1985

Mixing and decay of pollutants from shore-based outfalls discharging into cross-flowing streams.

Shaden Tawfik. Abdel-Gawad
University of Windsor

Recommended Citation
Abdel-Gawad, Shaden Tawfik., "Mixing and decay of pollutants from shore-based outfalls discharging into cross-flowing streams." (1985). *Electronic Theses and Dissertations.* Paper 2743.

CANADIAN THESES ON MICROFICHE

I.S.B.N.

THESES CANADIENNES SUR MICROFICHE

National Library of Canada
Collections Development Branch

Canadian Theses on
Microfiche Service

Ottawa, Canada
K1A 0N4

Bibliothèque nationale du Canada
Direction du développement des collections

Service des thèses canadiennes
sur microfiche

NOTICE

The quality of this microfiche is heavily dependent upon the quality of the original thesis submitted for microfilming. Every effort has been made to ensure the highest quality of reproduction possible.

If pages are missing, contact the university which granted the degree.

Some pages may have indistinct print especially if the original pages were typed with a poor typewriter ribbon or if the university sent us a poor photocopy.

Previously copyrighted materials (journal articles, published tests, etc.) are not filmed.

Reproduction in full or in part of this film is governed by the Canadian Copyright Act, R.S.C. 1970, c. C-30. Please read the authorization forms which accompany this thesis.

THIS DISSERTATION
HAS BEEN MICROFILMED
EXACTLY AS RECEIVED

AVIS

La qualité de cette microfiche dépend grandement de la qualité de la thèse soumise au microfilmage. Nous avons tout fait pour assurer une qualité supérieure de reproduction.

S'il manque des pages, veuillez communiquer avec l'université qui a conféré le grade.

La qualité d'impression de certaines pages peut laisser à désirer, surtout si les pages originales ont été dactylographiées à l'aide d'un ruban usé ou si l'université nous a fait parvenir une photocopie de mauvaise qualité.

Les documents qui font déjà l'objet d'un droit d'auteur (articles de revue, examens publiés, etc.) ne sont pas microfilmés.

La reproduction, même partielle, de ce microfilm est soumise à la Loi canadienne sur le droit d'auteur, SRC 1970, c. C-30. Veuillez prendre connaissance des formules d'autorisation qui accompagnent cette thèse.

LA THÈSE A ÉTÉ
MICROFILMÉE TELLE QUE
NOUS L'AVONS REÇUE

NL-339 (r. 82/08)

Canada

MIXING AND DECAY OF POLLUTANTS FROM SHORE-BASED OUTFALLS DISCHARGING INTO CROSS-FLOWING STREAMS

A Dissertation
submitted to the Faculty of Graduate Studies through
the Department of Civil Engineering in Partial
Fulfillment of the Requirements for the
Degree of Doctor of Philosophy at
The University of Windsor

by
Shaden Tawfik Abdel-Gawad

Windsor, Ontario, Canada
1985

ABSTRACT

In North America, it is a common practice to discharge municipal and industrial wastewaters through shore-based outfalls into rivers and lakes. In the case of the rivers located in the Great Lakes basin, a Limited Use Zone is specified to delineate the portion of the river channel wherein the contaminant concentrations can exceed the allowable limits.

The main objective of this thesis was investigation of the near-field mixing and dispersion of effluent based on physical modelling of buoyant and non-buoyant shore-based outfalls discharging into a cross-flowing ambient current in a trapezoidal channel. The physical model was scaled to represent a typical large outfall into one of the connecting channels of the Great Lakes system. This study also treated the decay kinetics of residual chlorine in sewage effluent diluted with the stream flow.

The hydrodynamic experiments were carried out in a 8.5 m long x 285 m wide x 0.34 m high flume with 3H to IV side slope and a bed roughness representative of the Detroit River. The jet was discharged normal to the channel flow through a round pipe of 50 mm diameter. The discharged jet was measured in detail to determine the velocity, concentration of fluorescein dye and temperature distributions in the near-field zone due to various jet to ambient current ratios, channel discharges, relative depths and densimetric

Froude numbers. Expressions for jet trajectories and minimum dilution for shore-based outfalls under buoyant, non-buoyant and heavy density conditions were derived and compared favourably with other available data.

The experimental results of this study were used to calibrate and validate the near-field models developed by Shirazi and Davis (1974) and Stolzenbach and Harleman (1971) for the surface and submerged outfalls. Good agreements between the measured and predicted jet trajectories and minimum dilution were obtained.

A field study was carried out in the Detroit River in the vicinity of West Windsor Pollution Control Plant. Water samples were collected for the total residual chlorine and temperature measurements. These field data were compared with the calibrated near-field models where a fair agreement was obtained. The field data were also compared with the predictions of the University of Windsor far-field model and a fair agreement was obtained.

Laboratory studies were conducted to develop a model for the overall decay of total residual chlorine, TRC, under various conditions. This model assumes that a portion of the initial chlorine concentration is used to satisfy the immediate chlorine demand and the remainder is subject to gradual decay. The important parameters influencing the gradual decay of TRC, after mixing in the rivers, were found to be photolysis, evaporation, free radical oxidation, temperature and turbulence.

It was observed that the rate coefficient obtained under alternating light and dark exposure was slightly higher than that obtained under complete darkness. The effect of evaporation on the decay rate was studied by changing the ratio of surface area to volume, A_s/V. It was found that the rate coefficient increased significantly as the A_s/V ratio was increased. The effect of temperature in the range of 2 to 30°C was studied and Arrhenius correction factor for temperature was found to be 1.08. The absence of turbulence may significantly influence the rate coefficient and thus provide erroneous value for the decay rate constant. Therefore, the influence of turbulence was investigated and it was found that the turbulence in stream can almost double the rate coefficients obtained under quiescent condition.

A separate study was conducted to gain a complete understanding of the effect of chlorination under various conditions on the Biochemical Oxygen Demand, BOD, progression. It was observed that all the tested samples showed a significant decrease in 5-day BOD values as the chlorine dose was increased. The experimental study also confirmed that the 5-day BOD and the ultimate oxygen demand values obtained in stirred bottles were consistently higher than those obtained with the standard procedure.

ACKNOWLEDGEMENTS

The author wishes to express her sincere gratitude to her advisor, Dr. J. K. Bewtra, for his continuous guidance, and generous aid during the course of this study.

My heartfelt thanks to my advisor, Dr. J. A. McCorquodale, whose continuous and patient guidance, along with constructive criticisms and thoughtful assistance have helped in the preparation of this work.

Thanks are due to Mr. F. Kiss, the Civil Engineering Technician, for his help and co-operation during the experimental investigation.

I am also grateful to the Department of Civil Engineering, the School of Graduate Studies at the University of Windsor and the Natural Sciences and Engineering Research Council of Canada for their financial support during this research work.

Appreciation and gratitude are extended to the author's parents, Dr. and Mrs. T. Abdel-Gawad, for their encouragement and inspiration. The author is most fortunate in having a very understanding husband, special thanks are due to him for his assistance, patience and encouragement.

Finally, I wish to express my sincere thanks to Mrs. A. Zeleney for typing this manuscript.

To my husband and my parents for
their sacrifices and moral support

TABLE OF CONTENTS

CHAPTER

LIST OF FIGURES

Figure | Page

Figure Page

Figure Page

Figure Page

LIST OF TABLES

LIST OF PHOTOGRAPHS

NOMENCLATURE

A	jet aspect ratio
A_j	area of the outfall
A_s	surface area
a	thermal diffusivity
a'	constant in Eq. 5.19
a_1	constant in Eq. 2.4
a_2	coefficient of thermal expansion
B	jet half width
B_f	buoyancy flux
B_o	outfall width
B_T	the value of η at which the concentration, C, takes the value of 0.37 C_m
b	channel width
b_1	constant in Eq. 2.5
$\bar{b}$	jet half-width for detached jet
$\bar{b}_1, \bar{b}_2$	jet half-width for attached jet
C	concentration of substance
$C_D, C_{D_{02}}, C_{D_{22}}$	drag coefficients
C_f	shear coefficient
C_i	initial chlorine concentration after dilution in pure water
$C_{i,j}$	pollutant concentration in the sub-section
C_{i_f}	pollutant concentration at the outfall

C_m	maximum concentration along the jet axis
C_o	initial chlorine concentration in rivers after mixing
C_p	specific heat
C_t	total residual chlorine at time t
C^*	immediate chlorine demand
c, c_1, c_2	constants
D	outfall diameter
D_r	outfall diameter ratio
D_y, D_z	horizontal and vertical turbulent mixing coefficients respectively
D_{z_1}	factor of diffusion, m^{-5}/s^2
E_H	dimensionless horizontal turbulent exchange coefficient
E_o	entrainment coefficient
E_v	ratio of vertical to horizontal turbulent exchange coefficient
F_D	drag force
F_o	densimetric Froude number
F_{TB}	turbulence factor
f_b	bottom friction factor
G	Grashof number
g	gravitational acceleration
g'	reduced gravitational acceleration = $g\frac{\Delta\rho}{\rho_a}$
H	depth of flow
H_o	discharge depth
H_r	depth ratio

H_1	water level above datum
h	jet depth
h_{max}	maximum jet depth
$\bar{h}$	jet depth for detached jet
$\bar{h}_1, \bar{h}_2$	jet depth for attached jet = H/2
$\bar{J}_y$	depth-averaged turbulent mass flux
K	thermal conductivity of the fluid
K_1	dimensionless surface heat exchange coefficient
k_{BD}	rate constant for biodegradation
k_{DI}	rate constant for dilution
k_{EV}	rate constant for evaporation
k_{HY}	rate constant for hydrolysis
k_{OL}	mass transfer rate for evaporation
k_{OX}	rate constant for oxidation
k_{PH}	rate constant for photolysis
k	first order decay rate
k_T	overall decay rate of chlorine
k_1	rate coefficient of BOD removal
k'	von Karman constant $\cong 0.4$
L_a	ultimate BOD
ℓ_b	buoyant length scale
ℓ_m	momentum length scale
ℓ_o	characteristic length scale = $\sqrt{H_o B_o}$
n	Manning's coefficient
$n_1, n_2, n_3,$ n_4, n_5	constants in Eq. 5.61

m_1, m_2, m_3 m_4, m_5	constants in Eq. 5.66
P	Prandtl number
P_d'	dynamic pressure due to turbulent fluctuations
P_d''	dynamic pressure due to mean flow
Q	channel flow rate
$Q'_{i,j}$	river flow through the area of influence of (i,j)
Q_f	volume flux
Q_{i_f}	outfall discharge
Q_o	flow rate at the nozzle
Q_p	prototype discharge
q_r	discharge per unit width ratio
R	velocity ratio = V_j/U_a
R_{i_o}	Richardson number
R_N	Reynolds number
r	radius of plume growth
S	minimum dilution
T	temperature at any distance
T_a	ambient temperature
T_{a_o}	initial ambient temperature
T_m	maximum temperature along the jet axis
T_o	initial jet temperature
t	time

U	velocity at any point
U_a	ambient velocity
U_{a_o}	ambient velocity at the end of the establishment zone
U_{a_ξ}	longitudinal ambient velocity at ξ position
U_m	maximum velocity along the jet axis
U_*	shear velocity
$\bar{U}$	average velocity in the cross-section
u	longitudinal velocity in the x-direction
$\bar{u}$	depth-averaged longitudinal velocity
$\forall$	volume
V_j	initial jet velocity
V_r	velocity ratio = prototype velocity/model velocity
v	lateral velocity in the y-direction
$\bar{v}$	depth-averaged lateral velocity
W_{jet}	jet width
W_p	prototype width
$\bar{w}$	depth-averaged vertical velocity
x	longitudinal distance measured from the outfall
x_{inj}	longitudinal injection distance
xk_1	spreading function coefficient
y	lateral distance measured from the outfall
y_{inj}	lateral injection distance
y_s	depth of submergence
z_p	pipe position

z	vertical distance measured from bed
z_1	cotangent of the side slope
α	dispersion factor
α_c	cross-flow entrainment coefficient
β	coefficient of expansion
ΔT	excess temperature at any distance
ΔT_m	maximum excess temperature along the jet axis
ΔT_o	initial excess temperature
ΔU	excess velocity at any point
ΔU_m	maximum excess velocity along the jet axis
ΔU_o	initial excess velocity
$\Delta \rho$	$\rho - \rho_a$ = density difference between the discharge and ambient
ε	rate of dissipation
ε_1	bed roughness
ε_m	momentum transfer coefficient
ε_s	mass transfer coefficient
ζ	vertical distance
η	the transverse distance from the jet axis
η_1	dimensionless cumulative discharge
η_c	the value of η for which ΔT is one half of ΔT_m
θ	discharge angle
θ_1	temperature correction factor
κ	depth averaged kinetic energy

ν	kinematic viscosity
ξ	the distance along the jet axis
ξ'	distance measured along the deflected jet from the virtual source
ξ_i	length of the flow establishment zone
ε_2	non-buoyant spreading rate for two-dimensional jets
ε_3	non-buoyant spreading rate for three-dimensional jets
ρ	discharged jet density
ρ_a	ambient density
σ_t	turbulent Prandtl-Schmidt number
σ_η	lateral length scale
σ_ζ	vertical length scale
τ_o	bed shear stress
$\bar{\tau}_{bx}$	bottom shear stress in the x-direction
$\bar{\tau}_{xy}$	depth-averaged turbulent stress
$\bar{\phi}$	depth-averaged scaler quantity

CHAPTER I

INTRODUCTION

1.1 OBJECTIVE

It is a common practice to dispose of treated municipal and industrial waste waters of varying magnitudes and quality into rivers and lakes using side discharge into a moving ambient fluid. This method of disposal can be misused by discharging pollutants in excess of the maximum assimilative capacity of the receiving body. The regulatory agencies have been continuously struggling to keep control on water quality both in near and far fields of such discharges.

In Ontario, the Ministry of Environment presented new policies in 1978 for surface water quality management to ensure that the surface waters remained satisfactory for water supply, aquatic life and recreation. These policies establish effluent requirements and specify and control the mixing zones where the water quality does not comply with the objectives. For proper implementation of such policies, it is imperative to use both physical and mathematical models to simulate the mixing, dispersion, decay and transport of different pollutants discharged into a receiving body.

This project was undertaken to study approaches to estimate near-field behaviour based on physical modelling of buoyant and non-buoyant shore-based outfalls discharged perpendicular to the ambient flow of trapezoidal cross-sections. The specific objectives were:

i. To study the factors affecting the near-field mixing and dispersion of effluent under buoyant and non-buoyant conditions.

ii. To modify and calibrate the near-field models developed by Stolzenbach and Harleman (1971) and Shirazi and Davis (1974) for surface and submerged jets to incorporate the conditions of this study.

iii. To validate the modified near-field models and the UOW-MOE far-field model by using the field data for total residual chlorine and temperature collected from the Detroit River in the vicinity of West Windsor Plant outfall.

iv. To investigate the decay kinetics of residual chlorine in sewage effluent diluted with the stream flow.

v. To study the effects of certain environmental factors on the influence of chlorine on BOD progression.

1.2 STATEMENT OF THE PROBLEM

A typical flow phenomenon occurring in a river in the vicinity of wastewater discharge is illustrated in Fig. 1.1. This is an example of shore-based outfall discharging perpendicular to the river direction, a condition that prevails in the Detroit River. The discharge jet is deflected by the river cross-flow which in turn is bent away from the bank by the jet. This phenomenon causes mixing in both lateral and

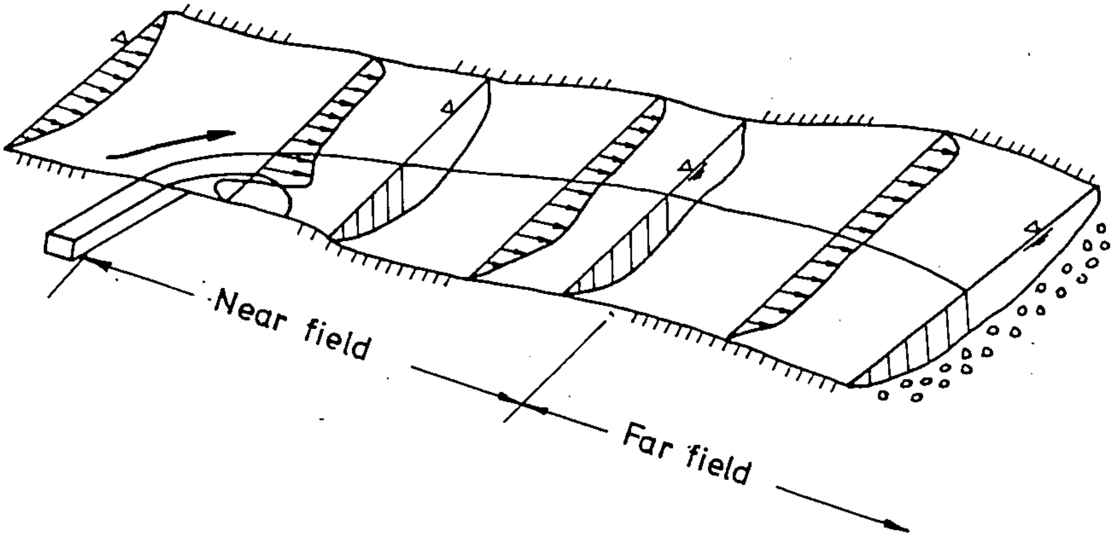

Fig. 1.1. Typical Discharge into a River Indicating Near and Far Fields.

longitudinal directions. The jet entrainment on the near-bank side is restricted by the presence of the solid boundary, causing a tendency for a recirculation region.

Apart from the occurrence of reverse flow, the flow in the vicinity of the discharge is usually complicated further by three-dimensional effects which are due to either the discharge geometry or buoyancy effects arising from a density difference between the wastewater and the river water. This is particularly true in the case of heated or cooling water discharges where significant density difference can be set up near the outlet.

The effluent jet influences the flow field in the river for a certain distance downstream from the outlet. This region is called the near-field. In this zone, the turbulence stems partly from generation within the shear induced by the effluent discharge and from generation at the river bed. Hence the turbulent mixing in the near-field is particularly difficult to simulate in a mathematical model (Rodi et al. 1981). Beyond the near-field, the flow in the river is no longer influenced by the outfall discharge and this region is called the far-field. In this zone, the turbulence is governed entirely by the generation due to channel geometry.

In order to understand what happens to a stream of effluent discharged into a river, it is necessary to discuss the mixing phenomenon in rivers. The effluent stream discharged into a river, bottom or surface, can be divided into three stages (Fisher et al. 1979). In the first stage, the initial momentum and buoyancy of the discharge determine the rate of dilution. This part has been discussed in detail in Chapter V. As the waste is diluted, the effects of the initial momentum and buoyancy are diminished, leading to a second stage in which the waste is mixed across the receiving channel primarily by turbulence in the receiving stream. Finally, when the waste is fully mixed across the channel, the process of longitudinal dispersion will tend to erase any longitudinal concentration variations.

There are no fixed limits for these three stages. Sometimes, the first stage may extend over the entire channel, effectively eliminating the second stage. A large discharge of heated water from the cooling system of a power plant containing relatively large amounts of initial momentum and buoyancy is a typical example. On the other hand, many industrial and municipal effluents contribute a negligible amount of flow, momentum, or buoyancy to the receiving stream and may be effectively treated as a point source for mass discharge of pollutant.

When a pollutant is discharged from an outfall into the river, the change in concentration occurs not only due to dilution but also due to its decay. Various physical, chemical and biological factors influence the decay rates of individual pollutants. Substances with very low decay rates may persist in stream for years whereas fast decaying substances may disappear even before complete mixing of effluent has occurred.

1.3 MOTIVATION

The distribution of pollutant concentrations, such as the temperature rise due to warm water discharged from wastewater treatment plants, is of great concern to environmentalists, who must assess possible detrimental effects on the ecology of the river. For rivers which are navigable and which carry appreciable ship and barge traffic, significant cross-river velocities induced by large discharges are also of interest. It is, therefore, important to be able to predict both velocity and pollutant fields caused by a proposed discharge.

Another type of important pollutant is the chlorinated effluent discharged from a sewage treatment plant into a nearby river or lake. The chlorination practice diminishes the presence of pathogens in the waterways. The significance of this practice is evident from the fact that all the Canadian Provinces and the American States around the Great Lakes require the disinfection of municipal wastewater effluents.

However, very little is known about the kinetics of chlorine decay in water and the organic particles that remain without being oxidized after chlorination. This is particularly important when wastewater effluents are introduced to rivers and lakes after chlorination for short contact times. Therefore, a need was felt to carry out a comprehensive study on the mixing and decay processes for chlorinated discharges in the near-field zone. Consequently, investigations on the velocity, concentration and temperature distributions as well as the decay of chlorine were carried out in this study.

1.4 APPROACH IN GENERAL

The flow pattern, temperature and concentration distribution due to side discharge of effluent into a river can be generated both by experimental model studies and by mathematical computer modelling.

The development of mathematical models for the far-field region where the velocity field has returned to its normal state has received considerable attention (Jirka et al. 1975, Akhtar 1978, Fischer et al. 1979, McCorquodale et al. 1983). However, all far-field models are dependent on accurate input of the starting profiles, which are governed by the near-field behaviour. In addition, regulatory requirements specify conditions which are most likely to be violated in the area close to the discharge points. Both these facts emphsize the importance of near-field mathematical models which still are in an early stage of development (Stolzenbach and

Harleman 1971, Shirazi and Davis 1974, Rodi et al. 1981). Moreover, these mathematical models contain a number of free variables such as entrainment coefficient, turbulent exchange coefficient, drag coefficient and shear coefficient which must be specified by the user. The magnitude of these coefficients are usually determined so that the mathematical model produces the best fit with the measured jet profiles and dilution. Consequently, recourse to laboratory modelling is usually required.

Laboratory measurements and physical scale models have always been an important part of hydraulic engineering because mathematical solutions cannot reproduce all the intricacies of real flow conditions. Therefore, in this study, a hydraulic model for a side discharge into a river was built and the velocity, concentration and temperature distributions were measured. These observations provided data that can be used to calibrate the existing near-field models (Stolzenbach and Harleman 1971, Shirazi and Davis 1974). Also, the physical model provided typical starting profiles that are required by the far-field models. In addition, the decay rate of chlorine under different conditions was determined experimentally and a mathematical model was developed.

The state-of-the-art review of turbulent jets in crossflow, modelling techniques and chlorine decay and its kinetics is provided in Chapter II. Description of the physical model and the experimental procedure are presented in Chapter III. The experimental results of both the hydrodynamic studies and the contaminant behaviour studies are given in Chapter IV. Data reduction, analysis and discussion of the results are treated in Chapter V. In Chapter VI, modifications of both PDS model (Shirazi and Davis 1974) and MIT model (Stolzenbach and Harleman 1971) and a comparison of the predicted and measured results are shown. An application of the near-field models and the University of Windsor far-field model using field data for a nonconservative pollutant, total residual chlorine, collected from Detroit River in the vicinity of West Windsor Pollution Control Plant is provided in Chapter VII. Finally, summary and conclusions are given in Chapter VIII.

The experimental investigation was carried out in the environmental and hydraulic laboratories of the University of Windsor during the period 1981-1983. The IBM 370/3031 computer facilities were used to execute all the computations in the mathematical model.

CHAPTER II

BACKGROUND AND LITERATURE REVIEW

2.1 GENERAL

The disposal of domestic and industrial wastewaters into natural streams has been practiced extensively because of the mixing and dilution of the pollutants by these streams. When a stream of effluent is discharged into a river, three stages in the mixing of the effluent can be distinguished: a) initial momentum and buoyancy of the discharge determine the mixing near the outlet, b) turbulence and currents in the receiving stream determine further mixing after initial momentum and buoyancy are dissipated, and c) after cross-sectional mixing is completed, longitudinal dispersion reduces longitudinal gradients caused by changes in effluent river discharges.

The literature review herein will deal with the work on:

- Turbulent jets and plumes
- Jets in liquid of different densities
- Jets in cross-flow
- Jets in coflowing streams

- Near-field and far-field models
- Kinetics of chlorine decay.

2.2 TURBULENT JETS AND PLUMES

In managing the wastewaters, municipal, industrial and thermal plants, different methods of treatment and disposal are used depending on economic, engineering and environmental quality considerations. For these wastes, a rapidly diluted discharge to the environment is often the selected means of disposal. An effective mechanism to accomplish the initial dilution is the turbulent jet and plume, because they entrain large volumes of ambient fluid and mix it with the discharge fluid.

The behaviour of jets or plumes issuing from round or slot ports are governed by (i) jet parameters, e.g., initial jet velocity, V_j, jet mass flux, jet momentum flux, and the flux of any tracer material such as heat, salinity or contaminant, (ii) environmental parameters, e.g., ambient currents, U_a, depth of flow, H, density stratification, $d\rho_a/dz$, bed roughness, ε_1, side slope and secondary currents, and (iii) geometrical factors, e.g., jet diameter, D, or port width, B_o, jet orientation, θ, depth of submergence, y_s, and density difference between the discharge and the ambient, $\Delta\rho$.

The densimetric Froude number is a convenient dimensionless parameter for describing the ratio of the inertia forces to the buoyancy (gravitational) forces, which can be expressed as:

$$F_o = V_j/(g'D)^{1/2} \text{ for a round/circular port} \quad (2.1)$$

$$= V_j/(g'B_o)^{1/2} \text{ for a slot/rectangular port} \quad (2.2)$$

where $g' = g(\Delta\rho/\rho_a)$; g is the acceleration due to gravity and ρ_a is the ambient density.

Near the outlet, inertia forces are often large enough to neglect the effect of buoyancy while at greater distances from the source the buoyancy forces are more important than the inertia (momentum) forces (Abraham 1960). The following three types of jets may be obtained depending on the Froude number.

2.2.1 The Simple Jet

A non-buoyant case in which the jet momentum is predominant is usually called a momentum source. The Froude number in this case is large, $F \to \infty$. Such jets have been studied extensively so that there is now a reasonably good understanding of their behaviour. The time-averaged measurement of tracer concentration, C, across the circular jet shows that it essentially follows a Gaussian distribution (Fischer et al. 1979) in the form of

$$C = C_m \exp[-(\eta/B_T)^2] \qquad (2.3)$$

in which the subscript m refers to the value of C on the jet axis, η is the transverse or radial distance from the jet axis and B_T is the value of η at which C takes the value of 0.37 C_m. The Gaussian distribution also applies to the time-averaged velocity profile across a jet but only in the region downstream of the jet known as the fully developed zone. This may be the case for C as well. Experimental observations on the mean turbulent velocity field indicate that in the axial direction of the jet, one could divide the jet flow into two distinct regions (Rajaratnam,1976). In the first region close to the jet, known as the flow development region, the turbulence penetrates inward towards the axis or centerline of the jet. This creates a wedge-like region of undiminished mean velocity equal to V_j. This wedge is known as the potential core (the establishment zone length) and is surrounded by a mixing layer on the top and bottom. In the second region, the fully developed flow region, the turbulence has penetrated to the axis and as a result, the potential core has disappeared. The length of the potential core was estimated by Rajaratnam (1976) and Fischer _et al_. (1979) to be about six times the jet diameter for a uniform velocity distribution at the outfall.

In the fully developed flow region, the velocity distributions are self-similar and can be represented by

$$U = U_m \exp\left[-a_1\left(\frac{\eta}{\xi}\right)^2\right] \qquad (2.4)$$

where U_m is the velocity along the jet axis, ξ, and a_1 has been found experimentally (Rajaratnam 1976) to vary from 70.7 to 75.

2.2.2 The Simple Plume

A buoyant case in which the initial momentum is negligible is usually called a buoyancy source. The Froude number in this case is small, F=o. The pure plume is usually easier to analyze than the pure jet because in the pure plume there is no initial volume or momentum flux. This means that all flow variables for a plume are functions of the buoyancy flux, B_f, the distance from origin, ξ, and the kinematic viscosity of the fluid, ν. The velocity at the centre line U_m is therefore given by:

$$U_m = b_1 (B_f/\xi)^{1/3} \qquad (2.5)$$

where B_f is the buoyancy flux and equal to $g'Q_f$, Q_f is the volume flux, and b_1 has been found experimentally by Rouse et al. (1952) to be 4.7.

2.2.3 The Buoyant Jet

Buoyant jet is an intermediate case, where both the buoyancy and the momentum are important. The Froude number in this case has a finite value, $0<F<\infty$. The initial density of the jet differs from the density of the receiving water by an amount equal to $\Delta\rho$. $\Delta\rho$ may be either positive or negative. A buoyant jet has jetlike characteristics depending on its initial volume and momentum fluxes and plumelike characteristics depending on its initial buoyancy flux. Far enough from the source, the plumelike characteristics are always dominant; that is, a buoyant jet will always turn into a plume if given enough free distance (Fischer, et al. 1979).

2.3 JETS IN LIQUID OF DIFFERENT DENSITIES

An early study on the influence of the density difference between a jet and the surrounding fluid on the jet diffusion was presented by Abraham (1960). He studied the case of a circular submerged turbulent jet issuing vertically upward in a surrounding water with a specific weight greater than that of the jet. The results were presented as nomographs for the concentration and velocity along the jet axis. The results showed that the density and the velocity depend on the initial density difference between the jet and the surrounding fluid and on the velocity of the jet at the nozzle. The theory was based on a dimensional analysis consideration and was confirmed with laboratory experiments. The experiments were performed in a glass-wall tank of 0.3m x 0.3m x 1.0m dimensions. The jet issued into the tank through pipes at the tank bottom with internal diameters of 15mm, 20mm and 25mm. The end of the vertical pipes was about 0.1m above the bottom of the tank. The density of the jet fluid was about 1000 kg/m^3 and the density of the surrounding fluid varied from 1020 to 1050 kg/m^3. The density-range covered by the experiments was such that the curves may be used when sewage disposal in the marine environment is considered.

Jen, Wiegel and Mobarek (1966) studied the characteristics of a warm water circular jet discharged horizontally at the surface of a body of initially quiescent deep water. They obtained the following relationship between temperature distribution and distance along the jet axis at the water surface for densimetric Froude number, F_o, ranging from 18 to 180,

$$\frac{T-T_a}{T_o-T_a} = 7.0\ \frac{D}{\xi}\ e^{[-3F_o^{1/2}(\eta/\xi)^2]} \qquad (2.6)$$

They also obtained an empirical relationship for the effective surface width η_c of the mixing plume,

$$\frac{\eta_c}{D} = 0.57 \frac{\xi}{DF_o{}^{1/4}} - 2.3 \qquad (2.7)$$

where T = the temperature, in degrees Fahrenheit

T_a = the temperature of the receiving water

T_o = the temperature of the jet

ξ = the horizontal distance along the center-line of the jet measured from the point of discharge

η = the horizontal distance measured normal to ξ

η_c = the value of η for which the temperature difference $(T-T_a)$ is one half the temperature difference (T_m-T_a)

T_m = the surface temperature at the point ξ,o (i.e., along the center-line of the jet).

All the temperature are in degrees Fahrenheit.

In 1984, Wallace and Wright studied a two-dimensional buoyant jet, discharged vertically into a stratified fluid with no cross-flow. They developed simple empirical equations using dimensional analysis to predict the location and concentration of effluent as it begins to spread horizontally from the buoyant jet axis because of an ambient density stratification. The dimensionless independent variables were determined by a stratification parameter and the jet source flux of either momentum or buoyancy. Scale model tests verified the form of these equations and provided experimental values for coefficients not provided by the dimensional analysis. Their results were easier to use than the integral equations and provided a good description of the location and thickness of the spreading layer.

2.4 JETS IN CROSS FLOWS

In recent years the subject of jets injected into cross-flows has received considerable attention from various researchers because of their applications to the disposal of effluents into rivers and the atmosphere. The resulting flow is a rather complex form of turbulent shear flow. The earlier studies were primarily of an experimental nature including qualitative empirical formulae (Abramovich 1963, Pratte and Baines 1967, Chassaing _et al_. 1973, Rajaratnam 1976). Based on these observations, three separate regions of the deflected jet can be identified as shown in Fig. 2.1. In the first region called the potential core zone, or the establishment zone, the external fluid starts to be entrained by the jet, which in turn spreads, slows down and curves. A characteristic of this zone is that only the circumferential part of the jet takes part in the mixing and the remainder forms the potential core or the establishment zone in which the axial velocity is of constant magnitude. When the maximum axial velocity begins to decrease, the second zone, known as the maximum deflection zone, is reached. This region is characterized by large ambient fluid entrainment, rapid jet velocity decay and large deflection. The characteristic kidney shaped velocity contours develop in this region (Abramovich 1963, Rajaratnam 1976). The third region, called the vortex zone, is characterized by a pair of counterrotating vorticies generated in the wake of the deflecting jet while the jet axis is nearly parallel to the ambient fluid direction (Pratte and Baines 1967, Moussa et al 1977, Rajaratnam and Gangadhariah 1980).

The above studies provided empirical expressions for the deflected jet axis usually in the form of a power law, i.e.,

$$\frac{y}{D} = cR^{n}\left(\frac{x}{D}\right)^{m} \tag{2.8}$$

where x = the longitudinal distance

y = the lateral penetration

R = the initial jet to cross-flow velocity ratio

D = the pipe diameter

c,n,m = empirical constants.

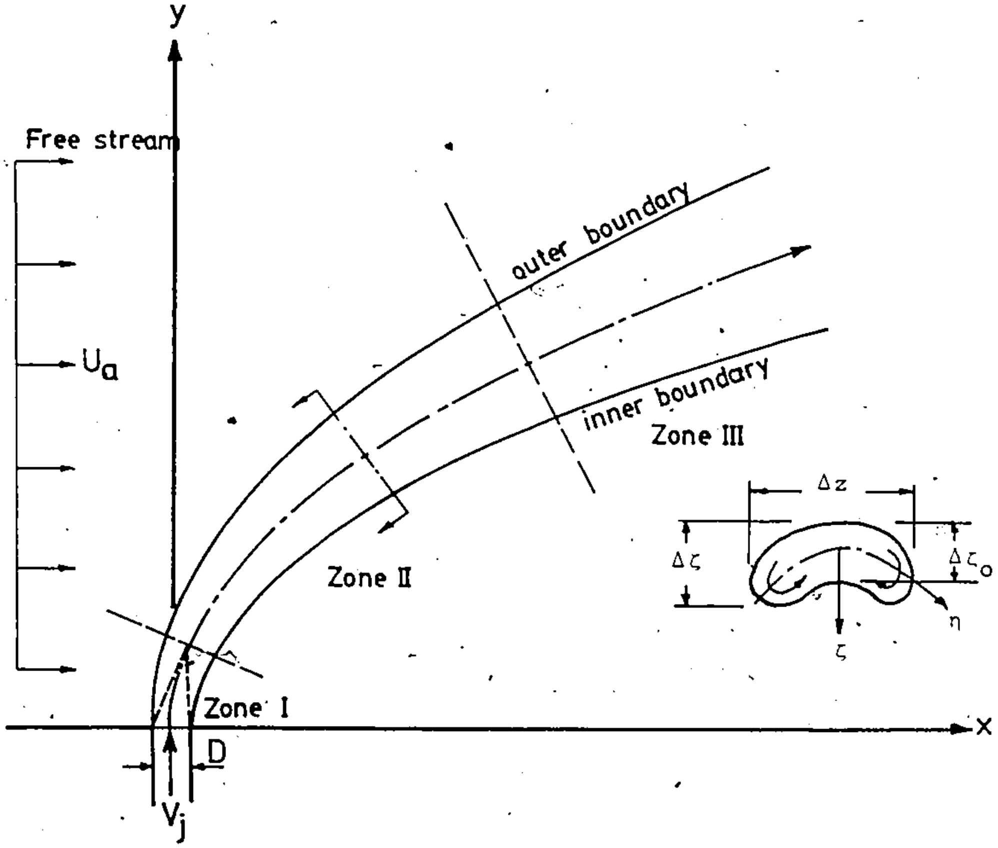

Fig. 2.1. Configuration of the Flow.

One of the early investigations of a flow related to the side discharge problem was the work done by Abramovich (1963). His analytical approach was based on the principle that the deflection of the jet is caused by a pressure differential analogous to that which causes the drag force on a cylinder. He found that the jet centre-line could be represented by the equation

$$\frac{Y}{D} = R^{0.87}(\frac{x}{D})^{0.33} \qquad (2.9)$$

Pratte and Baines (1967) studied the performance of momentum jets by measuring the profile and size of a smoke vertical jet in a 1.2 x 2.4m wind tunnel for a range of velocity ratios, R, from 5 to 35 and jet diameters of 4.0, 6.3 and 9.2mm. From their experimental study and dimensional analysis, they found that the inner and outer boundaries of the deflected jet can be described by the equations:

$$(\frac{Y}{D})_T = 1.35\ R^{0.72}(\frac{x}{D})^{0.28} \qquad (2.10)$$

and

$$(\frac{Y}{D})_B = 2.63\ R^{0.72}(\frac{x}{d})^{0.28} \qquad (2.11)$$

The jet centre-line was assumed to be midway between the inner and outer boundaries and was described by the equation

$$\frac{y}{D} = 2.05\ R^{0.72} (\frac{x}{D})^{0.28} \qquad (2.12)$$

They also observed that the length of the potential core increased with the diameter of the jet. However, this variation was very small, $\xi_i/D \equiv 2.5$ to 3.5, where ξ_i is the length of the potential core, and did not appear in the plotting of their data. Finally, they proved that the cross-section shape of the jet did not change and there is a self-preserving flow involving the vortices and large eddies.

Strazisar and Prahl (1973) evaluated the jet trajectory from photographs of injected dye and examined the influence of the velocity ratio, R, the jet Reynolds number, the jet depth to width ratio, H_o/B_o, and the channel to jet width, b/B_o. They found that the length and width of the recirculating eddy were little affected by Reynolds number, but increased with increasing R, H_o/B_o and decreasing b/B_o.

In 1980, Rajaratnam and Gangadhariah conducted an extensive experimental program to study the behaviour of a circular jet discharged vertically in cross-flow for velocity ratios, R=2.73, 4.52, 7.05 and 23.4. The experiments were performed in a rectangular water channel of 4.8m in length, 0.45m in width and 0.915m in depth. Their study concluded that:

1. For R up to about 7, the kidney shape of the deflected jet is developed only after the jet has travelled an axial distance of a few diameters past the end of the potential core.

2. In the deflected jet, after the end of the potential core, the distribution of the axial velocity in the η and ξ directions were similar.

3. For R up to about 7.0, the dimensionless volume flux, Q/Q_o, was found to be proportional to the axial distance ξ, i.e.,

   $$\frac{Q}{Q_o} = 0.54\left(\frac{\xi}{D}\right)^{1.22} \qquad (2.13)$$

   However, for high values of R equal to 23.4, Q has been found to be proportional to ξ, with a slope of the line about 30% larger than that of the simple circular jet, i.e.,

   $$\frac{Q}{Q_o} = 0.41\left(\frac{\xi}{D}\right) \qquad (2.14)$$

4. The entrainment velocity was found to be much larger than in the simple circular jet. For a circular jet

in cross-flow, the entrainment appears to come partly from the same mechanism which exists in the simple jet with additional entrainment caused by the circulation induced by the cross-flow. The circulation effect is almost 13 times the simple jet effect.

Buoyancy effects on cross jets were also investigated, particularly by Chu and Goldberg (1974), Wright (1977) and Jirka *et al*. (1981). In 1974, Chu and Goldberg studied the combined effects of exit momentum and buoyancy for forced-plumes entering normal to a horizontal cross-flow. Their experiments were performed in a 0.3m wide, 0.45m deep and 9.0m long tilting flume. The plume was simulated by injecting dyed solution vertically downward into uniform open channel flow through a hyperdermic needle. They obtained efflux velocities up to 4.6 m/s and cross-flow velocities up to 0.24 m/s. Salt solutions of different densities were used to study the buoyant case. They defined the turbulent entrainment coefficient, α, as

$$\alpha = \left(\frac{dr}{dx}\right) / \frac{U_m}{U_a} \qquad (2.15)$$

where r = radius of plume growth

U_m = plume rise centreline velocity

U_a = ambient velocity

Assuming that α is constant, the best fit for non-buoyant jet trajectory was obtained by taking $\alpha=0.5$, as:

$$\frac{z}{\ell_m} = 1.44\left(\frac{x}{\ell_m}\right)^{1/3} \tag{2.16}$$

For the buoyant case, they used the same value of $\alpha=0.5$ and the path of buoyant plume was described by:

$$\frac{z}{\ell_b} = 1.44\left[\frac{1}{2}\left(\frac{x}{\ell_b}\right)^2 + \left(\frac{\ell_m}{\ell_b}\right)^2\left(\frac{x}{\ell_b}\right)\right]^{1/3} \tag{2.17}$$

where x, z = horizontal and vertical distances

ℓ_m = momentum length scale

ℓ_b = buoyant length scale

They also found that the transition from the near-field, where the flow depended on exit momentum flux, to the far-field, where the effect of buoyancy dominated the flow, occurred at a distance, downstream from the exit, equal to:

$$x = \frac{2U_a V_j}{g\left(\frac{\rho-\rho_a}{\rho_a}\right)} \tag{2.18}$$

Wright (1977) presented a model for vertical round buoyant jets discharged normal to an ambient flow. The time averaged behaviour of this complex flow was derived by making analogies with simpler flows whose behaviour is better understood, e.g., buoyant jets in a stagnant ambient and non-buoyant jets in cross-flow. When this was combined with dimensional analysis, Wright obtained approximate solutions. The jet behaviour was analyzed by considering it to be a source of momentum and buoyancy flux. He neglected the effect of the initial volume flux except very near the source. His model consisted of four different flow regimes, e.g., momentum dominated near-field, momentum dominated far-field, buoyancy dominated near-field and buoyancy dominated far-field. The model predicted trajectories and dilutions for each particular flow regime to within a constant that must be experimentally determined. The values of the various constants were obtained in an experimental study conducted in 0.6m x 0.6m x 9.0m flume with no flow. The jet source was towed at a constant velocity through the stationary fluid to avoid any effects due to ambient turbulence and velocity gradients.

In 1981, Jirka _et al_. used a combination of dimensional analysis, simple physical arguments and inspection of data to define distinct geometric properties and mixing characteristics within the near-field of buoyant surface jets. For deep stagnant receiving water, the buoyant jet has a certain transition length which was used to define the near-field zone, a maximum penetration depth and a limited dilution capacity which was predominantly met through bottom entrainment. These parameters were found to scale with a densimetric Froude number, F_o, based on kinematic momentum and buoyancy fluxes, and characteristic source length, ℓ_o. They also presented a criterion to distinguish between free and shoreline-attached buoyant surface jets in cross-flowing receiving water. They used data reported by other researchers to derive the following equation for nonattaching jets:

$$R > 20\left(\frac{h_{max}}{H}\right)^{3/2} \tag{2.19}$$

in which h_{max} is the maximum jet depth and H is the depth of flow. Finally, they showed that the trajectory of surface buoyant jets in crossflowing deep receiving water can be described by simple trajectory relations in the form of:

$$\left(\frac{y}{\ell_o R}\right) = c_1\left(\frac{x}{\ell_o R}\right)^{1/2} \text{ - initial phase} \tag{2.20}$$

$$\left(\frac{y}{\ell_o R}\right) = c_2\left(\frac{x}{\ell_o R}\right)^{1/3} \text{ - final phase} \tag{2.21}$$

in which c_1 and c_2 are constants that must be determined experimentally.

2.5 JETS IN COFLOWING STREAMS

The previous studies in this review of literature were concerned with the deflection of jets discharged perpendicular to the ambient fluid direction. However, very little information is available on the horizontal cross jet that is being studied during this investigation. It is of interest to review the work on turbulent jets in coflowing streams as the horizontal cross jets, after certain distances become parallel to the ambient streams and the mechanism of coflowing jets can be applied thereafter.

Rajaratnam (1984) presented a two part paper on the behaviour of jets in coflowing streams. In the first part, he presented the results of an experimental study on the diffusion of circular non-buoyant turbulent surface jets in a coflowing channel. The experiments were performed with nozzles producing circular jets of diameters 6.35, 9.32 and 25.8mm located in a rectangular channel of 1.22m width, 0.67m depth and 18.3m length. The nozzles were attached to a 29mm pipe placed in the middle of the channel. Based on the experimental results, he found that the velocity scale and the vertical length scale could be predicted from the equations developed for submerged circular jets in coflowing streams using the excess momentum thickness as the length scale. But the transverse length scale and width appeared to grow at a rate equal to that of circular wall jets in coflowing streams for some distance from the nozzle.

In the second part, he presented the results of further experimental studies on the diffusion of circular buoyant jets in coflowing streams of large width and depth for values of R ranging between 1.5 to 20 and a source Richardson number, R_{i_o}, up to 0.1. The source Richardson number is defined by:

$$R_{i_o} = \frac{gD \, \Delta\rho/\rho_a}{V_j^2} = \frac{1}{F_o^2} \qquad (2.22)$$

The experiments were carried out in the same flume used for part one. However, in this case, hot water for the surface jets was provided by a boiler through a constant head arrangement. Based on the experimental results, Rajaratnam found that the velocity distribution in the centreplane as well as in the planes containing the maximum velocity were similar. The velocity scale as well as the vertical and transverse length scales were analyzed using the excess momentum thickness as the length scale and the source Richardson number as a parameter. He concluded that the variation of the velocity scale was not affected by the buoyancy effects whereas the transverse spreading rate had increased and the vertical spreading was almost zero for longitudinal distances greater than a few times the momentum thickness.

2.6 REVIEW OF NUMERICAL MODELS FOR NEAR AND FAR FIELDS

2.6.1 Near-Field Models

The near-field mathematical models are of great importance since all the far-field models are dependent on accurate input of the starting profiles, which are governed by the near-field behaviour. Unfortunately, the near-field models are in a less advanced stage of development, particularly for the flow situation of interest here. Some theoretical investigations of non-buoyant side discharges were carried out by Mikhail <u>et</u> <u>al</u>. (1975) who employed a global control volume analysis to obtain relations between the eddy size and the momentum flux ratio, and by Strazisar and Prahl (1973) who used an integral momentum analysis to determine the jet trajectory. McGuirk and Rodi (1978) calculated this flow with a two dimensional depth-averaged numerical model of the finite-difference type. Demuren and Rodi (1983) presented a three-dimensional numerical mathematical model for calculating the near-field of side discharges into open channel flow. This method employed the standard k-ε turbulence model for determining the turbulent stresses. Two discretization schemes were considered, namely, the hybrid central/upwind differencing scheme and the quadratic, upstream-weighted differencing scheme, QUICK. The surface flow patterns obtained with the higher order QUICK scheme were found to agree fairly well with previous experimental observations of Rodi. The influence of both the velocity ratio, R, and the bed roughness on the size of the recirculation zone were reproduced faithfully. The lower order hybrid differencing scheme was shown to suffer severely from numerical diffusion when the same fairly fine grid was used. This false diffusion led to a significant underprediction of the size of the recirculation zone. Although the model performed well for isothermal discharges, it did not include the buoyancy terms and consequently the model cannot be used in its present form to predict the temperature distribution of a buoyant jet. For the buoyant side discharges of this study, Shirazi and Davis model (1974) and Stolzenbach and Harleman model (1971) were tested and used for such flow situations. Therefore, these two models are reviewed in depth.

2.6.1.1 PDS Model

In 1974 Shirazi and Davis developed a mathematical model that describes the three dimensional behaviour of a surface heated jet discharged from a rectangular channel into a deep and wide body of homogeneous water. This water can be either at rest or moving with a uniform and steady velocity. The discharge angle, channel dimensions, discharge velocity and temperature were selected arbitrarily. The jet velocity and temperature distributions at the outlet were assumed to be uniform and constant.

The PDS model is based on the three-dimensional integral model developed by Stolzenbach and Harleman (1971). Prych (1972) sought to increase the computational efficiency and to improve the predictive capabilities of this model. Subsequently, Shirazi and Davis (1974) made numerous changes through an extensive data-fitting analysis.

The model is an integral model, in which specific mathematical shape functions are chosen for lateral and vertical profiles of temperature and velocity. Selection of these shape functions enables one to integrate the basic conservation equations over the cross section of the jet and make the problem one-dimensional in which all variables are a function only of the distance along the jet axis. Specific model features include the following:

1. The zone of flow establishment, ZOFE, is treated in a very simplified way, with the length defined by the following empirical equation:

$$\frac{\xi_i}{H_o} = 5.4\left(\frac{A^2}{F_o}\right)^{1/3} \qquad (2.23)$$

where ξ_i = Length of ZOFE

H_o = Discharge depth

A = jet aspect ratio = discharge width/discharge depth

F_o = initial densimetric Froude number.

2. Buoyant and non-buoyant jet spreading are assumed to be additive.

3. Diffusion due to ambient turbulence is treated as a form of added entrainment.

The similar profiles for temperature and velocity are Gaussian, as given by

$$\frac{\Delta T}{\Delta T_o} = \frac{\Delta T_m}{\Delta T_o} \exp(-\eta^2/B^2) \exp(-\zeta^2/h^2) \qquad (2.24)$$

$$U = U_m \exp(-\eta^2/B^2) \exp(-\zeta^2/h^2) + U_a \cos\theta \quad (2.25)$$

in which

ΔT_m = temperature rise at jet centerline

ΔT = temperature rise at distance η and ζ from jet axis

ΔT_o = initial temperature rise

η = horizontal distance from jet axis

[illegible] vertical distance from jet axis

[illegible] plume half-width

h = plume depth

U = jet velocity at distance η and ξ from jet axis
U_m = jet centerline velocity
U_a = ambient velocity
θ = angle between jet axis and ambient velocity.

In establishing the basic equations, the change of jet discharge with distance, $dQ/d\xi$, is assumed due to jet entrainment and ambient diffusion and is evaluated as

$$\frac{dQ}{d\xi} = \frac{dQ}{d\xi}\Big|_j + \frac{dQ}{d\xi}\Big|_a \tag{2.26}$$

The jet and ambient contributions are both divided into vertical and horizontal components. The horizontal jet entrained fluid is given by

$$\frac{dQ}{d\xi}\Big|_{j,h} = 2E_o \int_{-\sqrt{2}h}^{o} \Delta U d\zeta \tag{2.27}$$

where $\Delta U = (U^2+U_a^2\sin^2\theta)^{1/2}\exp(-\zeta^2/h^2)$ (2.28)

E_o = an entrainment coefficient

By inserting Eq. 2.28 into Eq. 2.27, one obtains

$$\frac{dQ}{d\xi}\Big|_{j,h} = \sqrt{\pi}\, hE_o(U^2+U_a^2\sin^2\theta)^{1/2} \tag{2.29}$$

The vertical jet entrained fluid is given by

$$\left.\frac{dQ}{d\xi}\right|_{j,v} = 2\int_{o}^{\sqrt{2}B} E\Delta U_v d\zeta \qquad (2.30)$$

where $\Delta U_v = [U^2\exp(-2\eta^2/B^2) + U_a^2\sin^2\theta]^{1/2}$ (2.31)

$E = E_o f(R_i)$ (2.32)

R_i = local Richardson number

$$= \frac{\sqrt{2}}{F_o^{\,2}}\,\frac{h(\Delta T)}{\Delta U_v^{\,2}}(\xi,\eta,o) \qquad (2.33)$$

ΔT = surface excess temperature at the distance η from the plume centreline.

The value of integral in Eq. 2.30 is determined numerically in the program.

According to an analysis by Prych (1972), the effective entrainment due to ambient turbulent mixing is given as

$$\left.\frac{dQ}{d\xi}\right|_{a,h} = 11.0\,\frac{h}{B}\,\frac{D_y}{V_j H_o} \qquad (2.34)$$

$$\left.\frac{dQ}{d\xi}\right|_{a,v} = 11.0\,\frac{B}{h}\,\frac{D_z}{V_j H_o}\,f(R_i') \qquad (2.35)$$

where D_y, D_z = horizontal and vertical turbulent mixing coefficients, respectively

$$R_i' = \sqrt{2}\ h(\Delta T)/[F_o^2(U+U_a\cos\theta)^2] \qquad (2.36)$$

The PDS model includes equations for conservation of momentum and heat flux, which also incorporate the expressions as in Eqs. 2.26, 2.29, 2.30, 2.34 and 2.35. The development yields seven simultaneous equations which are integrated stepwise along the plume axis, using the Hamming predictor-corrector method, to give values of jet coordinates, width, depth, velocity, temperature rise, angle and volumetric flux. Further details are given in Appendix C.

Like most other mathematical models, this model is greatly idealized, that is, it describes the behaviour of a plume whose discharge characteristics and ambient environment are closely controlled. There are some difficulties confronting the exact simulation of a real plume, which are not included in the model. For example (i) surface discharges are not confined to rectangular open channel, (ii) the jet is usually discharged over a sloping bank or beach, (iii) the ambient current is neither uniform nor constant, (iv) a natural body of water may be stratified, (v) there is some wind, and (vi) the discharge velocity and temperature profiles are usually nonuniform.

In order to use the PDS model, a number of free variables must be experimentally determined in advance.

These variables are the entrainment coefficient, E_o, horizontal and vertical turbulent exchange coefficients E_H and E_v, drag coefficient, C_D, and shear coefficient, C_f. Shirazi and Davis (1974) suggested values for these variables, however, they emphasized that these values were not universal correlations and could not be used outside the conditions for which they were derived.

2.6.1.2 MIT Model

Stolzenbach and Harleman (1971) developed a model to describe near field behaviour of buoyant surface discharges. Like the PDS, the MIT model also is based on the integral approach. However, the integral framework in MIT model is developed in terms of "jet averaged" properties rather than the Guassian distribution used in the PDS. This is equivalent to assuming a "top-hat" profile for excess temperature and longitudinal velocity.

In their model, Stolzenbach and Harleman took into account the jet interaction with a shallow receiving water bottom. The model also takes into account the re-entrainment of previously discharged heated water. The authors first developed a solution for the case of no re-entrainment using a set of ordinary differential equations. A different set of equations was used for detached and bottom-attached flows. Next, criteria were developed for the occurrence of various forms of near-field re-entrainment. A global near-field heat budget was used to derive additional algebraic equations and the governing set of differential equations was modified to include re-entrainment.

With no re-entrainment, the following distributions of u and T were assumed:

For detached flows

if $|\eta| < \bar{b}, \ -z_1 < \zeta < \bar{h}$

$$u = \bar{u} \tag{2.37}$$

$$T = T_a + \overline{\Delta T} \tag{2.38}$$

otherwise

$$u = U_a \cos\theta \tag{2.39}$$

$$T = T_a \tag{2.40}$$

where

u = velocity component in ξ direction

$\bar{u}$ = jet average or top hat velocity

U_a = ambient velocity

T_a = ambient temperature

$\overline{\Delta T}$ = jet average excess temperature

η, ζ = local coordinates following the jet centerline.

$\bar{b}$ = jet half width for detached portion

$\bar{h}$ = jet depth

z_1 = free surface elevation above z

θ = angle of jet centerline with respect to x-axis.

For Attached Flows

if $|\eta| < \bar{b}_2, -z_1 < \zeta < H$

or $\bar{b}_2 < |\eta| < \bar{b}_1, z_1 < \zeta < \bar{h}_1$

$$u = \bar{u} \tag{2.41}$$

$$T = T_a + \Delta\bar{T} \tag{2.42}$$

otherwise

$$u = U_a \cos\theta \tag{2.43}$$

$$T = T_a \tag{2.44}$$

where,

$\bar{b}_1, \bar{b}_2$ = jet half width for the upper and lower layers

$\bar{h}_1 = H/2$

Figure 2.2 shows the near-field definition sketch.

The following set of differential equations govern the flow under the assumptions of steady flow, high Reynolds number, small density differences and small curvature:

$$\frac{\partial\bar{u}}{\partial\xi} + \frac{\partial\bar{v}}{\partial\eta} + \frac{\partial\bar{w}}{\partial\zeta} = 0 \tag{2.45}$$

$$\frac{\partial\bar{u}^2}{\partial\xi} + \frac{\partial\bar{u}\bar{v}}{\partial\eta} + \frac{\partial\bar{u}\bar{w}}{\partial\zeta} = -g\frac{\partial}{\partial\xi}\int_z^H \frac{\Delta\rho}{\rho_a}\,dz - \frac{\partial}{\partial\eta}\overline{\bar{u}'\bar{v}'} - \frac{\partial}{\partial\zeta}\overline{\bar{u}'\bar{w}'} \tag{2.46}$$

$$\frac{\partial\bar{u}\bar{v}}{\partial\xi} + \frac{\partial\bar{v}^2}{\partial\eta} + \frac{\partial\bar{v}\bar{w}}{\partial\zeta} - \bar{u}^2\frac{\partial\theta}{\partial\xi} = -g\frac{\partial}{\partial\eta}\int_z^H \frac{\Delta\rho}{\rho_a}\,dz - \frac{1}{\rho_a}\frac{\partial P_d'}{\partial\eta}$$
$$- \frac{1}{\rho_a}\frac{\partial P_d''}{\partial\eta} - \frac{\partial}{\partial\eta}\overline{\bar{v}'^2} - \frac{\partial}{\partial\zeta}\overline{\bar{v}'\bar{w}'} \tag{2.47}$$

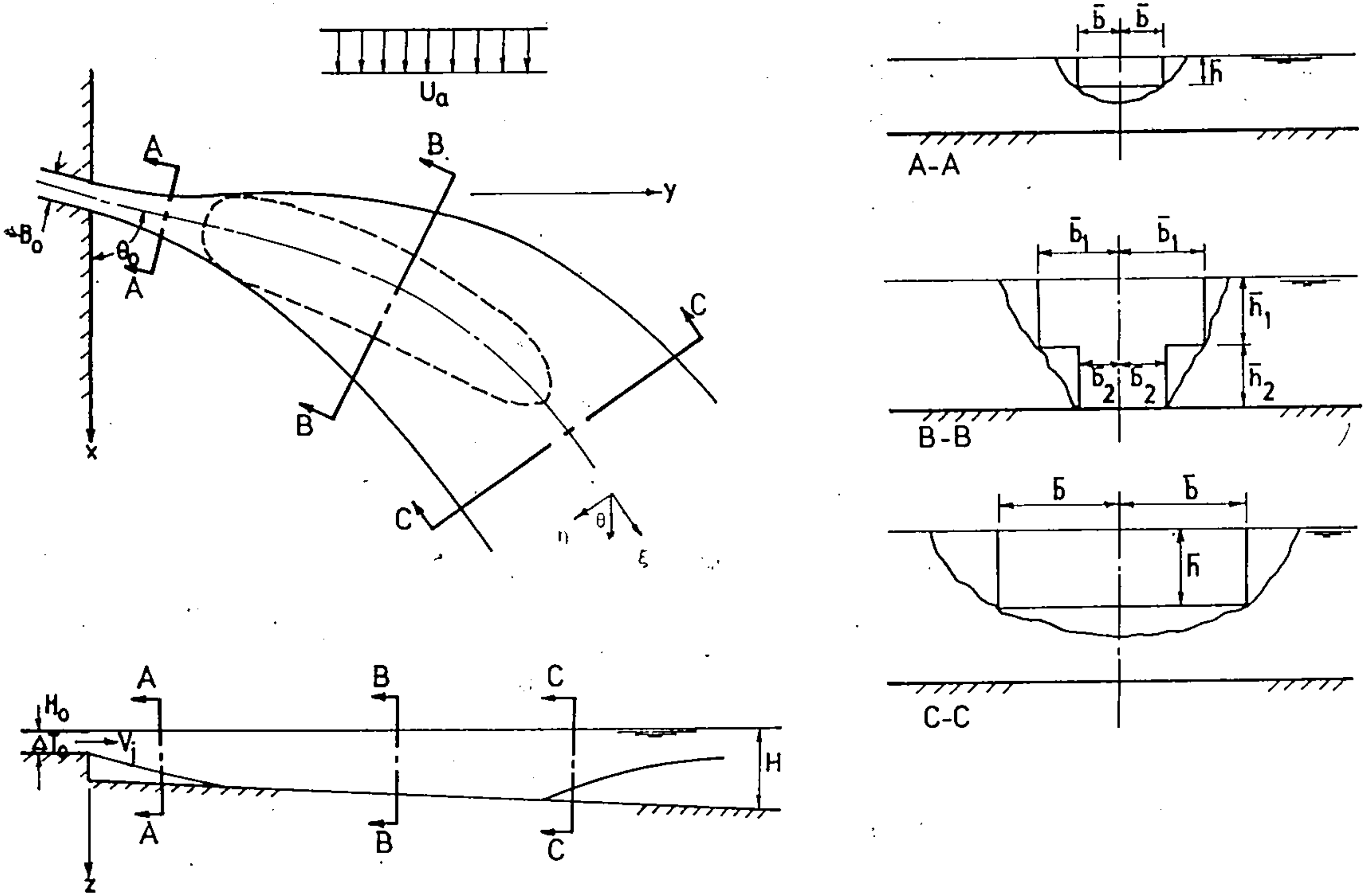

Fig. 2.2. Definition Sketch for MIT Model (after Stolzenbach and Harleman 1971).

$$\frac{\partial \bar{u}T}{\partial \xi} + \frac{\partial \bar{v}\bar{T}}{\partial \eta} + \frac{\partial \bar{w}\bar{T}}{\partial \zeta} = -\frac{\partial \overline{\bar{v}'\bar{T}'}}{\partial \eta} - \frac{\partial \overline{\bar{w}'\bar{T}'}}{\partial \zeta} \tag{2.48}$$

$$\Delta\rho = \rho_a - \rho = a_2(T-T_a) \tag{2.49}$$

where

$\bar{u},\bar{v},\bar{w}$ = velocity components in ξ, η, ζ directions

P_d' = dynamic pressure due to turbulent fluctuations

P_d'' = dynamic pressure due to mean flow

a_2 = coefficient of thermal expansion

The boundary conditions used in the integration of these equations, together with the details of the theoretical development are given elsewhere (Stolzenbach and Harleman 1971 and 1973). A summary of the integral equations for detached jets are presented in Appendix C.

The resulting set of ordinary differential equations were rendered non-dimensional by using V_j, $\sqrt{H_o B_o}$ and ΔT_o as normalizing velocity, length and temperature scales. Calculations were performed using a standard 4th order Runge-Kutta integration scheme assuming that the jet is attached at $\eta=0$.

The MIT model, despite its many fine features, has considerable computational difficulties. It has also some idealizations, for example, the cross flow has a constant velocity and the water depth is of the form

$$H(x) = H_o + \frac{dH}{dx} x \tag{2.50}$$

where $\frac{dH}{dx}$ is constant.

Like the PDS, this model also has several unknown coefficients that must be determined by fitting the theory to experimental data. These coefficients are the non-buoyant spreading rates for three-dimensional and two-dimensional jets, ε_3 and ε_2, the crossflow entrainment coefficient, α_c, drag coefficients, $C_{D_{02}}$ and $C_{D_{22}}$, and bottom friction factor, f_b. Stolzenbach and Harleman (1971) have suggested values for some of these coefficients based on experimental results of other researchers. However, these are not universal and must be changed according to the particular nature of the study. More details on the coefficients are given in Chapter VI.

2.6.2 Far-Field Models

An extensive review of the literature indicates that numerous models for predicting dispersion in natural streams are available (Fischer 1973, Jirka et al 1975 and Akhtar 1978). However, most of these models neglect the hydrodynamic aspect of the simulation and rather assume constant, parabolic or logarithmic velocity distributions. The following four models are reviewed in detail:

1. University of Windsor - MOE model, McCorquodale et al. (1983)

2. k-ε model, Rodi et al (1981)
3. Stream function model, Lau and Krishnappan (1981)
4. Cell model, U.S. EPA (1974).

2.6.2.1 University of Windsor - MOE Model

A two-dimensional mathematical model was developed jointly by the University of Windsor and the Ontario Ministry of the Environment to simulate the dispersion of soluble non-conservative and conservative pollutants discharged from multiple industrial outfalls along the St. Clair River (McCorquodale et al. 1983). This model takes into account the effect of depth and velocity variations in both longitudinal and lateral directions, the removal rates of degradable trace organic pollutants, lateral convection of mass, and the effect of jet mixing and dilution at the outfalls. Also, it can accommodate rapid convergence or divergence in stream width, influence of the presence of an island and the effect of flow diversion. The model was calibrated by using chloride ion concentration and validated by using phenol as a pollutant and comparing the computed values with the field data collected by the Ontario Ministry of the Environment.

The model has been divided into hydrodynamic submodel and pollutant transport submodel. The hydrodynamic submodel was based on a simplified field calibrated flow distribution using available data from St. Clair River.

The pollutant transport submodel was based on a reduced form of the depth averaged steady state convective-dispersion equation for concentration, C, of a conservative pollutant, i.e.,

$$\frac{\partial uHC}{\partial x} + \frac{\partial vHC}{\partial y} = \frac{\partial}{\partial y}(HD_y \frac{\partial C}{\partial y}) - k_T CH \qquad (2.51)$$

where

H = depth of flow

u,v = longitudinal and lateral velocities in the x and y directions respectively

k_T = overall decay rate constant

D_y = lateral dispersion coefficient.

The authors have assumed that the dispersion coefficient, D_y, is proportional to the shear velocity, U_* and the depth of flow, i.e.,

$$D_y = \alpha U_* H \qquad (2.52)$$

where α is a dimensionless dispersion factor and U_* is obtained from the assumed velocity profiles.

The model incorporates two methods of solution:

i. an implicit finite difference formulation for the convection-diffusion equation, and

ii. an explicit finite difference formulation in

which the pollutant is first convected along
the computed streamlines, then diffused and
finally decayed.

The numerical model uses the forward marching Crank-Nicholson Method (Smith 1965) for calculating the concentration values at different nodes.

This numerical model has been applied to the St. Clair River, Detroit River and St. Lawrence River and is capable of predicting the concentrations of various non-conservative pollutants discharged from multiple outfalls into the river. A reasonable agreement between the computed and observed concentration values was reported.

2.6.2.2 κ-ε Model

Rodi et al. (1981) realized the importance of hydrodynamics in developing any mathematical model for the transport of pollutants in natural streams and presented a two-dimensional depth-averaged model for the near field in the form of elliptic equations and for the far field in the form of parabolic equations. Because of the many assumptions and difficulties encountered in expressing some physical parameters in deriving the two-dimensional elliptic equations, the near field model is not considered in this review. The main emphasis is placed on the far field model which is governed by the parabolic equations.

Another important concept which has been introduced in Rodi's Work is the treatment of the turbulent transfer coefficients in the mean-flow equations. These terms represent the transfer of momentum, heat and mass by the turbulent fluctuations and need to be modelled or defined so that a closed set of equations is obtained. The turbulence model used is the κ-ε model, i.e., kinetic energy and its rate of dissipation.

The equations describing the mean flow in the parabolic model are:

$$\frac{\partial H\bar{U}}{\partial x} + \frac{\partial H\bar{V}}{\partial y} = 0 \tag{2.53}$$

$$\bar{U}\frac{\partial \bar{U}}{\partial x} + \bar{V}\frac{\partial \bar{U}}{\partial y} = -g\frac{dH_1}{dx} + \frac{1}{\rho H}\frac{\partial}{\partial y}(H\bar{\tau}_{xy}) - \frac{\bar{\tau}_{bx}}{\rho H} \tag{2.54}$$

$$\bar{U}\frac{\partial \bar{\phi}}{\partial x} + \bar{V}\frac{\partial \bar{\phi}}{\partial y} = \frac{1}{\rho H}\frac{\partial}{\partial y}(H\bar{J}_y) \tag{2.55}$$

in which

$\bar{U},\bar{V}$ = depth-averaged velocity components in the x and y directions

H = local water depth

H_1 = water level above datum

g = gravitational acceleration

$\bar{\tau}_{bx}$ = bottom shear stress in the x direction

$\bar{\phi}$ = depth-averaged scaler quantity

$\bar{\tau}_{xy}$ = depth-averaged turbulent stress

$\bar{J}_y$ = depth-averaged turbulent mass flux

The flow field in this model has been described solely by the x-momentum equation 2.54 and by the continuity equation 2.53. Equation 2.55 is the transport equation of any scaler quantity, $\overline{\Phi}$. Equations 2.53, 2.54 and 2.55 contain the depth-averaged turbulent shear stress $\overline{\tau}_{xy}$ and the depth-averaged turbulent mass flux $\overline{J}_y$ that must be determined to solve those set of equations.

Rodi employed a modified κ-ε turbulence model which has found wide application in many fields of engineering and is also considered one of the best-tested turbulence models. The κ-ε model employs the eddy viscosity/diffusivity concept which relates the turbulent stresses and heat or mass fluxes respectively to the gradients of the depth-averaged velocity components and the depth-averaged temperature or concentration. The model solves two transport equations for the depth-averaged kinetic energy κ and the depth-averaged rate of dissipation ε.

A forward marching finite difference scheme is used to approximate the governing equations 2.53, 2.54 and 2.55 the two transport equations of κ and ε.

The model was applied and compared to field data in Germany and a very good agreement between the measured and the predicted velocity and concentration profiles has been reported.

2.6.2.3 Stream Function Model

Yotsukura and Sayre (1976) derived a convective-diffusion equation in a general orthogonal curvilinear coordinate system in which the streamwise axis follows the meander of the river. Then by using the cumulative discharge to replace the transverse distance coordinate, the authors have shown that the equation for steady, two-dimensional mixing can be simplified to include only two terms, similar to the equation for straight, prismatic channels. Based on this equation, Lau and Krishnappan (1981) presented a numerical model in which they have shown that the effects of change in channel width and depth as well as channel curvature can be readily included in a "diffusion factor", which is particularly suitable for natural streams.

The form of the convective-diffusion equation as given by Lau and Krishnappan (1981) is:

$$\frac{\partial C}{\partial x} = \frac{1}{Q^2} \frac{\partial}{\partial \eta_1} [D_{z_1}(x, \eta_1) \frac{\partial C}{\partial \eta_1}] \qquad (2.56)$$

where

C = depth-averaged concentration

x = longitudinal distance coordinate in the orothogonal curvilinear system.

Q = total discharge of the channel

η_1 = dimensionless cumulative discharge

D_{z_1} = factor of diffusion, m^5/s^2

At the left bank, $\eta_1=0$ and at the right bank, $\eta_1=1$. The term $D_{z_1}=uh^2m_xD_z$ includes the turbulent mixing coefficient D_z, as well as the term uh^2m_x which reflects local changes in velocity, depth and stream curvature. If D_{z_1} is assumed to be constant, then Eq. 2.56 can be solved analytically. However, for accurate simulation, it is necessary to use local values for D_{z_1} and solve Eq. 2.56 numerically.

An implicit finite-difference scheme has been used to solve Eq. 2.56. A set of weighting coefficients was used to approximate the derivatives given in that equation. A Crank-Nicholson scheme was used in the differencing scheme. The system of the resulting equations were solved using the Gauss-Seidal method (Smith 1965) of successive substitutions.

The validity of this model for use in natural streams has been shown using data from a field test. Simulations of a dye concentration at various transects downstream from the source were carried out, using different assumptions for the factor of diffusion. The simulations can reproduce the narrowing and widening of the concentration profiles very well. For accurate simulation of the profiles, the authors suggest the use of local values of the velocity, depth, and metric coefficients together with a transverse dispersion coefficient which can vary in the downstream direction.

In 1984, Gowda used the same technique of stream tube to develop an analytical model to predict concentration distributions of conservative and nonconservative pollutants in the mixing zones of shallow rivers. Analytical solutions for pipes and diffuser outfall sources presented by other researchers were modified by Gowda to account for the reach-dependency of pollutant decay rate, transverse diffusion factor and channel hydraulic parameters. The model was calibrated and verified using data on the distribution of chloride ion naturally present in the Grand River at Waterloo, Ontario. The model was also validated for total residual chlorine, using field data from the Boyne River north of Toronto, Ontario. Gowda concluded that these models, in general, are useful to assess water quality in mixing zones of shallow rivers wherein the pollutant transport is governed by transverse dispersion and exponential decay.

2.6.2.4 Cell Model

The cell model has been used by the United States Environmental Protection Agency (1974) for the Detroit River and the St. Clair River. In this model, the mass balance is applied to a cell model of selected dimensions within the water body. The sources and sinks terms within the cell as well as convection and dispersion through the cell boundaries must be specified. This model is a simple one but requires a considerable amount of input data.

2.7 CHLORINE DECAY

2.7.1 Chlorine Chemistry

When chlorine is added to water it reacts rapidly with water to form a mixture of hypochlorous acid HOCl and hypochlorite ion OCl^- depending on pH, temperature, and dissolved solids or chlorinity (Johnson 1975). This mixture is referred to as free available chlorine, FAC, as shown below:

$$FAC = HOCl + OCl^- \qquad (2.57)$$

These two forms of FAC are produced when chlorine gas, Cl_2, or hypochlorite solution, NaOCl, or $Ca(OCl)_2$, are added to water

$$Cl_2 + H_2O \longrightarrow HOCl + H^+ + Cl^- \qquad (2.58)$$

$$OCl^- + H_2O \rightleftharpoons HOCl + OH^- \qquad (2.59)$$

The pH of the solution determines the proportion of the FAC present as HOCl or OCl^-. The FAC is half HOCl and half OCl^- at pH 7.5 and 25°C whereas at 0°C the 50:50 value is at pH 7.9. At higher pH values, the FAC shifts to more OCl^- and at lower pH to more HOCl for the same concentration of free available chlorine.

In wastewaters, and even in many drinking and river waters, sufficient ammonia is present to make it difficult to add enough chlorine to produce FAC. Combined available chlorine, CAC, forms rapidly at pH 7 to 10 to give monochloramine NH_2Cl:

$$HOCl + NH_3 \longrightarrow NH_2Cl + H_2O \qquad (2.60)$$

Further reactions may replace another H^+ from the nitrogen of ammonia to give dichloramine, $NHCl_2$, and trichloramine, NCl_3. These latter compounds are formed more slowly at higher concentrations of chlorine relative to ammonia and at lower pH.

As HOCl is added, easily oxidizable organic compounds, ferrous ion, sulfide, nitrite and other reducing agents are oxidized rapidly. After this demand is satisfied, combined available chlorine is formed that is primarily monochloramine. As additional chlorine is added beyond that needed to react with ammonia nitrogen (5 mg Cl_2/L for each 1 mg NH_3-N/L), dichloramine, $NHCl_2$ begins to form and decompose. In addition, reactions occur between different chlorine forms and difficult to oxidize chloro-organic compounds, $RNCl_z$, where R represents many possible organic compounds. Thus, combined available chlorine, CAC, is a complex mixture of chloramines of ammonia, NH_xCl_y, and organic chloramines, $RNCl_z$, where x, y and z are small whole numbers between 0 and 3.

$$CAC = NH_xCl_y + RNCl_z \tag{2.61}$$

In general the ammonia chloramines are good disinfectants as compared to the organic chloramines but are poor disinfectants when compared to HOCl (Johnson 1975). However, in the wastewaters, monochloramine is generally relied upon as the desired disinfectant.

2.7.2 Kinetics for Chlorine Decay

Residual chlorine in natural water systems can disappear either through volatilization or by reaction with ammonia and organics. When the chlorine gas is bubbled through water, and as the bubbles rise, it dissolves in water at a rate controlled by the mass transfer coefficient, the bubble surface area to volume ratio and the size distribution of bubbles (Snodgrass 1980). Since the partial pressure of chlorine in the atmosphere is essentially zero, dissolved chlorine is removed from the water body only through volatilization at a rate depending on the atmosphere mass transfer coefficient, unless chemical reactions occur. Chlorine, $Cl_2(g)$, reacts readily with water to form hypochlorous acid and this becomes the second major mechanism for removal of dissolved $Cl_2(g)$ from a water body.

Several investigators have studied the factors affecting the decay of chlorine residual concentration, both under laboratory and field conditions, and have proposed different kinetic models to describe the decay process. A study by Katz (1977) on the chlorine dissipation and toxicity in the presence of nitrogenous compounds suggested a first order kinetics. It was observed that the rate constant for chlorine decay in the presence of nitrogenous compounds was of the order of 0.01 min^{-1} and chlorine dissipation was more rapid in sea water as compared to the tap water with a rate constant of $k = 0.0446$ min^{-1}. Also, it was concluded that the rate constant had increased to 0.05 min^{-1} in the presence of sunlight but was substantially reduced upon addition of ammonia.

Hostgaard-Jensen et al. (1977) conducted a study to establish a model for the decay of chlorine in the cooling water from power plant and in the seawater. Their laboratory experiments suggested two models. The first model presumed two reactions, one being the reaction of chlorine with a component x in the water, perhaps organic material, and the other is a decomposition of chlorine. This model was discarded because, at long decay times - 18 hours or more - it yielded too small values of residual chlorine concentration and also because it did not fit at small time and initial concentrations, C_o, values. The second model considered two mechanisms, the instantaneous disappearance of chlorine essentially completed in 5 minutes and a decay according to second order kinetics. The rate constant for this second order reaction is a function of C_o', which is the amount of initial chlorine left when the instantaneously disappearing chlorine is subtracted. They estimated k-values for cooling waters from three power stations. The variation of k was almost the same for the three cooling waters when related to C_o'.

The main objectives of Gowda's work (1978, 1979) were: (i) to determine the relative effects of dispersion and chemical reaction on the diminution of instream total residual chlorine concentrations, (ii) to develop mathematical models applicable to the prediction of spatial distribution of TRC in streams receiving sewage effluent, and (iii) to investigate the effects of streamflow variations on the TRC levels in the mixing zones of shallow streams. Gowda assumed first order kinetics to govern chlorine decay for two river sites. It was observed that transverse dispersion of effluent in the Boyne River is estimated to cause a reduction of about 30% of the average TRC concentration in the effluent plume under survey conditions. For the Boyne River, he observed first order decay rates of 0.27 and 0.082 min^{-1} (to base 10) in two successive reaches during summer, 21.5°C. In Aurora Creek, the decay rates were 0.0052 and 0.012 per minute (to base 10) during the summer, 18°C, and 0.00095 and 0.0029 per minute (to base

10) during the winter, 5.5°C, in two successive reaches of the stream. The Aurora Creek rate constant values are consistent with the van't Hoff-Arrhenius temperature kinetics (Fair and Geyer 1958, White 1972) in the form of

$$k = k_{20}\theta_1^{T-20} \tag{2.62}$$

where k and k_{20} are the rate coefficients at temperatures T and 20° and θ_1 is the temperature correction factor. From Gowda's analysis, θ_1 was found to be equal to 1.08. But in his analysis, there was no explanation for the large difference in decay coefficients between the two rivers and between the successive reaches. Possible reasons could be the differences in chlorine concentrations and the oxidation of ammonia to form chloramines.

Snodgrass (1980) conducted literature surveys to obtain information on the degradation of various pollutants such as ammonia, chlorine, cyanide and phenol both in natural bodies of water and under controlled laboratory conditions. He suggested a first order kinetic model for chlorine dissipation for fresh water systems with temperature correction factor, θ_1 with respect to 20° of 1.009.

Bobra and Mackay (1980) developed a computational model describing the fate of selected non-conservative pollutants in an idealized section of St. Clair River. They proposed kinetic expressions to describe the conversion of the pollutants by volatilization, photolysis, oxidation, hydrolysis, biodegradation and dilution and arrived at the following equation for the decay of pollutants after mixing in the stream:

$$k = (k_{EV}+k_{PH}+k_{OX}+k_{HY}+k_{BD}+k_{DI}) \qquad (2.63)$$

where

k_{EV} = rate constant for evaporation (volatilization)
k_{PH} = rate constant for photolysis
k_{OX} = rate constant for oxidation
k_{HY} = rate constant for hydrolysis
k_{BD} = rate constant for biodegradation
k_{DI} = rate constant for dilution.

In their analysis, they assumed that all processes proceed independently. They suggested that these degradation processes can be added to hydraulic models to yield information on the relative importance of individual and total degradation rates with respect to dilution and diffusion processes.

Haas and Karra (1984) proposed a new kinetic model to describe the kinetics of chlorine demand exertion by assuming a parallel first order decay in the following form:

$$C=C_o(X)\exp(-k_1t) + C_o(1-X)\exp(-k_2t) \qquad (2.64)$$

The model considered that decay may proceed through two mechanisms, each of first order, and involving a different component of the chlorine residual; that is, component X with concentration $C_o(X)$, is subject to first order decay with a rate constant of k_1 and the remainder, the initial chlorine residual with component X, $C_o(1-X)$, is subject to first order decay with a rate constant of k_2. By definition, X is limited to a range between zero and unity. They showed that the use of a parallel first order decay model produced a satisfactory fit to large experimental data set obtained by other researchers. They estimated that 10 to 40% of the applied chlorine decays with a rate constant of approximately 1.0 min^{-1}, but the chemical basis for this rapid loss is uncertain. The second, slow rate of decomposition k_2, clusters around 0.003 min^{-1} and proceeds at a velocity consistent with that of pure inorganic and organic chloramines.

CHAPTER III

MATERIALS AND EXPERIMENTAL TECHNIQUES

3.1 HYDRODYNAMIC STUDIES

The effect of a circular jet injected laterally into a straight channel flow was investigated by means of a physical model. The set-up simulated conditions similar to those for many outfalls in the Detroit River.

3.1.1 Description of the Model

The laboratory experiments were performed in a half trapezoidal flume of 8.5 m long x 2.85 m wide x 0.34 m high with side slope of 3 horizontal to 1 vertical. The model was constructed of finished plywood to a scale of about 1 to 45 of the Detroit River. The flume bed was covered with a 50 mm layer of 6.5 to 12.5 mm river gravel which represents the frictional resistance of the Detroit River (Manning's coefficient n $\approx$0.026).

The jet was discharged perpendicular to the channel flow through a round pipe placed at 5.15 m from the upstream end of the channel. The ABS plastic pipe was 50 mm inside diameter and 4.5 mm thickness. The pipe size was scaled from the existing diffusers at Detroit River.

The flume was equipped with its own sump pump to supply water to the pipe and the jet discharge was controlled by a valve located on the ABS pipe, Fig. 3.1. In order to produce a uniform flow distribution across the flume and to damp the turbulence, the entrance to the flume was supplied with a screen, a fibre mesh and a 0.15 m high plywood weir. A tailgate at the downstream end of the test flume was used to control the water level in the model. Hot and cold water supplies were employed during the density current tests as shown in Photograph 3.2.

Flow for the model was supplied by a 9375 L/min (2500 USGPM) centrifugal pump. The flow rate was measured by a Foxbough magnetic flowmeter which was calibrated and checked before the tests. The reading error on the flow chart was approximately ±37.5 L/min (±10 USGPM). A general layout of the model and the principal dimensions are shown in Fig. 3.1. The overall views of the test facilities are shown in Photographs 3.1 and 3.2.

3.1.2 River Similitude

Detroit River was chosen as a typical case of study during this investigation and the following data were obtained from the U.S. Department of Commerce maps (1979):

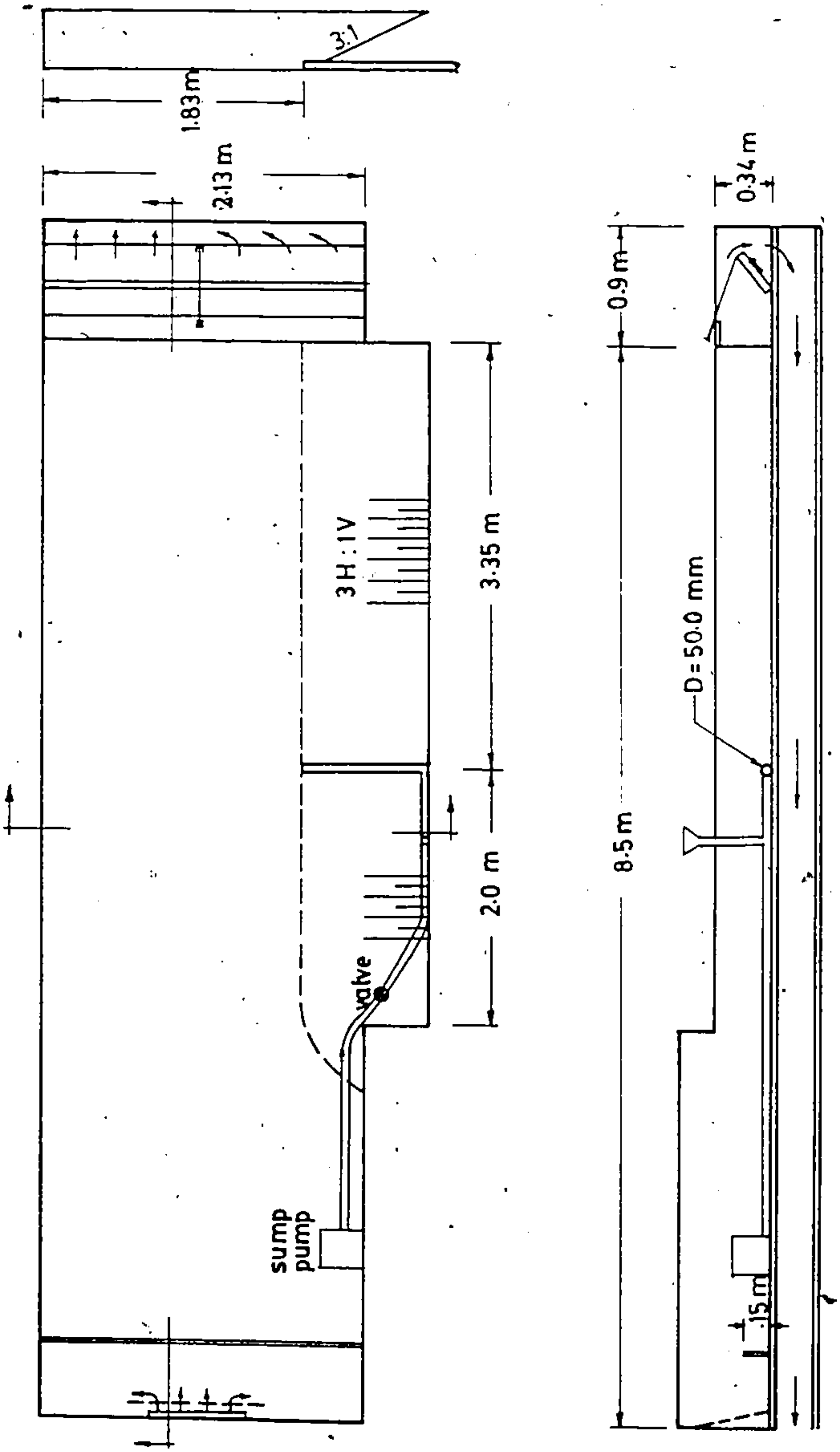

Fig. 3.1. Layout of the Physical Model.

COLOURED PICTURES
Images en couleur

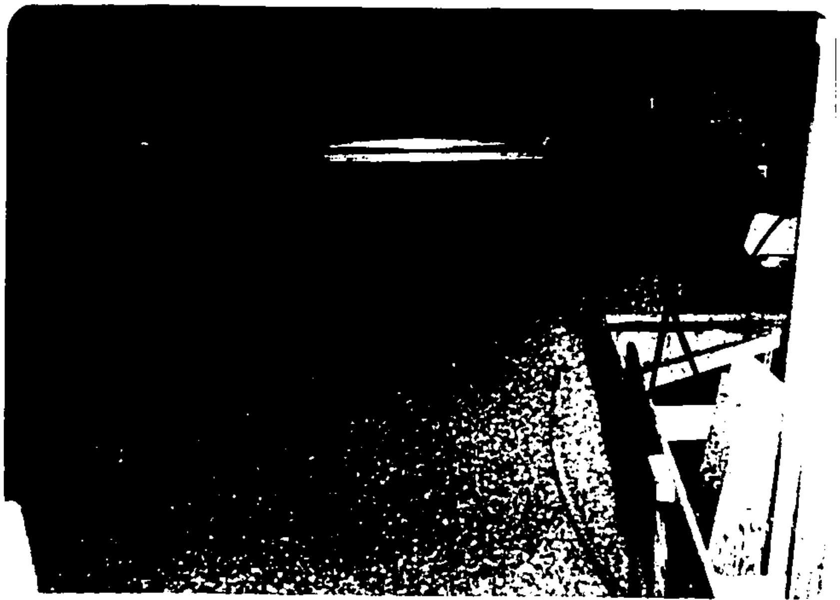

Photo 3.1. Overall view of the physical model looking downstream.

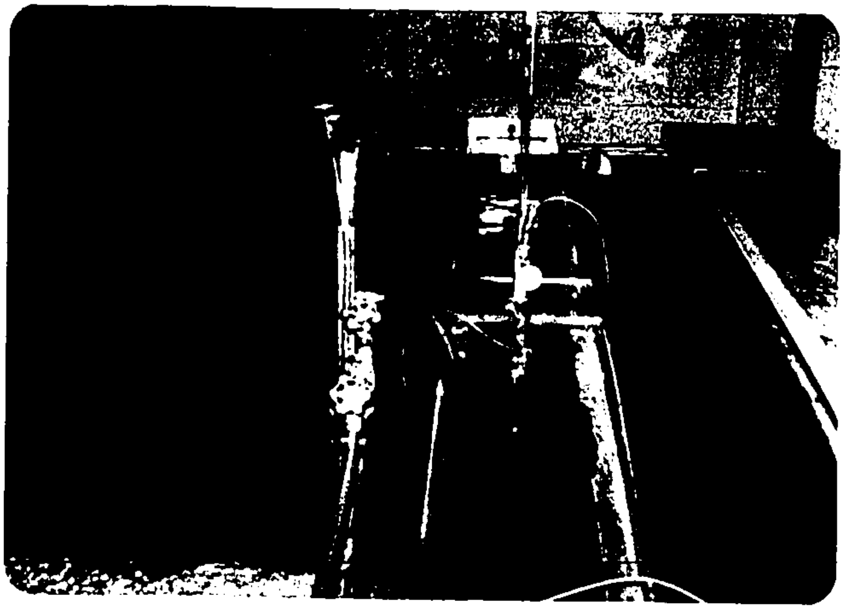

Photo 3.2. Overview of the test facility showing hot and cold water supplies and dye injection system.

Total length = 51.5 km (32 miles) from its head at Windmill Point Light to the Detroit River Light in Lake Erie

Maximum width = 1050 m (3500 ft.)

Minimum width = 580 m (1900 ft.)

Velocity = 0.5-1.2 m/s (1.65-4.0 ft/s)

Flow rate = 4100-6000 m^3/s (144,400-212,700 cfs)

Typical water depth = 6-9 m (20-30 ft.)

Typical diffuser diameter = 1.8-2.7 m (6-9 ft.)

For complete similitude, the model must be geometrically similar to the prototype and have the same Froude number, Reynolds number, Weber number, Euler number, and Mach number. It is practically impossible to satisfy all the similitude requirements; therefore the rigid similitude requirements must be relaxed in favour of the most important requirements. In most open surface hydraulic models, with Froude numbers of the order of 1, the Froude law is used as the operating law but the model scale is set to ensure similar turbulent conditions in the model and the prototype (McCorquodale 1977).

Therefore, the above hydraulic data were converted to the equivalent model values using the Froude Scaling Law, i.e., the Froude number was kept to be the same in both the model and the prototype while maintaining similar turbulent nature. This led to the following relationships:

(i) Geometric Similarity

Since the observed jet width in the field was confined to only 10 to 25% of the total river width, the flume width represented a part of the total river width. In fact, the width ratio did not represent the model scale and the discharge ratio was made per unit width.

Depth ratio H_r = Prototype depth/Model depth

= 30-60

Pipe diameter ratio D_r = Prototype diameter/Model diameter

= 36-54

(ii) Kinematic Similarity

It is apparent that in a Froude model,

Velocity ratio V_r = Prototype velocity/Model velocity

$= H_r^{1/2}$

= 5.5-7.7

Therefore, an average velocity in the model worked out to be 0.15 m/s. A range of velocity varying from 0.1 to 0.3 m/s was chosen in this study.

Discharge ratio q_r = Prototype discharge/Model discharge

$= V_r \cdot H_r$

$= H_r^{3/2}$

= 165-465

$$\text{but } q_p = \frac{Q_p}{W_p} = 7.2$$

Therefore, an average flow rate in the model worked out to be 65 L/s. Three values for flow rate, 35, 70 and 100 L/s, were chosen in this study.

In case of density currents, the same densimetric Froude number was maintained in the model as in the prototype according to the following equation:

$$F_o = V_j/\sqrt{g'D} \tag{3.1}$$

where

F_o = initial densimetric Froude number

V_j = jet velocity

g' = $g(\Delta\rho/\rho_a)$

ρ_a = ambient density

$\Delta\rho$ = the density difference between the discharge and the ambient.

g = acceleration due to gravity.

3.1.3 Measurement System

A traversing mechanism was used for the measuring system in the lateral, vertical and longitudinal directions. A plexiglass carriage was mounted on the traverse and it travelled on tracks to provide the lateral position while the vertical position was set using a point gauge with a vernier which was read to the nearest one hundredth of an inch.

Various parameters such as discharge, depth of flow, jet velocity/ambient velocity and position of the jet were varied. Table 3.1 indicates the parameters for each experiment. Figure 3.2 is the definition sketch for these data.

3.1.3.1 Velocity Measurements

Velocity measurements were made by means of a KENT current flow meter which had a propeller diameter of 10 mm, Photograph 3.3. Although the meter was provided with two high and low speed probes, all the measurements were made with the low speed probe. The accuracy of the meter is about ±2%.

The procedures for each set of measurements are listed below:

1. The pump was started and the flow was delivered to the the test flume.
2. The desired flow rate was established with the help of the control valve on the feed pipe.
3. The tailgate was adjusted to the desired position and the water surface elevation was measured using the point gauge.
4. The current meter was used to measure the velocity distribution across the channel and an average value was taken.
5. The sump pump was started and the exit velocity at the

pipe was measured by the current meter and adjusted to the desired value by a control valve on the outfall pipe.

6. The velocity distribution across the channel due to the jet injection was determined at four stations, i.e., at 0, 6, 12 and 24 times the pipe diameter downstream from the outfall. Each experiment involved taking a lateral and vertical velocity profile. The vertical readings were taken at 0.2H, 0.5H and 0.8H.

A series of 25 detailed runs was performed to obtain qualitative and quantitative information about the velocity distribution in the channel due to the jet injection. The only component of velocity measured was the "U" component; that is the component parallel to the direction of the ambient flow.

In addition to the above runs, five more detailed runs within 0.3 m downstream the discharged jet were conducted, in which both longitudinal and lateral velocity components, U and V, were measured. Velocity measurements in the lateral and vertical directions were taken at cross-sections every 50 mm downstream from the jet.

3.1.3.2 Photographs

A series of 37 runs was performed in order to qualitatively study the dispersion of jets with neutral and light densities. These runs used the equipment described above but no velocity measurements were made other than to obtain the initial jet velocity ratio. Instead, the pipe discharge was injected with potassium permanganate dye and the jet trajectories were visually studied. Photographs of the discharged dye were taken with a 35 mm SLR Nikon camera, provided with a wide angle lens (1:3.5, f=20mm), and mounted on a steel frame at 1.2 m above the flume. The steel frame was fixed on the traverse bridge as shown in Photograph 3.4.

3.1.3.3 Fluorescein Dye Tests

A dye test involved a rapid injection of a known amount of sodium fluorescein, supplied by Fisher Scientific Company as Uranine, into the main pipe through a dye injection system located at 0.5 m, 10D, upstream of the outfall, Photograph 3.2. A Turner Fluorometer, Model 111, was used to measure the concentration of the injected dye at selected points downstream of the outfall as shown in Fig. 3.3. The dye was prepared according to the procedure suggested in the Fluorometer instruction manual (1974). A continuous-flow attachment, along with a dye sample pump, were used for continuous measurement of dye concentration. A single channel chart recorder, Hitachi Perkin-Elmer type, was connected to the Fluorometer for recording the concentration. Photograph 3.5 shows the equipment used in the dye tests.

Table 3.1

Significant Details for the Experiments of Nonbuoyant Circular Jets

Run No.	Q L/s	H m	H/D	V_j m/s	U_a m/s	R = V_j/U_a	R_N = V_jD/ν $\times 10^3$	Position	Remarks
1	34	0.10	2.0	0.64	0.20	3.2	32	B	
2	34	0.20	4.0	0.20	0.10	2.0	10		
3	34	0.20	4.0	0.52	0.10	5.2	26		
4	70	0.10	2.0	0.64	0.40	1.6	32		
5	70	0.20	4.0	0.63	0.19	3.3	31.5		
6	70	0.28	5.5	0.28	0.13	2.2	14		
7	70	0.28	5.5	0.64	0.13	4.9	32		
8	100	0.20	4.0	0.63	0.30	2.1	31.5		
9	100	0.28	5.5	0.62	0.18	3.4	31		
10	34	0.20	4.0	0.20	0.10	2.0	10	M	
11	34	0.20	4.0	0.55	0.10	5.5	27.5		
12	70	0.20	4.0	0.75	0.19	4.0	37.5		
13	70	0.28	5.5	0.28	0.13	2.2	14		
14	70	0.28	5.5	0.75	0.13	5.8	37.5		
15	100	0.20	4.0	0.74	0.28	2.6	37		
16	100	0.28	5.5	0.76	0.18	4.2	38		
17	34	0.20	4.0	0.20	0.10	2.0	10	S	Extended outfall
18	34	0.20	4.0	0.52	0.10	5.2	26		
19	70	0.20	4.0	0.79	0.19	4.2	39.5		
20	70	0.28	5.5	0.28	0.13	2.2	14		
21	70	0.28	5.5	0.76	0.13	5.9	38		
22	100	0.20	4.0	0.79	0.30	2.6	39.5		
23	100	0.28	5.5	0.79	0.18	4.4	39.5		
24	34	0.20	4.0	0.20	0.10	2.0	10	S	Shore-based outfall
25	34	0.20	4.0	0.52	0.10	5.2	26		
26	70	0.28	5.5	0.64	0.13	4.9	32		

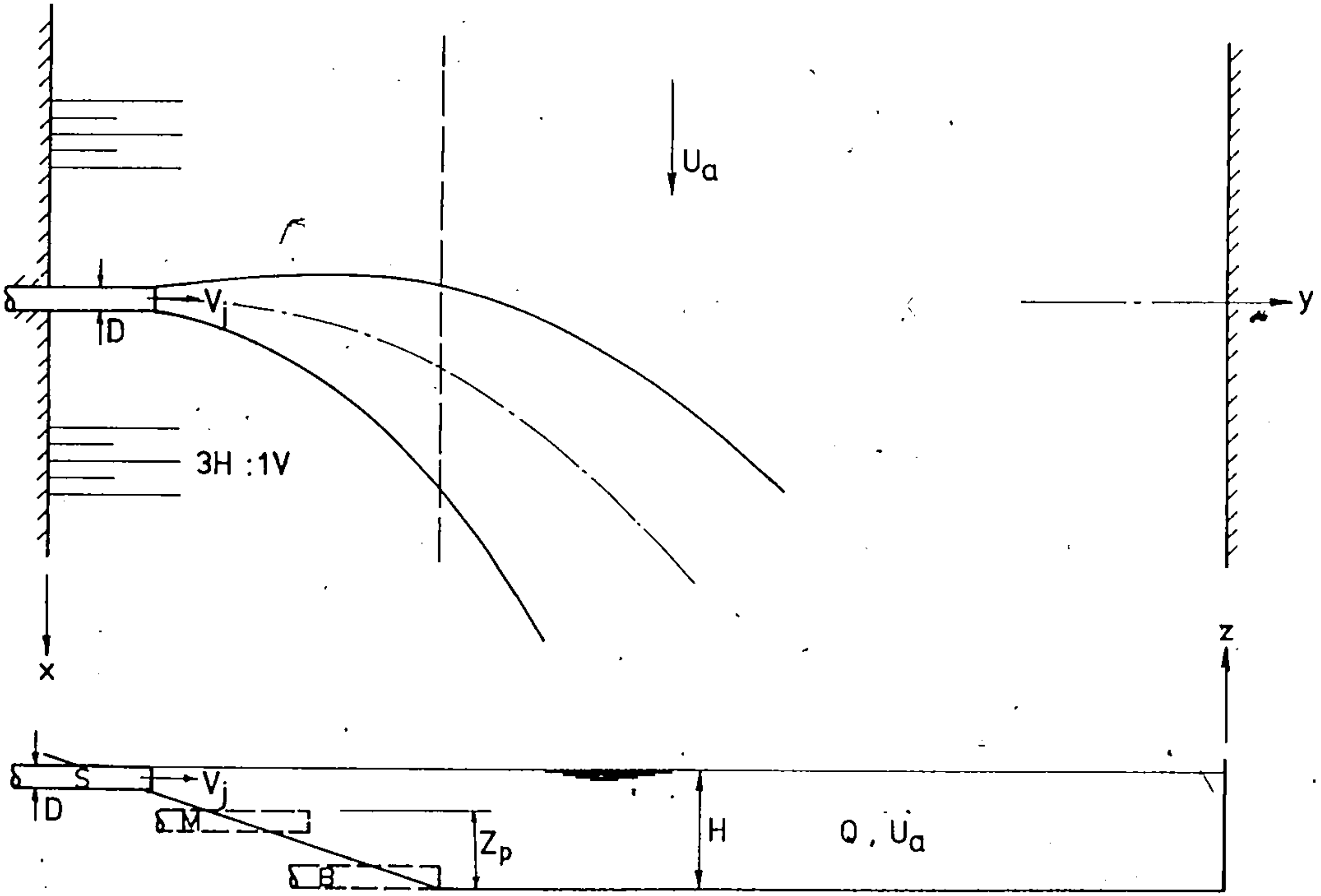

S = Surface ; M = Middle ; B = Bottom

Fig. 3.2. Definition Sketch for Experimental Set-up.

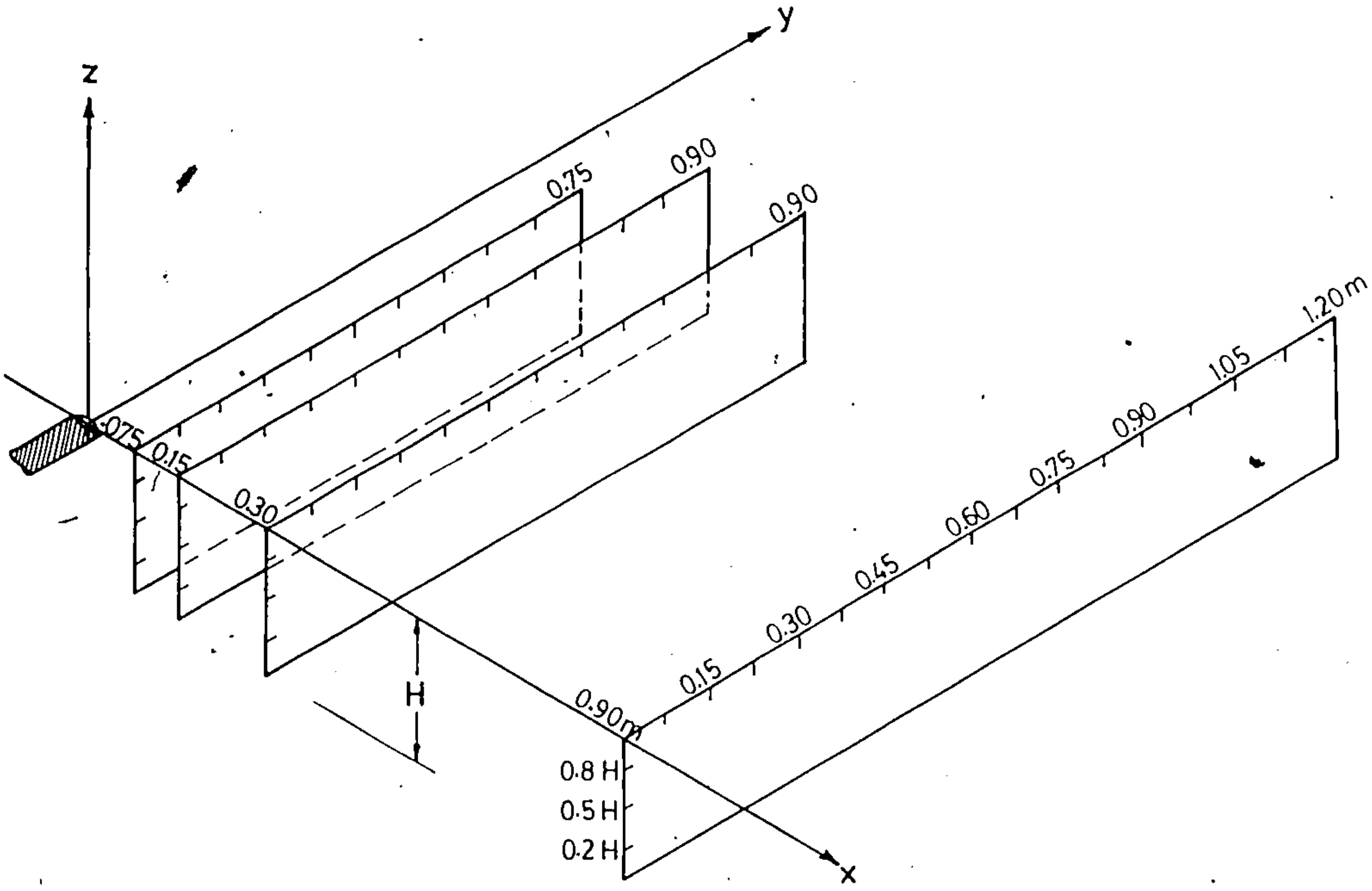

Fig. 3.3. The Three Dimensional Array of Measurement Points.

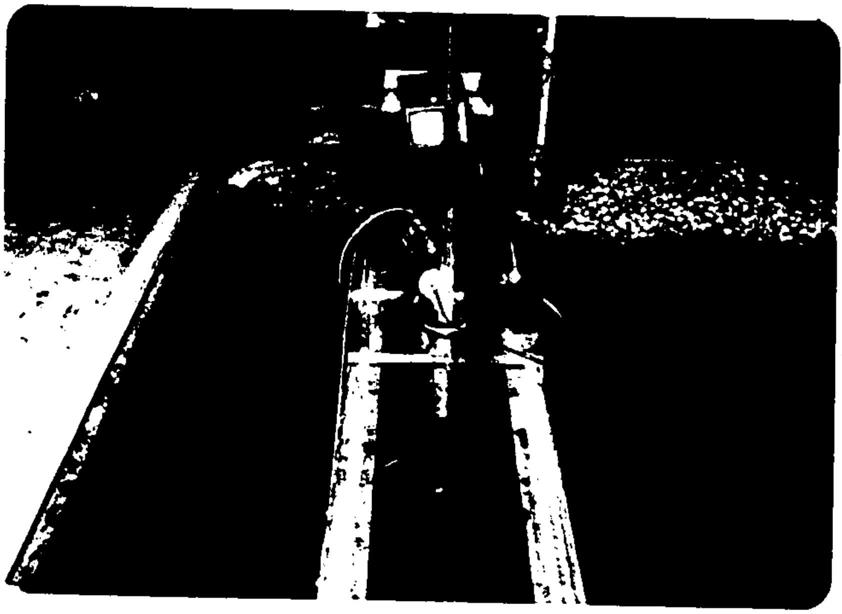

Photo 3.3 . Overview showing traverse mechanism, Current meter and the thermistor.

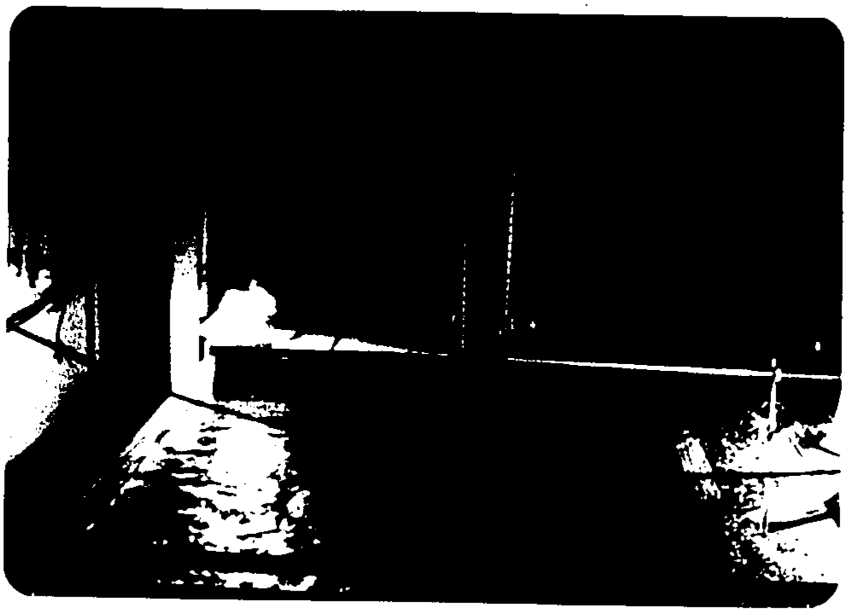

Photo 3.4 View of camera mount.

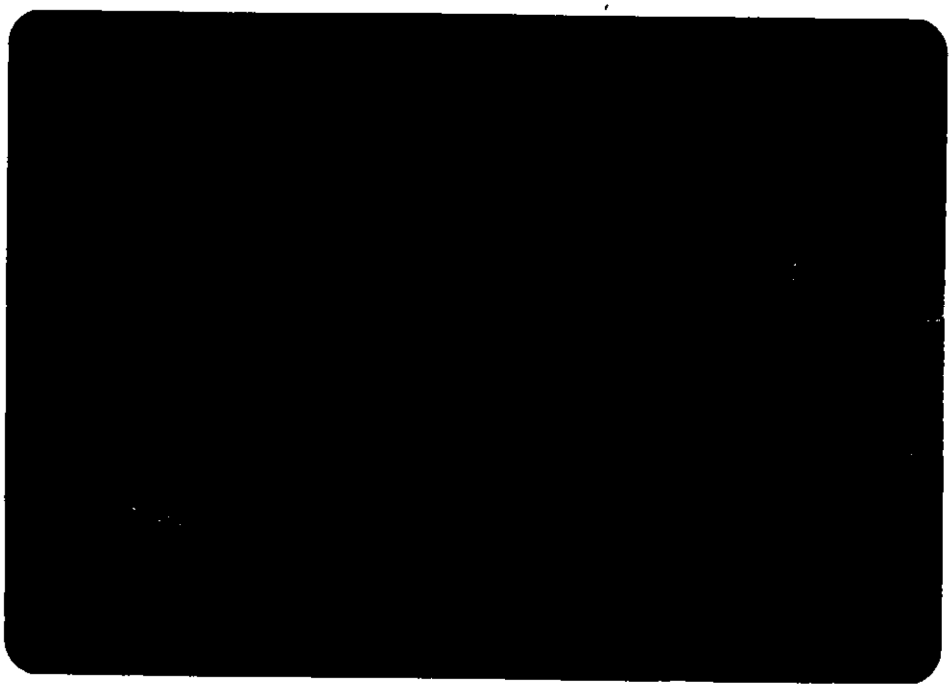

Photo 3.5. Turner fluorometer set-up for the concentration dye tests.

The following sequence of operations was adopted for a typical neutral density dye test:

1. The Fluorometer, chart recorder and dye sample pump were started and the Fluorometer was zeroed.
2. The dye was injected using a separate pump and the initial concentration at the outfall was marked on the recording paper after allowing the dye to reach a steady condition which took approximately two minutes.
3. The dye sample pump suction tube was moved to the first section, 75 mm downstream of the outfall. The vertical profile was taken first at five vertical positions, that is, at 0.0H, 0.2H, 0.5H, 0.8H and 1.0H depths. The results were recorded on the chart recorder as they were taken and the position of maximum concentration noted. The lateral profile was then taken at the position of maximum concentration. Seven to ten points were considered sufficient to describe the lateral profile.
4. Procedures described in 3 above were followed at 0.15 m, 0.30 m and 0.90 m downstream from the outfall.
5. The details of each test, i.e., discharge, depth of flow, amount of dye, measuring position and model arrangement, were cross-recorded on the recording paper.

The dye tests with density current were conducted in the same manner as described above except that hot or cold water of the desired temperature was injected laterally in the main flow to create buoyant density currents or heavy density currents respectively.

3.1.3.4 Temperature Tests

Temperature measurements were made by a thermistor probe which had an accuracy of about ±0.05°C. The probe was fixed to the point gauge which was mounted on the movable traverse as shown in Photograph 3.3. The measurement points were similar to those used for the concentration tests, Fig. 3.3. Temperature at downstream cross sections were measured until the temperature field became two-dimensional, i.e., nearly uniform temperature distribution in the vertical direction.

A typical temperature test procedure was as follows:

1. The temperature upstream of the outfall was recorded to obtain the initial ambient temperature, T_{a_o}.
2. The hot water was allowed to the pipe through a hot water supply and the initial jet temperature, T_o, was recorded after allowing two minutes for complete mixing.
3. The traverse mechanism was moved to the first section, 75 mm downstream of the outfall and the vertical profile was taken at five vertical positions. The lateral

profile was then taken at the location of maximum temperature as indicated by the vertical profile. Subsequent readings were taken at lateral spacings to allow the profile to be adequately defined with approximately seven points.

4. Procedures described in 3 above were followed at 0.15 m, 0.30 m and 0.90 m downstream of the outfall.

The heavy density current tests were conducted in the same manner as described above except that the flume was first warmed for a period of at least 30 minutes and then the hot valve was turned off while the cold valve was simultaneously turned on to inject cold water through the pipe. Table 3.2 presents the significant parameters for the experimental runs for the buoyant circular jets and heavy density jets.

Table 3.2

Significant Details for the Experiments of Buoyant and Heavy Density Circular Jets

Run No.	Q (L/s)	H (m)	H/D	$R=V_j/U_a$	T_o (°C)	T_a (°C)	ΔT_o (°C)	F_o	Remarks
1-1	34	0.10	2.0	3.2	30.1	20.4	9.7	17.30	bottom outfall
2-1	34	0.20	4.0	2.0	34.5	18.3	16.2	4.32	"
3-1	34	0.20	4.0	5.2	28.0	16.0	12.0	14.17	"
5-1	70	0.20	4.0	3.3	27.5	17.7	9.8	18.60	"
6-1	70	0.28	5.5	2.2	34.5	21.1	13.4	6.52	"
7-1	70	0.28	5.5	4.9	28.2	18.8	9.4	19.30	"
24-1	34	0.20	4.0	2.0	31.1	20.3	10.8	5.32	shore-based outfall
25-1	34	0.20	4.0	5.2	33.0	21.2	11.8	12.90	"
25-2	34	0.20	4.0	5.2	30.7	22.5	8.2	16.90	"
26-1	70	0.28	5.5	4.9	34.0	22.9	11.1	19.14	"
30-1	34	0.20	4.0	2.0	17.1	24.7	-7.6	4.05	"
31-1	34	0.20	4.0	5.2	16.2	22.3	-6.1	15.17	"

3.2 CONTAMINANT BEHAVIOUR STUDIES

Chlorine is used as a disinfecting agent in domestic wastewater treatment plants in order to destroy the pathogens of public health concern before discharging the effluent into a receiving waterbody.

Total residual chlorine, TRC, is the most common test for chlorine in receiving waters. Not only it indicates the efficiency of disinfection but also measures the concentrations of chlorine compounds particularly monochloramine, NH_2Cl. Monochloramine is important because of its toxicity to bacteria, rapid formation rate and widespread appearance due to the ubiquity of ammonia in natural water (White 1972).

Biochemical Oxygen Demand, BOD, is the most commonly used parameter to define the strength of a domestic wastewater or organic industrial wastewater. The BOD is considered to be an important parameter in controlling the amount of chlorine necessary to obtain satisfactory disinfection (White 1972).

3.2.1 Experimental Materials

In this investigation, treated wastewater samples, before chlorination, were collected both from the West Windsor Pollution Control Plant and the Little River Pollution Control Plant. The West Windsor Plant receives domestic wastewater and industrial wastes in equal amounts and provides physical-chemical treatment while the Little River Plant receives, primarily, domestic wastewater and some industrial wastes and provides secondary treatment using the activated sludge process.

The wastewater samples collected from the two plants were spiked with different amounts of a stock chlorine solution. In order to prepare the stock chlorine solution, bleach containing sodium hypochlorite was added to distilled water and the concentration was measured by amperometric titrant. The chlorinated samples were then diluted in the ratio of 1 to 19 with Detroit river water. Hostgaard-Jensen et al. (1977) have recommended this dilution factor based on their experiments. Also, from the field studies described later, this value was found to be reasonable for Detroit River. The river water was first saturated with dissolved oxygen by aerating with filtered air for about four days and then was left without aeration for one day in order to allow the water to reach equilibrium in case it was supersaturated.

3.2.2 Measurement Procedure

A series of tests was conducted on the diluted chlorinated samples to determine (i) the decay rates for residual chlorine in river water under various conditions, (ii) the influence of chlorination on progression of biochemical oxygen demand, BOD, in river water, and (iii) the fate of ammonia in river water.

3.2.2.1 Determination of Decay Rates for Residual Chlorine and Ammonia

A series of separate tests was performed to measure the changes in residual chlorine and ammonia concentrations in the diluted final effluent samples under the conditions shown in Fig. 3.4 and explained below:.

(i) Effect of Varying Chlorine Dose

Five sets of experiments were conducted on the same final effluent sample collected from West Windsor Plant to study the effect of varying the chlorine dose on the residual chlorine and ammonia concentrations. Sufficient stock chlorine solution was added to each effluent sample so as to obtain chlorine doses of 5, 7, 9, 11 and 13 mg/L. Then the samples were diluted in the ratio of 1 to 19 with water from Detroit River. These solution samples were poured in standard 250 mL glass beakers and were placed in a constant temperature chamber , Photograph 3.6. The residual chlorine and ammonia concentrations in these beakers were determined at selected time intervals.

(ii) Effect of Alternating Exposure to Light and Dark Environment

Two sets of tests were carried out on effluent samples in which 9 mg/L of chlorine was added and diluted with water

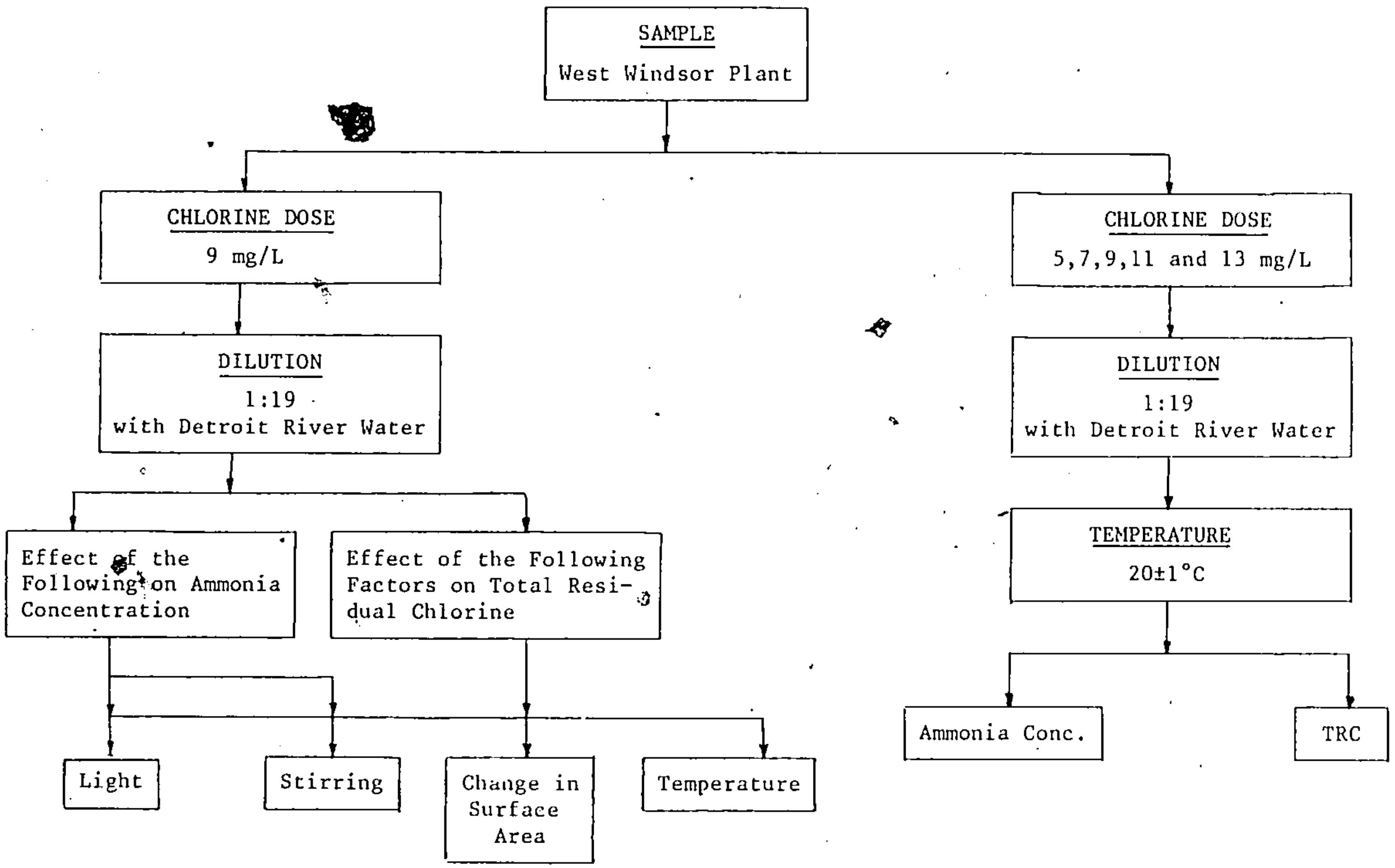

Determination of TRC, Ammonia and Decay Rate of Chlorine

Fig. 3.4. Flow Chart for Total Residual Chlorine and Ammonia Concentrations Tests.

from Detroit River. The first set of samples was placed in a 20±1°C constant temperature chamber provided with alternating exposure to 12 hours of light and 12 hours of darkness each day, while the second set was kept in complete darkness.

(iii) Effect of Stirring Samples

Two sets of experiments were performed on the wastewater samples dosed with 9 mg/L of chlorine and diluted. The first set was kept under continuous stirring with individual magnetic stirrers, manufactured by Fisher Scientific Co., Model No. SL. 7225, using 25 mm L x 8 mm D The magnetic bar was rotated at 680 rpm which represents a level of turbulence existing in natural streams (Ali 1972). (1"L x 5/16" D) teflon covered octagonal magnetic bars. Asbestos pads were placed between the magnetic stirrers and the beakers in order to reduce the heat transfer between them. The second set was kept under quiescent conditions. All the beakers were placed in a constant temperature chamber provided with alternating exposure to 12 hours of light and 12 hours of darkness each day.

(iv) Effect of Varying Surface Area

Five sets of experiments were conducted on the same final effluent provided with 9 mg/L chlorine dose and diluted with river water to study the effect of varying the surface area per unit volume. The samples were placed in different size glass beakers with area/volume of 0.0035, 0.0069, 0.011, 0.021 and 0.029 mm^{-1}. All beakers were placed at the same room temperature.

(v) Effect of Varying Temperatures

In order to study the effect of temperature on the decay rate of chlorine, four sets of experiments were conducted at 2, 11, 20 and 30±1°C respectively under identical conditions. Wastewater samples dosed with 9 mg/L of chlorine and diluted with river water were used for this study.

Unless otherwise specified, all the tests were conducted in standard 250 mL glass beakers containing 250 mL of diluted final effluent with a specified concentration of chlorine added. Residual chlorine was determined at different time intervals for several days, according to the procedures mentioned in the Standard Methods for the Examination of Water and Wastewater (1980). The free and combined residual chlorine concentrations were measured by the amperometric titration method using Wallace & Tiernan Titrator.

Concentration of ammonia ions was determined using an ammonia-electrode, Orion Model 95-10, connected to microprocessor ionalyzer, Orion Model 901, as shown in Photograph 3.7. The basic procedure used for ammonia measurements was essentially what has been recommended by

COLOURED PICTURES
Images en couleur

Photo 3.6. Experimental set-up for residual chlorine.

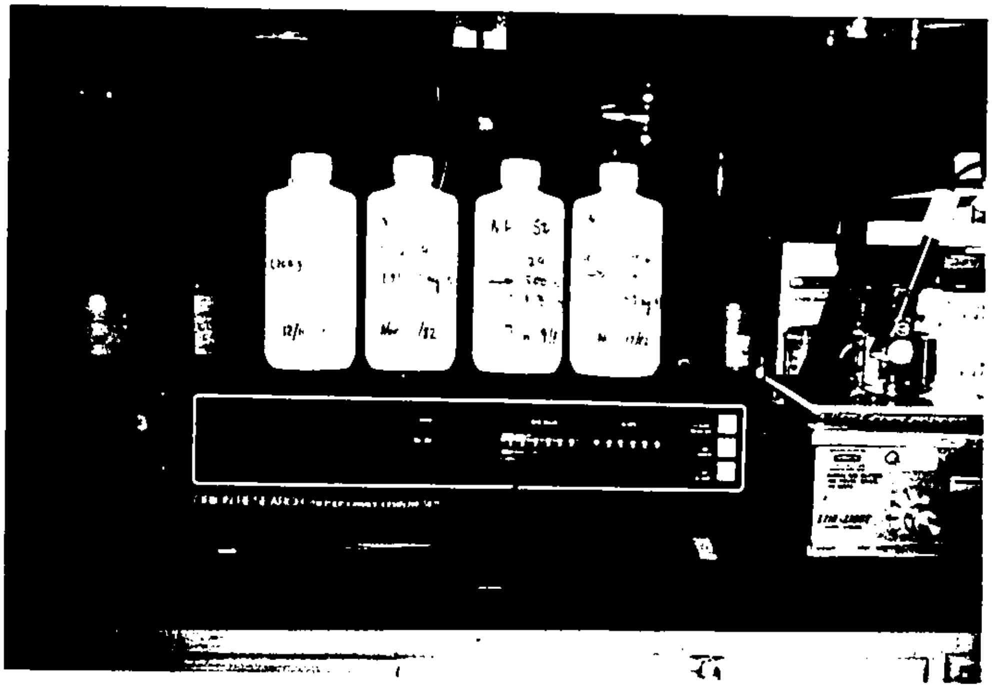

Photo 3.7. Ammonia-electrode set-up.

Orion Research (1979). Since the ammonia concentration was below the Nerstian response range of the electrode, the known-addition method using Gran's Plot proposed by Bailey (1976) was adopted for the analysis. All the samples were analyzed soon after collection and before adding chlorine to determine the ammonia level in the treated wastewater. Also, the ammonia concentration measurements were determined on chlorinated and diluted samples at different time intervals for several days. Measurements on blank solutions were conducted immediately before and after each determination in order to check the reproducibility of the electrode response. The required time to reach a stable electrode response varied from several seconds to several minutes. It was found that constant temperature, constant rate of stirring, and the recording of measurements at appropriate constant time intervals were of a crucial importance to the reproducibility of the results. Thus, these factors were closely controlled in the course of measurements.

3.2.2.2 Determination of the Influence of Chlorine on Biochemical Oxygen Demand

A series of separate tests was performed on the chlorinated solution samples to obtain the BOD progression curves under the conditions shown in Fig. 3.5 and explained below:

BOD PROGRESSION CURVE

(Determination of 5-day BOD, L_a, $\breve{k}_1$)

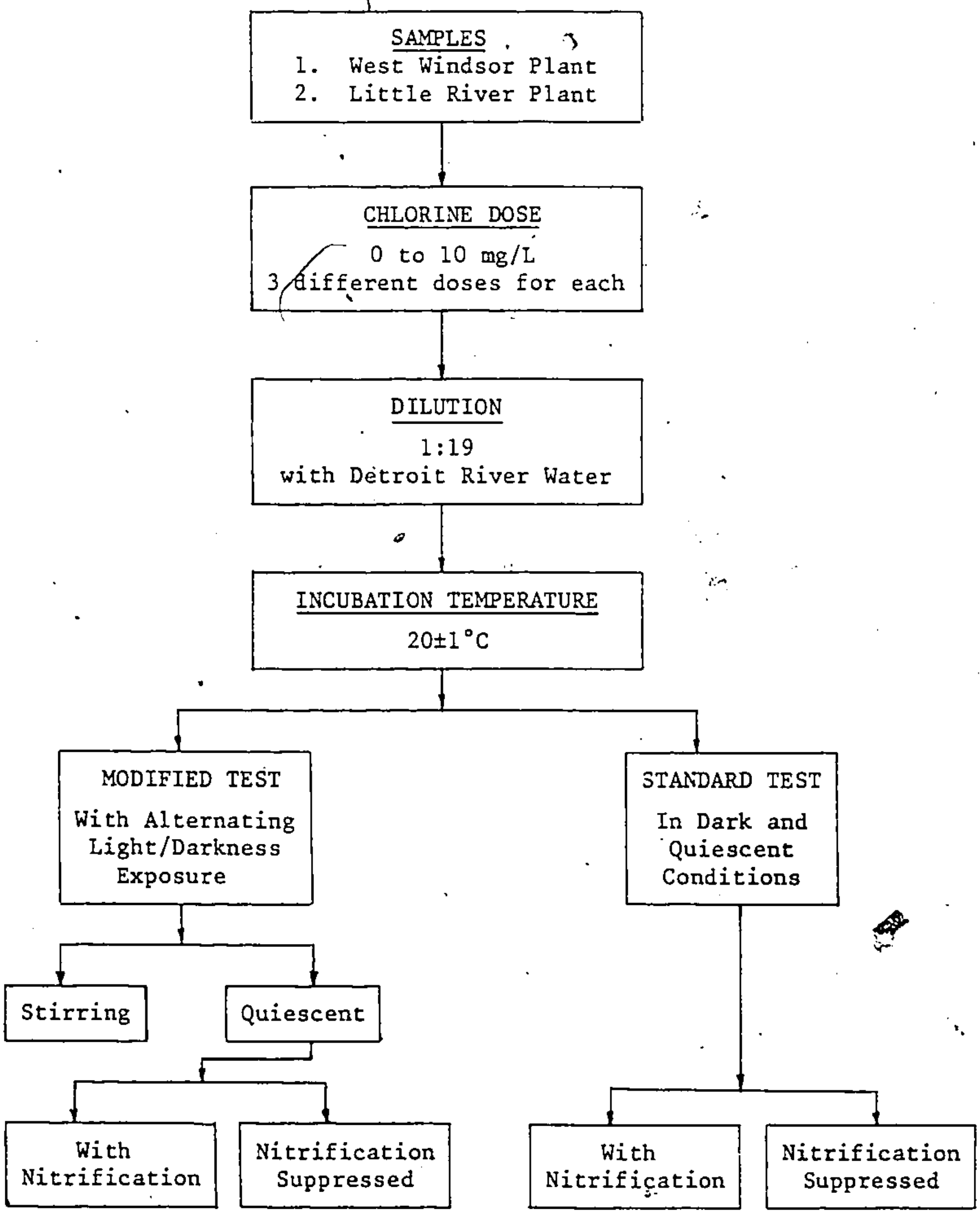

Fig. 3.5. Flow Chart for BOD Experiment Conditions.

(i) Effect of varying Chlorine Dose

Two sets of experiments were carried out on effluent samples collected before chlorination from both plants. Stock chlorine was added to provide three different dosages of 0, 5 and 10 mg/L in the same final effluent from West Windsor Plant and dosages of 0, 2 and 5 mg/L of chlorine in the same final effluent from Little River Plant. Then the chlorinated samples were diluted 1 to 19 with water from Detroit River. The chlorinated solution samples were poured in standard 300 mL BOD bottles and incubated in a standard BOD air incubator at 20±1°C. The dissolved oxygen readings were taken daily for 11 days.

Another series of six experiments was conducted in which chlorine was added to provide dosages of 0, 5 and 10 mg/L in the final effluent from West Windsor Plant and 0, 5 and 8 mg/L in the final effluent from Little River Plant. These sets were run for 7 days at temperature 20±1°C and the dissolved oxygen readings were taken after 0, 1, 2, 3, 5 and 7 days respectively.

(ii) Effect of Light

In order to study the effect of light on BOD progression, one set of samples was incubated with alternating exposure to 12 hours of light and 12 hours of darkness each day, while another set of samples was incubated in complete darkness. All the samples were dosed with the prespecified chlorine doses before starting the experiments.

(iii) . Effect of Turbulence

Two sets of BOD bottles were inoculated to evaluate the influence of turbulence on BOD progression. The first set was kept under continuous stirring with individual magnetic stirrers, using 25 mm Lx8 mm D (1"L x 5 1/16"D) teflon covered octagonal magnetic bars, while the second set was kept under the standard quiescent condition. All BOD bottles were incubated in a standard BOD air incubator provided with alternating exposure to 12 hours of light and 12 hours of darkness.

(iv) Effect of Nitrification Suppression

When nitrification was expected to occur simultaneously with oxidation of carbonaceous matter in samples from the Little River Plant, nitrifying bacteria were suppressed by pasteurization by heating the samples to 60-70°C and immediately cooling to 20°C (Sawyer et al. 1946). This suppression of nitrifying bacteria was done to determine the BOD values due to carbonaceous matter only. In a parallel run, a set of BOD bottles was inoculated without pasteurization. Both sets of samples were kept under quiescent condition.

All the tests were conducted according to the procedures suggested in the Standard Methods for the Examination

<u>of Water and Wastewater</u> (1980). The dissolved oxygen concentration was measured with the D.O. Analyzer, Model 57, manufactured by Yellow Springs Instrument Co. (YSI). The DO and temperature readings were taken by tightly inserting the oxygen probe and thermistor bead in the BOD bottle at predetermined time intervals. After taking the readings, the bottles were stoppered again and kept in the incubator. Proper care was taken to prevent loss or gain of oxygen between bottles contents and environment while measuring the dissolved oxygen concentration.

CHAPTER IV

EXPERIMENTAL RESULTS

4.1 HYDRODYNAMIC STUDIES

4.1.1 Velocity Profiles of Non-buoyant Jets

A set of 25 runs was made to measure the velocity distribution across the channel due to non-buoyant jet injection. Each experiment involved taking lateral and vertical velocity profiles at four downstream stations. The ranges for the experimental variables were:

Channel discharge, Q = 34, 70 and 100 L/s
Jet discharge, Q_o = 0.4 to 1.5 L/s
Relative Depth, H/D = 2, 4 and 5.5
Jet velocity/ambient velocity, R = 2.0, 3.2 and 5.2
Pipe diameter, D = 50 mm
Pipe position, Z_p = on bed, at mid depth and at the surface.

Typical lateral profiles of the longitudinal velocity, U, measured at various longitudinal distances, x, from the outfall with different flow rates, depths of flow, velocity ratios and pipe positions are shown in Figs. 4.1 to 4.4. The rest of the results are shown in Appendix A. The reported velocity U is the average of the vertical readings taken at 0.2H, 0.5H and 0.8H whereas velocity $\overline{U}$ is the average velocity in the cross-section containing the value U and was obtained by integrating the lateral velocity distribution. In all of these graphs, the local mean velocity, U, is normalized with respect to the average velocity, $\overline{U}$, and plotted against the lateral distance, y, normalized with the outfall diameter, D. These profiles are repeated for different longitudinal distances, i.e., x/D=0, 6, 12 and 24. Figures 4.1, 4.2 and 4.3 show the results of low and high velocity ratios for bottom, submerged and extended surface outfalls. A comparison of velocity results taken at 0.8H is made in Fig. 4.4 between Runs 17 and 18 for extended surface outfall for R=2 and 5.2, respectively.

Five additional detailed velocity tests for Runs 2, 3, 10, 11 and 25 were performed to obtain qualitative and quantitative information about the velocity distribution near the outlet. Typical velocity results are shown in Figs. 4.5 to 4.7.

4.1.2 Photographs

Exploratory photographs were taken with potassium permanganate dye carried in the jet as shown in Photographs 4.1 to 4.8. Photographs 4.1 and 4.2 show the turbulent

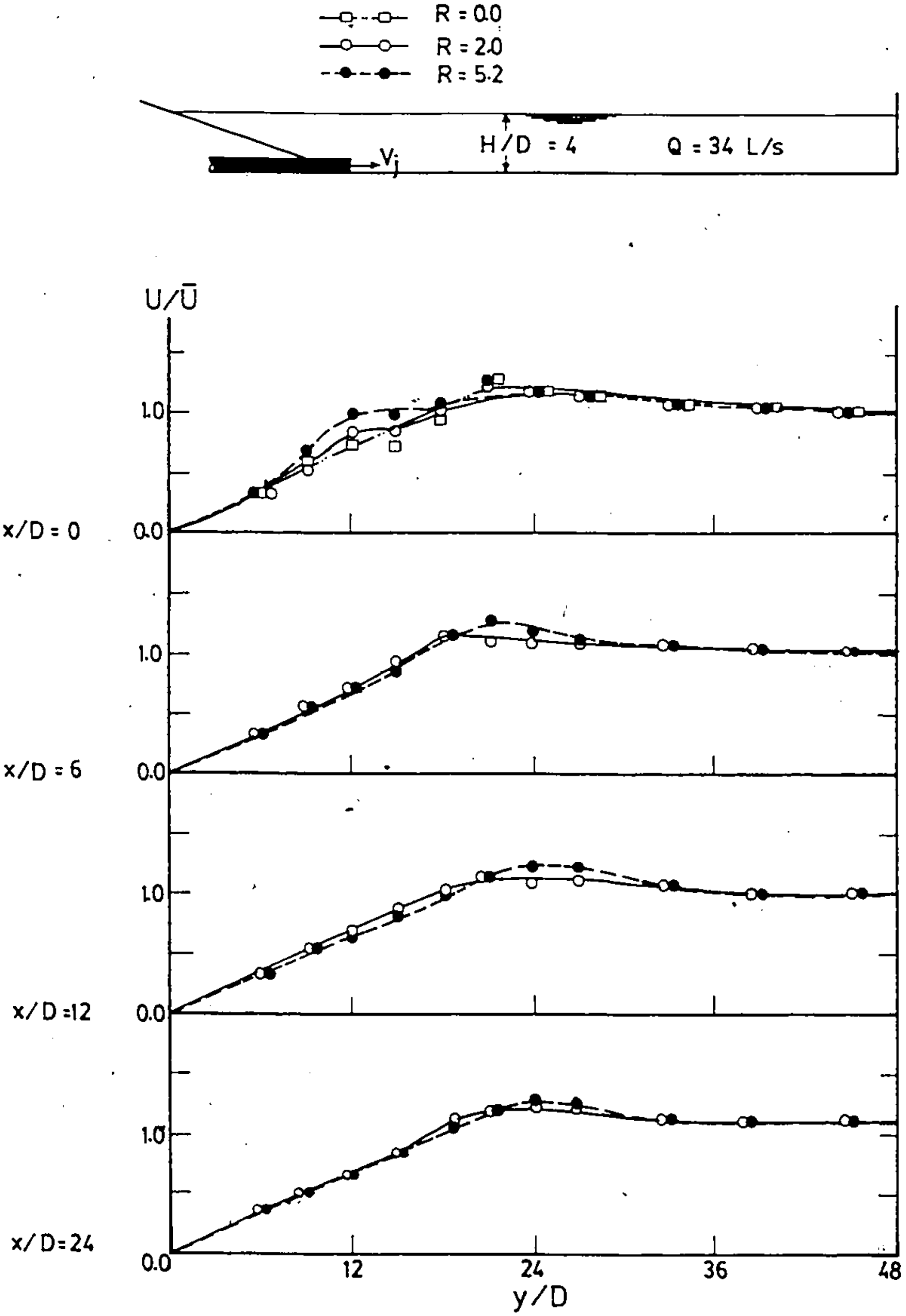

Fig. 4.1. Lateral velocity profiles for bottom outfall - Exps. 2 and 3.

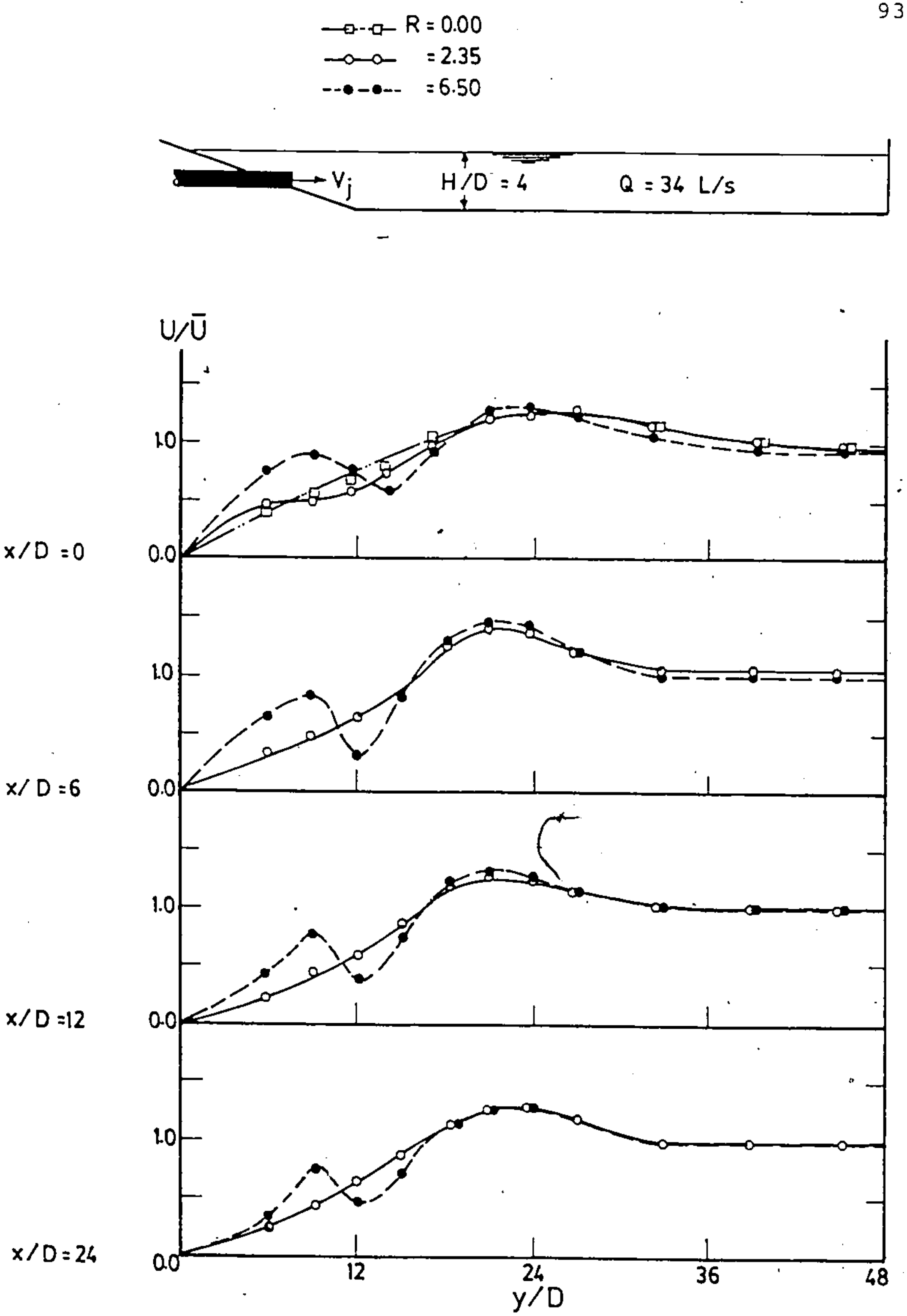

Fig. 4.2. Lateral velocity profiles for submerged outfall - Exps. 10 and 11.

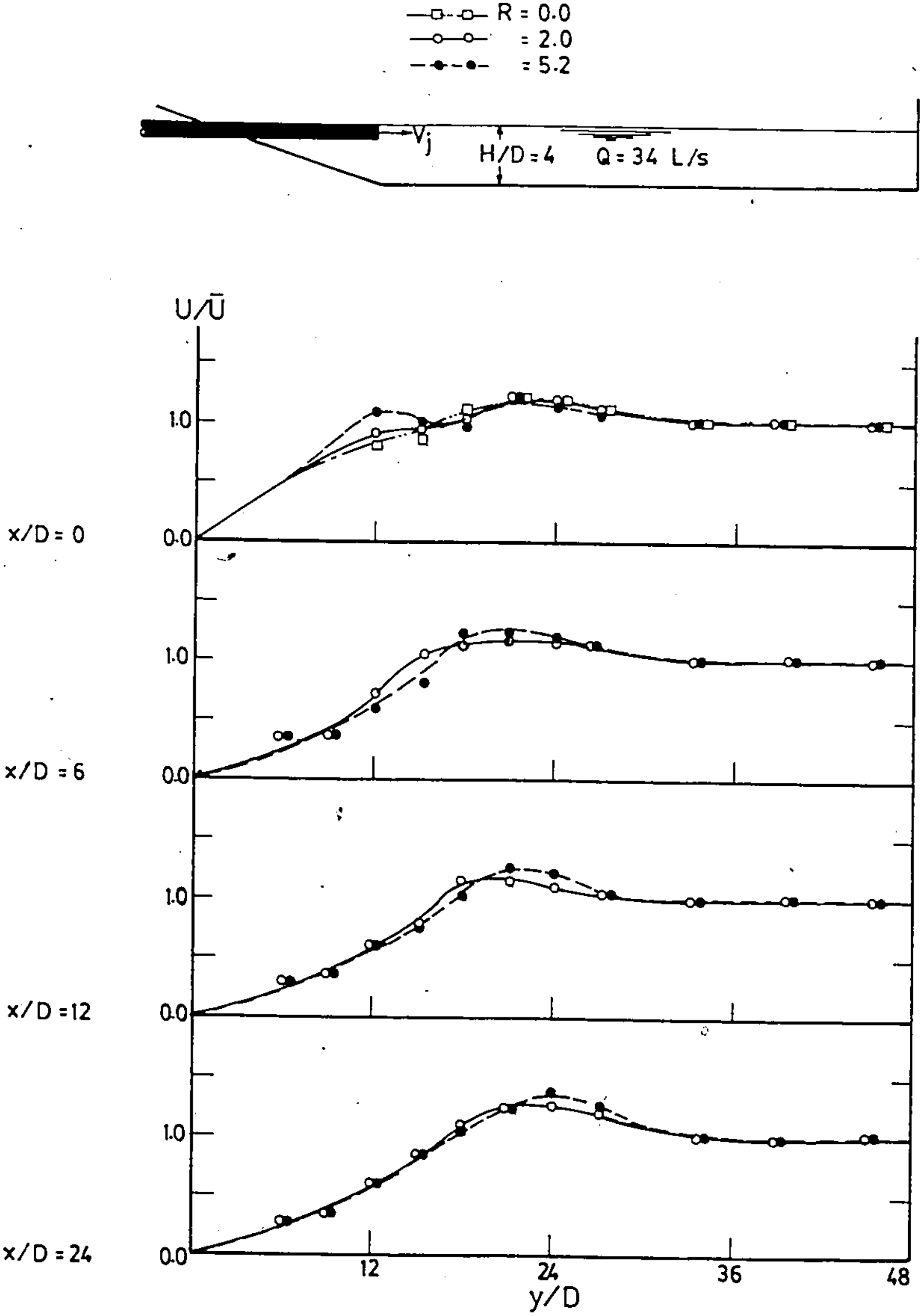

Fig. 4.3. Lateral velocity profiles for extended surface outfall - Exps. 17 and 18.

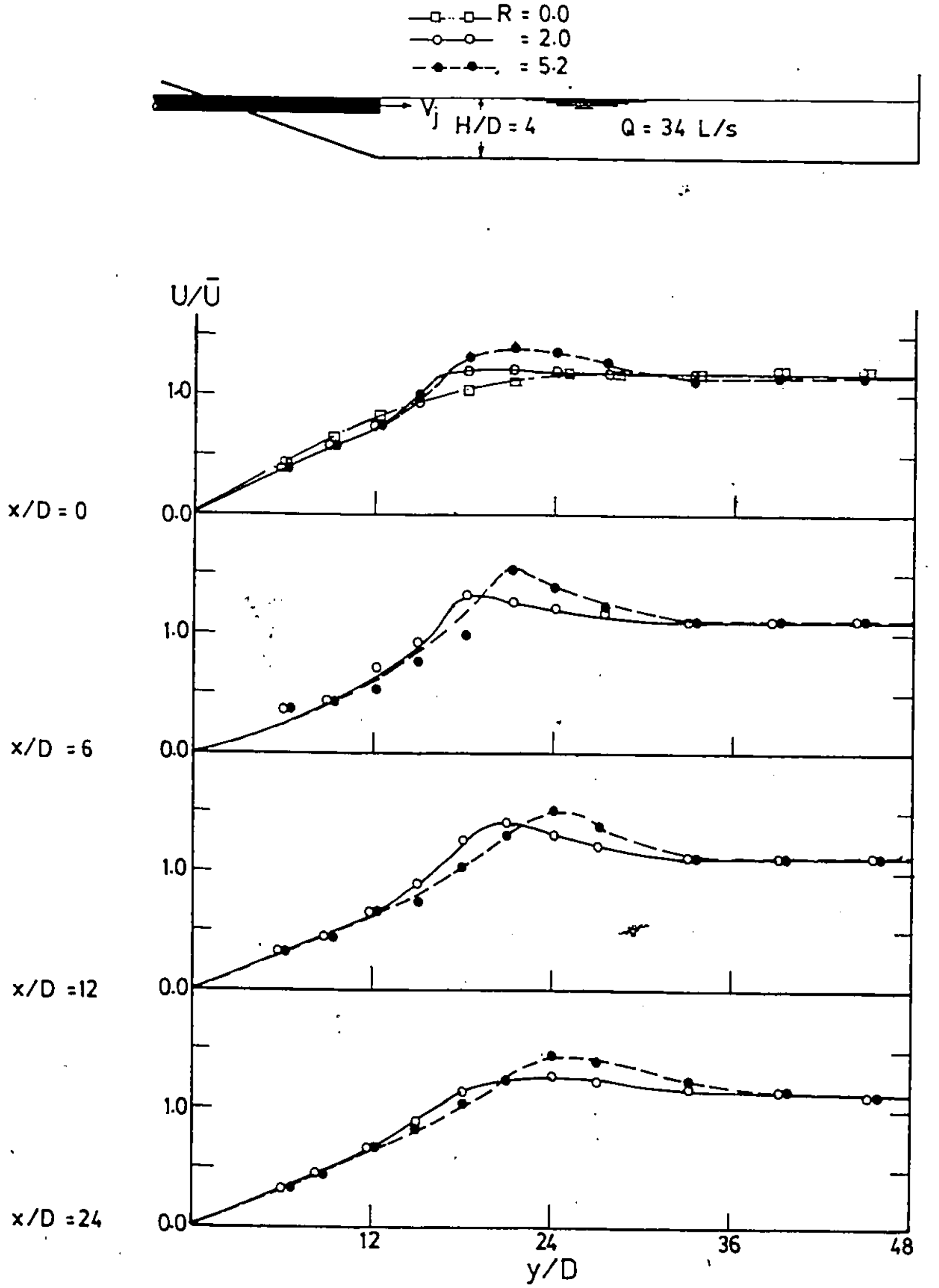

Fig. 4.4. Lateral velocity profiles for extended surface outfall taken at 0.8H - Exps. 17 and 18.

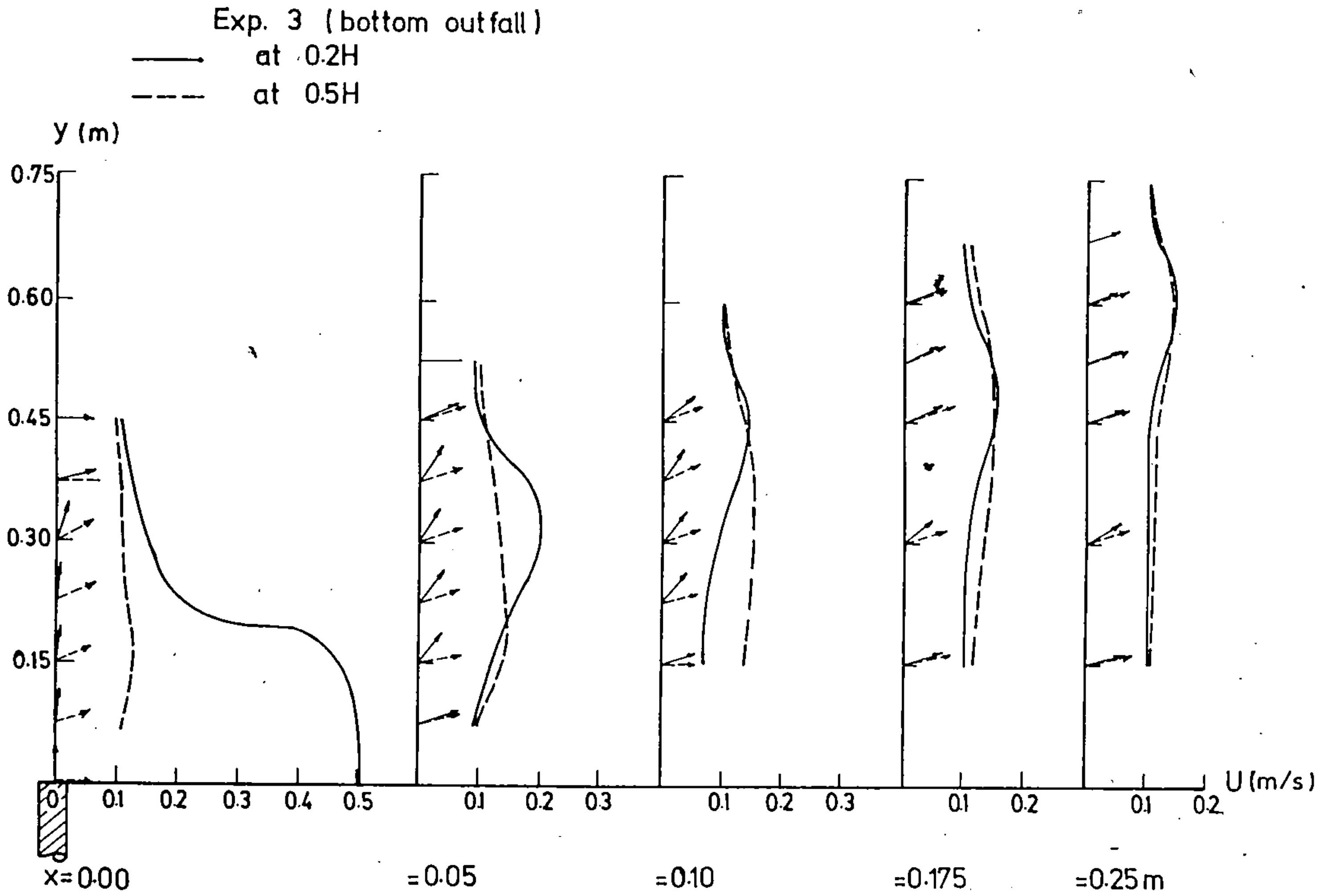

Fig. 4.5. Magnitude and Direction of Velocity vector of Exp. 3.

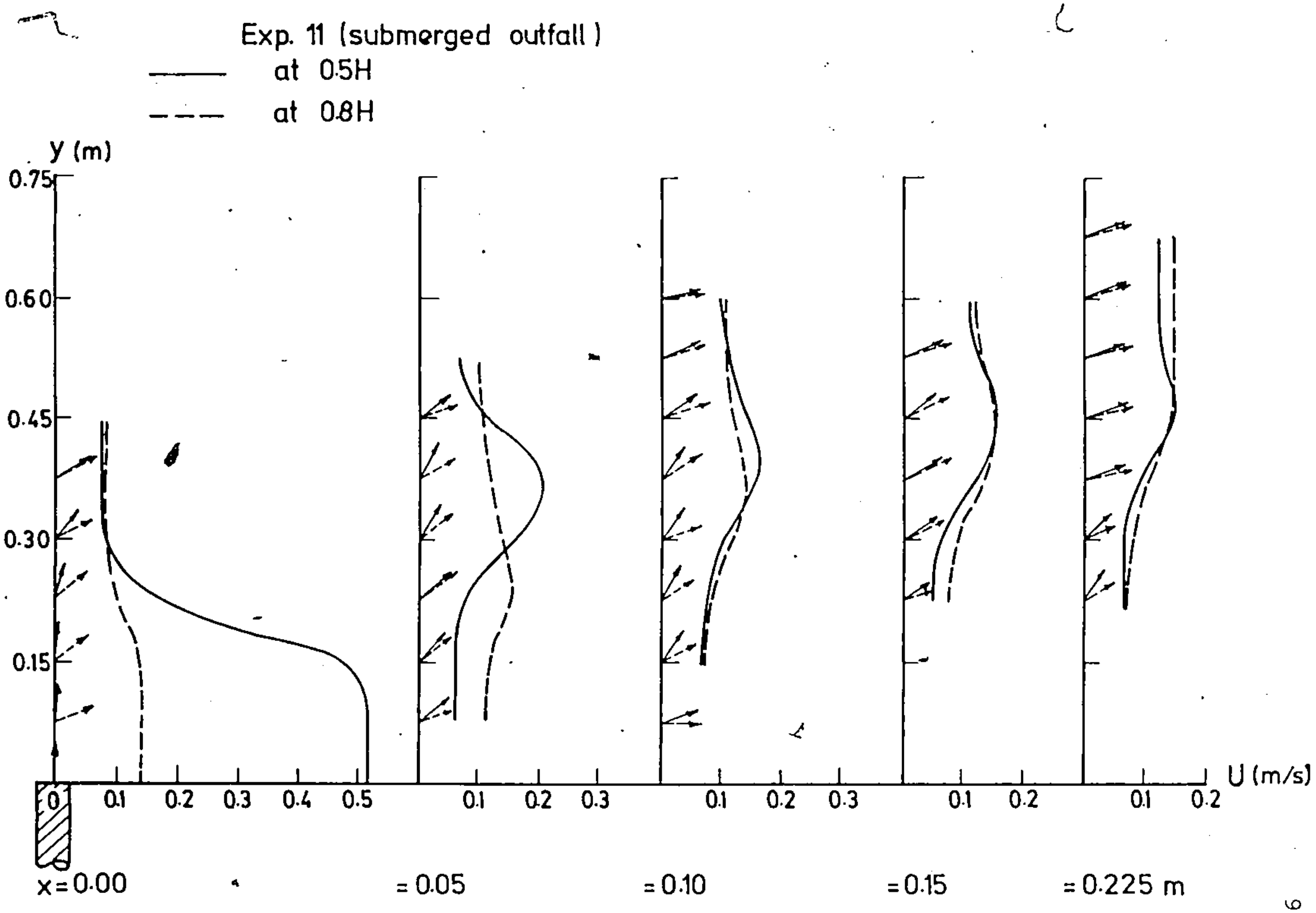

Fig. 4.6. Magnitude and Direction of Velocity Vector of Exp. 11.

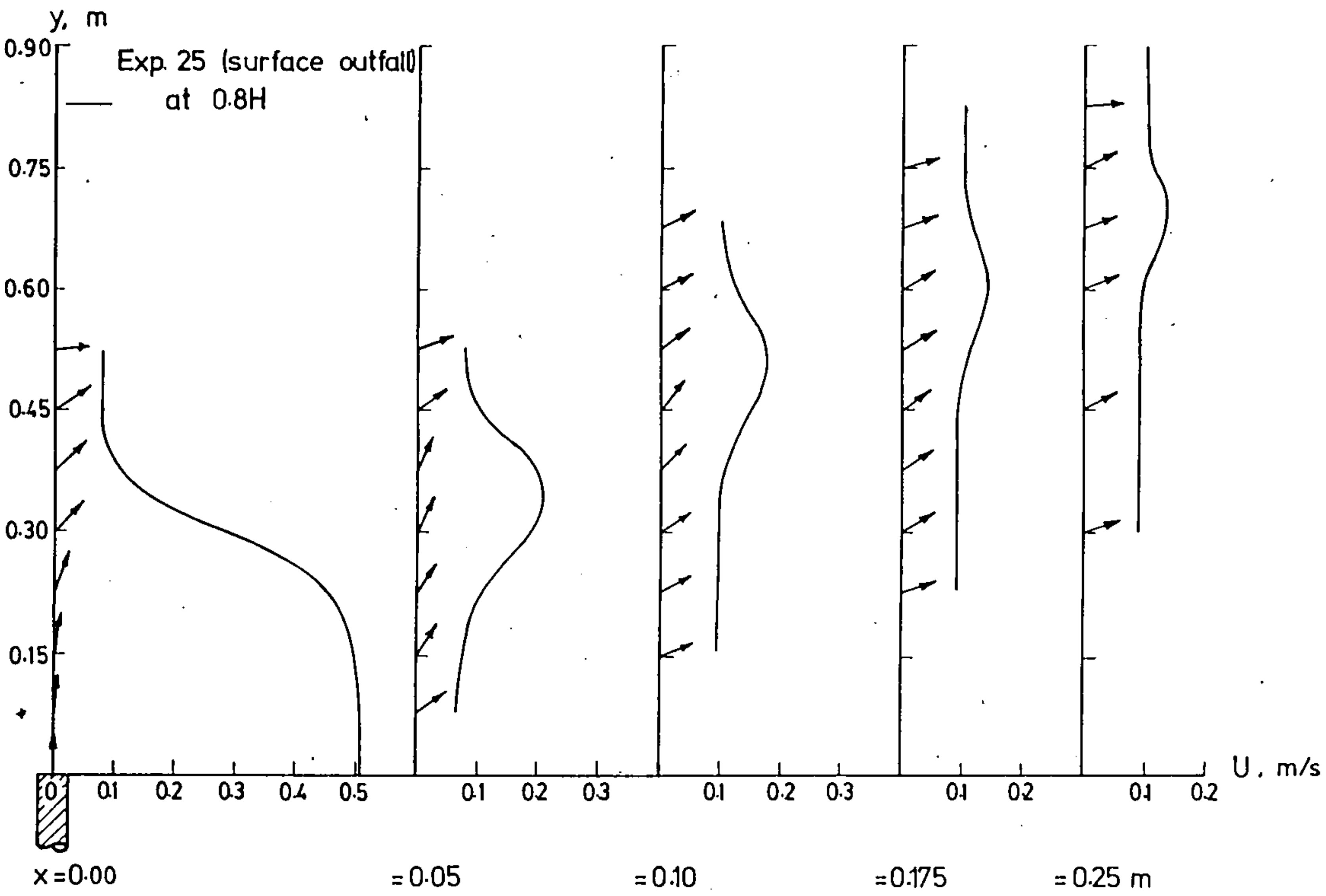

Fig. 4.7. Magnitude and Direction of Velocity Vector of Exp. 25.

jet discharged normal to the ambient flow, for two velocity ratios, where the outfall was initially at the bottom. In Photographs 4.3 and 4.4, the outfall was submerged between the water surface and the channel bed. For Photographs 4.5 and 4.6, the discharged jet was released at the surface through the extended outfall, whereas in Photographs 4.7 and 4.8 the outfall was set flush with the side slope of the channel.

Photographs 4.9 to 4.12 show laboratory simulations of turbulent buoyant jets in which Photographs 4.9 and 4.10 were taken for a bottom outfall and Photographs 4.11 and 4.12 were taken for a shore-based surface outfall. Plan view photographs for all dye tests were also taken and are shown in Appendix B.

4.1.3 Concentration Profiles of Non-buoyant Jets

A series of 9 tests was made to describe the behaviour of a non-buoyant circular bottom and surface jets discharged into cross-flowing ambients. The ranges for the experimental variables were the same as those given for the velocity tests. Typical concentration profiles of non-buoyant jets in vertical and lateral directions for Runs 1, 2, 3, 5, 6, 7, 24, 25 and 26 are shown in Figs. 4.8 to 4.19. In all these figures, the dye concentration, C, is noramlized with respect to the initial concentration, C_o, taken at the outfall.

COLOURED PICTURES
Images en couleur

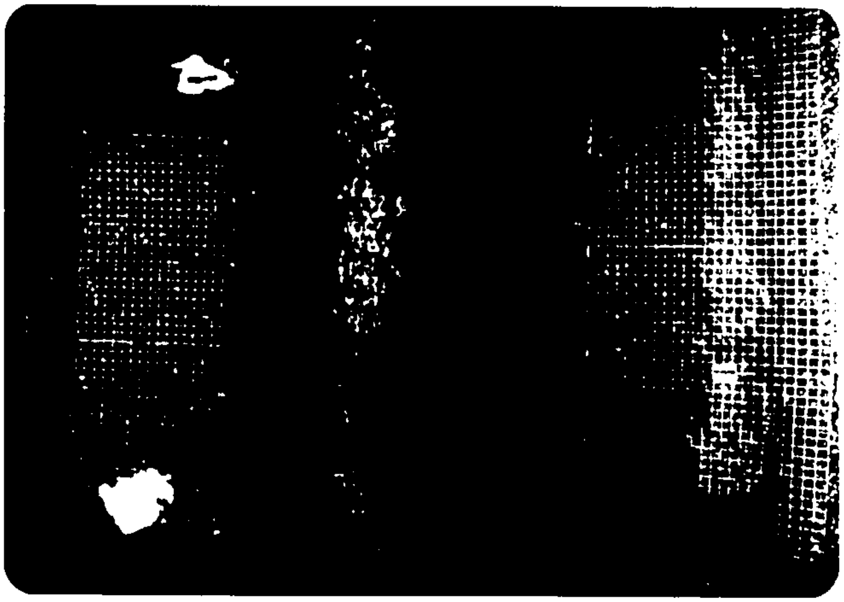

Photo 4.2. Plan view of non-buoyant bottom jet. Exp. 3 (R=5.2, H/D=4.0).

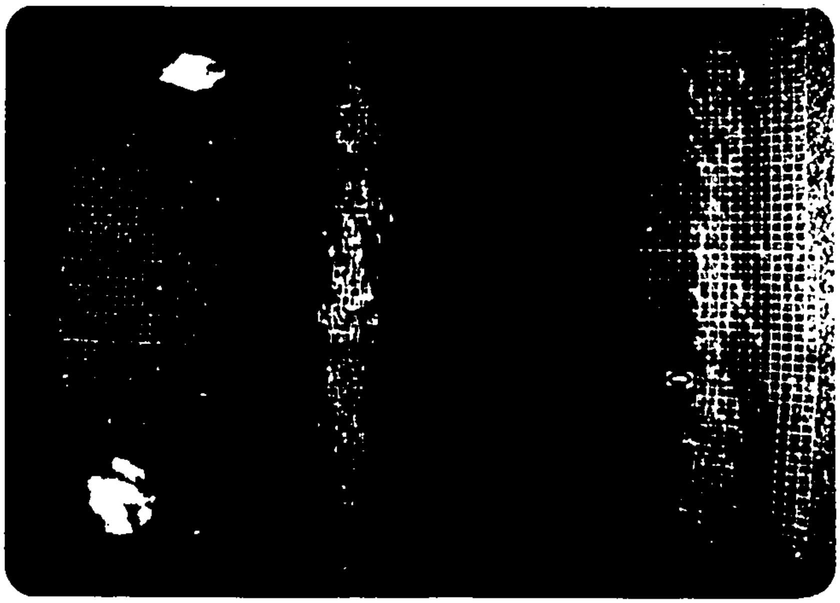

Photo 4.1. Plan view of non-buoyant bottom jet. Exp. 2 (R=2.0, H/D=4.0).

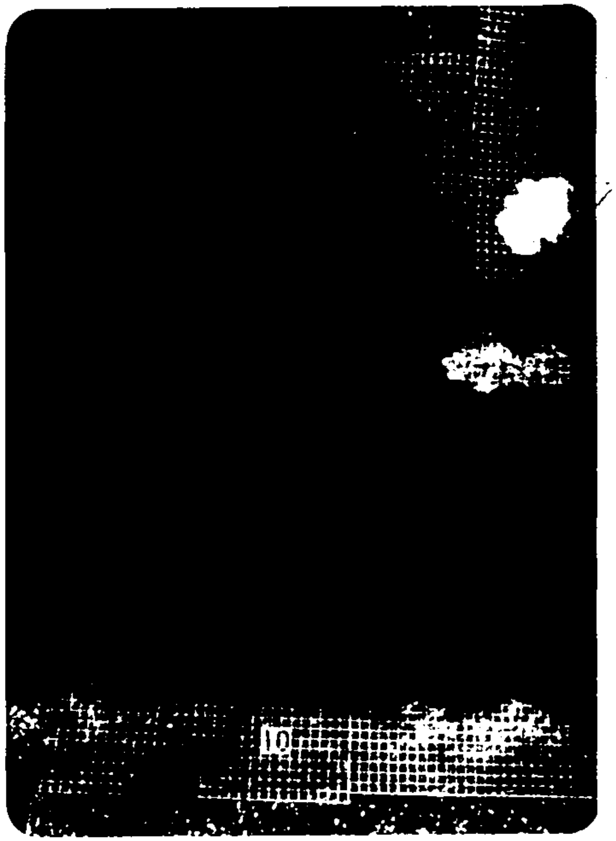

Photo 4.3. Plan View of non buoyant submerged Jet - Exp. 10 (R=2.0 , H/D=4.0)

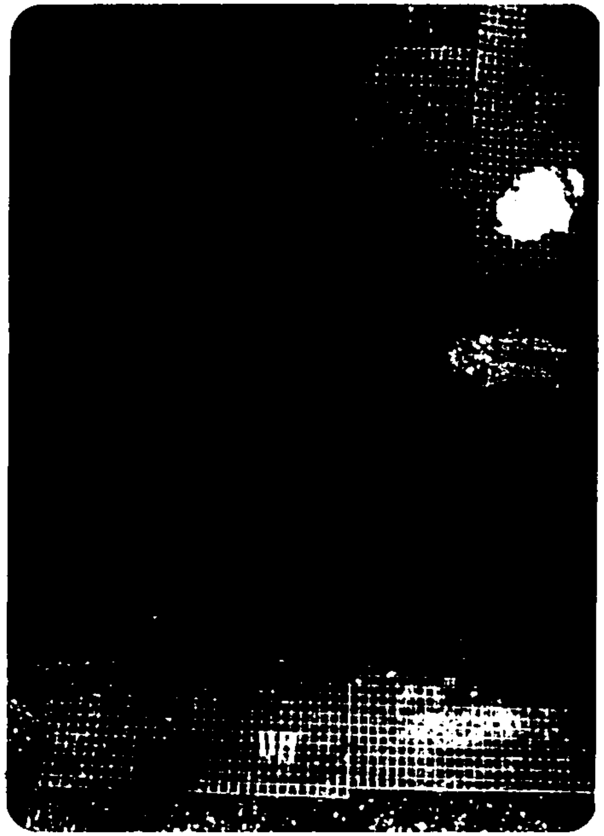

Photo 4.4. Plan View of non-boyant submerged jet - Exp. 11 (R=5.5, H/D=4.0).

COLOURED PICTURES
Images en couleur

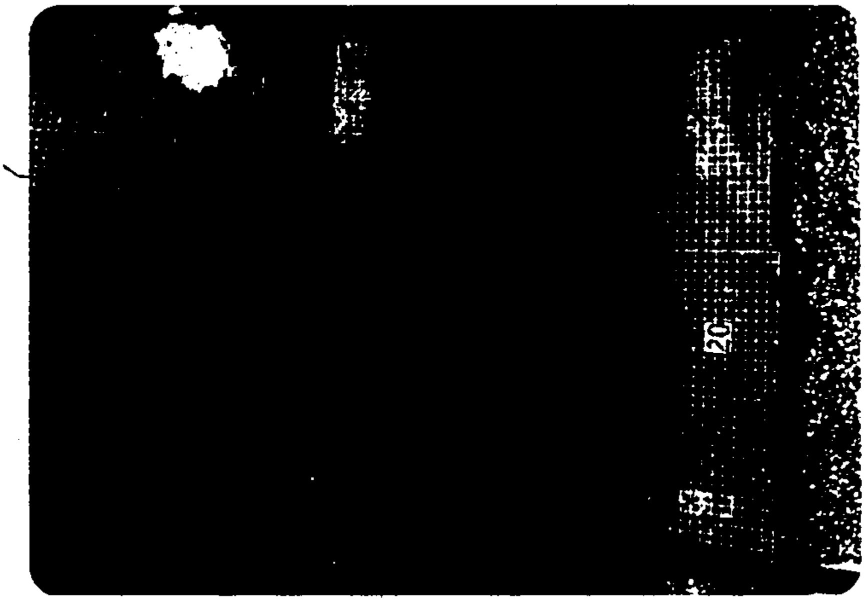

Photo 4.5. Plan view of non-buoyant extended surface jet - Exp. 17 (R=2.0, H/D=4.0)

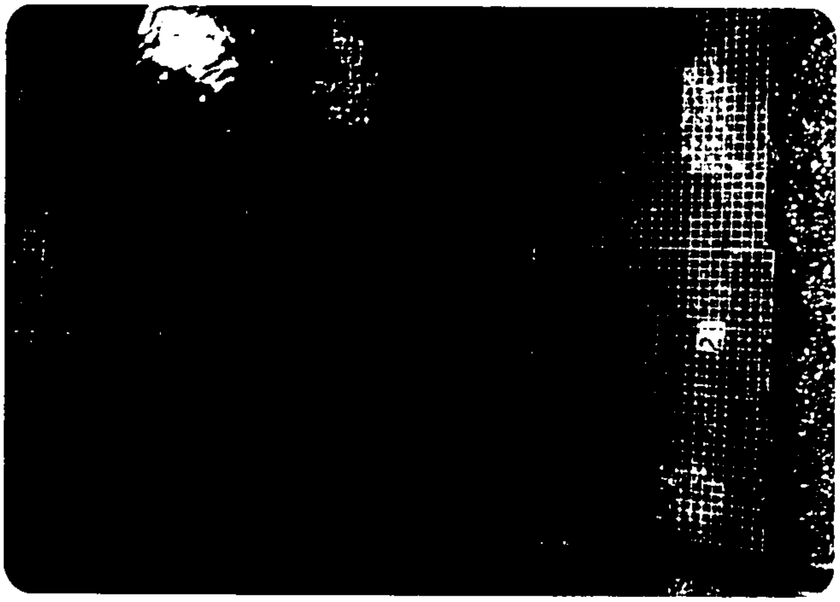

Photo 4.6. Plan view of non-buoyant extended surface jet - Exp. 18 (R=5, H/D=4.0).

COLOURED PICTURES
Images en couleur

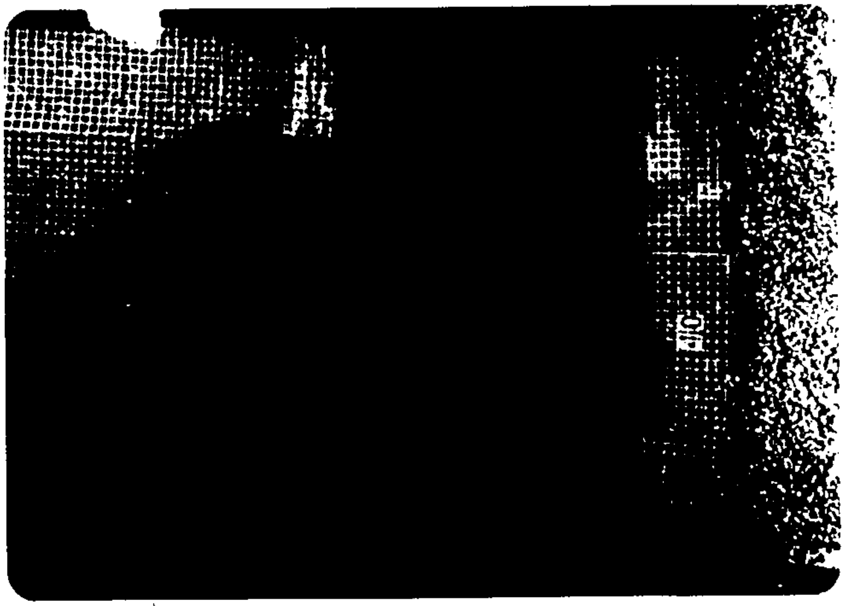

Photo 4.7. Plan view of non-buoyant shore-based surface Jet - Exp. 24 (R=2.0, H/D=4.0).

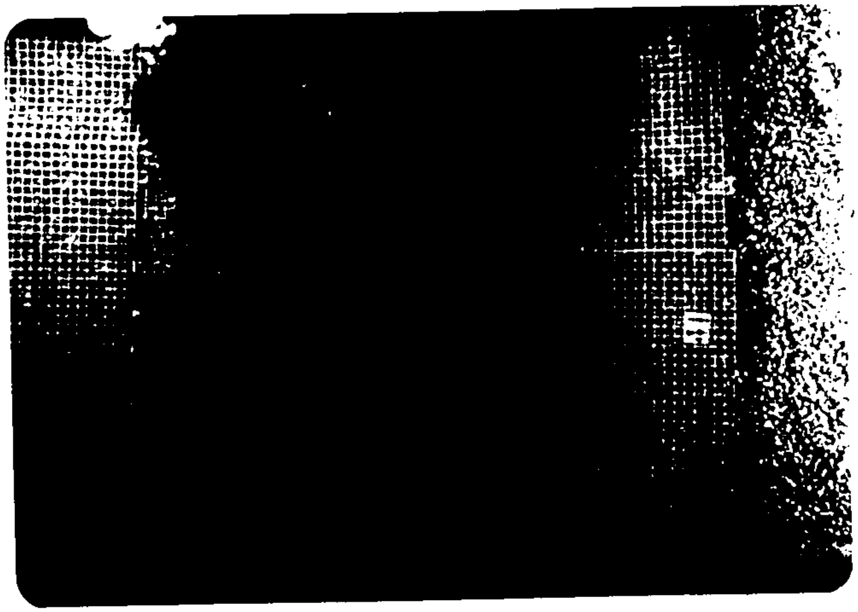

Photo 4.8 Plan view of non-buoyant shore-based surface jet - Exp. 25 (R=2.0, H/D=4.0).

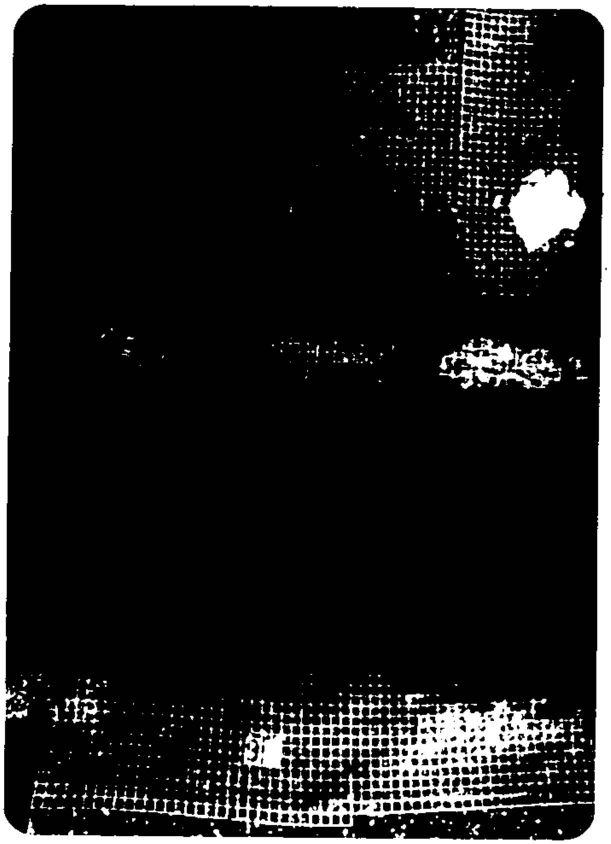

Photo 4.9. Plan view of buoyant bottom jet - Exp. 2-1 ($R=2.0$, $H/D=4.0$, $F_o = 4.32$).

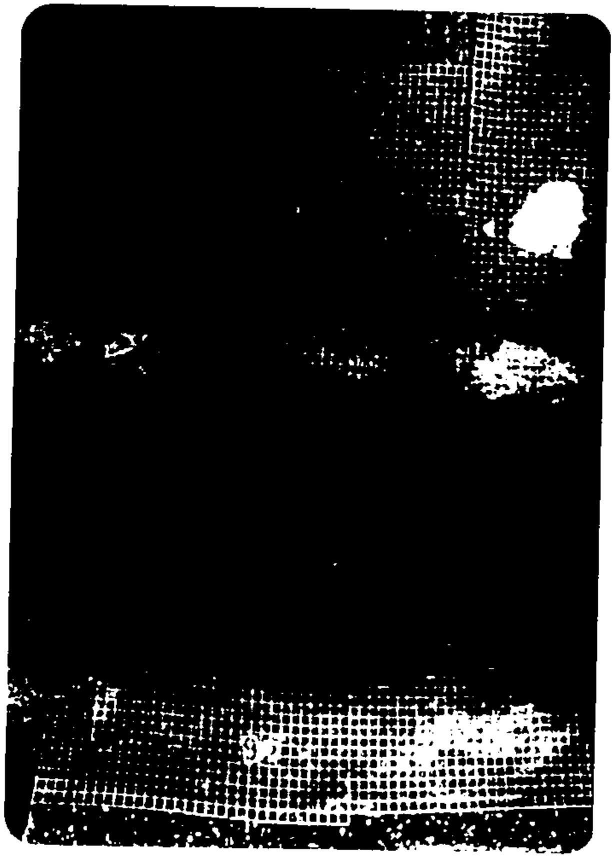

Photo 4.10 Plan view of buoyant bottom Jet - Exp. 3-1 ($R=5.2$, $H/D=4.0$, $F_o=14.17$)

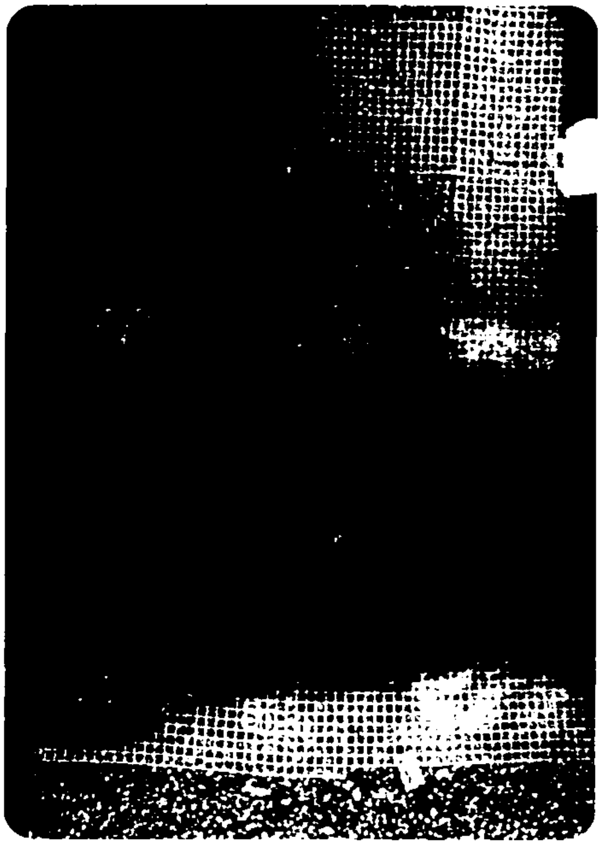

Photo 4.11. Plan view of buoyant shore-based surface jet - Exp. 24-1 (R=2.0, H/D=4.0, F_o=5.32).

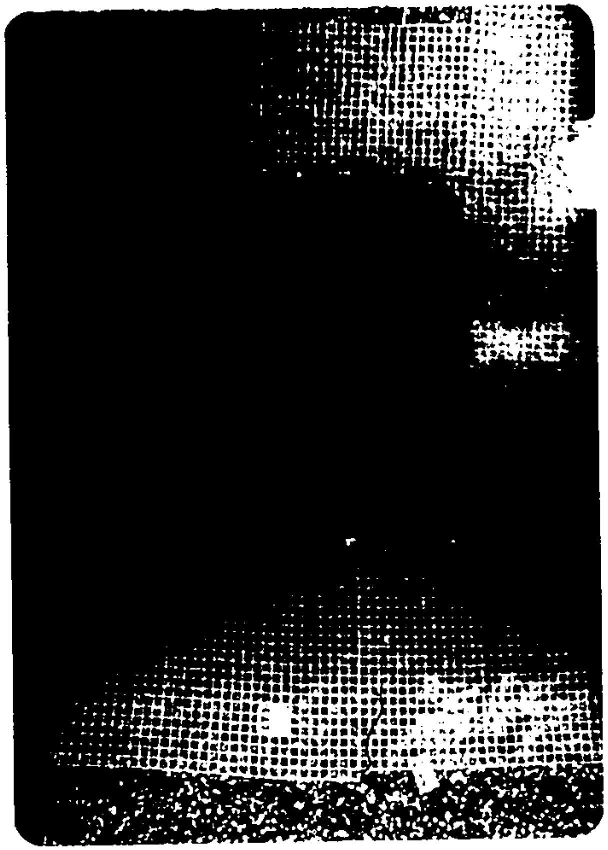

Photo 4.12. Plan view of buoyant shore-based surface jet - Exp. 25-2 (R=5.2, H/D=4.0, F_o=16.9).

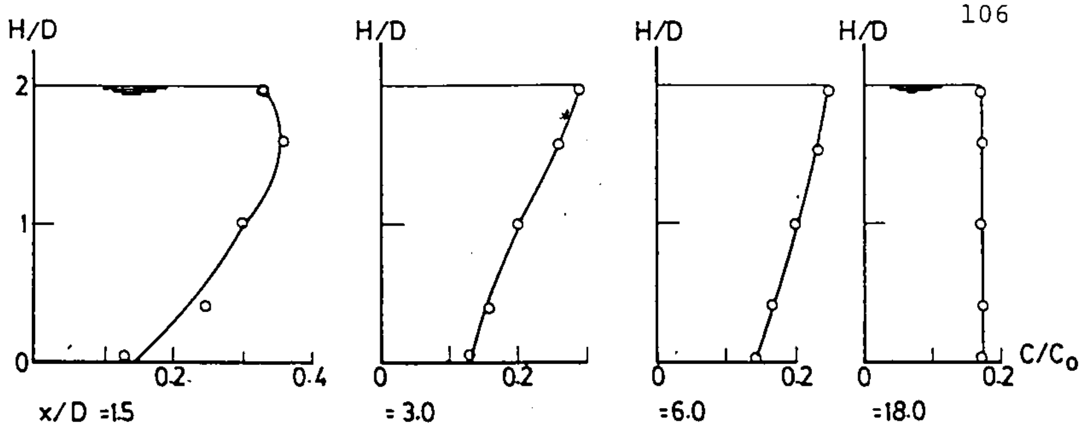

Fig. 4.8. Vertical concentration profiles for Exp. 1.

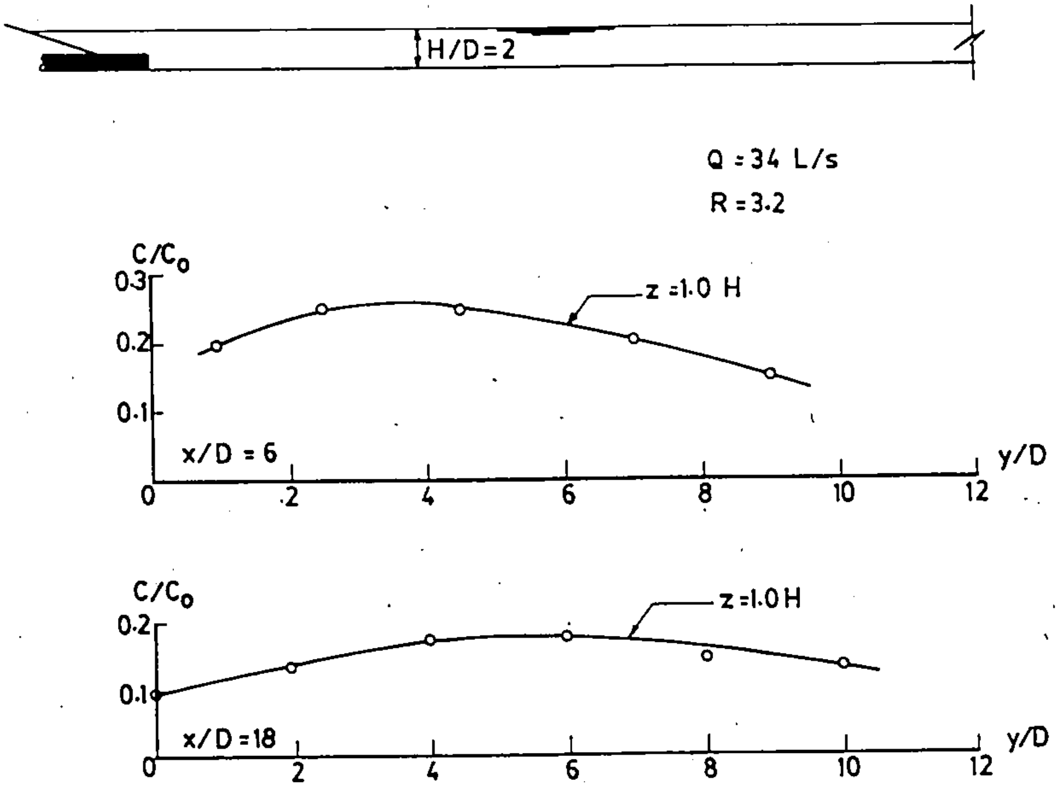

Fig. 4.9. Lateral concentration profiles for Exp. 1.

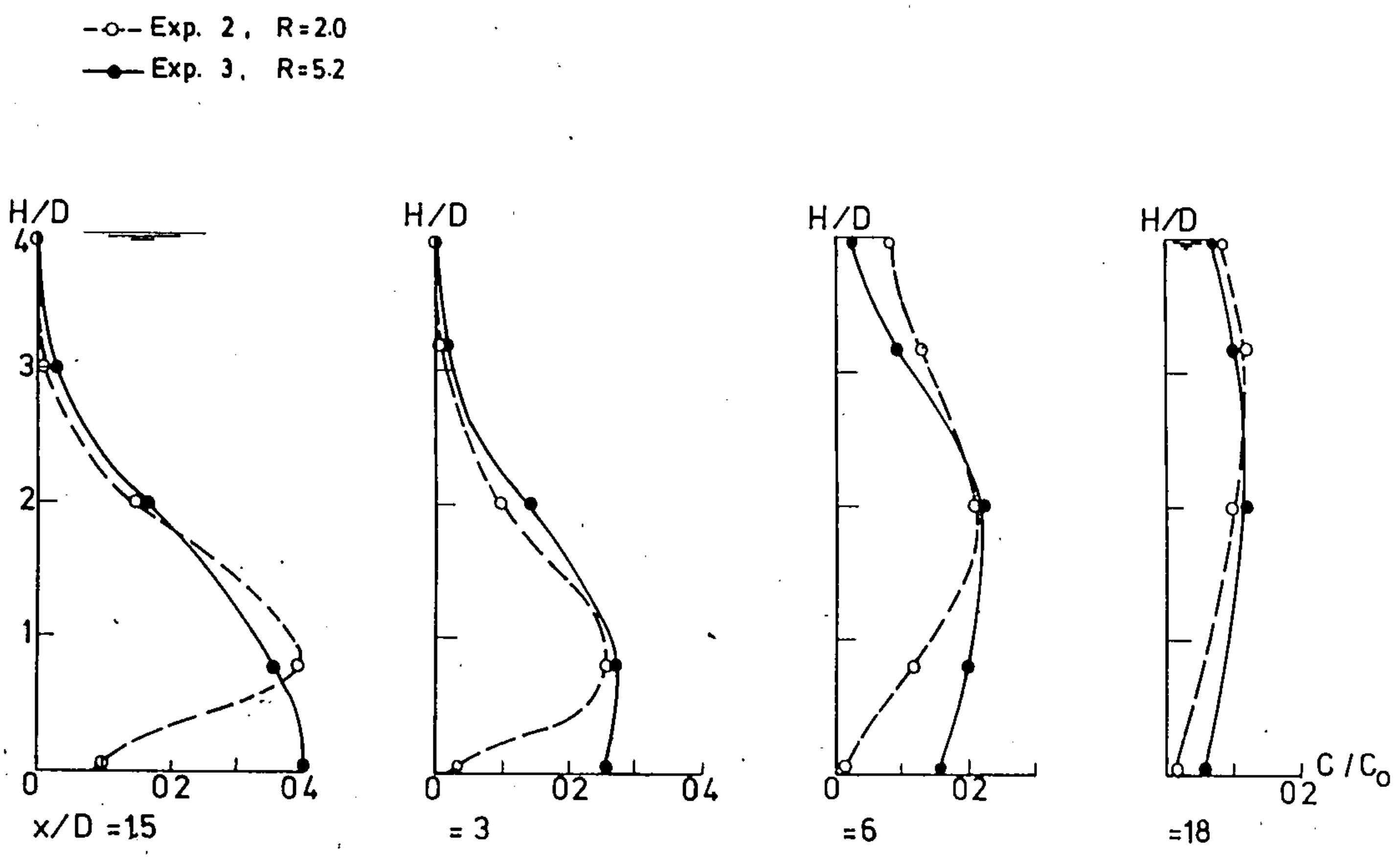

Fig. 4.10. Vertical concentration profiles for Exps. 2 and 3.

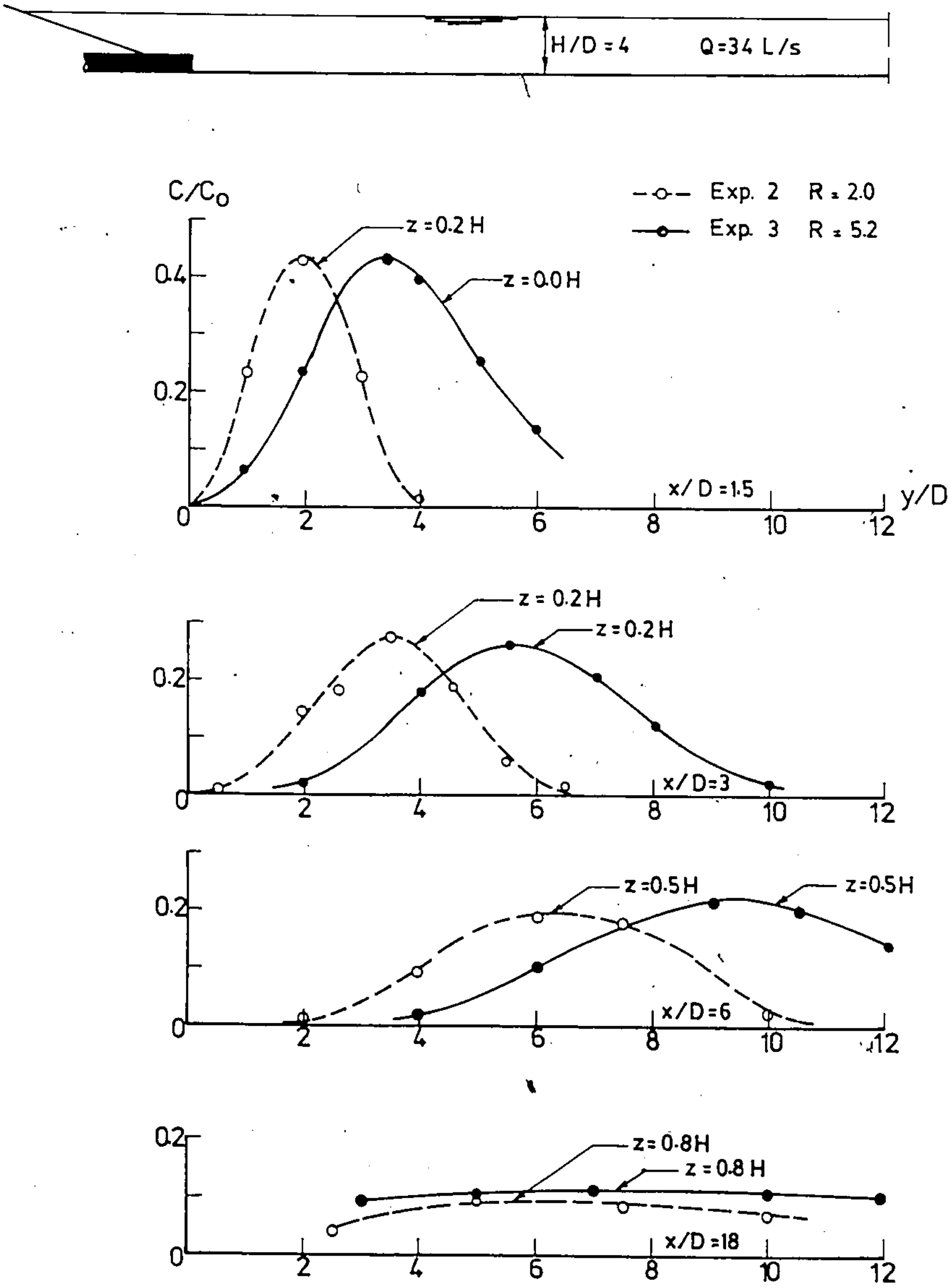

Fig. 4.11. Lateral concentration profiles for Exps. 2 and 3.

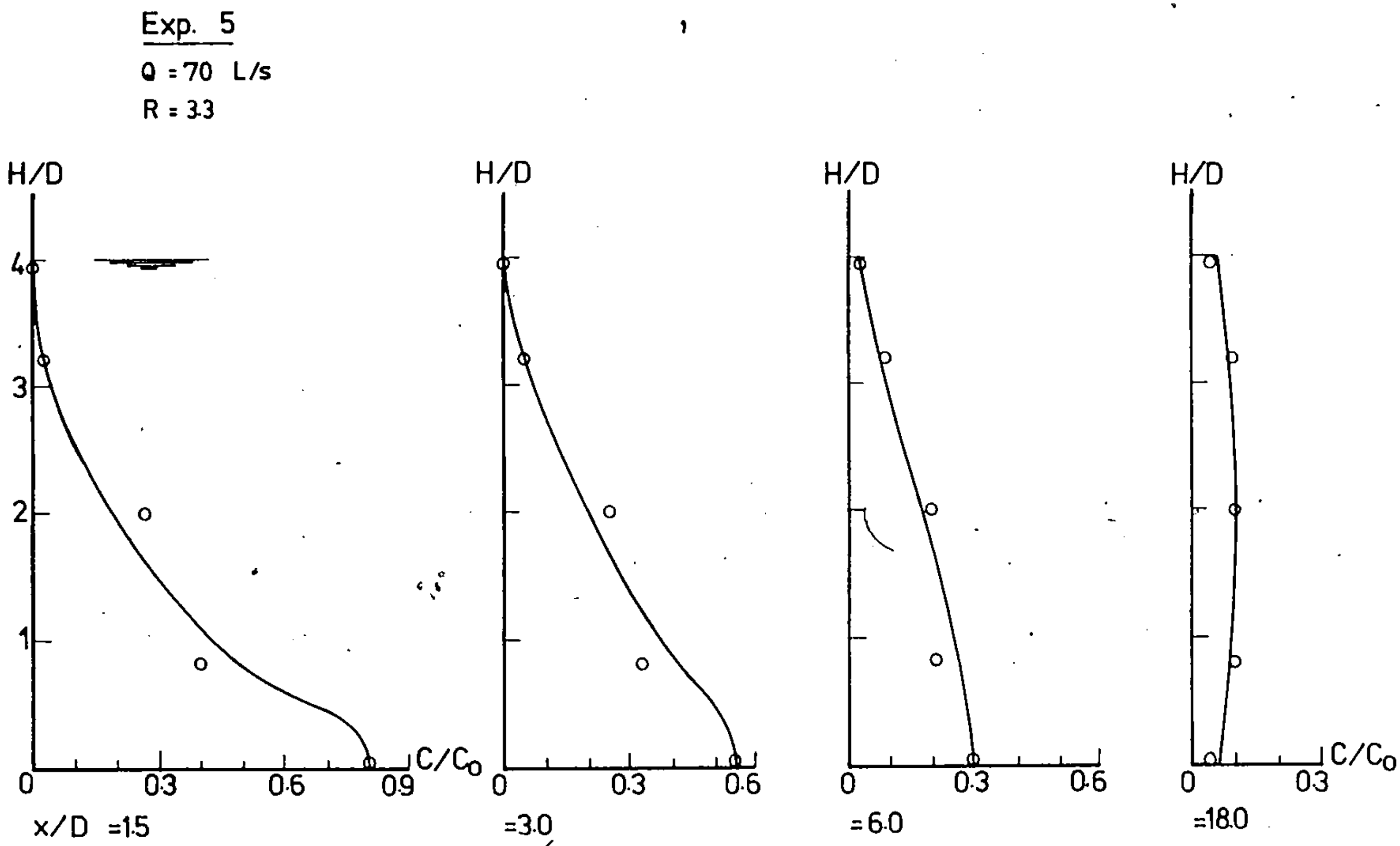

Fig. 4.12. Vertical Concentration Profiles for Exp. 5.

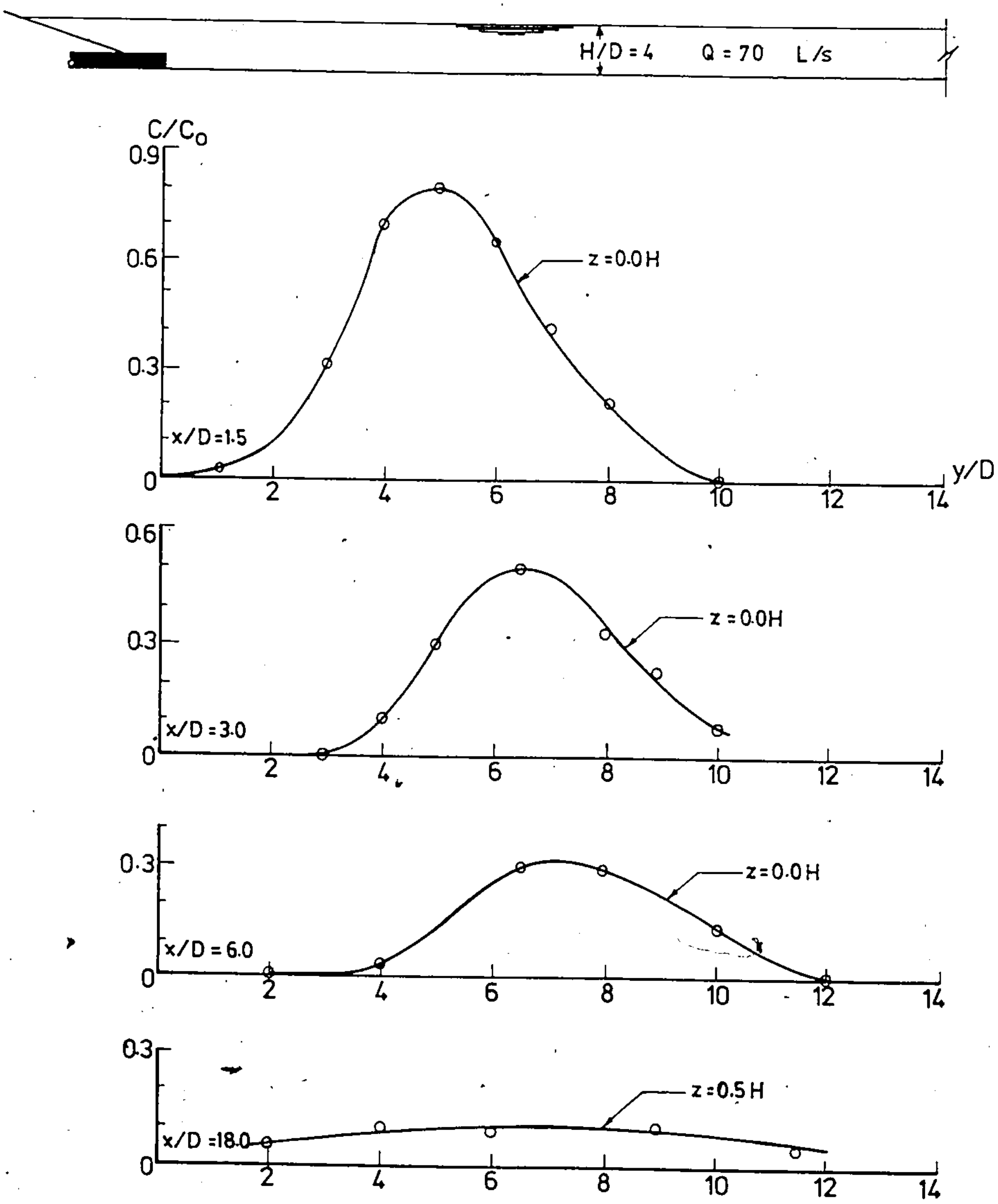

Fig. 4.13. Lateral Concentration Profiles for Exp. 5.

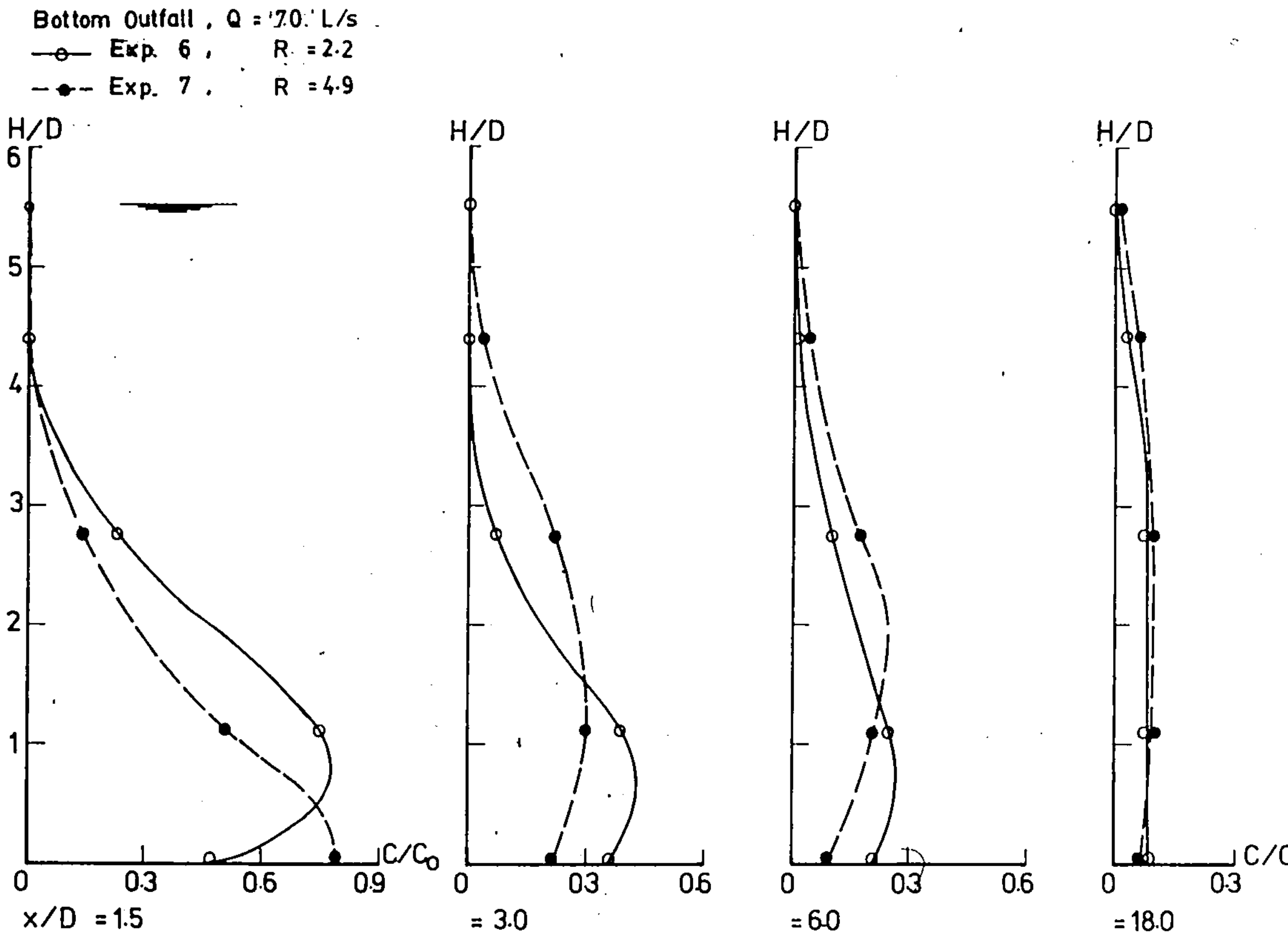

Fig. 4.14. Vertical Concentration Profiles for Exps. 6 and 7.

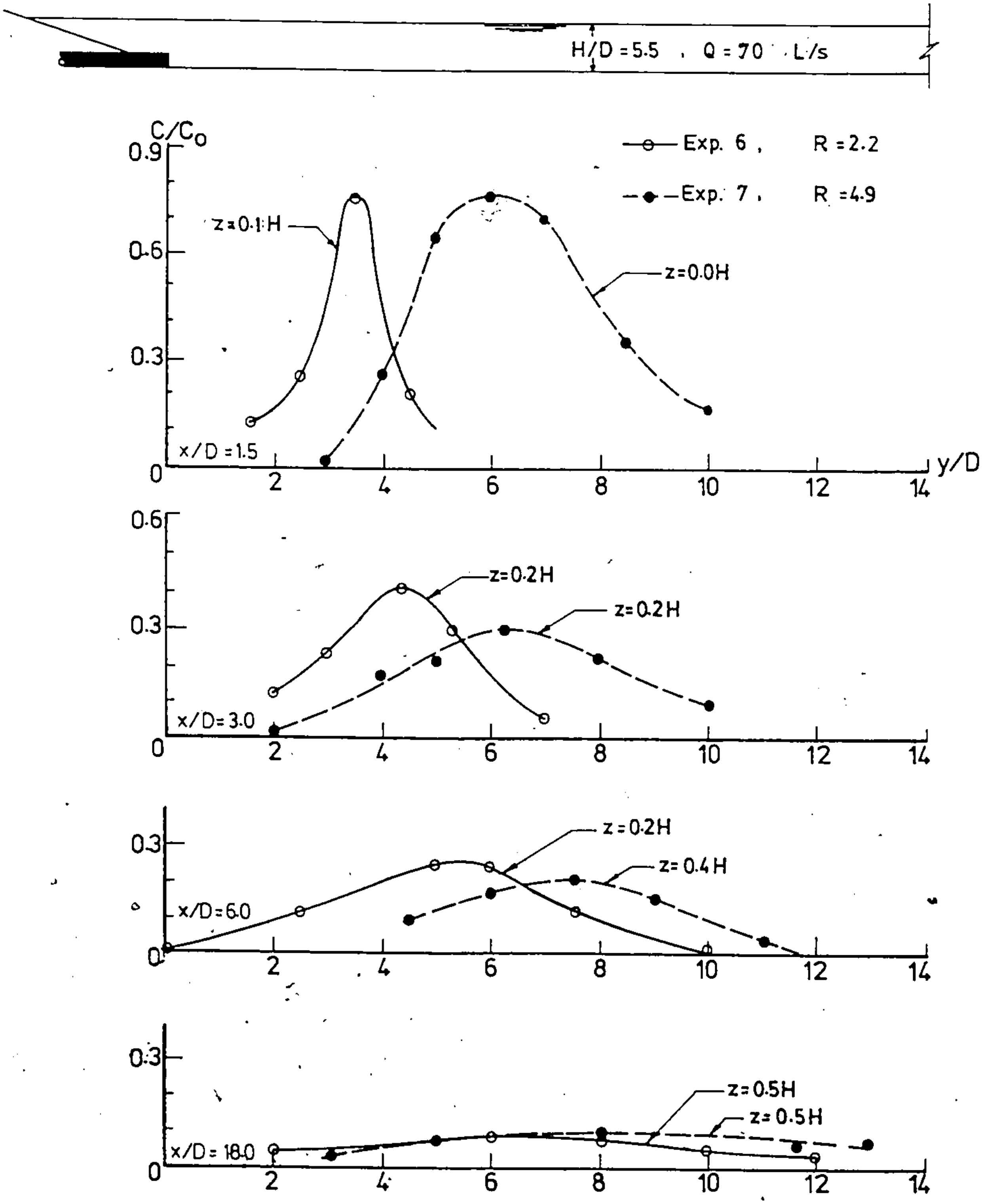

Fig. 4.15. Lateral Concentration Profiles for Exps. 6 and 7.

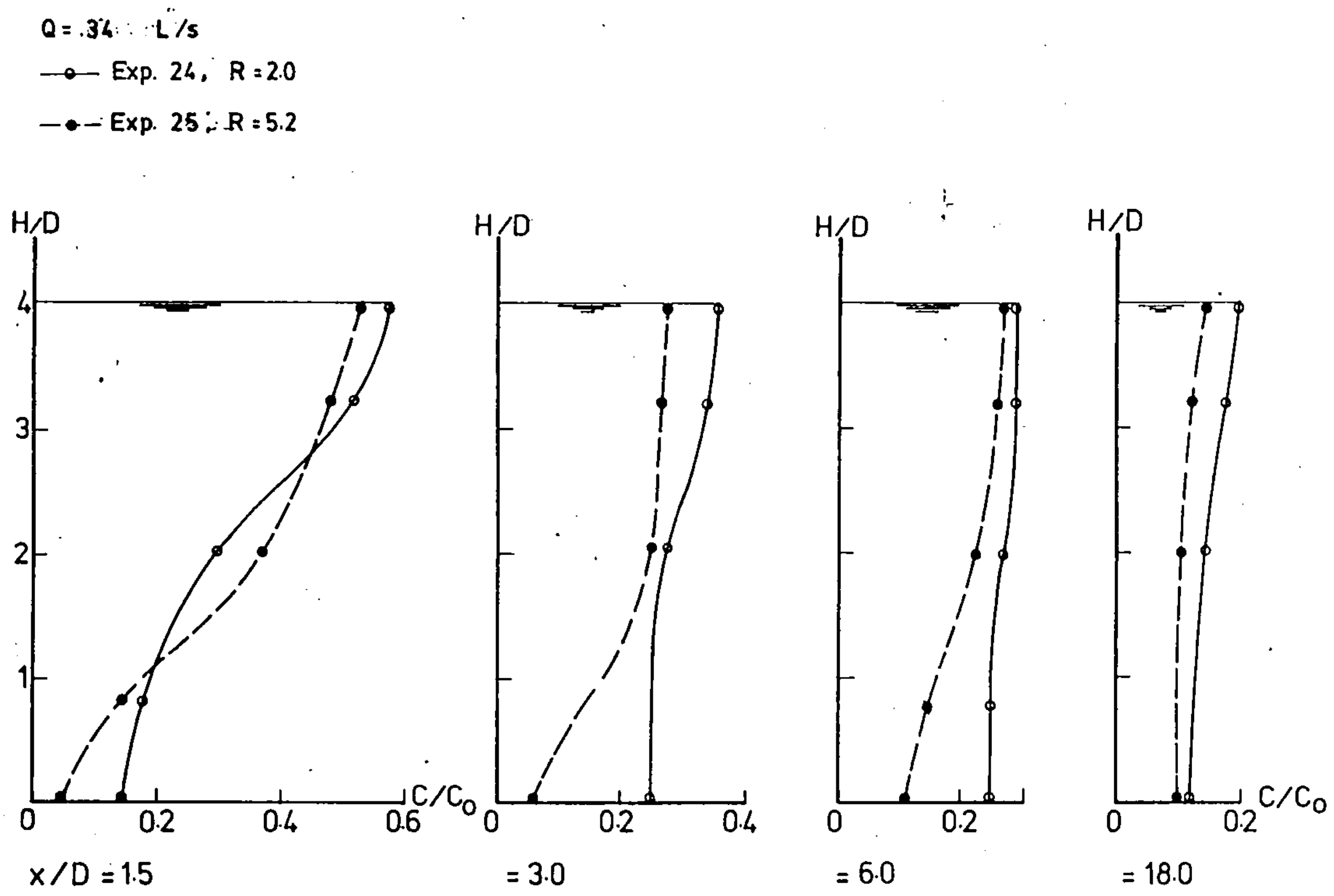

Fig. 4.16. Vertical Concentration Profiles for Exps. 24 and 25.

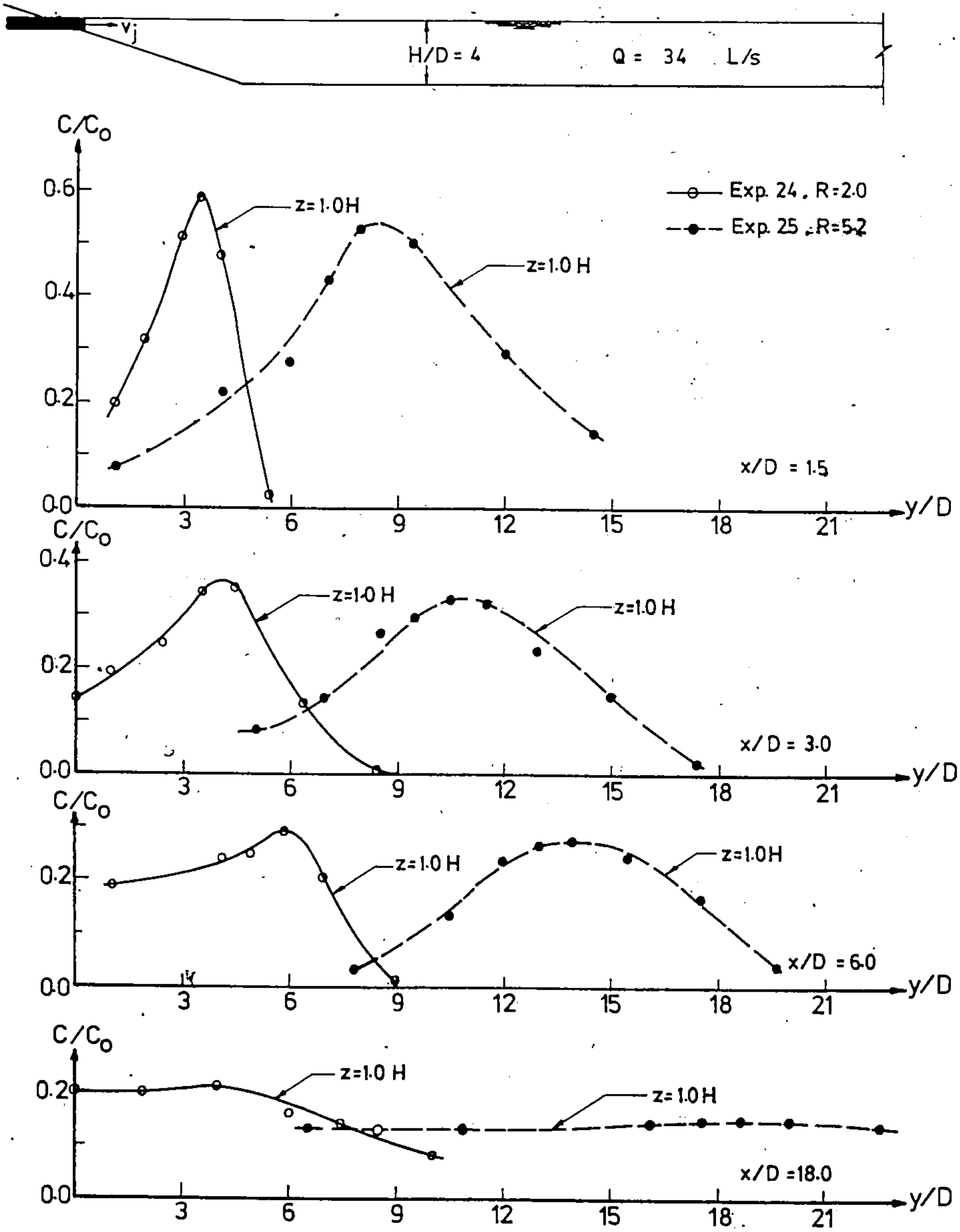

Fig. 4.17. Lateral Concentration Profiles for Exps. 24 and 25.

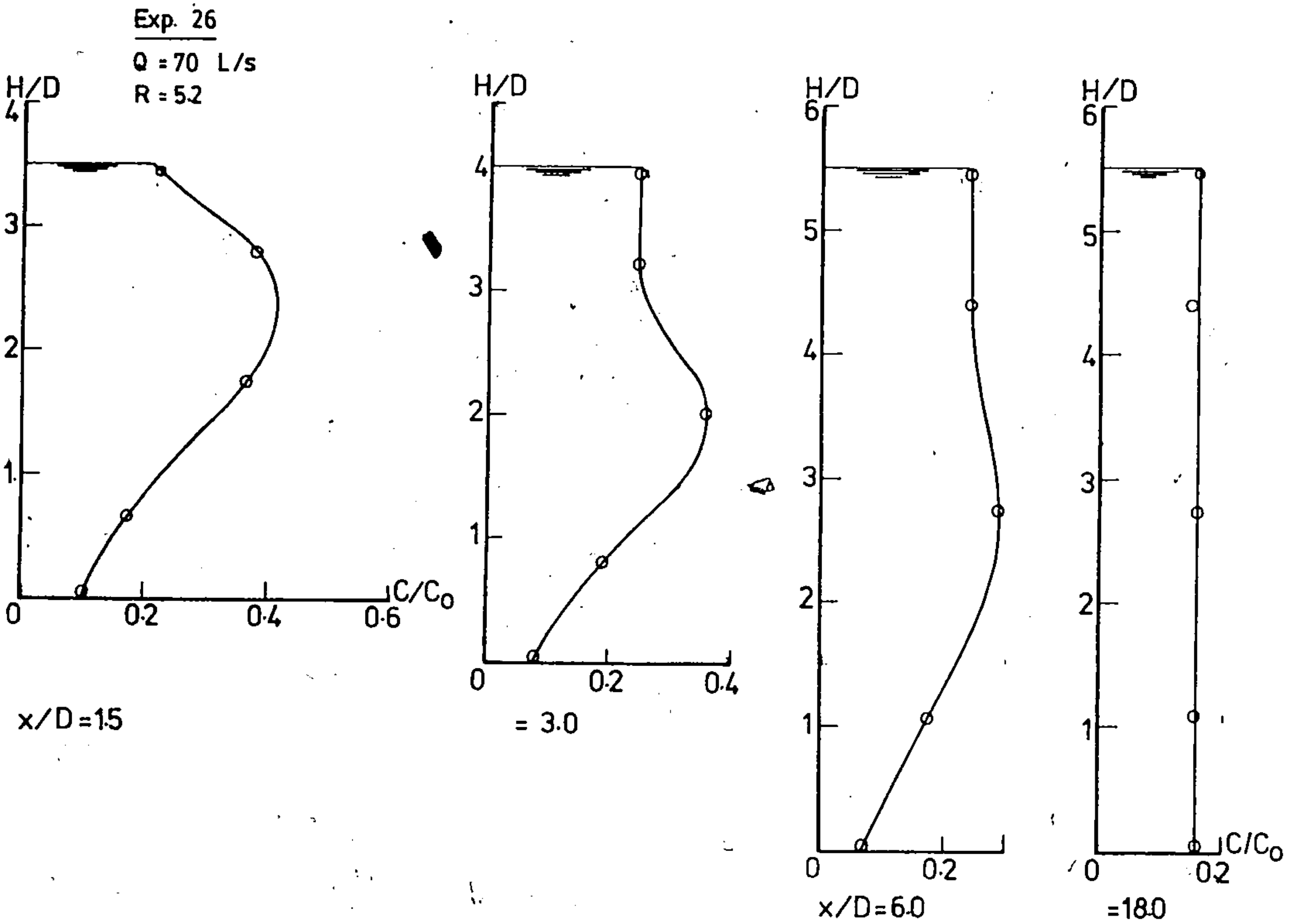

Fig. 4.18. Vertical Concentration Profiles for Exp. 26.

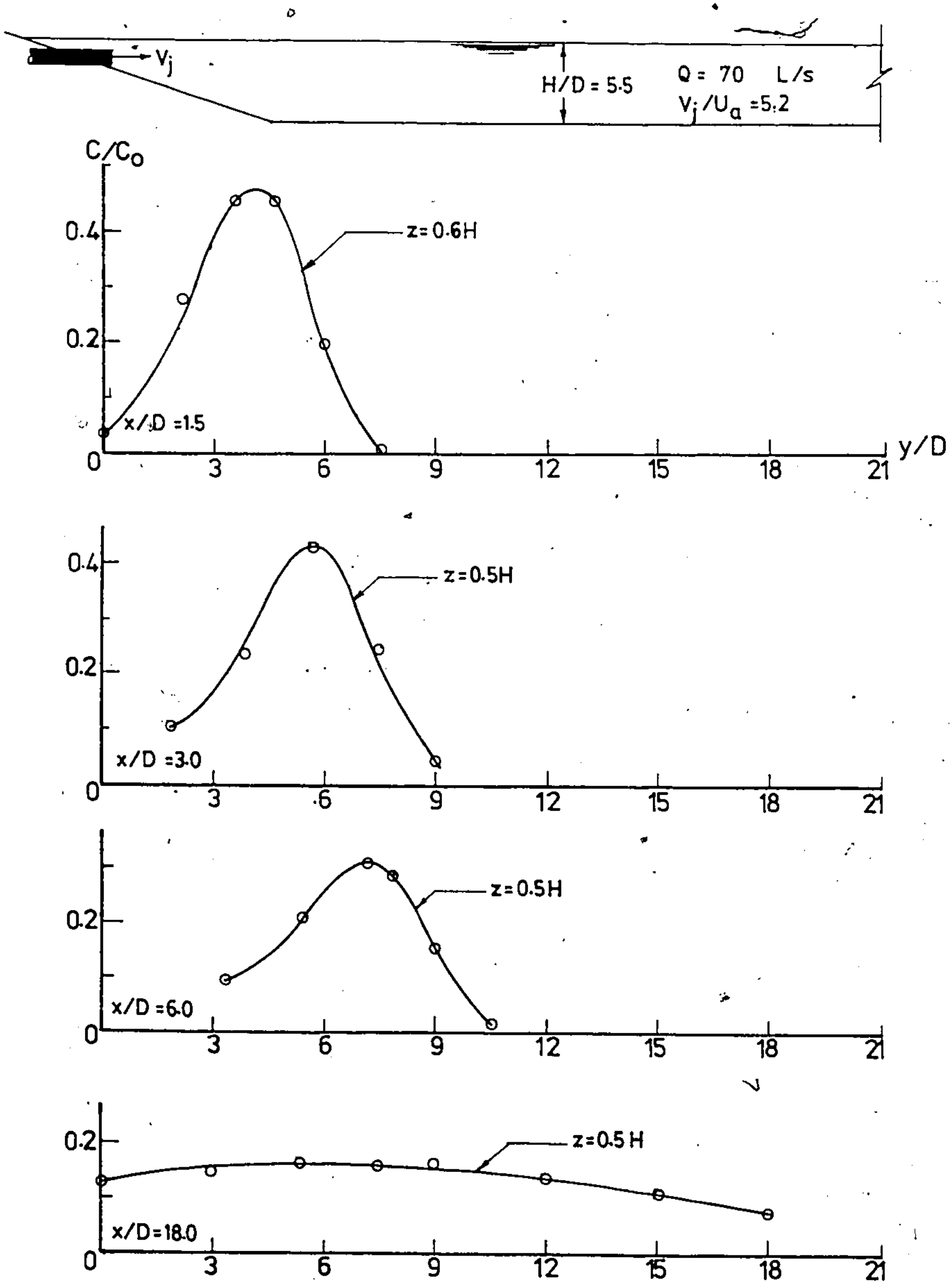

Fig. 4.19. Lateral Concentration Profile for Exp. 26.

4.1.4 Temperature Profiles

Nine tests were performed to describe the behaviour of a heated jet discharged from a round jet into cross flowing ambient. The ranges for the variables were:

Channel discharge, Q = 34 and 70 L/s

Jet discharge, Q_o = 0.4 to 1.5 L/s

Relative depth, H/D = 2, 4 and 5.5

Velocity ratio, R = 2.0, 3.2, 5.2

Initial temperature difference, ΔT_o = 8.2 to 16.2°C

Densimetric Froude no., F_o = 4.3 to 19.3

Pipe position, Z_p = on bed and at the surface.

Ambient temperature, T_a, was subtracted from the measured temperature, T, to obtain excess temperature, ΔT. Similarly, the initial ambient temperature, T_{a_o}, was subtracted from the initial jet temperature, T_o, to obtain the initial excess temperature, ΔT_o. All subsequent analyses were based on the ratio of these incremental variables, $\Delta T/\Delta T_o$. The excess temperature for Runs 1.1, 2.1, 3.1, 5.1, 6.1, 7.1, 24.1, 25.2 and 26.1 are presented in generalized form at four different longitudinal sections, i.e., x/D = 1.5, 3, 6 and 18. Figures 4.20 to 4.31 present the vertical and lateral profiles at each section of the above Runs.

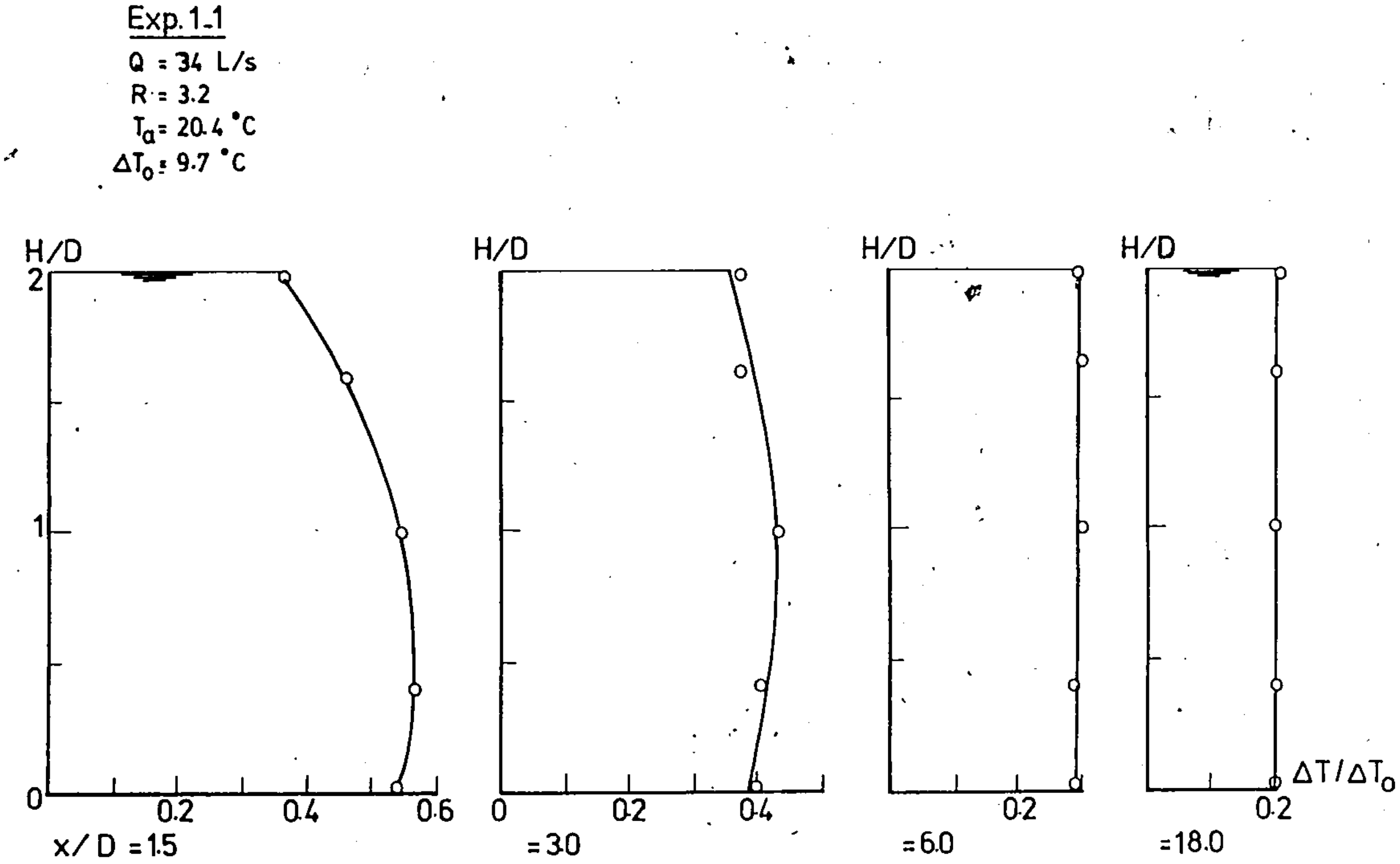

Fig. 4.20. Vertical temperature profiles for Exp. 1-1.

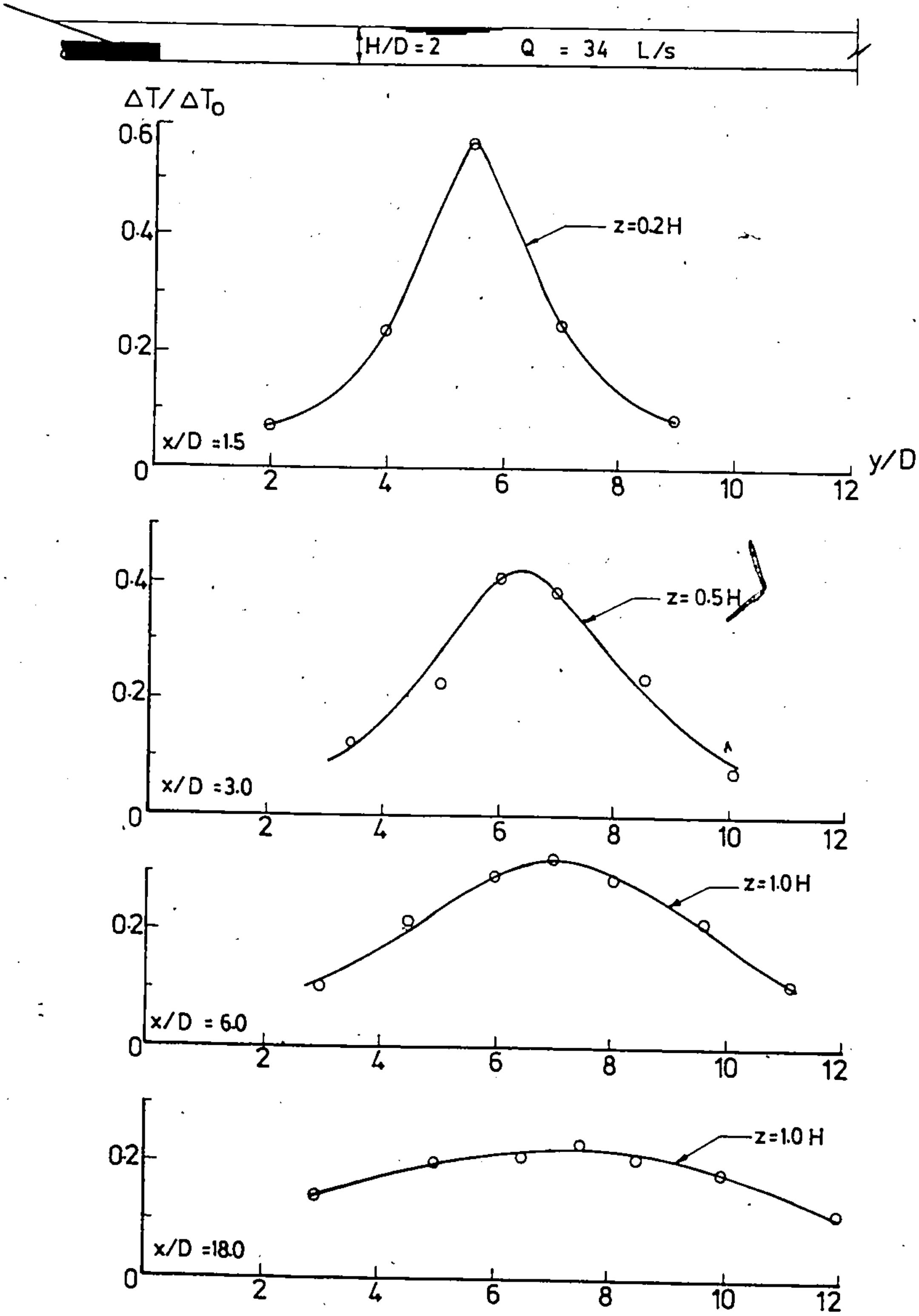

Fig. 4.21. Lateral Temperature Profiles for Exp. 1-1.

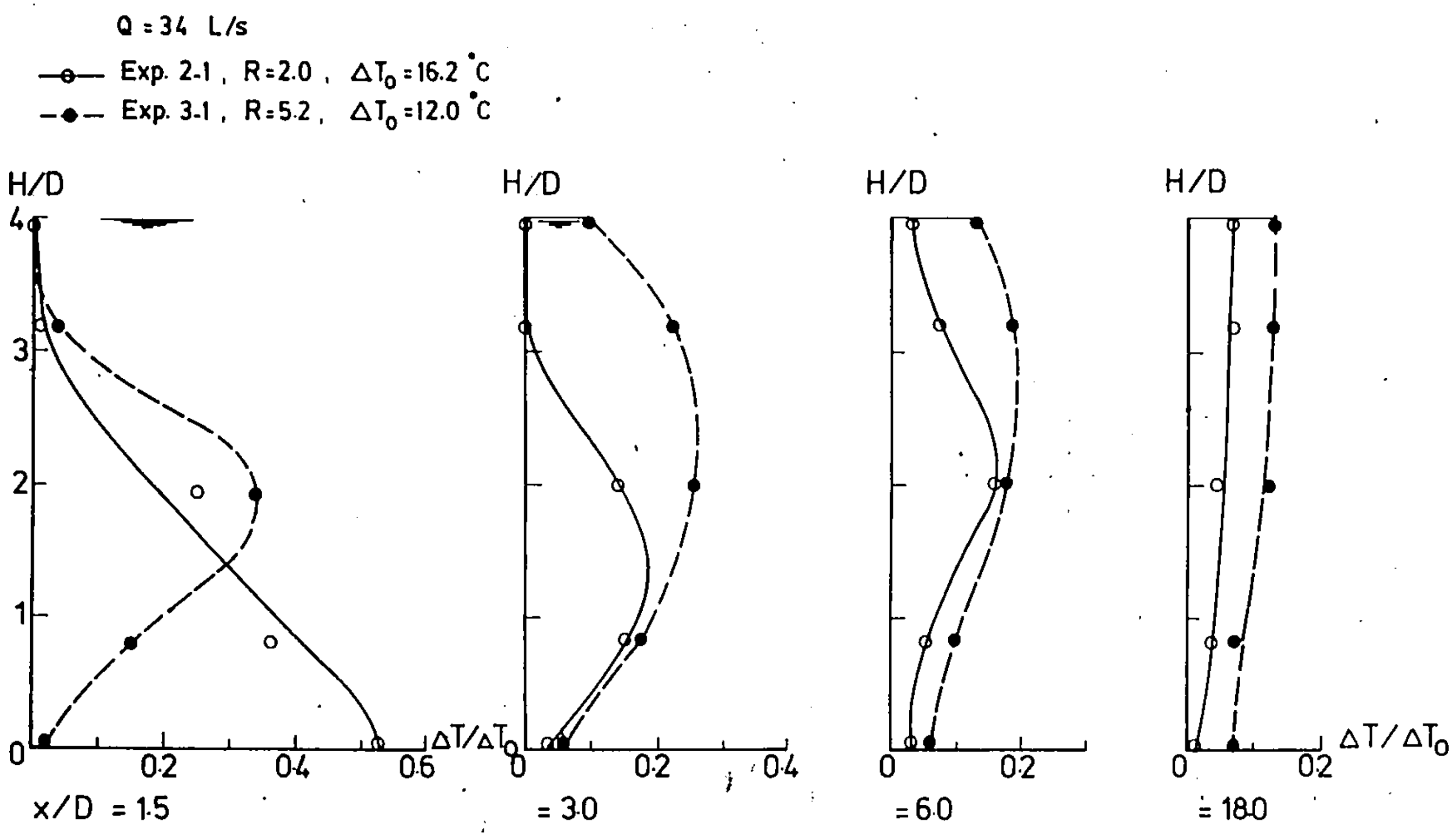

Fig. 4.22. Vertical Temperature Profiles for Exps. 2-1 and 3-1.

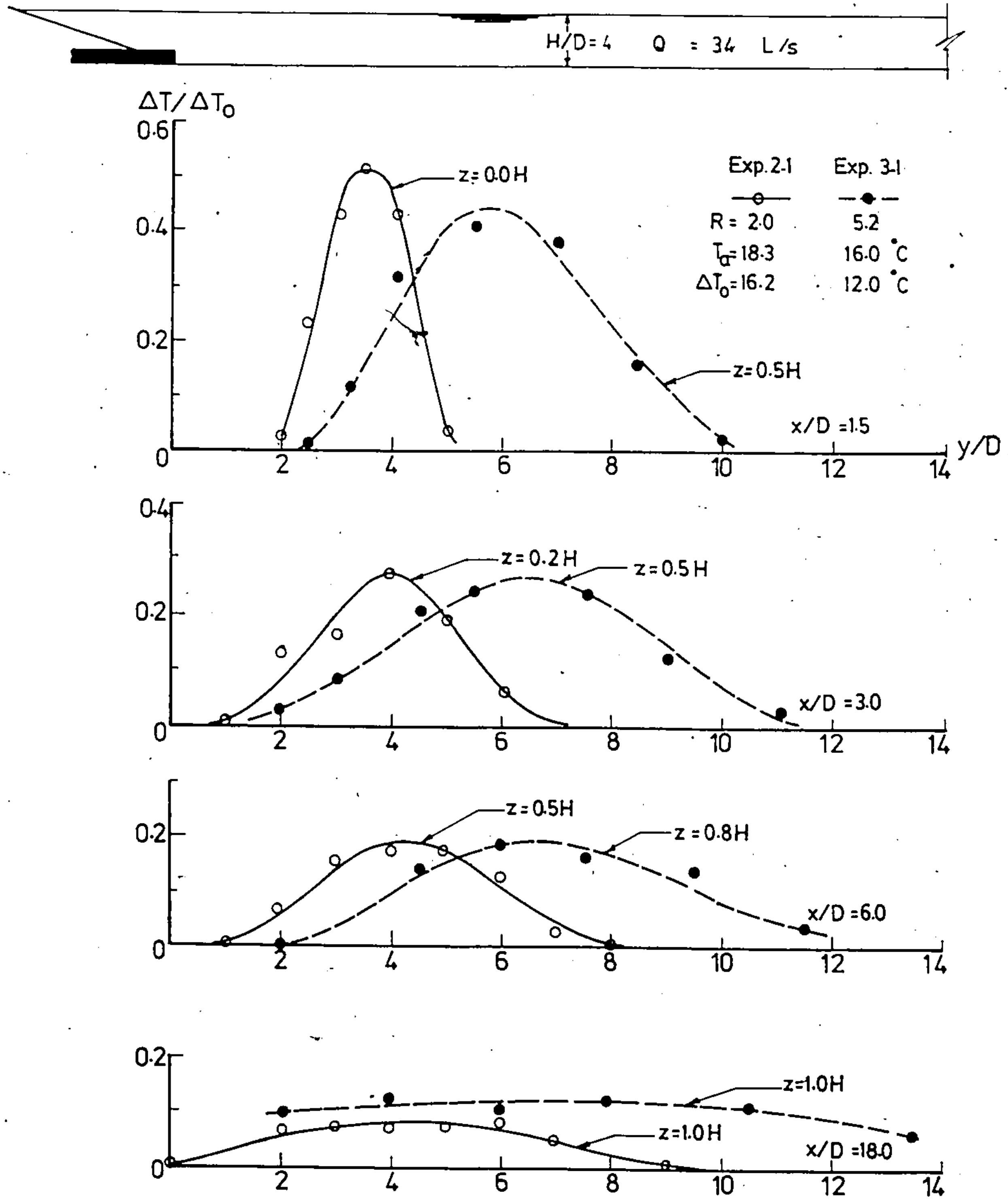

Fig. 4.23. Lateral Temperature Profiles for Exps. 2-1 and 3-1.

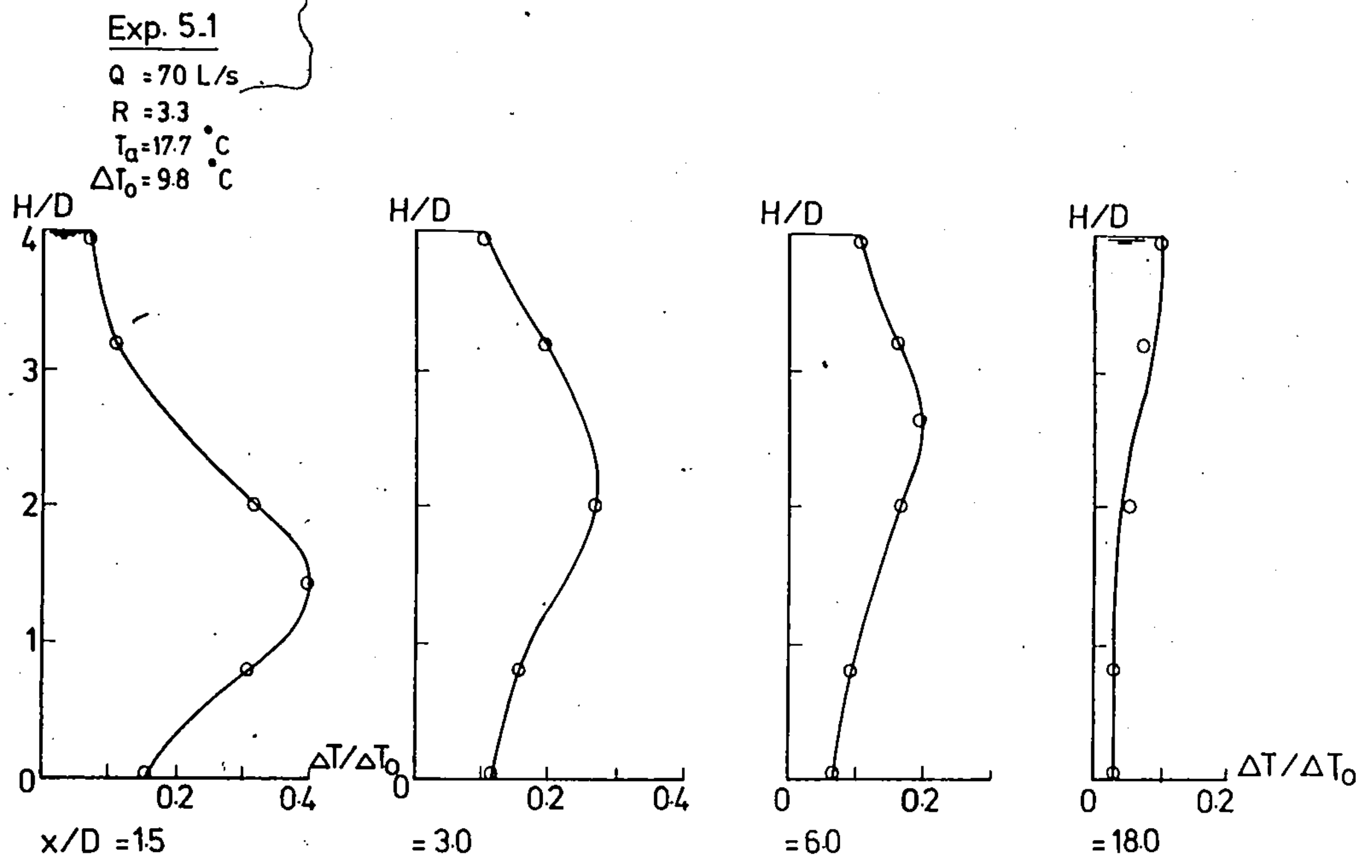

Fig. 4.24. Vertical Temperature Profiles for Exp. 5-1.

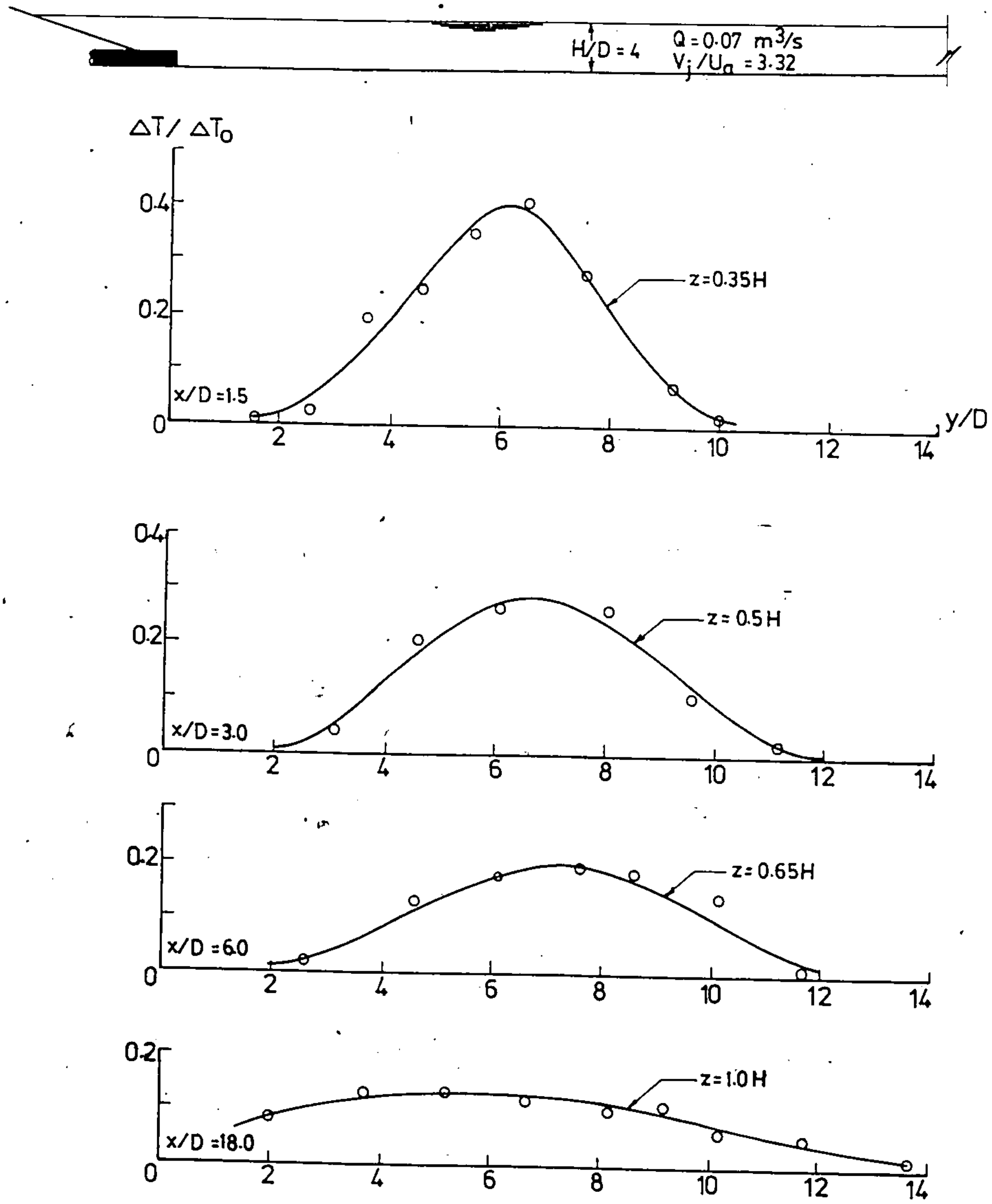

Fig. 4.25. Lateral Temperature Profiles for Exp. 5-1.

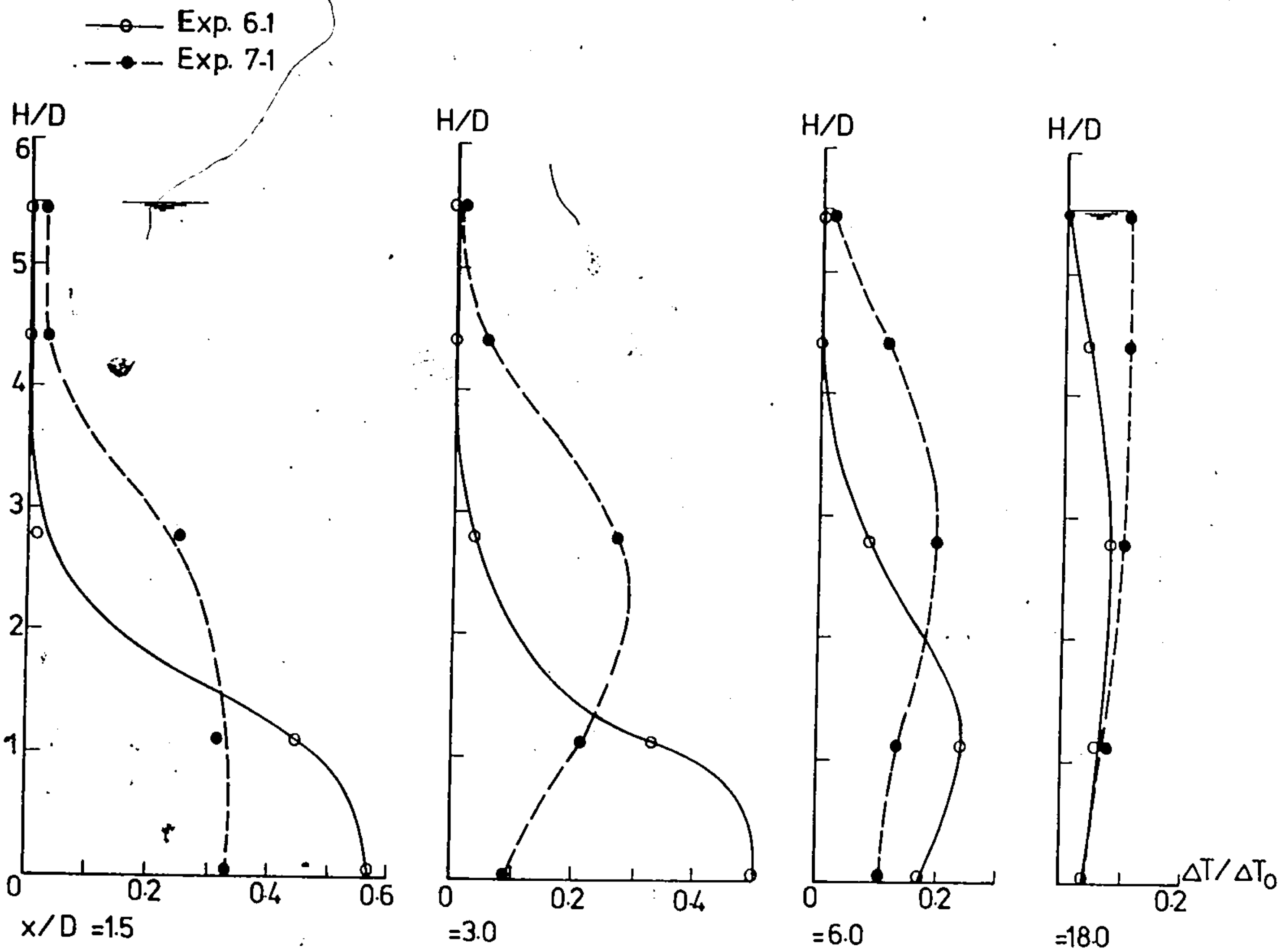

Fig. 4.26, Vertical Temperature Profiles for Exps. 6-1 and 7-1.

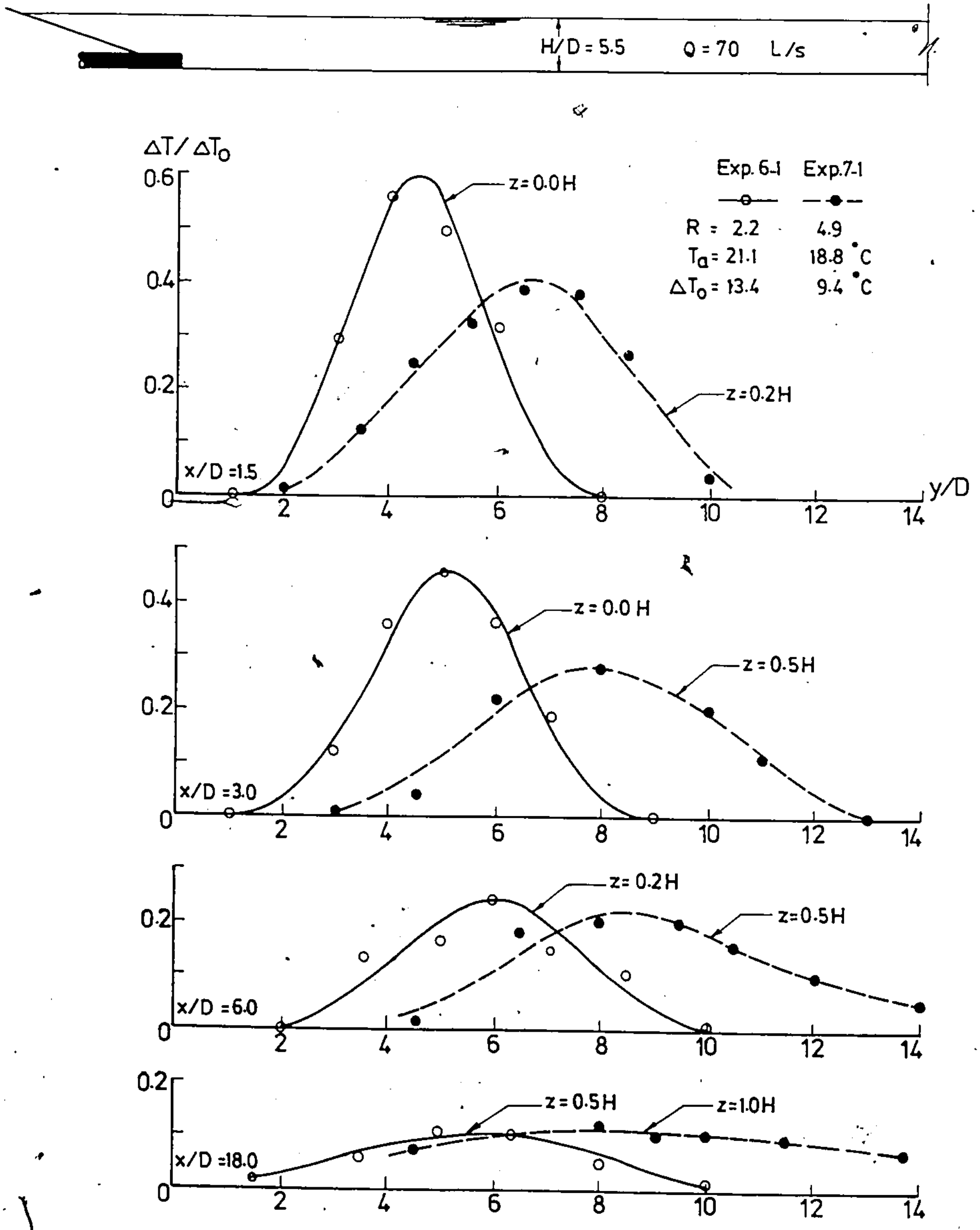

Fig. 4.27. Lateral Temperature Profiles for Exps. 6-1 and 7-1.

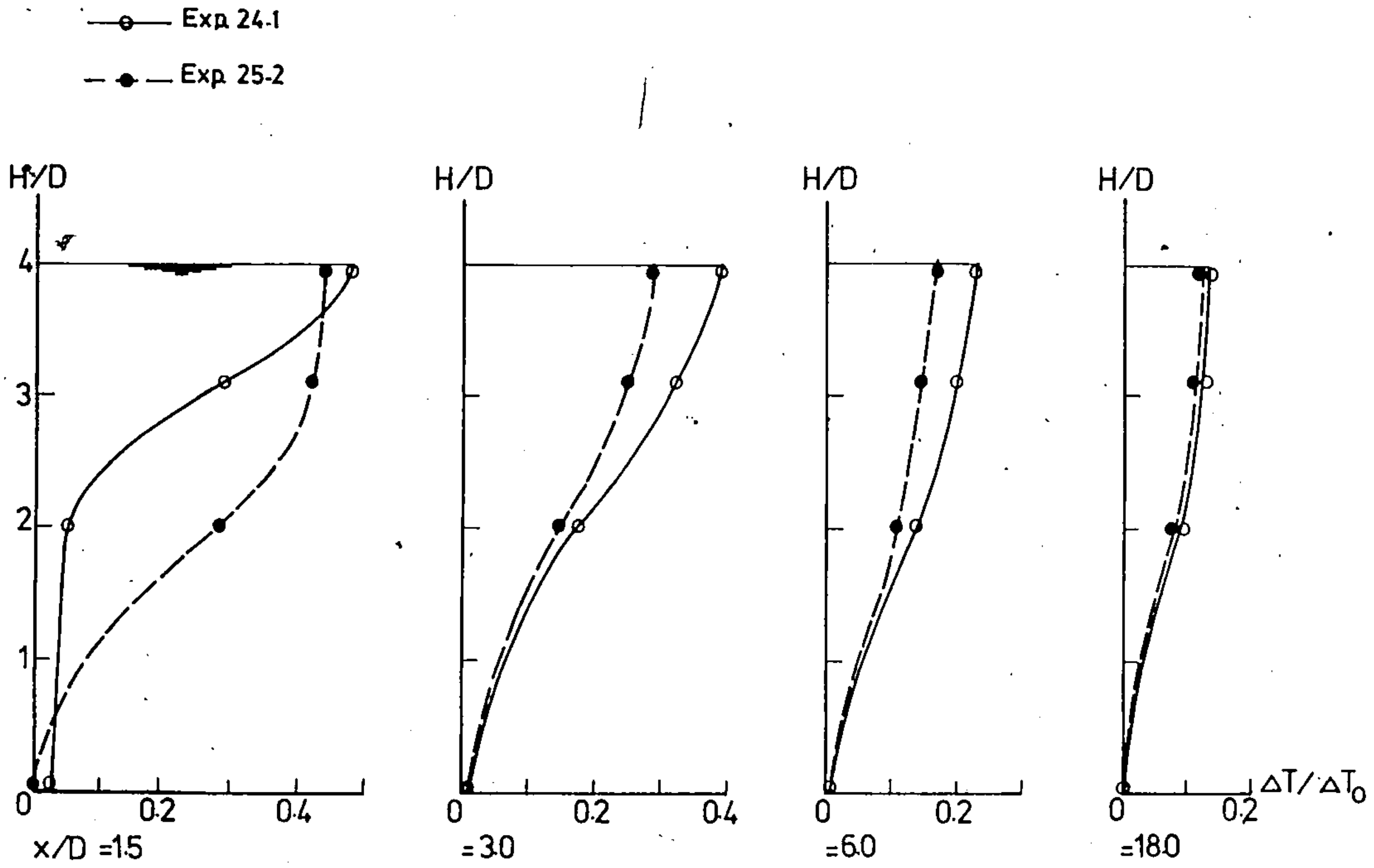

Fig. 4.28. Vertical Temperature Profiles for Exps. 24-1 and 25-2.

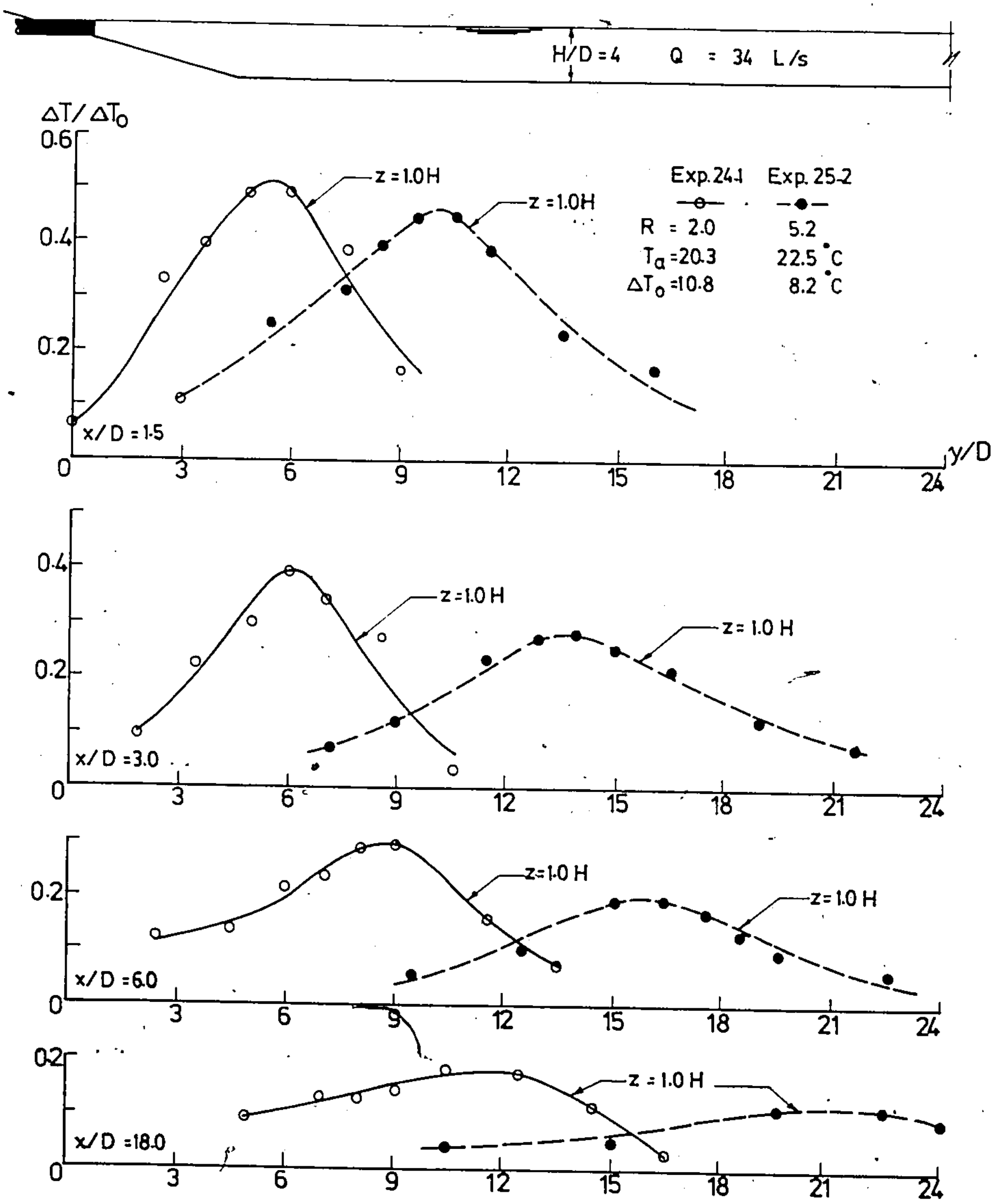

Fig. 4.29. Lateral Temperature Profiles for Exps. 24-1 and 25-2.

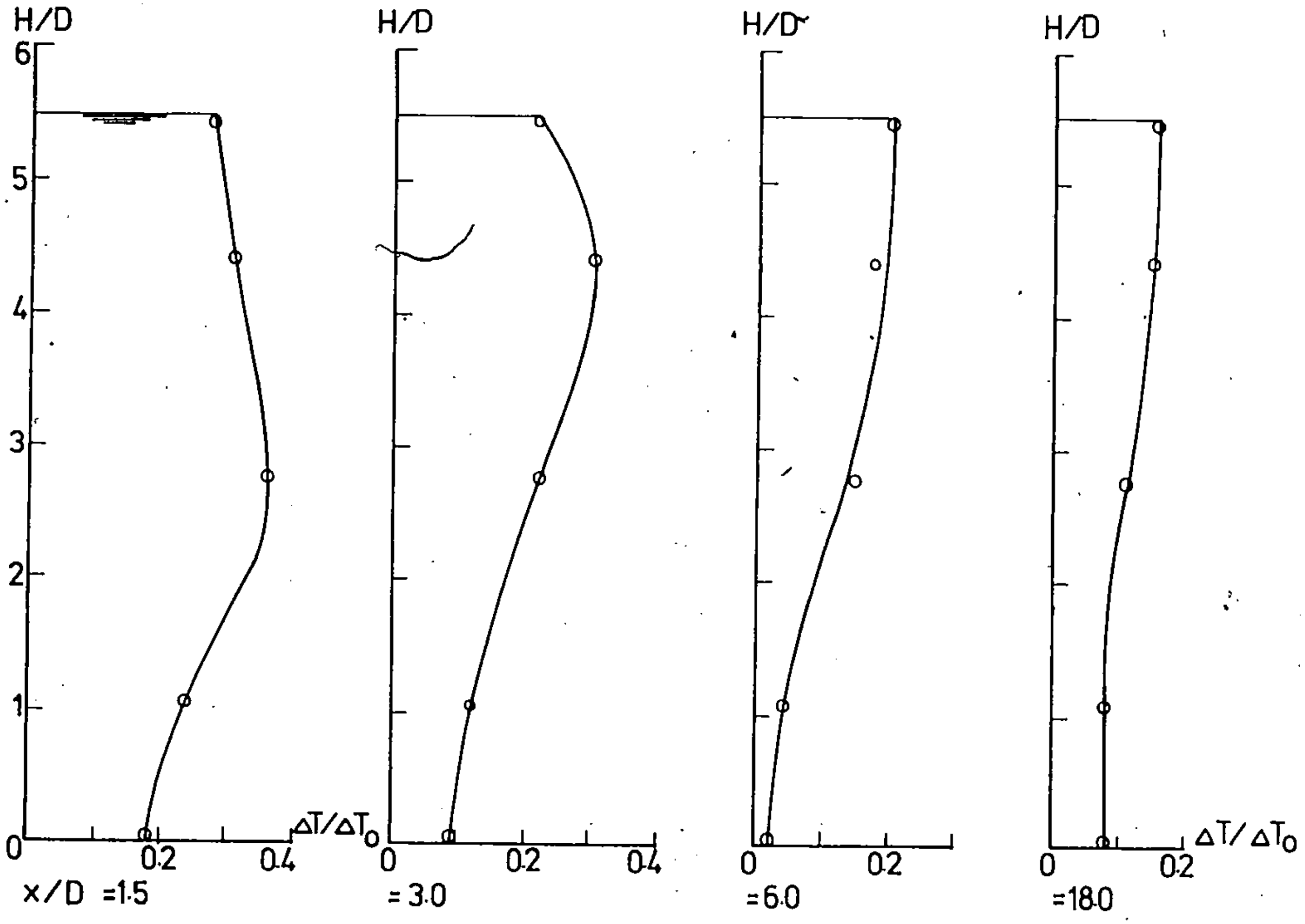

Fig. 4.30. Vertical Temperature Profiles for Exp. 26-1.

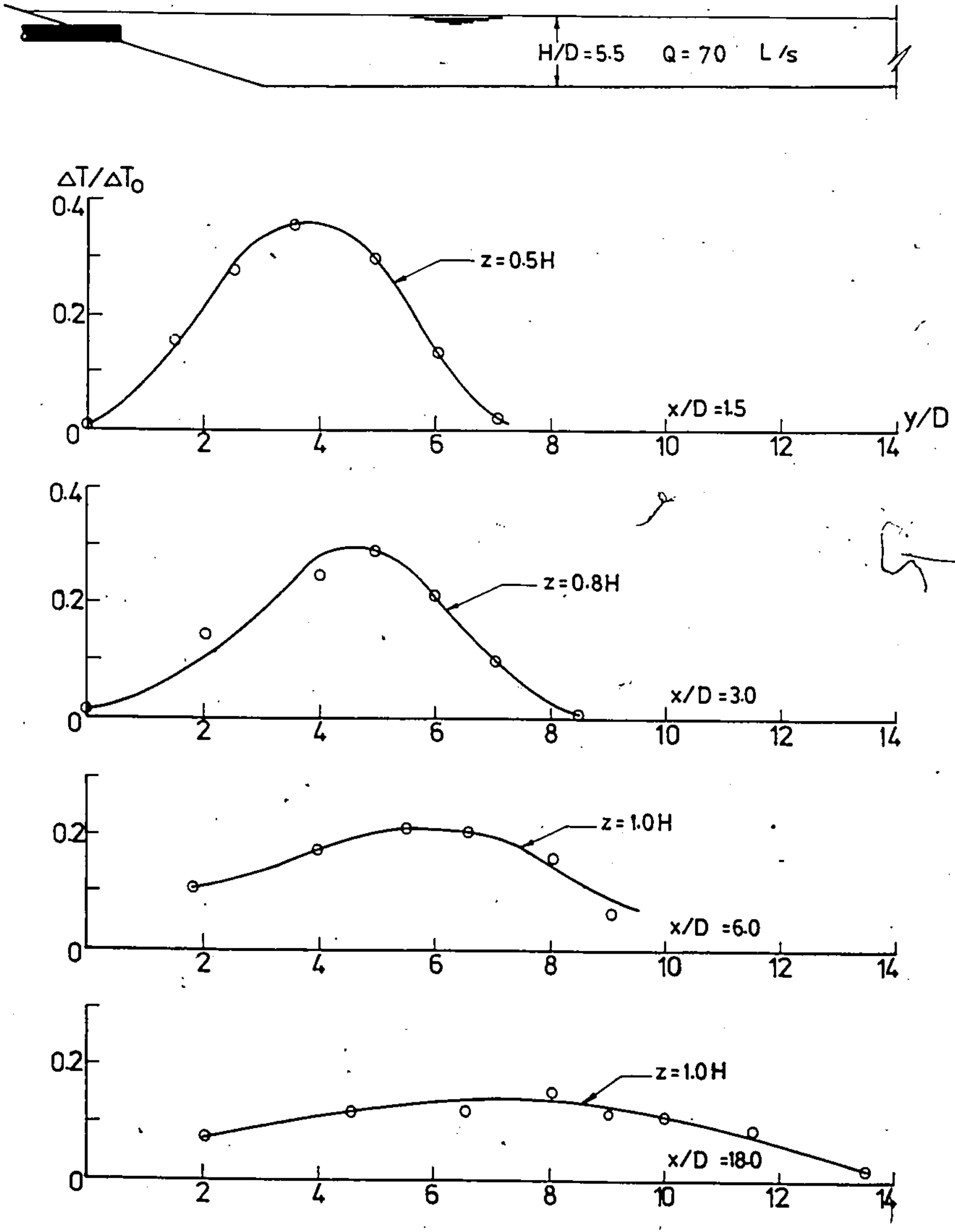

Fig. 4.31. Lateral Temperature Profiles for Exp. 26-1.

Two tests were conducted to study the behaviour of heavy density jet discharged at the surface. Figures 4.32 and 4.33 present the vertical and lateral temperature distributions resulting from cold water discharges for Runs 30.1 and 31.1 These figures show the results for low and high velocity ratios, R = 2 and 5.2, with initial temperature differences of -7.6 and -6.1°C, respectively.

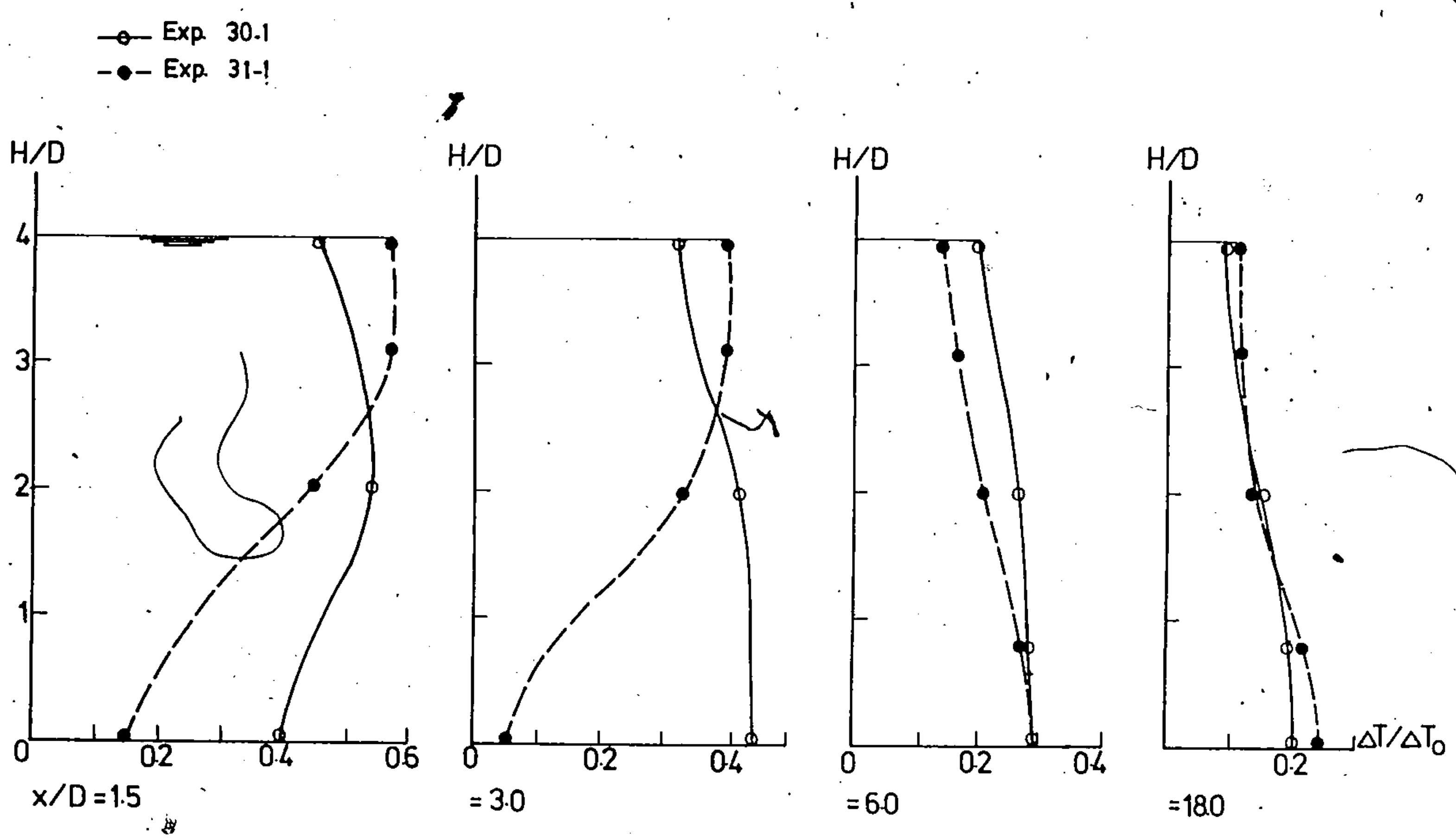

Fig. 4.32. Vertical Temperature Profiles for Exps. 30-1 and 31-1.

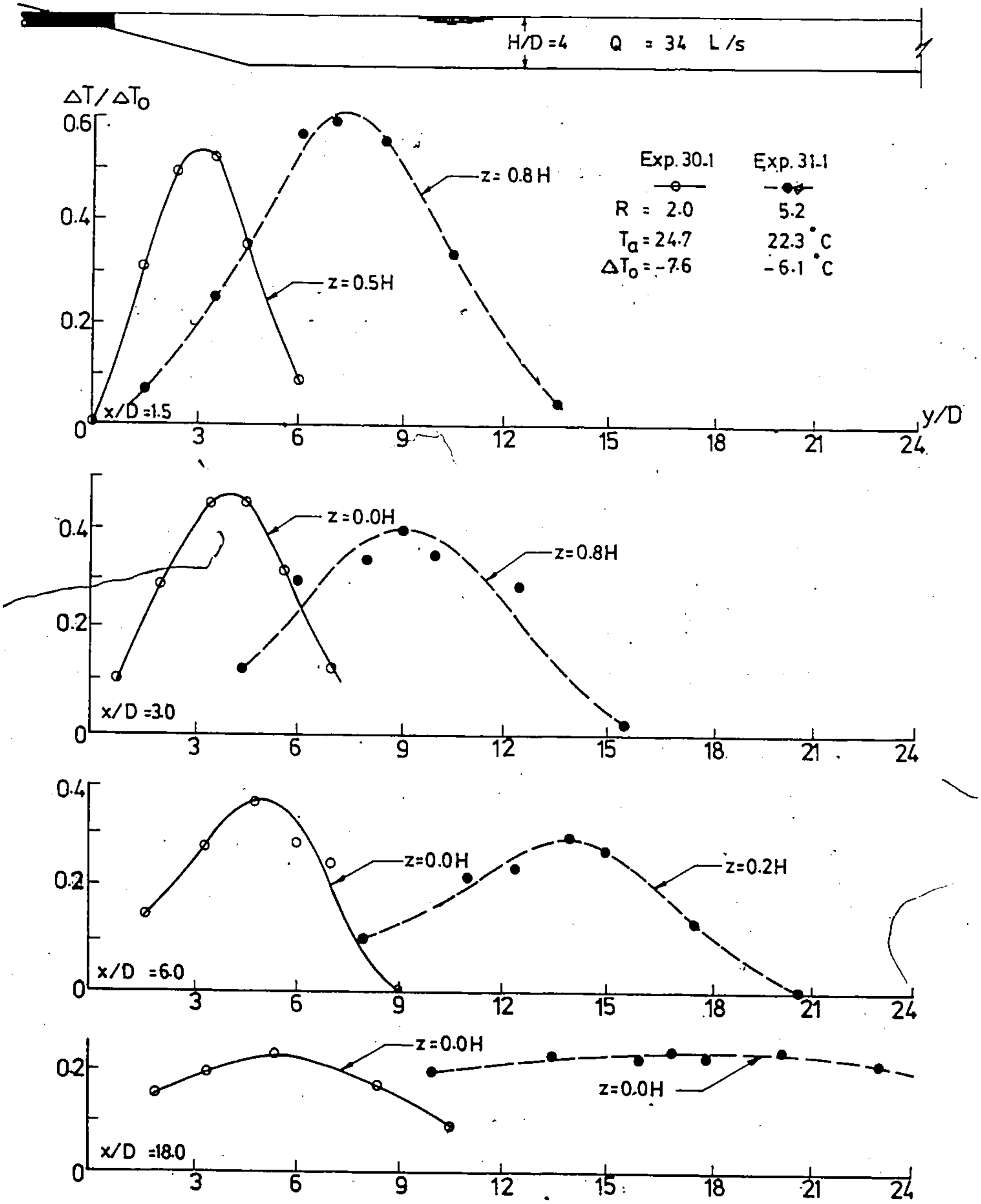

Fig. 4.33. Lateral Temperature Profiles for Exps. 30-1 and 31-1.

4.2 CONTAMINANT BEHAVIOUR STUDIES

4.2.1 Relationship Between Chlorine Dose and Residual Chlorine and Ammonia

Five sets of experiments were conducted on diluted final effluent samples to study the effect of chlorine dose on residual chlorine and ammonia concentrations. Various amounts of stock chlorine solution were applied to each sample so that chlorine dosages in a range from 5 to 13 mg/L were obtained. After thorough mixing of chlorine solution in the samples, they were diluted with the river water in the ratio of 1 to 19. After 30 minutes of contact time, all the samples were analyzed for free and combined residual chlorine by the amperometric titration method and for ammonia concentration by the ammonia electrode. Also, the final effluent samples, after collection from the treatment plant and before adding chlorine solution, were analyzed for ammonia concentration to determine the level of ammonia in the final effluent.

It was observed that no significant free residual chlorine was present in any of the samples. The chlorine demands exerted by the sample from Windsor Plant at various chlorine doses, together with the corresponding changes in ammonia concentration are shown in Fig. 4.34. Theoretical curve for pure water is drawn also on the figure.

Simultaneously, total residual chlorine and ammonia concentrations in the same sample were measured at different time intervals for several days. At the end of each contact period, 100 mL from each sample was withdrawn to residual chlorine determination and another 100 mL was withdrawn to measure ammonia concentration. The results are shown as a decay curve for residual chlorine in Fig. 4.35 and the corresponding ammonia concentrations are presented in Fig. 4.36.

4.2.2 Effect of Physical and Chemical Parameters on Chlorine Decay

4.2.2.1 Influence of Exposure to Light

Two sets of experiments were carried out on the same final effluent with a chlorine dose of 9 mg/L, to study the effect of light on residual chlorine and ammonia concentrations. The samples were placed in 250 mL beakers in 20±1°C constant temperature chambers with one set kept in complete darkness while the other set was exposed alternatively to 12 hours of light and 12 hours of darkness each day. The initial readings were taken within the first half-hour and the values reported are an average of two readings from two separate beakers.

Figure 4.37 shows the results of these runs with the total residual chlorine concentration plotted against the corresponding time. It can be seen from this figure that

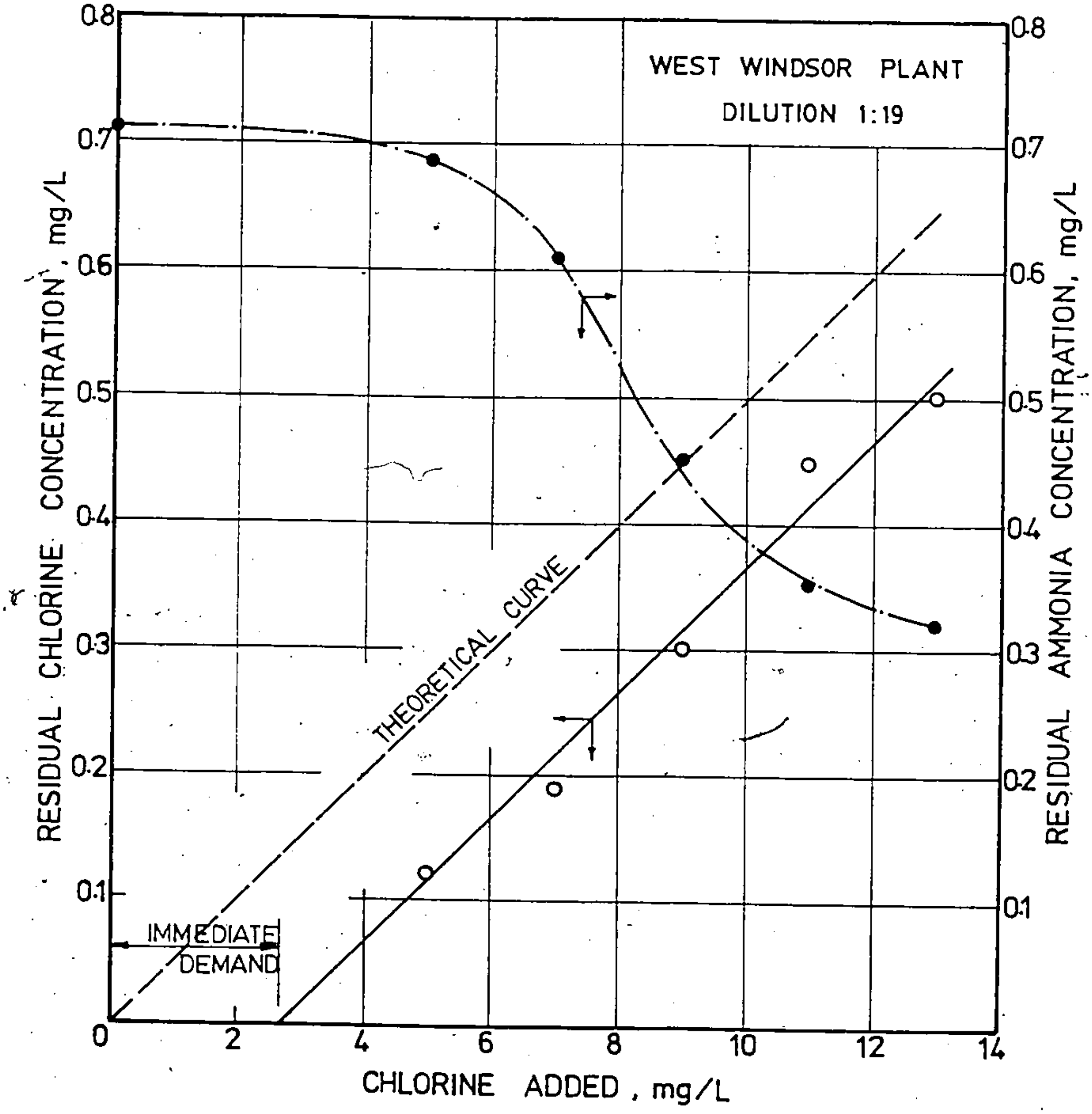

Fig. 4.34. Residual Chlorine and Ammonia Versus Chlorine Added after Half-Hour Contact Time.

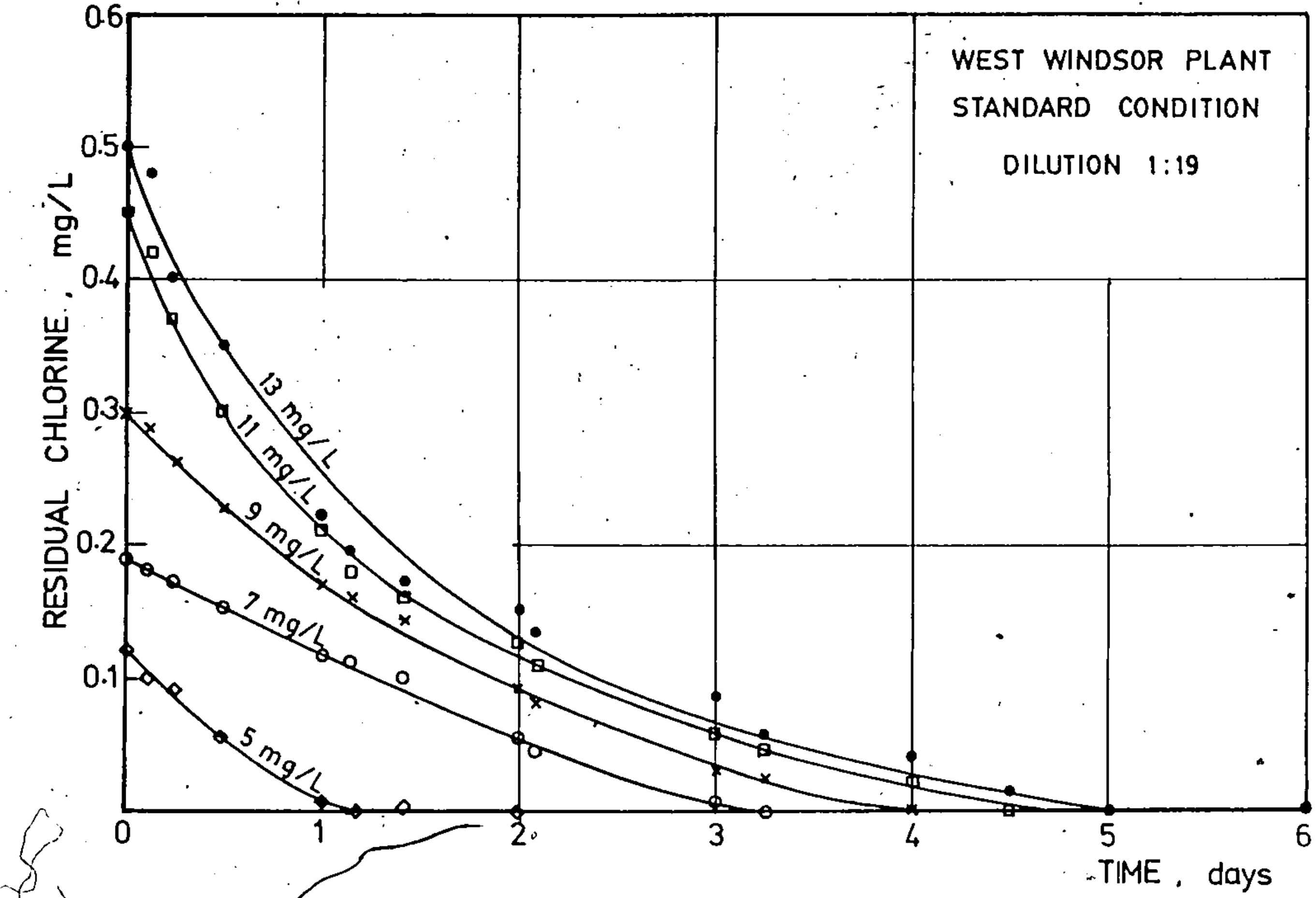

Fig. 4.35 Effect of Chlorine Dose on Total Residual Chlorine.

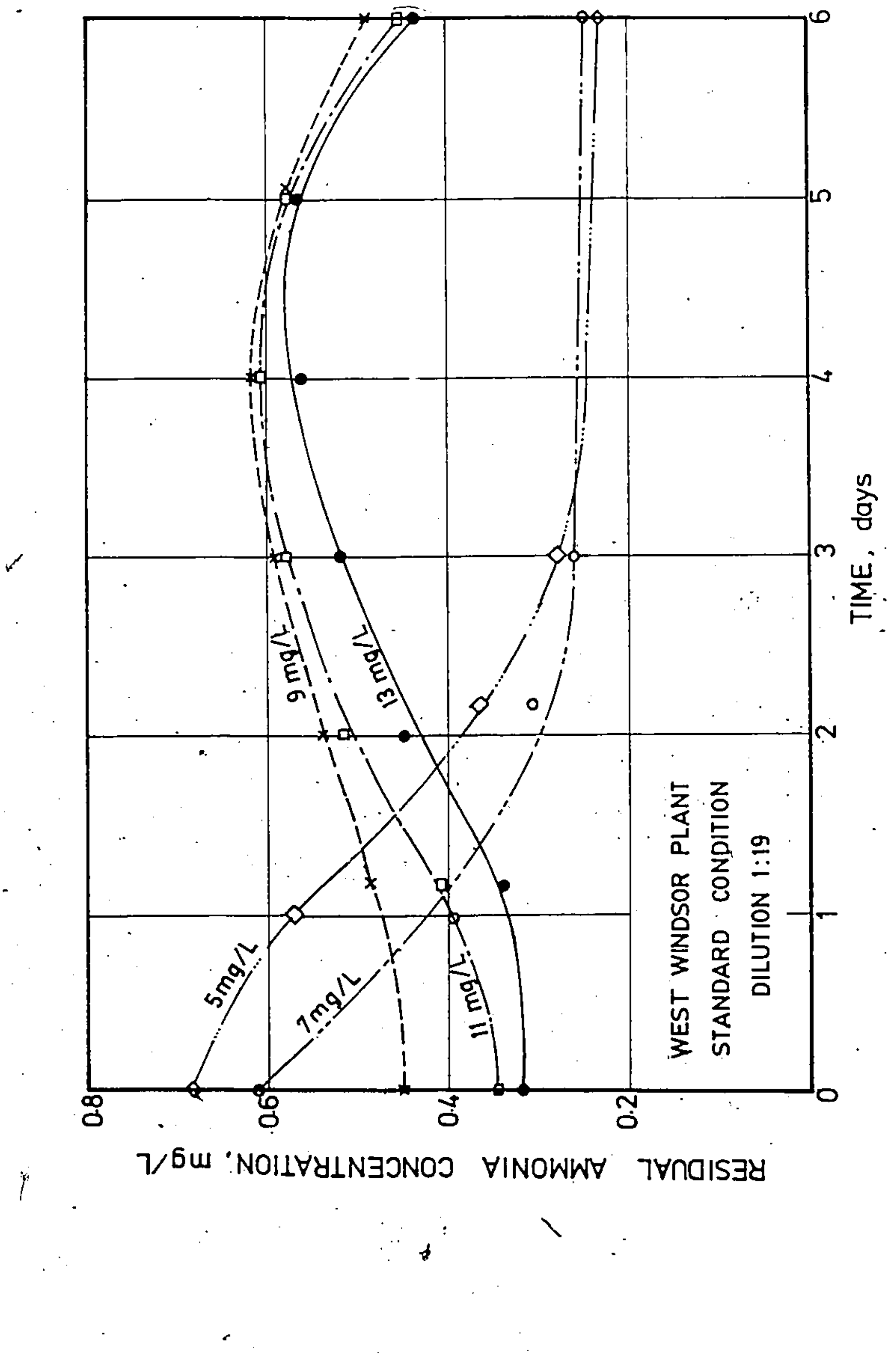

Fig. 4.36. Effect of Chlorine Dose on Residual Ammonia.

the residual chlorine levels under complete darkness are slightly higher than those obtained under alternating light and dark condition. Figure 4.38 shows the results of residual ammonia concentration plotted against time. It is observed that the effect of alternating exposure to light and darkness on the residual ammonia concentration is similar to that observed for the residual chlorine concentration.

4.2.2.2 Influence of Stirring

All the previous studies on the residual chlorine tests were conducted under standard quiescent conditions without considering the fact that turbulence is present in actual conditions. In this phase of the study the effect of turbulence on residual chlorine and ammonia concentrations was investigated in a sample exposed alternatively to 12 hours of light and 12 hours of darkness. Residual chlorine and ammonia concentrations were determined daily in separate beakers in which stirrers were rotated continuously at a constant speed. Figure 4.39 shows the residual chlorine concentration as a function of time. This figure clearly indicates that the stirring has a significant effect on the decay rate of chlorine. With no stirring, the time required for the disappearance of chlorine is 3 days, while 1.5 day of stirring is enough

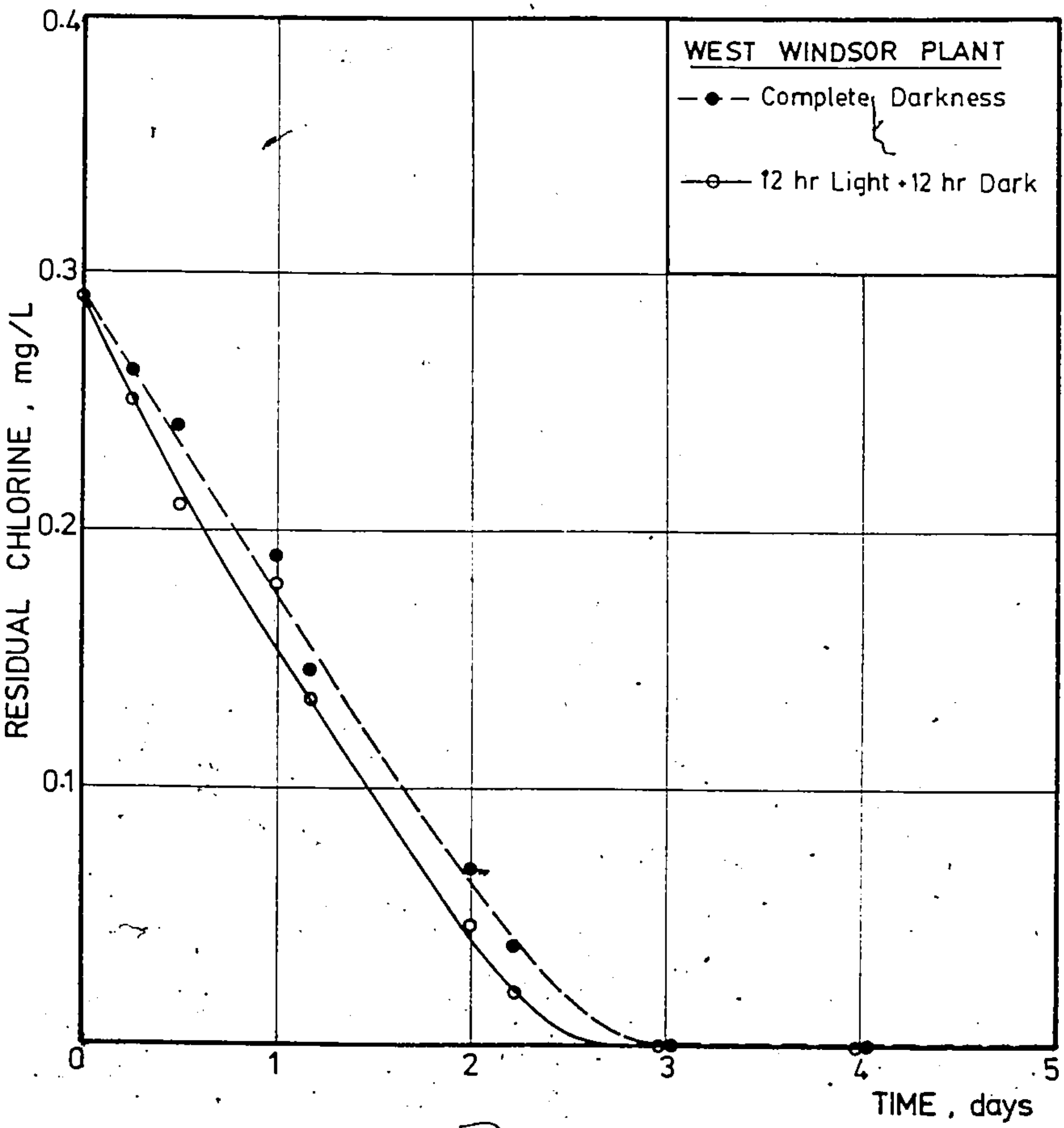

Fig. 4.37. Influence of Exposure to Light on Residual Chlorine.

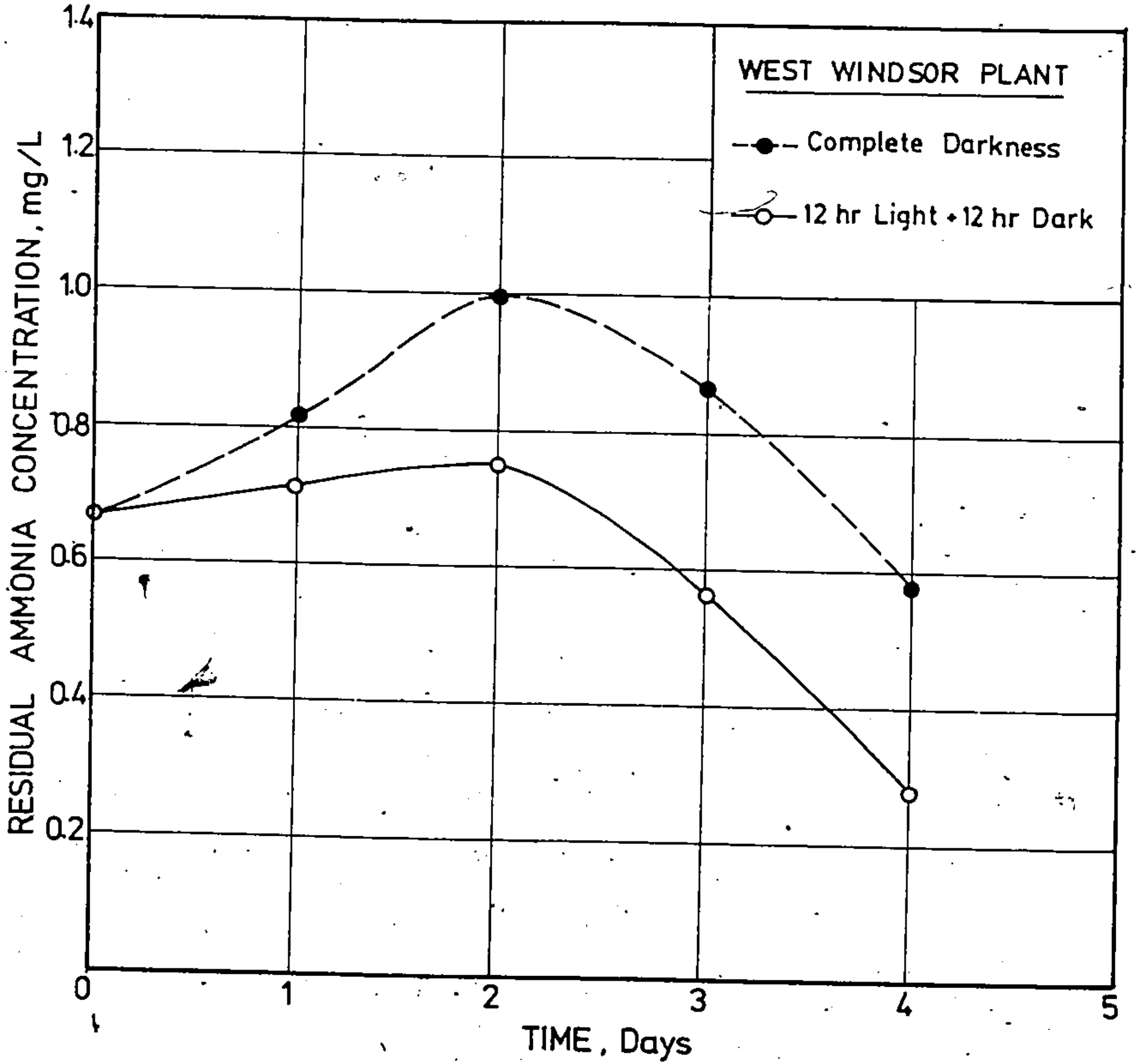

Fig. 4.38. Influence of Exposure to Light on Residual Ammonia.

for complete disappearance. The results of residual ammonia as a function of time are presented in Fig. 4.40.

4.2.2.3 Effect of Varying the Surface Area to Volume Ratios

Five sets of experiments were conducted on the same final effluent with chlorine dose of 9 mg/L, to study the effect of changing the surface area/volume on residual chlorine. The samples were placed in different size containers to obtain five different surface area to volume ratios and were kept at a constant room temperature. The residual chlorine concentrations were determined at different time intervals over a period of 5 days. Typical residual chlorine curves at different surface area to volume ratios are plotted in Fig. 4.41. The initial reading is an average of five readings. It is observed from these plots that the higher the A_s/V ratio, the lower is the residual chlorine concentration at any time.

4.2.2.4 Temperature Effect

In order to study the effect of temperature on the rate constant for chlorine decay, experiments were conducted at four different temperatures, 2, 11, 20 and 30±1°C. The results presented in Fig. 4.42 show that, in the diluted final effluent samples that have been dosed with 9 mg/L of chlorine, chlorine decays very

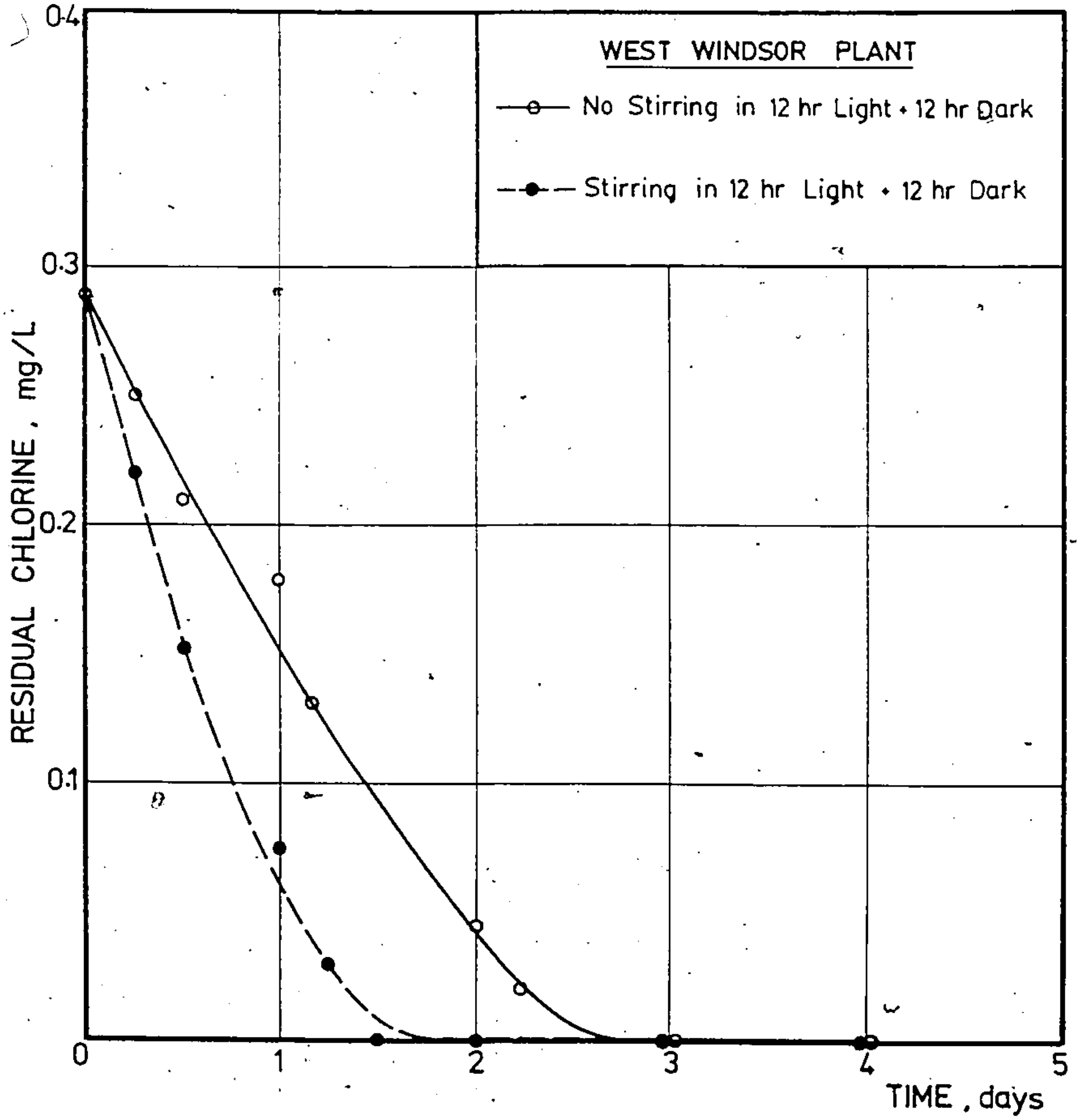

Fig. 4.39. Influence of Stirring on Residual Chlorine.

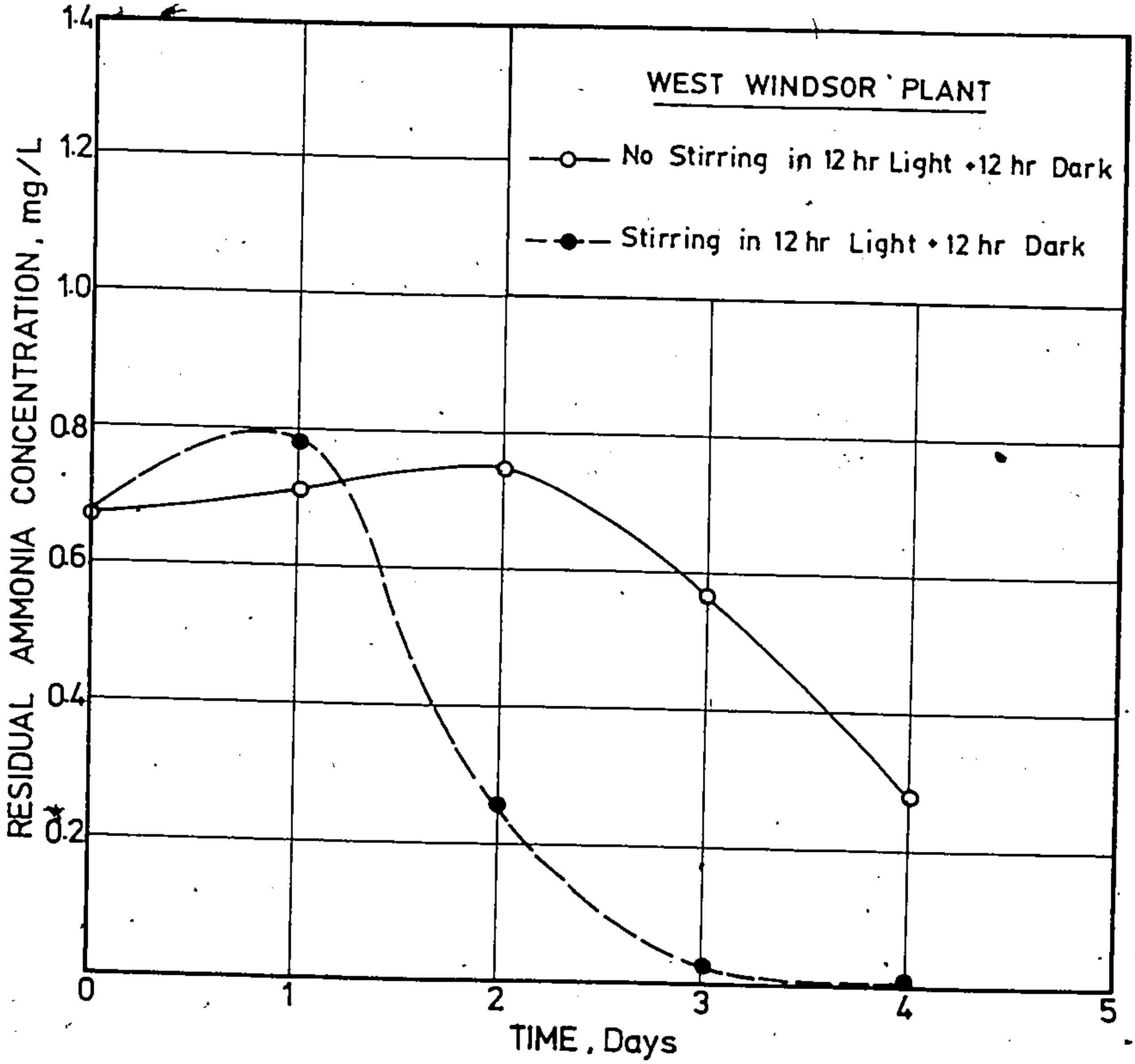

Fig. 4.40. Influence of Stirring on Residual Ammonia.

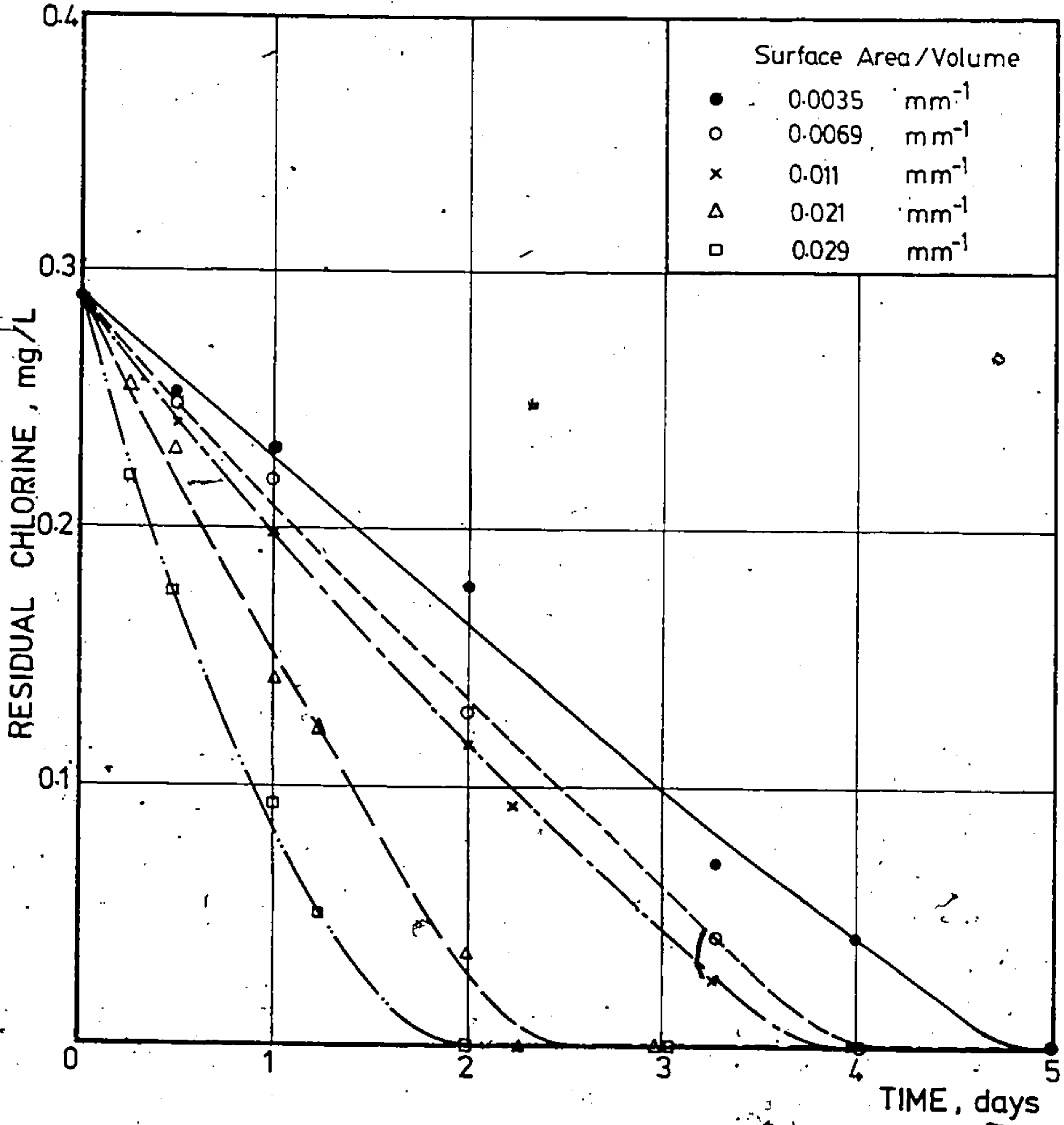

Fig. 4.41. Effect of Varying the Surface Area to Volume Ratios on Residual Chlorine.

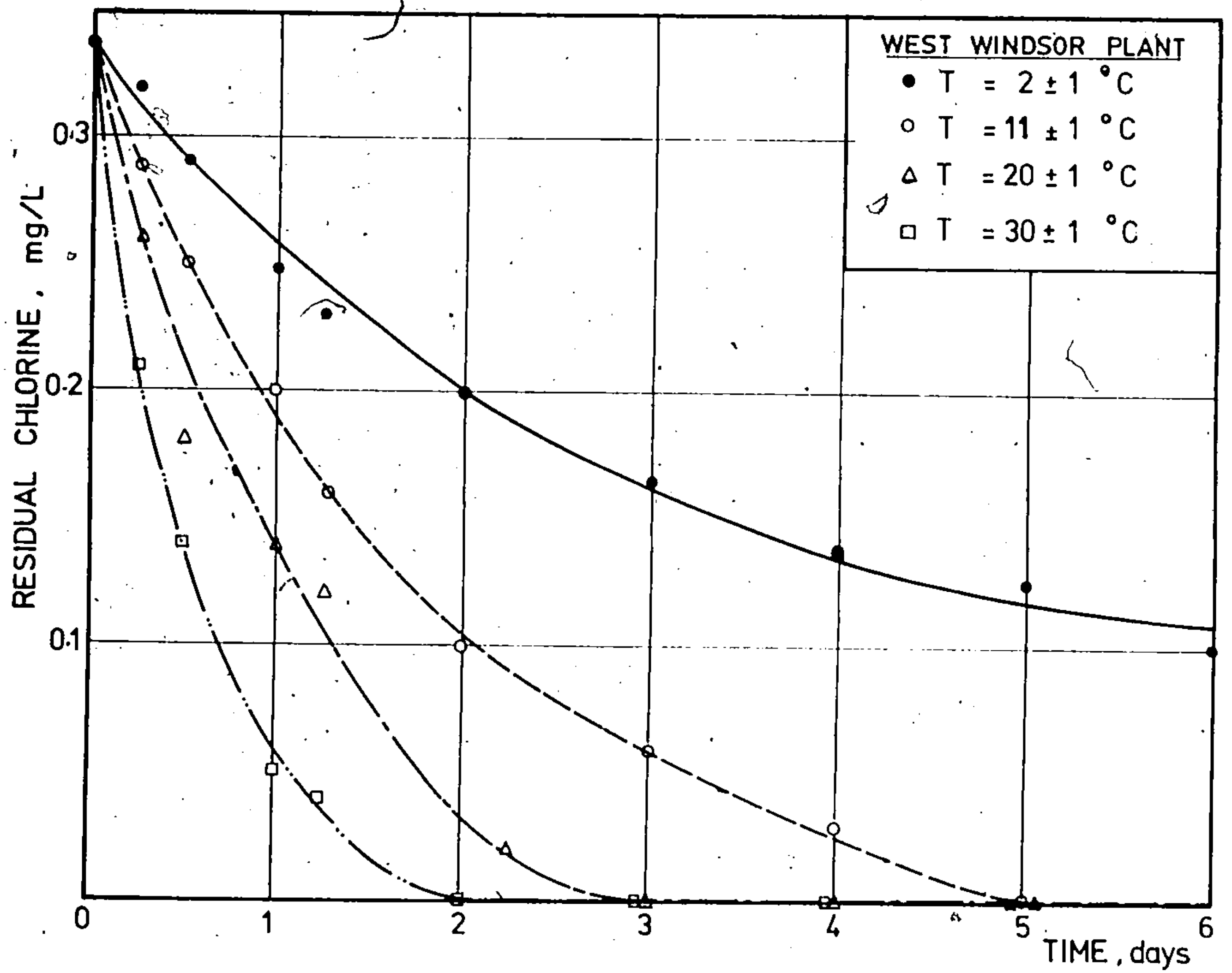

Fig. 4.42. Temperature Effect on Residual Chlorine.

slowly near freezing point as compared to that at room temperature.

4.2.3 Effect of Residual Chlorine on BOD Progression

4.2.3.1 Effect of Varying Chlorine Dosages on BOD Progression

Stock chlorine was added to provide three different dosages of 0, 5 and 10 mg/L in the same final effluent from West Windsor Plant and dosages of 0, 2 and 5 mg/L in the same final effluent from Little River Plant. BOD values were taken daily for 11 days in separate bottles under quiescent condition. Typical BOD progression curves at different chlorine dosages are plotted in Figs. 4.43 and 4.44. These figures clearly indicate that the BOD values for any incubation period decrease with increase in chlorine dose.

4.2.3.2 Effect of Light

The effect of chlorination with eutrophication was studied by running BOD progression tests providing alternating exposure to 12 hours of light and 12 hours of darkness each day. Identical runs were made under standard conditions in which BOD bottles were incubated all the time in darkness. Figures 4.45 and 4.46 compare the effect of eutrophication in chlorinated and unchlorinated

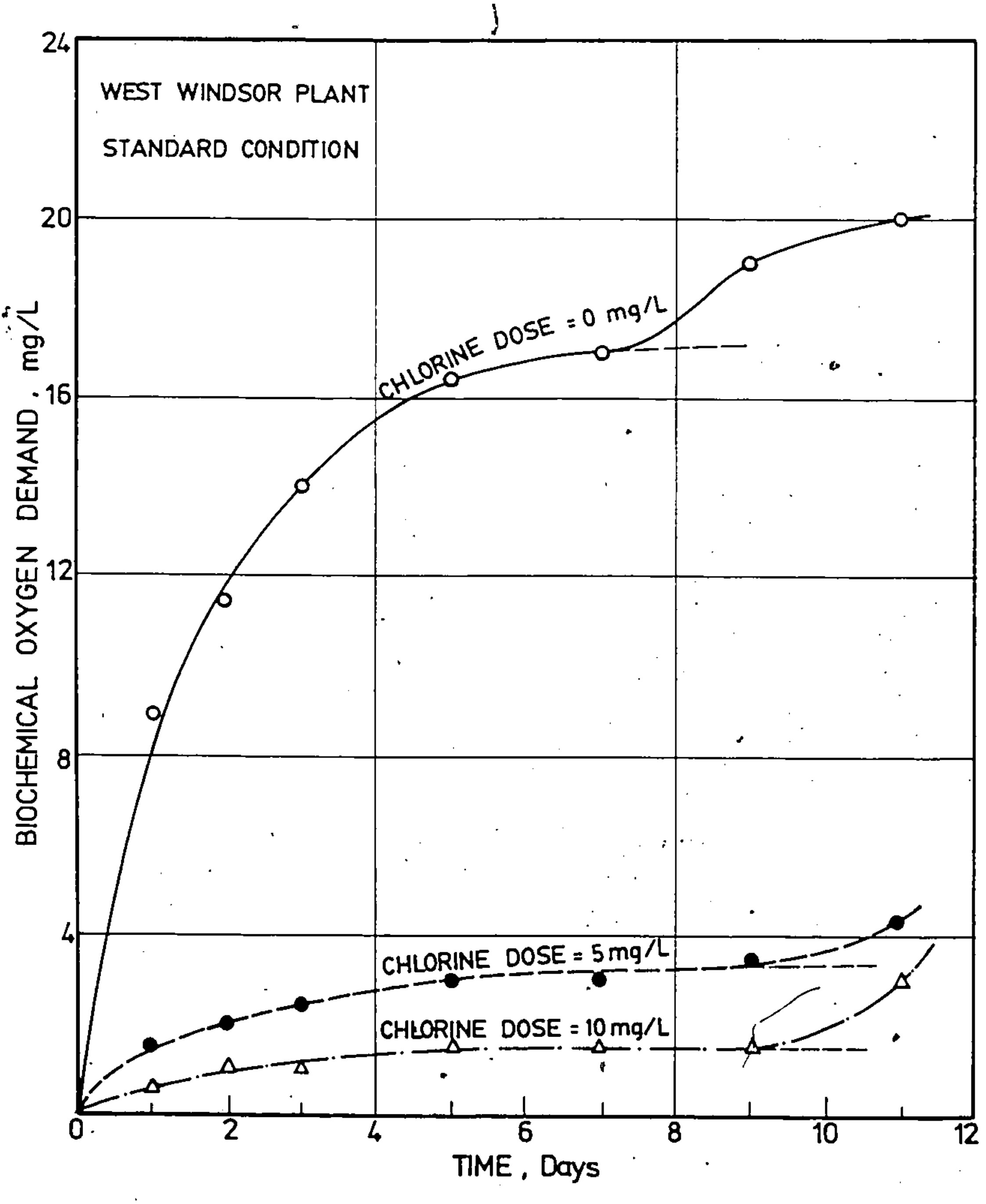

Fig. 4.43. Effect of Chlorine Dose on BOD Progression, West Windsor Plant.

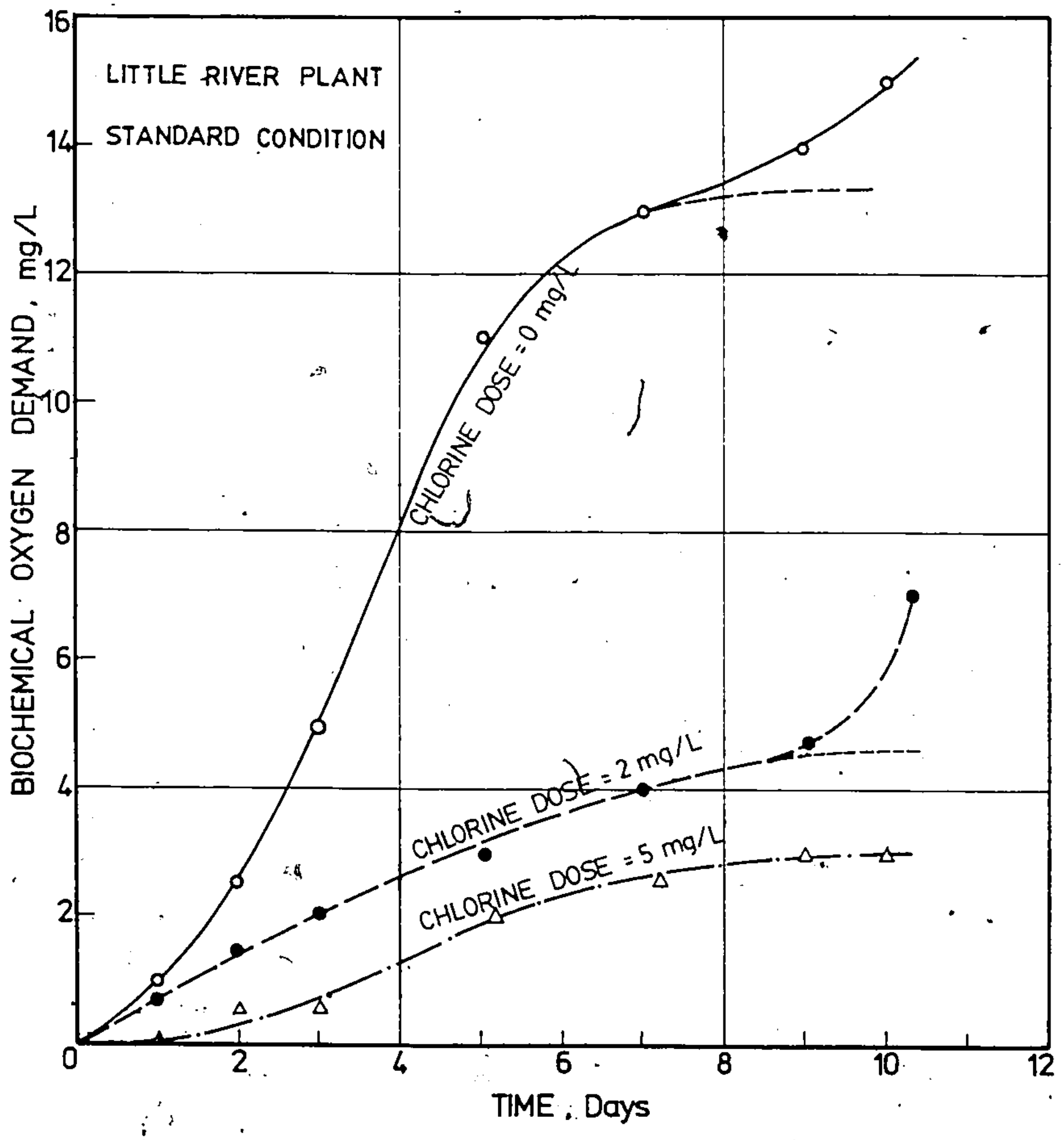

Fig. 4.44. Effect of Chlorine Dose on BOD Progression, Little River Plant.

samples. These figures show that lower BOD values were obtained by light and dark incubation than those obtained by the standard method in which BOD bottles were incubated all the time in darkness. In Fig. 4.46 it should be noted that when 8 mg/L chlorine was added to the samples, it yielded no measurable BOD.

4.2.3.3 Effect of Stirring

In practice, turbulence in streams and treatment plants is expected to result in different effects on the rate of oxygen utilization for biochemical reaction. Therefore, turbulence was introduced in BOD bottles by stirring their contents.

BOD tests were conducted on the final effluent from West Windsor Plant with three chlorine concentrations, 0, 5 and 10 mg/L, and on the final effluent from Little River Plant with three chlorine concentrations, 0, 5 and 8 mg/L. For each test, BOD values were taken daily for 7 days in two separate sets of bottles kept under standard and stirred conditions. The reported values are an average of two readings from two separate BOD bottles. Figures 4.47 and 4.48 show typical BOD progression curves from both plants under standard and stirred conditions with alternating exposure to light and darkness.

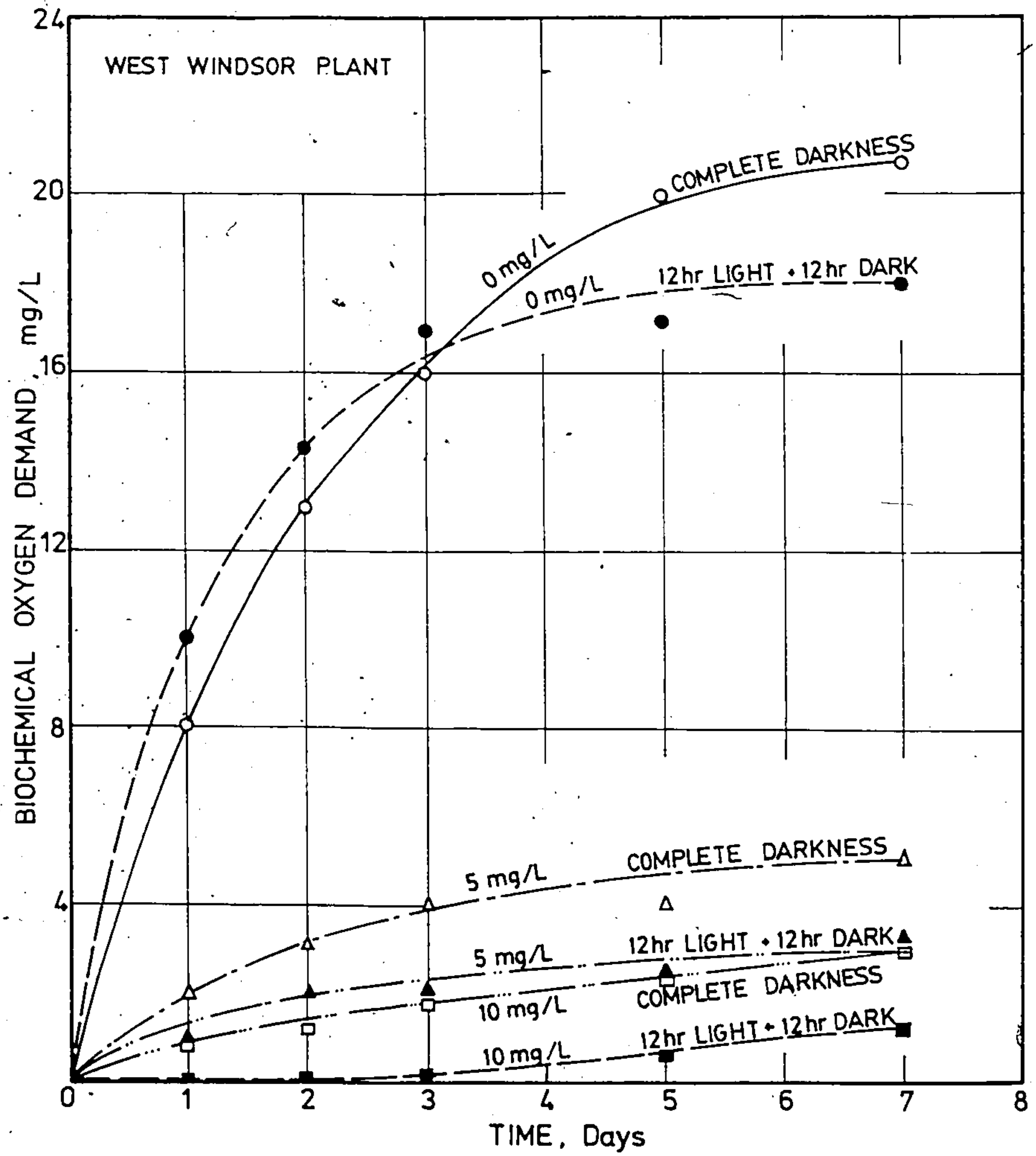

Fig. 4.45. Effect of Eutrophication on BOD Progression - West Windsor Plant.

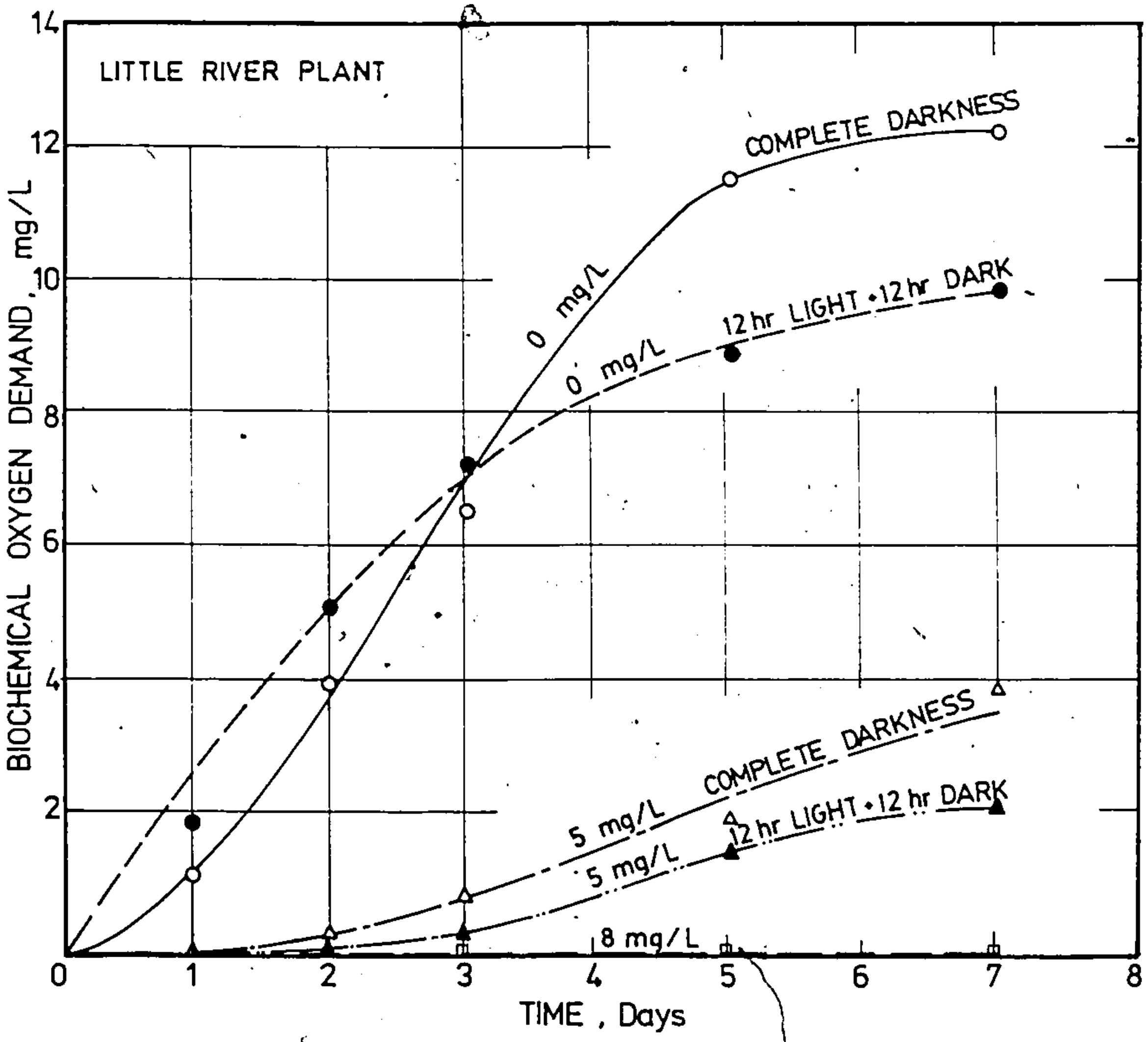

Fig. 4.46. Effect of Eutrophication on BOD Progression, Little River Plant.

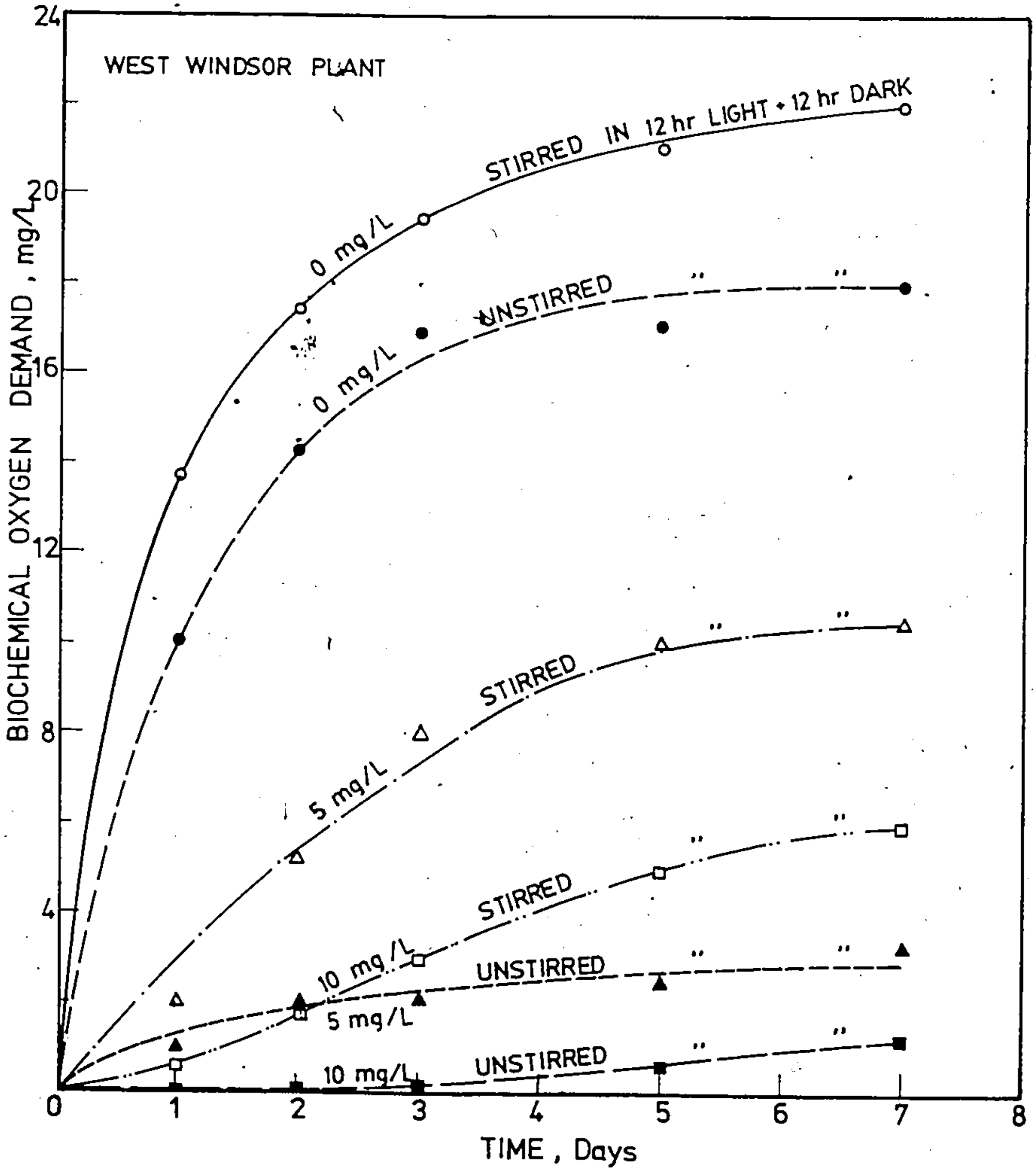

Fig. 4.47 Effect of Stirring on BOD Progression, West Windsor Plant.

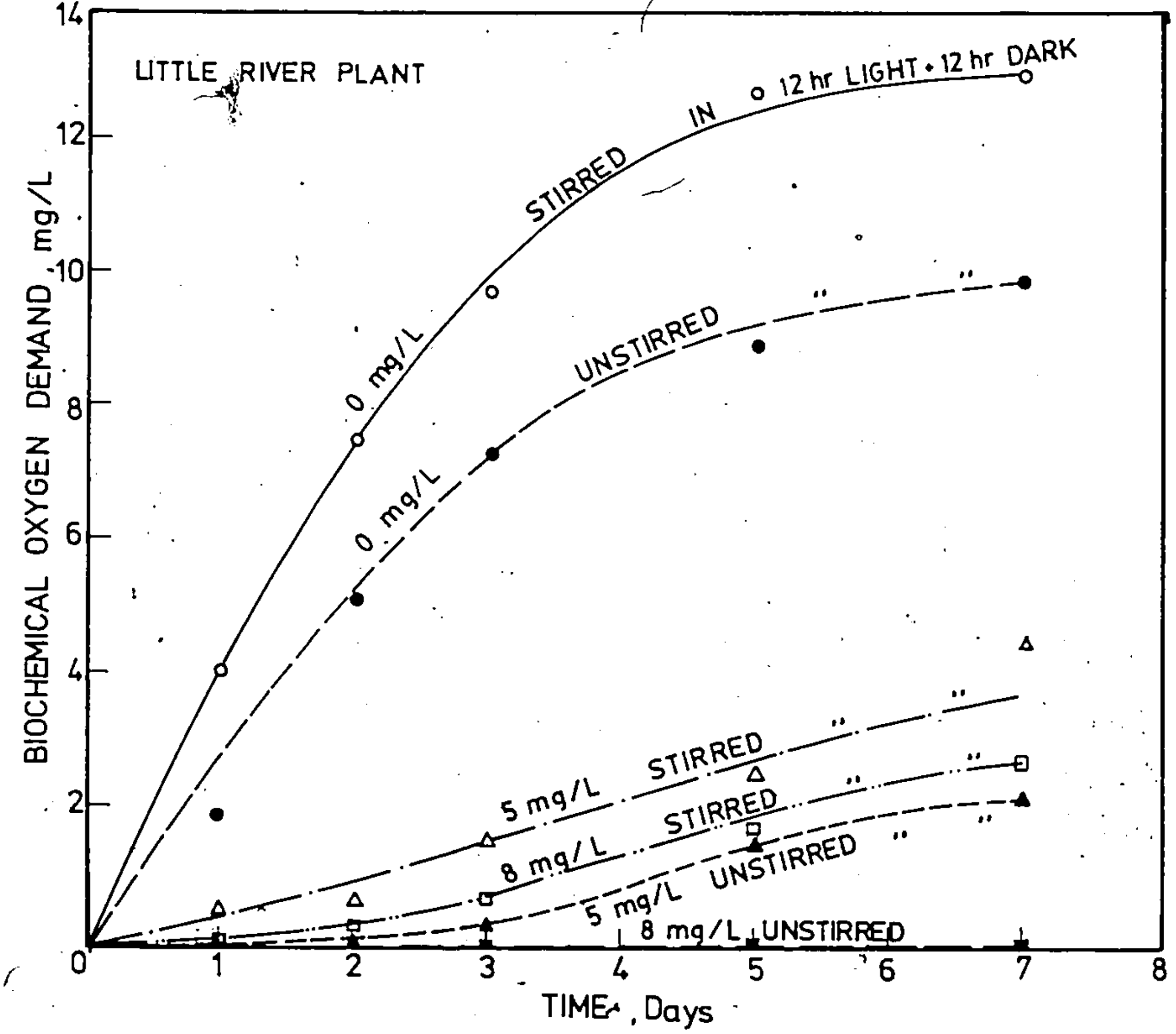

Fig. 4.48. Effect of Stirring on BOD Progression, Little River Plant.

4.2.3.4 Effect of Chlorination With and Without Nitrification Suppression by Pasteurization

In order to eliminate the influence of nitrifying bacteria on BOD progression, three sets of experiments were conducted with 0, 5 and 8 mg/L of chlorine dose in the pasteurized final effluent sample from Little River Plant. Typical BOD progression curves, with and without nitrification suppression under standard conditions, are plotted in Fig. 4.49. Figure 4.50 shows similar BOD progression curves with and without nitrification suppression when exposed to alternating 12 hours of light and 12 hours of darkness each day. Examining both figures, it can be seen that pasteurization of the samples yields BOD values slightly lower than those obtained without pasteurization.

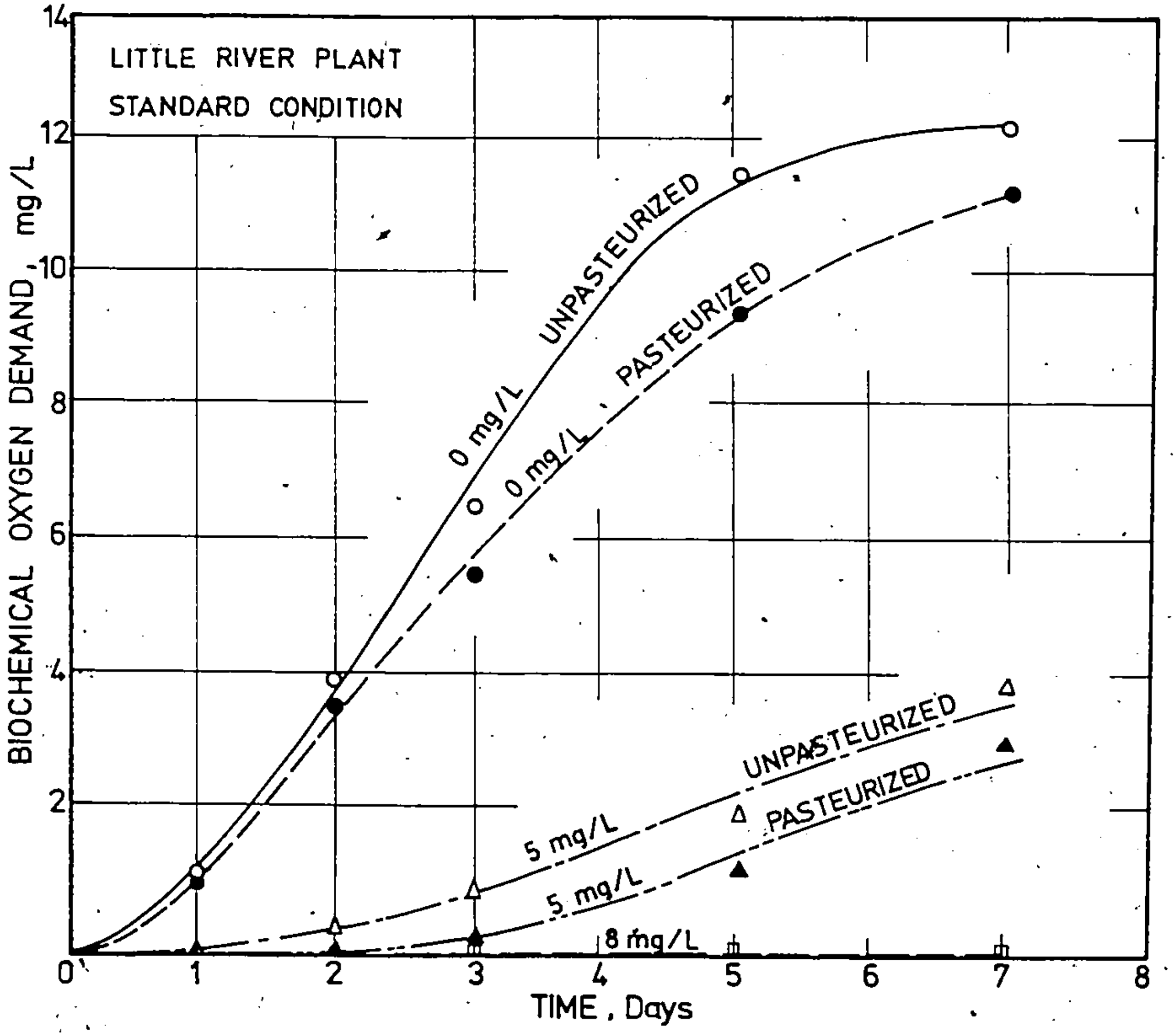

Fig. 4.49. BOD Progression With and Without Nitrification Suppression Under Standard Condition.

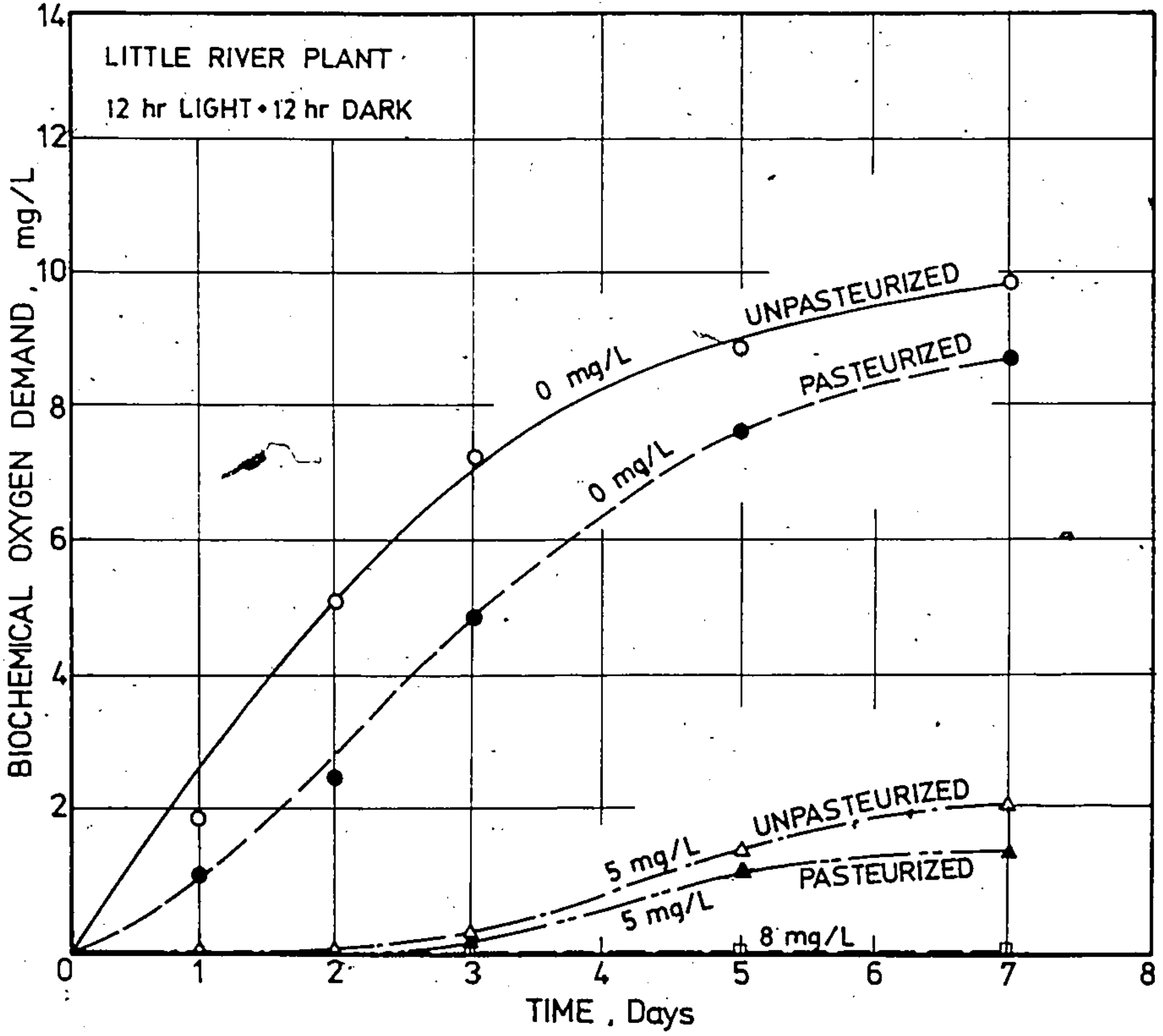

Fig. 4.50. BOD Progression With and Without Nitrification Suppression Under Alternating Exposure to Light and Dark.

CHAPTER V

ANALYSIS AND DISCUSSION

5.1 HYDRODYNAMIC STUDIES

In this section, the behaviour of buoyant and non-buoyant circular jets in cross-flow have been analyzed for the following variables: velocity ratio, R, relative depth of flow, H/D, pipe position, Z_p, and densimetric Froude number, F_o. First, the distribution of the velocity, concentration and temperature in the cross-sections of the deflected jet were analyzed. Secondly, the trajectories were analyzed for bottom and surface jets. Thirdly, the entrainment into the deflected jet was studied. Finally, general equations for both the jet trajectory and minimum dilution were derived.

5.1.1 Dimensional Analysis

In the case of a turbulent jet discharged into cross-flowing homogeneous ambient water, the jet profile, y=f(x), depends in general on the following variables:

x = the longitudinal distance measured from the outfall

H = the ambient water depth

D = the outfall diameter

V_j = the initial outfall velocity

U_a = the ambient velocity

g = acceleration of gravity

ρ_a = the ambient density

$\Delta\rho$ = the density difference between the fluid of the jet and the surrounding ambient

ν = the kinematic viscosity

Z_p = the vertical distance from channel bottom to pipe crown

θ = the angle of discharge

ε_1 = the bed roughness

z_1 = the cotangent of the side slope

Figures 2.1 and 3.2 show the definition sketch of this problem.

Considering the requirement for dimensional consistency, the jet profile can be written as

$$y = f_o(x,H,D,V_j,U_a,Z_p,g,\rho_a,\Delta\rho,\nu,\theta,\varepsilon_1,z_1) \qquad (5.1)$$

In dimensionless variables, Eq. 5.1 becomes

$$\frac{y}{D} = f(\frac{x}{D},\frac{H}{D},\frac{V_j}{U_a},F_o,R_N,\frac{Z_p}{H},\frac{\varepsilon_1}{H},\theta,z_1) \qquad (5.2)$$

in which F_o is a densimetric Froude number,

$$F_o = \frac{V_j}{\sqrt{\frac{\Delta\rho}{\rho_a}gD}} \qquad (5.3)$$

and R_N is a jet Reynolds number,

$$R_N = \frac{V_j D}{\nu} \tag{5.4}$$

Several assumptions are necessary in order to reduce the number of independent variables to be included. The jet Reynolds numbers in the tests described herein are of the order of 10^4 or larger as shown in Table 3.1. Thus, the shear stresses causing the jet spread and leading to the jet deflection are turbulent, and the Reynolds number is considered to be sufficiently large to have no influence on Eq. 5.2. This study is also restricted to turbulent jets discharged perpendicular to ambient water and the side slope of the experimental flume was 3H to 1V which is a typical natural stream slope. Therefore, θ and z_1 are deleted from Eq. 5.2. The bed roughness, ε_1, is due either to bed forms or dredging irregularities. A typical value of ε_1, is found to vary from 0.15 to 0.60 m for the Detroit River (U.S. Corps of Engineers, 1974). The water depth in the Great Lakes channels varies from 3 to 10 m (U.S. Department of Commerce, 1979). The ratio $\frac{\varepsilon_1}{H}$ generally lies between $\frac{1}{10}$ to $\frac{1}{60}$. In this study, the flume bed was covered with river gravel of 6.5 to 12.5 mm diameter and a typical water depth in the flume was 0.2 m. Thus, the average roughness to depth ratio of this study was $\frac{1}{20}$ and consequently the effect of the relative roughness on Eq. 5.2 was considered to be representative of the Great Lakes connecting channels.

Profile shape of the jet is thus described by

$$\frac{Y}{D} = f\left(\frac{X}{D}, R, F_o, \frac{H}{D}, \frac{Z_p}{H}\right) \tag{5.5}$$

where R = the velocity ratio = $\frac{V_j}{U_a}$

A natural system of coordinates based on the jet profile can be defined by ξ, η, ζ as shown in Fig. 2.1. Similarly, dimensional analysis shows that the maximum velocity, U_m, and concentration, C_m, along the jet axis, ξ, respectively, have the forms:

$$\frac{U_m}{V_j} = f\left(\frac{\xi}{D}, R, F_o, \frac{H}{D}, \frac{Z_p}{H}\right) \tag{5.6}$$

$$\frac{C_m}{C_o} = f\left(\frac{\xi}{D}, R, F_o, \frac{H}{D}, \frac{Z_p}{H}\right) \tag{5.7}$$

where ξ = the distance measured along the jet axis

C_o = the initial jet concentration.

In the case of buoyant jets, the factors affecting the temperature profiles are similar to those that affect the concentration in non-buoyant jets, Eq. 5.7. However, there is heat transfer between the jet and the surrounding water and also heat loss between the plume and the surrounding air. Therefore, the following additional parameters are introduced:

K = thermal conductivity of the fluid, $J.m^{-1}.s^{-1}.°K^{-1}$

C_p = specific heat, $J.kg^{-1}.°K^{-1}$

β = coefficient of expansion, $°K^{-1}$

From dimensional analysis (Schlichting 1968), the excess temperature, ΔT, is described by

$$\frac{\Delta T}{\Delta T_o} = f\left(\frac{\xi}{D}, R, F_o, \frac{H}{D}, \frac{Z_p}{H}, G, P\right) \tag{5.8}$$

where G = Grashof number = $\frac{g\beta D^3 \Delta T_o}{\nu^2}$

P = Prandtl number = $\frac{\nu}{a}$

and a = thermal diffusivity, m^2/s = $\frac{K}{\rho_a C_p}$.

The Grashof number becomes important only at very small velocities of flow, particularly if the motion is caused by buoyancy forces, e.g., plume rise problems and also for a relatively compressible fluid (Schlichting 1968). Since this study is mainly for jet flow in water, the Grashof number is dropped from any further consideration. The Prandtl number depends only on the properties of the medium (Schlichting 1968) and therefore it is deleted from Eq. 5.8. Thus Eq. 5.8 becomes

$$\frac{\Delta T}{\Delta T_o} = f\left(\frac{\xi}{D}, R, F_o, \frac{H}{D}, \frac{Z_p}{H}\right) \tag{5.9}$$

5.1.2 Velocity Profiles

In rivers which are navigable, such as the Great Lakes connecting channels, cross river velocities induced by cross discharges may be hazardous to ship and barge traffic. Most of the available literature has been concerned with measuring or predicting the jet velocity along the jet axis (Keffer and Baines 1962, Parr 1979 and Rajaratnam 1980). Little attention has been given to the actual velocity distribution across the river and the interference between the jet and the cross-flow. In this section, the effect of the jet velocity on the lateral distribution of the longitudinal velocity of the river is discussed and analyzed.

Three different sets of experiments were performed to measure the velocity distribution due to the jet injection for different velocity ratios, discharges and relative depths. In the first set, presented in Fig. 4.1 and Tables A.1 to A.3, the outfall was at the bottom, whereas, the second set represents a submerged outfall, Fig. 4.2 and Tables A.4 and A.5. In the third set, shown in Fig. 4.3 and Tables A.6 and A.7, the outfall was placed at the surface. In Figs. 4.1, 4.2 and 4.3, the undisturbed velocities, i.e., the longitudinal channel velocities without the jet, were plotted at x/D=0.0. Although the inlet to the laboratory flume was provided with a screen and a weir to distribute the flow uniformly across the channel, the measurements showed some nonuniformity in the flume velocity especially at high flows and depths, e.g., Experiments 7, 9, 14, 16, 21 and 23.

The effect of a bottom discharged jet on the velocity distribution is shown in Fig. 4.1 and Tables A.1 to A.3. In this figure, the local depth averaged velocity, U, is normalized with respect to the average velocity in the cross section, $\bar{U}$, and plotted against y/D. The locus of maximum velocity values were used as a basis for defining the jet trajectory. The maximum values, as expected, increase with increasing the velocity ratio, R, as shown in Tables A.1 to A.3. The normalized velocity, $U/\bar{U}$, is seen to decrease along the path of the jet from a maximum value to eventually merge with the undisturbed channel velocity. Also, the velocity induced by the jet decreases with the longitudinal distance to eventually attain the channel velocity at $x/D \geq 24$.

The normalized velocity profiles for a submerged outfall as measured across the channel are shown in Fig. 4.2 and Tables A.4 and A.5 for different parameters. In this case, the ambient cross-flow decelerates as it approaches the jet boundaries as if it was being blocked by a rigid obstacle, except that "the boundaries of the jet are compliant and entraining" (Moussa et al. 1977). Experiments 11, 12, 14 and 16 showed that there is a tendency of bifurcation in the velocity profiles and this tendency increases with increasing the velocity ratio. In Fig. 4.2 and for R=6.5, the jet bifurcates into a pair of vortices leading to two velocity maxima. This bifurcation becomes stronger with distance as the two velocity maxima diverging at an angle of 5-8°. This agrees with Rajaratnam et al. (1980) who reported that for the experiments with R=7.0, there are more than one maximum velocity points. Scorer (1959) and Turner (1960) had shown that a strongly buoyant plume in a cross-flow may actually bifurcate into two concentration maxima. The bifurcation shown in Fig. 4.2 is also confirmed by the Photographs 4.4, B.8 and B.11 where a splitting in the coloured dye is clear. For small velocity ratios, R<4.2, the measurements showed no bifurcation.

The velocity profiles due to jet injection from an extended surface outfall are shown in Fig. 4.3 and Tables A.6 and A.7. Experiments 17 to 23 showed no bifurcation and the jet trajectory can be detected by tracing the locus of the maximum velocity. The extended pipe obstructed the flow and decreases the cross-flow velocity downstream from the pipe location. This is demonstrated in Fig. 4.3 at x/D=6, 12 and 24 and for y/D≤12 which corresponds to the pipe length.

In all the velocity analysis presented in this section, the reported velocities are the average measurements based on 0.2, 0.5 and 0.8 the depth of flow. Figure 4.4 presents comparative plots of lateral velocities taken at 0.8H from the bed, for the case of extended surface outfall. Comparing Figs. 4.3 and 4.4 indicates that the measurements taken at 0.8H show a slight increase in the jet velocity and a slight shift in the jet trajectory away from the bank. However, this effect diminishes as the jet moves downstream from the outfall. All the velocity measurements at 0.2, 0.5 and 0.8H as well as the depth-averaged velocity are given in Appendix A.

In order to study the difference between the extended and shore-based surface outfall, the velocity profiles of Exps. 18 and 25 for these two cases are compared in Fig. 5.1. In the case of the extended outfall, the disturbance of the ambient flow is less and the velocity profile returns to the ambient profile at $\frac{x}{D}\geq 12$. For the shore-based case, the velocity profile is highly nonuniform and the effect of the jet is carried further downstream to $\frac{x}{D}\geq 24$. Moreover, the shore-based outfall causes a recirculation to occur at the lee side of the jet. This zone of negative velocity may have high concentrations of hazardous materials discharged through the outfall by an industry or treatment plant. Therefore, it may be advantageous to have outfalls extended a distance away from

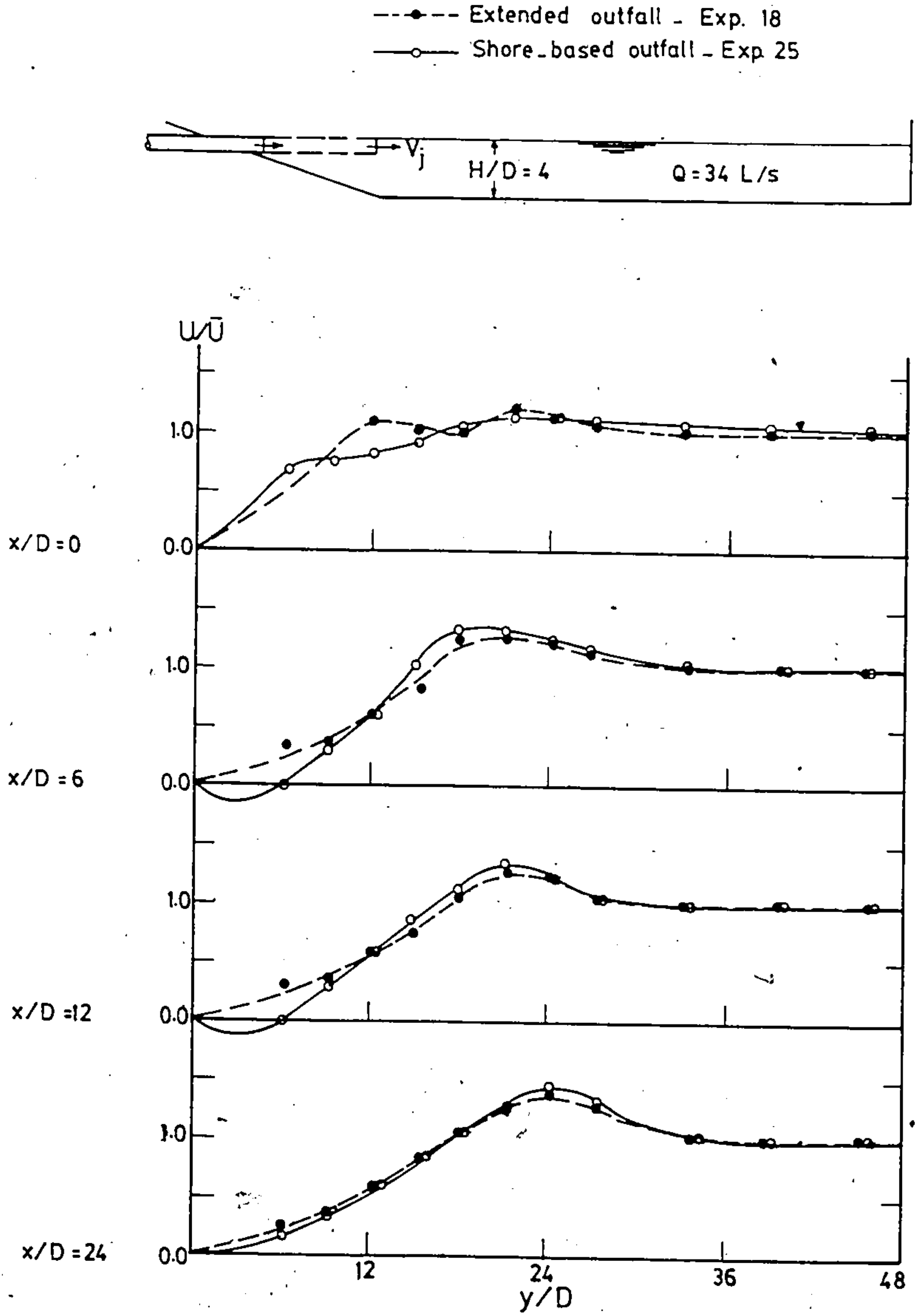

Fig. 5.1. Comparison of lateral velocity profiles between shore-based and extended surface outfalls - Exps. 25 and 18.

the shore so that the waste directly mixes with the receiving stream resulting in a rapid dispersion. However, the costs and maintenance involved in extending outfalls further from the shore may offset this advantage.

5.1.2.1 Bed Shear Stresses

In order to check the development of the boundary layer for the turbulent flow encountered in the present experimental investigation, a plot of the velocity, U, with no jet, versus the vertical distance, $\frac{z}{H}$, is depicted in Fig. 5.2. These velocity profiles show a fully developed turbulent shear flow for different flow rates. The shear stresses at the bed are counterbalanced by the driving forces-pressure gradients and gravity. The velocity distribution reported by Fischer et al. (1979) is observed to be excellently approximated by a logarithmic function as follows:

$$U-\bar{U} = \frac{U_*}{k'} + \frac{2.3}{k'} U_* \log_{10} \frac{z}{H} \qquad (5.10)$$

where

k' = the von Karman constant $\cong 0.4$

z = the vertical distance measured from the bed

H = the depth of flow

U_* = the shear velocity = $\sqrt{\tau_o/\rho}$

τ_o = the bed shear stress

$\bar{U}$ = the average river velocity ($U=\bar{U}$ at $\frac{z}{H} = 0.368$).

The linear velocity profiles of Fig. 5.2 were replotted on a semi-log scale as shown in Fig. 5.3. These profiles follow a straight line indicating that the ambient velocity in the flume follows a logarithmic distribution. The logarithmic profiles are obtained as follows:

$$U-\bar{U} = 2.45 + 5.64 \log \frac{z}{H} \quad \text{for} \quad Q = 34 \text{ L/s} \qquad (5.11)$$

$$U-\bar{U} = 3.60 + 8.30 \log \frac{z}{H} \quad \text{for} \quad Q = 70 \text{ L/s} \qquad (5.12)$$

$$U-\bar{U} = 3.90 + 8.97 \log \frac{z}{H} \quad \text{for} \quad Q = 100 \text{ L/s} \qquad (5.13)$$

The shear velocity, U_*, and the shear stress, τ_o, for each experiment run of Fig. 5.3 can be obtained by comparing Eqs. 5.11, 5.12 and 5.13 with Eq. 5.10. The shear stresses correspond to Eqs. 5.11, 5.12 and 5.13 are 0.0098, 0.021 and 0.025 N/m^2, respectively. A typical distribution of shear stress on the side and bottom of the flume is shown in Fig. 5.4 for Q = 34 L/s.

5.1.2.2 Velocity Similarity Analysis

When a jet is discharged into a stream, the local vertical velocity distributions no longer follow a logarithmic profile. This is shown in Figs. 5.5 and 5.6 where the dimensionless excess velocity, $\frac{\Delta U}{\Delta U_o} = \frac{U-U_a}{\bar{V}_j-U_a}$, is plotted against relative depth, $\frac{z}{H}$ for bottom and extended surface outfalls, respectively.

The dimensionless excess velocity profiles in the

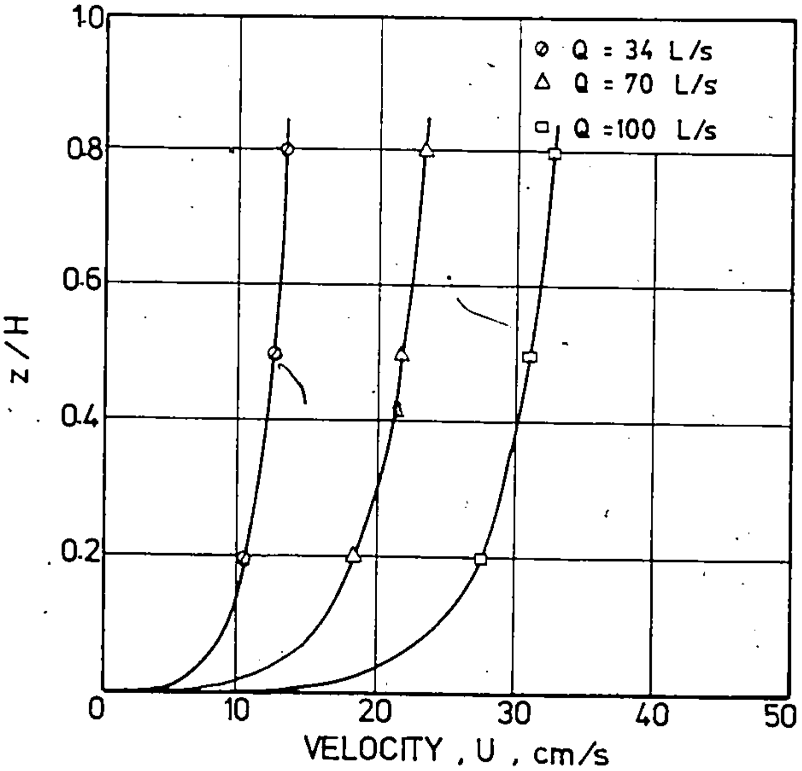

Fig. 5.2. Variation of U(without jet) with $\frac{z}{H}$ for different flow rates.

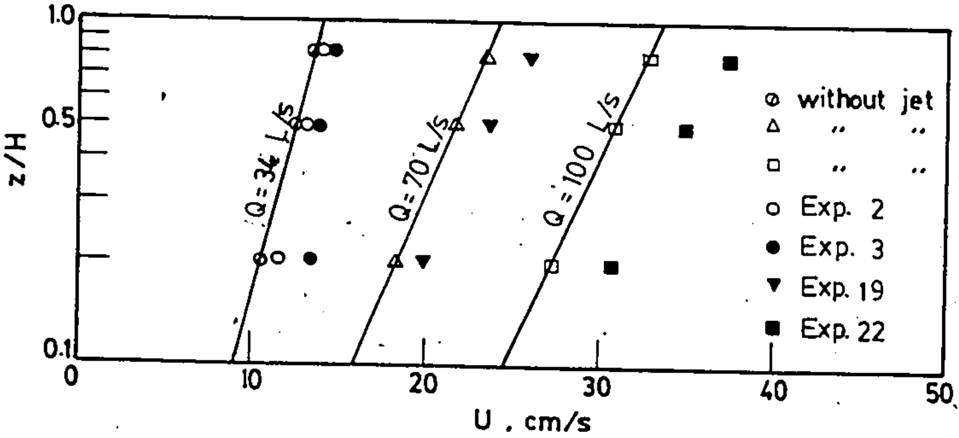

Fig. 5.3. Logarithmic variation of the velocity U with $\frac{z}{H}$.

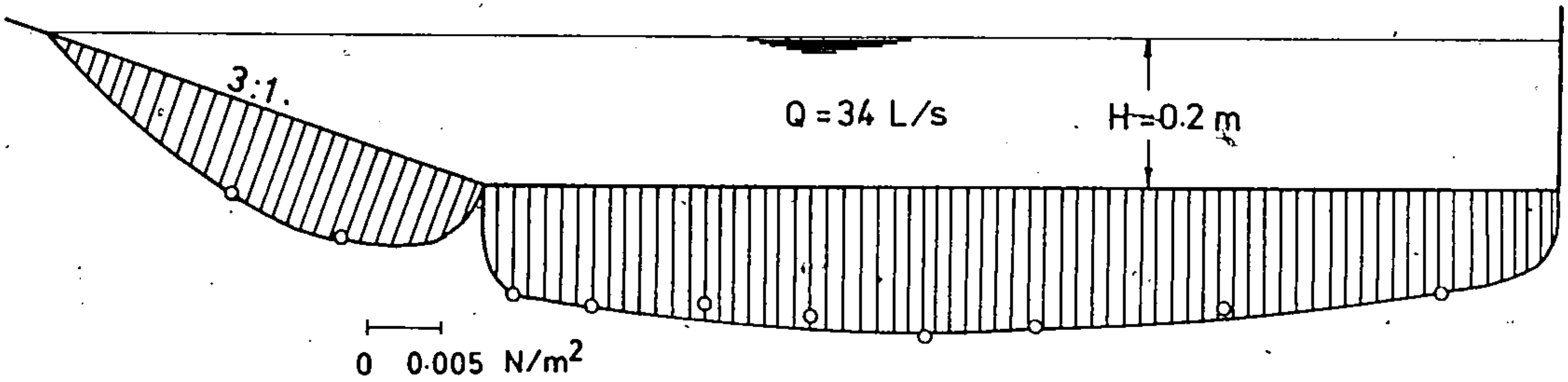

Fig. 5.4. Typical distribution of shear stresses in the flume.

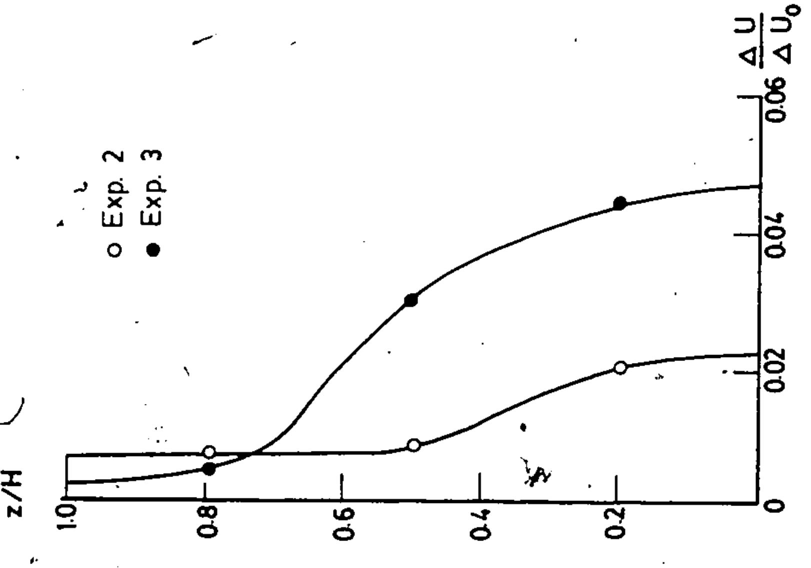

Fig. 5.5. Vertical excess velocity profile for bottom outfall (neutral density).

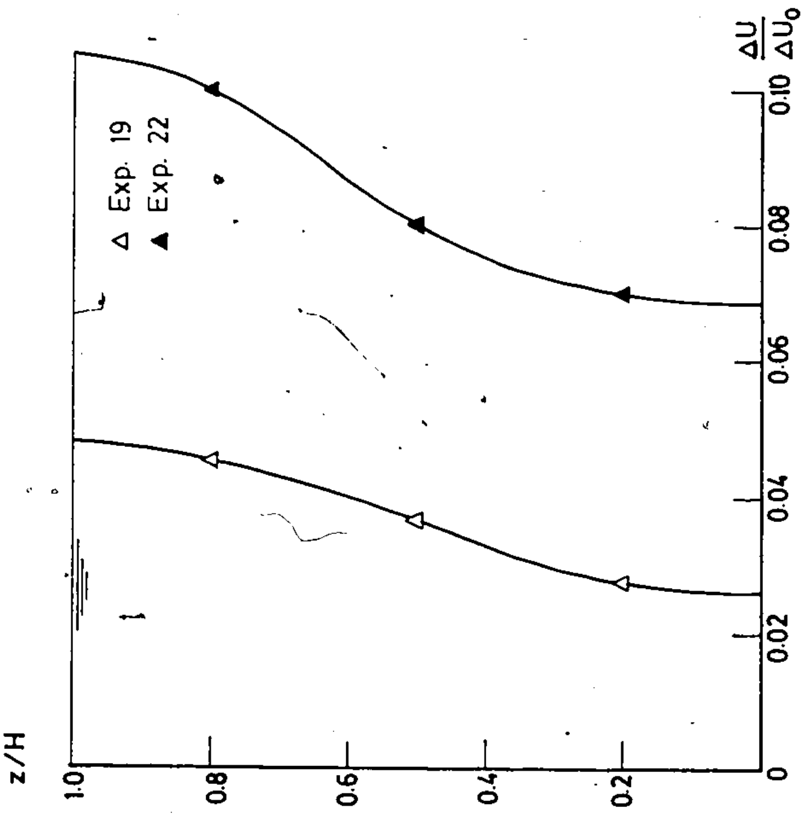

Fig. 5.6. Vertical excess velocity profiles for extended surface outfall (neutral density).

lateral direction were analyzed for similarity. Figure 5.7 shows $(\frac{\Delta U}{\Delta U_o})/(\frac{\Delta U_m}{\Delta U_o})$ plotted against η/σ_η where the subscript m refers to the maximum value of $\frac{\Delta U}{\Delta U_o}$, η is the coordinate normal to the jet trajectory, ξ, and σ_η is the standard deviation, i.e., the width at which 0.683 of the total area is enclosed by the lateral profile. From Fig. 5.7 it can be seen that the excess velocity profiles are similar and are best described by a Gaussian form. Similarly, it was found that the velocity profiles in the vertical direction were similar if values of $(\frac{\Delta U}{\Delta U_o})/(\frac{\Delta U_m}{\Delta U_o})$ were plotted against $\frac{\zeta}{\sigma_\zeta}$ where ζ is the vertical distance and σ_ζ is the velocity length scale in the vertical direction. A typical plot is shown in Fig. 5.8 where a Gaussian form describes the data reasonably well. Thus the excess velocity distribution can be taken as

$$(\frac{\Delta U}{\Delta U_o})/(\frac{\Delta U_m}{\Delta U_o}) = e^{-0.5\{(\eta/\sigma_\eta)^2 + (\zeta/\sigma_\zeta)^2\}} \tag{5.14}$$

Variations of the lateral and vertical length scales in terms of D are shown in Figs. 5.9 and 5.10 respectively, where values of $\frac{\sigma_\eta}{D}$ and $\frac{\sigma_\xi}{D}$ are plotted against $\frac{\xi}{D}$ for bottom and shore-based surface outfalls. In Fig. 5.9, both variations have the same trend but σ_η for surface outfall increases at a rate slightly higher than that of bottom outfall. However, σ_ζ for surface outfall grows at a rate approximately 1.20 times the rate of growth of σ_ζ for bottom outfall. From

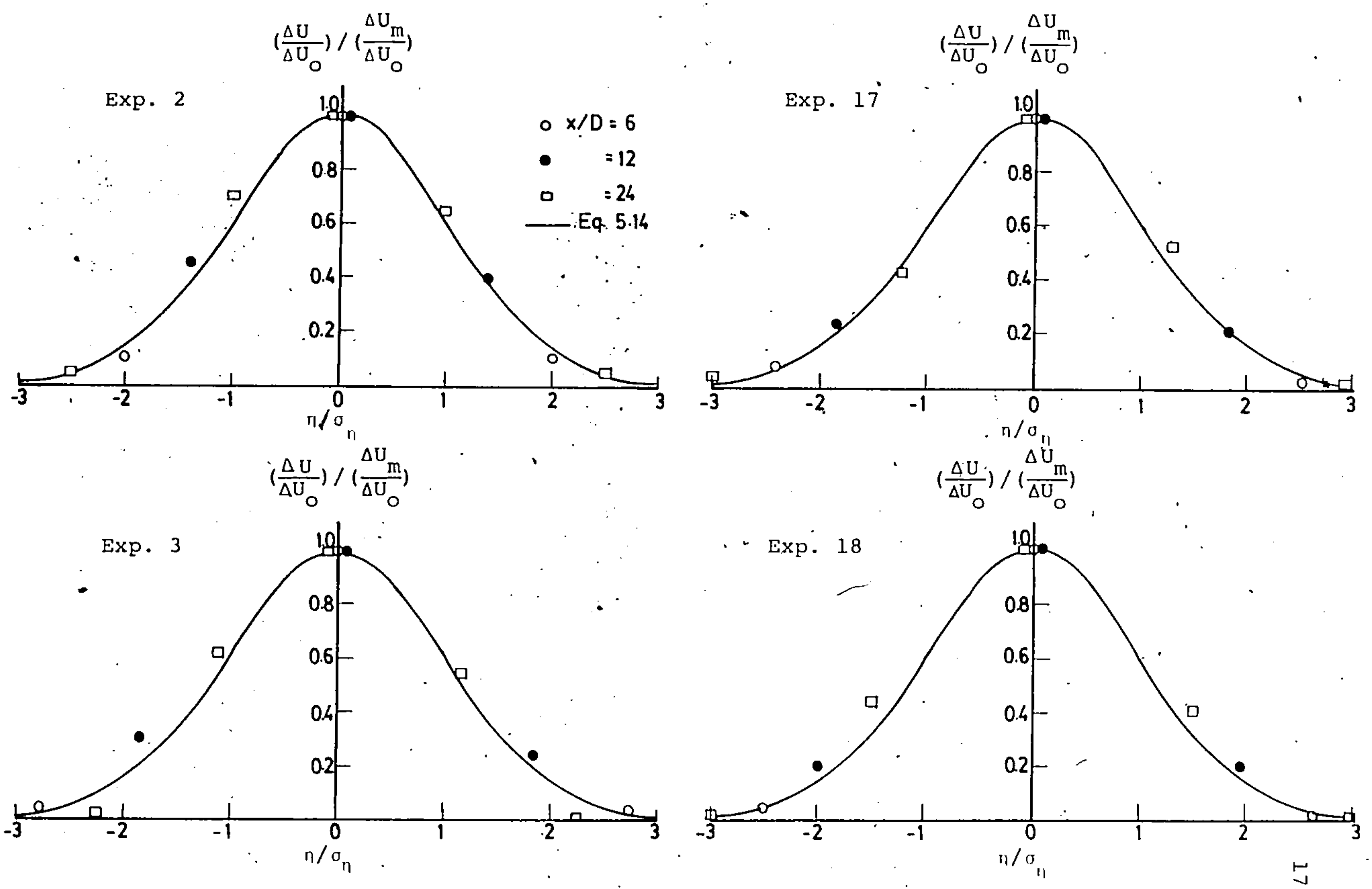

Fig. 5.7. Similarity of lateral velocity profiles.

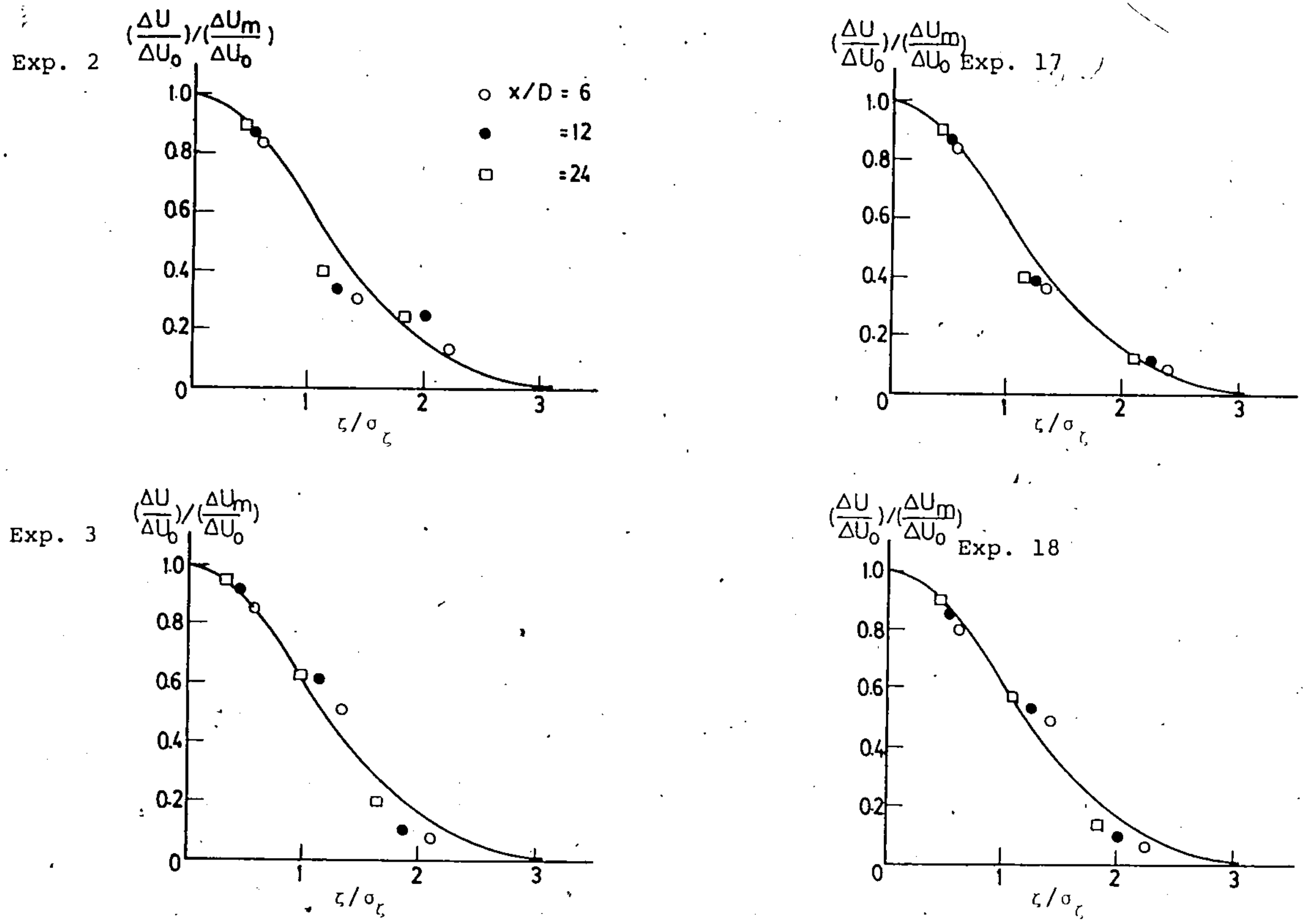

Fig. 5.8. Similarity of vertical velocity profiles.

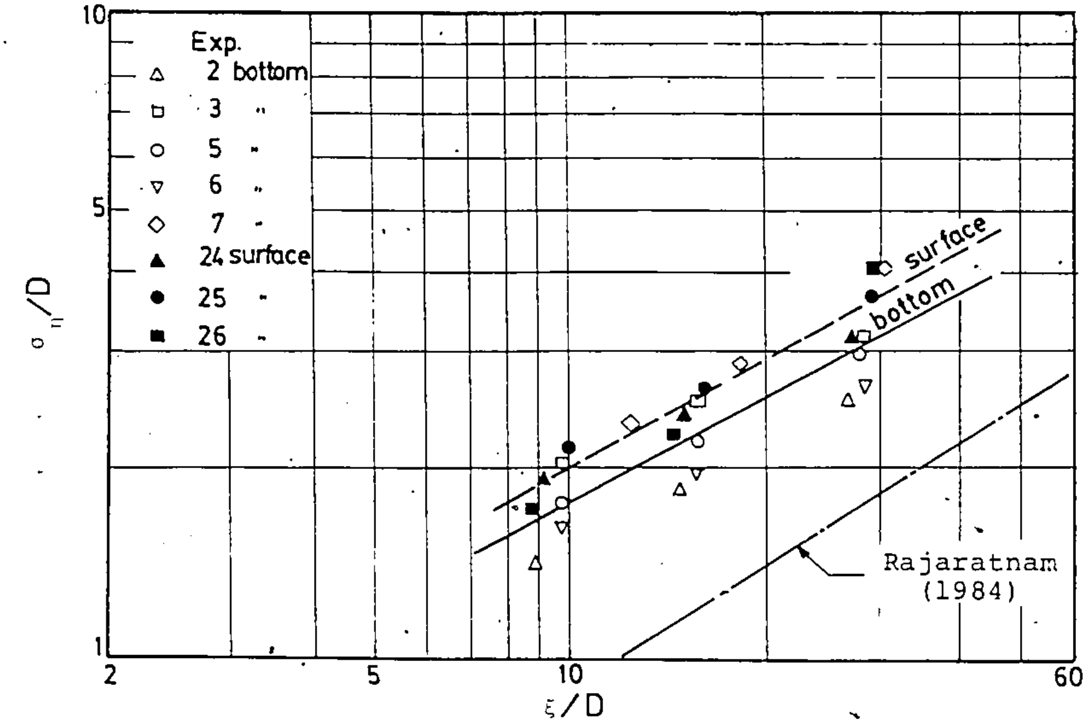

Fig. 5.9. Lateral length scale for velocity profiles.

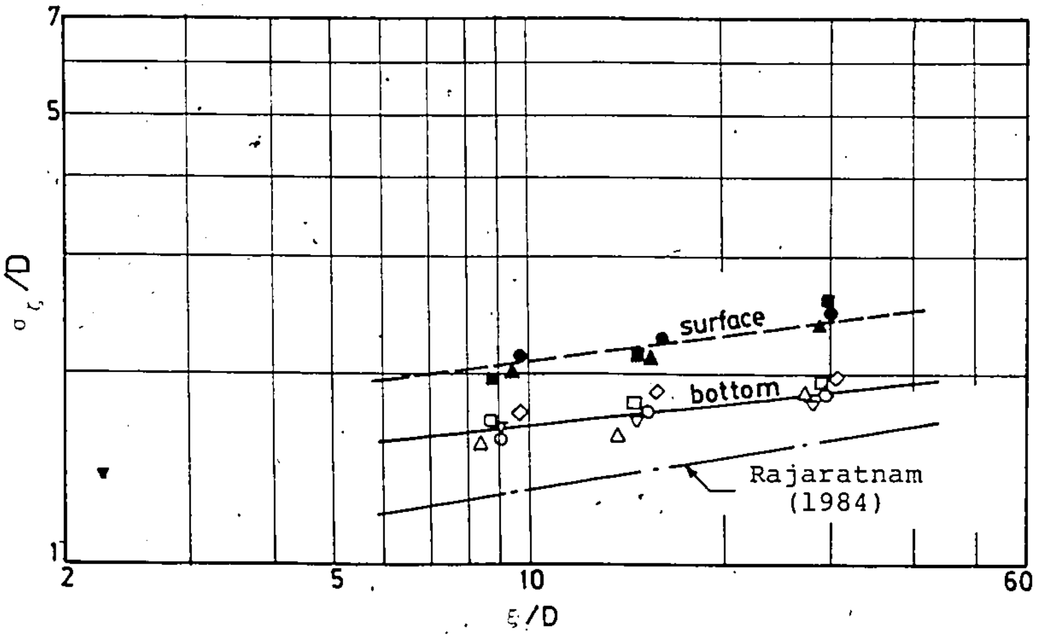

Fig. 5.10. Vertical length scale for velocity profiles.

Figs. 5.9 and 5.10, one can write that:

For bottom outfall

$$\frac{\sigma_\eta}{D} = 0.51\left(\frac{\xi}{D}\right)^{0.53} \qquad (5.15)$$

$$\frac{\sigma_\zeta}{D} = 1.30\left(\frac{\xi}{D}\right)^{0.10} \qquad (5.16)$$

For surface outfall

$$\frac{\sigma_\eta}{D} = 0.53\left(\frac{\xi}{D}\right)^{0.56} \qquad (5.17)$$

$$\frac{\sigma_\zeta}{D} = 1.56\left(\frac{\xi}{D}\right)^{0.12} \qquad (5.18)$$

The results for surface jets were compared with Rajaratnam's (1984) scales for a surface circular jet in coflowing streams as shown in Figs. 5.9 and 5.10. It is noted that the lateral and vertical scales are greater than those of Rajaratnam.

5.1.2.3 Decay of Jet Excess Velocity

Considering the decay of the velocity field, the variation of $(U_m - U_a)$ for bottom outfall with ξ/D is shown in Fig. 5.11 for different values of R, where U_m is the maximum velocity at any section along the jet. This figure shows that $(U_m - U_a)$ decreases very rapidly with ξ/D especially for high R. It is also seen from Fig. 5.11 that these profiles, although having a common shape, are not independent of the velocity ratio. For comparison purposes with bottom outfall, results of a similar analysis on extended surface outfall are shown in Fig. 5.12. Figures 5.11 and 5.12 indicate that the decay of the velocity fields in both cases are almost identical. Therefore, both bottom and extended surface outfalls can be considered as better means for disposal an effluent into natural streams than shore-based surface outfall.

Regarding the velocity scales, Figs. 5.13 and 5.14 depict the excess velocity made dimensionless by dividing by the initial maximum excess velocity (V_j-U_a), plotted in a log-log system with ξ/D. It is seen that the points lie on straight lines and the decay of U_m-U_a is a function of the velocity ratio, R, when plotted from the origin. However, when the data points are plotted for some distance after the end of the establishment zone, the points are described by a straight line and are independent of the velocity ratio as shown in Figs. 5.15 and 5.16 for bottom and surface outfalls, respectively. Also included in Fig. 5.15, the data of Keffer and Baines (1962) for bottom jets discharged vertically to a cross-flow. It can be seen that the reported results for bottom jets discharged horizontally to a cross-flow show a linear variation, while the curve developed by Keffer and Baines is nonlinear. The results of bottom outfall shown in Fig. 5.15 are analogous to those of the free jet by Albertson et al. (1950). The excess velocity, however, decreases much more rapidly than for the free jet results and the rate of decrease increases with distance away from the source. This is because the entrainment is augmented by secondary effects, primarily the twin vortices, which do not exist in the free jet. Finally, it can be concluded that a single functional behaviour of the jet velocity exists for various velocity ratios if the jet is considered after the establishment zone. The decay of the maximum excess velocity can be represented by the following linear relationships:

$$\frac{\Delta U_m}{\Delta U_o} = \frac{U_m - U_{a_\xi}}{V_j - U_{a_o}} = a'\left(\frac{\xi'}{D}\right)^{-1} \tag{5.19}$$

where

U_m = longitudinal ambient velocity in ξ direction

U_{a_ξ} = longitudinal ambient velocity at ξ position

U_{a_o} = ambient velocity at the end of the establishment zone

ξ' = distance measured along the deflected jet after the establishment zone.

a' = constant

= 1.89 for bottom outfall

= 1.80 for extended surface outfall

= 3.20 for shore-based surface outfall

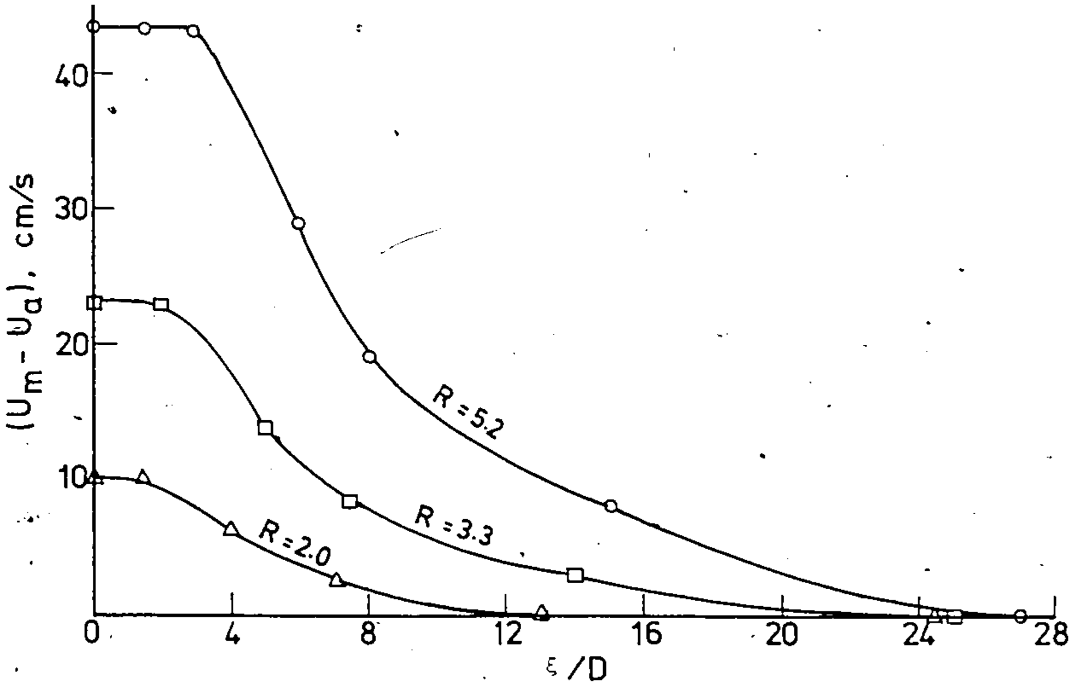

Fig. 5.11. Decay of maximum jet velocity at different velocity ratios for bottom outfall.

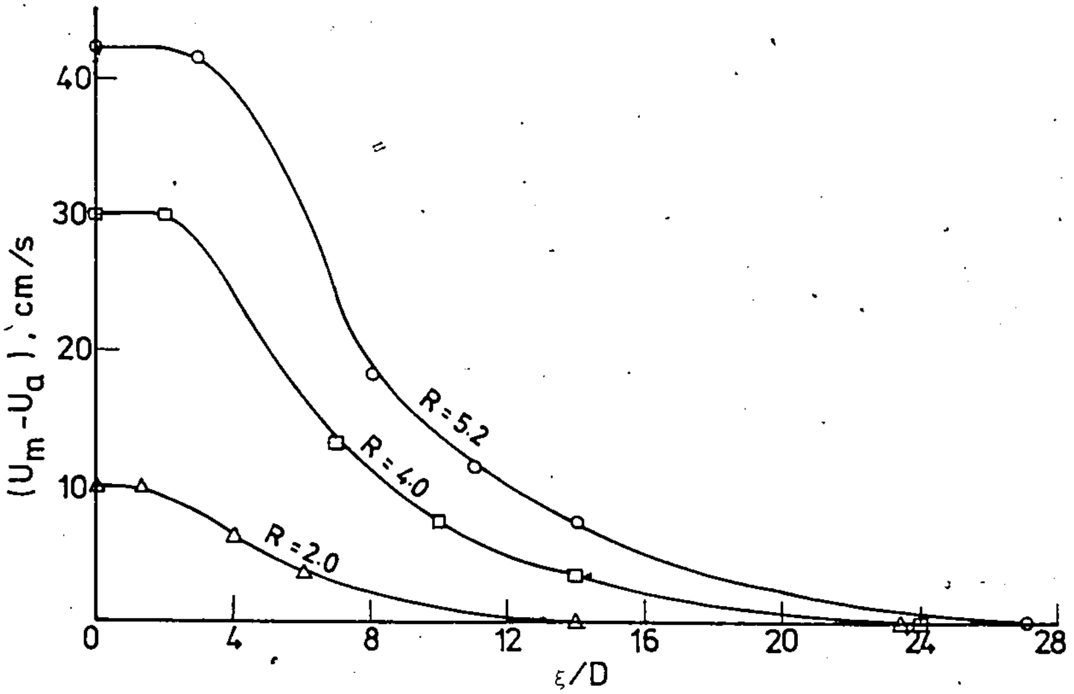

Fig. 5.12. Decay of maximum jet velocity at different velocity ratios for extended surface outfall.

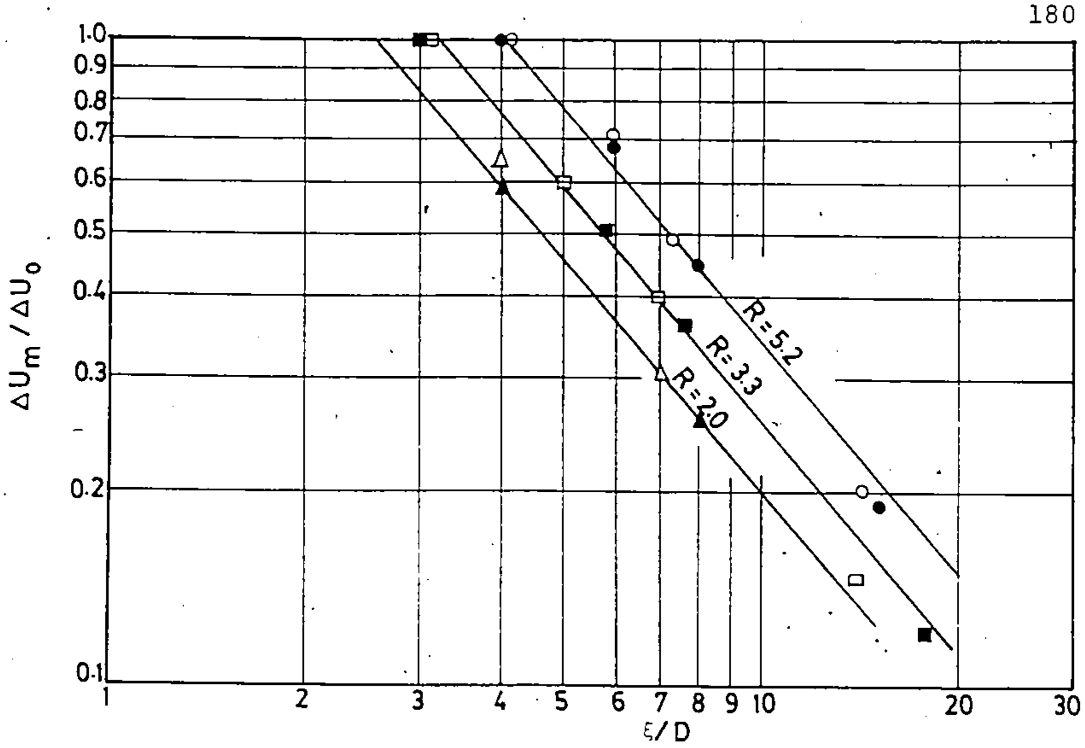

Fig. 5.13. Decay of maximum jet excess velocity from the nozzle for bottom outfall.

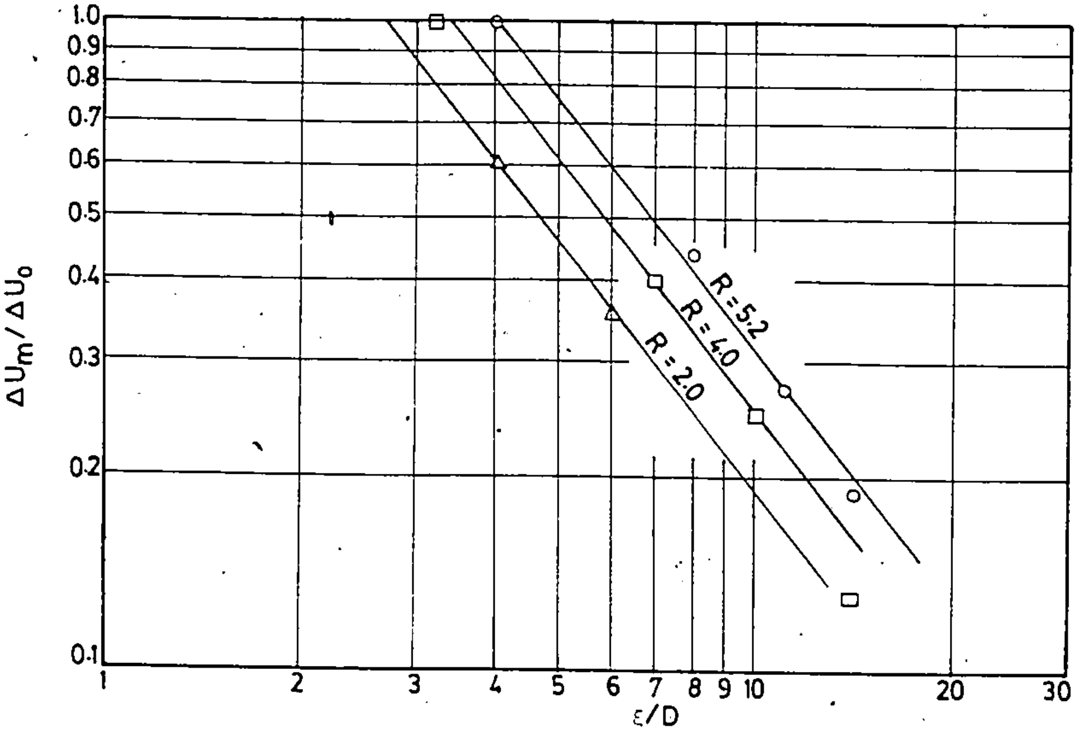

Fig. 5.14. Decay of maximum jet excess velocity from the nozzle for extended surface outfall.

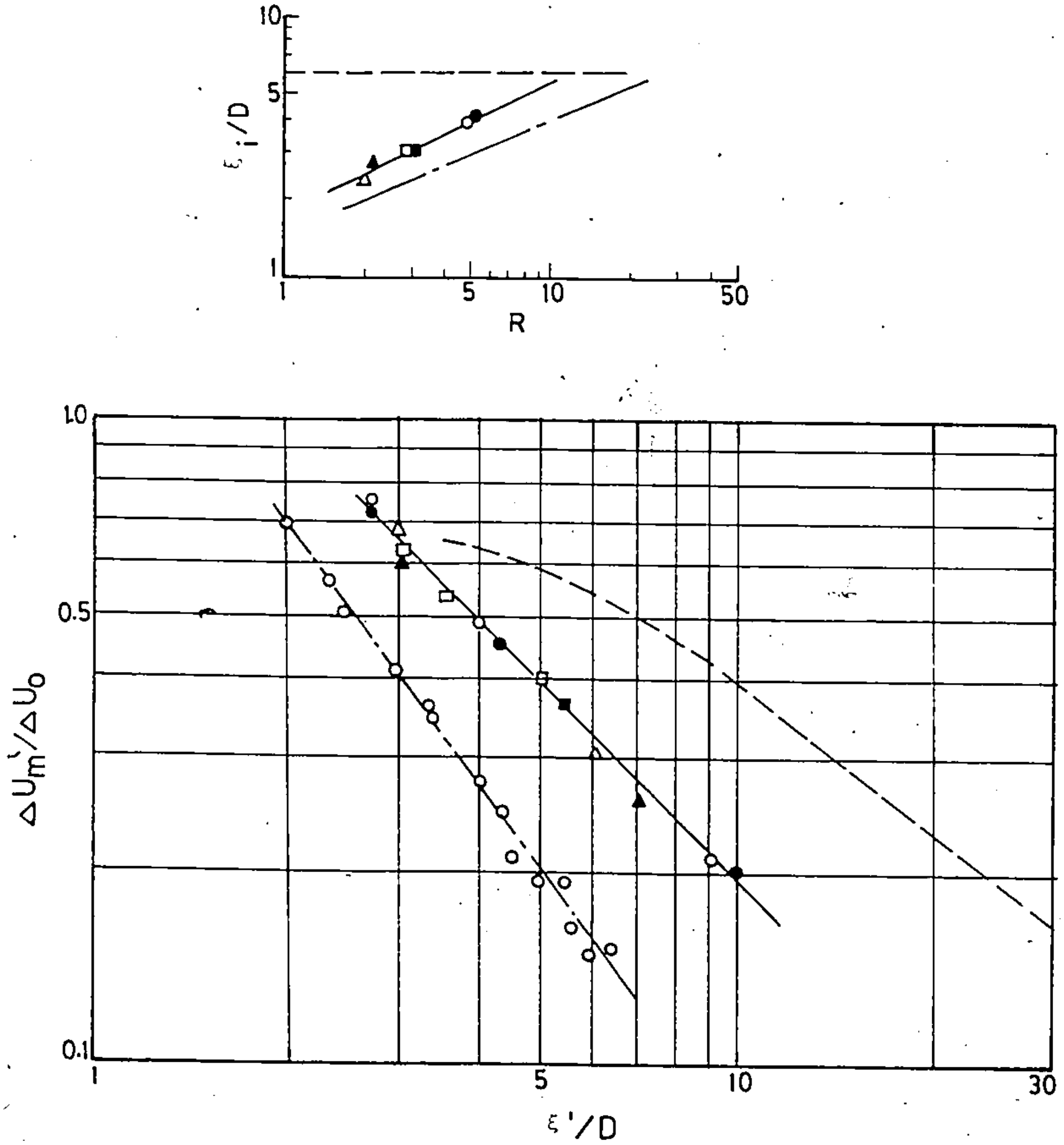

Fig. 5.15 Decay of maximum jet excess velocity after the establishment zone for bottom outfall.

– – – free jet by Albertson *et al*. (1950)

— — vertical jet in cross-flow by Keffer and Baines (1962)

——— results of this study..

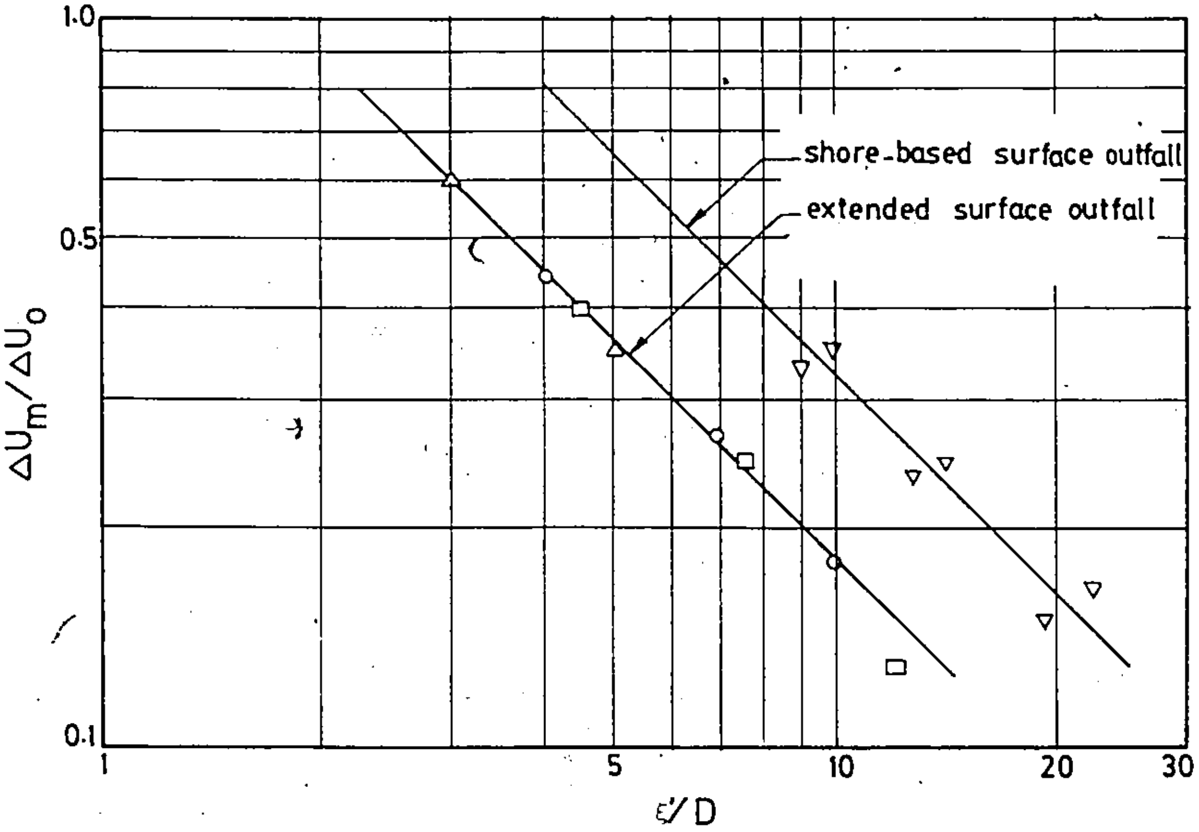

Fig. 5.16. Decay of maximum jet excess velocity after the establishment zone for surface outfall.

5.1.3 Concentration Profiles of Non-Buoyant Jets

The zone in which there exists significant variation of concentration in the lateral direction is termed a mixing zone. Once the turbulent mixing is fully developed, it is assumed that the shape of the mean profiles of the concentration and the temperature, as it will be seen later, do not change throughout the jet trajectory and these profiles follow almost the Gaussian distribution. Ultimately, the concentration profiles attain uniformity at some distance below the outfall.

The variations of the concentration, C, in the vertical and lateral directions are shown in Figs. 4.8 to 4.19 in a normalized form at various longitudinal sections, i.e., $\frac{x}{D} = 1.5$, 3, 6 and 18. The figures are plotted for different test variables, e.g., channel discharge, depth of flow, jet velocity to ambient velocity ratio and position of the outfall. The curves shown in these figures tend to be skewed to one side or the other. The asymmetry is mostly due to the nonuniform distribution of the flow across the trapezoidal channel. Also, the cross-flow may disturb the symmetry within the jet. The lateral concentration profiles shown in the above mentioned figures spread out and attenuate with x/D approaching uniformity at some distance downstream from the outfall. Two dimensional flow was observed in this study at a longitudinal distance of approximately 18D. In

Figs. 4.11, 4.15 and 4.17, lateral concentration profiles are compared for low and high velocity ratios, R. These figures clearly show that, for high velocity ratios, the concentration profiles spread out more rapidly and the concentration peaks penetrate further into the ambient flow.

5.1.3.1 Concentration Similarity Analysis

Similarity analysis was applied to reduce the experimental data to a manageable and useful form. Practically, this involved plotting each profile in the η-plane at successive longitudinal sections and fitting a smooth curve through the data points. Figure 5.17 and 5.18 were prepared wherein $(\frac{C}{C_o})/(\frac{C_m}{C_o})$ is plotted against η/σ_η for non-buoyant bottom and surface outfalls, respectively. From these figures, it can be seen that the concentration profiles are similar in the lateral direction and are satisfactorily described by the Gaussian equation (Hinze 1975 and Townsend 1976)

$$(\frac{C}{C_o})/(\frac{C_m}{C_o}) = e^{-0.5\{(\eta/\sigma_\eta)^2 + (\zeta/\sigma_\zeta)^2\}} \qquad (5.20)$$

In most of the non-buoyant experiments, the data points agreed with Eq. 5.20 as shown in Figs. 5.17 and 5.18. However, in Exps. 24 and 26, some points deviated from the solid curve; these correspond to a reattachment to the shoreline. This is also shown in Photographs 4.7 and B.18 for Exps. 24 and 26, respectively. Similarly, the concentration profiles in the vertical direction were also found to be similar as shown in Fig. 5.19. In this figure, the Gaussian equation describes the experimental results reasonably well, Eq. 5.20.

The variations of the length scales $\frac{\sigma_\eta}{D}$ and $\frac{\sigma_\zeta}{D}$ against $\frac{\xi}{D}$ are shown in Figs. 5.20 and 5.21, respectively for both bottom and surface outfalls. In these figures, solid symbols signifying bottom conditions and open symbols signifying surface conditions. These figures clearly indicate that the length scales for the surface outfall are higher than those of bottom outfall. Also, the jet cross-section is larger in the η-direction than in the ζ-direction. The length scales are thus described by:

For bottom outfall

$$\frac{\sigma_\eta}{D} = 0.56\left(\frac{\xi}{D}\right)^{0.54} \qquad (5.21)$$

$$\frac{\sigma_\zeta}{D} = 1.04\left(\frac{\xi}{D}\right)^{0.24} \qquad (5.22)$$

For surface outfall

$$\frac{\sigma_\eta}{D} = 0.73\left(\frac{\xi}{D}\right)^{0.54} \qquad (5.23)$$

$$\frac{\sigma_\zeta}{D} = 1.46\left(\frac{\xi}{D}\right)^{0.24} \qquad (5.24)$$

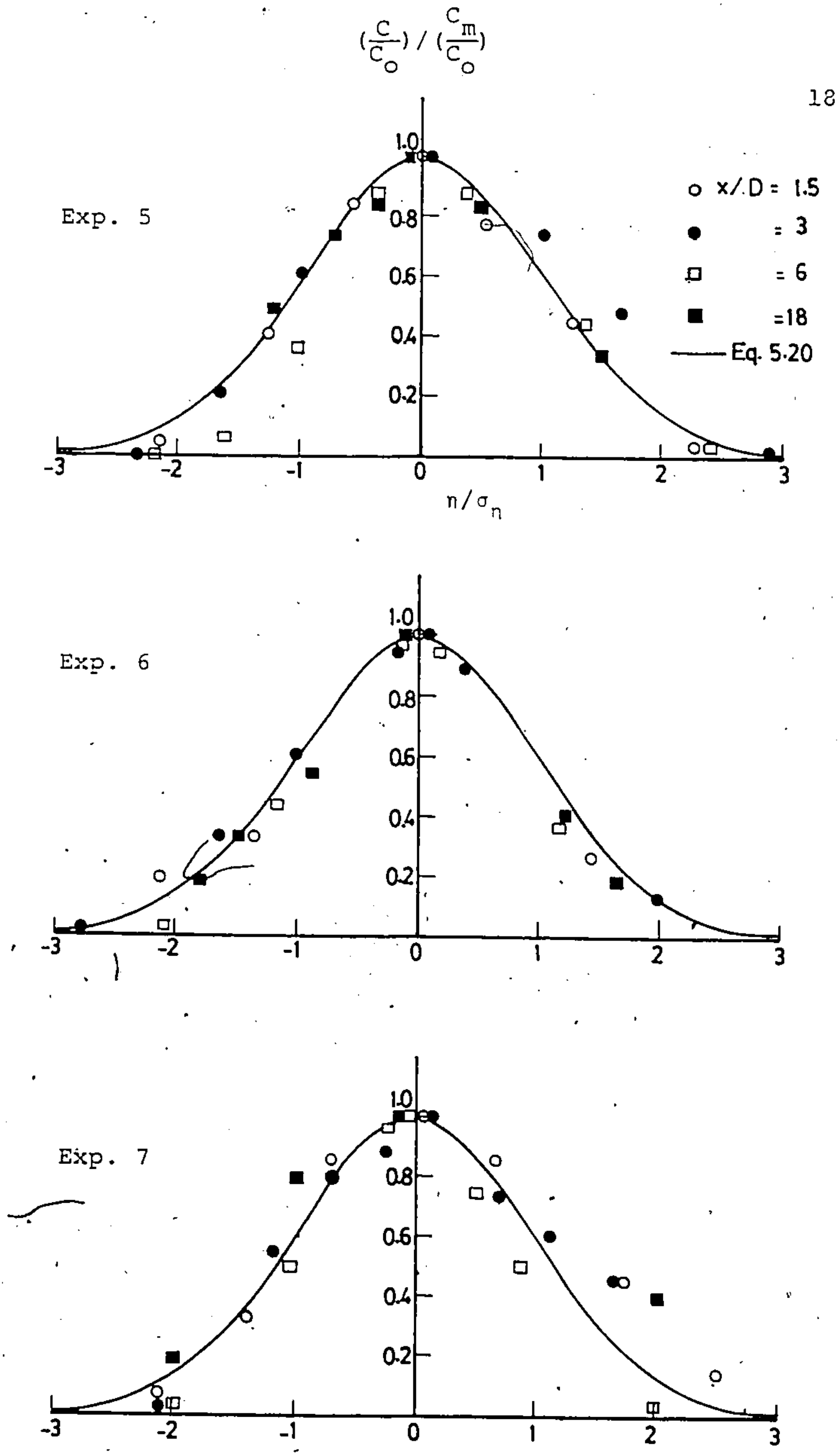

Fig. 5.17. Similarity of lateral concentration profiles for non-buoyant bottom outfall.

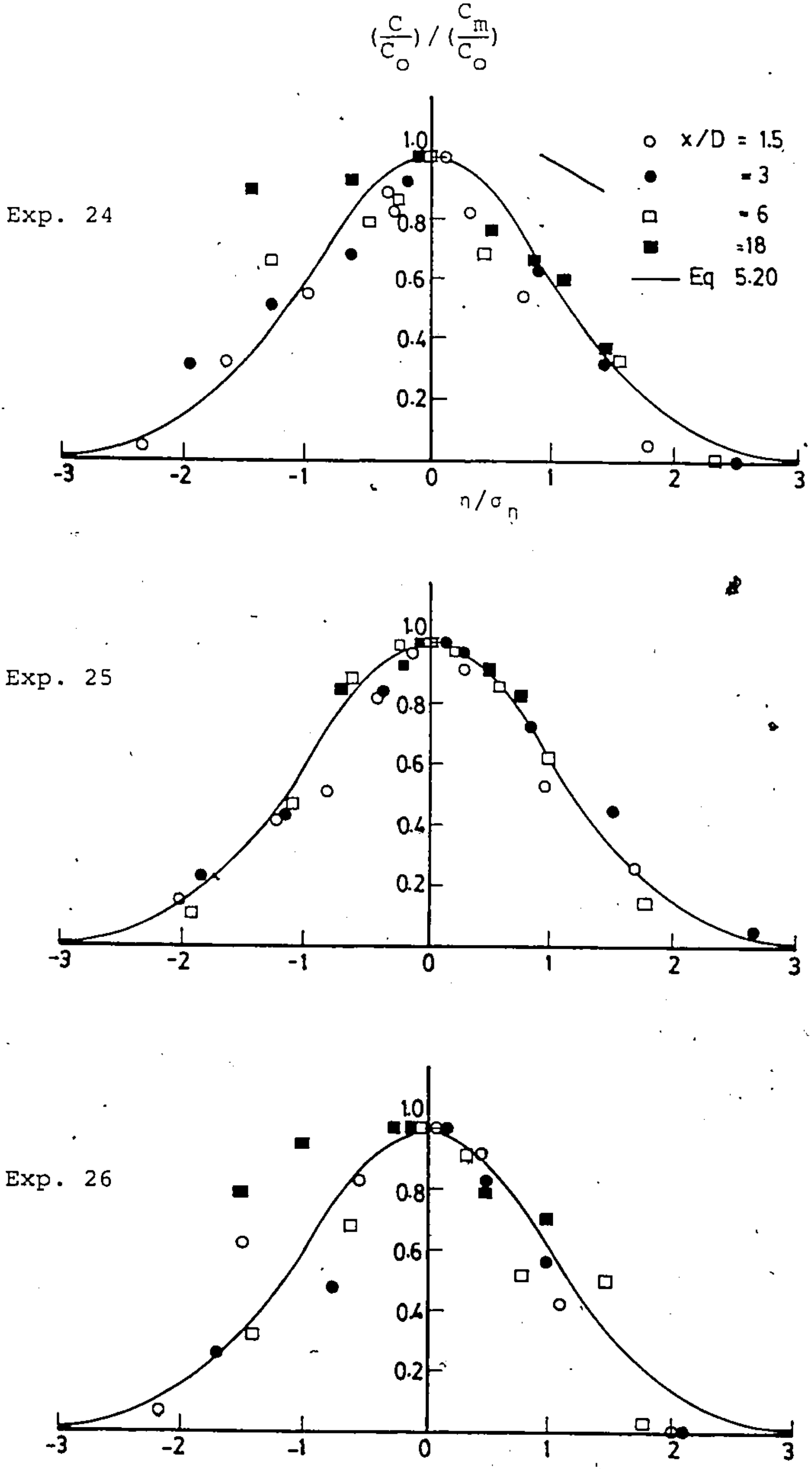

Fig. 5.18. Similarity of lateral concentration profiles for non-buoyant surface outfall.

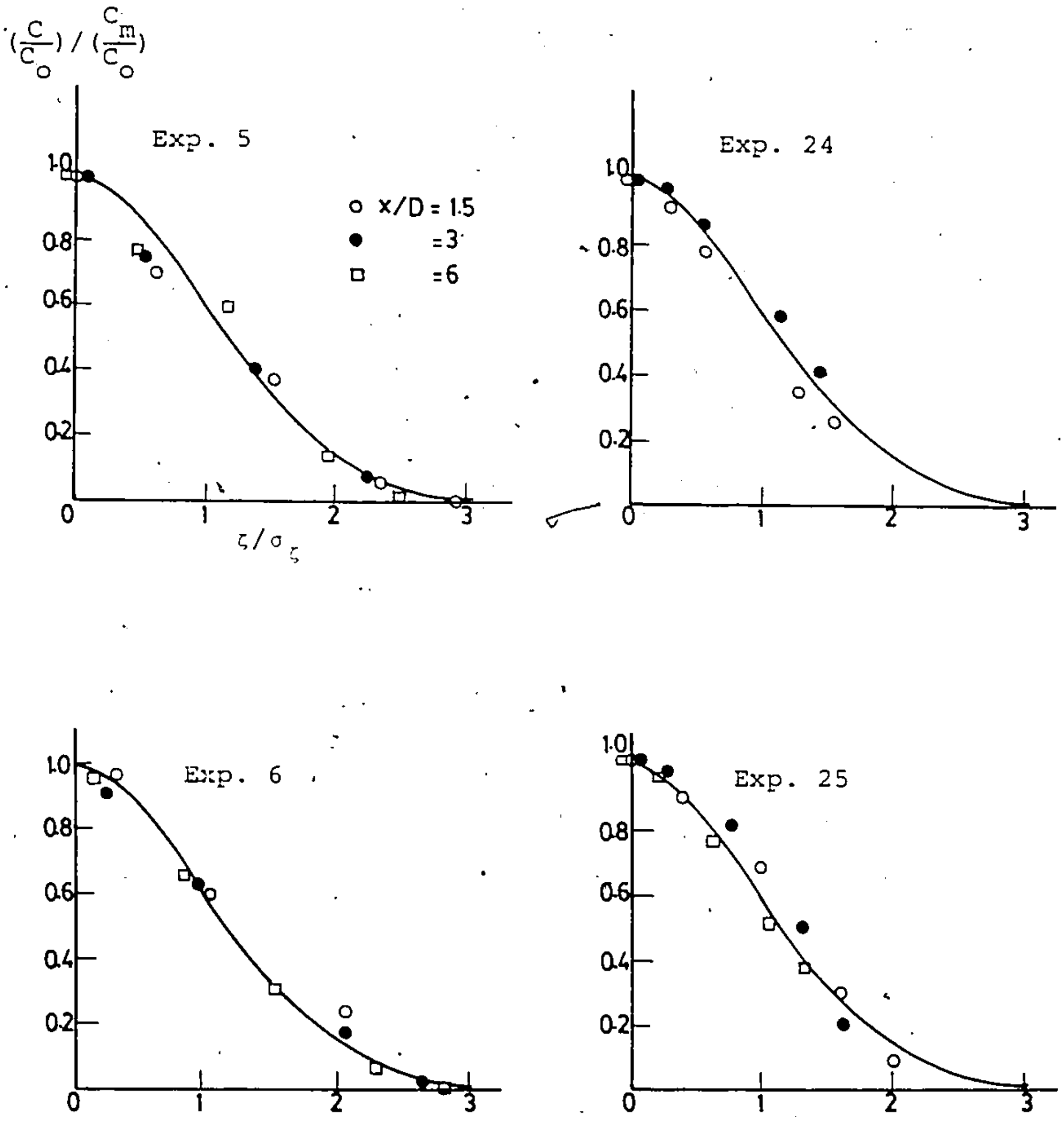

Fig. 5.19. Similarity of vertical concentration profiles.

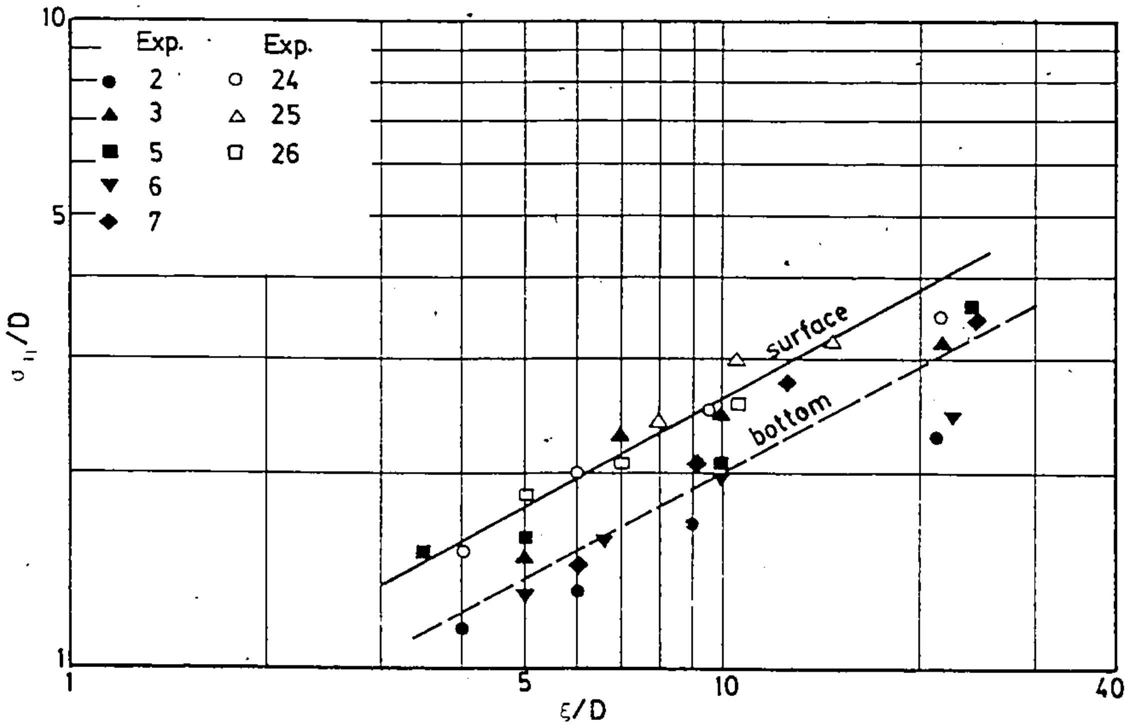

Fig. 5.20. Lateral length scale for non-buoyant jets.

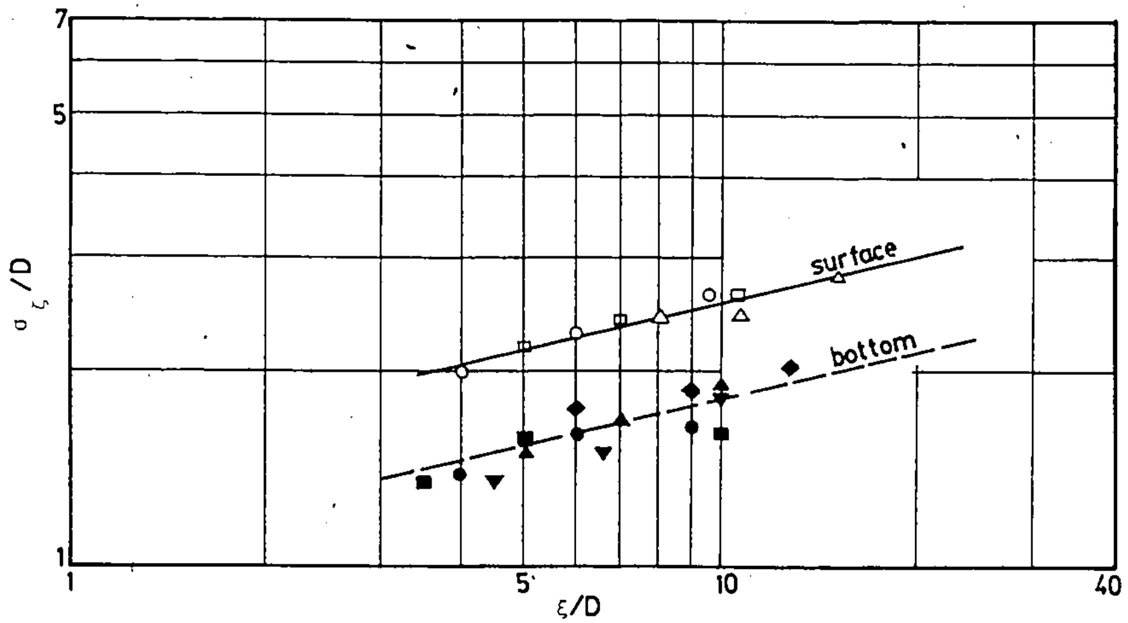

Fig. 5.21. Vertical length scale for non-buoyant jets.

Comparing Eqs. 5.21 with 5.15 and 5.23 with 5.17 shows that the concentration length scales grow at a rate approximately 1.10 and 1.37 times the rate of growth of velocity scales for bottom and surface outfalls, respectively. This result means that the concentration profile is wider than the velocity profile. This agrees with Fischer et al. (1979) who reported a value of 1.19 for $\frac{\sigma_{\eta_c}}{\sigma_{\eta_v}}$.

5.1.3.2 Effect of Ambient Water Depth

It has been well established that boundaries in the receiving fluid have a significant effect on jet behaviour (Keffer and Baines 1962, Stolzenbach and Harleman 1971 and Jirka et al. 1981). The effect of water depth on the concentration distribution of bottom outfall can be studied by comparing Figs. 4.8, 4.10 and 4.14 for H/D=2, 4 and 5.5, respectively. For the shallow water depth H/D=2, Fig. 4.8, the jet expanded vertically to occupy the whole depth at $\frac{\xi}{D} \geq 5$. The cross-flow was blocked and this caused a highly curved jet trajectory. As a result, a recirculation area near the shore-line was noticed with relatively high concentrations, Fig. 4.9. When the relative depth H/D was increased to 4, the bottom jet remained attached to the bottom up to x/D =3, (ξ/D=7) and then started to rise, Fig. 4.10. For the deep water condition, H/D=5.5, as represented by Runs 6 and 7, the bottom jet remained attached to the bed of the channel with a zero concentration at the surface for $\frac{\xi}{D}<24$, Fig. 4.14.

For surface outfalls over a sloping side, e.g., Runs 24, 25 and 26, bottom attachment began at the source and the jet remained attached to the sloping bottom throughout the near-field zone as shown in Figs. 4.16 and 4.18. The vertical distribution of C/C_o became uniform in a fairly short distance, approximately 6 times the jet diameter. The entering jet occupied a portion or all of the available water depth, and thus the ambient flow was blocked, leading to high stagnation pressure and a strong jet deflection towards the shore-line. At the same time, the entrainment on the downstream side of the jet was inhibited leading to an unequal pressure distribution on the jet boundary. Eventually, the jet became partially attached to the shoreline with a build-up of concentration as a result of recirculation. This is demonstrated in Figs. 4.17 and 4.19 where the value of C/C_o for Run 24 was constant and equal to 0.2 near the shoreline. For Run 25, the concentration at the shore side had a significant value of 0.1.

5.1.4 Temperature Profiles

The flow situation considered here is hot or cold water with temperature T_o and velocity V_j which is discharged from a circular outfall of diameter D into a cross-flowing ambient of velocity U_a and temperature T_a. A warm or cold water jet develops whose spreading is governed by momentum, buoyancy and ambient turbulence. The main parameters governing the jet behaviour are the densimetric Froude number, F_o, and the discharge diameter, D. Buoyancy is usually of minor importance near the source and the flow is dominated by momentum. The local Froude number decreases in the downstream direction and also towards the edges of the jet. As $F_o \to 1$, buoyancy effects start to dominate and the flow loses its jet character. The flow field in the mixing zone is extremely complex and not amenable to general analytical description until two-dimensional flow is established. At this point, the depth-averaged temperature field becomes essentially uniform in the transverse direction.

The excess temperature, $\Delta T/\Delta T_o$, for the experimental Runs presented in Table 3.2, are shown in Figs. 4.20 to 4.31 at four downstream sections, i.e., x/D=1.5, 3, 6 and 18. Figures 4.20 to 4.27 present the vertical and lateral excess temperature profiles for bottom outfalls whereas Figs. 4.28 to 4.31 show the surface outfall results. From Figs. 4.20 to 4.27, it can be seen that the discharged jet rises to the surface and spreads since it is lighter than the surrounding ambient water. For buoyant surface jets over a sloping bottom shown in Fig. 4.28 and 4.30 for experimental Runs 24-1, 25-2 and 26-1, bottom attachment begins at the source similar to the non-buoyant case. However, the jet remains attached for a short distance until the lateral pressure force caused by buoyancy succeeds in contracting or uplifting the bottom of the jet.

Figures 4.32 and 4.33 present the vertical and lateral excess temperature distributions resulting from cold water discharges. In these figures, a comparison was made between low velocity ratio, R=2 with initial temperature difference ΔT_o= -7.6°C and high velocity ratio, R=5.2 with ΔT_o= -6.1°C. It can be seen that the discharged cold water sinks to the bottom because it is denser than the ambient water forming a bottom spreading layer of cool water. This stable stratification pattern occurs immediately after the point of discharge and the jet remains attached to the bottom as shown in Fig. 4.32. Figure 4.33 shows that the strong ambient current deflects the jet towards the shoreline and a recirculation occurs with a zone of cold water. At x/D=3, the low jet sinks completely and the section of maximum excess temperature is found to be at the bed. The relatively stronger jet, R=5.2, attaches to the bottom at $x/D \cong 6$. The vertical profiles shown in Fig. 4.32 indicate that complete bottom attachment for the two velocity ratios occurs at $x/D \geq 6$ and at x/D=18, where the excess temperature distributions become nearly uniform.

5.1.4.1 Temperature Similarity Analysis

The temperature profiles were tested for similarity in a similar manner to the concentration profiles. Figures 5.22, 5.23 and 5.24 present the temperature profiles along the lateral direction, η-axis, at successive ξ positions in the zone of established flow. The scales needed were maximum excess temperature $(\frac{\Delta T_m}{\Delta T_o})$ and distance from point of maximum excess temperature to the point where the area under the profile is equal to 0.683, i.e., one standard deviation. Using these scales, the similarity profiles of each run were plotted in Figs. 5.22 and 5.23 for bottom buoyant outfalls and in Fig. 5.24 for surface buoyant outfalls. These profiles were found to be similar for most of the runs and were best described by the often used Gaussian equation

$$(\frac{\Delta T}{\Delta T_o})/(\frac{\Delta T_m}{\Delta T_o}) = e^{-0.5\{(\eta/\sigma_\eta)^2 + (\zeta/\sigma_\zeta)^2\}} \qquad (5.25)$$

which is shown in Figs. 5.22 to 5.24 as a solid line.

Similarly, it was found that the excess temperature profiles in the vertical direction were similar and the Gaussian distribution also describes the data reasonably well as shown in Fig. 5.25. This confirms the assumption of PDS model where Shirazi and Davis (1974) assumed Gaussian distribution for the temperature profile in the lateral and vertical directions.

The temperature profiles for heavy density surface

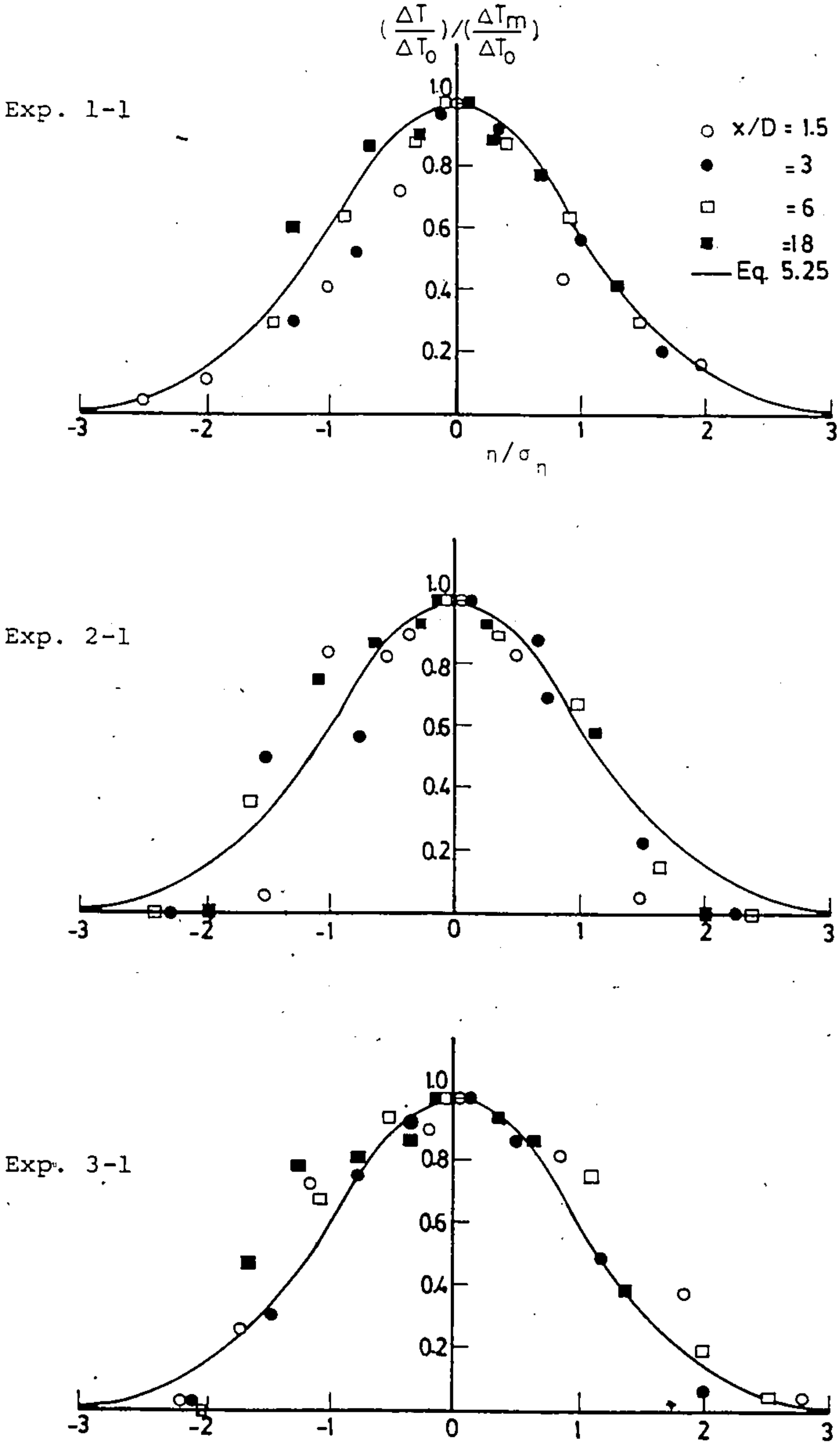

Fig. 5.22. Similarity of lateral temperature profiles for buoyant bottom outfalls (Exps. 1-1, 2-1, and 3-1).

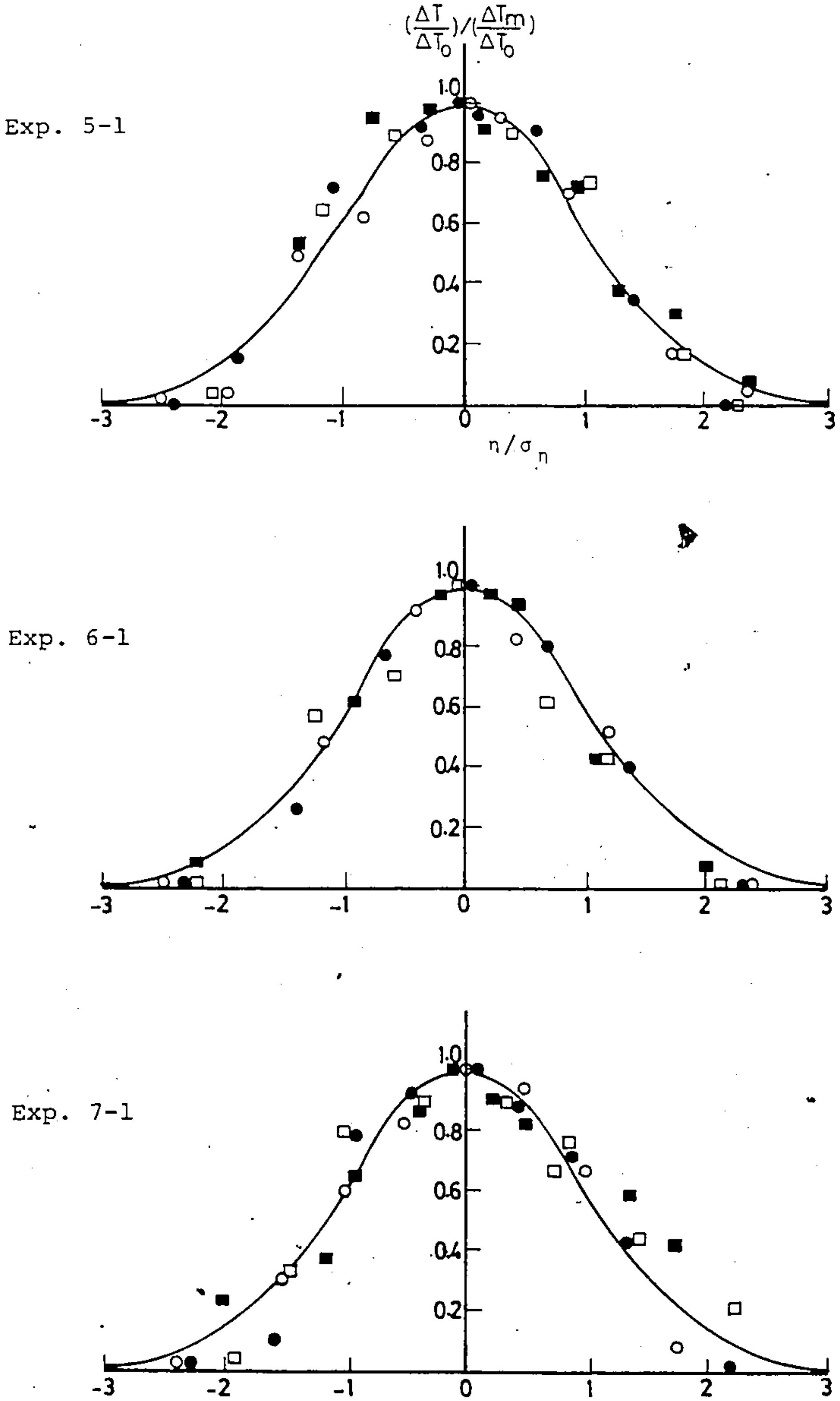

Fig. 5.23. Similarity of lateral temperature profiles for buoyant bottom outfall (Exps. 5-1, 6-1 and 7-1).

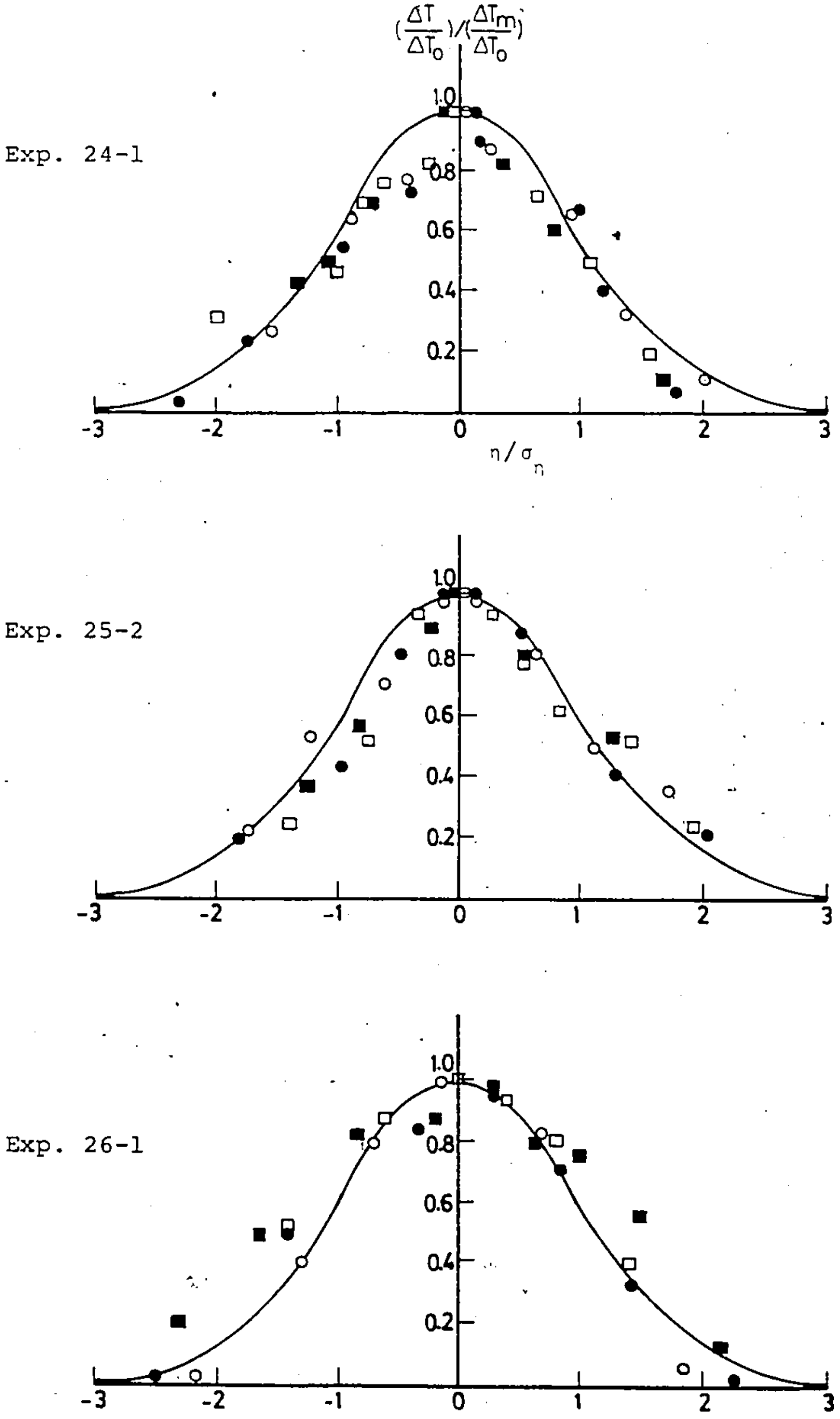

Fig. 5.24. Similarity of lateral temperature profiles for buoyant surface outfall (Exps. 24-1, 25-2 and 26-1.

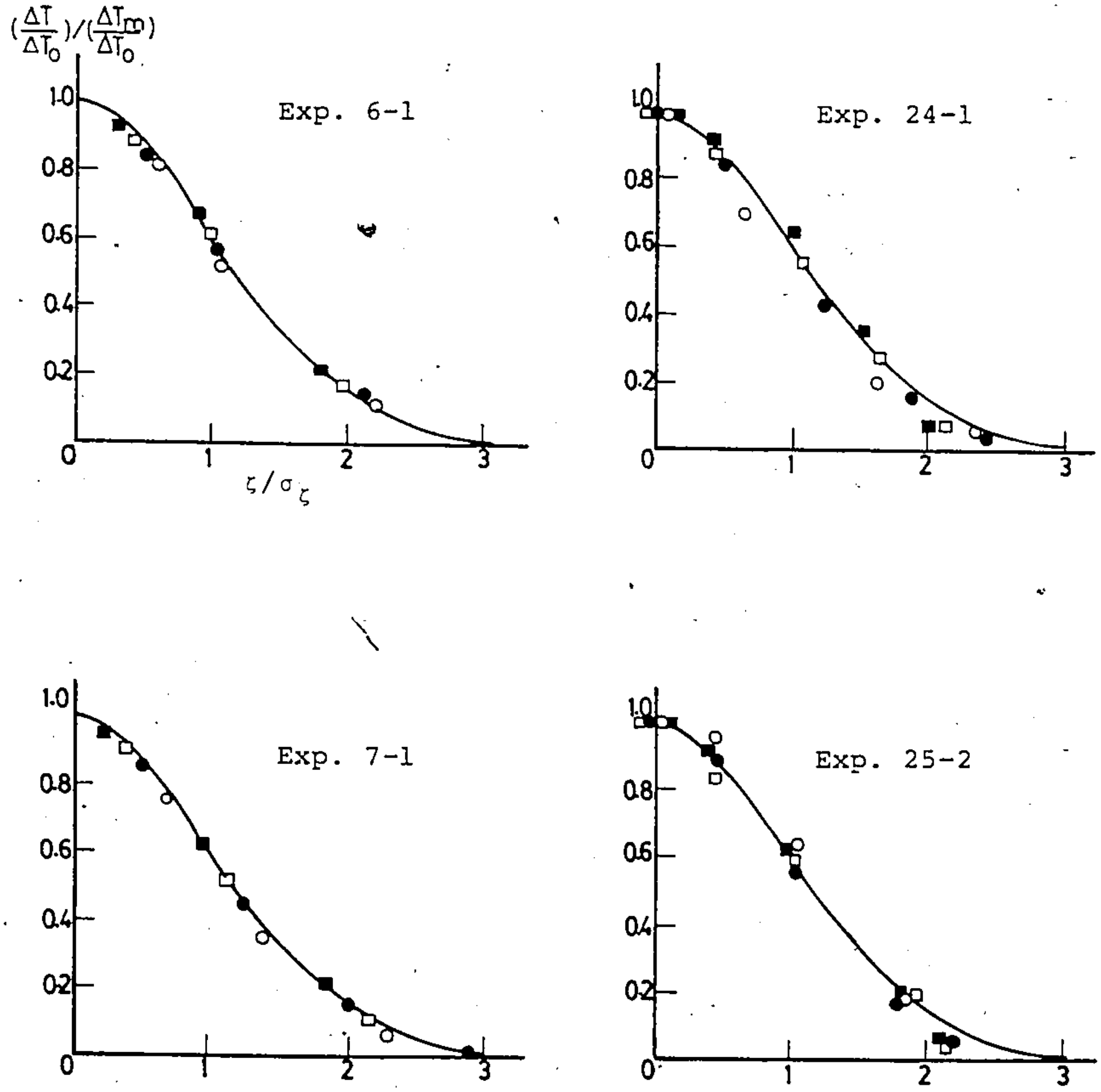

Fig. 5.25. Similarity of vertical temperature profiles for buoyant outfall.

jets shown in Fig. 4.33 were tested for similarity in a way similar to buoyant and non-buoyant jets as shown in Fig. 5.26. It was found that the lateral profiles for both cases were similar and exhibited Gaussian distribution.

Regarding the length scales σ_η in the transverse direction, from Figs. 5.27 and 5.28, for bottom and surface outfalls, respectively, it appears that the expansion rate is greater than that of the corresponding non-buoyant case (that is, $F_o=\infty$). This is because an additional lateral spreading is produced by the hydrostatic pressure of the lighter fluid resting on the surface of the heavier. For the vertical length scales σ_ζ, the experimental results plotted in Figs. 5.29 and 5.30 show that the vertical spreading is smaller for a buoyant jet than it is for a non-buoyant jet. This is because buoyancy induces an upward motion counteracting vertical spreading, and the vertical entrainment is reduced by buoyancy. From Figs. 5.27 to 5.30, one can write that:

For bottom outfall

$$\frac{\sigma_\eta}{D} = 0.63 \ (\frac{\xi}{D})^{0.56} \qquad (5.26)$$

$$\frac{\sigma_\zeta}{D} = 0.90 \ (\frac{\xi}{D})^{0.28} \qquad (5.27)$$

For surface outfall

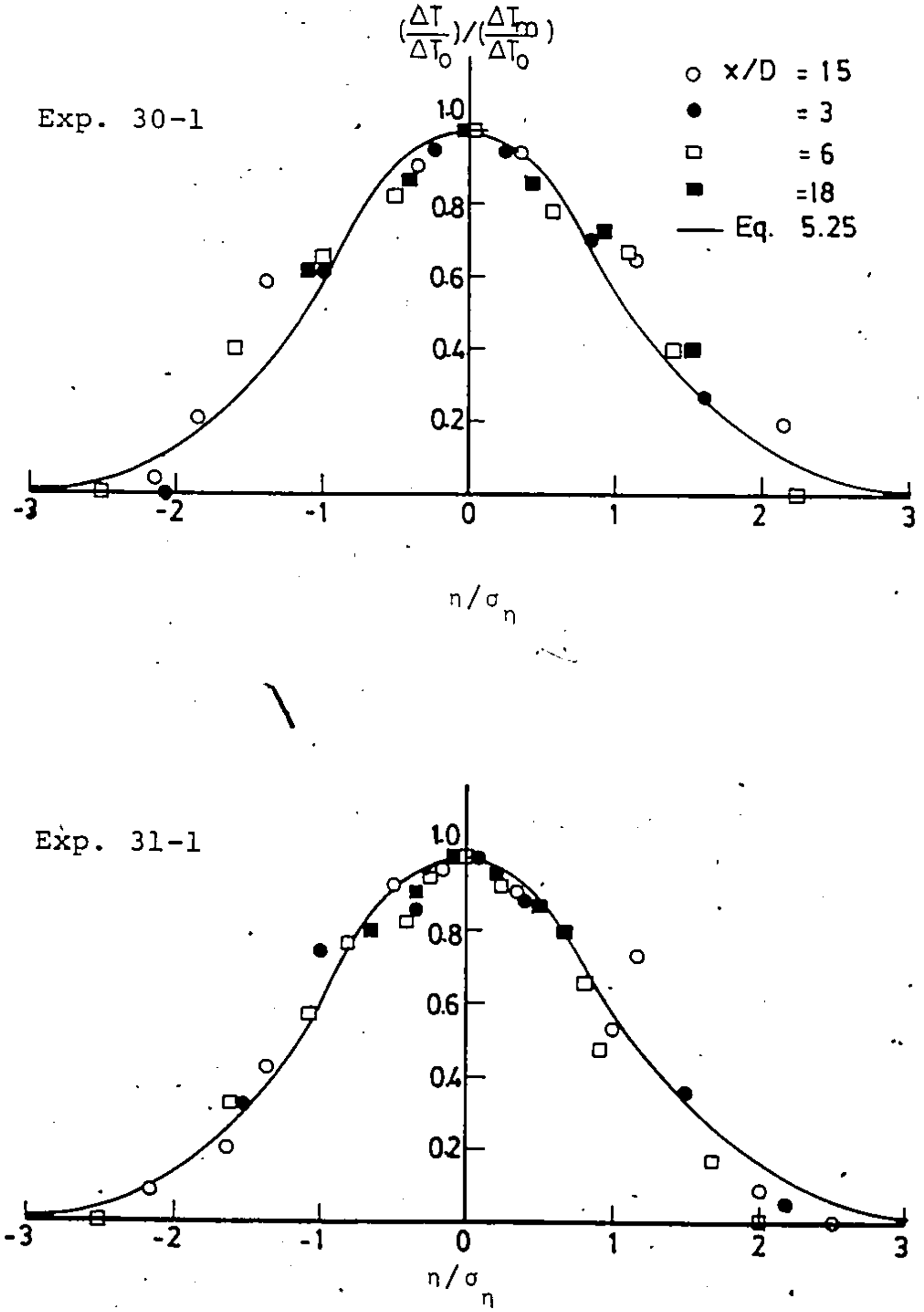

Fig. 5.26. Similarity of lateral temperature profiles for heavy density surface outfall.

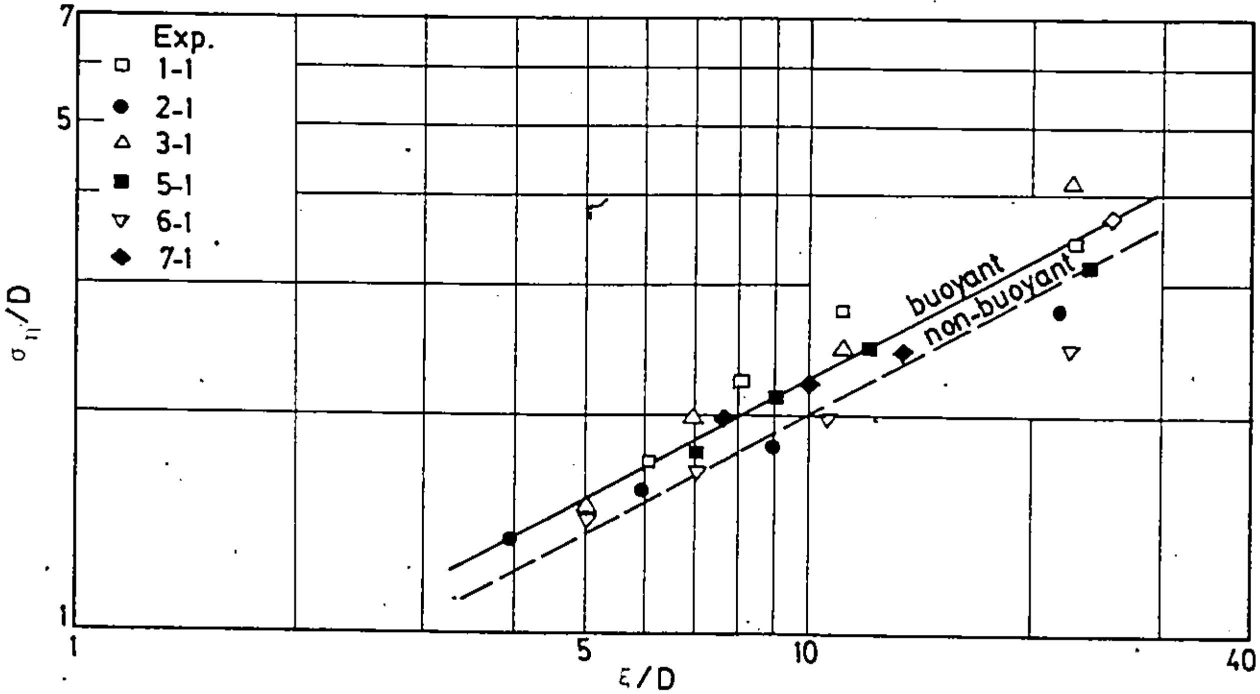

Fig. 5.27. Lateral length scale for buoyant bottom jets.

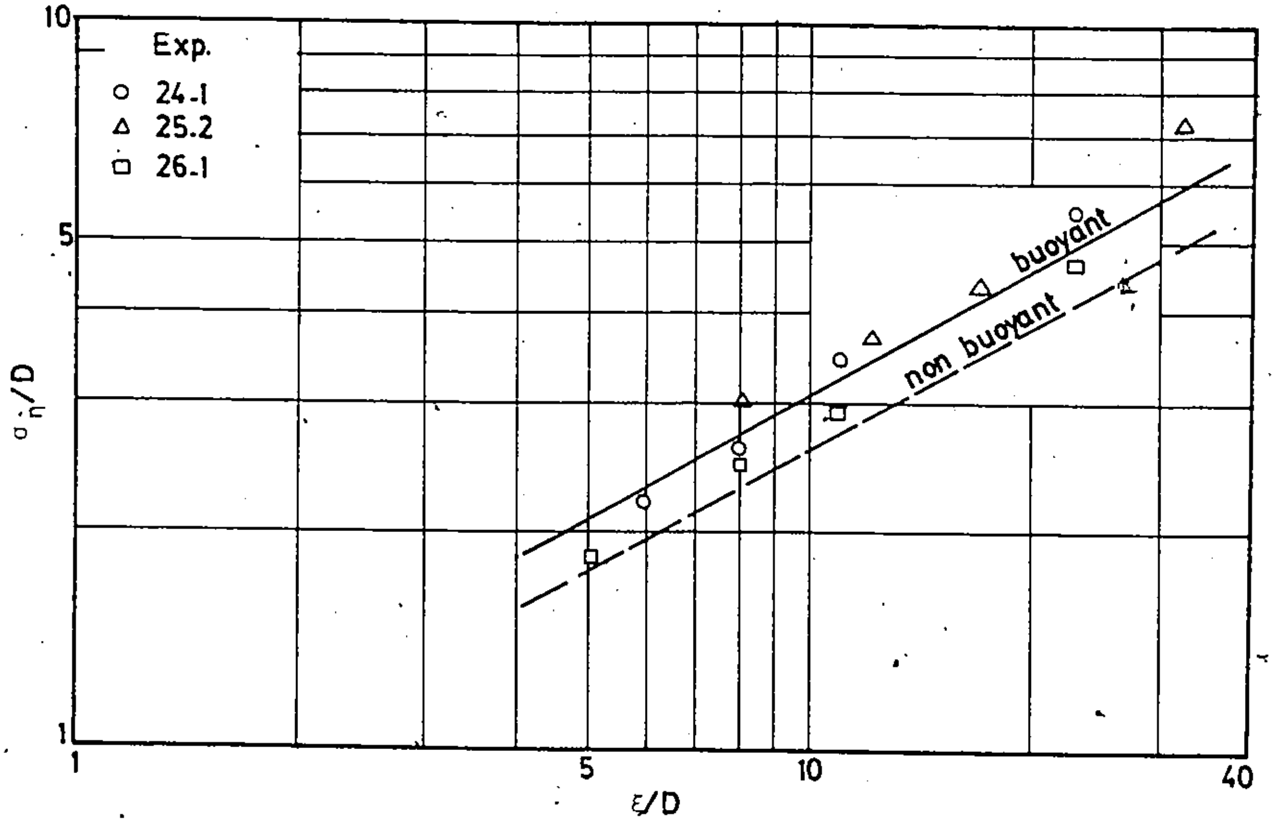

Fig. 5.28. Lateral length scale for buoyant surface jets.

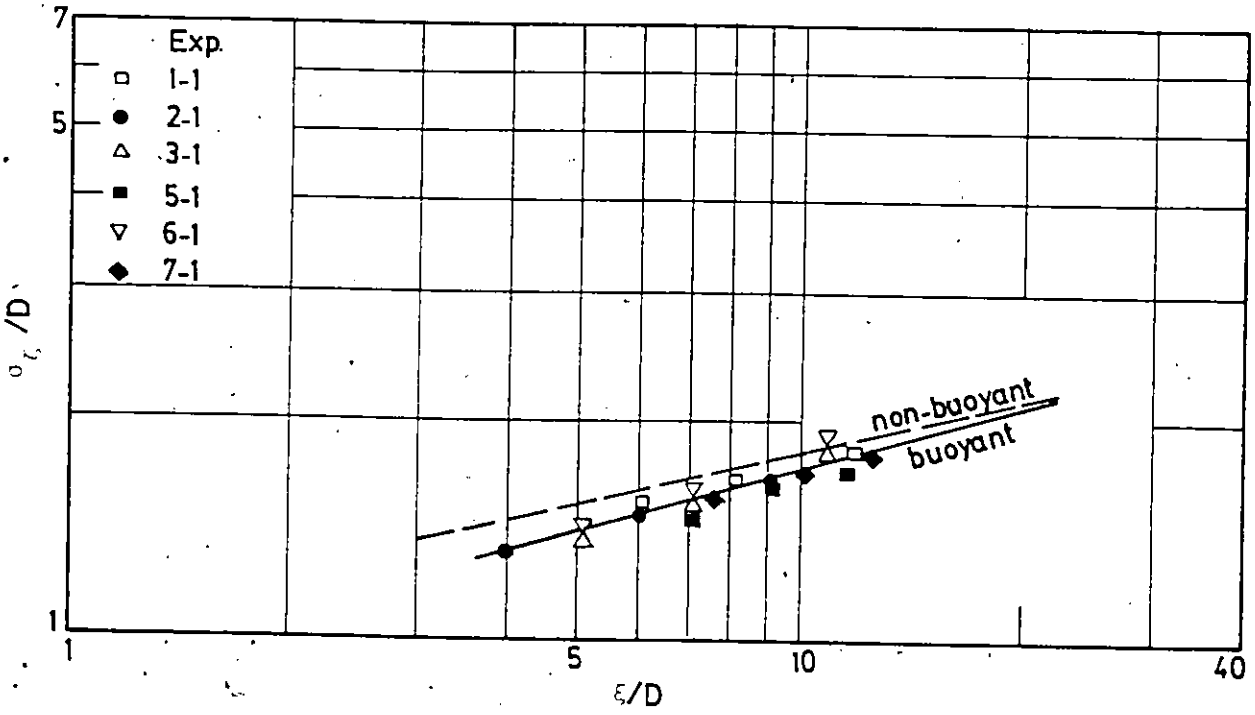

Fig. 5.29. Vertical length scale for buoyant bottom jets.

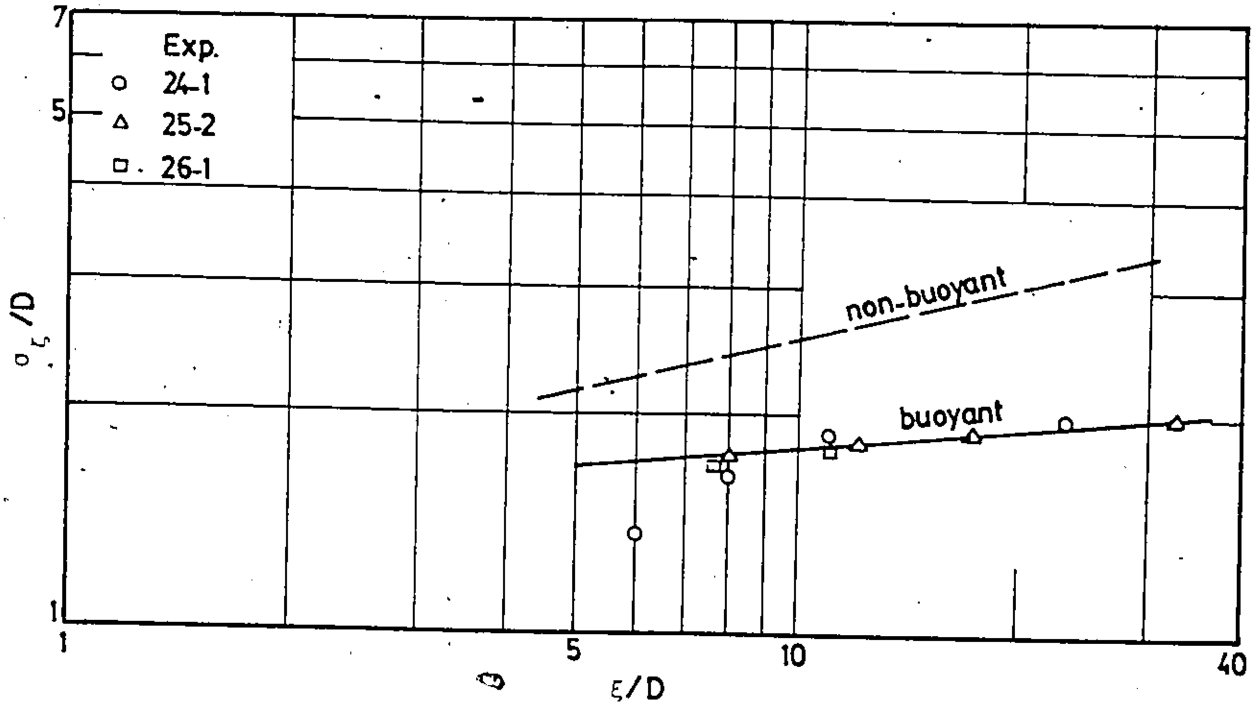

Fig. 5.30. Vertical length scale for buoyant surface jets.

$$\frac{\sigma_\eta}{D} = 0.86 \left(\frac{\xi}{D}\right)^{0.56} \qquad (5.28)$$

$$\frac{\sigma_\zeta}{D} = 1.53 \left(\frac{\xi}{D}\right)^{0.13} \qquad (5.29)$$

5.1.4.2 Criterion for Shoreline Attachment

Jirka et al. (1981) derived an empirical formula for the shoreline attachment in rectangular channel through a correlation with the velocity ratio, R, and the shallowness parameter, h_{max}/H, as follows:

$$R < 20 \left(\frac{h_{max}}{H}\right)^{3/2}; \qquad z_1=0 \qquad (2.19)$$

The shallowness parameter is considered to be a convenient measure of the blocking condition and the entrainment limitation as it includes the effect of buoyancy as well as the depth. They used data reported by other researchers to derive the following equation for the maximum jet depth:

$$\frac{h_{max}}{\sqrt{A_j/2}\ F_o} \cong 0.42 \qquad (5.30)$$

in which A_j is the area of the outfall. However, when the measurements of h_{max} of this study were plotted against F_o, the data points fell below the curve developed by Jirka et al. as shown in Fig. 5.31 and Eq. 5.30 was modified to

$$\frac{h_{max}}{\sqrt{A_j/2}\ F_o} \cong 0.3 \qquad (5.31)$$

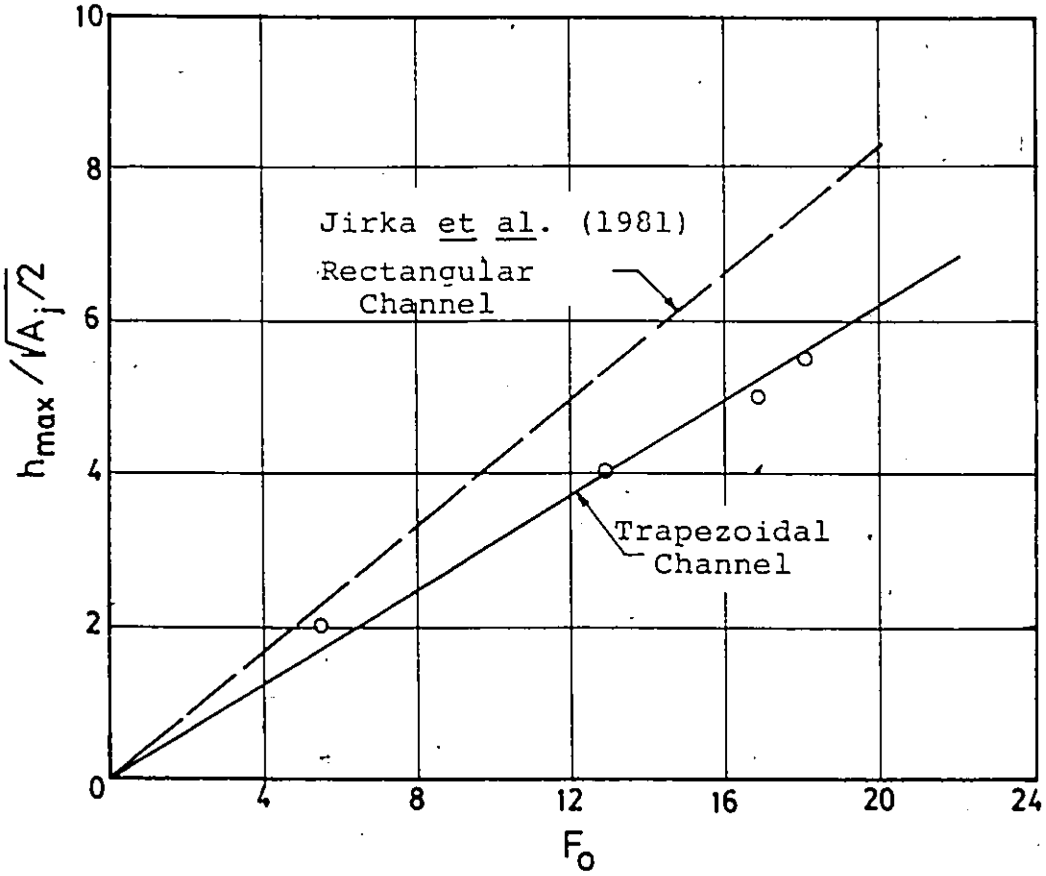

Fig. 5.31. Maximum jet depth, h_{max}, for buoyant surface jets in deep and shallow receiving water.

and consequently Eq. 2.19 was modified to

$$R < 14.3\left(\frac{h_{max}}{H}\right)^{3/2} \qquad \text{for } F_o < 20 \ ; \quad z_1 = 3 \qquad (5.32)$$

They also classified the jet as shoreline-attached if at any longitudinal section, x, of the near-field zone, the reduced shoreline excess temperature is more than half of the centreline value. This definition looks arbitrary but seems acceptable to distinguish between significant and insignificant shoreline influence. The relatively high crossflow of Run 24-1, R=2, forced the jet to attach to the shore. This shoreline attachment causes a recirculation to occur with a build-up of excess temperature as shown in Fig. 4.29 and Photograph 4.11. However, the discharge with weak crossflow represented by Exp. 25-2 and shown in Fig. 4.29 and Photograph 4.12 shows no attachment. Also, in Fig. 4.31, the jet discharging into relatively large depth, H/D=5.5, do not seem to attach. This agrees with the data of Keffer and Baines (1962) which showed nonattaching jets for high depths.

5.1.4.3 Decay of Maximum Excess Temperature

Considering the decay of maximum excess temperature $\Delta T_m/\Delta T_o$, Figs. 5.32 and 5.33 show the decrease of $\Delta T_m/\Delta T_o$ with x/D for bottom and surface outfalls respectively, for various densimetric Froude numbers. In these both figures, the excess temperature decays slower and levels off sooner for the lower F_o case; the former is due to the buoyancy induced, longitudinal pressure gradient and the latter due to the reduction of entrainment due to buoyancy. In Fig. 5.33, the decay of maximum excess temperature of Experiments 25-1 and 25-2 (same velocity ratio, R=5.2) is essentially the same, but that the decay for the lowest Froude number is slower. The excess temperature for surface outfall, Fig. 5.33, can be seen to decay slower than that for bottom outfall, Fig. 5.32. This is due to the fact that the surface outfall is discharged over the sloping side, hence, the jet entrainment is restricted by the presence of the solid boundary.

5.1.5 Jet Trajectory Analysis

Jet trajectories were examined by injecting coloured dye into the jet fluid and photographing the discharging jets (see Appendix B). Additional trajectory information were obtained by tracing fluorescein dye added to the jet fluid as explained in Chapter III.

Slides (35 mm) of the dyed jet were projected and the jet trajectories were determined by tracing the dye outlines on coordinate paper. A smooth curve was visually drawn midway between the upper and lower dye boundaries and was taken as the apparent jet trajectory. The results from the velocity, concentration and temperature measurements were considered separately from the photographic data since the

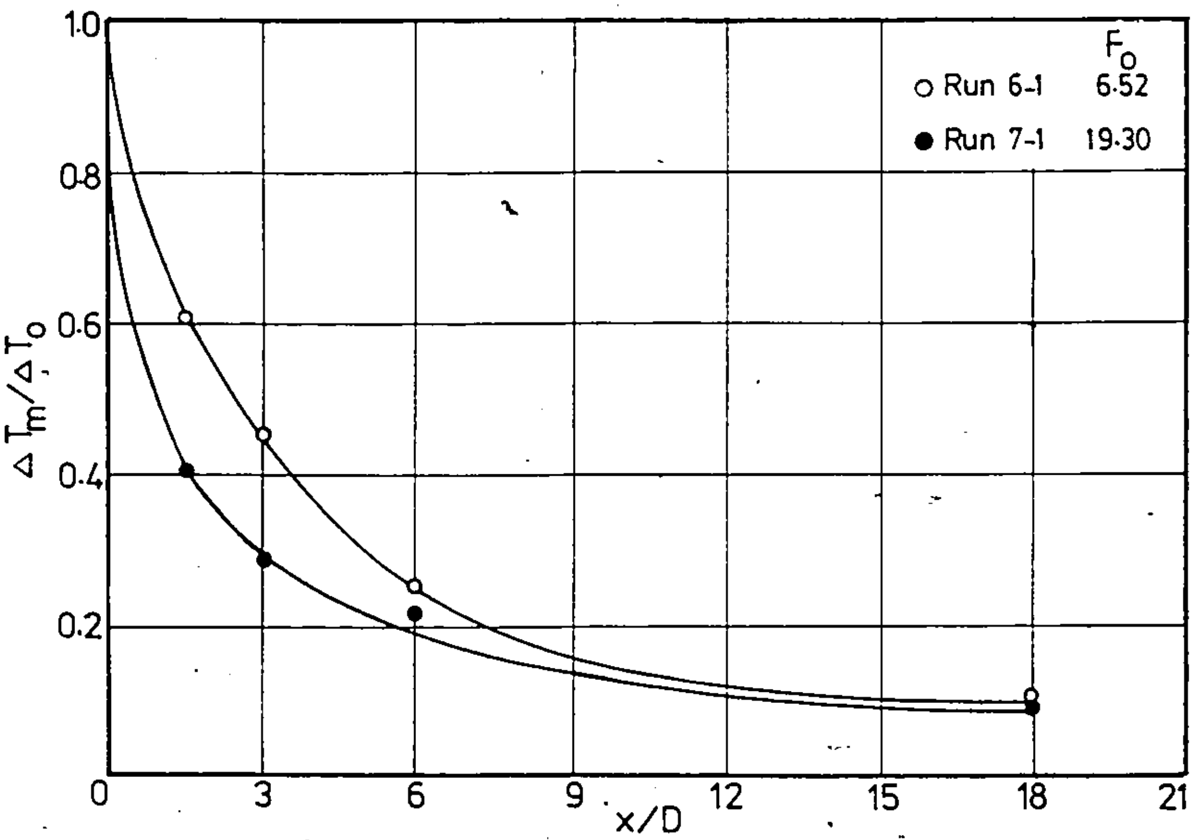

Fig. 5.32. Decay of maximum excess temperature for bottom outfall.

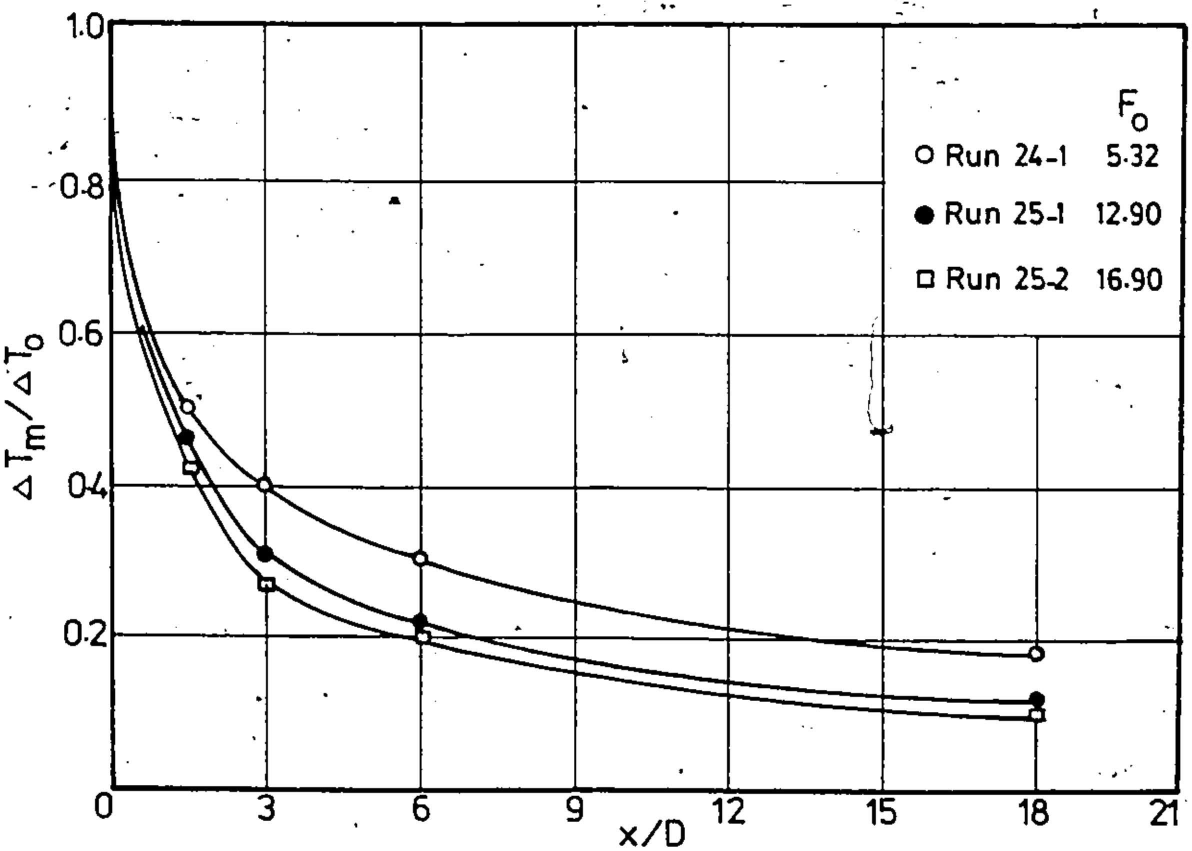

Fig. 5.33. Decay of maximum excess temperature for surface outfall.

trajectory definitions were different. In this case, the jet trajectory is the locus of maximum velocity, concentration or temperature. Typical results of the data points based on this definition are given in Figs. 5.34 and 5.35. In these figures, measured jet trajectories are compared for different velocity ratios. Velocity ratios ($R=V_j/U_a$) of 2.0, 3.3 and 5.0 were chosen to cover a range that might be expected in practice. Measurements of the axis of the jet, defined as the locus of maximum points are compared in Fig. 5.34 for neutral, light and heavy density surface jets at two velocity ratios, R=2.0 and 5.2. From Fig. 5.34, it can be seen that in the case of light density, the measured jet trajectories for both velocity ratios penetrate further into the channel than the neutral and heavy density cases. This is due to the buoyancy induced pressure in the light density case. In Fig. 5.35, a comparison of the jet trajectories, obtained from the photographs, is made between bottom and extended surface outfalls at two velocity ratios. As expected, both trajectories show a similar trend because they are restricted by the presence of a plane boundary.

A number of methods have been proposed to predict the configuration of the axis of a circular jet in cross-flow. In the method of Abramovich (1963), the deflection of the jet is attributed entirely to the pressure differential

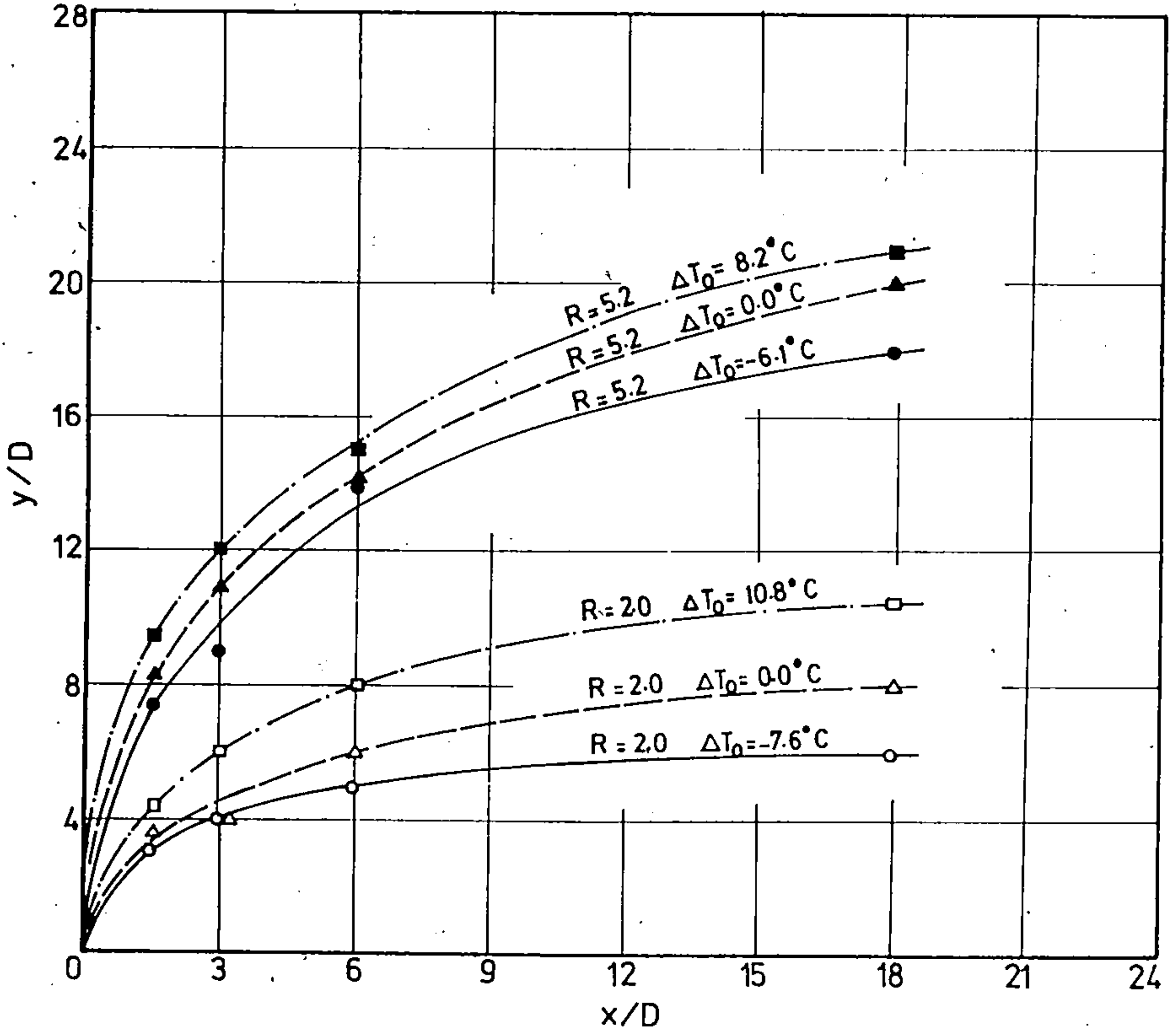

Fig. 5.34. Comparison of jet trajectories for neutral, light and heavy densities surface jets.

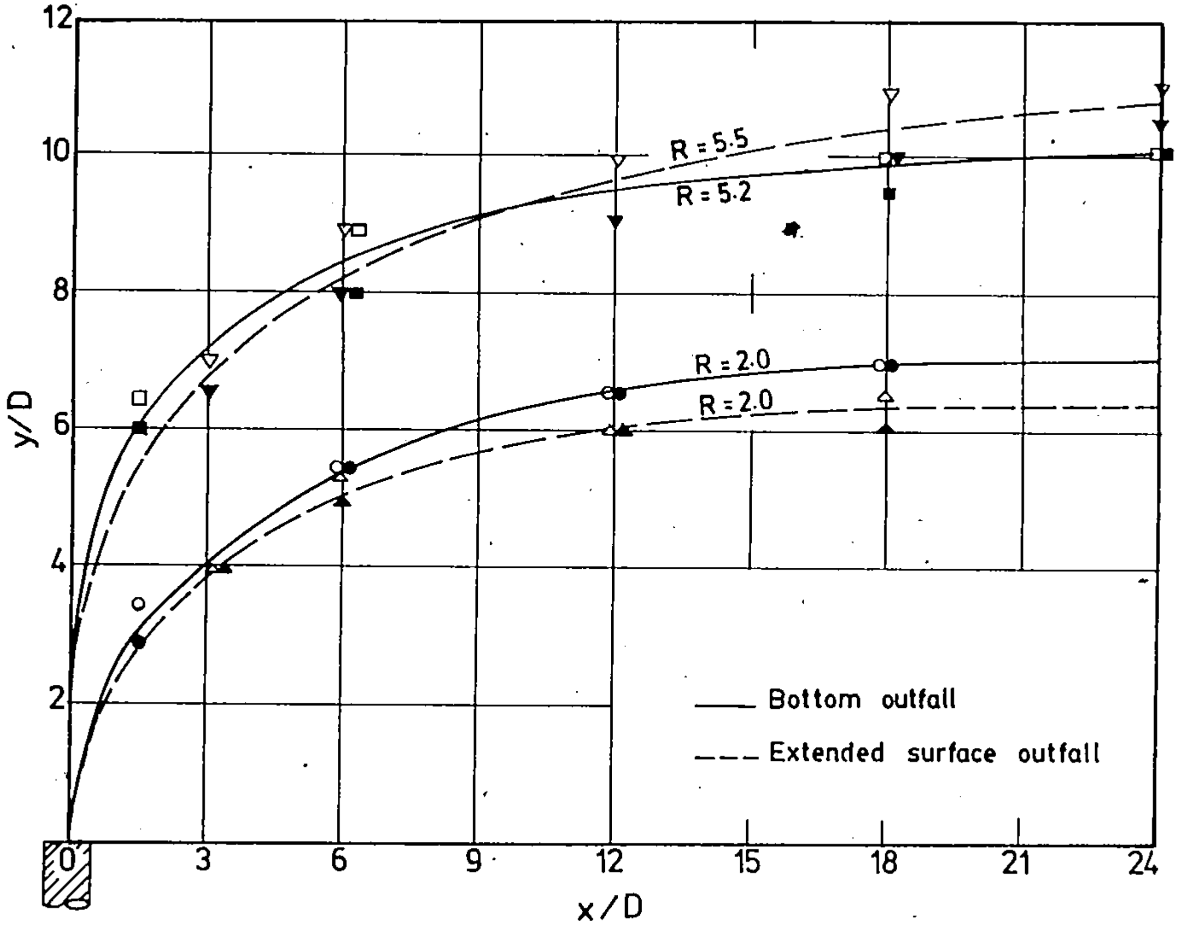

Fig. 5.35. Comparison of jet trajectories for bottom and extended surface outfalls.

between the upstream and downstream faces of the jet whereas in the method of Keffer and Baines (1962), Pratte and Baines (1976) and Rajaratnam and Gangadhariah (1980), the deflection is attributed to the entrained momentum of the free stream. These studies provided empirical expressions for the deflected jet axis usually in the form of a power law, i.e.,

$$\frac{y}{D} = c_1 \left(\frac{x}{D}\right)^{n_1} R^{n_2} \tag{5.33}$$

where, c_1, n_1, and n_2 are constants to be determined from experiments. All the available results for predicting the jet trajectory are collected together in Table 5.1.

Using the present experimental measurements, Eq. 5.33 was evaluated for non-buoyant bottom and surface jets. For a bottom outfall, the data points were obtained from the concentration profiles while for a surface outfall, the jet trajectory points were obtained by analyzing the concentration profiles as well as the photographs. The results are shown in Figs. 5.36 and 5.37 for bottom and surface jets, respectively. Variations in the data points shown in Fig. 5.37 are due to the fact that the photographs represent an instantaneous view of the jet behaviour. The regression analysis using the data points yielded the following equations:

Table 5.1

Jet Trajectory Predictions for Circular Jets in Cross-Flow

Investigators	Equations or Curves	Remarks
Gordier (1959)	$y/D=1.31\ (x/D)^{0.37}R^{0.74}$	Total pressure measurements in water
Abramovich (1963)	$y/D=(x/D)^{0.33}\ R^{0.87}$	R varied from 3.5 to 32
Keffer and Baines (1963)	Experimental curves	R = 2,4,6,8 and 10
Patrick (1967)	$y/D = (x/D)^{n}\ R^{0.87}$ $n = 0.38$ (from velocity measurements) $= 0.34$ (from concentration measurements)	R varied from 6 to 50
Pratte and Baines (1967)	$y/D = 2.05\ (x/D)^{0.28}\ R^{0.72}$	R varied from 5 to 35
Rajaratnam and Gangadhariah (1980)	Experimental curves	R= 2.73, 4.52, 7.05, and 23.4

For non-buoyant bottom jets

$$\frac{y}{D} = 2.33(\frac{x}{D})^{0.23} R^{0.54} \tag{5.34}$$

For non-buoyant surface jets

$$\frac{y}{D} = 1.53(\frac{x}{D})^{0.35} R^{0.95} \tag{5.35}$$

The predictions of Eqs. 5.34 and 5.35 are also presented in Figs. 5.36 and 5.37. Good agreement between the measured and predicted jet trajectories are shown in these figures. This indicates that both Eqs. 5.34 and 5.35 can be satisfactorily used to predict the trajectory for non-buoyant jet.

In the case of a buoyant jet, the trajectory is governed by the combined effects of buoyancy and momentum. Near the source, the momentum will dominate over the buoyancy, and at larger distances from the source, buoyancy exerts an increasing influence on the jet behaviour. It is expected, therefore, that Eq. 5.33 must include the densimetric Froude number, F_o, as an independent variable. However, the available research data in literature usually neglects the effect of F_o and uses the same form of Eq. 5.33 for buoyant case. For comparison purposes, the data points of this study on buoyant jets were used to determine the coefficients of c_1, n_1 and n_2 of Eq. 5.33. The regression analysis yielded the following equations:

For buoyant bottom jets

$$\frac{Y}{D} = 2.52\left(\frac{X}{D}\right)^{0.14} R^{0.59} \tag{5.36}$$

For buoyant surface jets

$$\frac{Y}{D} = 2.43\left(\frac{X}{D}\right)^{0.33} R^{0.77} \tag{5.37}$$

The predictions of these equations together with the measured data points are shown in Figs. 5.38 and 5.39 for bottom and surface outfalls, respectively. Good agreement between the measured and the predicted trajectories were obtained.

Comparing Eqs. 5.35 and 5.37 for non-buoyant and buoyant surface outfalls, it is shown that both cases are similar but in the buoyant jet, the constant c_1 is 57% higher than that of the non-buoyant case. It is also observed that, for bottom outfalls, both Eqs. 5.34 and 5.36 are similar. It can be seen that n_1 has lower values for both buoyant and non-buoyant bottom outfalls compared to the surface outfall. This can be attributed to the bed friction that could limit the effect of mixing. Equation 5.35, for non-buoyant surface jets, agrees with the results of Gordier (1959) as shown in Table 5.1. However, other values of the constants presented in this study cannot be compared to other results since the relations developed do

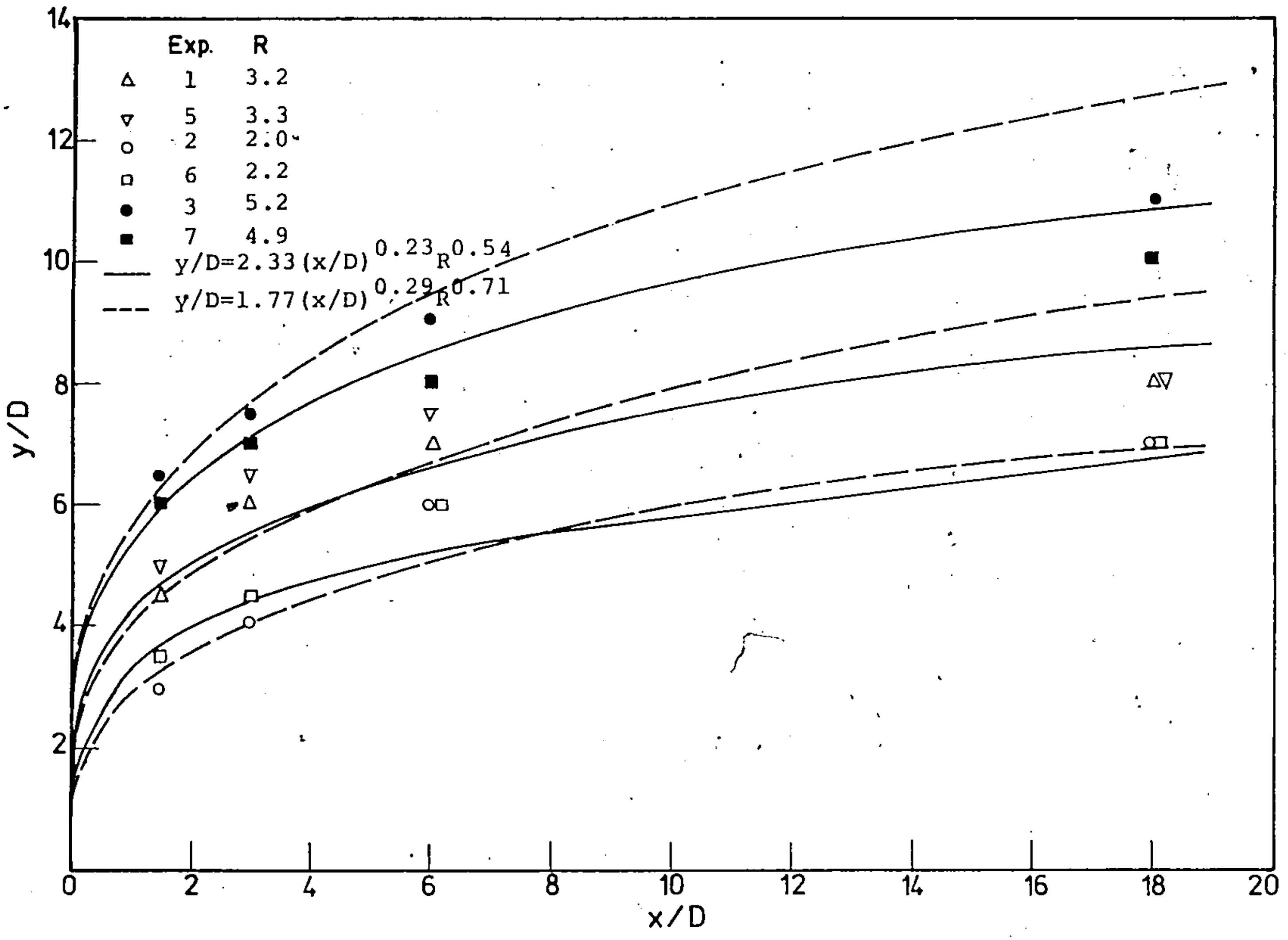

Fig. 5.36. Jet trajectories for non-buoyant bottom outfalls.

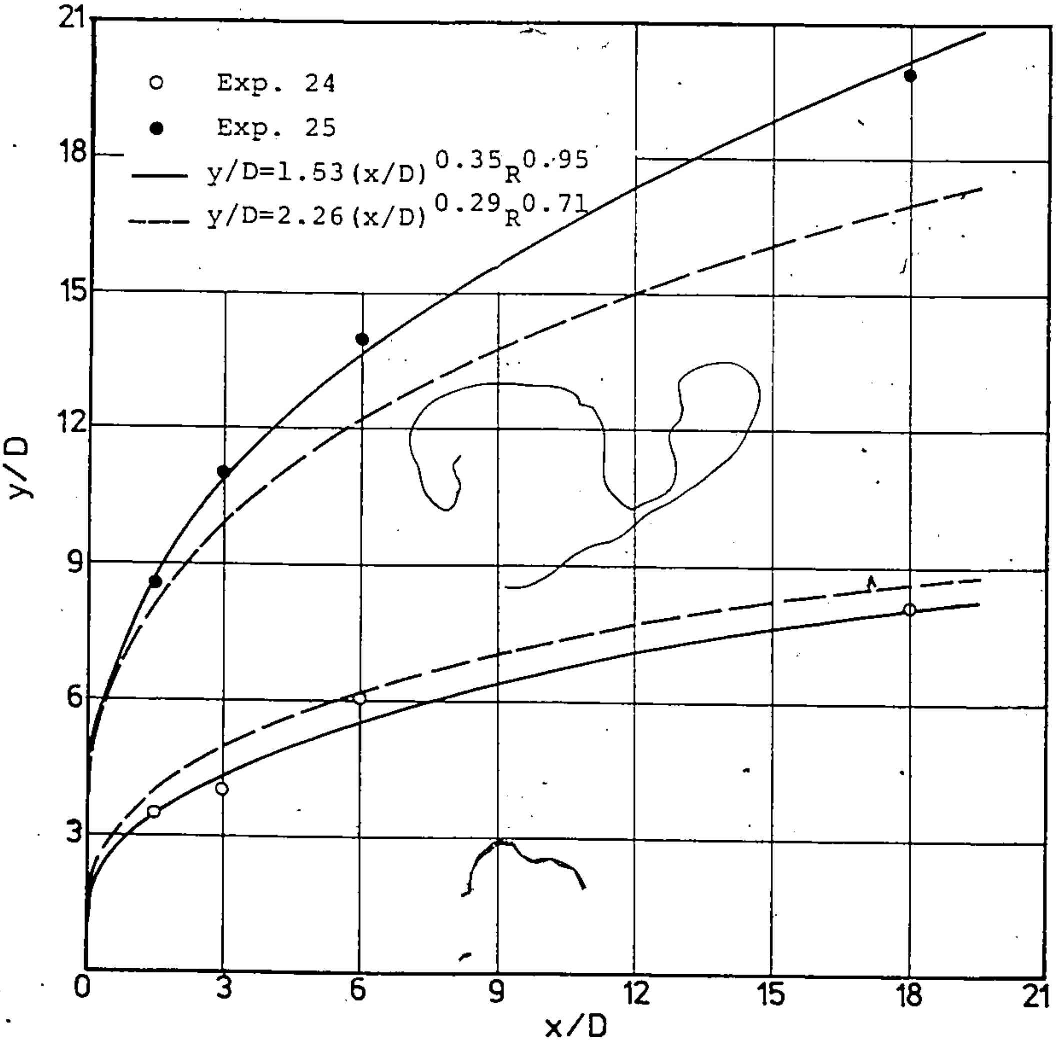

Fig. 5.37. Jet trajectories for non-buoyant surface outfalls.

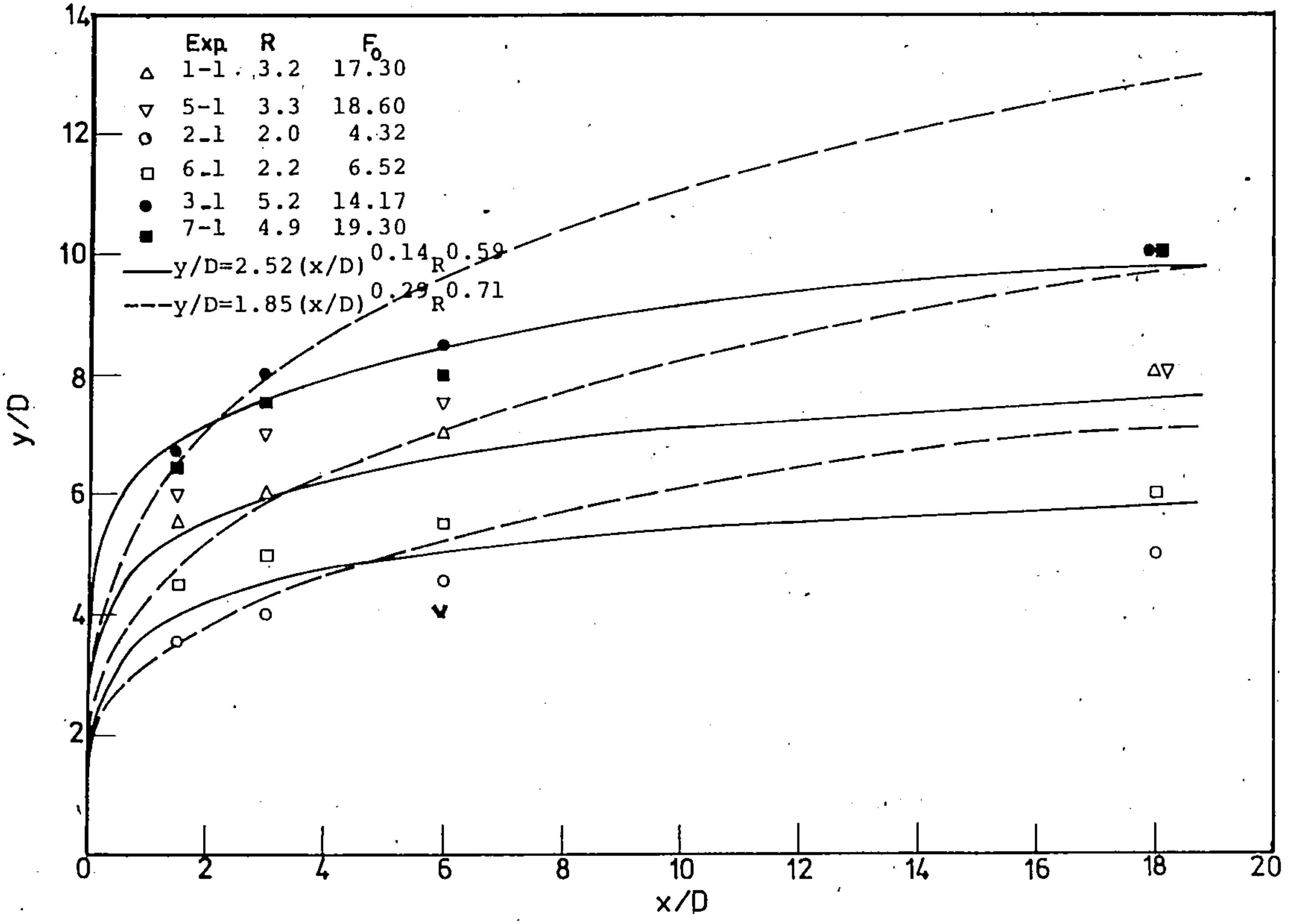

Fig. 5.38. Jet trajectories for buoyant bottom outfalls.

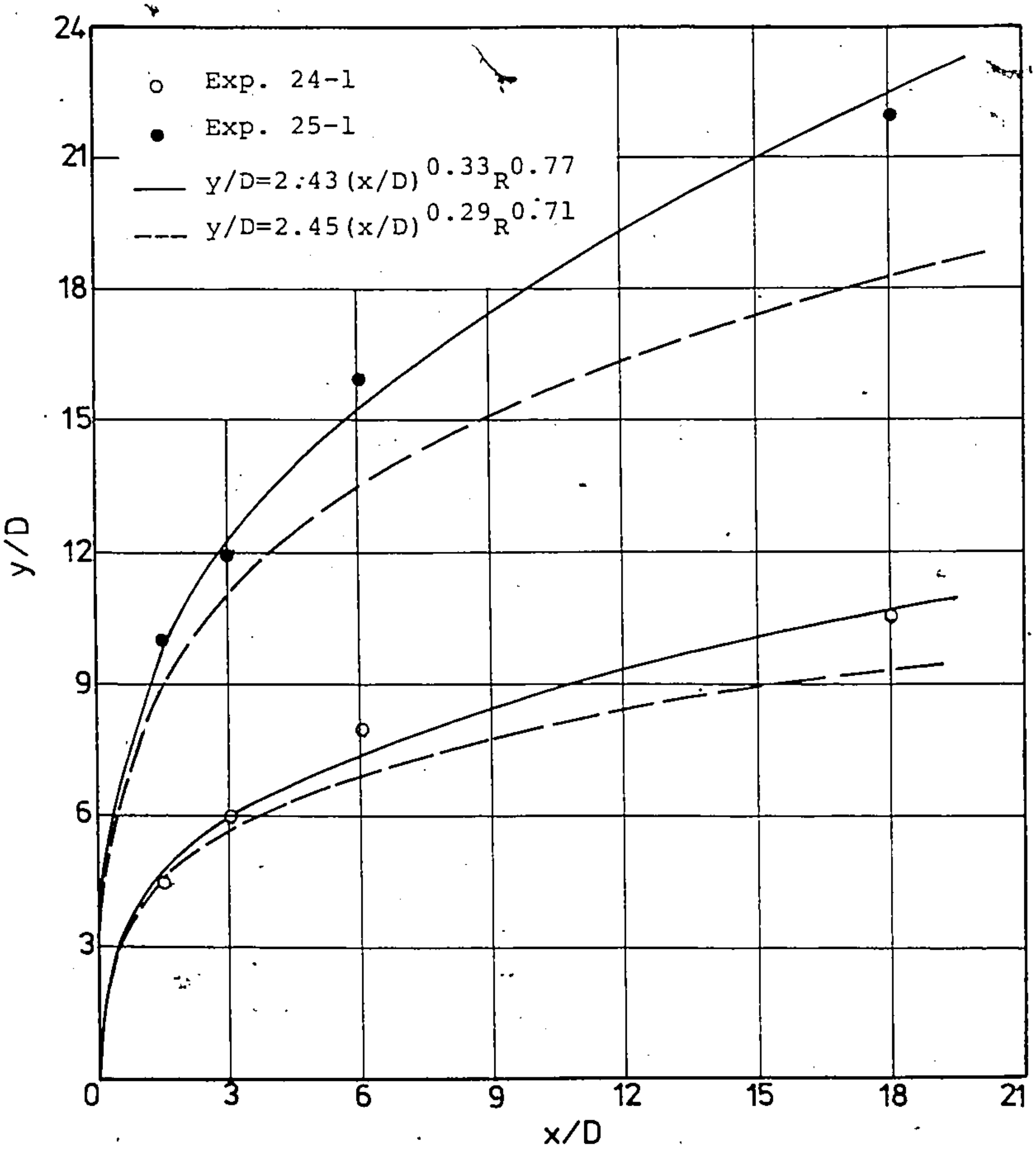

Fig. 5.39. Jet trajectories for buoyant surface outfalls.

not directly correspond with other researchers relations.

It would be useful to study the trajectory of a heavy density surface jet discharging normal to a uniform density ambient fluid using the results of Runs 30-1 and 31-1. The following equation was derived from the regression analysis:

$$\frac{y}{D} = 1.31\left(\frac{x}{D}\right)^{0.32} R \qquad (5.38)$$

In Fig. 5.40, the jet trajectories predicted by Eq. 5.38 are compared with the corresponding measurements. Although Eq. 5.38 gives good agreement, it should be considered approximate since only two experiments were available for analysis.

A similar analysis was made by Pratte and Baines (1967) who proposed an empirical formula for submerged jet of air in a cross-flow. They assumed that $(n_1+n_2) = 1$ in Eq. 5.33 and the equation becomes

$$\frac{y}{RD} = c_1\left(\frac{x}{RD}\right)^{n} \qquad (5.39)$$

The best fit of their data gives

$$\frac{y}{RD} = 2.05\left(\frac{x}{RD}\right)^{0.28} \qquad (5.40)$$

Using their approach, the measured data points are

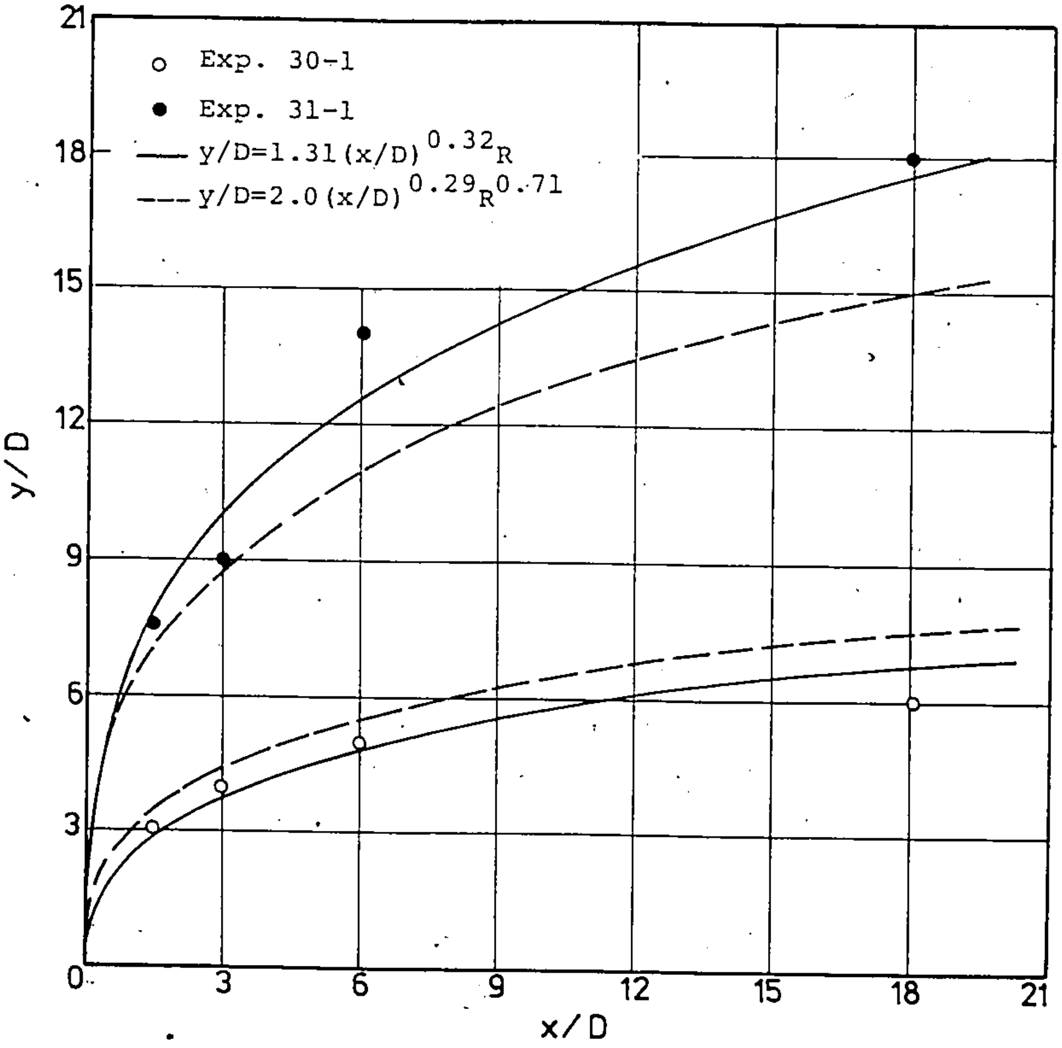

Fig. 5.40. Jet trajectories for heavy density surface outfalls.

presented on logarithmic scales where $\frac{y}{RD}$ is plotted versus $\frac{x}{RD}$ for various values of R. A typical trajectory plot is given in Fig. 5.41 for a horizontal non-buoyant bottom outfall. The regression analysis of this study showed that the plotted points follow a single line in the form of

$$\frac{y}{RD} = 1.77\left(\frac{x}{RD}\right)^{0.29} \tag{5.41}$$

The trajectory obtained by Pratte and Baines is also shown in Fig. 5.41. Comparing Eqs. 5.40 and 5.41 shows that the two equations have the same trend but the Pratte and Baines equation predicts larger values of $\frac{y}{RD}$ for any given $\frac{x}{RD}$ than Eq. 5.41. The basic difference in their setup as compared to the present experiments was that their injection was vertical and there were no surface or wall effects. The same procedure was adopted to predict a jet trajectory equation for non-buoyant surface jets using the data points from both the photographs and the concentration profiles. The regression analysis gave the following equation:

$$\frac{y}{RD} = 2.26\left(\frac{x}{RD}\right)^{0.29} \tag{5.42}$$

For the case of buoyant jet, the jet profile equation must include the effect of F_o, i.e.,

$$\frac{y}{RD} = f\left(\frac{x}{RD}, \frac{F_o}{R}\right) \tag{5.43}$$

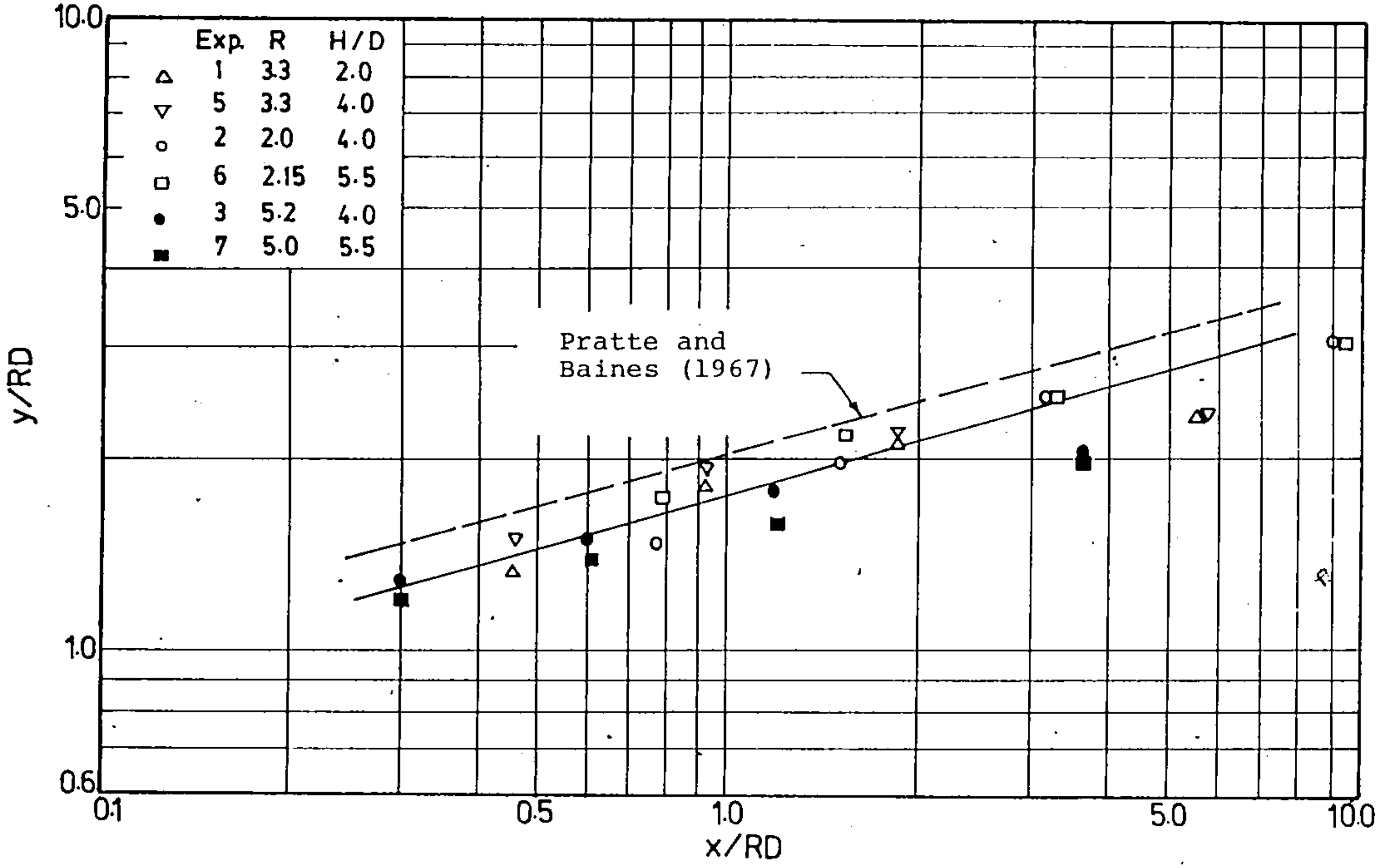

Fig. 5.41. Variation of y/RD versus x/RD.

Following the arguments of Jirka et al. (1981) the ratio F_o/R should provide an indication of the effect of buoyancy on the trajectory. If $F_o/R \gg 1$, then buoyancy should play a minor role as the cross-flow deflection occurs more quickly than the buoyant influences. In this case, the jet trajectory follows Eq. 5.39 for bottom and surface jets. For $F_o/R \ll 1$, buoyancy should play a significant role and the buoyant jets are expected to penetrate more deeply into the receiving water than non-buoyant jets, since both cross-flow forces, entrainment and drag force, decrease (Jirka, et al. 1981). The ranges of the ratio F_o/R for the experimental data of this study were 2.2 to 5.4 for bottom outfall and 2.5 to 3.3 for surface outfall. These values are intermediate between the two bounds given by Jirka et al. Therefore, it is expected that the buoyant jet trajectory would follow the same trend as the non-buoyant case with a slightly greater penetration. The regression analysis shows that the plotted points for buoyant jet trajectories follow a single line with the same slope as the non-buoyant case but with more penetration. The jet penetration is thus given by:

For buoyant bottom jet

$$\frac{y}{RD} = 1.85\left(\frac{x}{RD}\right)^{0.29} \qquad (5.44)$$

For buoyant surface jet

$$\frac{y}{RD} = 2.45\left(\frac{x}{RD}\right)^{0.29} \qquad (5.45)$$

Comparing Eq. 5.42 for non-buoyant surface outfalls with Eq. 5.45 for buoyant surface outfall, in which the experimental data in both cases corresponding to the same values of R, it is shown that the buoyant jet penetrates further into the channel than the non-buoyant jet with an increase of 8% in the penetration constant c_1. It was also observed that for bottom outfall, the buoyant jet penetration constant is 4.5% higher than that of non-buoyant jet.

A similar analysis was made on heavy density surface jet and the following equation was derived:

$$\frac{y}{RD} = 2.0\left(\frac{x}{RD}\right)^{0.29} \qquad (5.46)$$

For comparison purposes, the predictions of Eqs. 5.41, 5.42, 5.44, 5.45 and 5.46 are plotted in Figs. 5.36, 5.37, 5.38, 5.39 and 5.40, respectively. An apparent deviation between the measured points and the predicted results from Eq. 5.39 can be seen especially for high values of R. The experimental evidence supports the concepts presented in the empirical formulation of Eq. 5.33.

A summary of the experimental jet trajectory equations together with the regression constants, using 95 and 99 percent confidence intervals are presented in Tables 5.2 and 5.3. Data points for surface outfalls were obtained from experimental runs as well as photographs. Since the photographs represent an instantaneous view of the jet behaviour, therefore, poor confidence limits were obtained. Also, for heavy density surface outfall, only two experimental runs were available for analysis which resulted in poor confidence limits as shown in Tables 5.2 and 5.3.

5.1.6 Dilution Analysis

The dilution rate was determined from the fact that the point of minimum dilution at any section is the point in the section with the maximum concentration or maximum excess temperature. These points occur along the jet trajectory (see Section 5.1.5). Ratios of the initial to the maximum concentration, C_o/C_m, are plotted against ξ/D as shown in Figs. 5.42 and 5.43 for bottom outfall and in Fig. 5.44 for surface outfall. For the range of ξ/D covered by the measurements, the experimental data points can be described by two linear variations. The first part represents the length of the establishment zone which was found to vary from 2 to 4 times the pipe diameter depending on the velocity ratio. The second part starts at the end of the establishment zone and describes how the dilution

Table 5.2

Summary of Jet Trajectories and Confidence Limits Based on Eq. 5.33

$\frac{Y}{D} = c_1 (\frac{x}{D})^{n_1} R^{n_2}$	Confidence Limits of n_1		Confidence Limits of n_2	
	95%	99%	95%	99%
Non-buoyant bottom outfall $\frac{Y}{D} = 2.33 (\frac{x}{D})^{0.23} R^{0.54}$	±0.02	±0.03	±0.03	±0.04
Non-buoyant extended surface outfall $\frac{Y}{D} = 2.00 (\frac{x}{D})^{0.29} R^{0.51}$	±0.18	±0.22	±0.16	±0.21
Non-buoyant shore-based surface outfall $\frac{Y}{D} = 1.53 (\frac{x}{D})^{0.35} R^{0.95}$	±0.20	±0.28	±0.18	±0.26
Buoyant bottom outfall $\frac{Y}{D} = 2.52 (\frac{x}{D})^{0.14} R^{0.59}$	±0.02	±0.03	±0.03	±0.04
Buoyant shore-based surface outfall $\frac{Y}{D} = 2.43 (\frac{x}{D})^{0.33} R^{0.77}$	±0.26	±0.31	±0.20	±0.28
Heavy density surface outfall $\frac{Y}{D} = 1.31 (\frac{x}{D})^{0.32} R$	±0.22	±0.27	±0.20	±0.26

Table 5.3

Summary of Jet Trajectories and Confidence Limits Based on Eq. 5.39

$\frac{y}{RD} = c(\frac{x}{RD})^n$	Confidence Limits of c		Confidence Limits of n	
	95%	99%	95%	99%
Non-buoyant bottom outfall $\frac{y}{RD} =$ [illegible] $)^{0.29}$	±0.18	±0.23	±0.05	±0.07
Non-buoyant extended surface outfall $\frac{y}{RD} = 1.70(\frac{x}{RD})^{0.29}$	±0.31	±0.42	±0.12	±0.16
Non-buoyant shore-based surface outfall $\frac{y}{RD} = 2.26(\frac{x}{RD})^{0.29}$	±0.48	±0.67	±0.12	±0.15
Buoyant bottom outfall $\frac{y}{RD} = 1.85(\frac{y}{RD})^{0.29}$	±0.17	±0.23	±0.05	±0.07
Buoyant shore-based surface outfall $\frac{y}{RD} = 2.45(\frac{y}{RD})^{0.29}$	±0.21	±0.29	±0.06	±0.08
Heavy density surface outfall $\frac{y}{RD} = 2.00(\frac{x}{RD})^{0.29}$	±0.53	±0.70	±0.14	±0.20

behaves in the near-field. From Figs. 5.42 and 5.43, it can be seen that the variation is proportional to ξ/D with the slope of the line varying from 0.36 to 0.45. An average value of a 0.40 was taken for these five runs and the dilution equation for bottom outfall can be written as:

$$\frac{C_o}{C_m} = 1 + 0.40\ \xi/D \qquad \text{for } \xi/D > 2\text{-}4 \tag{5.47}$$

From studies by Albertson *et al*. (1950) and Rajaratnam (1976) for a momentum jet discharging into a quiescent fluid, they found that the dilution is given by

$$\frac{C_o}{C_m} = 1 + 0.32\ \xi/D \tag{5.48}$$

Comparing Eqs. 5.47 and 5.48, both show a linear variation for the dilution with the slope of the line obtained in this study is 30% steeper than that for a simple circular jet. This is attributed to the increased entrainment caused by the cross-flow. A recent study by Rajaratnam and Gangadhariah (1980) on the behaviour of a circular jet discharged vertically in cross-flow shows that the dilution variation is non-linear with ξ/D for values of R up to 7.0. Their dimensionless equation is in the form of:

$$\frac{C_o}{C_m} = 0.54(\xi/D)^{1.22} \tag{5.49}$$

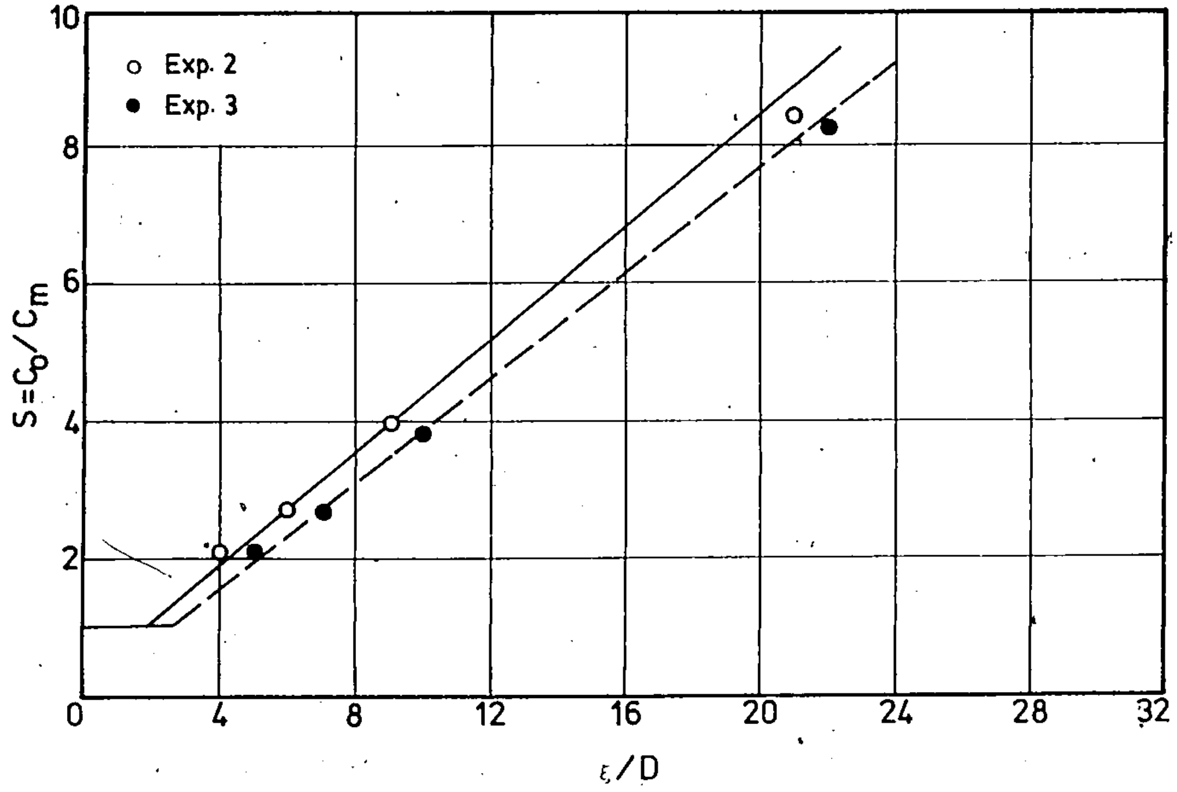

Fig. 5.42. Variation of $\frac{C_o}{C_m}$ with $\frac{\xi}{D}$ - Exps. 2 and 3.

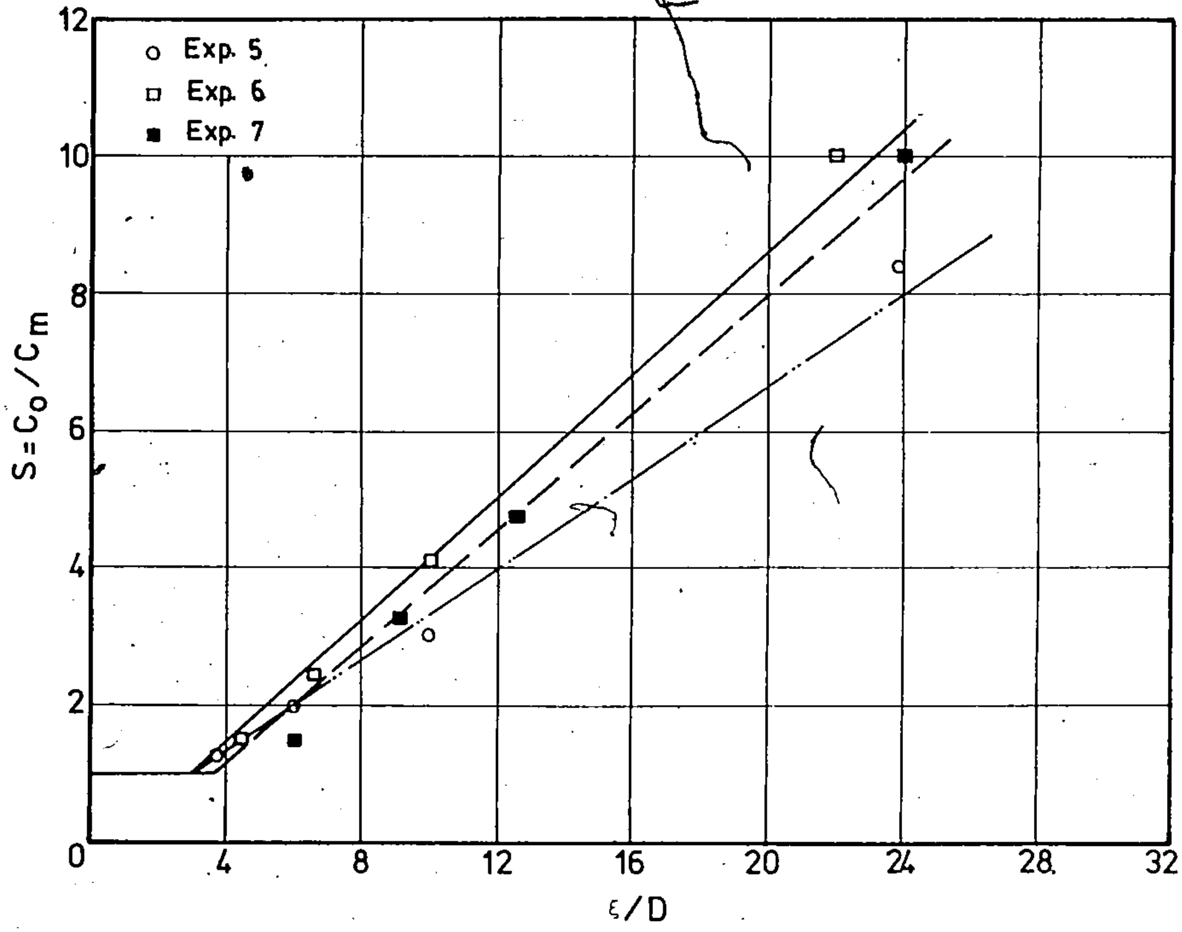

Fig. 5.43. Variation of $\frac{C_o}{C_m}$ with $\frac{\xi}{D}$ - Exps. 5, 6 and 7.

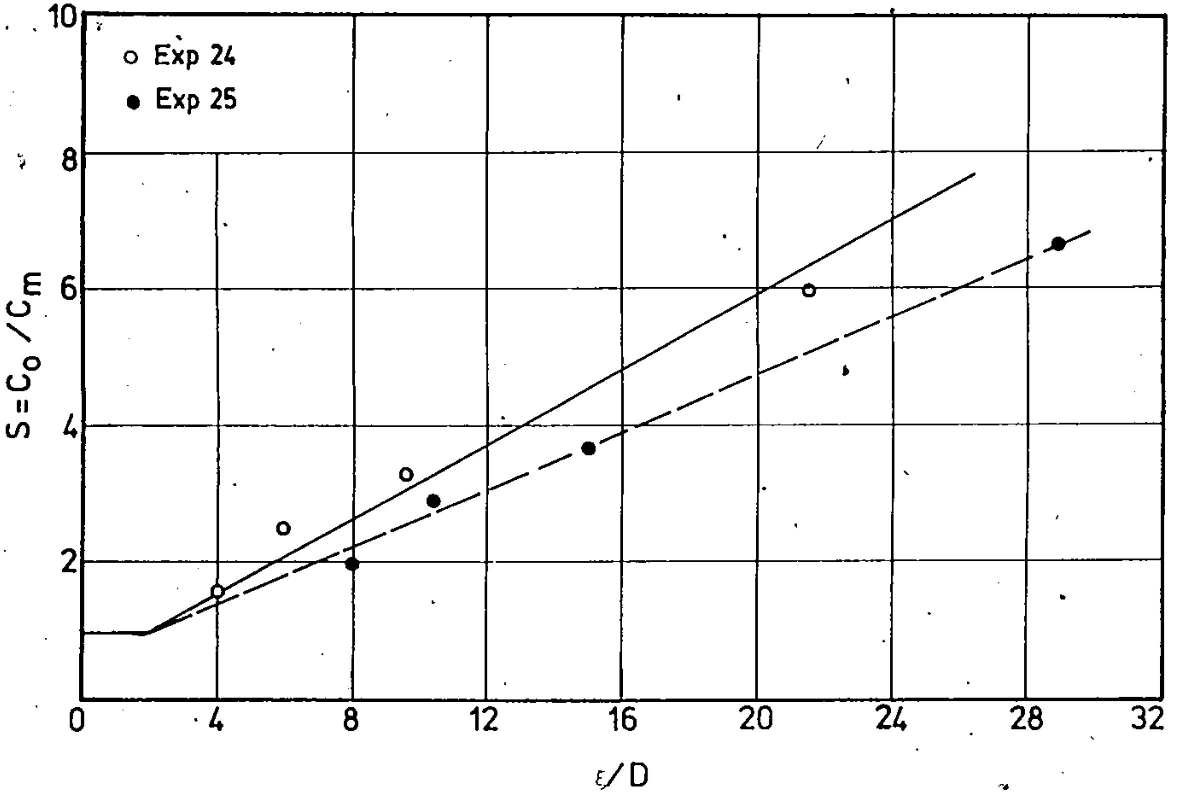

Fig. 5.44.. Variation of $\frac{C_o}{C_m}$ with $\frac{\xi}{D}$ - Exps. 24 and 25.

They also found that with larger values of R (e.g., R=23.4) the minimum dilution is linear with the slope of the line about 30% larger than that for a simple jet. The results of the five experiments, (Runs 2, 3, 5, 6 and 7) with R between 2.0 and 5.2, are shown replotted on log-log paper in Fig. 5.45. The results show that the minimum dilution for a horizontal non-buoyant bottom outfall can be represented by the following linear relationship:

$$\frac{C_o}{C_m} = 0.4(\xi/D) \qquad (5.50)$$

Figure 5.45 also presents the minimum dilution curve obtained by Rajaratnam <u>et</u> <u>al</u>. (1980) for a non-buoyant jet that discharges vertically into a cross-flowing deep ambient stream. It is noted that the dilution for the vertical outfall is approximately double that for the horizontal bottom jet. Reasons for this substantial difference include: the effect of the near-shore boundary layer relative to the bottom boundary layer in the central part of the ambient; the greater surface exposure to entrainment on the vertical jet and the greater vortex development in the vertical jet.

Figure 5.44 presents the results for a surface outfall in the region downstream the establishment zone. The dilution rate was found to vary from 0.26 to 0.29 with an average value of 0.27. Table 5.4 presents the results of

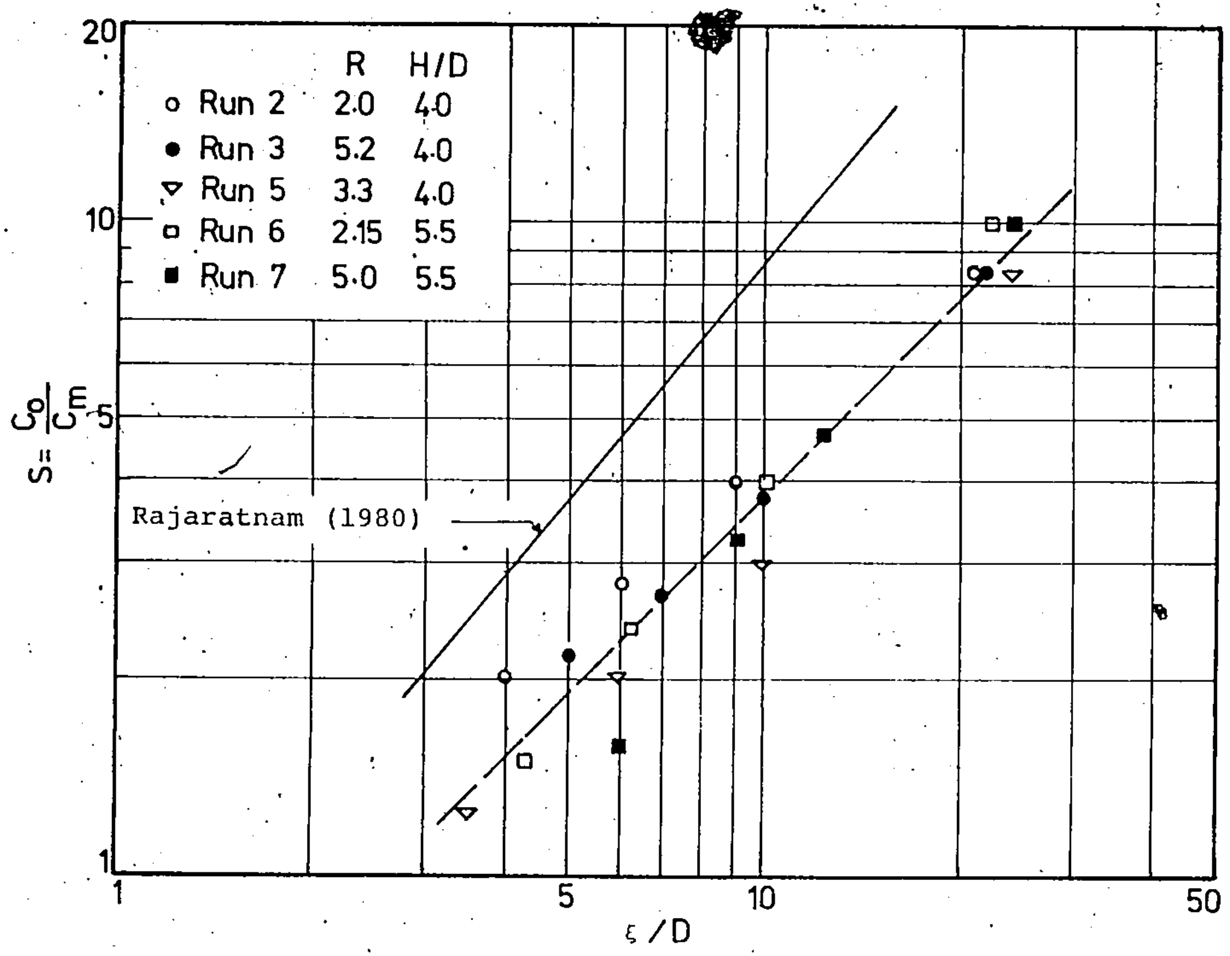

Fig. 5.45. Minimum Dilution Curve for Non-buoyant bottom outfalls.

Table 5.4

Dilution Rates for Non-Buoyant Jets

Run No.	Q L/s	H/D	$R=V_j/U_a$	Pipe Position	Dilution Rate	ξ_i
1	34	2	3.2	bottom	0.18	2D
2	34	4	2.0	bottom	0.42	2D
3	34	4	5.2	bottom	0.40	3D
5	70	4	3.3	bottom	0.36	3D
5	70	5.5	2.15	bottom	0.45	3D
7	70	5.5	4.92	bottom	0.425	3.7D
24	34	4	2.0	surface	0.29	2D
25	34	4	5.2	surface	0.26	4D
26	70	5.5	4.92	submerged	0.31	2D

the dilution rate for non-buoyant bottom and surface outfalls.

5.1.6.1 Determination of Prandtl-Schmidt Number

The turbulent velocity-concentration correlation are related to the mean concentration through the eddy diffusivity. The eddy diffusivity ε_s is also not a fluid property but depends on the state of turbulence. In fact, the Reynolds analogy between mass transfer, ε_s, and momentum transfer, ε_m, suggests the following relationship:

$$\sigma_t = \frac{\varepsilon_m}{\varepsilon_s} \tag{5.51}$$

where σ_t is the turbulent Prandtl-Schmidt number. Many models make use of Eq. 5.51 with Prandtl-Schmidt number as constant and equal to unity. The results of the variation of $\frac{C_o}{C_m}$ and $\frac{\Delta U_o}{\Delta U_m}$ with $\frac{\xi'}{D}$ for bottom jets is shown in Fig. 5.46 where ξ' is the distance along the deflected jet measured after the establishment zone. A study of Fig. 5.46 shows that both the variation of $\frac{C_o}{C_m}$ and $\frac{\Delta U_o}{\Delta U_m}$ can be represented by the following linear relationships

$$\frac{C_o}{C_m} = 0.60 \frac{\xi'}{D} \tag{5.52}$$

$$\frac{\Delta U_o}{\Delta U_m} = 0.53 \frac{\xi'}{D} \tag{5.53}$$

Comparing Eqs. 5.52 and 5.53 indicates that σ_t should be in the order of 0.88 for bottom jets. Similar analysis was made for shore-based surface outfall and the results are depicted in Fig. 5.47. Both $\frac{C_o}{C_m}$ and $\frac{\Delta U_o}{\Delta U_m}$ show linear variations with $\frac{\xi'}{D}$ in the form of:

$$\frac{C_o}{C_m} = 0.40\ \frac{\xi'}{D} \tag{5.54}$$

$$\frac{\Delta U_o}{\Delta U_m} = 0.31\ \frac{\xi'}{D} \tag{5.55}$$

Equations 5.54 and 5.55 suggest that σ_t is equal to 0.78 for shore-based surface jets. This agrees with Rodi's work (1980) as he stated that the value of σ_t varies from 0.5 in free mixing to 0.9 in near wall. Also, Fischer et al. (1979) reported a value for σ_t=0.8 for free turbulent jets.

5.1.6.2 Excess Temperature Dilution

The excess temperature dilutions $\Delta T_o/\Delta T_m$ are plotted as a function of ξ/D in the same manner as the concentration dilutions. Typical results of the dilution data are given in Figs. 5.48 to 5.50 and a summary of the experimentally determined constants is presented in Table 5.5. Each dilution curve can be described by two linear variations. The first part of the plot describes the establishment zone and the second part describes the dilution curve.

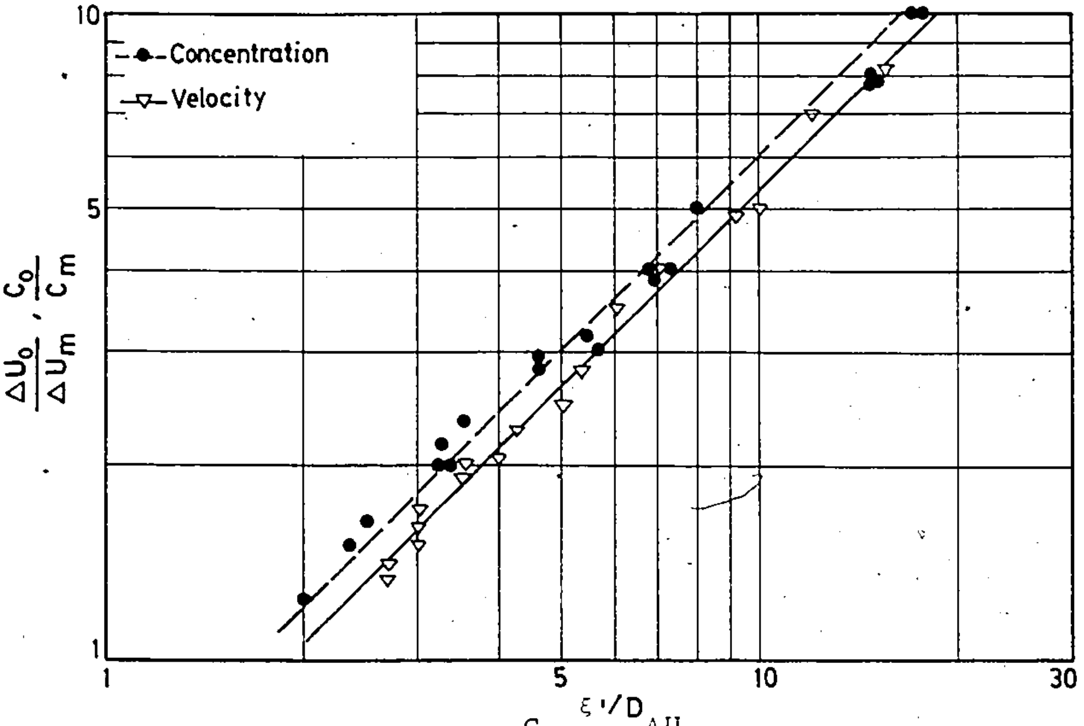

Fig. 5.46. Variation of $\frac{C_o}{C_m}$ and $\frac{\Delta U_o}{\Delta U_m}$ with $\frac{\xi'}{D}$ for bottom jets.

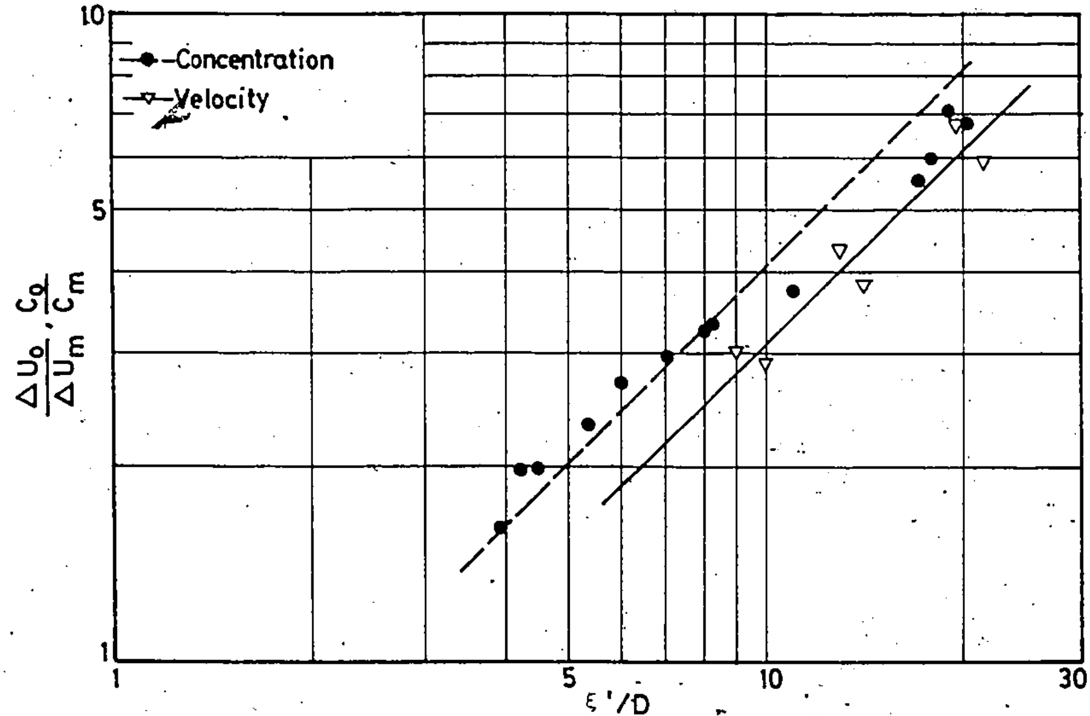

Fig. 5.47. Variation of $\frac{C_o}{C_m}$ and $\frac{\Delta U_o}{\Delta U_m}$ with $\frac{\xi'}{D}$ for surface jets.

beyond the establishment zone. The latter appears to start at $\xi/D \simeq 2$ to 3 and corresponds to the start of the deflection zone. This point was noted by Shirazi and Davis (1974) who developed an empirical equation to define the length of the establishment zone in the form of:

$$\frac{\xi_i}{D} = 5.4\left(\frac{A^2}{F_o}\right)^{1/3} \qquad (2.23)$$

in which

ξ_i = length of the establishment zone

A = jet aspect ratio (width to depth ratio)

Using this equation to calculate the length of the establishment zone, it was found that ξ_i is equal to 2D for high velocity ratio (R=5) and 3D for low velocity ratio (R=2). The measured and the predicted lengths of ξ_i for each run are shown in Table 5.5.

The dilution along the jet trajectory is compared in Figs. 5.49 and 5.50 for different velocity ratios. The results show that the dilution is influenced very little by the velocity ratio although the measurements indicate that the rate of dilution decreases slightly with increasing the velocity ratio R. This observation has been confirmed by the experiments of McGuirk and Rodi (1978).

Considering the region downstream the end of the establishment zone, the curves shown in Figs. 5.48 to 5.50

depict a linear increase of $\Delta T_o/\Delta T_m$ with ξ/D. The dilution rate was found to vary from 0.33 to 0.5 for bottom outfalls and from 0.2 to 0.23 for surface outfalls. Average value of 0.40 and 0.21 were taken for buoyant bottom and surface outfalls, respectively. The equations can be written as

for $\xi/D>2\text{-}3$

$$\frac{\Delta T_o}{\Delta T_m} = 1 + 0.40\,\frac{\xi}{D} \qquad \text{(bottom outfall)} \qquad (5.56)$$

$$\frac{\Delta T_o}{\Delta T_m} = 1 + 0.21\,\frac{\xi}{D} \qquad \text{(surface outfall)} \qquad (5.57)$$

In Fig. 5.48, the dilution rate for Exp. 1-1 was found to be 0.19. This Experiment was excluded from the analysis as the depth of flow is shallow, $H/D=2.0$. Therefore, it is possible that the entrainment demand of the jet could not be met, and the jet became attached to the bottom and all the entrainment flow entered from the sides. Consequently, Eq. 5.56 is only valid for ratio of $H/D\geq 4.0$.

The relatively high value of dilution rate found for Run 26-1 (Fig. 5.50 and Table 5.5) was the result of placing the issuing pipe of the jet a little beneath the water surface. This run can be treated as a submerged case and the equation can be written as:

$$\frac{\Delta T_o}{\Delta T_m} = 1 + 0.35\,\frac{\xi}{D} \qquad (5.58)$$

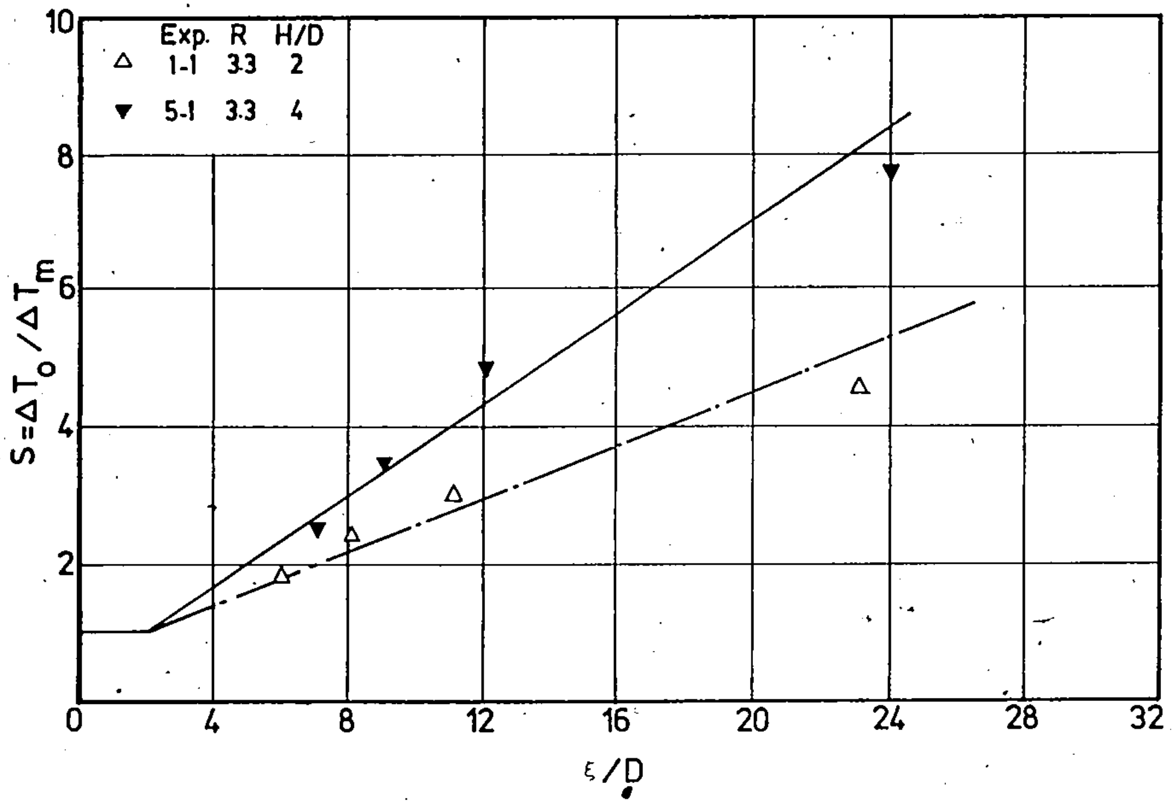

Fig. 5.48. Variation of $\frac{\Delta T_o}{\Delta T_m}$ with $\frac{\xi}{D}$, Exps. 1-1 and 5-1.

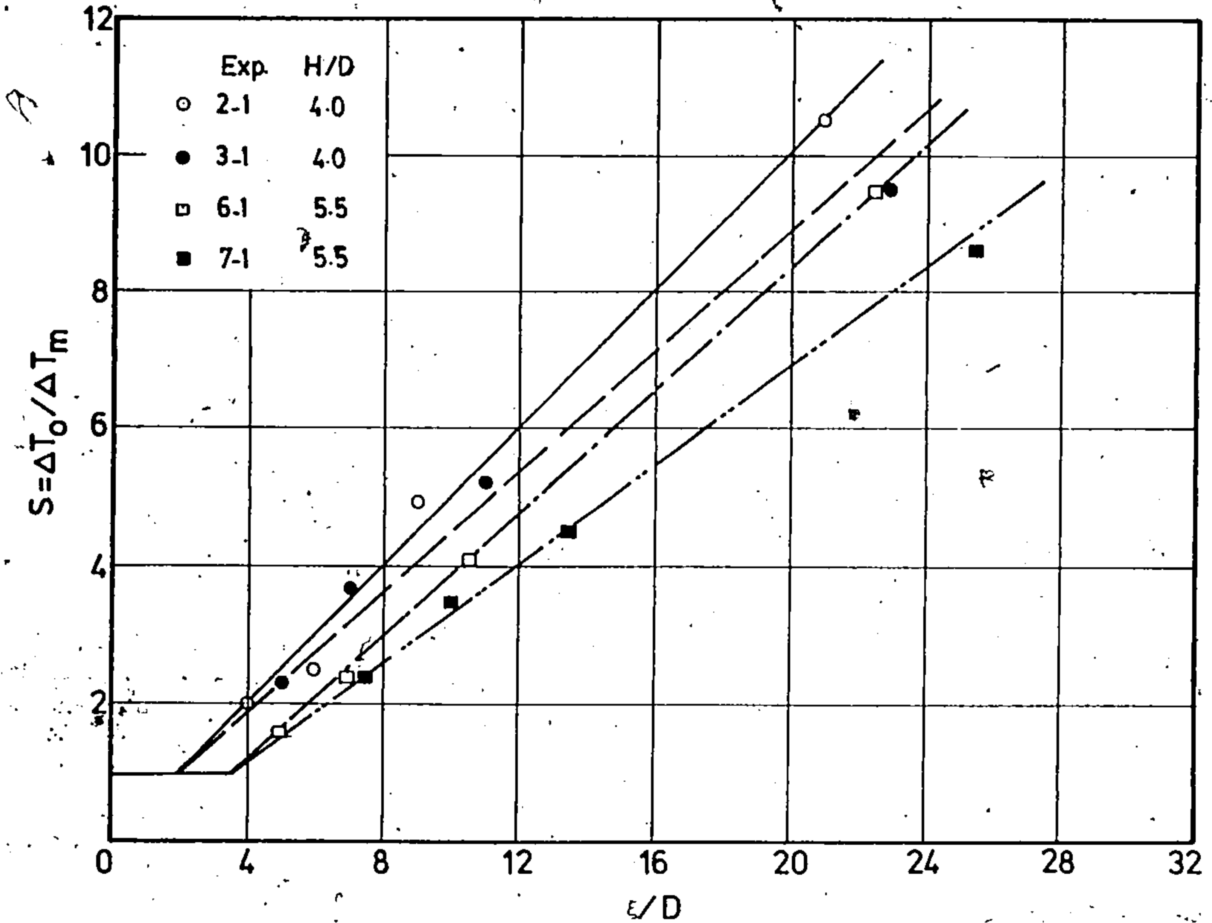

Fig. 5.49. Variation of $\frac{\Delta T_o}{\Delta T_m}$ with $\frac{\xi}{D}$, Exps. 2-1, 3-1, 6-1 and 7-1.

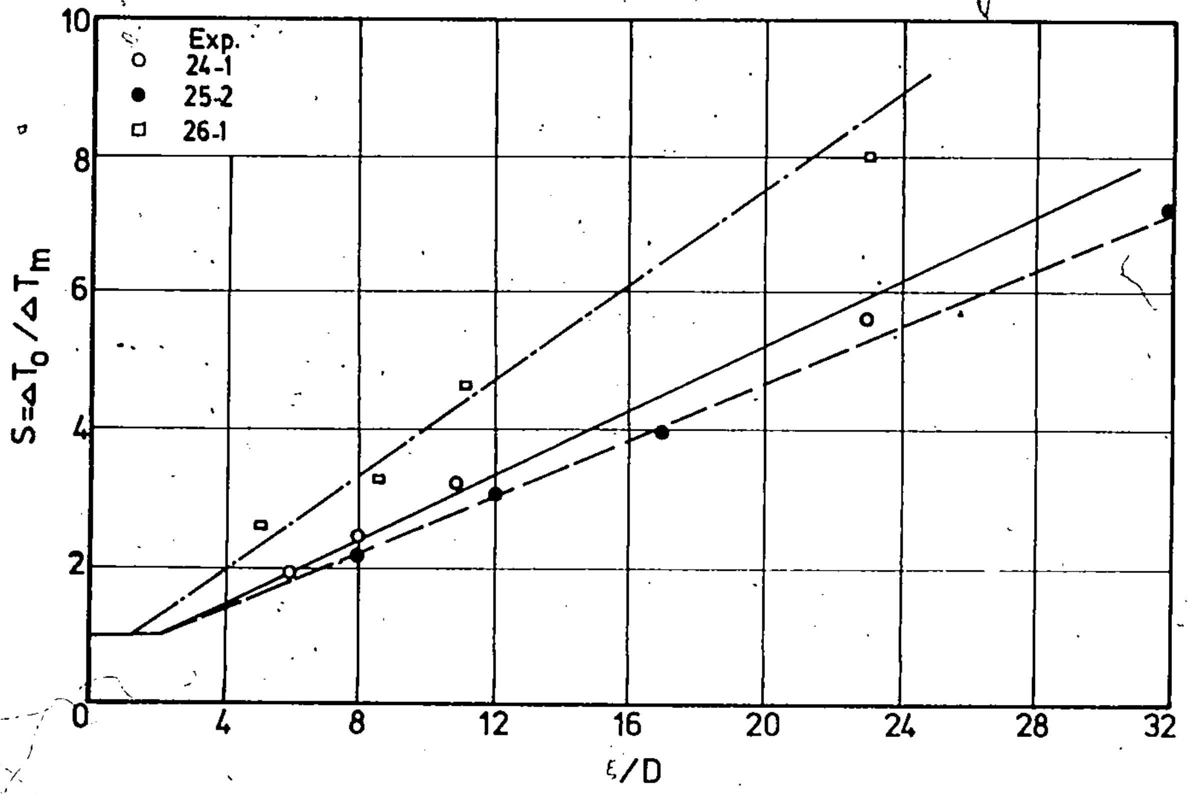

Fig. 5.50. Variation of $\frac{T_o}{T_m}$ with $\frac{\xi}{D}$, Exps. 24-1, 25-2 and 26-1.

Table 5.5

Dilution Rates for Buoyant Jets

Run No.	Q L/s	H/D	$R=V_j/U_a$	Pipe Position	Dilution Rate	Establishment Zone Length	
						Measured	Predicted
1-1	34	2	3.2	bottom	0.19	2D	2D
2-1	34	4	2.0	bottom	0.50	2D	3D
3-1	34	4	5.2	bottom	0.44	2D	2D
5-1	70	4	3.3	bottom	0.33	2D	2D
6-1	70	5.5	2.15	bottom	0.44	3.5D	3D
7-1	70	5.5	4.92	bottom	0.36	3.5D	2D
24-1	34	4	2.0	surface	0.23	2.3D	3D
25-2	34	4	5.2	surface	0.20	2.1D	2D
26-1	70	5.5	4.92	submerged	0.35	2D	2D

The higher dilution rate given by the above equation for Run 26-1 also indicates the effect of the depth of flow. For a relatively shallow receiving water represented by Runs 24-1 and 25-2, the bottom entrainment flow has to approach laterally within a restricted fluid layer under the jet. Consequently, the induced velocities are higher, leading to more frictional dissipation and a reduced vertical entrainment flow.

Two tests were carried out on heated discharges where the concentration and temperature were measured simultaneously. Ratios of the initial to the maximum concentration, C_o/C_m, and the initial to the maximum temperature, $\Delta T_o/\Delta T_m$, were plotted versus ξ/D in Figs. 5.51 and 5.52 for bottom and surface outfalls, respectively. As expected, the minimum dilution, S, as estimated for both approaches were very close.

Similar analysis was made on a heavy density surface jet to obtain a general equation for the dilution. Figure 5.53 presents the results of the dilution curves for two velocity ratios. Both curves show that the dilution starts at $\xi/D=2$. The dilution rate was found to be 0.16 and 0.22 for R=5.2 and 2.0 respectively as shown in Table 5.6. An average value of 0.19 was taken and the equation became

$$\frac{\Delta T_o}{\Delta T_m} = 1 + 0.19 \frac{\xi}{D} \quad (5.59)$$

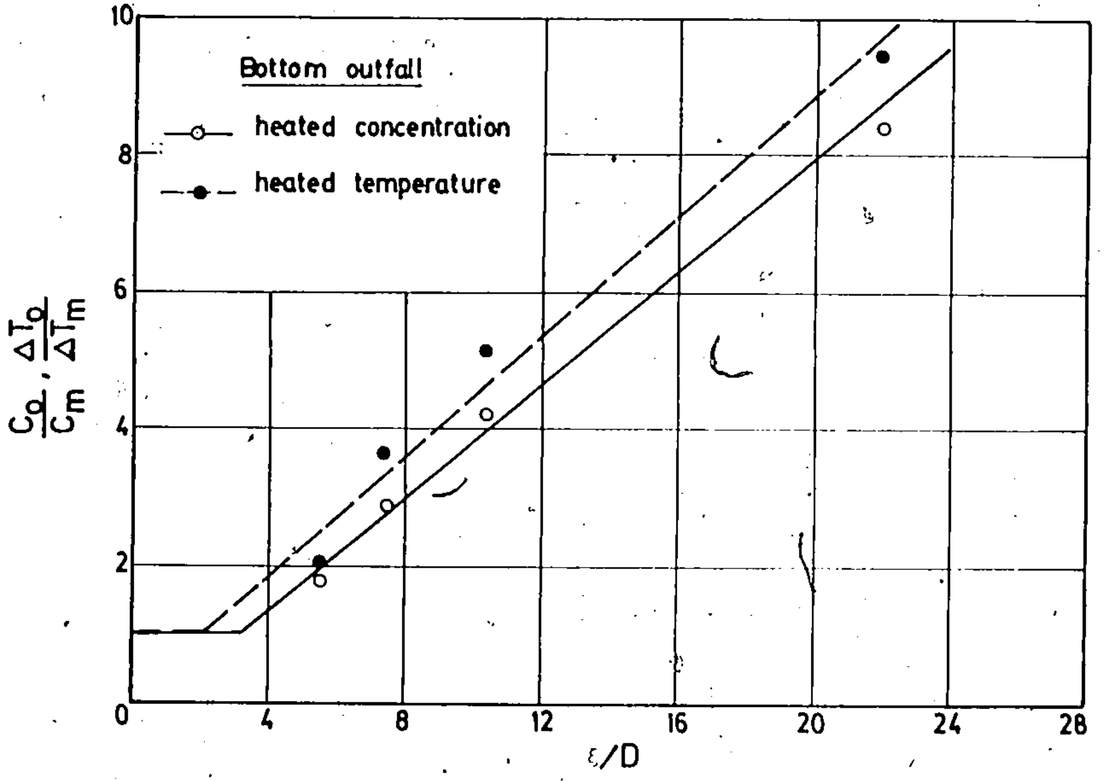

Fig. 5.51. Variation of $\frac{C_o}{C_m}$ and $\frac{\Delta T_o}{\Delta T_m}$ with $\frac{\xi}{D}$ - bottom outfall.

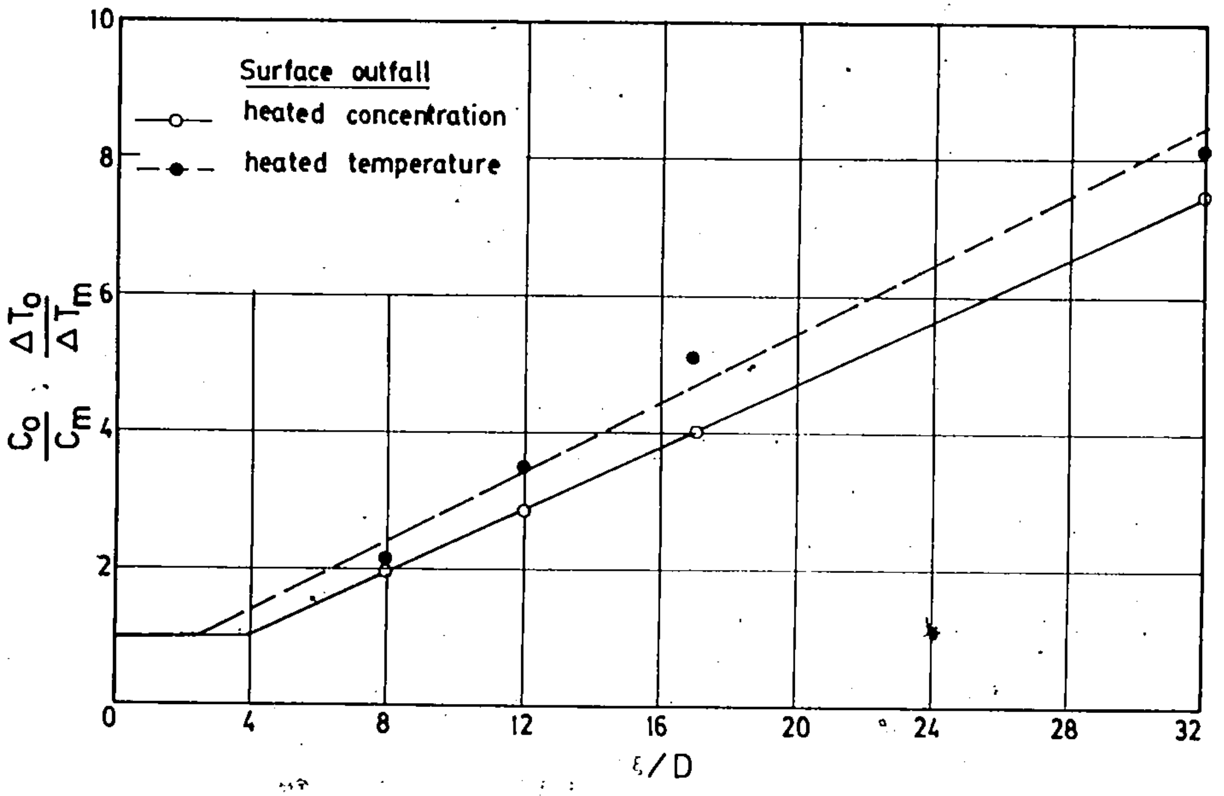

Fig. 5.52. Outfall of $\frac{C_o}{C_m}$ and $\frac{\Delta T_o}{\Delta T_m}$ with $\frac{\xi}{D}$ - surface outfalls.

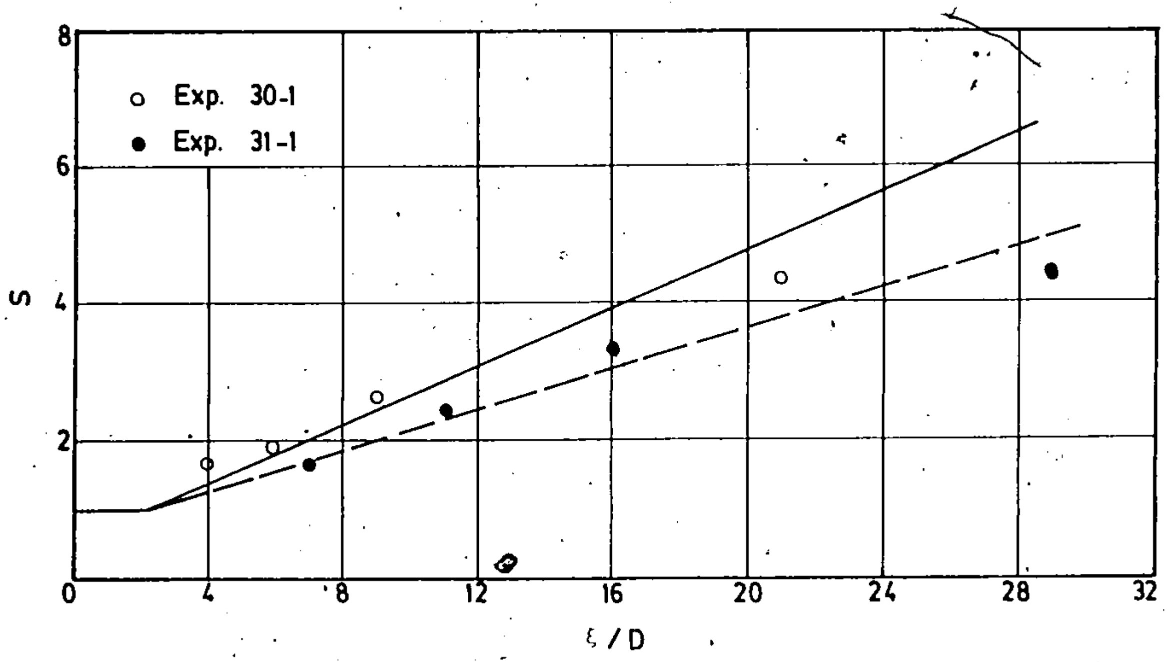

Fig. 5.53. Minimum dilution curve for heavy density surface outfalls.

Table 5.6

Dilution Ratio for Heavy Density Jets

Run No.	Q L/s	H/D	$R=V_j/U_a$	Pipe Position	Dilution Rate	ξ_i
30-1	34	4	2.0	surface	0.22	2D
31-1	34	4	5.2	surface	0.16	2D

In general, the variation of minimum dilution, S, with ξ/D is linear only for ξ/D>2 to 4. S is found to decrease with decreasing the depth of flow, H/D, raising the outfall to the surface and to a lesser extent with increasing the velocity ratio, R.

5.1.7 General Equations of Jet Trajectories and Minimum Dilution

Most of the research work in the area of jets in cross-flow have neglected the geometrical parameters in deriving the jet trajectory and dilution equations. In this section, consideration is given to the geometrical and environmental parameters so that a useful analytical description can be devised for the jet in a cross-flow. The experimental results of this study and the dimensional analysis presented in section 5.1.1 indicated that the jet profile and the dilution are strongly affected by the longitudinal distance, x, the depth of flow, H, the ambient velocity, U_a, the jet velocity V_j, density difference between the jet and the ambient $\Delta\rho$ and pipe position, Z_p, i.e.,

$$\frac{y}{D} = f\left(\frac{x}{D}, R, F_o, \frac{H}{D}, \frac{Z_p}{H}\right) \qquad (5.5)$$

$$S = f\left(\frac{\xi}{D}, R, F_o, \frac{H}{D}, \frac{Z_p}{H}\right) \qquad (5.60)$$

5.1.7.1 Jet Trajectory

The suggested form for the general jet trajectory equation is:

$$\frac{y}{D} = c_1 \left(\frac{x}{D}\right)^{n_1} R^{n_2} \left(\frac{1}{1+F_o} + 1\right)^{n_3} \left(e^{-\frac{H}{D}} + 1\right)^{n_4} \left(\frac{Z_p}{H} + 1\right)^{n_5} \tag{5.61}$$

where c_1, n_1, n_2, n_3, n_4 and n_5 are coefficients that must be determined using multiple linear regression analysis. A total of 88 data points were used to obtain these coefficients. In general, Eq. 5.61 gave a good agreement with the measurements for the bottom outfall. However, the predicted equation underestimated the jet profile for both buoyant and non-buoyant surface outfall with high velocity ratios, $R \geq 4.9$. This suggested a modification in the pipe position term, $\frac{Z_p}{H}$. Several combinations of R and $\frac{Z_p}{H}$ were tried until the best-fit with the measurements was obtained. Therefore, it was concluded that the general form of the jet trajectory should be

$$\frac{y}{D} = c_1 \left(\frac{x}{D}\right)^{n_1} R^{n_2} \left(\frac{1}{1+F_o} + 1\right)^{n_3} \left(e^{-H/D} + 1\right)^{n_4} \left(e^{R(Z_p/H)^2}\right)^{n_5} \tag{5.62}$$

or

$$\log \frac{y}{D} = \log c_1 + n_1 \log \left(\frac{x}{D}\right) + n_2 \log (R) + n_3 \log \left(\frac{1}{1+F_o} + 1\right) + n_4 \log \left(e^{-\frac{H}{D}} + 1\right) + n_5 \log \left(e^{R(Z_p/H)^2}\right) \tag{5.63}$$

The results of the multiple linear regression analysis are summarized in Table 5.7. From Table 5.7, the generalized equation of the jet trajectory can be rewritten as:

$$\frac{Y}{D} = 2.24\left(\frac{X}{D}\right)^{0.245}(R)^{0.493}\left(\frac{1}{1+F_o}+1\right)^{0.435}\left(e^{-H/D}+1\right)^{0.83}\left(e^{R(Z_p/H)^2}\right)^{0.092} \qquad (5.64)$$

The term PR>|T| in Table 5.7 indicates the probability that the value of the parameter is equal to zero. Thus, the parameters c_1, $\frac{X}{D}$, R and $\frac{Z_p}{H}$ are not likely to equal zero and they contribute significantly to the value of $\frac{Y}{D}$. The parameters F_o and $\frac{H}{D}$ have a relatively small effect on the prediction of $\frac{Y}{D}$. The experimental data of this study showed that F_o significantly affected the jet width not the trajectory.

A statistical analysis was carried out on Eq. 5.64 and a summary of this analysis is given as follows:

i. Equation 5.64 as a whole, significantly accounts for the dependent variable $\frac{Y}{D}$ behaviour (PR>|F| = 0.0001).

ii. The multiple correlation coefficient of Eq. 5.64 is 83%.

Comparison between measured and predicted jet trajectories are shown in Figs. 5.54 to 5.57. The predicted Eq. 5.64 shows good agreement for both non-buoyant and buoyant bottom outfalls (Figs. 5.54 and 5.55). However, when comparing the prediction of Eq. 5.64 with the results of surface outfall, good agreement was obtained with low velocity ratio, R=2.0, as shown in Figs. 5.56 and 5.57. Also reasonable agreement were observed for submerged outfall. This indicates that Eq. 5.64 is valid for shoreline attached surface jets with R up to 2.0. For high value of R, the jet becomes detached and Eq. 5.64 underestimates the jet trajectory. This suggests that a correction factor should be included in Eq. 5.64 to account for the detachment. Thus, Eq. 5.64 becomes

$$\frac{y}{D} = 2.5\left(\frac{x}{D}\right)^{0.245}(R)^{0.493}\left(\frac{1}{1+F_o}+1\right)^{0.485}\left(e^{-H/D}+1\right)^{0.83}\left(e^{R(Z_p/H)^2}\right)^{0.092} \tag{5.65}$$

A criterion for detached and attached jets was presented in section 5.1.4.2. Equation 5.32 is used as a criterion for shoreline attachment of surface jets.

5.1.7.2 Minimum Dilution

Relationship for characteristic dilution with buoyant and non-buoyant jet can be determined by a similar method. The independent variables to be considered are the same as those for jet trajectory. The independent variable, ξ,

Table 5.7

Regression Analysis Results of Jet Trajectory Equation

Variable	Parameter Estimate	Standard Error	PR>|T|
c_1	2.24	±0.09	0.0001
n_1	0.245	±0.02	0.0001
n_2	0.493	±0.06	0.0001
n_3	0.435	±0.41	0.2911
n_4	0.830	±0.56	0.1445
n_5	0.092	±0.01	0.0001

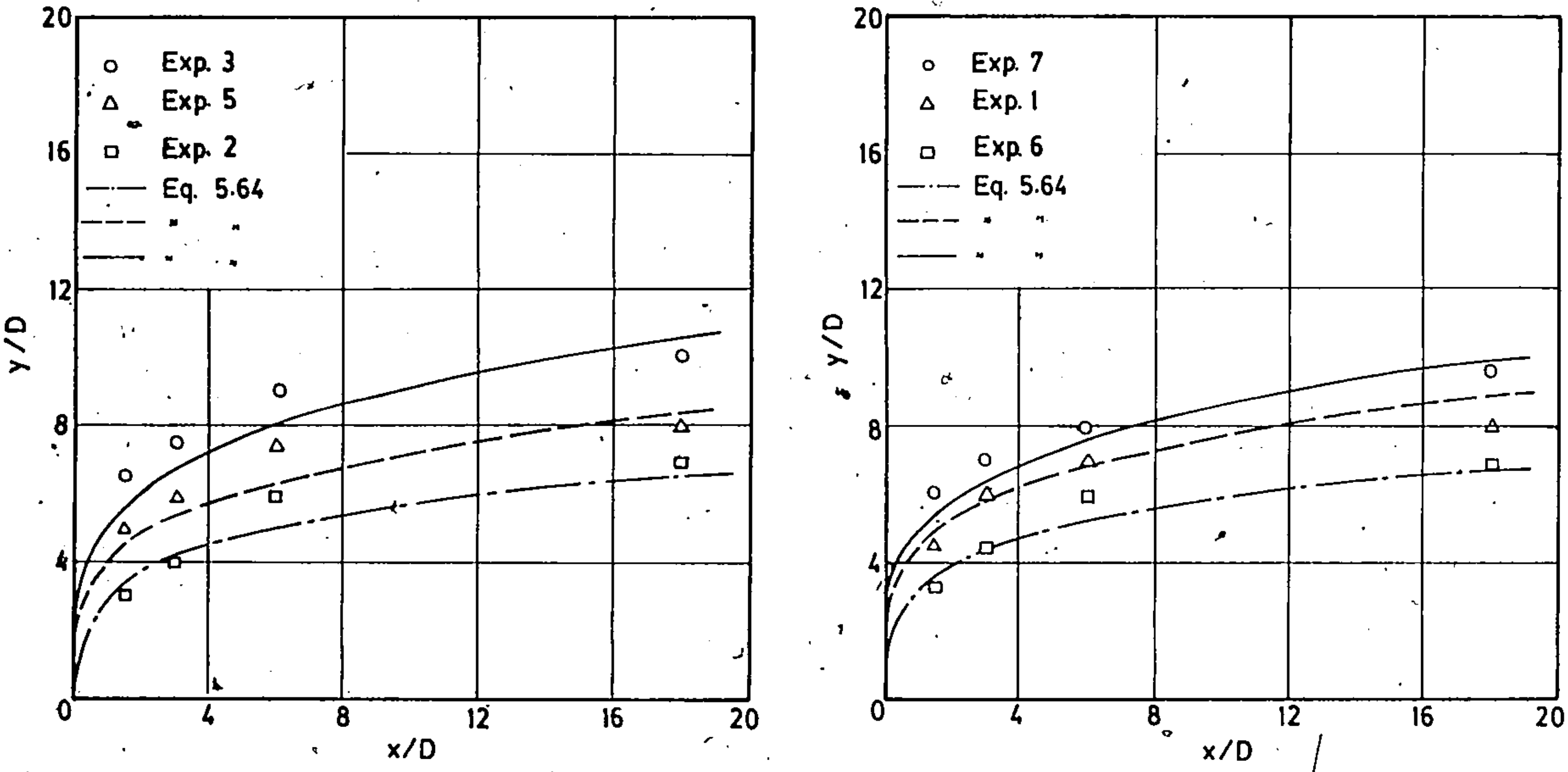

Fig. 5.54. Comparison between measured and predicted jet trajectories for non-buoyant bottom outfalls.

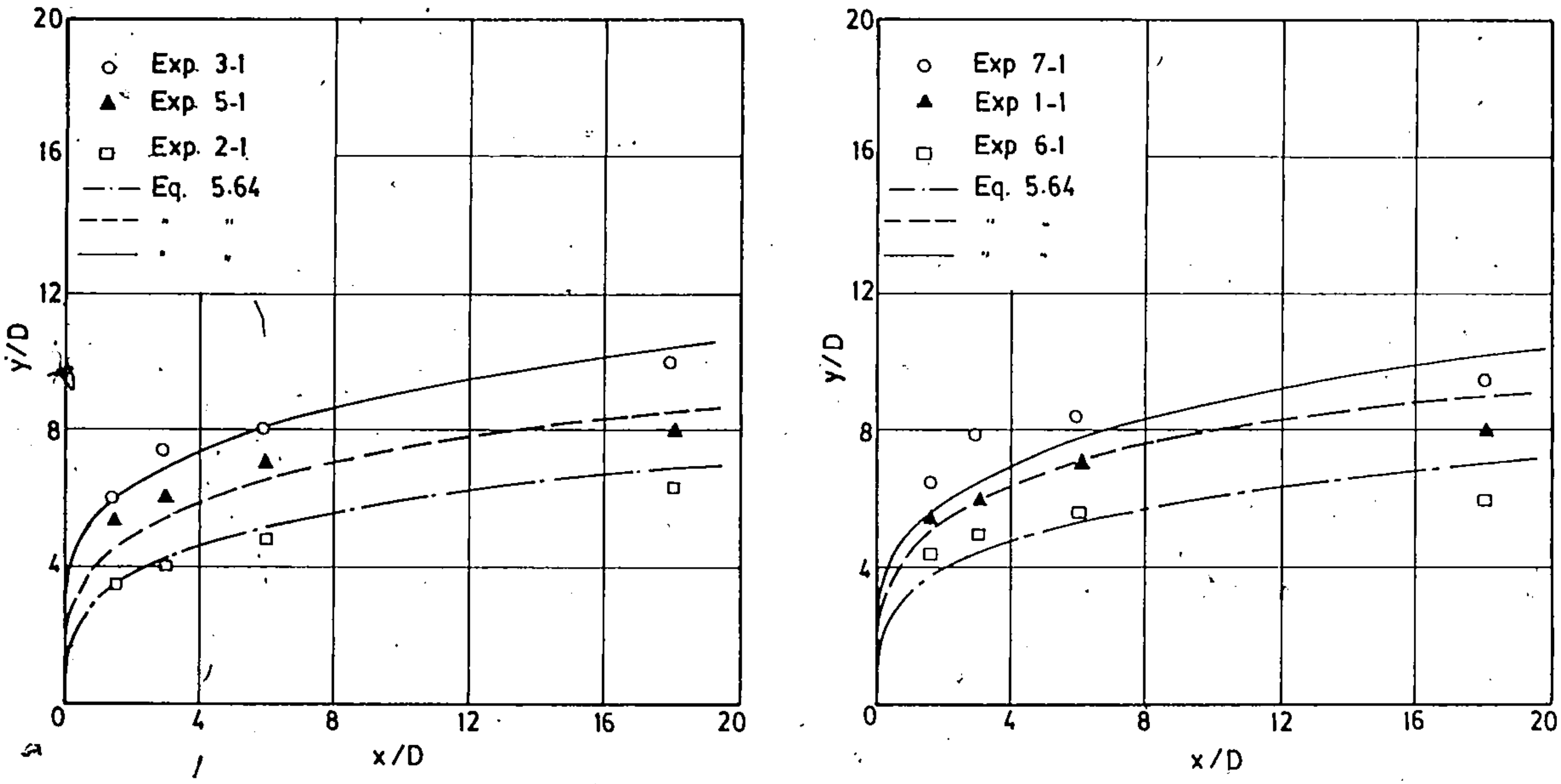

Fig. 5.55. Comparison between measured and predicted jet trajectories for buoyant bottom outfalls.

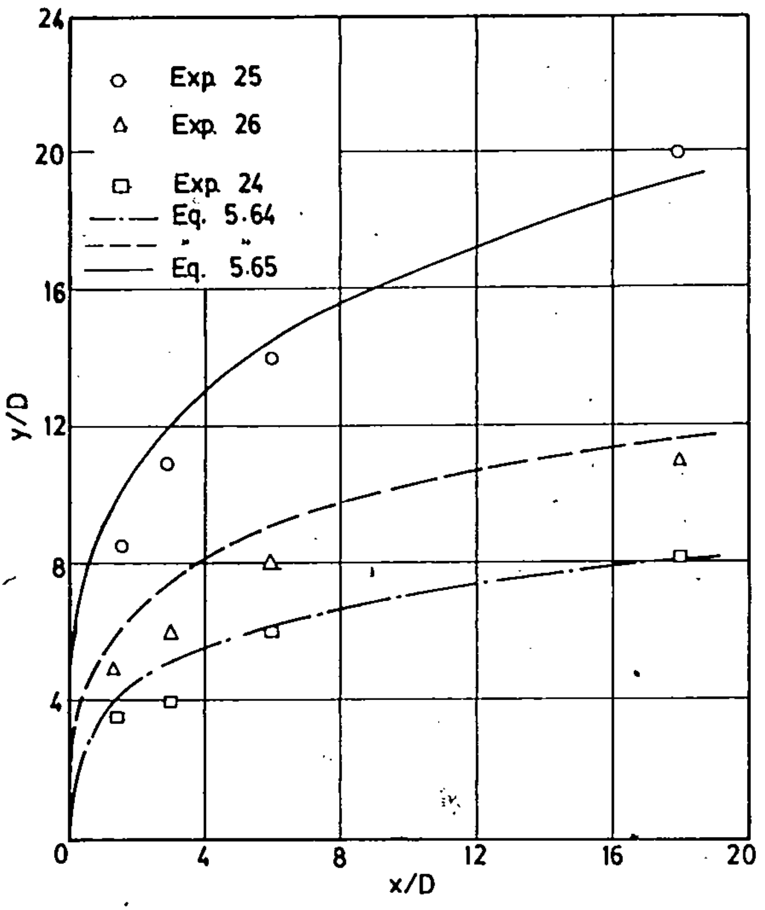

Fig. 5.56. Comparison between measured and predicted jet trajectories for non-buoyant surface outfalls.

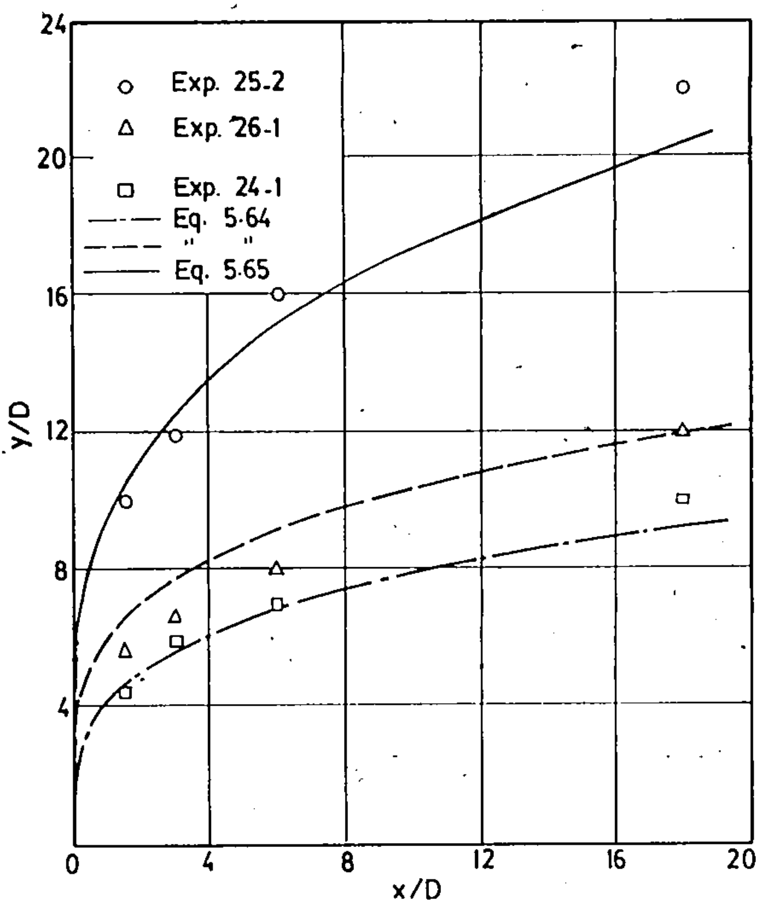

Fig. 5.57. Comparison between measured and predicted jet trajectories for buoyant surface outfalls.

should be considered instead of x and y. The suggested form of the dilution equation is:

$$S = c_2 \left(\frac{\xi}{D}\right)^{m_1} R^{m_2} \left(\frac{1}{1+F_o} + 1\right)^{m_3} \left(e^{-H/D}+1\right)^{m_4} \left(\frac{Z_p}{H} + 1\right)^{m_5} \tag{5.66}$$

where c_2, m_1, m_2, m_3, m_4 and m_5 are coefficients to be determined from a multiple linear regression analysis using the data points obtained during this study. Best fit with the measurements were obtained and the results are summarized in Table 5.8. The generalized equation of the minimum dilution is:

$$S = 0.564 \left(\frac{\xi}{D}\right)^{0.894} R^{-0.059} \left(\frac{1}{1+F_o}+1\right)^{0.152} \left(e^{-H/D}+1\right)^{-4.015} \left(\frac{Z_p}{H} + 1\right)^{-0.319} \tag{5.67}$$

It can be seen from Table 5.8 that c_2, $\frac{\xi}{D}$, $\frac{H}{D}$ and $\frac{Z_p}{H}$ are the most significant variables affecting S. The regression analysis also showed that:

i. Equation 5.67 significantly accounts for the dependent variable, S, behaviour $(PR>|F| = 0.0001)$.

ii. The multiple correlation coefficient of Eq. 5.67 is 90%.

Typical comparison plots between the measured and the predicted minimum dilution are shown in Figs. 5.58 and 5.59 for non-buoyant and buoyant outfalls respectively. Good agreements were observed in these two figures.

Table 5.8

Regression Analysis Results of Minimum Dilution Equation

Variable	Parameter Estimate	Standard Error	PR>|T|
c_2	0.564	±0.11	0.0001
m_1	0.894	±0.04	0.0001
m_2	-0.059	±0.06	0.3312
m_3	0.152	±0.43	0.7264
m_4	-4.015	±0.60	0.0001
m_5	-0.319	±0.07	0.0001

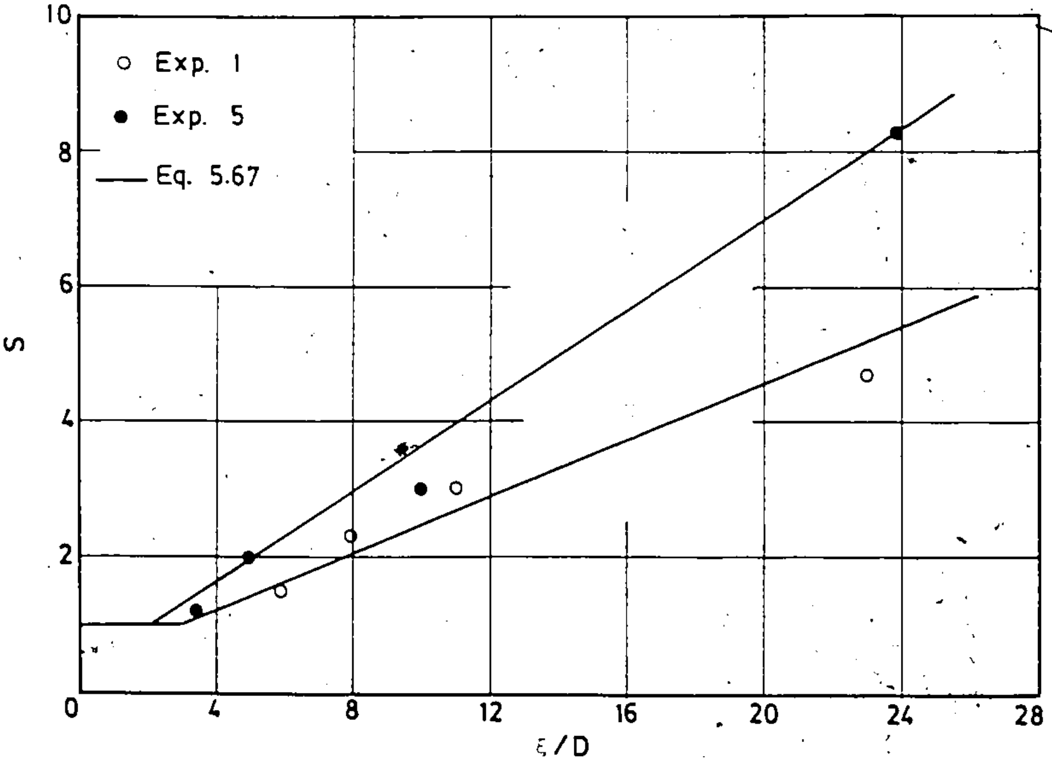

Fig. 5.58. Comparison between measured and predicted minimum dilution for non-buoyant outfalls.

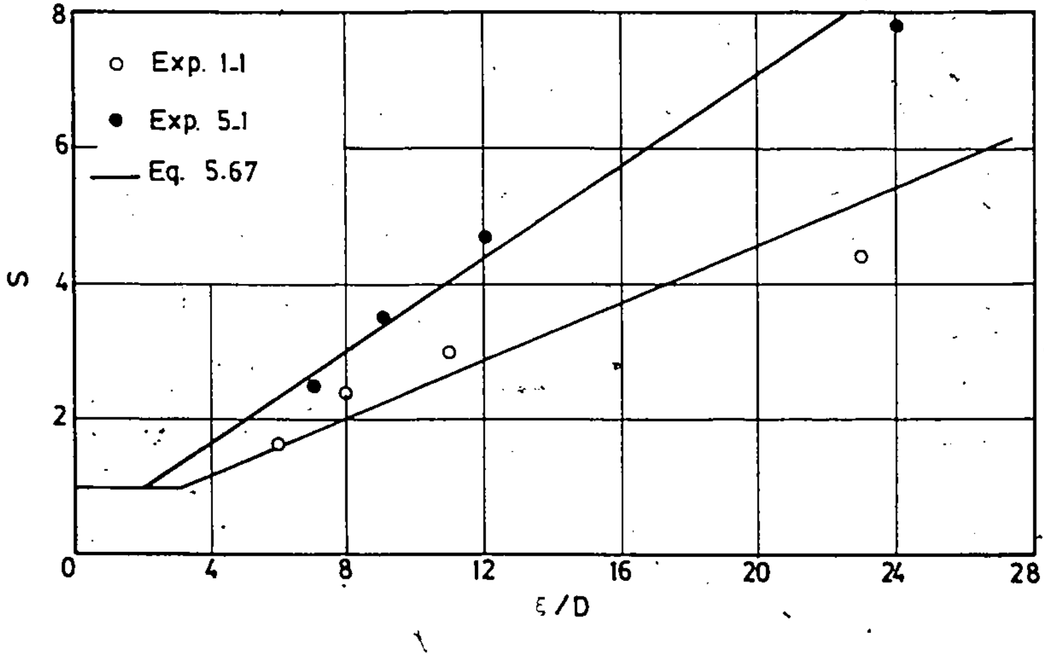

Fig. 5.59. Comparison between measured and predicted minimum dilution for buoyant outfalls.

5.2 CONTAMINANT BEHAVIOUR STUDIES

5.2.1 Relationship Between Chlorine Dose and Residual Chlorine

The chlorine demand exerted by various concentrations of chlorine added to the diluted final effluent from West Windsor Pollution Control Plant is shown in Fig. 4.34. In this figure, the residual chlorine is plotted as a function of chlorine added following a contact time of 30 minutes. The immediate chlorine demand of 2.7 mg/L shown in Fig. 4.34, is due to the reaction with easily oxidizable organic compounds, ferrous ions, sulfides, nitrites and other reducing agents present in the effluent. Using the data shown in the above figure, values for increase in moles of total residual chlorine per mole of chlorine added, $\Delta TRC/\Delta Cl_2$ added, are tabulated in Table 5.9 . Both the slope of residual chlorine plot in Fig. 4.34 and the average $\Delta TRC/\Delta Cl_2$ added value in Table 5.9 clearly indicate that, after the immediate chlorine demand is satisfied, all chlorine added appears as combined residual chlorine.

The removal of ammonia in natural water system can occur via three main routes (i) biological decay, (ii) chemical oxidation by materials such as chlorine to form chloramines, and (iii) degassing via water-atmosphere exchange (Snodgrass 1980). The ammonia concentration in the treated wastewater was determined soon after collection

Table 5.9

Effect of Chlorine on Residual Chlorine and Ammonia

Cl_2 added and diluted mg/L	TRC mg/L	Residual NH_3 mg/L	ΔCl_2 Added mg/L	ΔTRC mg/L	$-\Delta NH_3$ mg/L	$\frac{\Delta TRC}{\Delta Cl_2 \text{ added}}$	$\frac{-\Delta NH_3}{\Delta Cl_2 \text{ added}}$
0.00	0.00	0.710					
0.135	0.00	0.710	0.135	0.00	0.00	0.00	0.00
0.25	0.12	0.685	0.115	0.12	0.025	1.04	0.22
0.35	0.19	0.610	0.100	0.07	0.075	0.70	0.75
0.45	0.30	0.450	0.100	0.11	0.160	1.10	1.60
0.55	0.45	0.350	0.100	0.15	0.100	1.50	1.00
0.65	0.50	0.320	0.100	0.05	0.030	0.50	0.30
					Average	0.97	

and before adding chlorine and was found to be 14.2 mg/L. This value would correspond to initial concentration of 0.71 mg/L after dilution. The corresponding residual ammonia concentrations in the diluted final effluent samples that have been dosed with 5, 7, 9, 11 and 13 mg/L of chlorine following a 30 minute contact time are shown also in Fig. 4.34. Values for decrease in moles of ammonia per mole of chlorine added, $-\Delta NH_4/\Delta Cl_2$ added, are tabulated in Table 5.9. These values range between 0.22 and 1.6. According to White (1972) and Johnson (1975), a value above 0.2 indicates the formation of monochloramines. Thus, in this study all the residual chlorine combined with ammonia was present as monochloramine.

The curves in Fig. 4.35 show the total residual chlorine in the diluted final effluent samples from West Windsor Plant that have been dosed with 5, 7, 9, 11 and 13 mg/L of chlorine. Without chlorine demand, these doses would correspond to initial concentrations of 0.25, 0.35, 0.45, 0.55 and 0.65 mg/L respectively. As it is shown, the most accelerated chlorine reaction occurs within the few hours and this is followed by a gradual decay in chlorine concentration for several days.

The following model is proposed to describe the decay of total residual chlorine with time in diluted effluent samples:

$$C_t = (C_i - C^*)\exp(-k't) \quad (5.68)$$

or $$C_t = C_o \exp(-k't) \quad (5.69)$$

or $$C_t = C_o 10^{-kt} \quad (5.70)$$

where

C_t = total residual chlorine after time t, mg/L

C_i = initial chlorine concentration after dilution in pure water, mg/L

C^* = immediate chlorine demand, mg/L

C_o = $(C_i - C^*)$ = Initial residual chlorine concentration in river after mixing, mg/L

$k = 0.4343\ k'$ = first order decay rate coefficient, day^{-1}

t = time, days

This equation comprises of two adjustable parameters, k and C^*. This model assumes that a portion of the initial chlorine concentration, C_i, is used to satisfy the immediate chlorine demand, C^*, and the remainder, C_o, is subjected to gradual decay. Table 5.10 presents the results of this study using Eq. 5.70. As Table 5.10 indicates the use of a first order decay model with an immediate chlorine demand yielded an average value of the immediate chlorine demand, C^*, clustering around 0.135 mg/L in diluted sample or 2.7 mg/L in effluent. This agrees with the value of C^*

Table 5.10

Immediate Chlorine Demand of Various Chlorine Doses

Chlorine Dose mg/L	Initial Conc. without Chlorine Demand C_i, mg/L	Immediate Chlorine Demand C*, mg/L	Initial Conc. after half hour C_o, mg/L
5	0.25	0.13	0.12
7	0.35	0.16	0.19
9	0.45	0.15	0.30
11	0.55	0.10	0.45
13	0.65	0.15	0.50
9	0.45	0.16	0.29
9	0.45	0.14	0.31
9	0.45	0.12	0.33
	Average	0.135	

Dilution factor = 20

C_i = chlorine dose/dilution factor

obtained earlier from Fig. 4.34.

It is known that chlorine in natural water system can disappear via reaction with ammonia and organics and by volatilization (Snodgrass 1980). This immediate chlorine demand is supposedly due to chemical reaction with reducing agents in wastewater. The subsequent gradual decay shown in Fig. 4.35 is due to chemical reactions and volatilization. A similar pattern of rapid initial chlorine demand, followed by a persistent residual, was observed by Baker (1970) in Passaic River water at Little Falls, New Jersey. When the effluent was dosed with 20 mg/L chlorine, 77% of its total 2-hour demand was exerted in the first four minutes. Very recent work by Haas and Karra (1984) showed that 10 to 40% of the applied chlorine decayed very fast with a rate constant of approximately 10 min^{-1} followed by a slow rate of decomposition.

In Fig. 5.60, the total residual chlorine, TRC, is plotted on logarithmic scale against time, t, for different initial chlorine concentrations. The results for initial chlorine dose of 5 mg/L are not shown in this figure because the chlorine decayed very fast within the first day. Figure 5.60 clearly indicates that there is a linear relationship between log TRC and t and the decay rates, given by the slopes of the plots, for all four concentrations are nearly the same for a given sample.

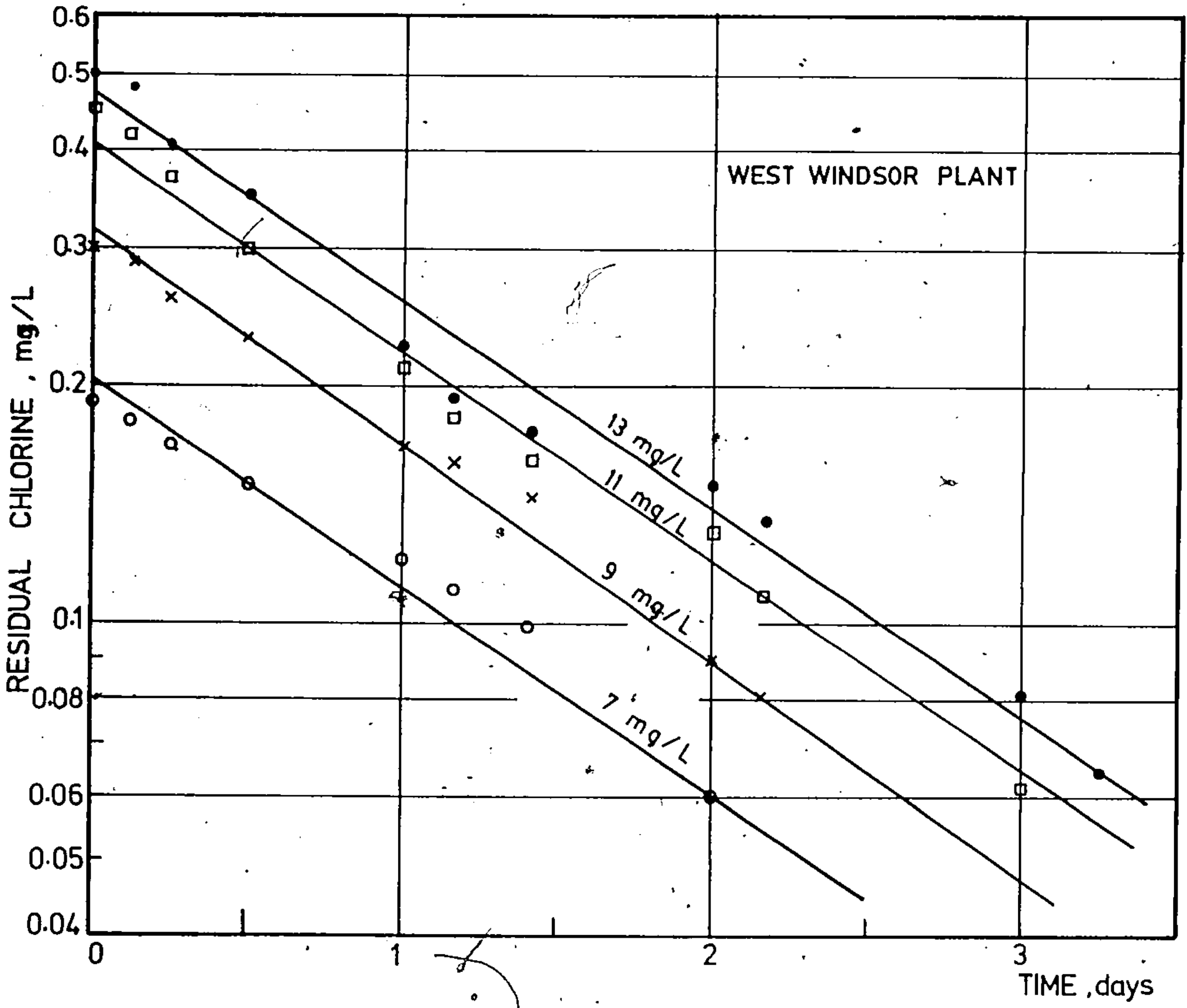

Fig. 5.60. Variation of residual chlorine with time under different chlorine doses.

This indicates that the decay rate of chlorine does not depend on the initial dose of chlorine.

5.2.2 Kinetics of Chlorine Decay

It was mentioned in Chapter II that several investigators have studied the factors affecting the decay of residual chlorine both in laboratory experiments and under field conditions, and have proposed different kinetic models to describe the decay process. (Katz 1977, Høstgaard-Jensen et al. 1977, Gowda 1978, 1979, Snodgrass 1980, Bobra and Mackay 1980, Haas and Karra 1984). In this investigation, it is hypothesized that the majority of the chlorine is in a monochloramine form, with its disappearance being controlled by first order kinetic model in the form shown by Eq. 5.70.

The model represented by Eq. 5.70 was evaluated by plotting the data from Figs. 4.37, 4.39, 4.41 and 4.42 on semi-log scales in Figs. 5.61, 5.62, 5.63 and 5.65. These figures show the relative remaining concentrations, C_t/C_o, plotted on logarithmic ordinates versus time, t, under the following experimental conditions:

A. Alternating exposure to 12 hours of light and 12 hours of darkness and complete darkness.

B. With and without stirring of samples with alternating light and dark exposure.

C. Varying surface area/volume under standard conditions, and

D. Varying temperature under standard conditions.

Linear regression analysis was used to analyze the data and obtain lines of best fit for each case.

A. In order to determine the TRC decay rate coefficient due to photolysis, k_{PH}, semi-log plots of the relative remaining concentrations versus time were drawn both for complete darkness and for alternating exposure to 12 hours of light and 12 hours of darkness, Fig. 5.61. An examination of the plots indicates that the rate coefficient under alternating light and dark exposure is slightly higher than that obtained for complete darkness. From the regression analysis, the estimated rate constants under complete darkness and with alternating light and dark exposure are 0.208 and 0.238 day^{-1} respectively, at a mean temperature of 20±1°C. Therefore, the rate constant due to photolysis, k_{PH}, is estimated to be equal to 0.03 day^{-1}.

The increase in rate coefficient can be attributed to the fact that the decay rate is catalyzed by ultraviolet light. This agrees with the studies conducted by Johnson (1975) and Høstgaard-Jensen, _et_ _al_. (1977) in which they reported higher removal rates under daytime conditions. Snoeyink and Markus (1974) measured the decay rates for free chlorine in nitrified secondary effluent at pH values of 8.2 to 8.5. Samples exposed to prevailing winds and daylight, and dosed with 3.12 mg/L chlorine, gave first

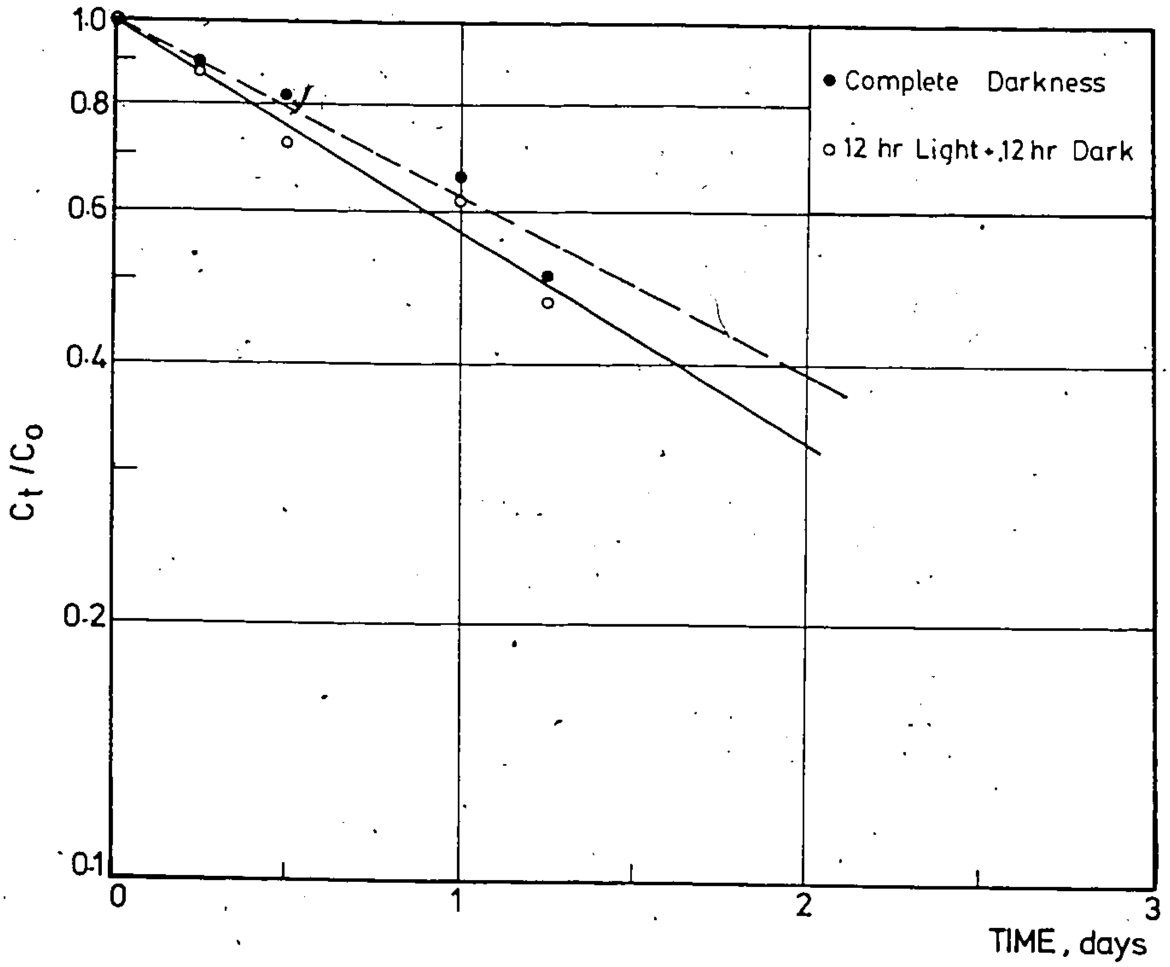

Fig. 5.61. Effect of exposure to light on C_t/C_o.

order decay rates from 2.1 to 7.4 hr^{-1} with half-lives of 8 to 28 min. For samples kept indoors, without stirring and exposure to ultraviolet light, first order decay constants in the range of 0.19 to 0.77 hr^{-1} were obtained.

Figure 4.38 shows the corresponding residual ammonia concentrations plotted against time. It is observed that the residual ammonia concentrations for any incubation period in complete darkness are significantly higher than those obtained for the same period under 12 hours of light and 12 hours of darkness exposure. However, the residual ammonia in both cases are observed to increase initially with the increase of time, up to 2 days, and then decrease with time. The reasons for this increase is not known and needs further investigation.

B. In practice, turbulence is present in streams and is expected to show a distinct effect on the decay rate coefficient. Therefore, in this phase of study, the effect of turbulence on the TRC decay rate of a sample exposed alternatively to light and darkness was investigated. Results of parallel runs, with and without stirring of samples, are plotted in Fig. 5.62 on semi-log scales. It can be observed that under quiescent conditions, the decay rate coefficient was 0.238 day^{-1}. When the stirrers were used, the decay rate coefficient had increased significantly to 0.487 day^{-1}. The increase in decay rate due to stirring can be attributed to

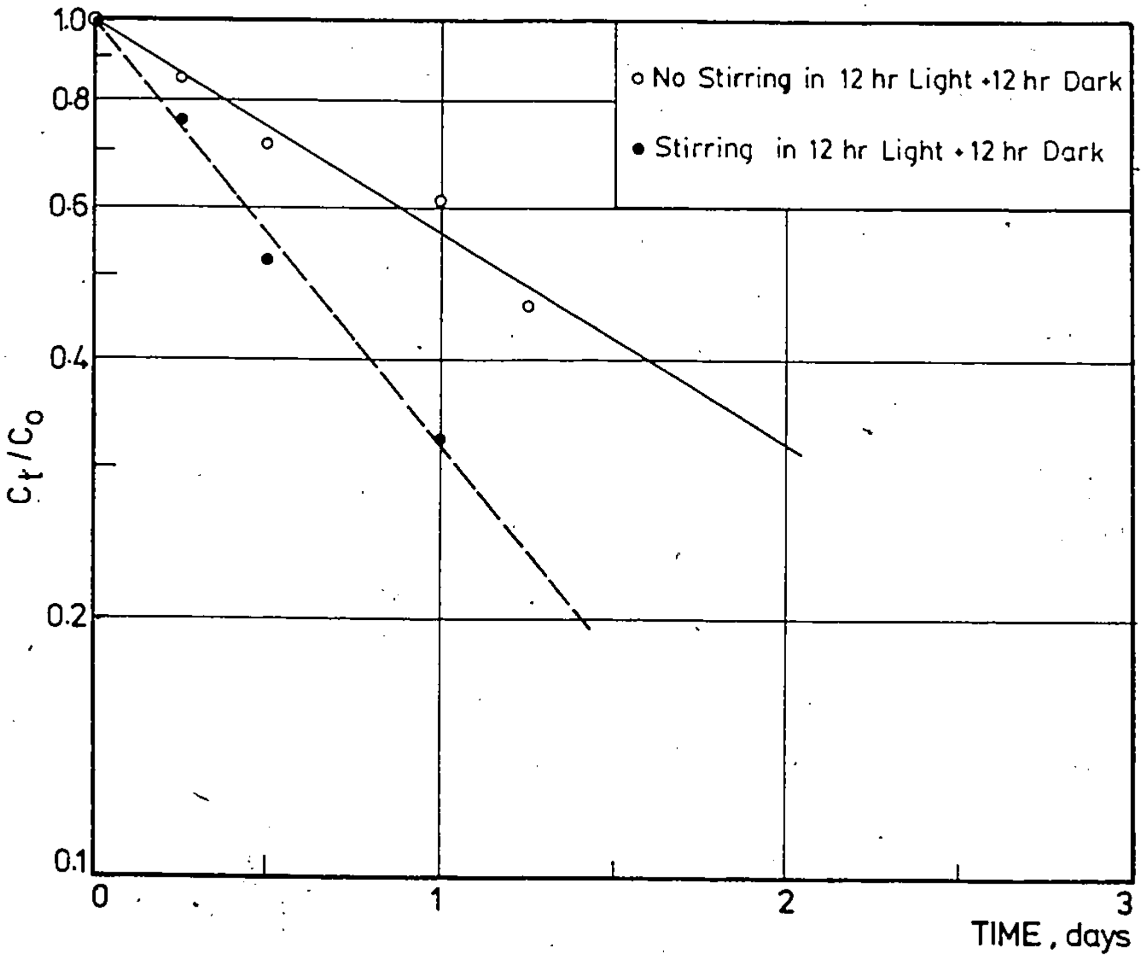

Fig. 5.62. Effect of Stirring on C_t/C_o.

to the removal of chlorine accumulated in the atmosphere above the liquid surface and possibly to some breakdown of the gas film at the interface. Therefore, it can be concluded that the TRC decay rate coefficient due to turbulence is approximately 2.05 times as fast as that under no stirring.

Figure 4.40 illustrates the results of runs with and without stirring the samples when exposed alternatively to 12 hours of light and 12 hours of darkness. It is observed that the residual ammonia concentrations obtained in stirred beakers are lower than those obtained in unstirred beakers. The higher decay rates attained when the stirrers are used can be attributed to the increased degassing via water-atmosphere exchange and the rapid renewal of the interface. This agrees with the findings of Wachs et al. (1972) and Weiler (1979) on the rate of ammonia loss from water to the atmosphere due to stirring.

C. In order to investigate the effect of evaporation or volatilization on TRC decay rate coefficient, different ratios of surface area to volume, $A_s/\forall$, ranging from 0.0035 mm^{-1} to 0.029 mm^{-1} were used. The TRC decay rate coefficient, $k_{A/\forall}$ for different $A_s/\forall$ values were determined from the semi-log plots of C_t/C_o versus time as shown in Fig. 5.63. A visual inspection of the plot indicates that the rate coefficient increases significantly as the $A_s/\forall$ ratio increases. The following regression equations were obtained for each case:

$$\log C_t/C_o = -0.116\,t \quad \text{for } A_s/\forall=0.0035 \text{ mm}^{-1} \tag{5.71}$$

$$\log C_t/C_o = -0.156\,t \quad \text{for } A_s/\forall=0.0069 \text{ mm}^{-1} \tag{5.72}$$

$$\log C_t/C_o = -0.196\,t \quad \text{for } A_s/\forall=0.011 \text{ mm}^{-1} \tag{5.73}$$

$$\log C_t/C_o = -0.324\,t \quad \text{for } A_s/\forall=0.021 \text{ mm}^{-1} \tag{5.74}$$

$$\log C_t/C_o = -0.434\,t \quad \text{for } A_s/\forall=0.029 \text{ mm}^{-1} \tag{5.75}$$

In natural streams, $A_s/\forall$ is approximately equal to $\frac{1}{H}$ where H is the depth of flow. Since the rate constant, $k_{A/\forall}$, is expected to vary inversely proportional to the depth of flow, therefore, the k values are plotted against $\frac{1}{H}$ in Fig. 5.64. The line of best fit can be represented by the following equation:

$$k = k_{OX} + k_{OL}\left(\frac{1}{H}\right) \tag{5.76}$$

where

k_{OX} = rate coefficient for free radical oxidation, day^{-1}

k_{OL} = mass transfer rate for evaporation, m day^{-1}.

This plot shows that the rate coefficient is made up of two components - k_{OX}, the decay rate corresponding to infinite depth and k_{EV}, the decay rate due to evaporation. k_{OX} is assumed to be the rate coefficient for free radical

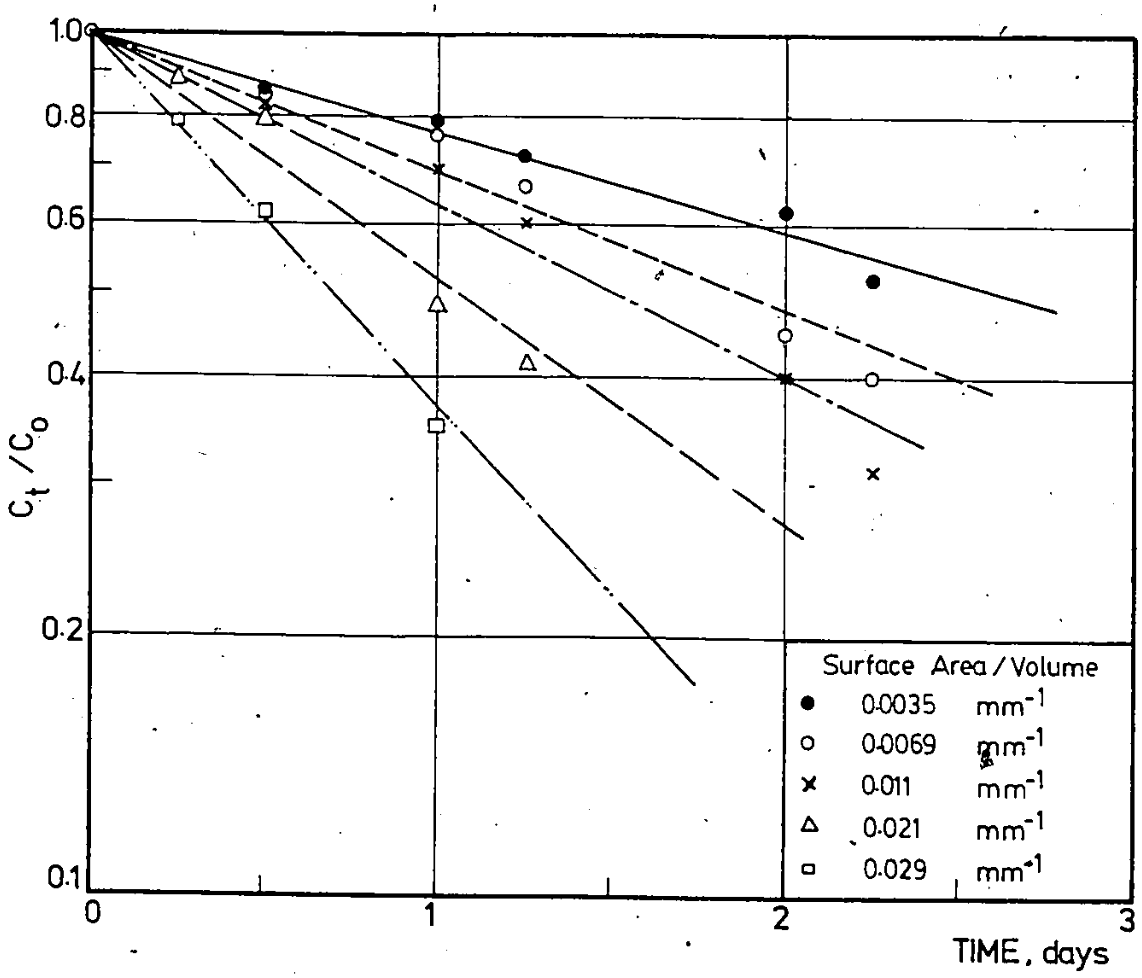

Fig. 5.63. Effect of varying A_s/V on C_t/C_o.

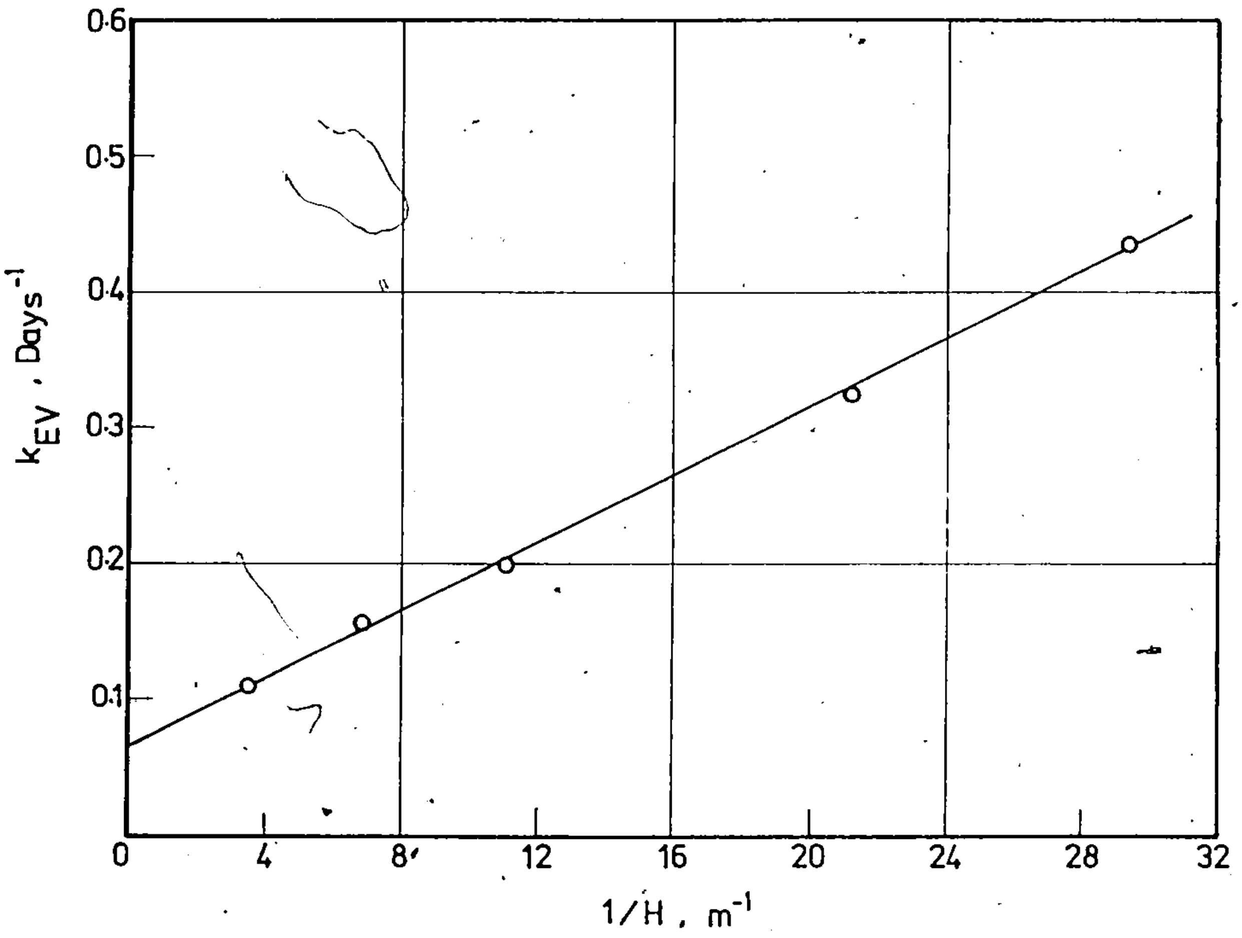

Fig. 5.64. Variation of the rate coefficient, k, with 1/H.

oxidation and k_{EV} is equal to k_{OL}/H where k_{OL} is the mass transfer rate for evaporation.

D. The temperature at which any reaction occurs has a significant influence on the rate of reaction. The effect of temperature on TRC decay rate coefficient was determined from semi-log plots, Fig. 5.65, of C_t/C_o versus t at different temperatures. The line of best fit at each temperature was determined statistically and the following regression equations were obtained:

$$\log C_t/C_o = -0.092\ t \quad \text{at } 2\pm1°C \tag{5.77}$$

$$\log C_t/C_o = -0.222\ t \quad \text{at } 11\pm1°C \tag{5.78}$$

$$\log C_t/C_o = -0.390\ t \quad \text{at } 20\pm1°C \tag{5.79}$$

$$\log C_t/C_o = -0.816\ t \quad \text{at } 30\pm1°C \tag{5.80}$$

All test conditions including the depths of samples were constant during the four experiments. Therefore, the following ratios of the rate coefficients at temperatures T and 20°C, k_T/k_{20}, calculated from the above regression equations indicate the influence of temperature on rate constant

$$k_2/k_{20} = 0.235 \tag{5.81}$$

$$k_{11}/k_{20} = 0.57 \tag{5.82}$$

$$k_{30}/k_{20} = 2.09 \tag{5.83}$$

The following expression based on the van't Hoff-Arrhenius relationship (Fair and Geyer 1958) has been used to correlate the effect of temperature on k:

$$k_T = k_{20}\ \theta_1^{(T-20)} \qquad (2.62)$$

in which

k_T = the rate coefficient at temperature T,
k_{20} = the rate coefficient at 20°C,
θ_1 = the temperature correction factor.

The above values of k_T/k_{20} are plotted versus (T-20) in Fig. 5.66. The line of best fit was obtained statistically for the regression of k_T/k_{20} on T and the temperature correction factor, θ_1, was found to be 1.08. This value agrees well with Gowda's study (1979a,b). He observed first order decay rates of 0.0052 and 0.012 per minute during the summer at mean temperature of 18°C, and 0.0095 and 0.0029 per minute during the winter at mean temperature of 5.5°C in two successive reaches of Aurora Creek. His data are consistent with the van't Hoff-Arrhenius Eq. 2.62 with θ_1 = 1.08. However, Snodgrass (1980) reported that the temperature correction factor with respect to 20°C for chlorine to be 1.009.

5.2.3 Overall Decay Model for TRC

Bokra and Mackay (1980) had investigated the degradation characteristics of certain chemicals. They proposed that the important parameters influencing decay of these

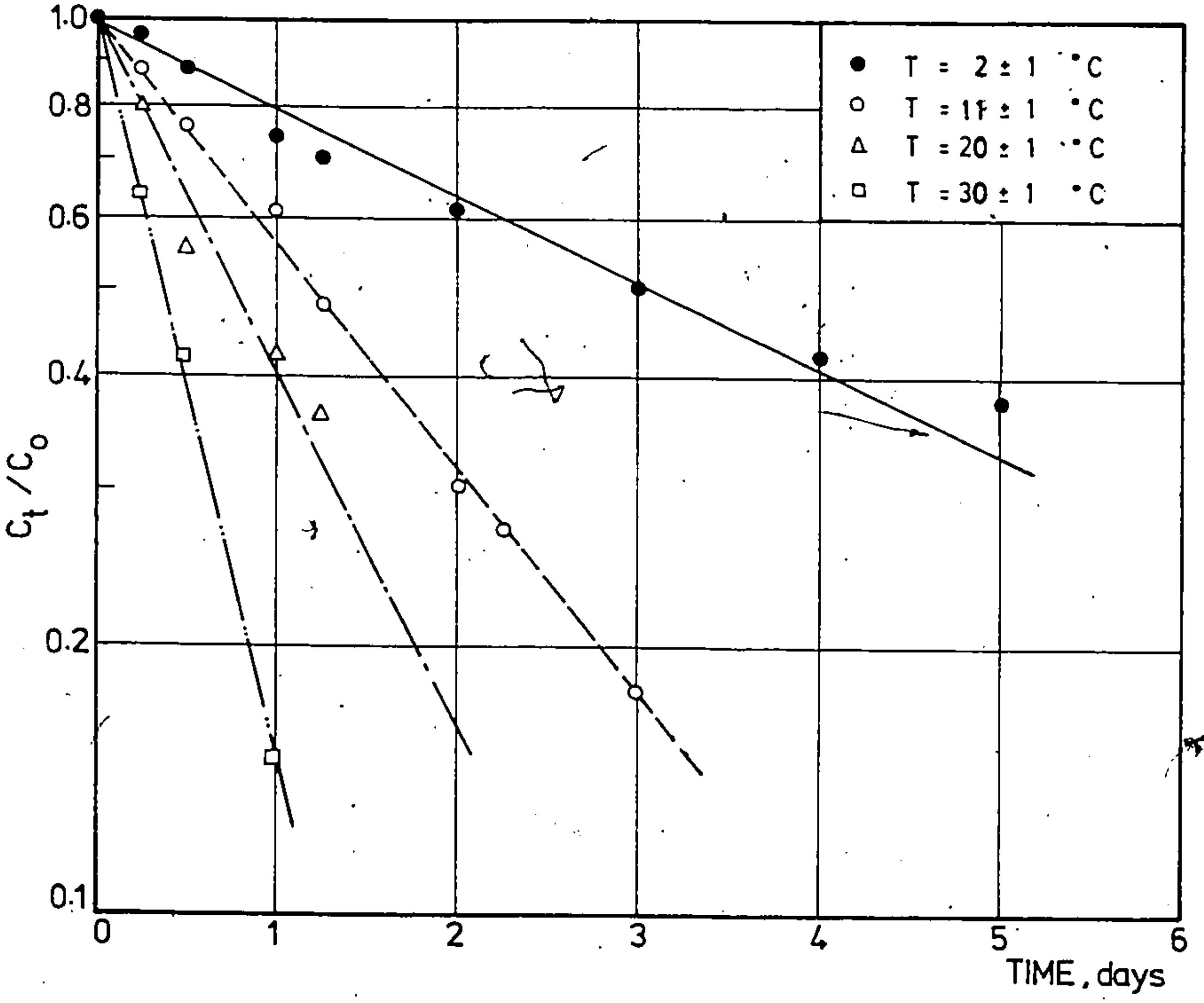

Fig. 5.65. Temperature effect on C_t/C_o.

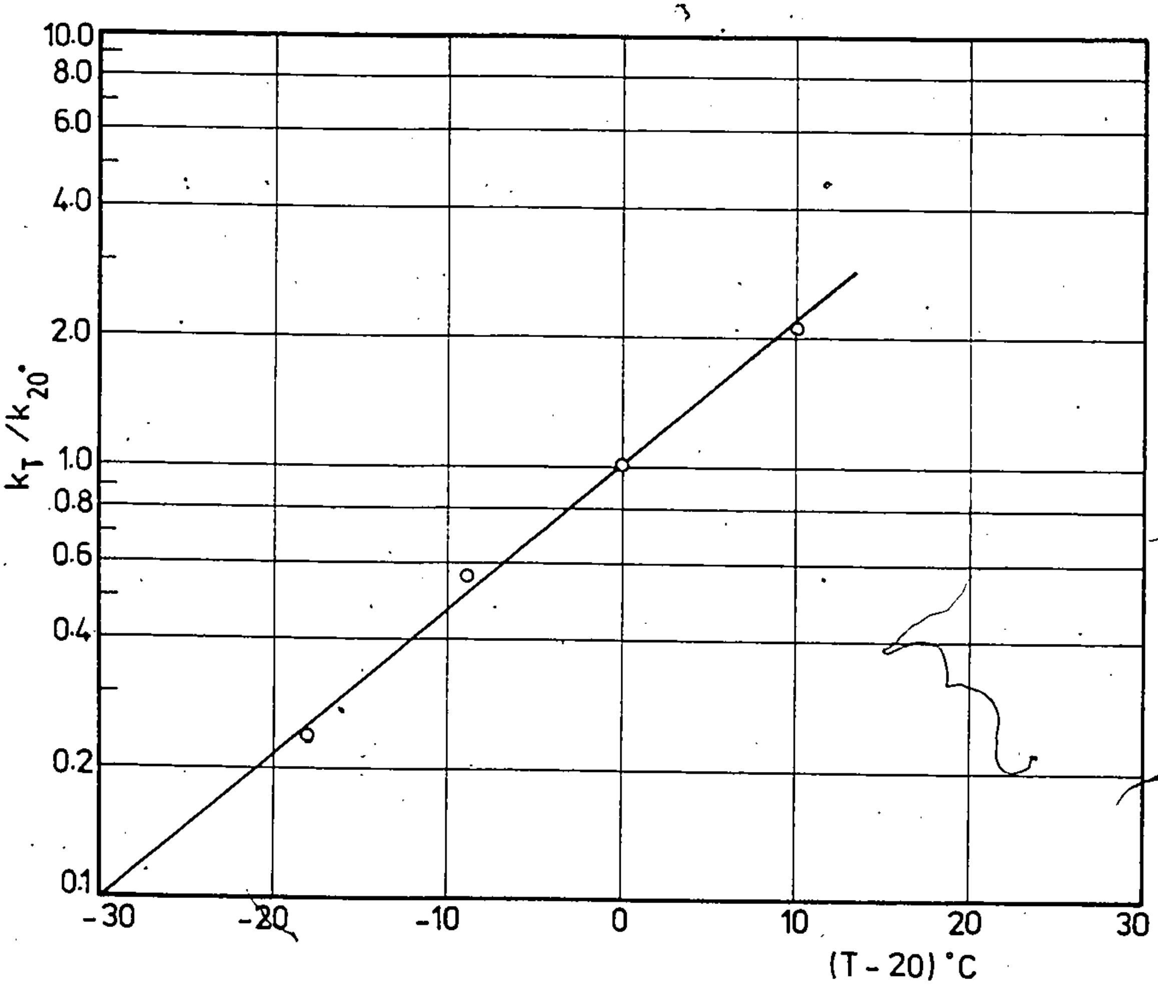

Fig. 5.66. Effect of temperature on k_T/k_{20}.

chemicals, after mixing in the streams, are volatilization (evaporation), biodegradation, photolysis, free radical oxidation and hydrolysis. They assumed that all these processes proceed independently and the overall decay rate is given by:

$$k_T = k_{EV} + k_{BD} + k_{PH} + k_{OX} + k_{HY} \qquad (2.63)$$

where,

k_{EV} = rate coefficient for evaporation = k_{OL}/H
k_{OL} = mass transfer rate for evaporation
k_{BD} = rate coefficient for biodegradation
k_{PH} = rate coefficient for photolysis
k_{OX} = rate coefficient for free radical oxidation
k_{HY} = rate coefficient for hydrolysis

However Bobra and Mackay (1980) had neglected the effect of turbulence on the overall decay rate. Undoubtedly, the degradation process is significantly influenced by the turbulence in the streams. This effect has been shown in Fig. 5.62. Therefore, Eq. 2.63 is modified to include the turbulence factor, F_{TB}; as well as the temperature correction factor, θ_1, and can be written as follows:

$$k_T = F_{TB}[k_{EV} + k_{BD} + k_{PH} + k_{OX} + k_{HY}]\theta_1^{T-20} \qquad (5.84)$$

For chlorine, the overall decay rate, k_T, depends in general on turbulence, evaporation, photolysis, oxidation and temperature (Snoeyink and Markus 1974). Therefore Eq. 5.84 can be written as

$$k_T = F_{TB}[k_{EV}+k_{PH}+k_{OX}]\theta_1^{T-20} \tag{5.85}$$

This study has shown the following values for various rate constants:

F_{TB} = 2.05 for stirred conditions
= 1.00 for quiescent conditions
k_{OL} = 0.013 m day^{-1}
k_{EV} = 0.013/H day^{-1}
k_{PH} = 0.03 day^{-1}
k_{OX} = 0.065 day^{-1}
θ_1 = 1.08

The observed and computed overall decay rates under different conditions of operation in this study together with their deviation are presented in Table 5.11. It is clear that the deviations between observed and computed rate constants range from -6.2 to +5.5, except for one run conducted at a temperature of 11±1°C, when substantially higher deviation of 19.4 was obtained. This may be a result of an error of taking the temperature reading which sometimes fluctuated considerably.

Table 5.11

Comparison Between Measured and Calculated Decay Rates

Condition				Measured k_T, day^{-1}	Calculated k_T, day^{-1}	Deviation %
Photolysis	Turbulence	Depth m	Temperature °C			
NP	NP	0.085	20	0.208	0.218	-4.6
P	NP	0.085	20	0.238	0.248	-4.0
P	P	0.085	20	0.487	0.508	-4.1
NP	NP	0.288	20	0.116	0.110	5.5
NP	NP	0.145	20	0.156	0.155	0.6
NP	NP	0.090	20	0.196	0.209	-6.2
NP	NP	0.047	20	0.324	0.340	-4.7
NP	NP	0.034	20	0.434	0.447	-2.9
P	NP	0.047	2	0.092	0.093	-1.1
P	NP	0.047	11	0.222	0.186	19.4
P	NP	0.047	20	0.390	0.372	4.8
P	NP	0.047	30	0.816	0.803	1.6

P = Present

NP = Not present

5.2.4 Effect of Chlorine on BOD Progression

Reduction in BOD of effluent on chlorination depends on the concentration of chlorine employed. With the proper application of chlorine, the desired dissolved oxygen levels of the receiving water can be maintained (White 1972). The BOD test determines the dissolved oxygen required to oxidize the decomposable matter when discharged into the streams. Since chlorine is a strong oxidizing agent, it rapidly reacts with the decomposable organic matter present in the wastewater and reduces its concentration. Therefore, effluent BOD has been considered to be an important factor controlling the chlorine dose necessary to obtain satisfactory disinfection.

The effect of varying the chlorine dose on BOD progression was evaluated by subjecting the same final effluent sample to different amounts of chlorine. The progression curves are shown in Figs. 4.43 and 4.44 for both West Windsor and Little River Pollution Control Plants, respectively. Both figures clearly indicate that the BOD values for any incubation period decrease with an increase in chlorine dose. In Fig. 4.43 for West Windsor Plant, the carbonaceous oxygen demand for the zero chlorine curve follows the first order reaction and the second stage of nitrification is observed to begin after seven days of incubation. The other two curves, for 5 and 10 mg/L chlorine doses, show a significant suppression of BOD kinetics, i.e., rate constant, 5-day BOD and ultimate BOD. The second stage is observed to develop after nine days of incubation. The BOD values are lower in both cases because chlorine had oxidized the organic matter and retarded the activity of micro-organisms. Also, chlorine, when added to the effluent sample, reacted with ammonia to form chloramines. This reaction could have delayed the start of nitrification stage. Figure 4.44 for Little River Plant shows a similar trend for the effect of chlorine dose on BOD progression. Similar observations on the effect of chlorine dose have been reported by Lee and Fung (1979).

Therefore, it can be concluded that addition of chlorine causes suppression of rate constant and ultimate values for both carbonaceous and nitrogenous oxygen demands. The start of nitrification phase is dependent on waste characteristics, particularly with respect to the number and stage of growth of nitrifying flora present at the time of adding chlorine and the extent of reaction between chlorine and ammonia.

After having established the effect of chlorine dose on BOD progression under standard conditions, the impact of the following factors on BOD progression in chlorinated effluents is discussed.

- Light

- Stirring the BOD contents
- Nitrification suppression.

5.2.4.1 Effect of Light on BOD Progression

Based on the information available in the literature, light is considered to have significant effects on BOD progression (Varma et al. 1963, Ali, 1972). Varma, et al. (1963) investigated the effect of algae on the BOD determination for synthetic sewage samples containing algae, incubated alternatively for 12 hours in darkness and 12 hours in light. These observations were compared with continuous incubation in darkness and they noticed lower BOD values obtained by light and dark technique. The alternating light and dark technique assumes that the biological reactions in BOD bottles proceed in a manner similar to the BOD progression in natural streams.

Figures 4.45 and 4.46 illustrate the results obtained in this study for runs with the light and dark technique. It is observed that generally lower BOD values were obtained with 12 hours of light and 12 hours of darkness exposure than those obtained by the standard method in which BOD bottles were incubated all the time in dark. This effect is more pronounced in chlorinated samples as compared to unchlorinated samples.

5.2.4.2 Effect of Stirring

Ali (1972a,b) criticized the light and dark technique without imparting turbulence in the BOD bottles as the lack of turbulence means major deviation from stream conditions. The turbulence in streams and treatment plants is expected to result in different effect on the rate of oxygen utilization for biochemical reaction as compared to the quiescent conditions maintained in BOD bottles under standard method. Consequently, in this phase of study, turbulence was introduced in BOD bottles by stirring their contents.

Irrespective of the source of sample and chlorine dose, the six sets of experiments in Figs. 4.47 and 4.48 show that the BOD values obtained in stirred bottles were significantly higher than those obtained in unstirred bottles. It is believed that the growth of algae is faster in the stirred bottles and it yields more organic load to be stabilized by bacteria. Ali (1972) had conducted extensive BOD progression studies on wastewater samples collected from raw sewage, primary settled sewage and final effluent. He concluded that significant increases in BOD values were obtained for all types of samples when the contents of BOD bottles were stirred continuously.

The average increase in 5-day BOD due to stirring with zero chlorine dose was 21% for final effluent collected from West Windsor Plant, Fig. 4.47 and 40% for

Little River Plant, Fig. 4.48. Ali (1972a,b) had arrived at a similar conclusion from his studies when he observed an average increase of 44% in BOD values for unchlorinated final effluent from the Little River Plant. For West Windsor Plant, significant increases in 5-day BOD values were noticed with 5 and 10 mg/L chlorine doses. It can be seen from Fig. 4.47 that the 5-day BOD due to stirring is approximately 3.5 times of that with no stirring. For the Little River Plant, an average increase of 60% was obtained with 5 mg/L chlorine dose, Fig. 4.48.

5.2.4.3 Effect of Chlorination With and Without Nitrification Suppression

Tests on final effluent from activated sludge treatment were conducted after suppressing nitrification by pasteurization. The typical BOD progressions with and without pasteurization are plotted in Figs. 4.49 and 4.50 under standard dark condition and in alternating incubation for 12 hours in light and for 12 hours in dark, respectively. Both figures show lower BOD values when the incubated samples were pasteurized. For zero chlorine, an average decrease of 34% in 5-day BOD was noticed under standard condition. For alternating light and dark exposure, the corresponding decrease was 22%. When 5 mg/L chlorine was added to the samples, pasteurization also yielded lower

5-day BOD values under both standard and alternating incubation conditions.

The progressive exertion of the BOD of freshly polluted water normally breaks down into two stages: a first stage in which the carbonaceous material is largely oxidized and a second stage in which significant amount of nitrification takes place as shown in Figs. 4.43 and 4.44. The first stage has generally been interpreted as a first-order reaction, dependent on the concentration of oxidizable organic material present, but independent of the oxygen concentration. The resulting first-order equation can be written in the form of:

$$y = L_a(1-10^{-k_1 t}) \qquad (5.86)$$

where

L_a = ultimate oxygen demand due to carbonaceous matter in mg/L

k_1 = rate coefficient of BOD removal in day^{-1}

and t = time in days.

Practical evaluation of Equation 5.86 is usually unknown. A number of methods for finding the magnitudes of L_a and k_1 from a series of observations of y and t have been proposed. The "Graphical Method" developed by Lee (1954) was adopted to analyze the data obtained in this study.

The values of k_1, L_a and 5-day BOD for final effluent samples from both plants, with different chlorine doses, are tabulated in Tables 5.12 and 5.13. Regardless of the source of the sample, it is found that the ultimate oxygen demand and 5-day BOD values show significant decrease as the chlorine dose increases. Likewise, k_1 values decrease as the chlorine dose is increased but this decrease in k_1 values is not significant. It can be seen from both these Tables that alternating light and dark exposures resulted in decrease in L_a and 5-day BOD. When the incubated samples are stirred continuously, both L_a and 5-day BOD values show an appreciable increase in all samples that have been dosed with different amount of chlorine. Also, L_a and 5-day BOD show a significant decrease due to pasteurization but k_1 values are not affected significantly. A decrease of 34% and 22% in 5-day BOD due to pasteurization is observed under standard condition and alternating exposure to light and darkness, respectively. It should be noted that some k_1 values are unreliable since their BOD progression curves did not obey the first order reaction. This had occurred when there was a relatively high residual chlorine in diluted sample.

Table 5.12

BOD Kinetic Values for Final Effluent from West Windsor Plant Under Various Chlorine Doses

Chlorine Dose mg/L	Conditions	k_1 day^{-1}	L_a mg/L	5-day BOD mg/L
0	standard condition	0.20	18.5	16.6
5	standard condition	0.19	3.2	2.9
10	standard condition	0.18	1.7	1.5
0	standard condition	0.20	22.3	18.0
	12 hr. light + 12 hr. dark	0.25	20.2	19.1
5	standard condition	0.19	5.5	4.6
	12 hr. light + 12 hr. dark	0.16	2.9	2.6
10	standard condition	0.16	3.7	2.8
	12 hr. light + 12 hr. dark	0.09	2.2	1.4
0	stirred in 12 hr. light + 12 hr. dark	0.28	24.4	23.0
	unstirred in 12 hr. light + 12 hr. dark	0.25	20.2	19.1
5	stirred in 12 hr light + 12 hr. dark	0.21	12.2	10.2
	unstirred in 12 hr. light + 12 hr. dark	0.16	2.9	2.6
10	stirred in 12 hr. light + 12 hr. dark	0.05	11.6	4.7
	unstirred in 12 hr. light + 12 hr. dark	0.09	2.2	1.4

Table 5.13

BOD Kinetic Values for Final Effluent from Little River Plant Under Various Chlorine Doses

Chlorine Dose mg/L	Conditions	k_1 day^{-1}	L_a mg/L	5-day BOD mg/L
0	standard condition	0.08	17.5	10.8
2	standard condition	0.06	9.3	3.2
5	standard condition	0.05	4.6	2.0
0	standard condition	0.08	19.1	11.5
	12 hr. light + 12 hr. dark	0.14	11.5	9.25
5	standard condition	0.05	4.0	1.8
	12 hr. light + 12 hr. dark	0.06	2.8	1.5
0	stirred in 12 hr. light + 12 hr. dark	0.14	16.5	13.0
	unstirred in 12 hr. light + 12 hr. dark	0.14	11.5	9.3
5	stirred in 12 hr. light + 12 hr. dark	0.04	9.4	3.2
	unstirred in 12 hr. light + 12 hr. dark	0.12	2.7	2.0
8	stirred in 12 hr. light + 12 hr. dark	0.05	4.3	2.0
	unstirred in 12 hr. light + 12 hr. dark	-	-	-
0	Unpasteurized in standard condition	0.08	19.1	11.5
	Pasteurized in standard condition	0.08	12.4	7.5
0	Unpasteurized in 12 hr. + 12 hr.	0.14	11.5	9.25
	Pasteurized in 12 hr. + 12 hr.	0.08	10.0	7.2

CHAPTER VI

COMPARISON OF THE EXPERIMENTAL RESULTS AND THE PREDICTIONS OF NEAR-FIELD MODELS

6.1 GENERAL

A buoyant surface jet arises from a combined source of momentum and buoyancy injected at the free surface of the receiving water body. Since the buoyant force acts normal to the free surface, complicated distortions of the cross-sectional jet geometry take place. This fact, together with the buoyant damping of the jet turbulence has prevented the development of relatively simple analytical solutions to the problem (Jirka et al. 1981). The presence of shallow receiving water near the discharge point and of ambient cross-flows further complicate the physical situation.

Among the three-dimensional surface jet models used in this study are those by Stolzenbach and Harleman (1971) known as MIT model and Shirazi and Davis (1974) known as PDS model. Both have shortcomings and limitations and more important there are the unknown coefficients which must be experimentally determined. These two models were chosen because of their availability and relatively simple input requirements. In this chapter, an attempt is made to determine the model coefficients for the study case of a trapezoidal channel and to test the validity of both models.

6.2 THE PDS MODEL

6.2.1 Background

The PDS model contains a number of free variables such as the entrainment coefficient, E_o, the turbulent exchange coefficients, E_H and E_V, the drag coefficient, C_D, the shear coefficient, C_f, and the spreading function coefficient, xk_1. Shirazi and Davis (1974) used the experimental results reported in literature to determine these coefficients and they used a different set of data for each coefficient.

To determine the effect of ambient turbulence on jet behaviour, Shirazi and Davis used the data set provided by Weil (1972) which has an initial densimetric Froude No., F_o=16, outfall aspect ratio (width to depth), A=2 and initial discharge angle, θ_o=0.0. They recommended the following values for the turbulent exchange coefficients:

- Dimensionless horizontal turbulent exchange coefficient, $E_H = \frac{D_y}{V_j H_o} = 0.02$
- Ratio of vertical to horizontal turbulent exchange coefficient, $E_V = \frac{D_z}{D_y} = 0.2$

- Spreading coefficient, xk_1 = 1.4

For the entrainment coefficient, E_o, the range of the data used were F_o=1.0 to 4.1, 1/R=0 to 0.01 and A=2 to 3.3. They recommended a value of 0.05 for E_o.

For the drag coefficient, C_D, the range of the experimental data were F_o=1.2 to 5.6, R=1.4 to 11.5 and A=0.5 to 3.1. They suggested a value of C_D=1.0.

In all the above, it was assumed that the interfacial shear coefficient, C_f=0.0 and the dimensionless surface heat exchange coefficient, $K_1=10^{-5}$.

6.2.2 Sensitivity Analysis of PDS Model

It is of considerable practical importance to study the sensitivity of PDS model to the above coefficients. Several computer runs were made using different values of these coefficients and the influence of parameter changes on the jet trajectory as well as the dilution curve were noted. Table 6.1 shows the variables included in the sensitivity analysis. In the following analysis, if one variable is being varied, all other parameters take on the base values shown in Table 6.1.

The effects of changing densimetric Froude No., F_o, velocity ratio, R, drag coefficient, C_D, spreading function coefficient, xk_1, entrainment coefficient, E_o, and horizontal turbulent exchange coefficient, E_H, on the jet trajec-

Table 6.1

Parameters in Sensitivity Analysis of PDS Model

Parameter	Value Suggested by Shirazi & Davis	Base Value	Range Studied
C_D	1.0	1.0	0.5-1.5
xk_1	1.4	1.4	1.0-2.0
E_0	0.05	0.05	0.02-0.08
E_H	0.02	0.02	0.01-0.04
F_0	-	12.9	2.0-100.0
R	-	5.2	1.5-20.0
A	-	1.0	0.5-4.0

tory are shown in Figs. 6.1 to 6.6, and the effects of the same parameters on the minimum dilution are shown in Figs. 6.7 to 6.12. The computer trials indicated that the densimetric Froude No., F_o, exhibits a significant impact on both jet trajectory and dilution as shown in Figs. 6.1 and 6.7. For a low value of F_o, the buoyancy spreading is high and the jet penetrates further into the channel. When F_o varies from 2.0 to 5.3, the jet penetration decreases by 48% at x/D=18, whereas an increase of F_o from 16.9 to 50.0 produces a decrease of only 16% at the same distance. For F_o=100.0, the jet trajectory is almost the same as for F_o=50.0, indicating that the buoyancy effect is negligible and the jet momentum is dominant. In fact, this case approaches the non-buoyant case where F_o is no longer a significant parameter.

Figure 6.2 shows that the velocity ratio, R, has also a significant effect on the jet trajectory. However, bank interference at a low ratio (R=1.5 and 2.0) may distort some of the model results. Shirazi and Davis indicated that the model is only valid for R≥1.5. Below this value, the edge of the jet contacts with the shoreline and the model cannot handle this complication.

The aspect ratio, A, (width to depth) was also found to have a significant effect on both the jet trajectory and the minimum dilution. Generally, F_o, R and A are well defined numbers based on specific discharge and outfall conditions.

The drag coefficient, C_D, as expected, affects the jet trajectory but has a very little effect on the dilution as shown in Figs. 6.3 and 6.9. An increase in C_D from 0.5 to 1.0 reduces the jet penetration by 10% at x/D=18 (Fig. 6.3) and reduces the dilution factor by 2% at the corresponding value ξ/D=27.5 (Fig. 6.9).

Figures 6.4 and 6.10 indicates that both the jet trajectory and the dilution are not sensitive to the spreading function coefficient, xk_1. The spreading coefficient relates the spreading due to buoyancy, dB/dξ, to the local excess density ratio and jet aspect ratio (Shirazi and Davis 1974) such that

$$\frac{dB}{d\xi} = \frac{xk_1}{(\frac{B}{h}F^2 - 1)^{1/2}} \qquad (6.1)$$

where F is the local densimetric Froude number. The value of xk_1 was set equal to 1.4 in this study as suggested by Shirazi and Davis.

In developing the PDS model, Shirazi and Davis assumed that the change of jet discharge with distance is due to contributions of the jet entrainment and ambient turbulent mixing. The coefficient of jet entrainment is

E_o, while the coefficient of entrainment due to ambient turbulent mixing is E_H. Therefore, it is expected that E_o and E_H have a similar effect on both the jet trajectory and the minimum dilution curve. Figures 6.5 and 6.11 show that an increase in E_o causes a decrease in jet penetration and an increase in the dilution factor as a result of more ambient fluid is being entrained by the jet. An increase in E_o from 0.02 to 0.08 decreases the jet penetration by 18% at $x/D=18$ and increases the dilution factor by 36% at the corresponding distance $\xi/D=27.5$ The same trend is observed for E_H as shown in Figs. 6.6 and 6.12. When E_H increases from 0.01 to 0.04, the jet penetration decreases by 23% at $x/D=18$ and the dilution factor increases by 47% at $\xi/D=27.5$.

From the sensitivity analysis, one can conclude that the jet trajectory is sensitive to E_o, E_H and C_D and insensitive to xk_1. Also the minimum dilution is sensitive to E_o and E_H but relatively insensitive to C_D and xk_1. Benedict and Preston (1980) studied the sensitivity of Prych, Davis, Shirazi (PDS) model. Their findings conclusively show that, E_H and to a lesser degree, E_v, are the most important parameters on the model predictions.

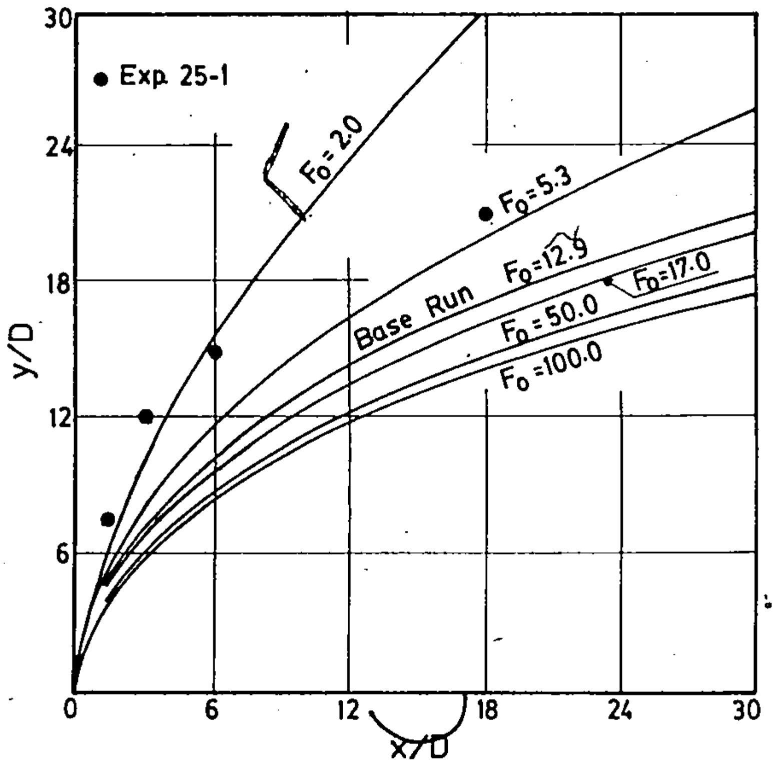

Fig. 6.1. Sensitivity of jet trajectory to Froude Number, PDS Model.

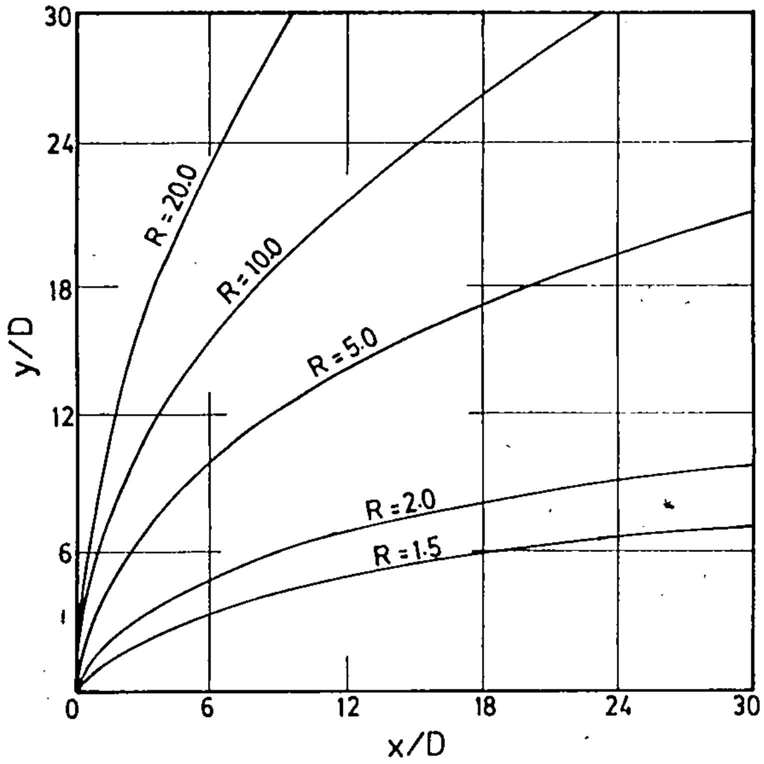

Fig. 6.2. Sensitivity of jet trajectory to velocity Ratio.

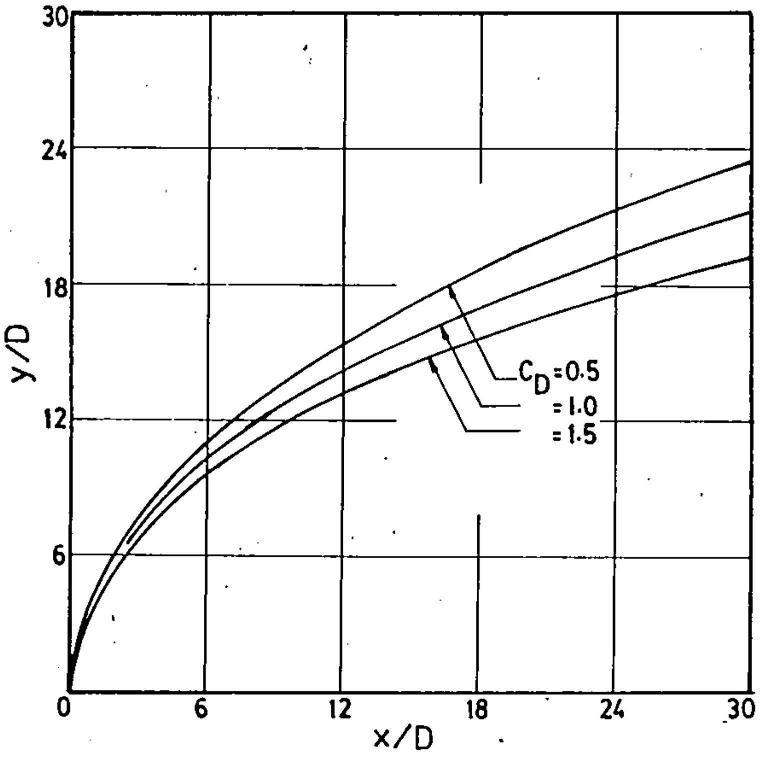

Fig. 6.3. Sensitivity of jet Trajectory to drag coefficient.

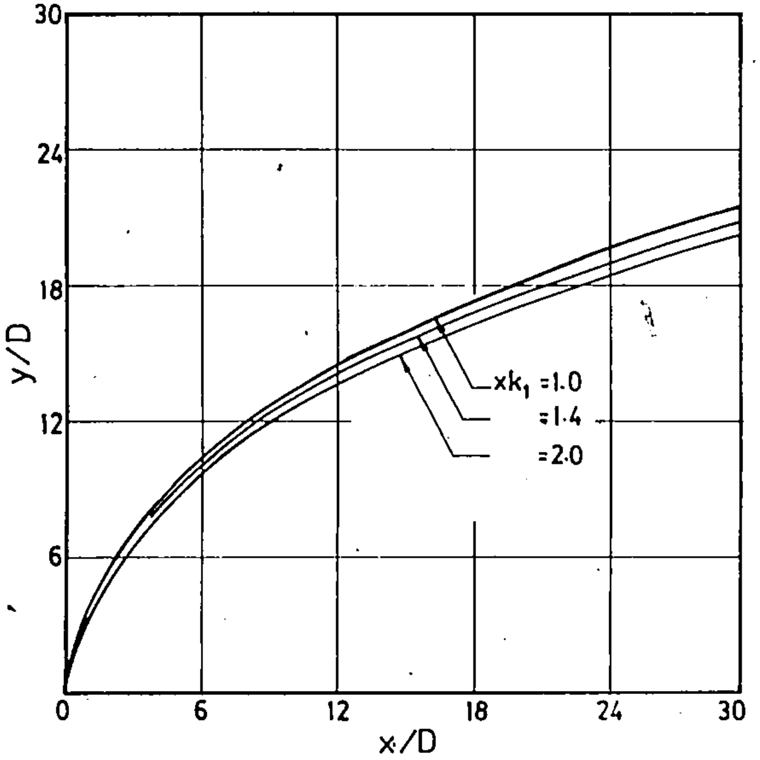

Fig. 6.4. Sensitivity of jet trajectory to spreading coefficient.

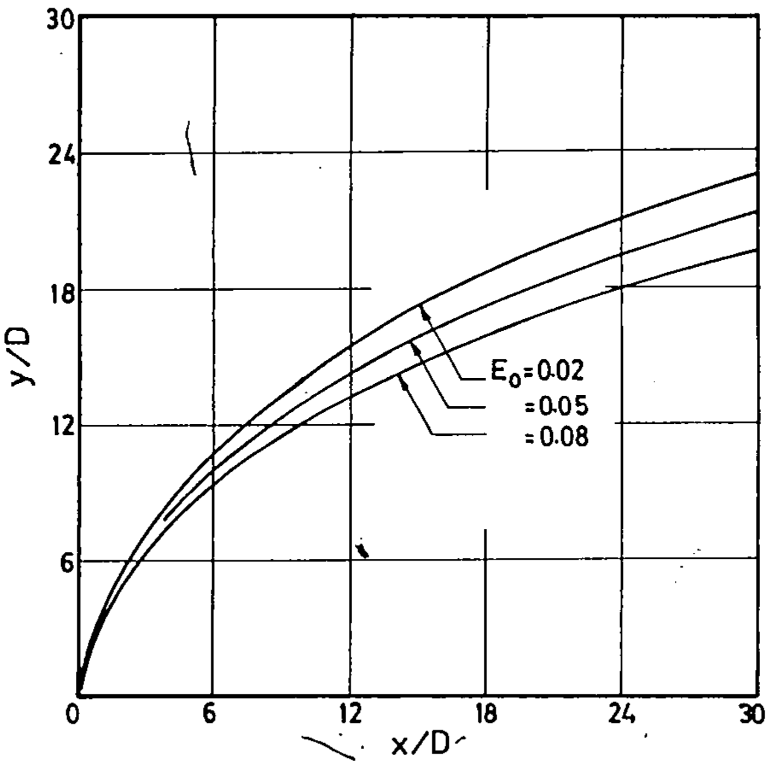

Fig. 6.5. Sensitivity of jet trajectory to entrainment coefficient.

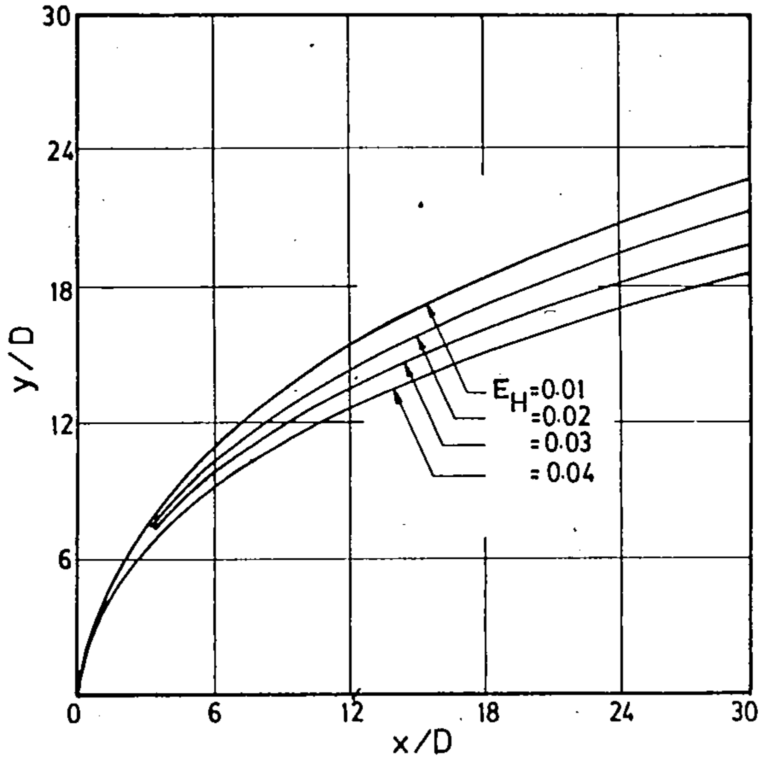

Fig. 6.6. Sensitivity of jet trajectory to horizontal turbulent coefficient.

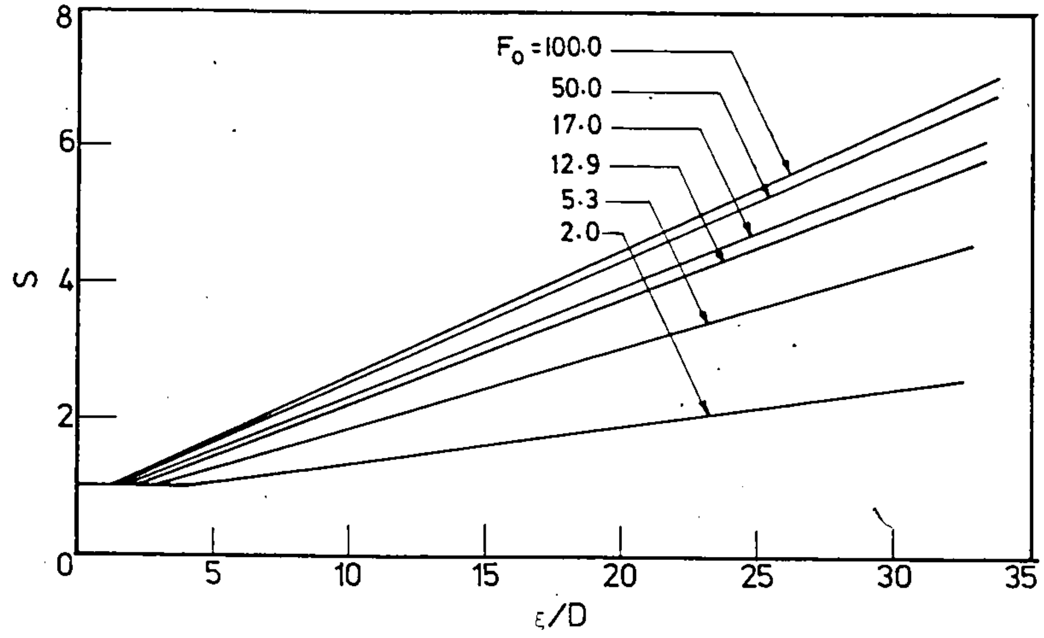

Fig. 6.7. Sensitivity of minimum dilution to Froude Number, PDS Model.

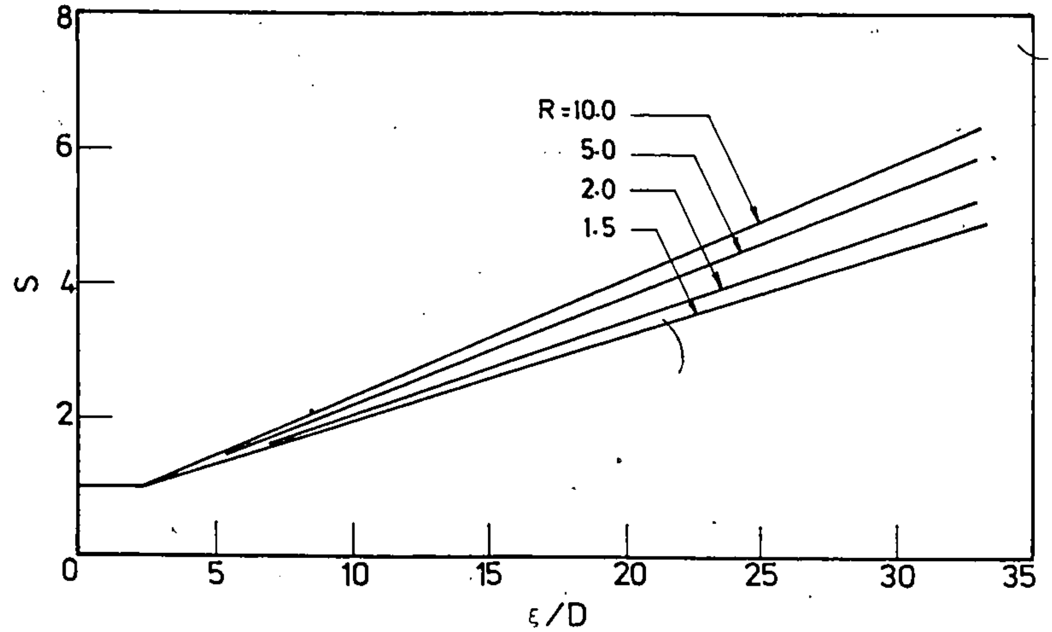

Fig. 6.8. Sensitivity of minimum dilution to velocity ratio.

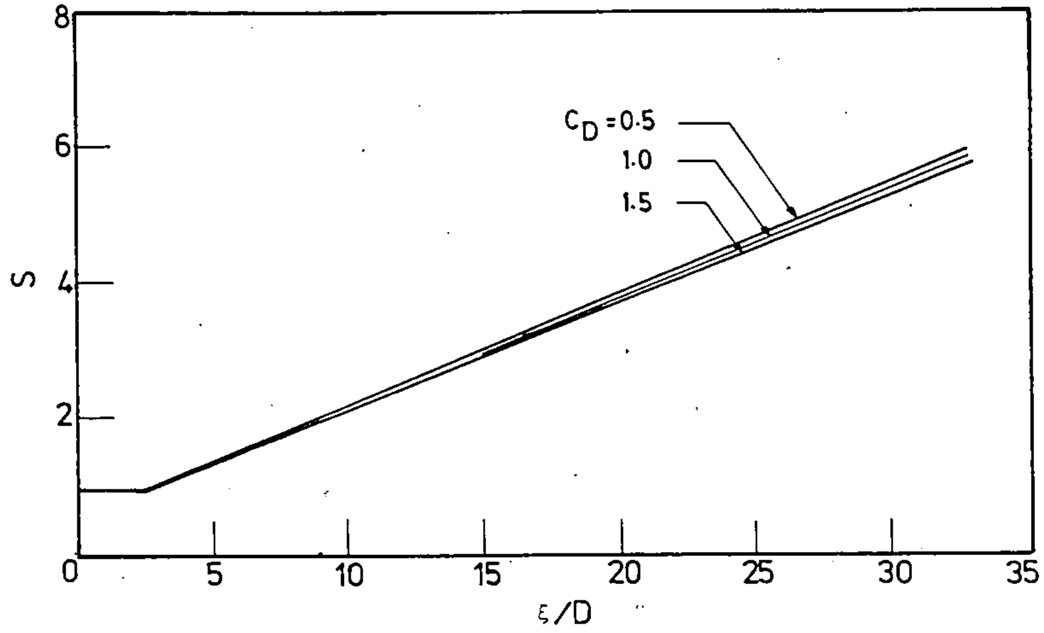

Fig. 6.9. Sensitivity of minimum dilution to drag coefficient.

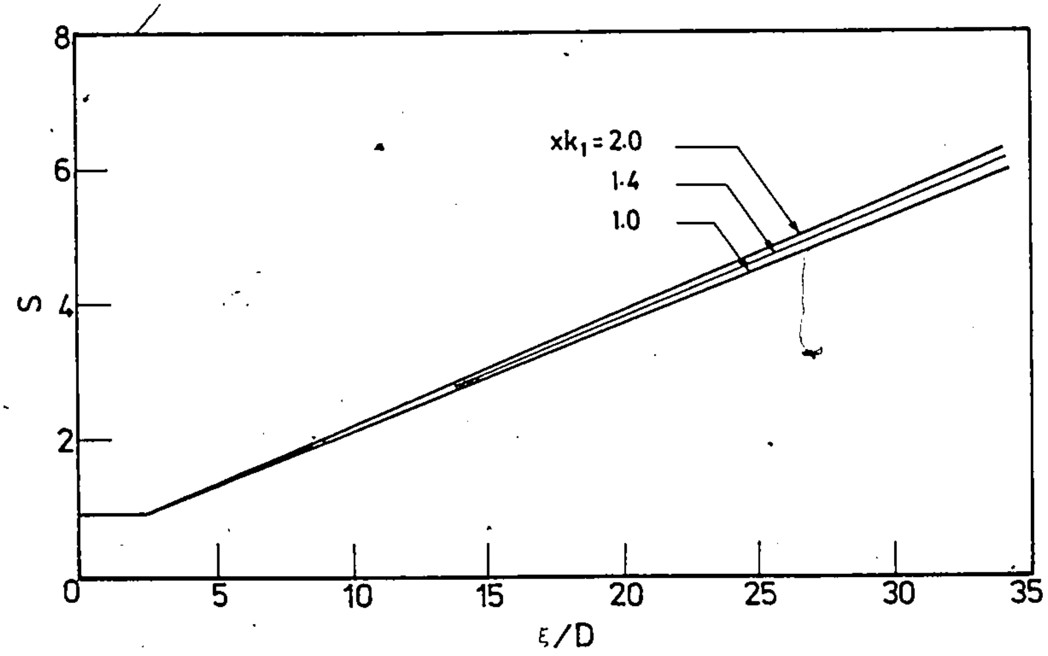

Fig. 6.10. Sensitivity of Minimum dilution to spreading coefficient.

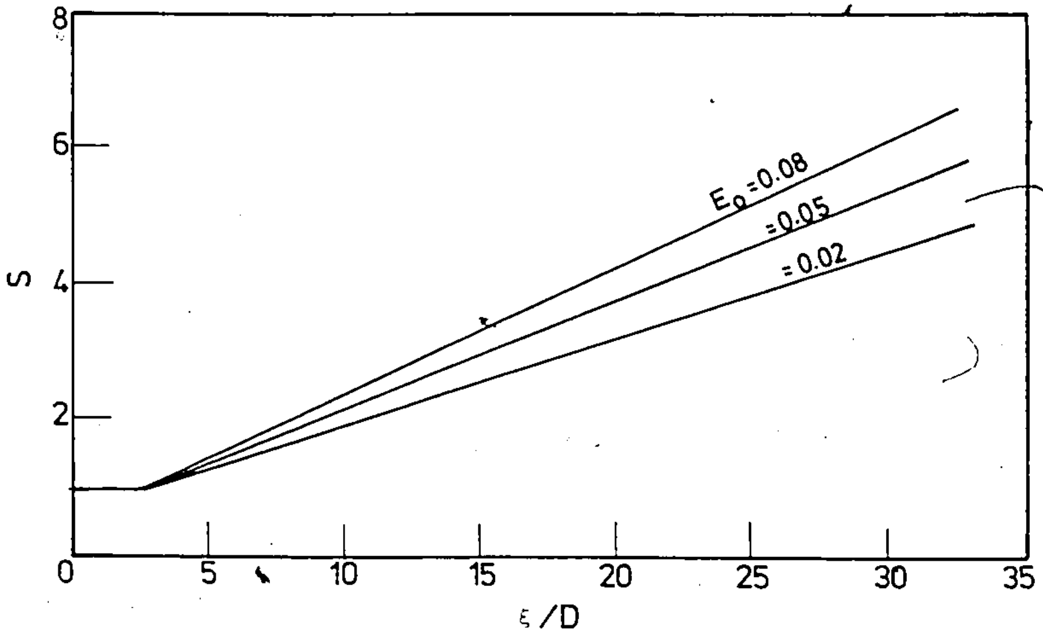

Fig. 6.11. Sensitivity of minimum dilution to entrainment coefficient.

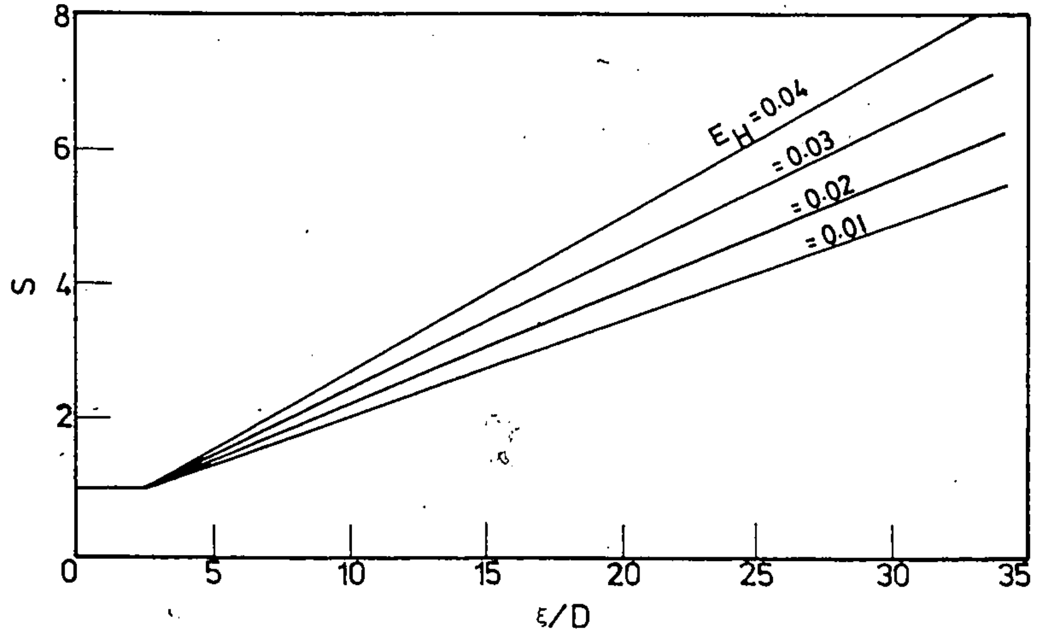

Fig. 6.12. Sensitivity of minimum dilution to horizontal turbulent coefficient.

6.2.3 Model Calibration

The suggested values of the PDS free coefficients given by Shirazi and Davis (1974) were based on specific experiments as pointed out in section 6.2.1. These coefficients are not universal and cannot be used outside the range they presented. In this section, an attempt was made to check and refine, if necessary, these coefficients using the experimental data of this study. The experimental Run 25-1 which has F_o=12.9 and R=5.2 was selected for the PDS calibration. In fact, the base values of F_o, R and A given in Table 6.1 are those of Run 25-1. The experimental Run 25-1 is compared in Fig. 6.1 with the base run. It is clear that there is a poor agreement between the measured and the predicted results as the PDS model is derived for a deep rectangular channel and does not take into account the sloping bank. The sloping bank interference at lower ambient velocities causes the disagreement. Since the experimental program of this study was performed in a trapezoidal flume, a slight change in the PDS program was made to allow for the velocity variation across the channel. The ambient velocity on the sloping side was obtained from the velocity measurements and the velocity ratio R was decreased from 8.3 on the sloping side to 5.2 on the main channel.

Taking the changes of velocity ratio into account and adjusting one or more of the model coefficients, better agreement between the experimental and predicted results was sought. Figures 6.13 and 6.14 are plots of the mean trajectory and dilution showing the comparison of the measured results with the predicted values due to changes in E_o. From Fig. 6.13, it appears that a good agreement with the measured jet trajectory is obtained with $E_o=0.05$, however, Fig. 6.14 indicates that the minimum dilution is best predicted with the value of $E_o=0.08$. The next step is to test these two values of E_o with different values of E_H. Figures 6.15 and 6.16 depict the effect of changing E_H on the mean trajectory for $E_o=0.05$ and 0.08, respectively, while the variations on the dilution curve are shown in Figs. 6.17 and 6.18. Examining these four figures, one can conclude that the best fit is obtained if $E_o=0.05$ while E_H varies from 0.03 on the side slope to 0.02 in the main channel. The value of E_o is the same value suggested by Shirazi and Davis (1974), while the value of E_H on the sloping side is 50% higher than the value recommended for the model. In fact, the value of $E_H=0.02$, reported by Shirazi and Davis is very low as indicated by Benedict and Preston (1980).

Since E_o and E_H are prespecified from the above analysis, only the drag coefficient, C_D, can be used to further adjust the trajectory. By using different values

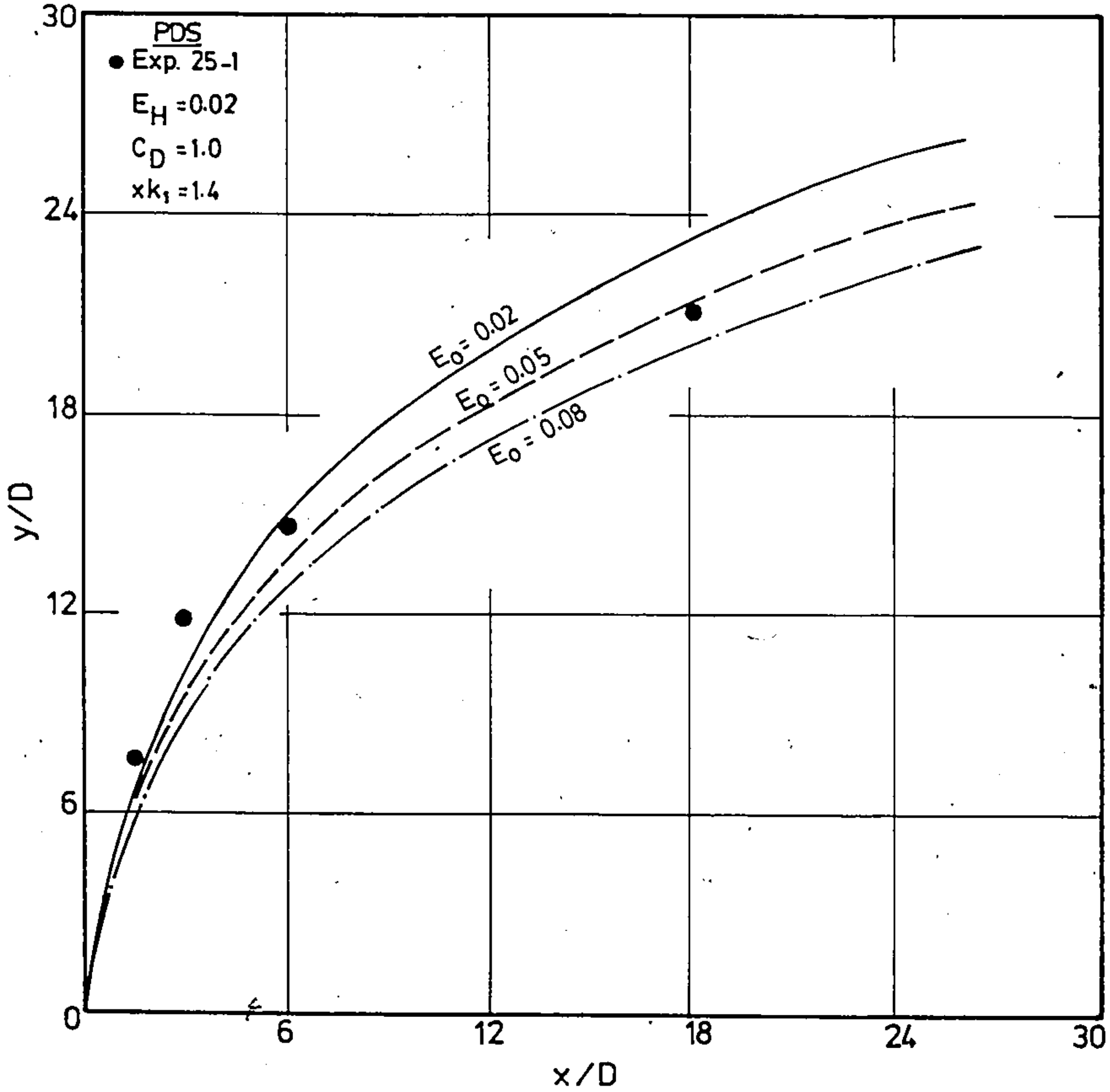

Fig. 6.13. Comparison of measured and predicted jet trajectories for different values of entrainment coefficient, Exp. 25-1.

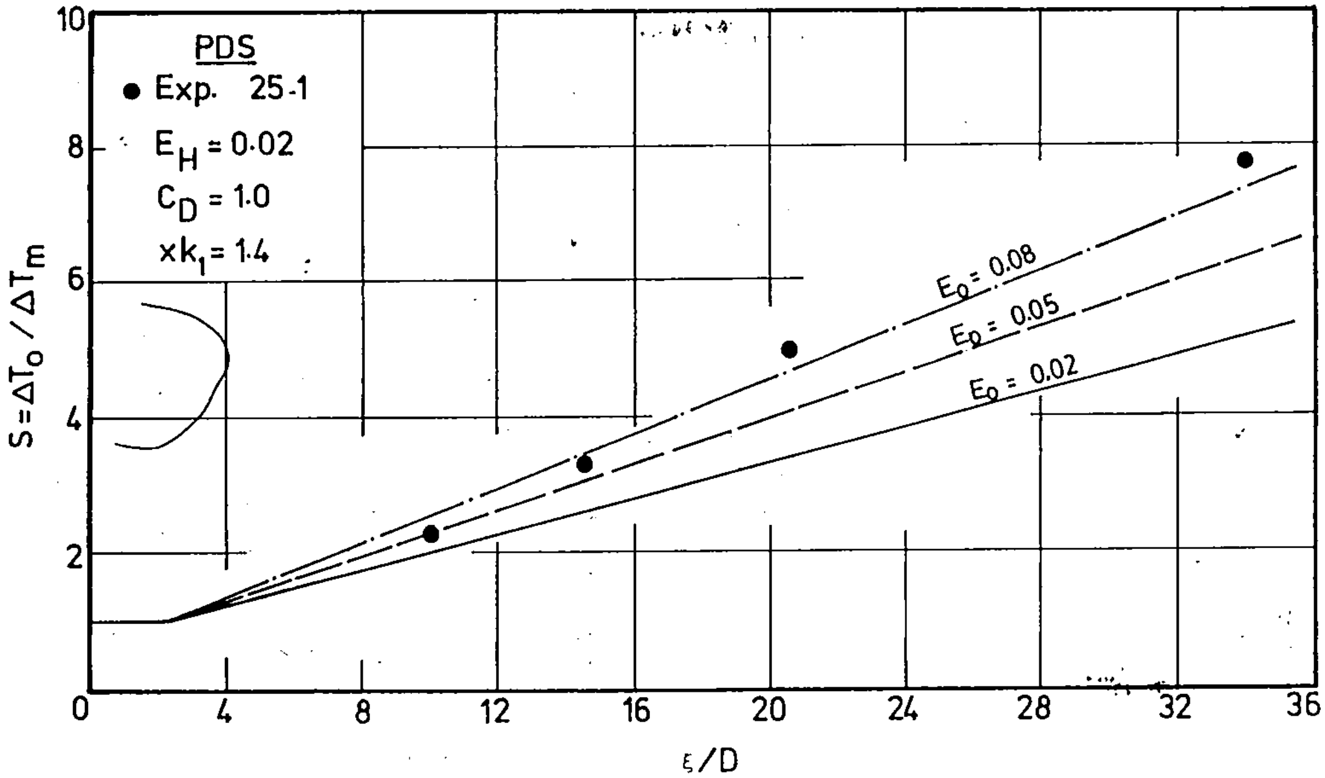

Fig. 6.14. Comparison of measured and predicted dilution for different values of entrainment coefficient, Exp. 25-1.

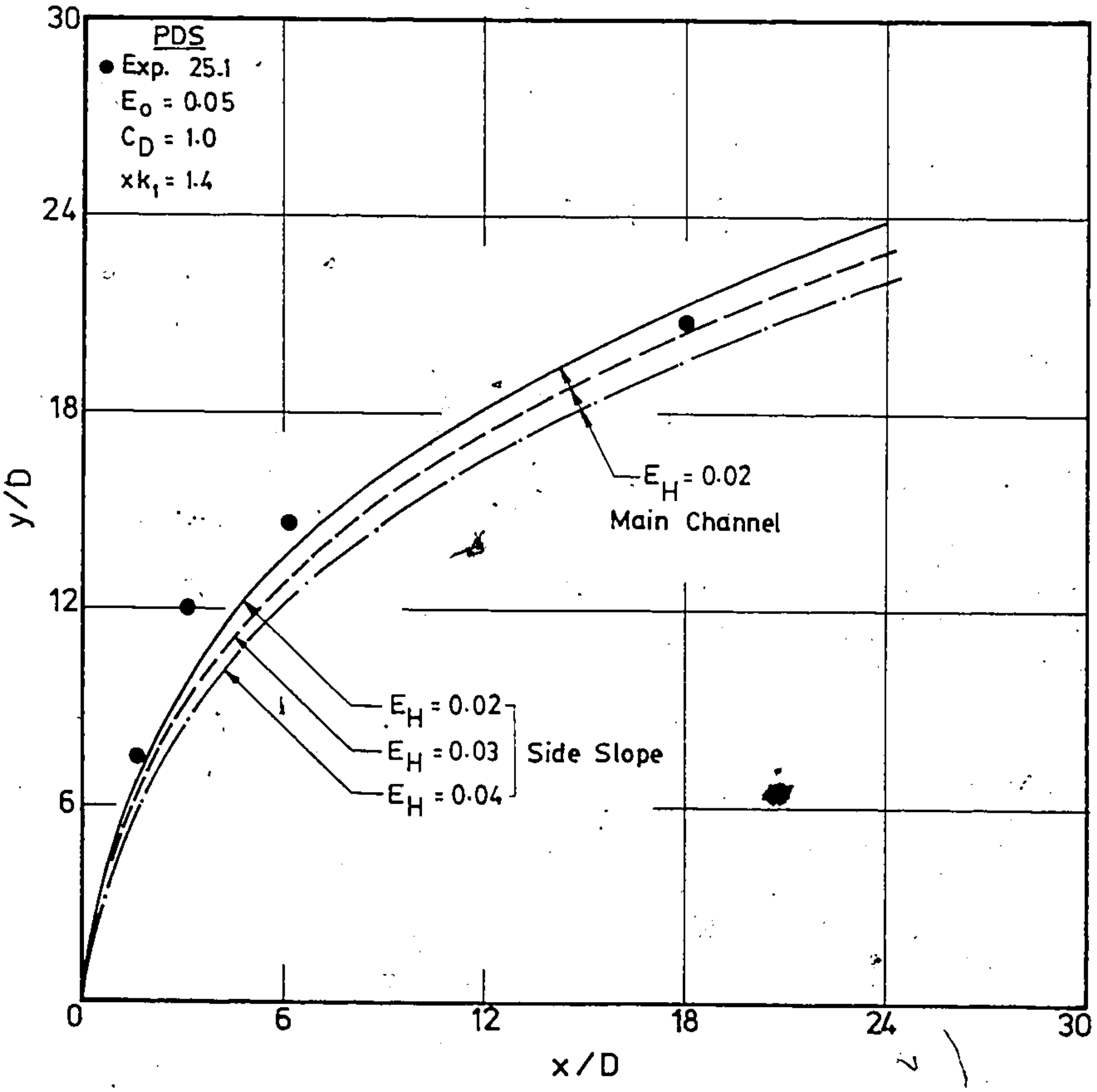

Fig. 6.15. Comparison of measured and predicted jet trajectories for different values of horizontal turbulent coefficient, E_o=0.05.

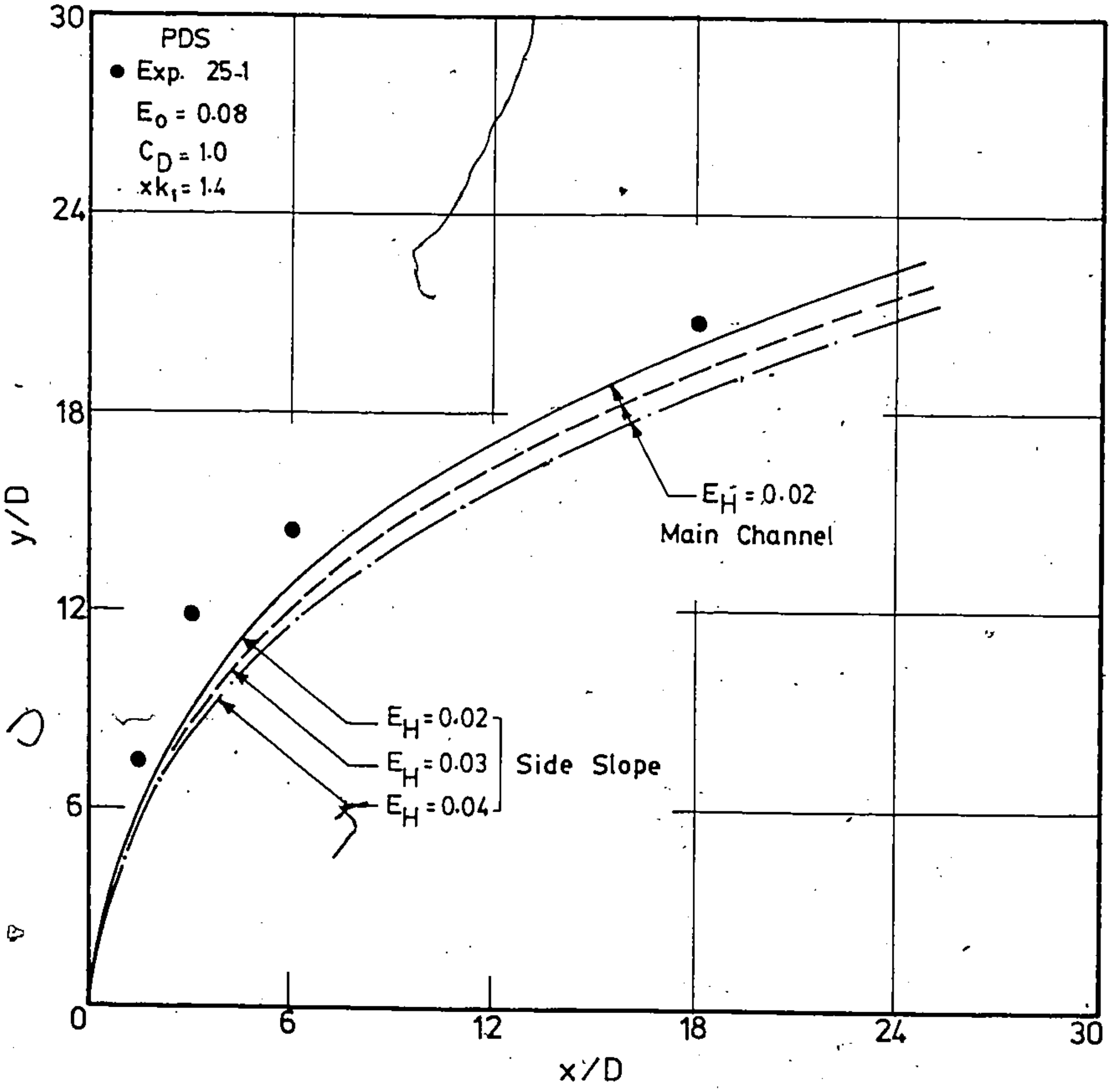

Fig. 6.16. Comparison of measured and predicted jet trajectories for different values of horizontal turbulent coefficient, E_o=0.08.

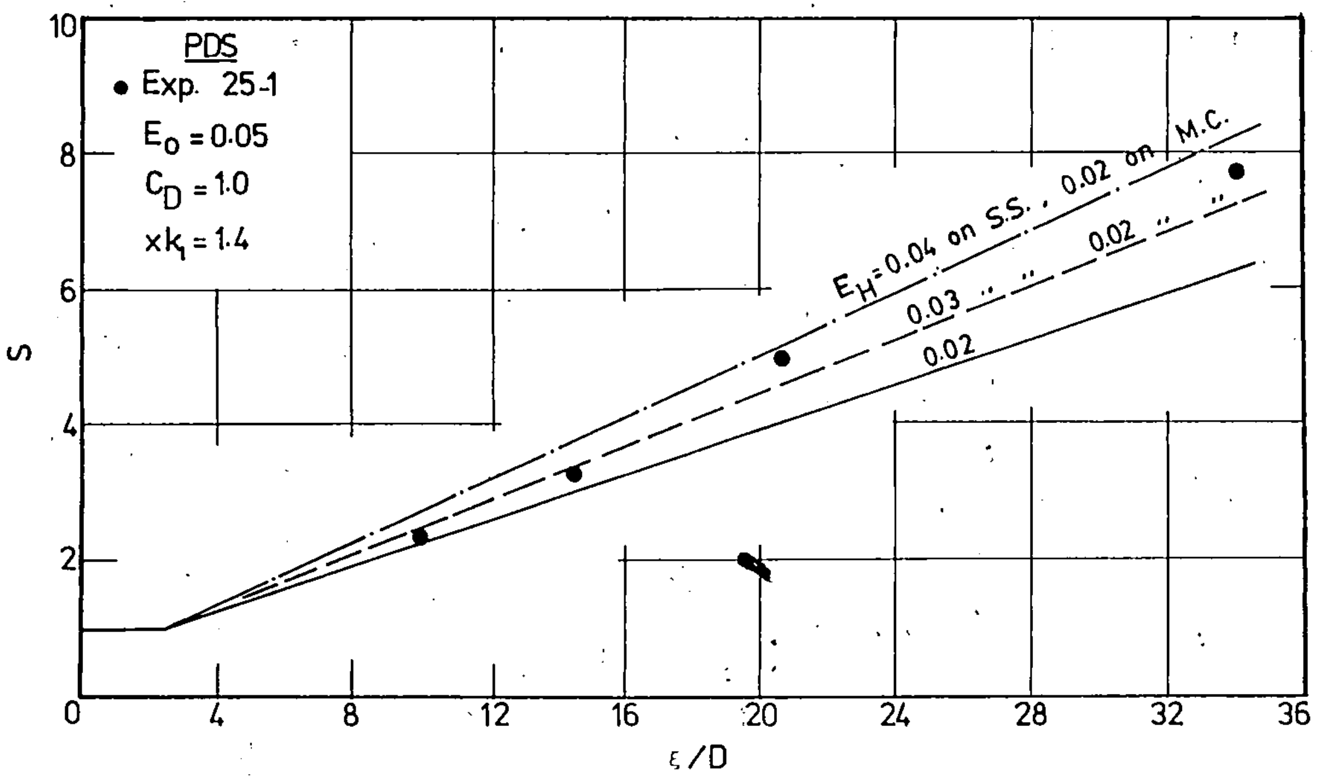

Fig. 6.17. Comparison of measured and predicted dilution for different values of horizontal turbulent coefficient, E_o=0.05.

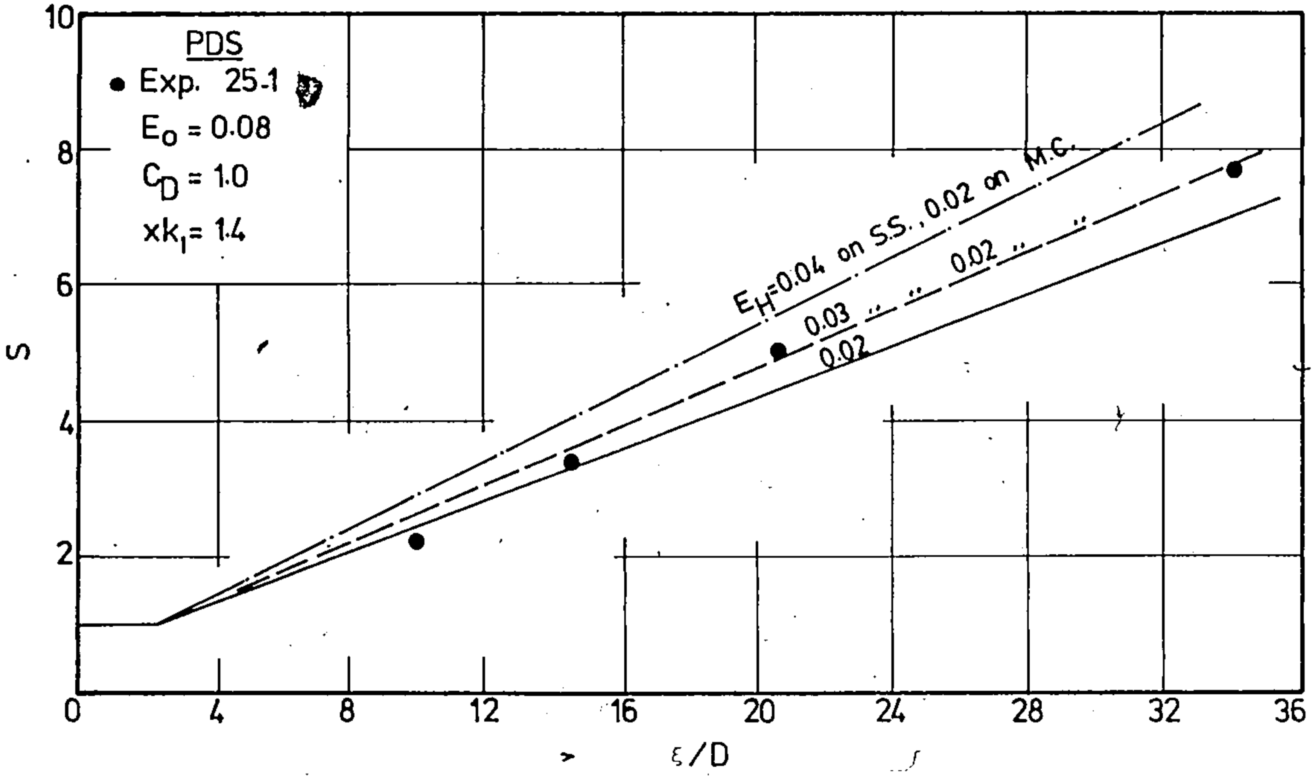

Fig. 6.18. Comparison of measured and predicted dilution for different values of horizontal turbulent coefficient, E_o=0.08.

of C_D, it was found that best fit is obtained with $C_D=1.0$ which agrees with the value reported by Shirazi and Davis.

In order to complete the calibration of PDS model to fit the data, it is necessary to compare the model with measured width and dilution for the prespecified parameters on Run 25-1. The results are shown in Figs. 6.19 and 6.20 for jet width and dilution. The measured jet width was plotted for 0.95 of the area under the normal curve of Fig. 4.29, which corresponds to $4\sigma_\eta$, where σ_η is the standard deviation. The agreement obtained from the comparison of predicted and measured jet width is excellent and the agreement for jet dilution is good.

It is, therefore, concluded that the calibrated values of the PDS coefficients are:

. Drag coefficient, C_D	= 1.0	
. Spreading function coefficient, xk_1	= 1.4	
. Entrainment coefficient, E_o	= 0.05	
. Horizontal turbulent exchange coefficient, E_H	= 0.02	on the main channel
	= 0.03	on the side slope

6.2.4 Model Verification

In order to verify the PDS model, the predicted results must be compared with other experimental results.

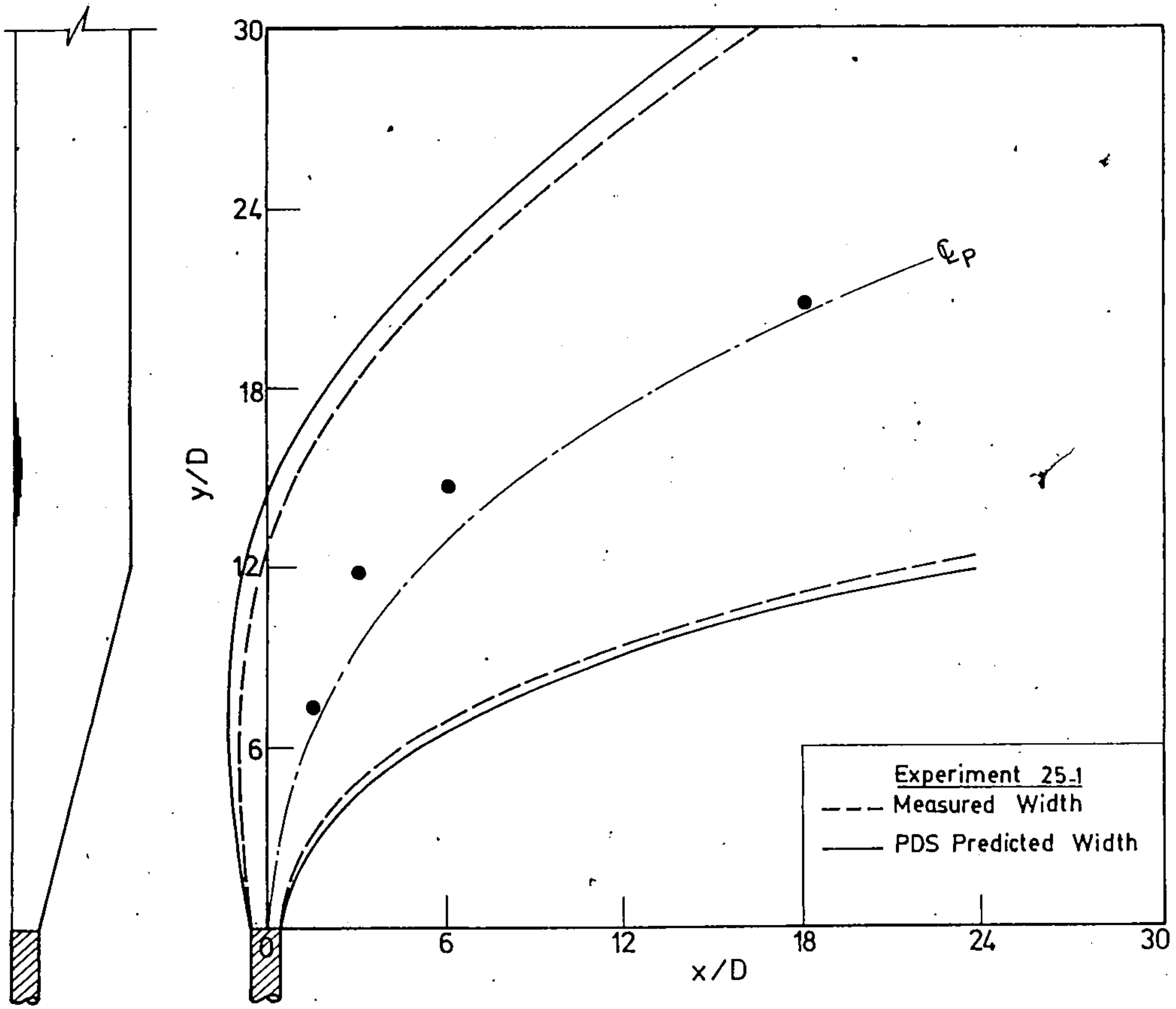

Fig. 6.19. Comparison of measured and predicted jet widths - Exp. 25-1.

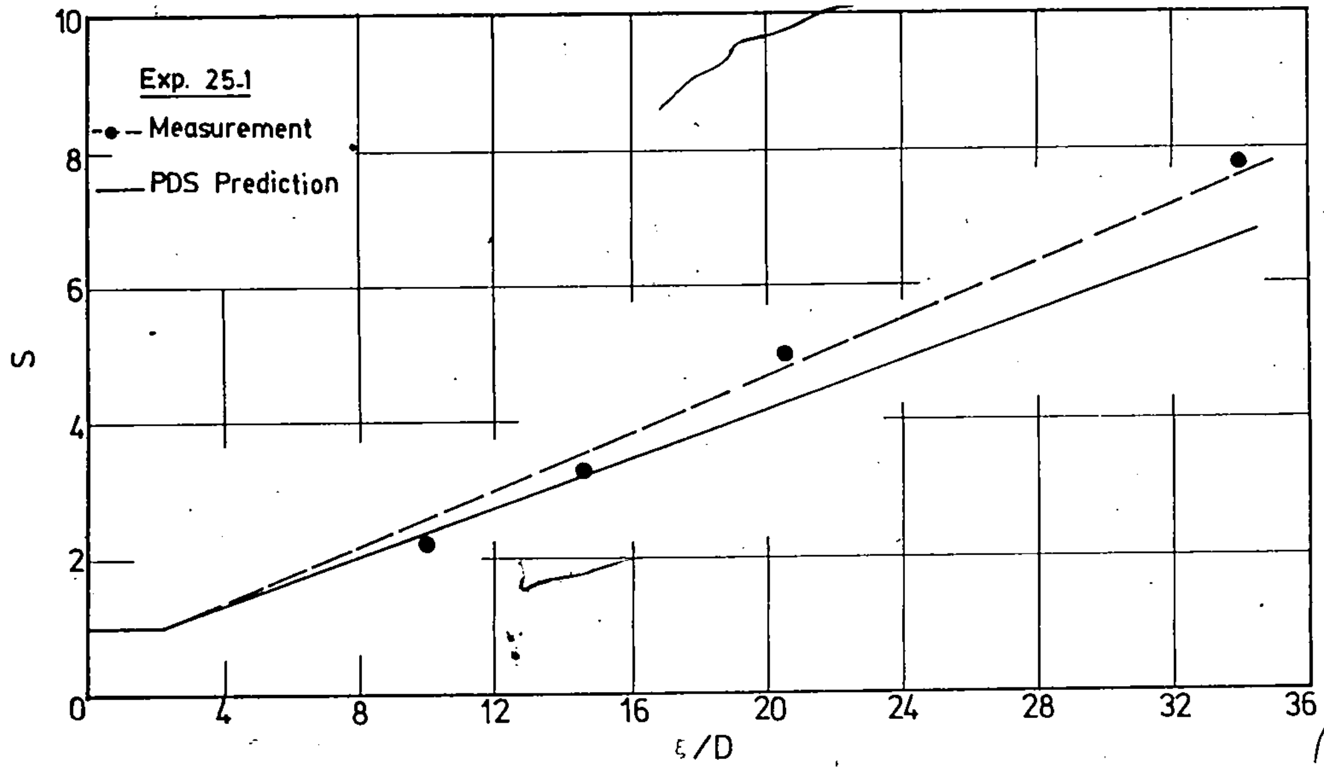

Fig. 6.20. Comparison of measured and predicted dilution - Exp. 25-1.

If reasonable agreement is obtained with such data without readjusting the previously specified coefficients, then the fitting of PDS with the data is considered complete. The experimental raw data and the predicted results based on the previously determined coefficients are compared in Figs. 6.21 and 6.22 for jet width and in Figs. 6.23 and 6.24 for the dilution for Runs 24-1 and 25-2, respectively. There are reasonably good agreement in these figures for both jet widths and dilution analysis. A full agreement is not expected because the integral approach used by Shirazi and Davis (1974) in developing the PDS model usually fails to account for physical boundaries, leading to difficulties when the river bank is sloped and when the entrainment is restricted by the bed. The prediction of the jet width for the high velocity ratio, R=5.2, shown in Fig. 6.22 is better than those for low velocity ratio, R=2.0, as shown in Fig. 6.21. This is also true for the dilution curve, where the agreement of the measured and predicted results for high R is excellent, Fig. 6.24, and for low R is only good, Fig. 6.23. The discrepancy in the case of low velocity ratio (strong cross-current) is possibly due to the assumptions of a uniform constant ambient current which is not true as shown from the velocity measurements. Moreover, when the ambient current is strong, it tends to force the jet towards the shoreline thereby confining entrainment mainly to one side of the jet. This complication cannot be handled by the PDS model.

More validation tests were performed on the PDS model to simulate the neutral density jets. For this case, the densimetric Froude number was set very high, $F_o=100$, and the spreading coefficient due to buoyancy, xk_1, was set equal to zero. These will tend to eliminate any effect of the buoyancy and treat the jet, to some extent, as non-buoyant.

The PDS predictions are compared with the experimental measurements of sodium fluorescein concentrations for neutral density experimental Runs 24 and 25 in Fig. 6.25 and 6.26, respectively. The measured jet widths of these figures were plotted for 0.95 of the area under the normal curves of Fig. 4.17, which corresponds to $4\sigma_\eta$. It is clear that the PDS shows lower jet trajectories for both cases. The reason is that the model assumed an infinite depth and did not take into account the sloping side. Also, for low velocity ratio, Fig. 6.25, the jet is confined by the shoreline giving rise to a boundary effect which cannot be handled by the PDS model.

The corresponding measured and predicted dilutions for Runs 24 and 25 are depicted in Figs. 6.27 and 6.28. Again, the PDS model successfully predicted the dilution of the neutral density jets with a deviation of ±10% from the

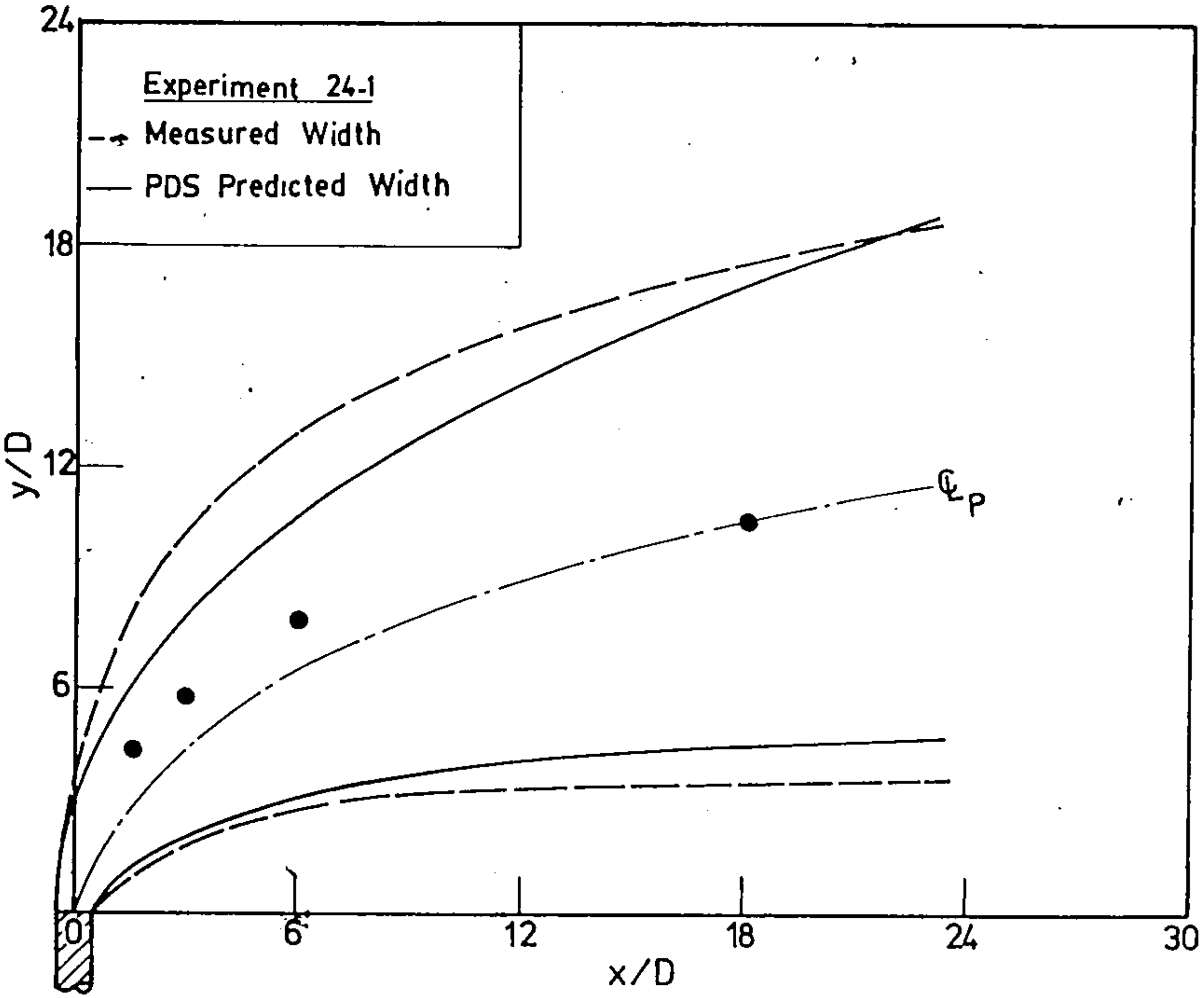

Fig. 6.21. Comparison of measured and predicted jet widths - Exp. 24-1.

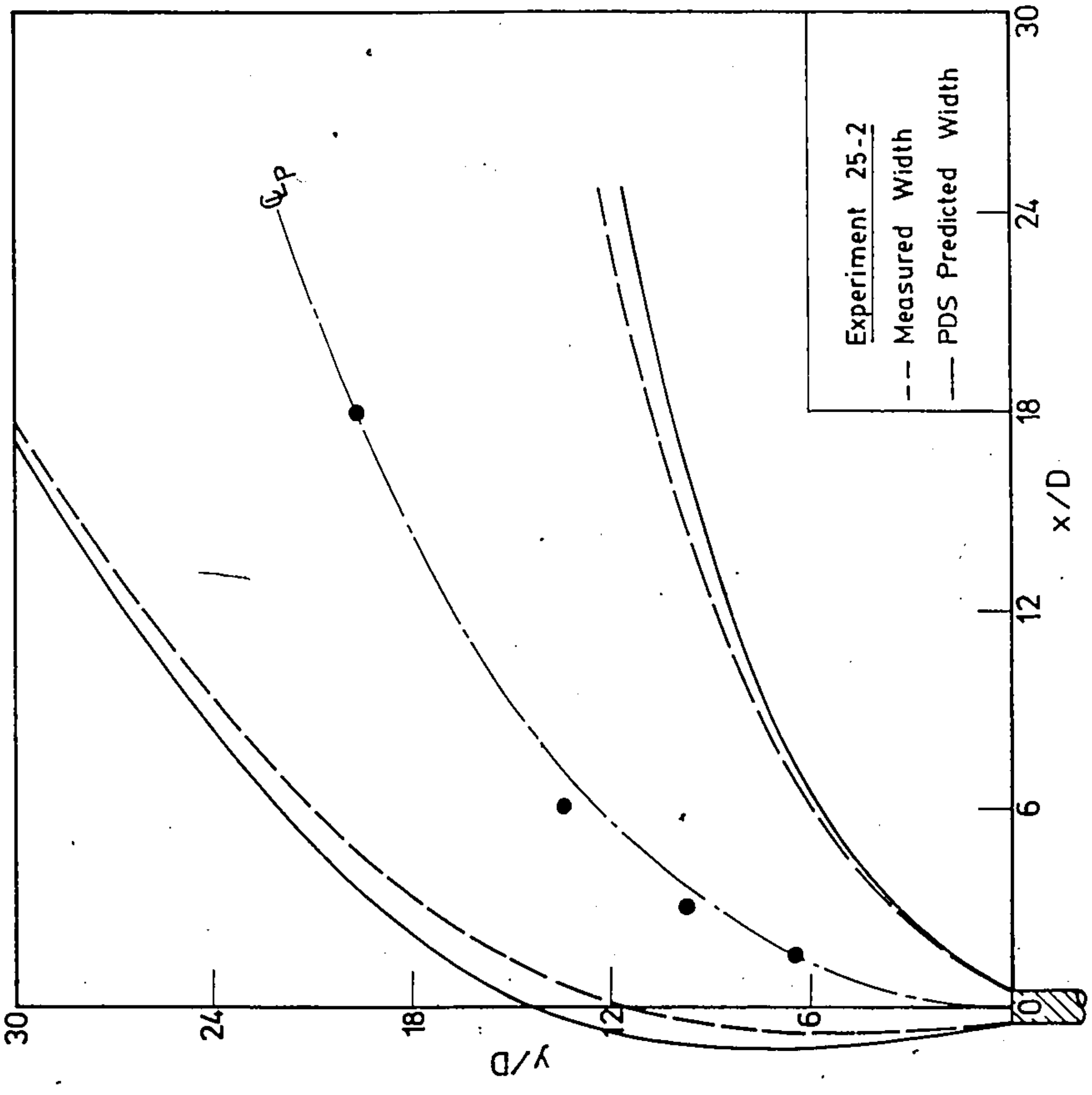

Fig. 6.22. Comparison of measured and predicted jet widths - Exp. 25-2.

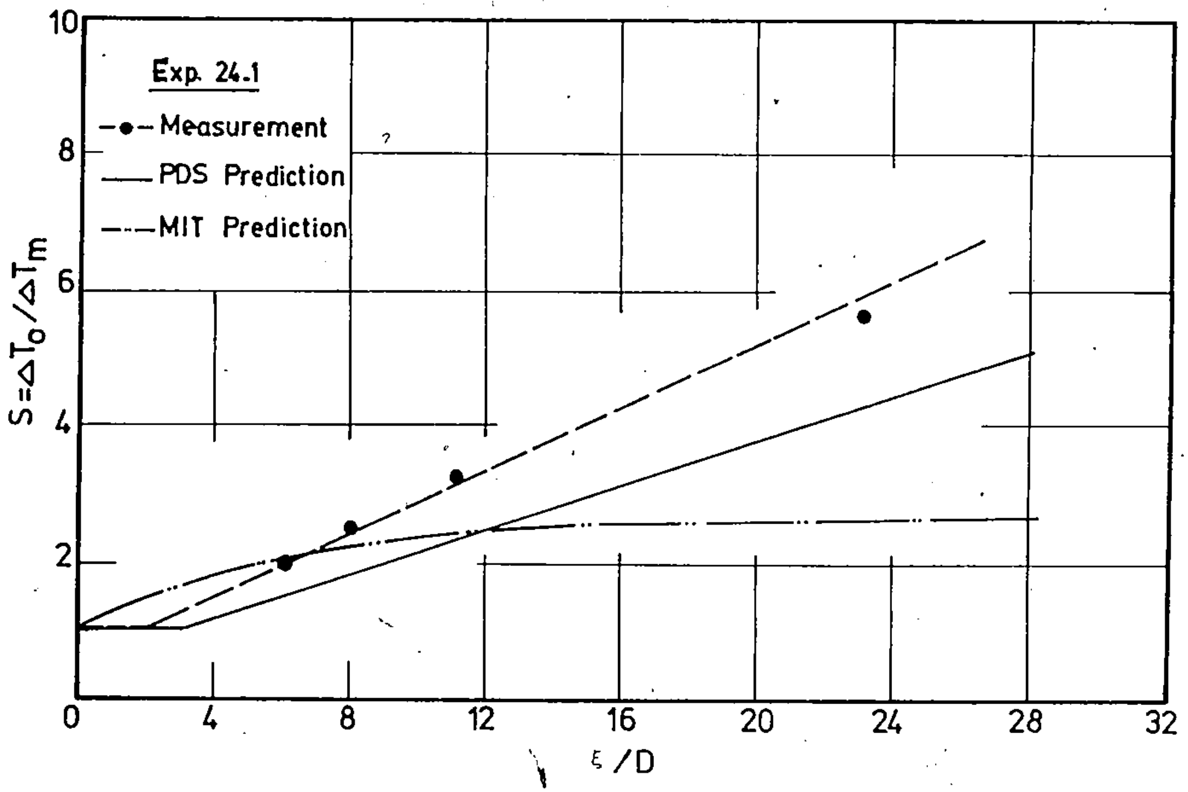

Fig. 6.23. Comparison of measured and predicted dilution - Exp. 24-1.

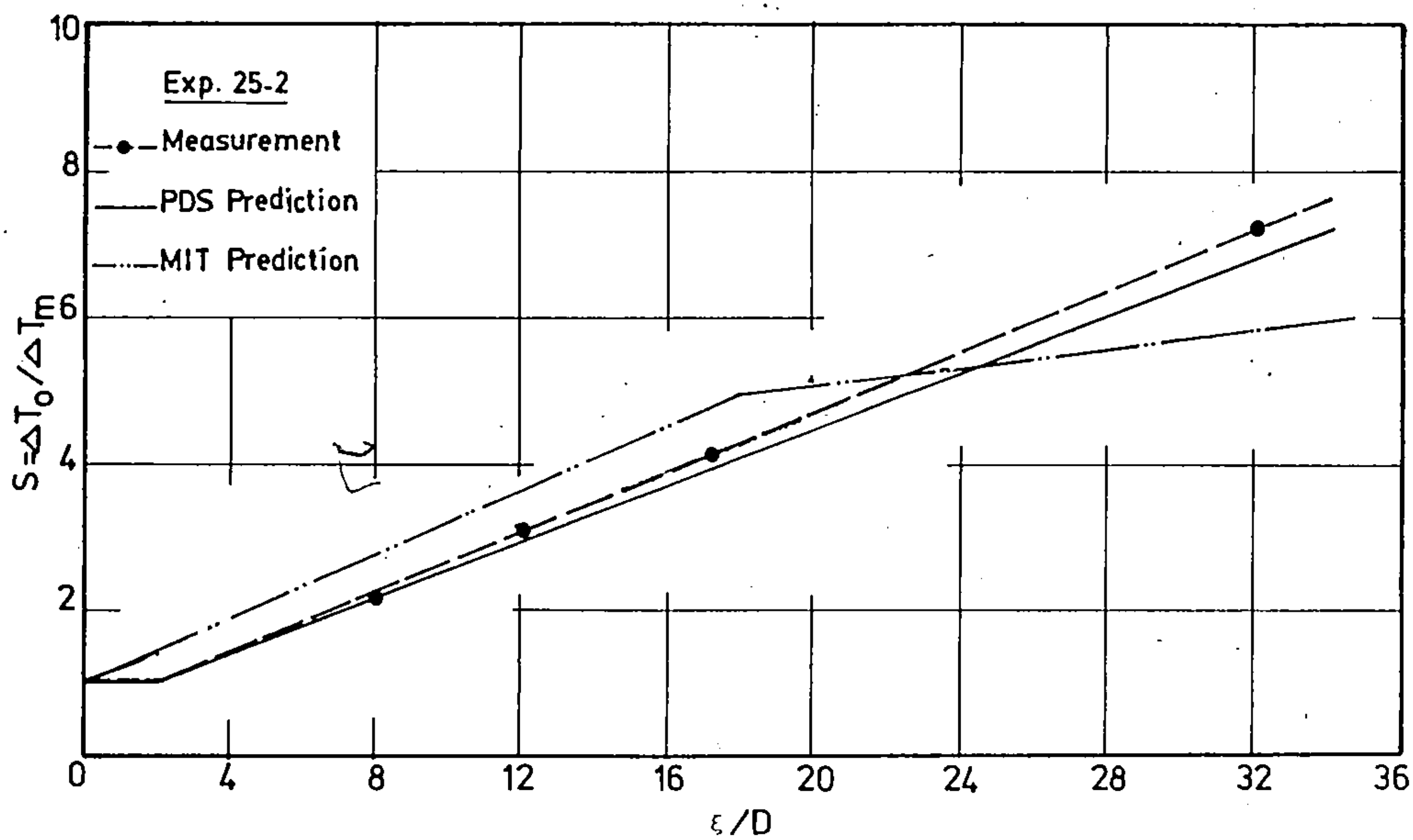

Fig. 6.24. Comparison of measured and predicted dilution - Exp. 25-2.

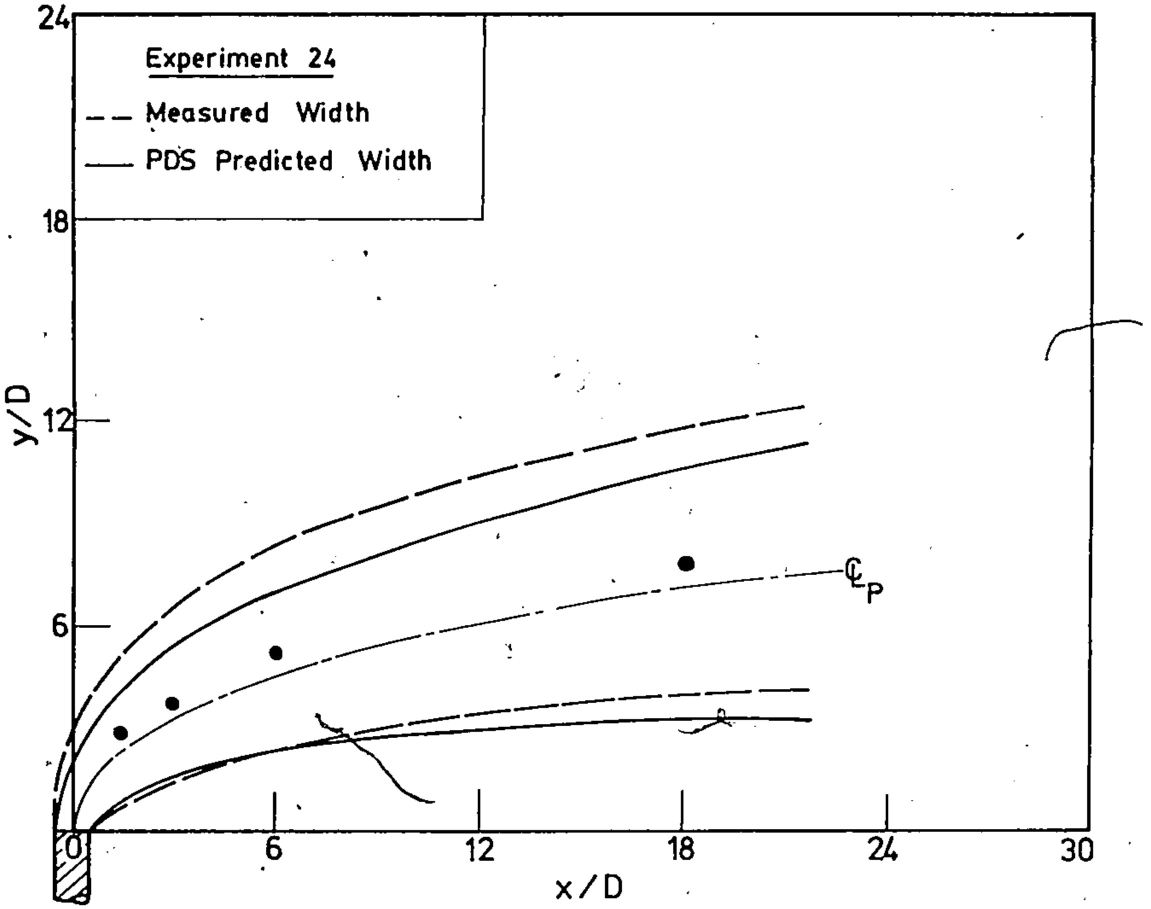

Fig. 6.25. Comparison of measured and predicted non-buoyant jet widths of Exp. 24.

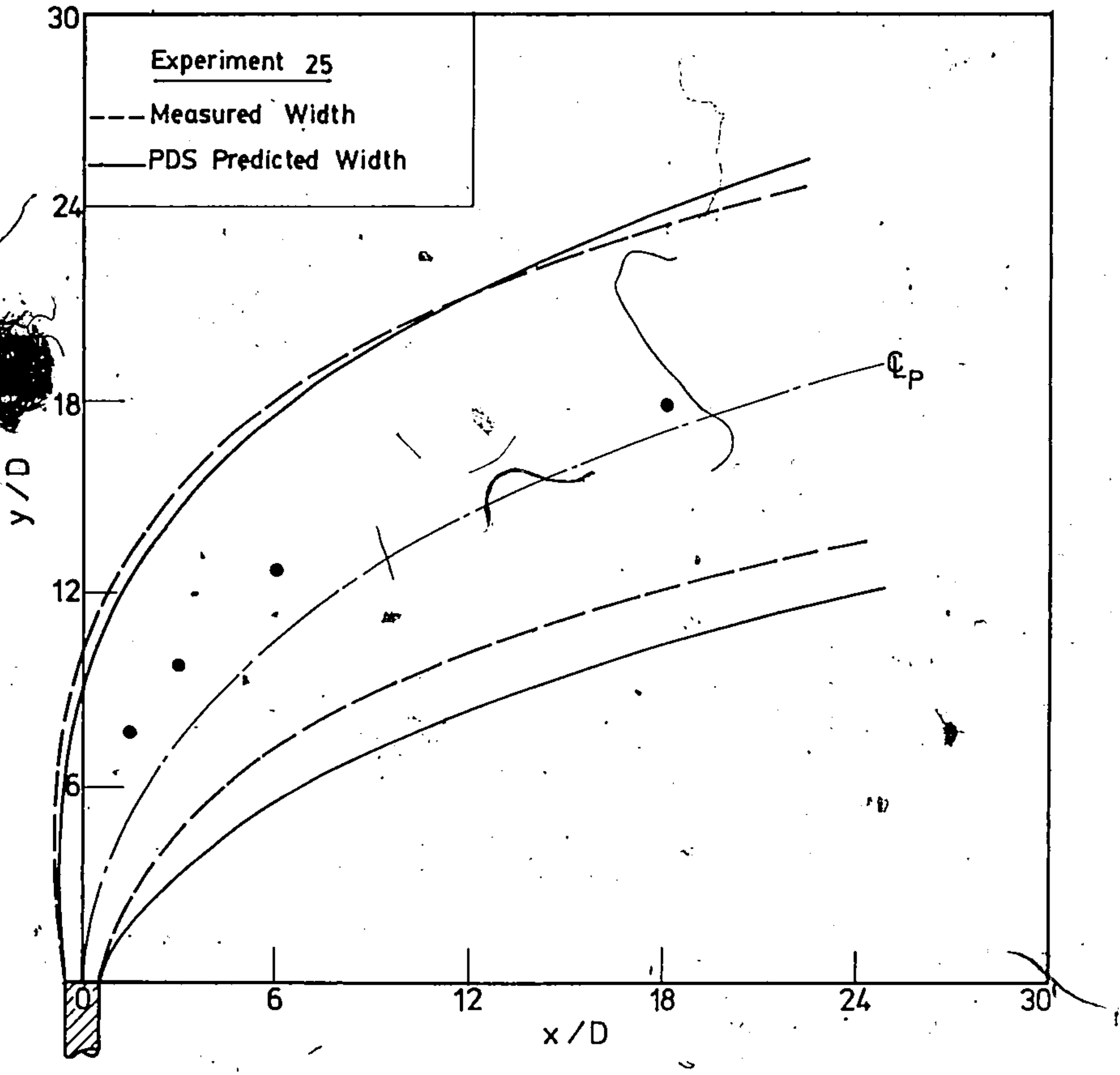

Fig. 6.26. Comparison of measured and predicted non-buoyant jet widths of Exp. 25.

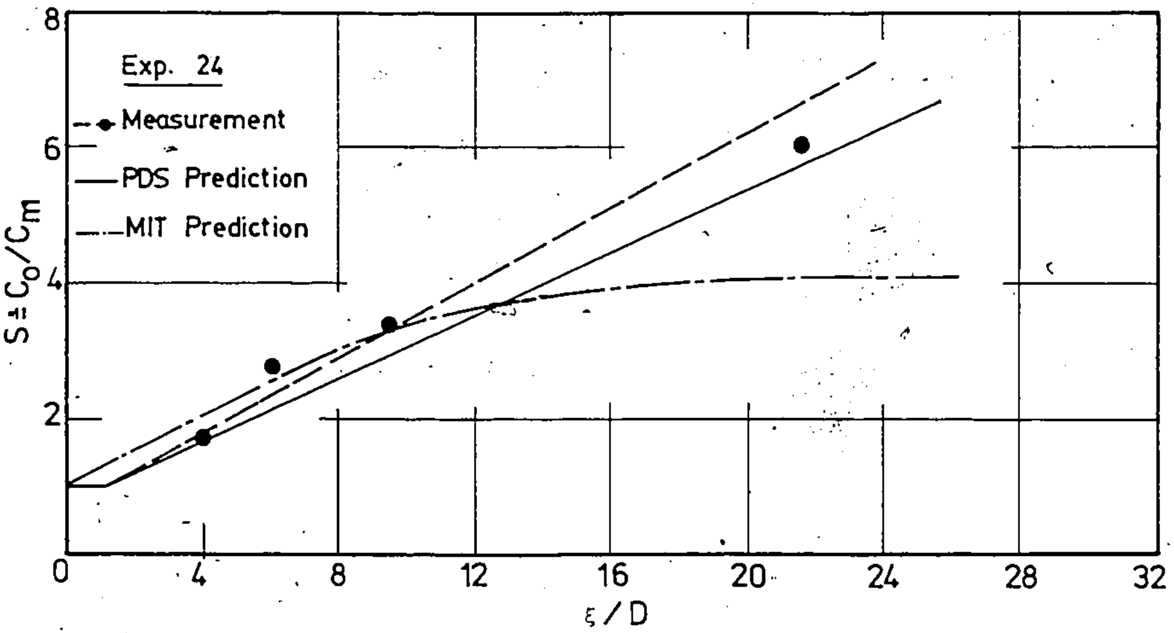

Fig. 6.27. Comparison of measured and predicted dilution for non-buoyant jet - Exp. 24.

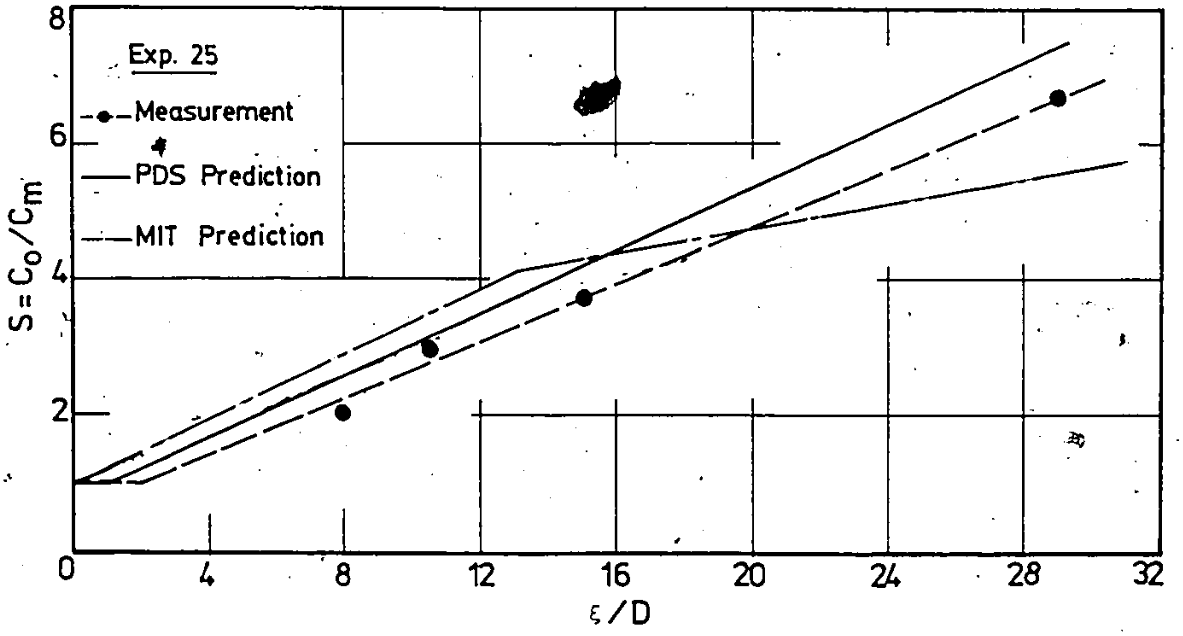

Fig. 6.28. Comparison of measured and predicted dilution for non-buoyant jet - Exp. 25.

measured results. In Fig. 4.16, the vertical concentration profile for Run 25 shows a jet attachment to the bottom, whereas, the PDS model did not predict any attachment, and therefore, it overestimated the dilution. However, when the jet is confined with the channel side slope, the measurement of Run 24 showed a higher dilution rate than the PDS prediction as indicated in Fig. 6.27. In this case, the cross-flow is strong and a recirculation pattern was observed as shown in both, Photograph 4.7, and the fluorescein concentration distribution in Fig. 4.17. The concentration at the lee side is high due to the re-entrainment. Therefore, the dilution analysis based on the concentration values could be deceiving for the recirculatory type of jet.

6.3 THE MIT MODEL

6.3.1 Background

The coefficients to be determined experimentally for MIT model are the non-buoyant spreading rates for three and two dimensional jets, ε_3 and ε_2, the cross-flow entrainment coefficient, α_c, the drag coefficients $C_{D_{02}}$ and $C_{D_{22}}$ and the bottom friction factor, f_b.

The values of ε_3 and ε_2 were determined by Stolzenbach and Harleman (1971) from the experiments of Albertson et al. (1950). They suggested the values 0.22 and 0.30 for ε_3 and

ε_2, respectively.

For determining the cross-flow entrainment coefficient, α_c, they fitted the theoretical solution of their study to experimental data by other researchers on the trajectories of axisymmetrical jets in deep stagnant water. The range of velocity ratio, R, were 8 to 16 and the jet trajectory has been normalized by the jet diameter. However, the experimental results were for non-buoyant jets or slightly buoyant jets (F_o=40 to 80). An average value of α_c=0.3 was recommended.

The drag force as defined in the MIT model is given by

$$F_D = \frac{1}{4}\bar{h}U_a^2\ [C_{D_o} + C_{D_2}\sin^2\theta] \qquad (6.2)$$

in which

$\bar{h}$ = the jet depth
θ = the angle of jet trajectory
C_{D_o}, C_{D_2} = the drag coefficients

The values of C_{D_o} and C_{D_2} were determined by interpolating between the values for 3-D jets in deep water ($C_{D_o}=C_{D_2}= 0$) and values for 2-D plane jets in shallow water. Those values of the drag coefficients of two dimensional jets, $C_{D_{02}}$ and $C_{D_{22}}$, were determined by using experimental data presented by Rouse (1957) on two-dimensional non-buoyant jets in a cross-flow with R=2.9, 6.3 and 13.7. A constant value of $C_{D_{22}}=1.7$ was suggested; and values of $C_{D_{02}}$ were related to 1/R as given by Rouse (1957) as

$$C_{D_{02}} = 0.06(1/R)^{-0.77} \tag{6.3}$$

For the bottom friction factor, f_b, a value of 0.025 was suggested and used by Stolzenbach and Harleman for computations.

6.3.2 Sensitivity Analysis of MIT Model

A comprehensive sensitivity analysis was performed on the MIT model by varying the coefficients mentioned in section 6.3.1 and depicting the effect of each coefficient on both the jet trajectory and minimum dilution. Table 6.2 presents the variables used in the sensitivity analysis together with the values recommended by Stolzenbach and Harleman (1971).

The effects of changing F_o, R, α_c, $C_{D_{22}}$ on the jet trajectory are shown in Figs. 6.29 to 6.32, and the effect of α_c and $C_{D_{22}}$ on the dilution are shown in Figs. 6.33 and 6.34. Figures 6.29 and 6.30 indicate that both densimetric Froude number and velocity ratio exhibit significant effects on the jet trajectory. The MIT model is similar to PDS model at low values of F_o, i.e., the jet penetrates

Table 6.2

Paramaters in Sensitivity Analysis of MIT Model

Parameter	Value Suggested by Stolzenbach and Harleman	Base Value	Range Studied
α_c	0.3	0.3	0.1-0.4
$C_{D_{02}}$	*	*	*
$C_{D_{22}}$	1.7	1.7	0.5-2.2
ε_3	0.22	0.22	0.11-0.33
ε_2	0.3	0.30	0.2-0.4
F_o	–	12.9	2-100
R	–	5.2	2-20

*$C_{D_{02}}$ depends on 1/R according to Eq. 6.3.

further into the channel. When F_o increases to 100, there is no affect on the jet trajectory indicating that the jet tends to behave as a non-buoyant case. Figure 6.30 depicts the significant effect of R on the jet trajectory. A reduction of R from 10 to 5.0 decreases the jet penetration by more than 100%. However, when the ambient current is strong R<2.0, the jet attaches to the shoreline.

The computer trials indicated that the bottom friction factor, f_b, had no effect on either the trajectory or the dilution. f_b is a function of Reynolds number and the roughness of the receiving basin bottom. In general, the Reynolds number is a function of the distance travelled by the jet, ξ, and it is not expected that the behaviour of the jet in the near-field would be very sensitive to f_b. The sensitivity analysis also indicated that neither ε_2 nor ε_3 had an effect on the jet trajectory or dilution. An increase in ε_2 from 0.3 to 0.5 decreases the penetration by 3% and an increase in ε_3 from 0.11 to 0.33 decreases the penetration by 3.8% at x/D=20. This agrees with the finding of PDS, considering that ε_2 and ε_3 are similar to the spreading coefficient xk_1.

The sensitivity analysis indicated that the most important parameters are the cross-flow entrainment coefficients, α_c, and the drag coefficient $C_{D_{22}}$. Figure 6.31 shows that an increase in α_c from 0.1 to 0.4 reduces the jet penetration by 42% at x/D=30. In Fig. 6.32, an increase in C_D from 0.5 to 2.2 decreases the penetration by 72%. However, when $\alpha_c \geq 0.3$, the MIT model predicts bottom attachment at $\xi/D \leq 4$ as shown in Fig. 6.33. In general, the minimum dilution increases with increasing α_c for either detached or attached jets. The effect of changing $C_{D_{22}}$ on the dilution is shown in Fig. 6.34. Each curve can be described by two linear variations. The first part describes the dilution for detached jet and the second part represents the linearity of the dilution curve for an attached jet. The latter appears to start at $\xi/D \cong 4.0$. Generally, the dilution curve is slightly affected by $C_{D_{22}}$. An increase in $C_{D_{22}}$ from 0.5 to 2.2, decreases the dilution by 6%.

6.3.3 Model Calibration

The experimental Run 25-1, used previously for the PDS calibration, was also chosen to calibrate the MIT model. The base values of F_o, R and A given in Table 6.2 are those of Run 25-1. Originally, when a constant value of the velocity ratio, R, was used across the channel, deviation of the predicted values versus experimental data was found, as shown in Fig. 6.31. Like the PDS, this deviation was corrected by increasing the velocity ratio, R, on the side slope of the channel to account for the

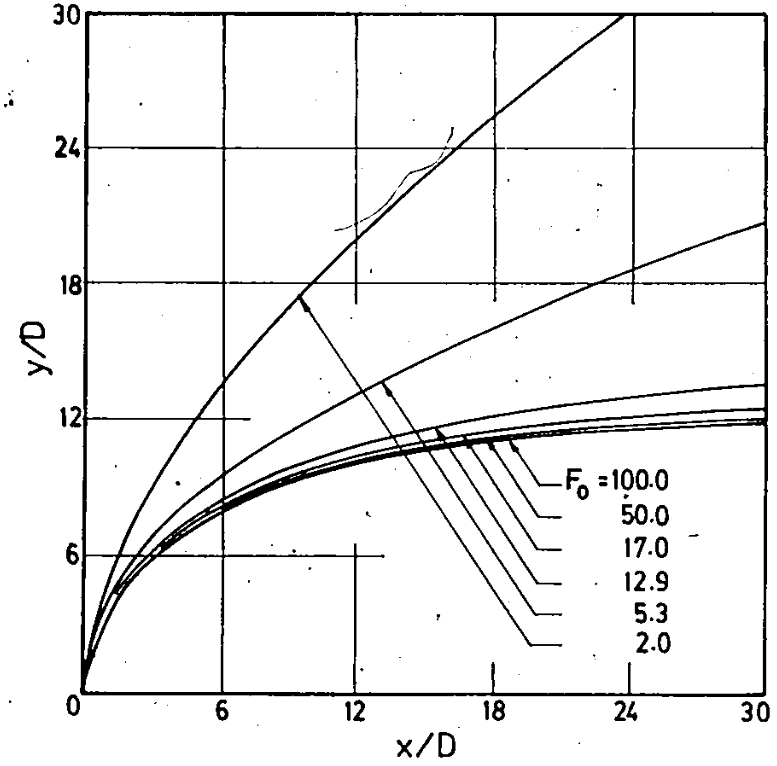

Fig. 6.29. Sensitivity of jet trajectory to Froude Number, MIT Model.

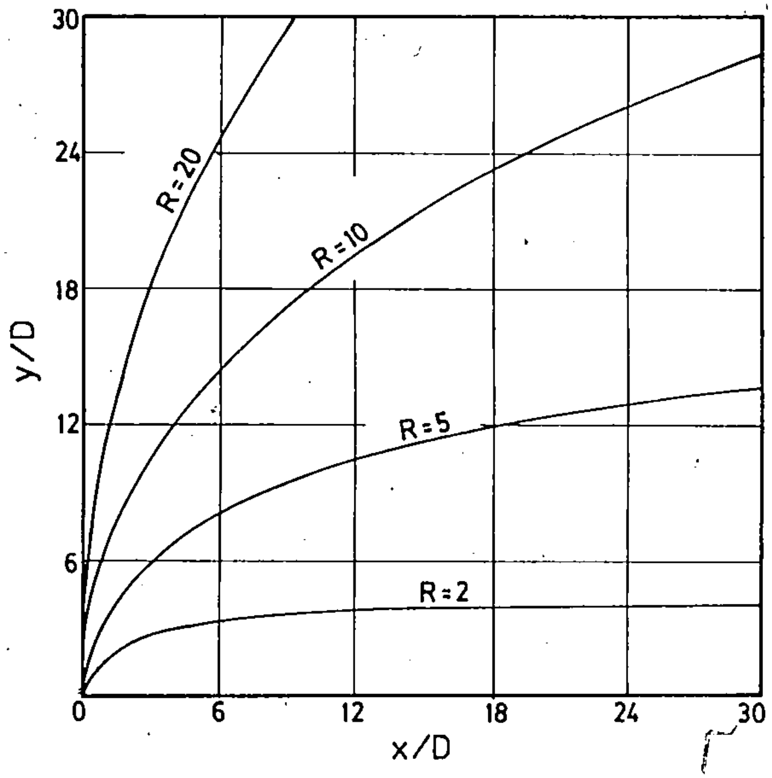

Fig. 6.30. Sensitivity of jet trajectory to velocity ratio.

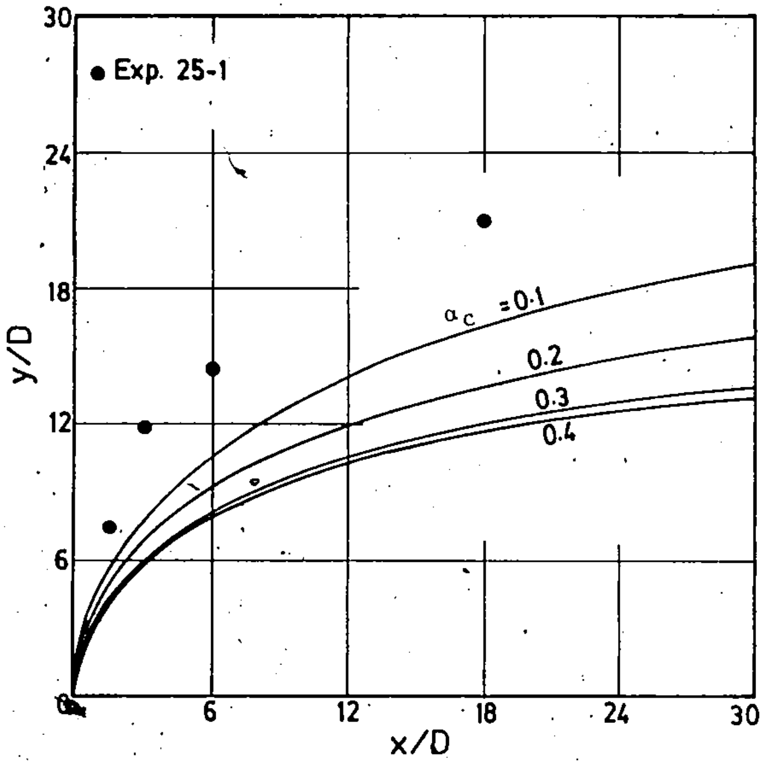

Fig. 6.31. Sensitivity of jet trajectory to cross-flow entrainment coefficient.

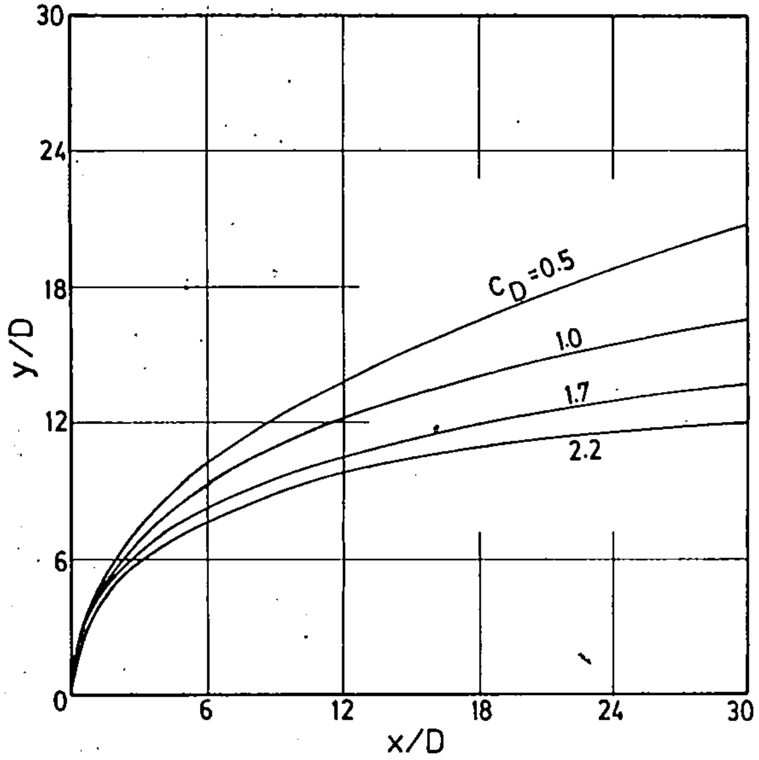

Fig. 6.32. Sensitivity of jet trajectory to drag coefficient.

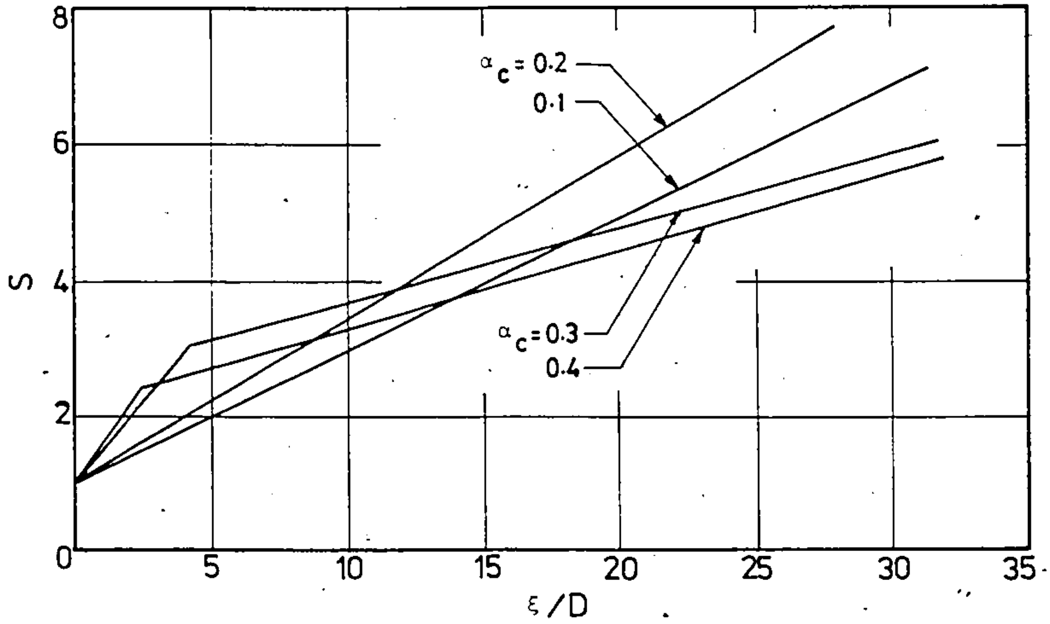

Fig. 6.33. Sensitivity of minimum dilution to cross-flow entrainment coefficient, MIT Model.

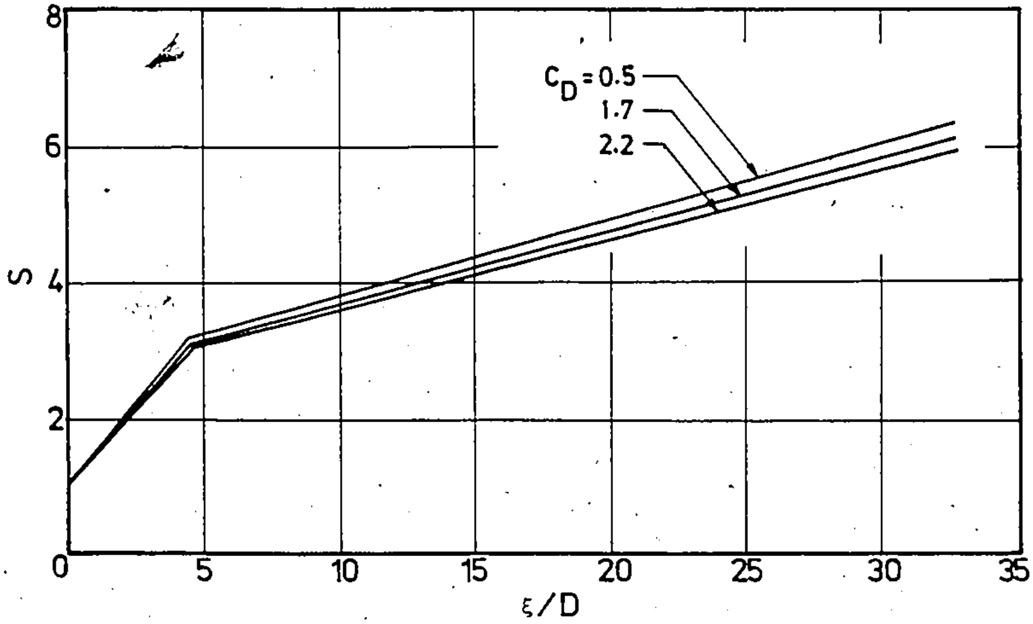

Fig. 6.34. Sensitivity of minimum dilution to drag coefficient.

lower ambient velocity. Agreement between the experimental data and the model results were sought by adjusting one or more of the model coefficients and taking the changes of velocity ratio into account. The sensitivity analysis indicated that the most important factors affecting the trajectory are the cross-flow entrainment coefficient, α_c, and the drag coefficient $C_{D_{22}}$. Figure 6.35 shows the plot of measured jet trajectory and several numerical results of MIT model with different preassigned values of α_c and C_{D22}. A visual inspection of this figure reveals that the best fit of the model with the experimental data is obtained with α_c=0.1 and $C_{D_{22}}$=1.0. In Fig. 6.36, a comparison of the measured dilution with the results of several computer runs is made. Again, it appears that a reasonably good agreement is obtained with α_c=0.1 and $C_{D_{22}}$=1.0. The values of α_c and $C_{D_{22}}$ are lower than those suggested in the MIT model report. In determining these coefficients, Stolzenbach and Harleman (1971) used experimental results for non-buoyant jets. When they used data for slightly buoyant jets (F_o=40 to 80) with α_c=0.3, the jet trajectory fell below the non-buoyant jets. This indicates that α_c must be less than 0.3 for buoyant jets. For determining $C_{D_{22}}$, they used an experimental data for two-dimensional non-buoyant jets in a cross-flow with R up to 13.7. This high value of R reduces the effect of cross-flow and tends

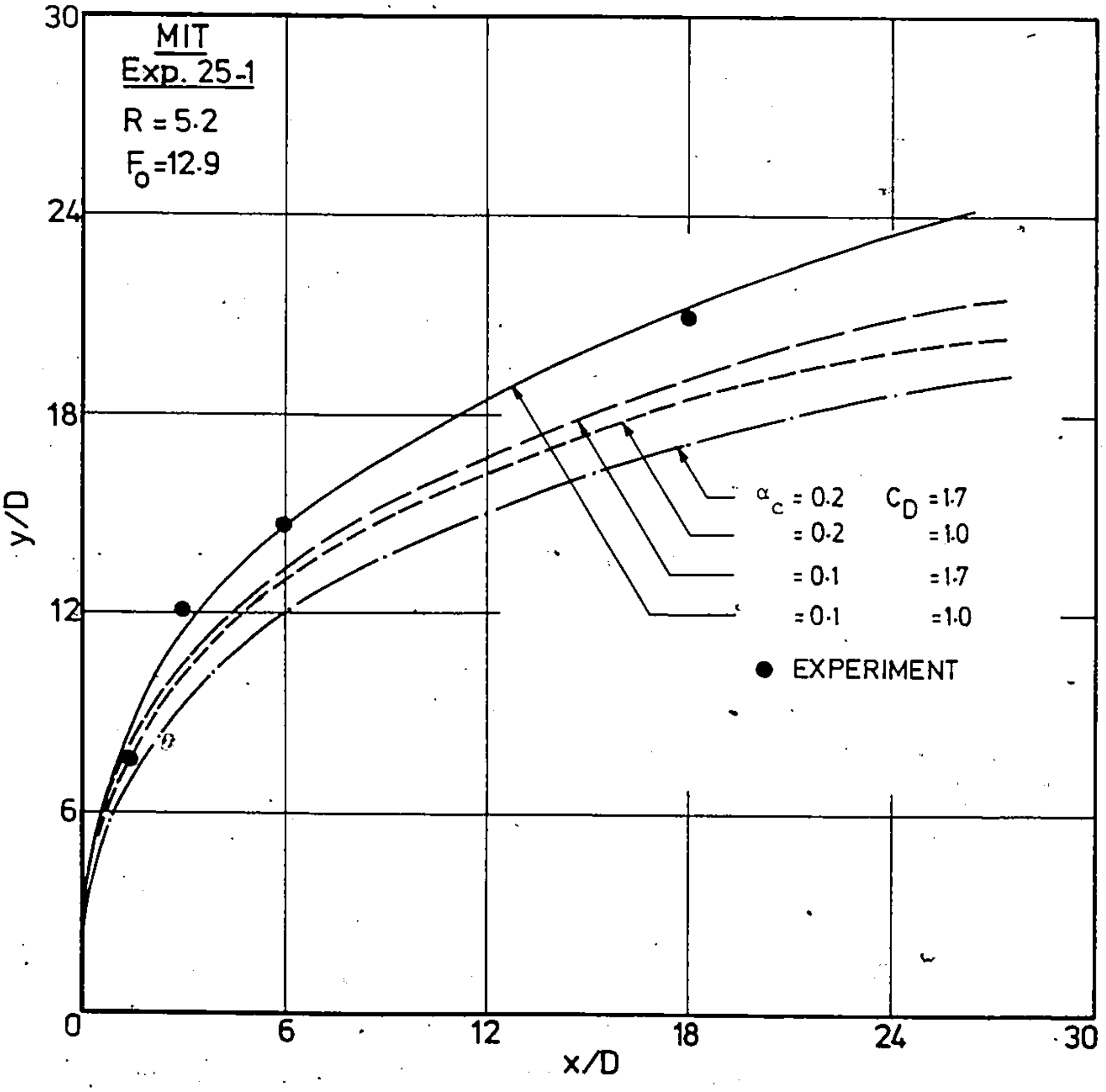

Fig. 6.35. Comparison of measured and predicted jet trajectories for different values of entrainment coefficient and drag coefficient - Exp. 25-1.

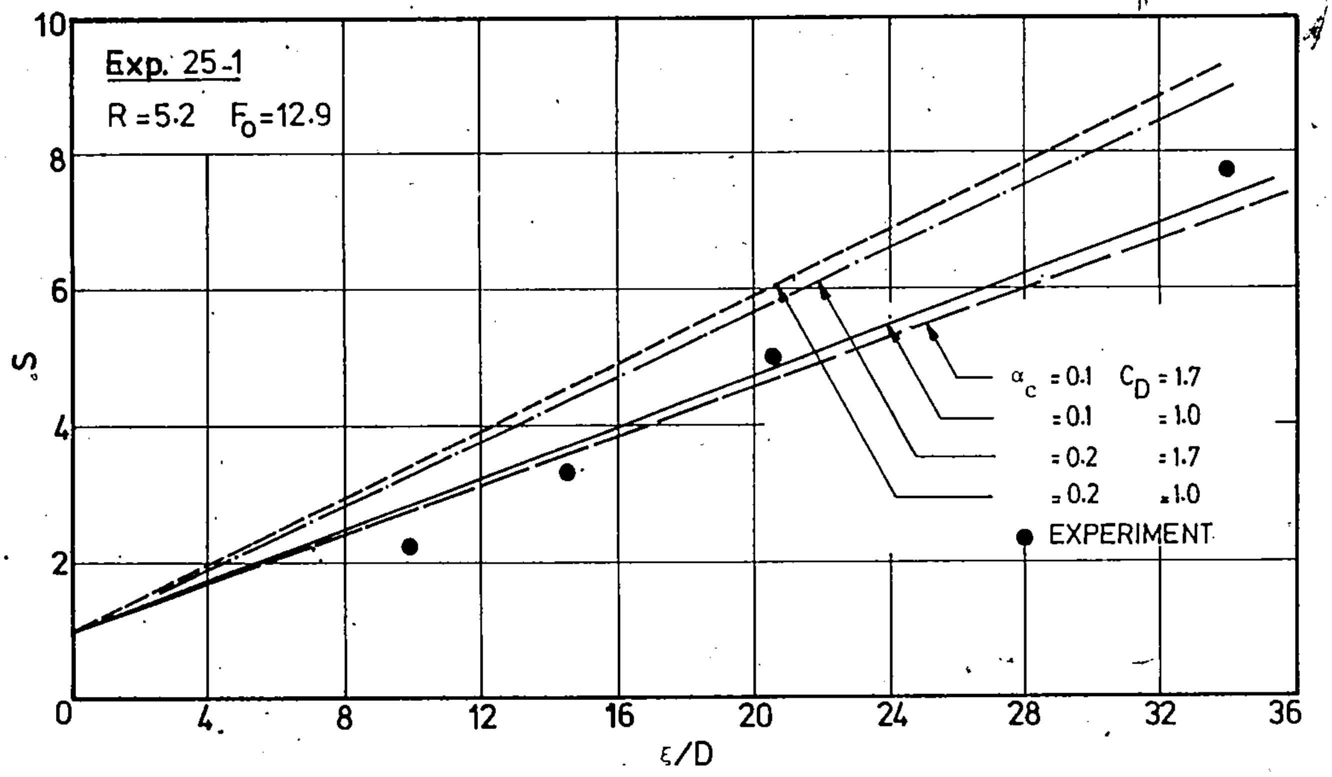

Fig. 6.36. Comparison of measured and predicted dilution for different values of entrainment coefficient and drag coefficient - Exp. 25-1.

to overestimate the drag coefficient.

The final step in the MIT model calibration is to compare the measured jet width and dilution of Run 25-1 with the prediction of MIT model using the new suggested value, i.e., $\alpha_c=0.1$ and $C_{D_{22}}=1.0$. The other coefficients take the same values suggested by Stolzenbach and Harleman and are given in Table 6.2. The jet width of Run 25-1 is compared with the MIT prediction in Fig. 6.37 whereas the comparison of the dilution is shown in Fig. 6.38.

6.3.4 Model Verification

The MIT model was verified by using experimental data that were not used in the calibration, e.g., experimental Runs 24-1 and 25-2. The velocity ratios of Run 24-1 are $R_1=2.5$ on the side slope and $R_2=2.0$ on the main channel, whereas for Run 25-2, $R_1=8.33$ and $R_2=5.2$. The experimental raw data and the predicted values based on the above coefficients are compared in Figs. 6.39 and 6.40 for jet width and in Figs. 6.23 and 6.24 for dilution for Runs 24-1 and 25-2 respectively. A fair agreement between the measured and the predicted jet widths is indicated by Figs. 6.39 and 6.40. In Fig. 6.40, for Run 25-2, the MIT predicted bottom attachment at $x/D=7.0$. The experimental measurements of the vertical temperature profile of Run 25-2 shown in Fig. 4.28 showed slight jet

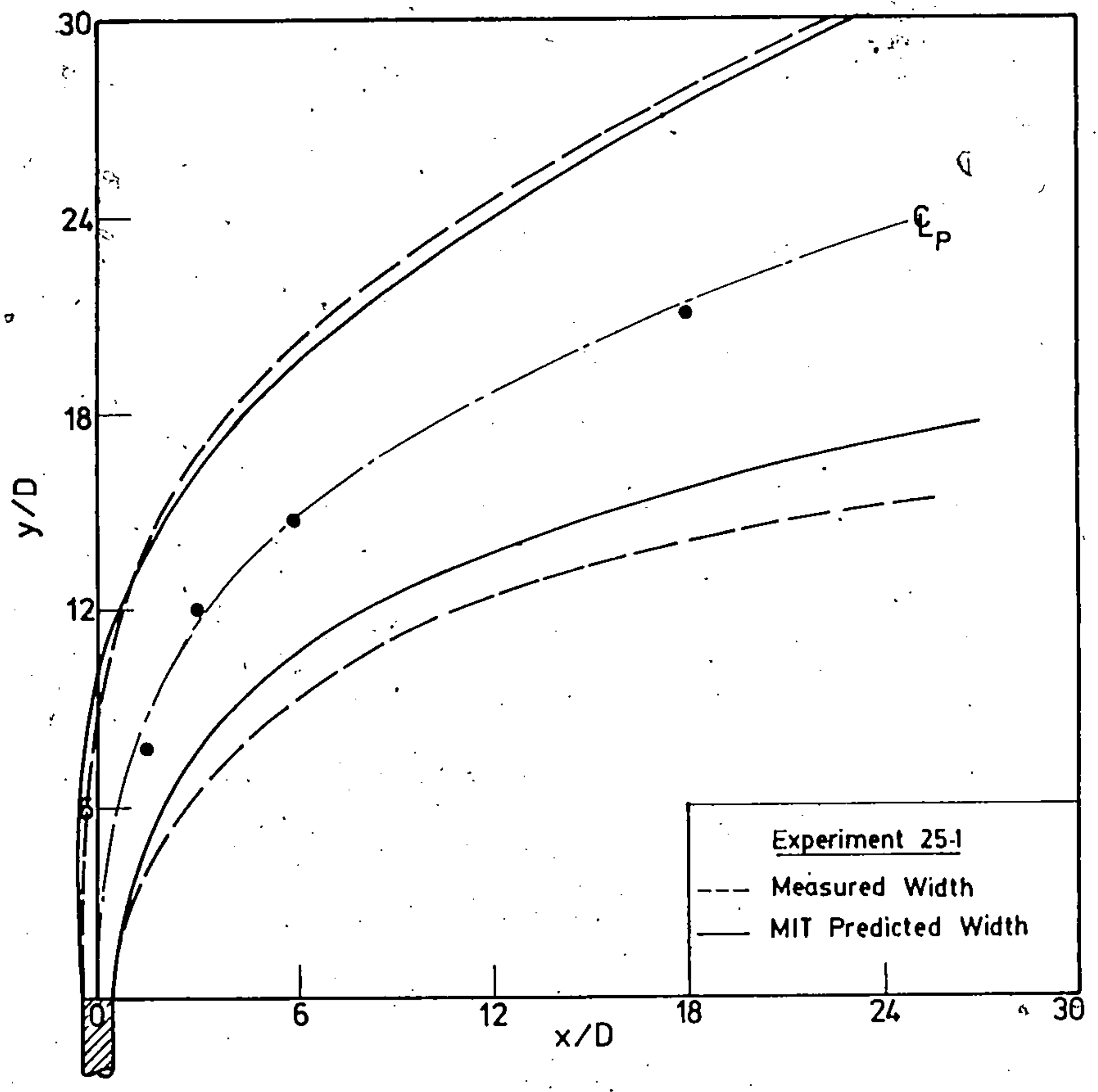

Fig. 6.37. Comparison of measured and predicted jet widths - Exp. 25-1.

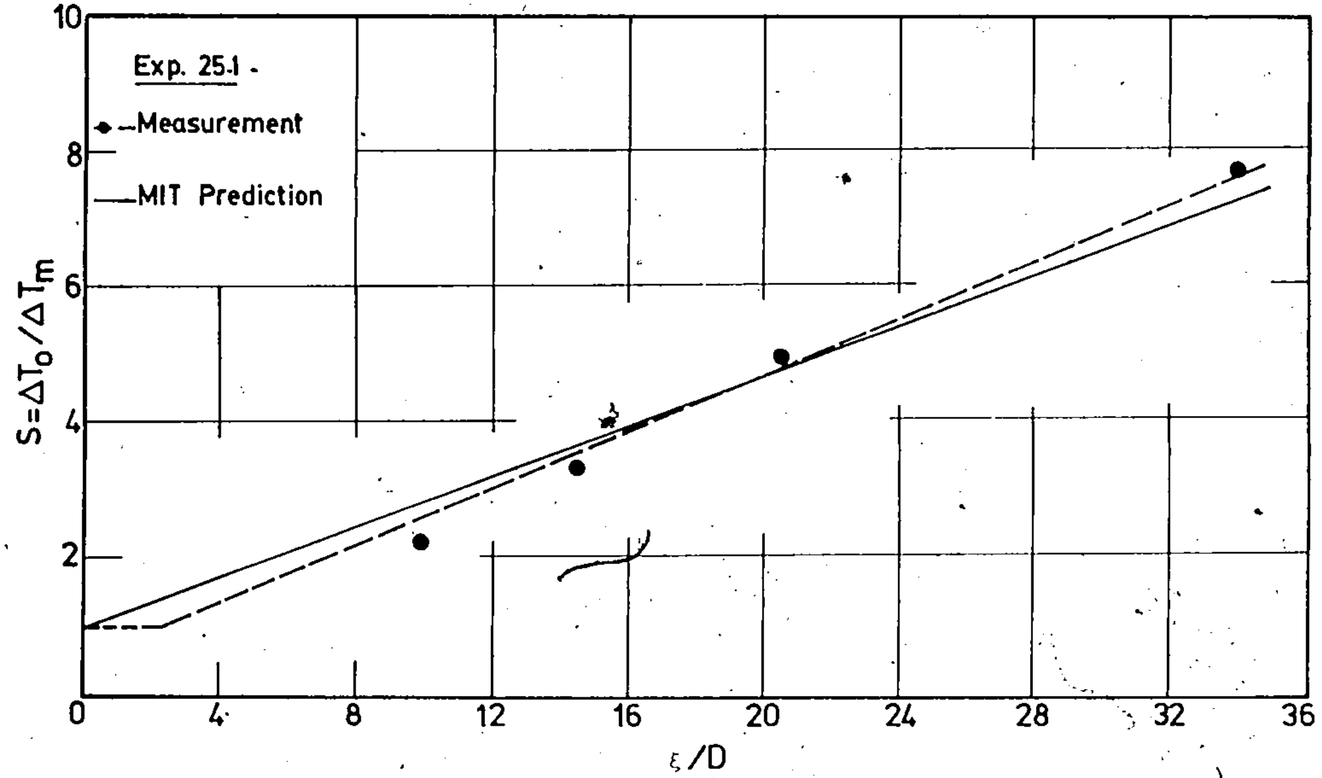

Fig. 6.38. Comparison of measured and predicted dilution - Exp. 25-1.

bottom attachment at x/D=3 where 10% of the maximum excess temperature at x/D=3 was measured at the bottom. However, due to the top hat profiles assumed by the MIT model, the model predicted a decrease in the jet width at the point of attachment, while the measurement of this study showed no reduction in jet width as a result of the attachment. For a smaller densimetric Froude number, Run 24-1, the agreement between the measured and the predicted jet width is fair near the source and becomes poor away from the source as shown in Fig. 6.39. One reason is that the MIT model assumed that buoyant and non-buoyant jet spreading are linearly additive. Therefore, when the inertia and the buoyant forces are of the same order, i.e., of magnitude, such as when F_o is not too large, the model tends to give inaccurate results.

Comparisons of the measured dilution, S , and the prediction of both MIT and PDS models are shown in Figs. 6.23 and 6.24 for experimental Runs 24-1 and 25-2, respectively. The agreement between the MIT prediction and the measurements is, in general, not as good as the PDS model. For a strong cross-flow, R=2.0, the MIT tends to underestimate the dilution factor whereas, for a weak cross-flow, R=5.2, the MIT model overestimates the dilution. In Fig. 6.23, the MIT predicts a reasonable value

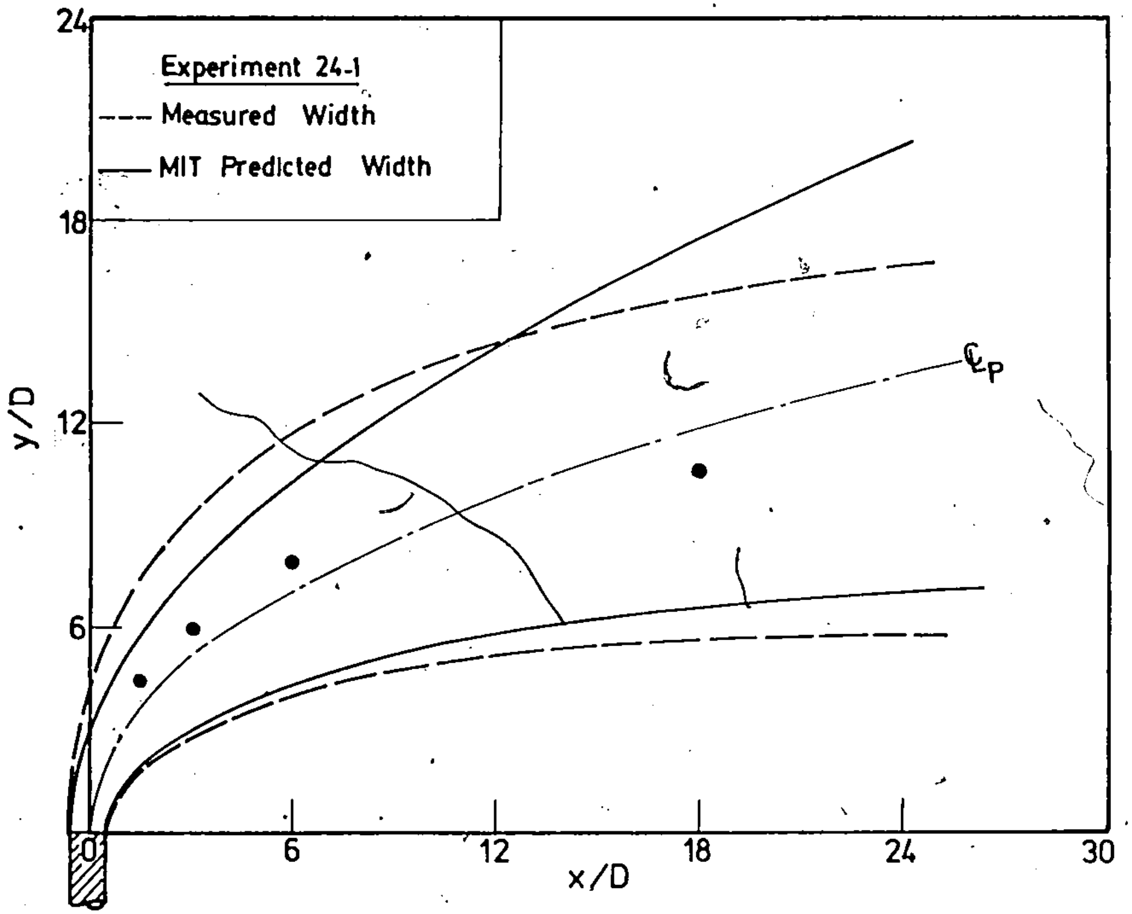

Fig. 6.39. Comparison of measured and predicted jet widths of Exp. 24-1.

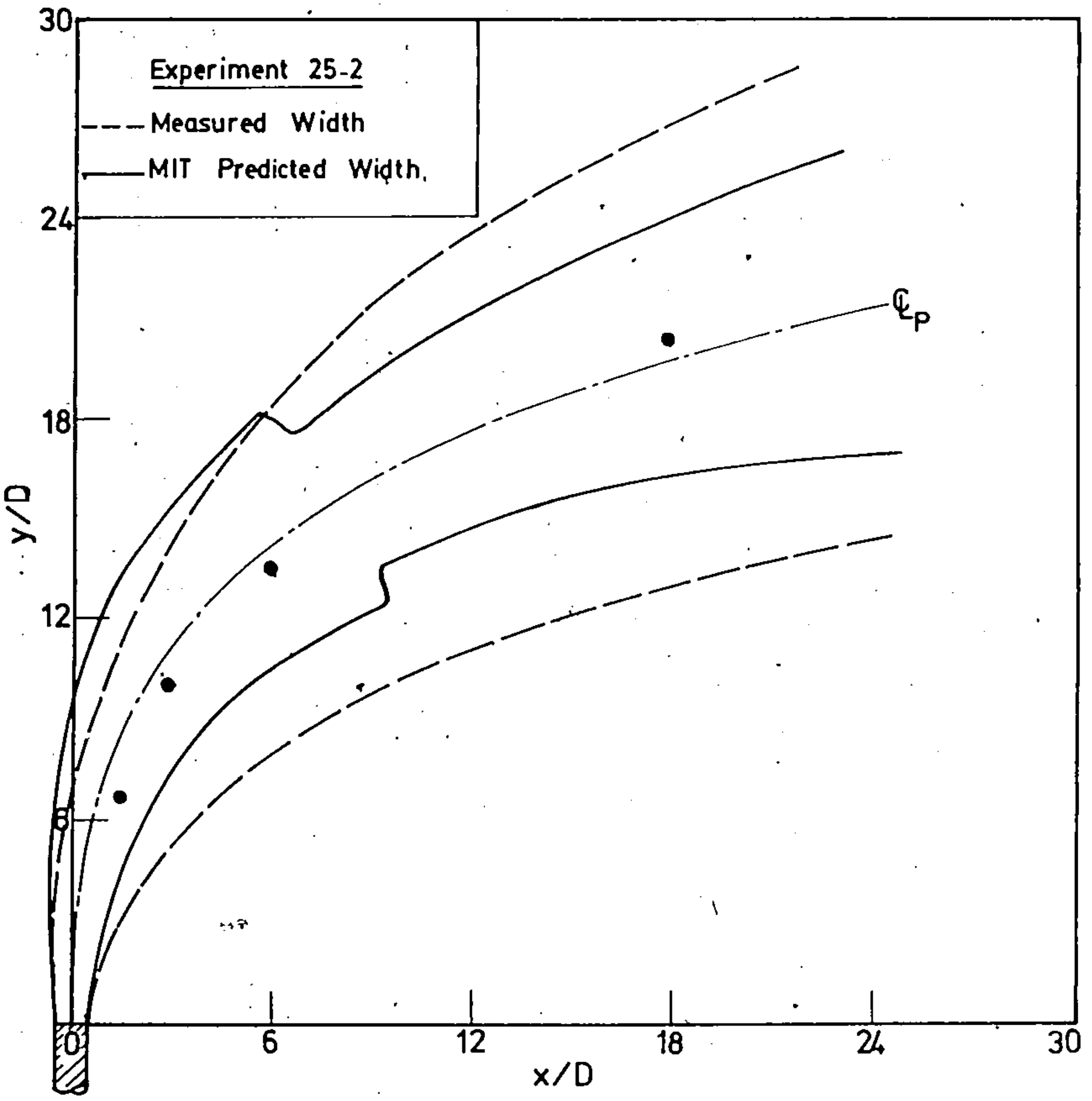

Fig. 6.40. Comparison of measured and predicted jet widths of Exp. 25-2.

of the dilution rate only when there is significant momentum mixing, i.e., close to the outfall. When the dilution is mainly due to buoyancy or stream generated turbulence, i.e., away from the outfall, the prediction is poor. In Fig. 6.24, the MIT shows a discontinuity in the slope of the dilution curve as a result of jet bottom attachment at $\xi/D=18$ and the dilution rate decreases henceforth. This is due to two assumptions made in deriving the model for attached jet. Firstly, Stolzenbach and Harleman set the entrainment velocity in the vertical direction equal to zero. This assumption is not exactly correct as some entrainment takes place at the interface. Secondly, they assumed that the mechanism of cross-flow entrainment is absent because the cross-flow can no longer penetrate under the jet to produce vortex motion.

The PDS has an advantage over the MIT in treating the zone of flow establishment. The MIT model neglects this zone and does not predict the length of the establishment zone. While in the PDS model, this zone is treated in a very simplified way; with the length of the establishment zone, ξ_i, was defined using the following empirical equation:

$$\frac{\xi_i}{D} = 5.4\left(\frac{A^2}{F_o}\right)^{1/3} \qquad (2.23)$$

The use of Eq. 2.23 to estimate ξ_i gave a good agreement with the experimental data as shown in Figs. 6.20, 6.23 and 6.24.

The MIT model is applied to the case of non-buoyant jet. The densimetric Froude number was set equal to 100. The experimental Runs 24 and 25 are compared with the MIT prediction in Figs. 6.41 and 6.42 for jet widths and in Figs. 6.27 and 6.28 for dilution. The measured jet widths were plotted for 0.683 of the area under the normal curves of Fig. 4.17 which correspond to $2\sigma_\eta$ to agree with the assumed shape functions of MIT model. The model shows a good agreement for both jet trajectory and width. Both the MIT model prediction and the measurements showed that the jet of Run 24 is confined with the sloping side of the channel (Fig. 6.41). For Run 25, Fig. 6.42, the MIT predicts jet attachment at longitudinal distance, x, equal to 4 times the pipe diameter, whereas, the experiment shows that the jet is completely attached at x/D=6 as shown in Fig. 4.33. However, the experimental measurements showed no reduction in the jet width as the MIT predicts. The reduction in the MIT is due to the discontinuity in the assumed shape function of the detached and attached jets.

Finally, the measured dilution and the MIT prediction are shown in Figs. 6.27 and 6.28 for Runs 24 and 25, respectively. For the purpose of comparison, the PDS predictions are also shown in Figs. 6.27 and 6.28. It appears that the PDS model shows a better agreement with the measurements than the MIT model. The PDS also estimates the length of the development zone which agrees with the measurements. The MIT shows a reasonable agreement with experimental data of Run 24 which has R=2.0, but only up to $\xi/D=9$. In this zone, the mixing is mainly due to momentum. Beyond this zone, the MIT predicted dilution starts to level off and the agreement with the measurements is poor (Fig. 6.27). Figure 6.28 shows that the MIT model tends to overestimate the dilution when the jet is detached and underestimate the dilution for the attached part.

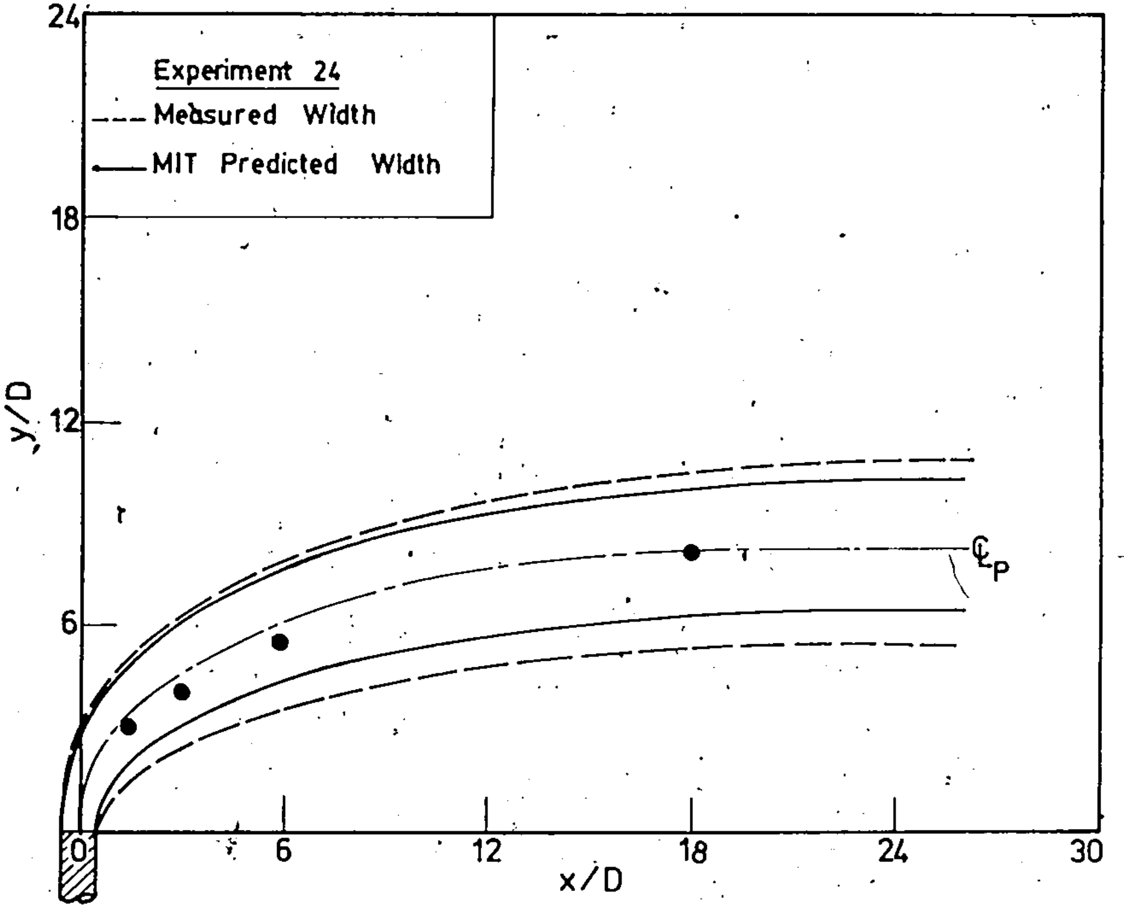

Fig. 6.41. Comparison of measured and predicted non-buoyant jet widths of Exp. 24.

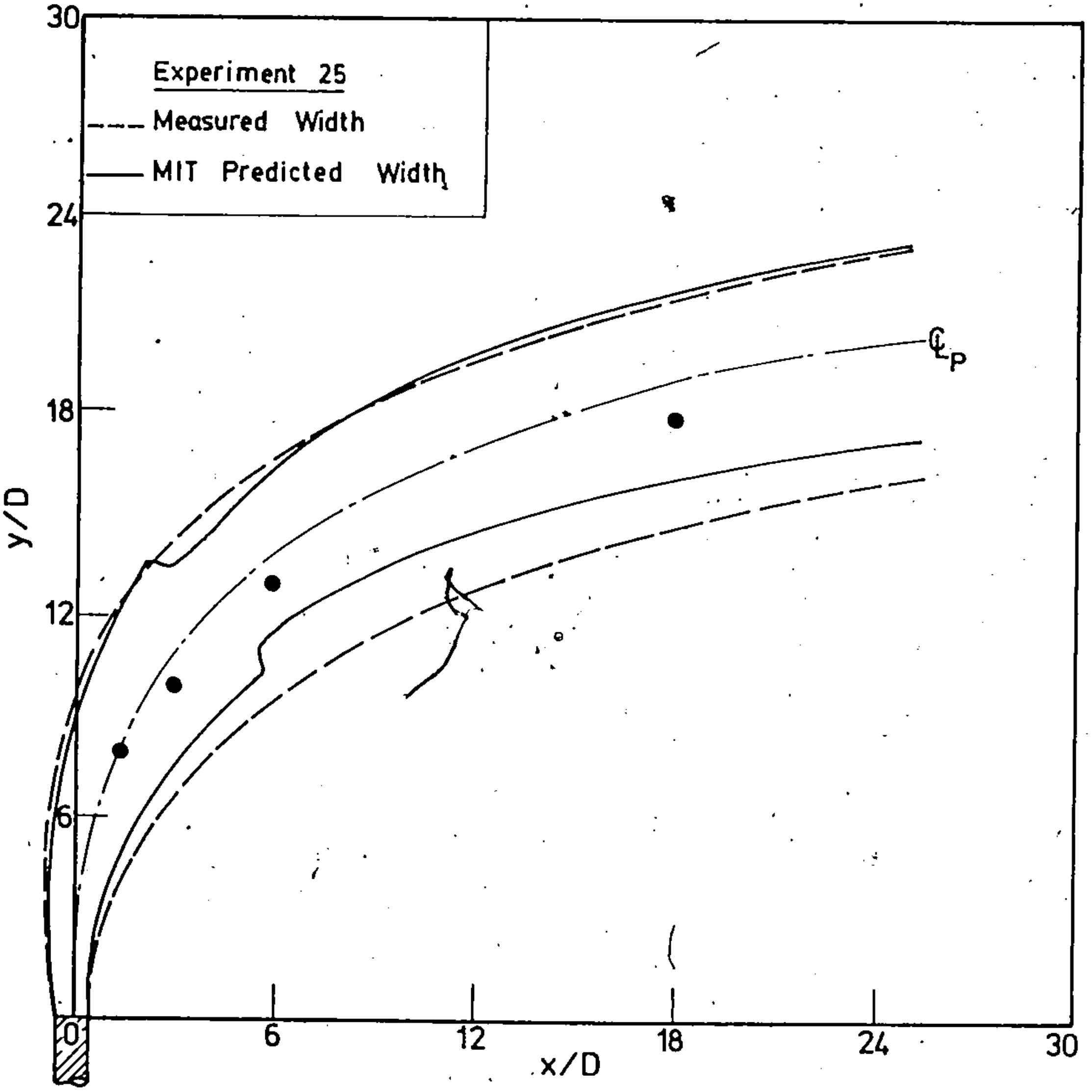

Fig. 6.42. Comparison of measured and predicted non-buoyant jet widths of Exp. 25.

CHAPTER VII

CASE OF STUDY: MODELLING OF CHLORINE RESIDUALS IN THE DETROIT RIVER IN THE VICINITY OF WEST WINDSOR POLLUTION CONTROL PLANT

7.1 GENERAL

The near-field models (PDS and MIT) were calibrated for the case of submerged outfall using the experimental data of this study. The near-field models and the far-field model (UOW-MOE) were validated using the field data for a nonconservative pollutant, total residual chlorine, collected from the Detroit River in the vicinity of West Windsor Pollution Control Plant (WWPCP).

7.2 DESCRIPTION OF FIELD STUDY

The study reach of the Detroit River, shown in Fig. 7.1, is 1000 m long. The field study is located downstream West Windsor Pollution Control Plant outfall, i.e., between latitudes 42°16'40" to 42° 17'15" and longitudes 83°05'30" and 83°06'00". The field tests were carried out on September 7, 1984. During the test, cross-sectional distribution of various parameters required for the modelling studies were collected at eight longitudinal sections, identified on

Fig. 7.1 by stations ST. 1 to ST. 8.

The West Windsor Pollution Control Plant (WWPCP) is located on a 36 acre site on the south-east corner of Ojibway Parkway and Sandwich Street, having an ultimate capacity of 265 million litres per day (60 MGD). The existing plant provides physical chemical treatment for 155 million litres per day (34 MGD). It also provides grit removal and chlorination for additional 265 MLD (65 MGD) of combined sewer-storm water (Harding and Romano, 1981). The effluent from WWPCP is discharged into the Detroit River through a circular pipe of 800 m long and 2.7 m diameter that extended 5.0 m from the east bank into the River. The crown of the pipe is 2.5 m below the water surface. Views of the river in the vicinity of the outfall are presented in Photographs 7.1 and 7.2.

At the time of the field study, the effluent flow rate was 3.0 m^3/s (260 million litres per day) and the mean total residual chlorine concentration in the effluent was 0.5 mg/L (Faust 1984). The average river flow was 5000 m^3/s (U.S. Army Corps of Engineers 1979) and the average upstream temperature was 18.8°C. The average and maximum wind speeds were 15 and 26 $km.h^{-1}$ from the south. At the time of the test, the wind speed was 17 $km.h^{-1}$ from the south, i.e., blowing from the Canadian shore towards the American shore, and the precipitation was 1.8 mm. The cross-sectional depth

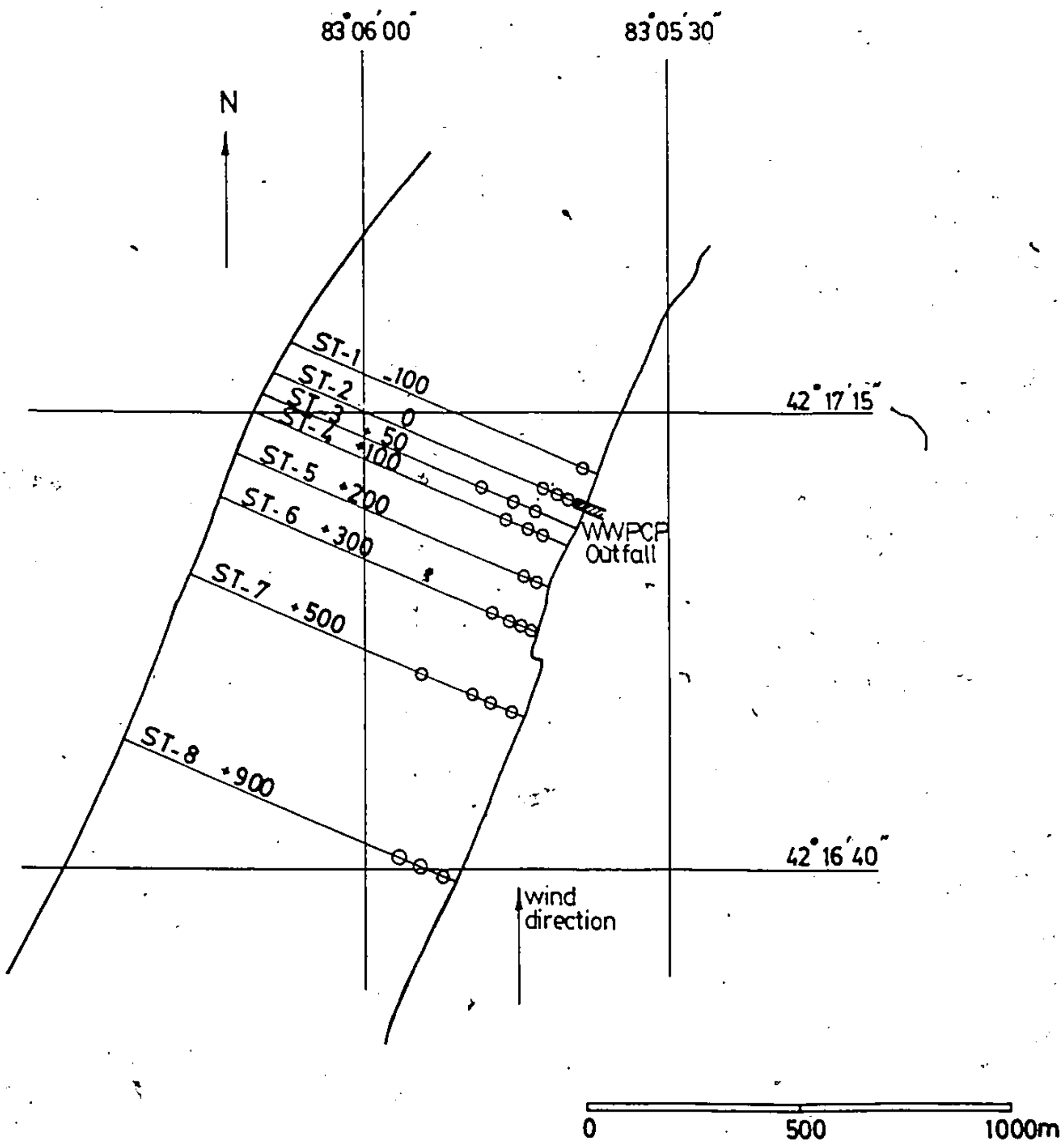

Fig. 7.1. Layout of the Detroit River study stretch.

COLOURED PICTURES
Images en couleur

Photo 7.1 View of WWPCP outfall.

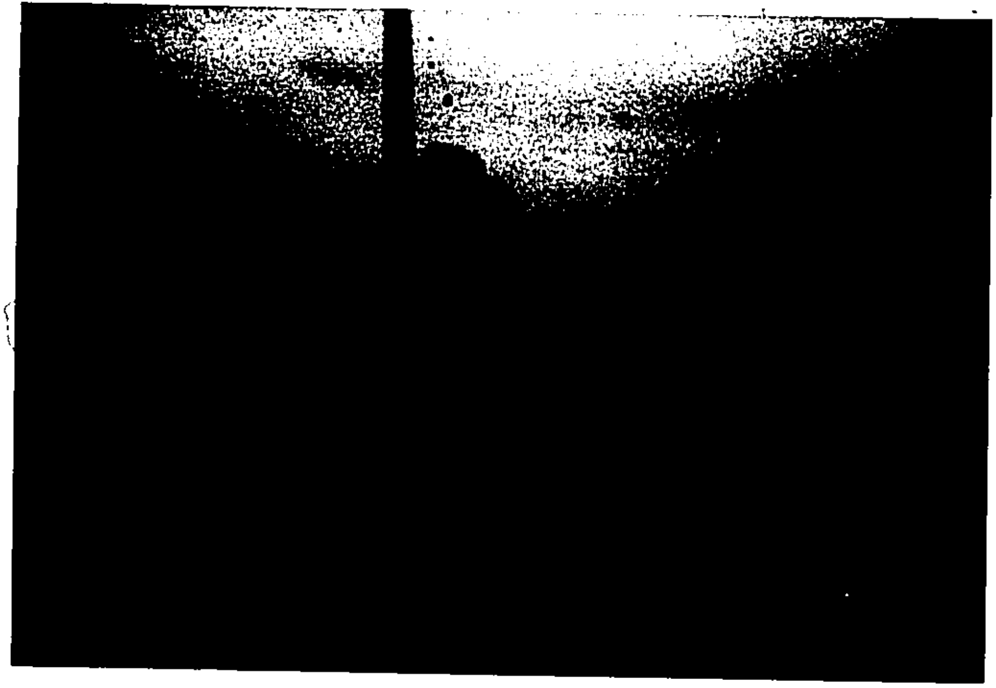

Photo 7.2. View of the effluent plume looking downstream.

profiles were obtained from the U.S. Department of Commerce maps (1979).

During the tests, water samples were taken from a depth of 3.0 m below the water surface using the sampler shown in Photograph 7.3. The samples were poured into 300 mL bottles and the temperature was measured using a thermistor with an accuracy of ±0.1°C. The samples were preserved by adding 1 mL of potassium iodide solution and 1 mL of acetate buffer solution pH4 and kept away from light. The river surface velocity was measured at selected stations using a magnetic current meter manufactured by Marsh and McBirney. At each station, the current meter was lowered to 1.5 m below the water surface and the velocity reading was taken when the boat was anchored. The samples were analyzed for total residual chlorine by the amperometric technique within two hours of sample collection. A correction factor was calculated using Eq. 5.70 to account for the chlorine decay between the time of data collection and analyzing the samples. A correction factor of 2% was added to all the TRC data. The TRC concentrations, temperature and velocity at various sampling points for the duration of the survey are summarized in Table 7.1.

The excess surface temperature contours and the total residual chlorine contours for the stretch reach was plotted in Fig. 7.2 and 7.3 respectively. These figures indicate

Table 7.1

Summary of the Collected Field Data (Total Residual Chlorine, Temperature and Velocity)

	y, m x, m	10	15	50	100	200
	ST. 1 -100			0.0mg/L 18.8°C 0.25m/s		
	ST. 2 0.0	0.2mg/L 20.9°C	0.14mg/L 20.1°C 0.1m/s	0.0mg/L		
	ST. 3 +50			0.1mg/L 20.0°C	0.03mg/L	0.0mg/L
	ST. 4 +100		0.04mg/L 18.9°C 0.15m/s	0.1mg/L 19.4°C	0.09mg/L 19.5°C	
	ST. 5 +200		0.04mg/L 18.8°C	0.07mg/L 19.2°C		
	ST. 6 +300	0.04mg/L 19.0°C	0.04mg/L 19.3°C	0.07mg/L 19.2°C	0.05mg/L 19.3°C	
ST.7 +500	0.04mg/L 19.1°C			0.045mg/L 19.2°C	0.03mg/L 19.1°C	0.018mg/L 19.1°C 0.6m/s
ST.8 +900	0.03mg/L 19.1°C 0.02m/s			0.035mg/L 19°C	0.03mg/L 18.9°C 0.3m/s	

Photo 7.3. The sampler and the thermistor used in the field data sampling.

that the initial mixing near the effluent is very high due to the combined effects of outfall protrusion and momentum of the jet. The maximum jet spreading is approximately 250 m from the east bank. The TRC concentrations were found to be below the detection level, i.e., below 0.01 mg/L, at 2000 m downstream of the outfall. The shallow zone shown in Figs. 7.2 and 7.3 and between $x=400$ and 900 m, represents a stagnant flow with recirculation and a build up of both temperature and TRC concentration. Due to the nonuniformity in the river velocity and the presence of the sudden increase in the river width at $x=400$ m, the jet bends over towards the shoreline as shown in Figs. 7.2 and 7.3 The jet trajectory changes its direction by approximately 30° towards the shore at $x=300$ m, ST-6. The contour patterns of both the excess temperature and total residual chlorine show a similar trend indicating that the jet trajectory and the dilution can be detected from either data.

A contour plot of the surface velocity distribution for the study stretch is shown in Fig. 7.4. The contour lines were based on the field measurements and the data obtained from U.S. Army Corps of Engineers (1974). The jet tends to block the stream flow and deflect the velocity contours away from the shore. The velocity returned to its normal distribution at $x \geq 200$ m. Figure 7.4 also indicates that the stream velocity is nonuniform, especially near the out-

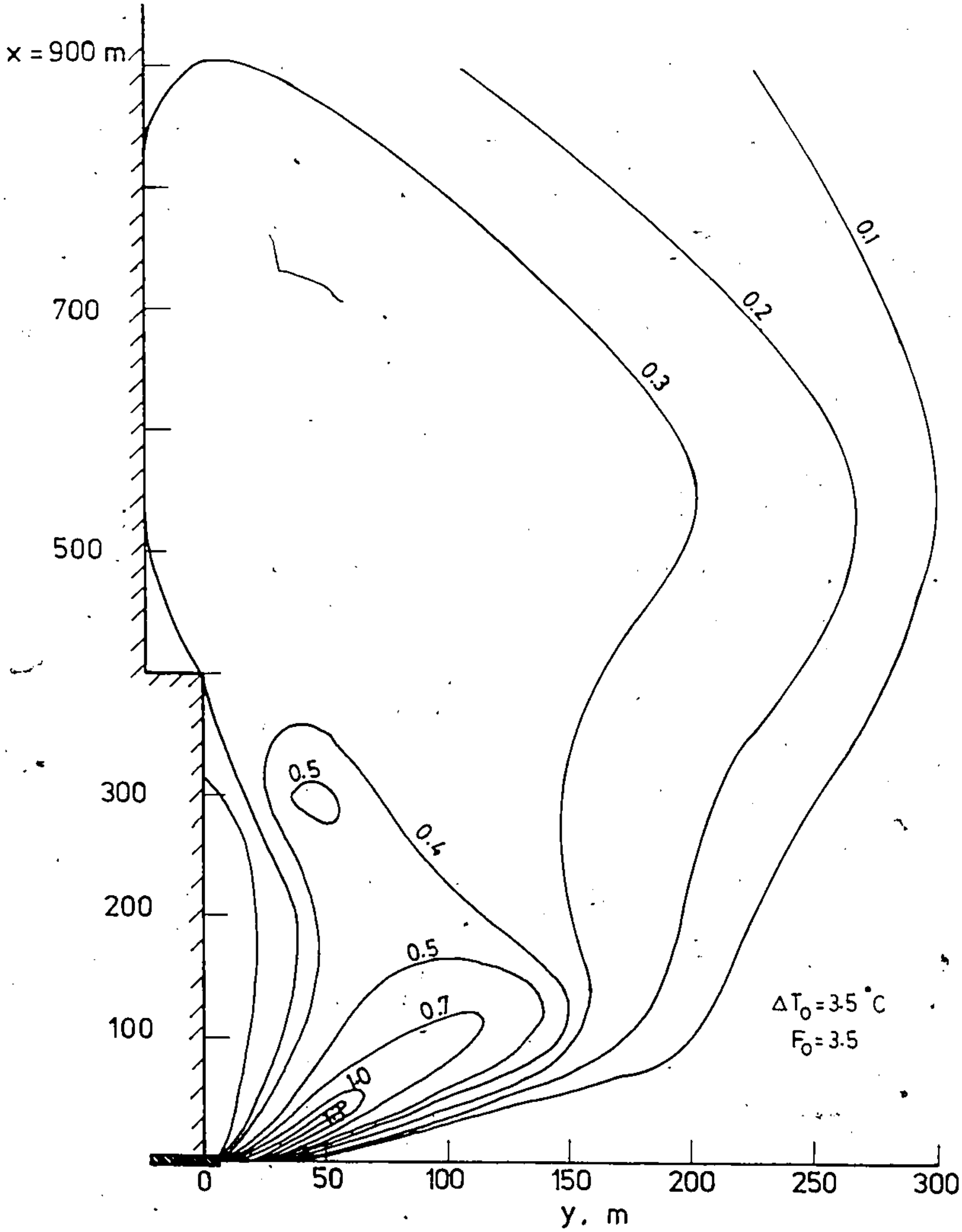

Fig. 7.2. Contours of excess temperature, ΔT, °C.

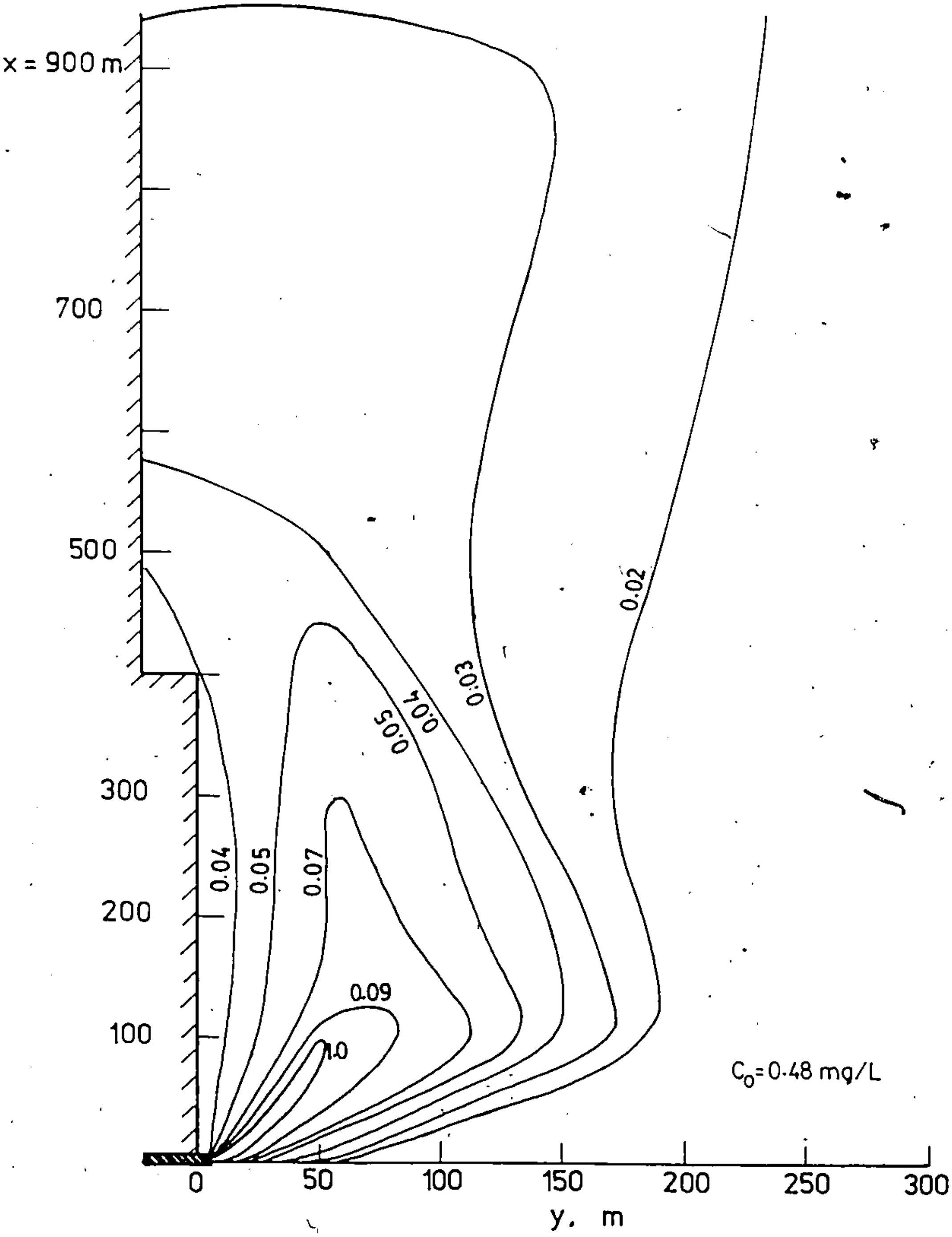

Fig. 7.3. Contours of total residual chlorine, TRC, mg/L.

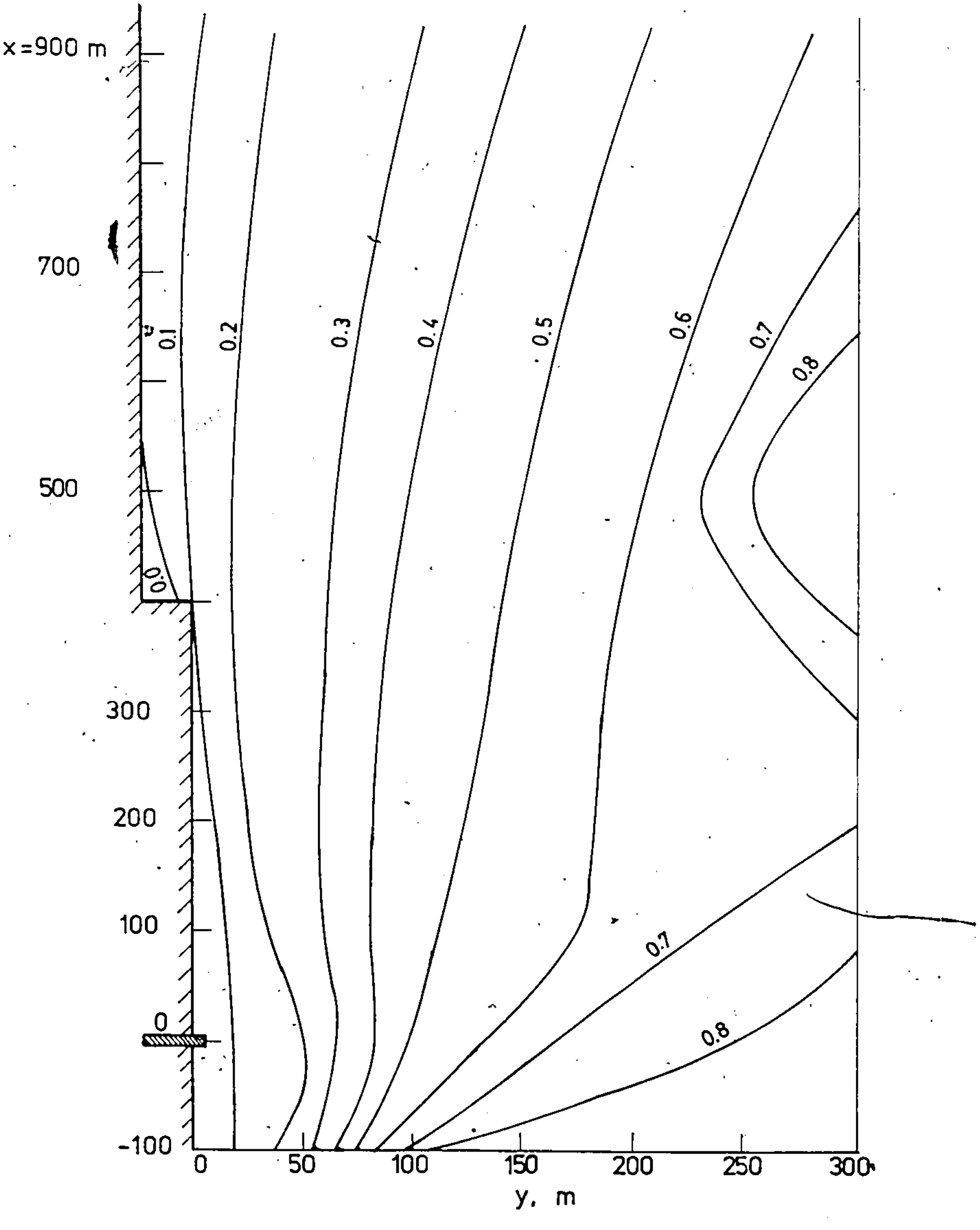

Fig. 7.4 Contours of surface velocity in m/s.

fall. A small recirculation area was detected at x=400 m where the river width is suddenly increased.

7.3 CALIBRATION OF THE NEAR-FIELD MODELS FOR THE CASE OF SUBMERGED OUTFALLS.

The PDS and MIT near-field models focus on surface discharges. Since the WWPCP outfall is submerged, calibration of both near-field models was needed in order to apply these to this case. The experimental run 26-1 which had F_O=19.14, R=7.8 on the side slope and 4.9 on the main channel and H/D=5.5 was selected for the calibration. The pipe was located 3 inches below the water surface as shown in Fig. 4.31.

7.3.1 PDS Model Calibration

In Chapter VI, it was found that the jet trajectory is sensitive to the entrainment coefficient, E_O, the horizontal turbulent exchange coefficient, E_H, and the drag coefficient, C_D. Therefore, the model calibration was made by adjusting E_O,E_H and C_D and comparing the predicted jet trajectory and minimum dilution with the measured results.

For the submerged jet, it is expected that E_O and E_H would be higher than those of the surface jet because the entrainment occurs on all sides of the jet. The drag coefficient is also expected to increase due to the increase of the differential pressure on the sides of the jet. Several computer runs were made with different values of E_o, E_H and C_D and compared with the experimental results of Run 26.1. The predictions of the run that were in close agreement with the measurements were obtained with $E_o=0.15$, $E_H=0.05$ and $C_D=3.0$ and are shown in Figs. 7.5 and 7.6 for mean trajectory and dilution respectively.

7.3.2 MIT Model Calibration

The sensitivity analysis of MIT model indicated that the most important coefficients affecting the trajectory are the cross flow entrainment coefficient, α_c, and the drag coefficient, $C_{D_{22}}$. Therefore, several computer runs were made by selecting different combinations of α_c and $C_{D_{22}}$. Fair agreements between the observations and the predictions of the jet trajectory and dilution, shown in Figs. 7.5 and 7.6, were obtained with $\alpha_c=0.3$ and $C_{D_{22}}=3.0$. The model calibration attempt resulted in a significant increase in α_c and $C_{D_{22}}$ values compared to those obtained for the surface jets. The higher value of α_c reflects the effect of more entrainment from all sides of the jet and the increase of gravity (buoyancy) mixing. The high value of $C_{D_{22}}$ indicates an increased differential pressure on the sides of the jet.

7.4 VALIDATION OF THE ~~NEAR-FIELD~~ MODELS

The field data have been utilized for the validation

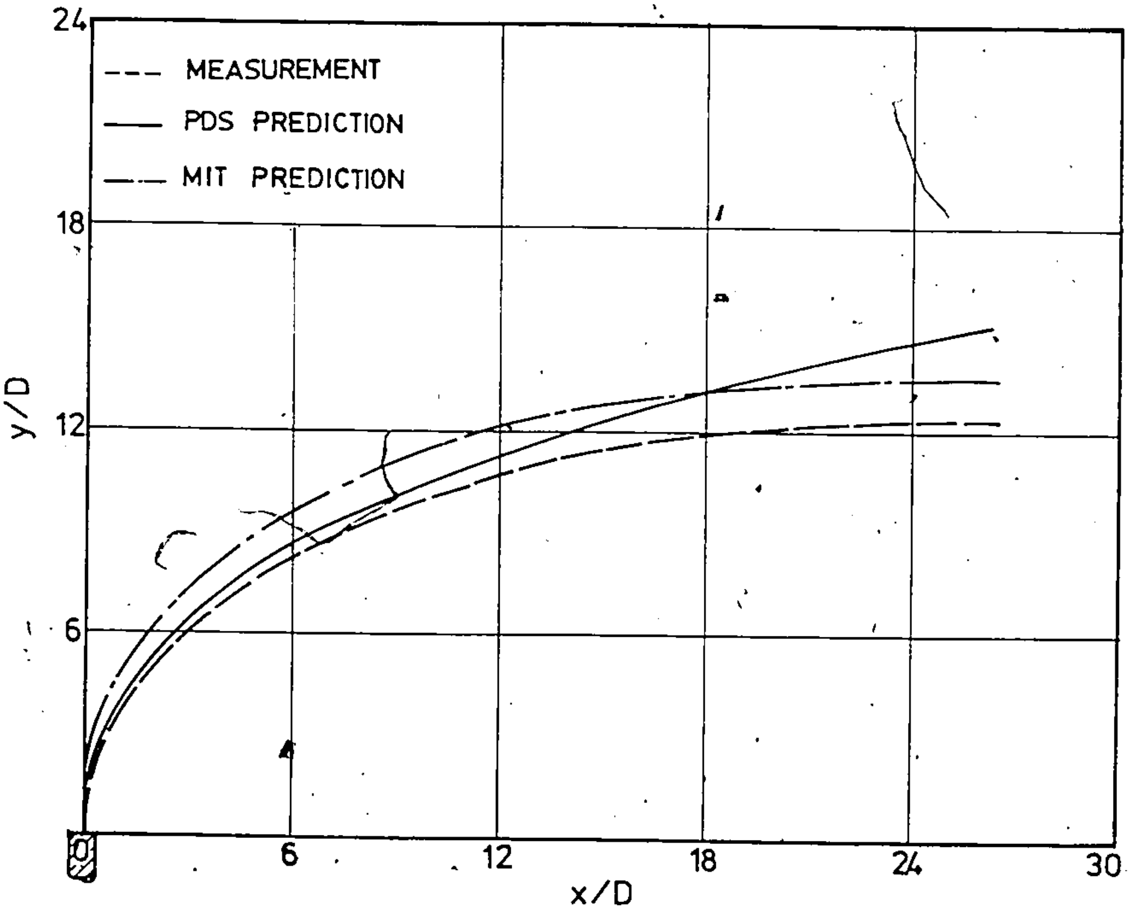

Fig. 7.5. Comparison of measured and predicted jet trajectories for submerged outfall, Run 26-1.

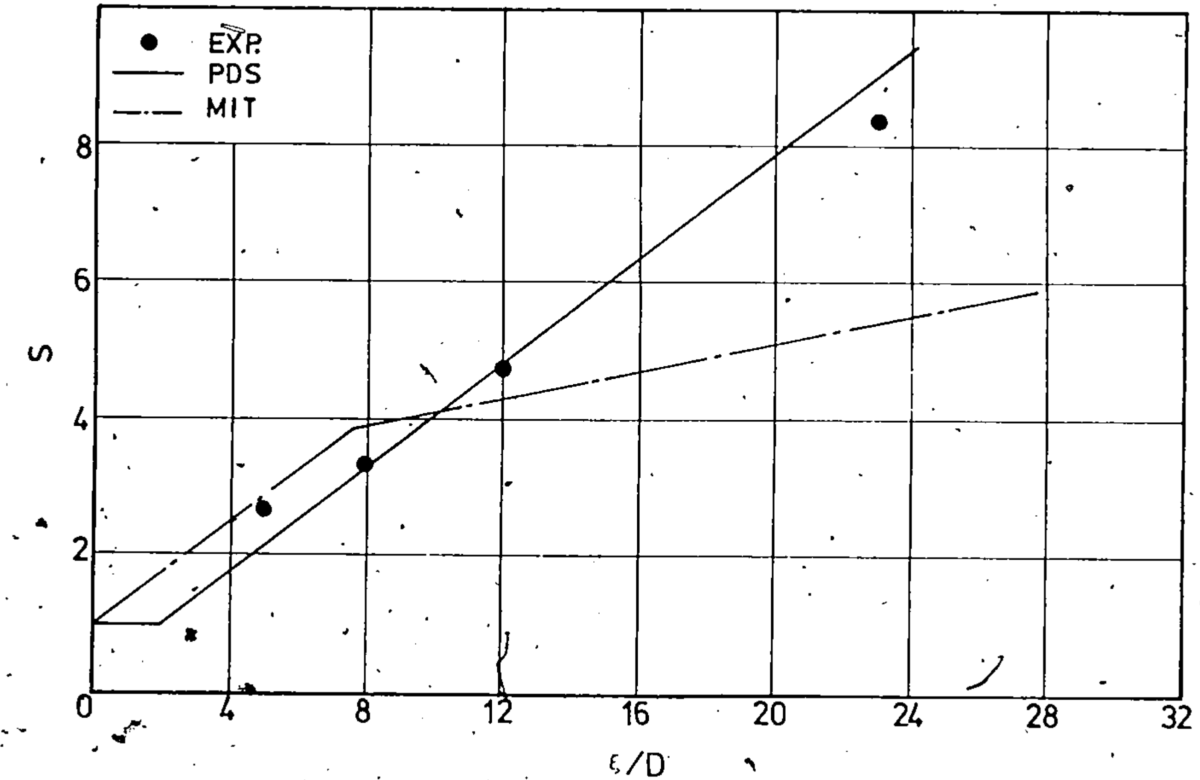

Fig. 7.6. Comparison of measured and predicted dilution for submerged outfall, Run 26-1.

of both the PDS and MIT near-field models. The field jet trajectory was obtained by tracing the locus of maximum excess temperature shown in Fig. 7.2 and that of maximum TRC concentraion shown in Fig. 7.3. Figures 7.7 and 7.8 show comparative plots of the observed results and the PDS and MIT predictions for the jet trajectory and dilution, respectively. The values of the coefficients used in both models were the same as those obtained from the model calibration. The PDS jet trajectory predictions were terminated at longitudinal distance x=130 m downstream of the outfall because the area enclosed by the isotherm is less than a specified value and the local Froude no. became too small resulting in a singularity in the solution and a discontinuity in the jet data. The comparison of the observed jet trajectory and the PDS prediction showed some differences at x>40 m. The observed trajectory may have been affected by initial mixing due to the combined effect of the momentum of the jet and the protrusion of the outfall, thus resulting in deeper penetration of the jet. Also, the field results showed that the velocity ratio, R, varies significantly from 5.0 at the outfall to 0.5 at other locations which undoubtedly affected the trajectory; the PDS assumes a uniform velocity ratio. Moreover, the offshore wind may affect the jet resulting in wider and greater penetration of the jet; the PDS neglects the wind effect.

Ratios of the initial to the maximum TRC concentration, C_o/C_m, and the initial to maximum excess temperature, $\Delta T_o/\Delta T_m$, are plotted in Fig. 7.8 as a function of ξ/D where ξ is measured along the jet trajectory. As expected, the minimum dilution as estimated for both approaches are very close. The minimum dilution predictions from both the PDS and MIT models are also shown in Fig. 7.8. The PDS predictions are generally in a good agreement with the observed data. However, the dilution rate for $\xi/D \leq 7.5$ was underestimated by the PDS as shown in the figure. This indicates that the initial mixing in the river in the vicinity of the outfall is very high and the existing near-field models fail to predict this dilution level.

The MIT predictions were terminated at longitudinal distance, x=60 m, as shown in Fig. 7.7 where the jet attaches to the side wall. However, the agreement between the predicted and the field jet trajectories for this distance is better than the PDS prediction. This is a result of including the depth variation in the MIT model. Nevertheless, it was decided to use the PDS model predictions as input to the University of Windsor far-field model.

It would be useful to check the validity of the general Eqs. 5.64 and 5.67 for jet trajectory and minimum dilutions, respectively on the field stretch under consideration using the following values:

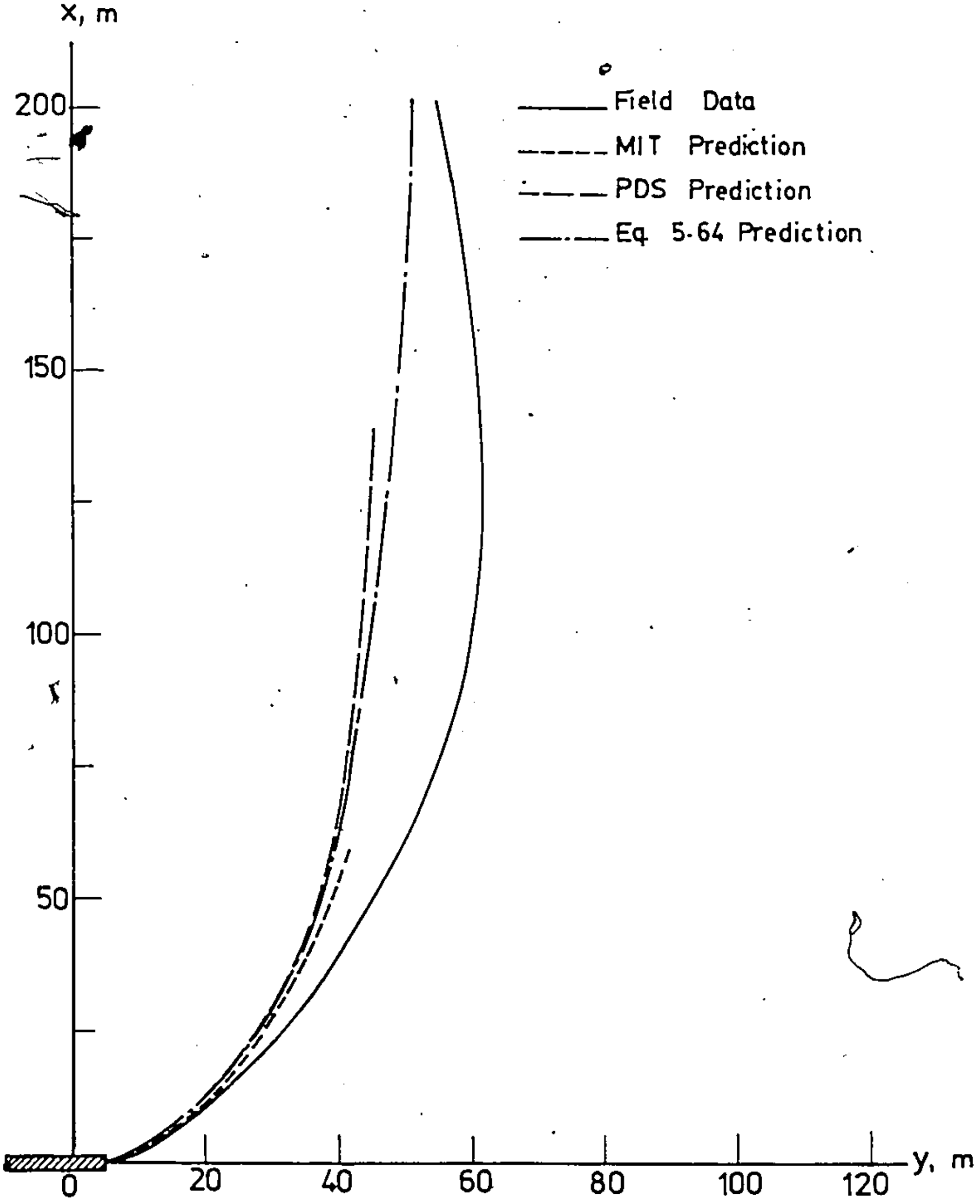

Fig. 7.7. Comparison of predicted and observed near-field jet trajectories.

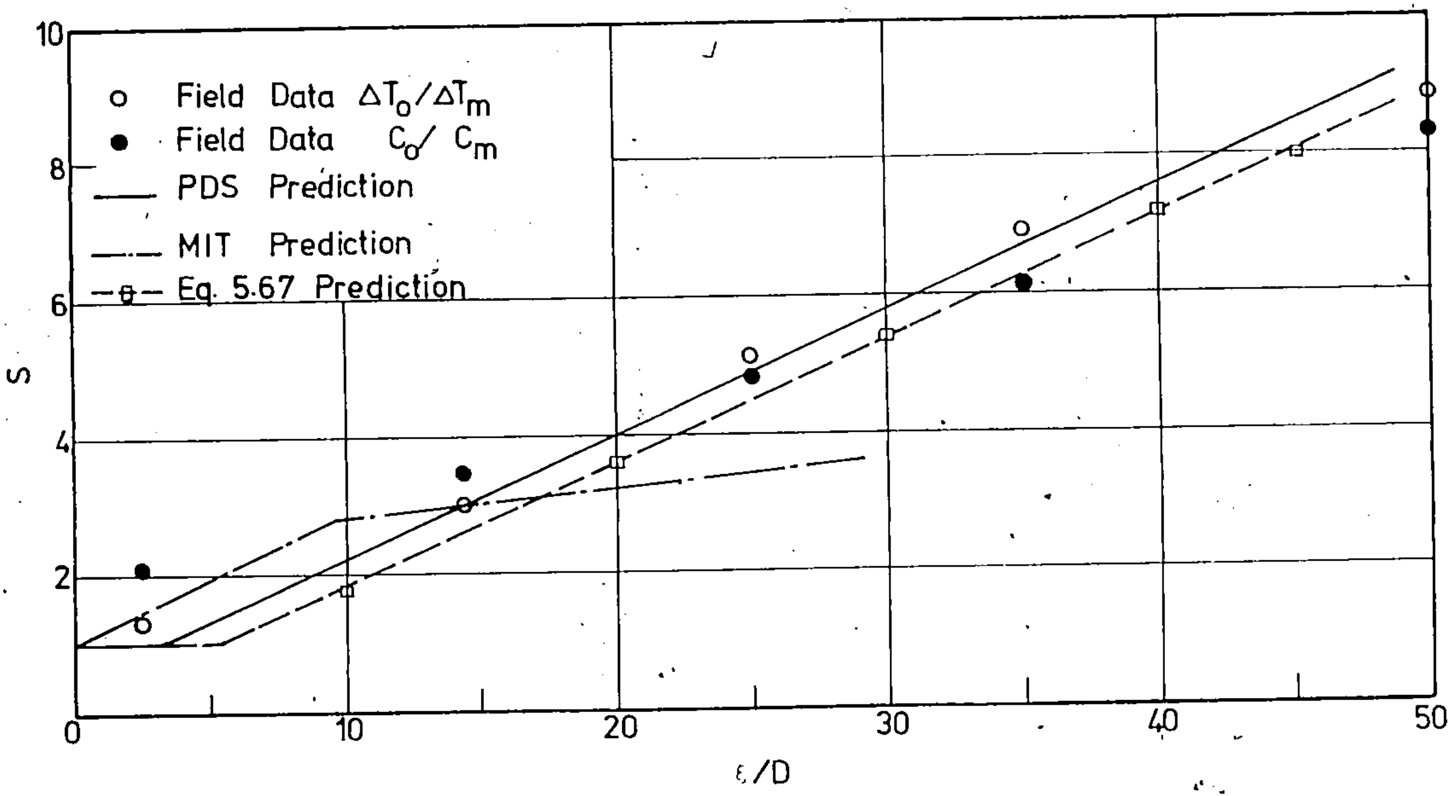

Fig. 7.8. Comparison of predicted and observed near-field dilution.

velocity ratio $R = 3.0$

densimetric Froude no. $F_o = 3.5$

relative depth $\frac{H}{D} = 2.7$

pipe position $\frac{Z_p}{H} = 0.8$

The predicted jet trajectory and dilution curve are shown in Figs. 7.7 and 7.8. In general, the predictions are in a good agreement with the observed data especially near the source. However, some differences were observed further downstream from the outfall due to the wind effect and the assumption of constant velocity ratio.

7.5 DESCRIPTION OF THE FAR-FIELD MODEL

The far-field numerical model developed by the University of Windsor - MOE group (McCorquodale et al. 1983) was used to simulate the dispersion of the total residual chlorine discharged from WWPCP into Detroit River. The river is discretized by using a rectangular grid in the longitudinal, x, and lateral , y, directions as shown in Fig. 7.9. The grid size must be specified such that:

$$DX = DSTN/N \tag{7.1}$$

$$DY = DDY/M \tag{7.2}$$

where

DSTN = distance between input cross-sections, m

DDY = width increment between input depth in each cross-section, m

N,M = integers.

In this study, Eq. 5.85 for the overall decay rate of pollutants after mixing in the rivers has been proposed:

$$k_T = F_{TB}[k_{EV}+k_{PH}+k_{OX}+k_{HY}]\theta_1^{T-20} \qquad (5.85)$$

For chlorine, the overall decay rate, k_T, depends on turbulence, evaporation, photolysis, oxidation and temperature. The experimental investigation of this study gave the following values for various rate constants:

F_{TB} = turbulence factor = 2.05

k_{EV} = rate coefficient for evaporation $= \frac{k_{OL}}{H}$

$= \frac{0.013}{H}$ day^{-1}

k_{PH} = rate coefficient for photolysis = 0.03 day^{-1}

k_{OX} = rate coefficient for free radical oxidation

= 0.065 day^{-1}

θ_1 = temperature correction factor = 1.08.

A special initial condition is required at the WWPCP outfall to start the finite-difference solution. The pollutant is mixed into a preselected stream sub-section, shown shaded in Fig. 7.9, by applying the mass balance equation. The location and dimensions of this sub-section depend

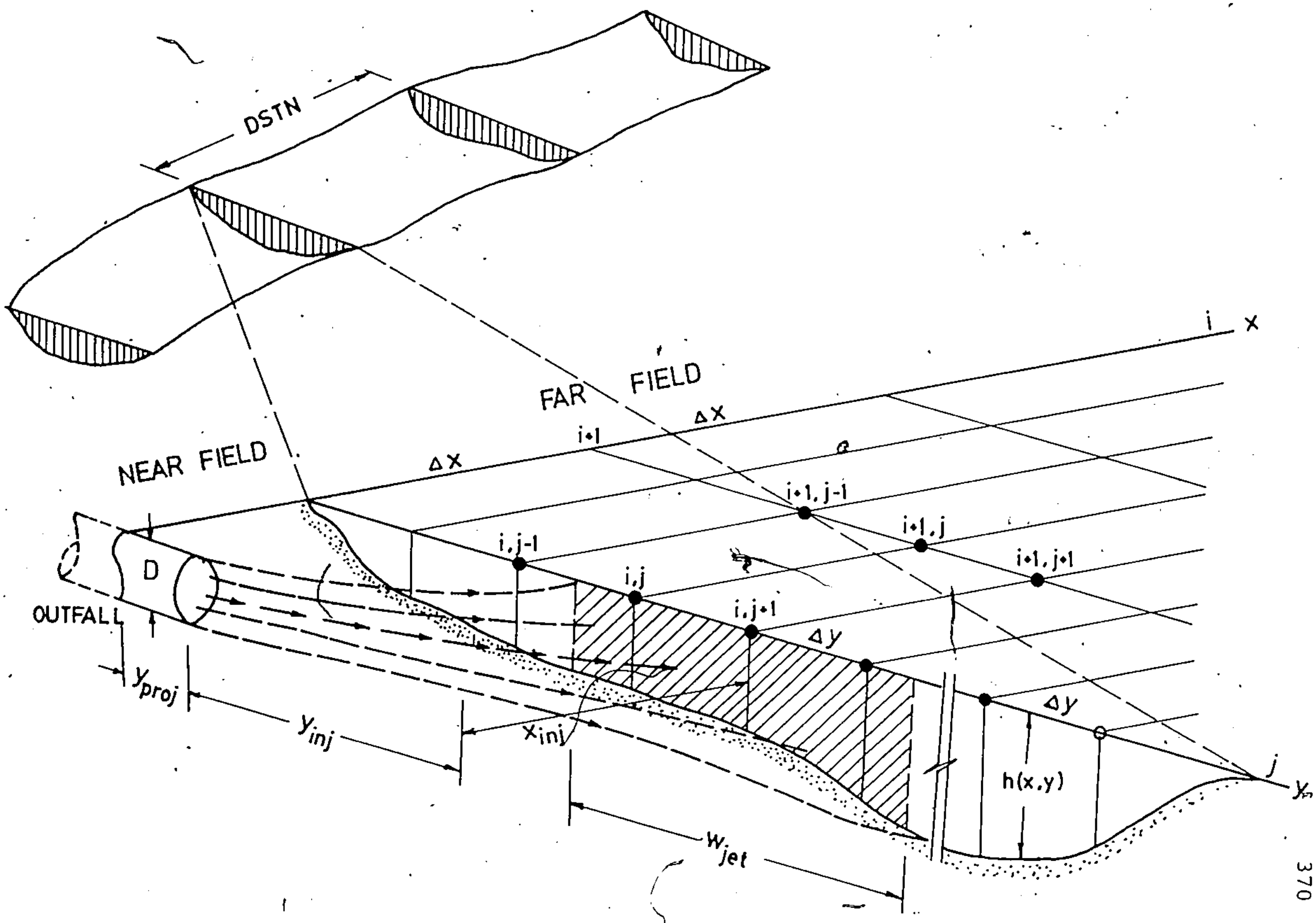

Fig. 7.9. Discretization of the River (after McCorquodale *et al.* 1983).

on the outfall characteristics and the flow distribution in the river. The pollutant concentration in this sub-section, $C_{i,j}$, is obtained from McCorquodale et al. (1983):

$$C_{i,j} = \frac{C'_{i,j}Q'_{i,j} + C_{i_f}Q_{i_f}}{Q'_{i,j} + Q_{i_f}} \qquad (7.3)$$

where

$C'_{i,j}$ = concentration at (i,j) without the outfall contribution

$Q'_{i,j}$ = river flow through the area of influence of (i,j)

C_{i_f} = pollutant concentration at the outfall

Q_{i_f} = outfall discharge

They approximated the lateral injection distance, y_{inj}, the minimum dilution, S, and the jet width, w_{jet}, respectively by:

$$y_{inj} = 2.05\ (RD)^{0.72}\ (x_{inj})^{0.28} \cos\theta_o \qquad (7.4)$$

$$S = \frac{1}{2}\left(8\frac{H}{\sqrt{A_j}} \cdot \frac{1}{R}\right) \qquad (7.5)$$

$$w_{jet} = \frac{SQ_{i_f}}{U_a H} \qquad (7.6)$$

where

x_{inj} = the longitudinal injection distance

U_a, H = the local ambient velocity and depth of the point (X_{inj}, Y_{inj})

A_j = outfall area

In the University of Windsor-MOE model, the dispersion coefficient was assumed to be proportional to the shear velocity, U_*, and the depth of flow, H, (Hamdy and Kinkead 1979),

$$D_y = \alpha U_* H \qquad (2.52)$$

where α is the dispersion factor and the shear velocity was obtained from

$$U_* = n\, U_a \sqrt{g}/H^{1/6} \qquad (7.7)$$

where n is Manning's coefficient = 0.026. A value of α =1.0 was observed by Hamdy and Kinkead (1979) for the St. Clair River and was used by McCorquodale et al. (1983) and also in the present study.

A preliminary computer run showed that Eq. 7.3 tends to overestimate the values of $C_{i,j}$ near the shore. This is due to the smaller depth and lower velocities at the side slope which resulted in a smaller $Q_{i,j}$ and higher $C_{i,j}$. Therefore, it was decided to use Eqs. 5.64 and 5.67, derived from this study, to estimate the initial values of $C_{i,j}$. Those values follow a Gaussian distribution, which was found to agree with the measured values of $C_{i,j}$.

The equivalent jet width, w_{jet}, the lateral injection distance, y_{inj}, and the longitudinal injection distance, x_{inj}, must be specified to the program. These values are also available from the PDS near-field model prediction or from direct field measurements shown in Fig. 7.3. The program also has an option to calculate y_{inj} from the trajectory equation, Eq. 5.64, and the dilution from Eq. 5.67 as derived from the experimental investigation of this study. A distance y_{proj} must be added to y_{inj} to determine the lateral position of the mixing sub-section.

7.6 APPLICATION OF THE FAR-FIELD MODEL

The numerical far-field model was applied on the 1000 m stretch of Detroit River, shown in Fig. 7.1, to obtain lateral and longitudinal concentration profiles of total residual chlorine. The near-field zone was assumed to end at x=150 m from the outfall as shown in Figs. 7.2 and 7.3. The width of the effluent jet, w_{jet}, and the penetration, y_{inj}, at this transect were estimated from the PDS model and the observed TRC distributions. They are 130 m and 42 m from the PDS and 150 m and 55 m from the field data. Equations 5.64 and 5.67 give values for w_{jet} and y_{inj} of 110 m and 45 m respectively. Comparative plots of measured distributions and far-field predictions at x=200, 300, 500 and 900 m downstream the outfall are presented in Fig. 7.10. In this figure, the predictions of the University of Windsor far-field model (McCorquodale et al 1983) were obtained using various initial values of y_{inj}, w_{jet} and $C_{i,j}$ at the end of the near-field, i.e., predictions based on (a) the empirical equations of this study, (b) the PDS output, and (c) the field measurements.

The far-field predictions based on the empirical equations showed some differences at x=200 and 300 m. The predicted jet width did not agree with the observed width because the initial width at x=150 m was smaller than the actual initial width. However, at x≥500 m, a reasonable agreement was observed in the jet width and TRC values.

The predictions based on the initial values from the PDS model gave a good agreement with the observed distributions at x≥300 m as shown in Fig. 7.10. However, the predictions show lower jet width than the observed values at each transect. The assumed initial Gaussian distributions by the PDS model and Eq. 2.24 appear to give a better representation than Eqs. 7.3 to 7.6. However, Eq. 7.3 must be used as a check on the mass conservation. In fact, both the PDS and the empirical Eqs. 5.64 and 5.67 satisfied Eq. 7.3.

The comparison of the observed and predicted distributions based on the initial field data shown in Fig. 7.10 detects good agreement in all transects. However, at x≥900 m, the predicted values are higher than those observed and the predicted width is somewhat smaller than the observed jet width.

The reason of the discrepancy between the observed and the predicted distributions shown in Fig. 7.10 can be attributed to the peculiar shape of the observed jet trajectory, shown in Fig. 7.3, as the jet bends sharply at x≥200 m and becomes attached to the shoreline with a build up of TRC concentrations. The far-field model cannot handle the recirculation zone which occurred at x≥400 m (McCorquodale et al 1983). The wind is considered an important factor which is often neglected in the numerical models. In this study, it was observed that the south wind of 17 km.h^{-1} tends to spread out the surface jet causing the discrepancy between the observed and the predicted jet widths. Also, dispersion in natural streams is essentially a three-dimensional problem. The two-dimensional simulation of this type of problem could result in an unrealistic representation.

A computer run was made, using the field data as an initial condition, but assuming that the decay of TRC is equal to zero. The result of this run was compared with the case in which the decay is considered. The comparison showed that the decay of TRC has a small effect on the decrease of TRC values. A decrease of 3% in TRC concentrations at the downstream transects was noticed.

The previous discussion suggests the use of elliptic

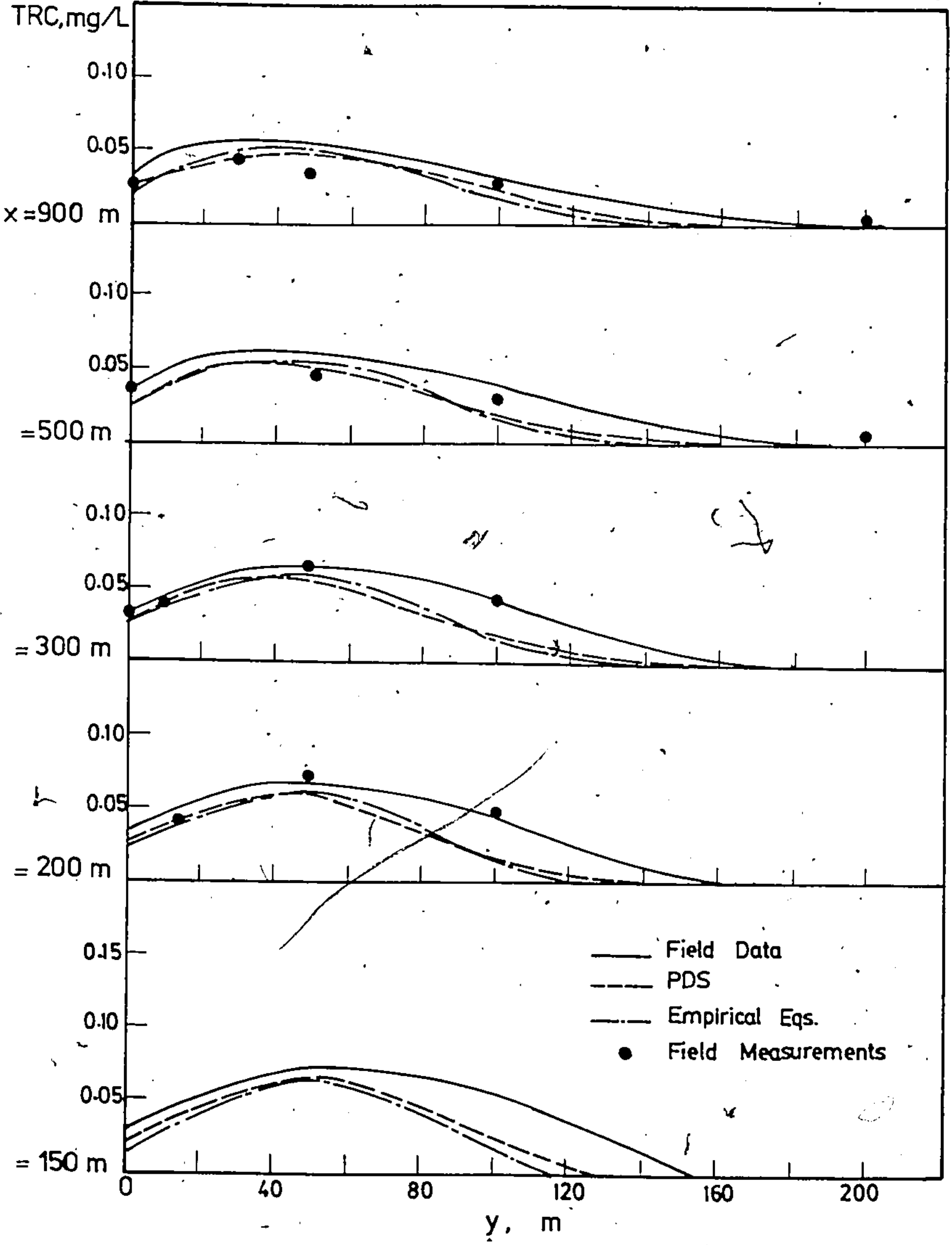

Fig. 7.10. Comparison of observed and predicted total residual chlorine concentrations in the Detroit River.

type models (Rodi et al. 1981) rather than the parabolic models. Nevertheless, the predictions of the far field model used in this study, incorporating the predictions of the empirical equations obtained from this study, and the predictions of the PDS model for the near-field zone, showed a good agreement with the observed values as indicated in Fig. 7.10. It is also noticed that the far-field dispersion coefficient, α=1.0, based on St. Clair River data, is appropriate for this reach of Detroit River.

CHAPTER VIII

SUMMARY AND CONCLUSIONS

8.1 HYDRODYNAMIC STUDIES

Experimental studies were performed to investigate the behaviour of buoyant and non-buoyant jets in cross-flowing ambients near the outfall where mixing zones are critical. Velocity, concentration and temperature in the lateral and vertical directions were measured in the region extending from the discharge section to about 24 pipe diameters downstream. Bottom, submerged and surface outfalls were investigated. Shore-based and extended surface outfalls were considered. The velocity ratio ranged from 2.0 to 5.9 and the ambient water depth varied from 2.0 to 5.5 pipe diameters. The experimental data was used to define distinct geometric properties and mixing characteristics within the near-field zone. An examination of the analysis led to the following conclusions:

1. The near-field mixing of jets from shore-based outfalls, that discharge into trapezoidal channels, can be characterized by the relative distance from the outfall, ξ/D, the velocity ratio, R, the jet densimetric Froude number F_o, the relative depth, H/D and

the position of the outfall, Z_p/H.

2. The experimental evidence and the similarity analysis indicate that the excess velocity, concentration and excess temperature profiles display similarity in the lateral and vertical directions and are best described by the Gaussian distribution; however, similarity was not achieved when strong re-attachment and recirculation occurred.

3. A single functional behaviour of the excess velocity along the jet axis exists for various velocity ratios if the jet is considered after the establishment zone.

4. For submerged outfalls (above the bottom), the experiments showed that there is a tendency of bifurcation in the lateral velocity profiles and this tendency increases with increasing the velocity ratio.

5. It has been found that the lateral concentration length scales grow at a rate 1.10 and 1.37 times the growth rate of velocity scales for bottom and surface outfalls, respectively. Also, the lateral spreading of the buoyant jets of this study was larger by about 16% than that of non-buoyant jet, and the vertical spreading on the other hand is smaller by about 15%.

6. A criterion is presented to distinguish detached and shoreline attached buoyant jets in cross-flow. The tendency for attachment increases with increasing the cotangent of the side slope and decreasing the velocity ratio.

7. A generalized trajectory relation given by Eq. 5.64 describes the deflection of buoyant and non-buoyant jets in cross-flow. The jet penetration, y/D, is found to increase with increasing x/D, R and Z_p/H. The parameters F_o and H/D have a relatively small effect on the prediction of y/D.

8. A generalized equation for the minimum dilution, S, is described by Eq. 5.67. It has been found that ξ/D, H/D and Z_p/H are the most significant variables affecting S.

Verification of the near-field models (PDS and MIT) against experimental data is, of course, only the first test of any proposed model. The experiments of this study on buoyant and non-buoyant surface jets were used to assess the performance of these models. The results presented herein indicate that:

9. For the PDS model, the jet trajectory is sensitive to the entrainment coefficient, E_o, horizontal turbulent exchange coefficient, E_H and the drag coefficient, C_D

and insensitive to spreading function coefficient, xk_1. Also, the minimum dilution is sensitive to E_o and E_H but relatively insensitive to C_D and xk_1.

10. The agreement between the measured and PDS predicted jet widths and dilution was in general acceptable over the major portion of the mixing zone. A discrepancy is observed near the source for the case of low velocity ratio, R=2.0, because the strong ambient current tends to force the jet towards the shoreline. This shoreline attachment is not treated by the PDS model which assumes an infinite depth with a uniform ambient current.

11. For the MIT model, the most important parameters influencing the trajectory are the cross-flow entrainment coefficient, α_c, and the drag coefficient $C_{D_{22}}$. Also the minimum dilution is affected by α_c.

12. For low velocity ratios, the agreement between the measured and MIT predicted jet widths is fair near the source and becomes poor away from the source. This is because the MIT model assumes that buoyant and non-buoyant jet spreading are linearly additive, therefore, when the inertia and the buoyant forces are of the same order, the model gives inaccurate results. The MIT predicts a reasonable value of dilution rate

when there is significant momentum mixing, i.e., close to the outfall. When the dilution is mainly due to buoyancy or stream generated turbulence, i.e., away from the outfall, the prediction is not as good.

13. For high velocity ratios, a reasonable agreement between the measured and MIT predicted jet widths and dilution was obtained.

14. The PDS model has an advantage over the MIT model in calculating the length of flow establishment zone. The measured and predicted lengths are in good agreement.

15. In general, the MIT and PDS models yielded comparable predictions with the measurements. However, the PDS model seems to perform as well or better than the MIT model when compared with data.

Validation of the far-field model (UOW-MOE) is made using the field data for total residual chlorine collected from the Detroit River in the vicinity of West Windsor Pollution Control Plant. The predicted results of this numerical model, incorporating the predictions of the empirical Eqs. 5.64 and 5.67 and the predictions of the PDS model for the near-field zone, were compared with the field data. A good agreement in the concentration values was observed.

8.2 CONTAMINANT BEHAVIOUR STUDIES

An examination and analysis of the contaminant behaviour studies on chlorinated effluent samples has led to the following conclusions:

1. When various concentrations of chlorine are added to the diluted final effluent, an immediate chlorine demand is exerted due to chemical reaction with reducing agents and easily oxidizable organic compounds in wastewater. This is followed by a gradual decay in the chlorine concentration due to reaction with ammonia and volatilization. A first order model is proposed to describe the kinetics of chlorine demand exertion based on the above observations.

2. The important parameters influencing the gradual decay of total residual chlorine, after mixing in the rivers, are photolysis, evaporation, free radical oxidation, temperature and turbulence.

    (A) The decay rate of chlorine under alternating exposure to light and darkness is slightly higher than that obtained under complete darkness. This increase can be attributed to the fact that the decay rate is catalyzed by ultraviolet light.

(B) The decay rate of chlorine increased significantly as the ratio of area to volume of the container increased. In streams, this ratio is equal to 1/depth.

(C) The rate constant values were consistent with the van't Hoff-Arrhenius temperature kinetics and the temperature factor, θ_1, was found to be equal to 1.08. The value of θ_1 depends on the nature of the waste and it should be determined experimentally before applying the first order model.

(D) The absence of turbulence may significantly influence the rate coefficient and thus provide erroneous value for the decay rate. The turbulence was found to approximately double the decay rate obtained under quiescent condition. This increase in rate constant due to stirring can be attributed to the removal of chlorine accumulated in the atmosphere above the liquid phase and to some breakdown of the gas film at the interface.

Therefore, the light and dark method, with continuously stirring of sample, would more nearly simulate existing conditions in the streams, and if properly used, would give more representative kinetic decay rate than that obtained with the standard method.

3. The BOD progression studies conducted on chlorinated effluent samples under various test conditions showed that:

   (A) BOD rate kinetics decrease as the chlorine dose is increased. Addition of chlorine delays the start of nitrification stage in the biochemical oxygen demand due to reaction of chlorine with ammonia. When high concentration of chlorine was added, almost all the bacteria were killed or un-activated and the BOD progression curve did not follow the first order reaction.

   (B) Under quiescent conditions, lower BOD values were obtained with alternate light and dark incubation of a sample when compared to values obtained with standard incubation in dark.

   (C) All the experiments conducted on BOD progression with different chlorine doses and with alternating light and dark exposure showed that, irrespective of the source of sample, the 5-day BOD and the ultimate oxygen demand values obtained in stirred bottles were consistently higher than those obtained with the standard procedure.

   (D) Suppression of nitrification with pasteurization was accompanied by a slight decrease in the ultimate oxygen demand and 5-day BOD in both chlorinated and unchlorinated samples.

8.3 RECOMMENDATIONS

Based on this study, several additional research topics in this area have been identified.

1. Further investigation is required in the applicability of similarity analysis of mass and momentum transports in the near-field (Townsend, 1976).
2. Further investigation of negative buoyancy effects on near-field mixing is required.
3. The effect of different channel geometries on near-field mixing should be carried out.
4. The decay of ammonia in streams receiving chlorinated sewage effluents is not well understood at present. Further investigations on the effect of chlorine dose on residual ammonia will be beneficial.

REFERENCES

Abraham, G., (1960). "Jet diffusion in liquid of greater density." J. Hyd. Div., Proc. ASCE 6, pp. 1-13.

Abramovich, M., (1963). The Theory of Turbulent Jets. MIT Press.

Akhtar, W., (1978). Study of Mixing in Natural Streams and Air Agitated Tanks. Ph.D. dissertation, University of Windsor, Windsor, Ontario.

Albertson, M. L., Dai, Y. B., Jensen, R. A. and Rouse, H., (1950). "Diffusion of submerged jets." Trans. ASCE, Vol. 115, pp. 639-697.

Ali, H. I., (1972). Influence of Turbulence on BOD Progression. Ph.D. Thesis, University of Windsor, Ontario.

Ali, H. I. and Bewtra, J. K., (1972). "Effect of turbulence on BOD Testing." J. Water Pollution Control Federation, Vol. 44, No. 9, pp. 1798-1807.

Bailey, P. L., (1976). Analysis with Ion-Selective Electrodes. Heyen & Son.

Baker, R. J., (1970). "Engineering considerations in disinfections." ASCE, Proc. of the National Specialty Conf. on Disinfection, Massachusetts, pp. 685-697.

Benedict, B. A., and Preston, J. W., (1980). "Sensitivity of the Prych- Davis-Shirazi Model." Proc. of the Spec. Conf. on Computer and Physical Modelling in Hydraulic Eng., Chicago. Published by ASCE, N. Y., pp. 322-332.

Bobra, A., and Mackay D. R., (1980). "Calculation of the degradation characteristics of selected pollutants in the St. Clair River," University of Toronto, private communication.

Chassaing, P., George J., Claria A. and Sananes, F., (1974). "Physical characteristics of subsonic jets in a cross-stream." J. Fluid Mechanics, Vol. 62, Part 1, pp. 41-64.

Chu, V. H., and Goldberg, M. B., (1974). "Buoyant forced-plumes in cross-flow." J. Hyd. Div., ASCE, Vol. 100, HY9, pp. 1203-1214.

Demuren, A. O., and Rodi, W., (1983). "Side discharges into open channels: Mathematical model." J. Hyd. Eng., ASCE, Vol. 109, No. 12, pp. 1707-1722.

Fair, G. M., and Geyer, J. C., (1958). Elements of Water Supply and Wastewater Disposal. John Wiley and Sons, Inc., New York, N. Y.

Faust, J., (1984). Personal communication. Chemist with the City of Windsor Wastewater Laboratory.

Fischer, H., (1973). "Longitudinal dispersion and transverse mixing in open-channel flow." Ann. Rev. Fluid Mech. 5, pp. 59-78.

Fischer, H. B., List, E. J., Koh, R.C.Y., Imberger, J., and Brooks, N. H., (1979). Mixing in Inland and Coastal Waters. Academic Press.

Gordier, R. L., (1959). "Studies on fluid jets normally into moving liquid." St. Anthoni Falls Hydraulics Lab., Univ. of Minneapolis, Tech. Paper, 28, Ser. B.

Gowda, T.P.H., (1978). "Prediction of chlorine residuals and toxic ammonia in mixing zones of streams." Presented at Transport Process Workshop, N.W.R.I., Canada Centre for Inland Waters, Burlington, Ont.

Gowda, T.P.H., (1979). "Modelling chlorine residuals in streams receiving sewage effluent." Presented at the 14th symposium on Water Pollution Research in Canada, Univ. of Toronto.

Gowda, T.P.H., (1984). "Water quality prediction in mixing zones of rivers." Journal Environmental Eng., ASCE, Vol. 110, No. 4, pp. 751-769.

Great Lakes Institute, (1983). "A case study of selected toxic contaminants in the Essex region." Progress Report No. 1, pp. 80-84.

Haas, C. N., and Karra, S. B., (1984). "Kinetics of wastewater chlorine demand exertion." J. Wat. Poll. Cont. Fed. Vol. 56, No. 2, pp. 170-173.

Hamdy, Y. S., and Kinkead, J. D., (1979). "Waste dispersion in the St. Clair River." Ontario Ministry of the Environment, Toronto, Ont.

Harding, G. T., and Romano, L. S., (1981). "City of Windsor Pollution Control Systems." Department of Works, City of Windsor, 18 p.

Hinze, J. O., (1975). Turbulence. McGraw-Hill Co., New York.

Høstgaard-Jensen, P., Klitgaard, J., and Pedersen, K. M., (1977). "Chlorine decay in cooling water and discharge into seawater." J. Water Poll. Cont. Fed., Vol. 49, No. 8, pp. 1832-1841.

Jen, Y., Wiegel R. L., and Mobarek, I., (1966). "Surface discharge of horizontal warm-water jet." J. of the Power Div. ASCE, Vol. 92, No. PO2, pp. 1-28.

Jirka, G. H., Abraham, G., and Harleman, D.R.F., (1975). "An assessment of techniques for hydrothermal prediction." Final Report to U.S. Atomic Energy Comm., Dept. Civil Eng. MIT R. M. Parsons Lab., Rep. No. 203.

Jirka, G. H., Adams, E. E., and Stolzenback, K. D., (1981). "Buoyant Surface Jets." Journal of the Hyd. Div., ASCE, Vol. 107, No. HY11, pp. 1467-1487.

Johnson, J. D., (1975). "Measurement and persistence of chlorine residuals in natural waters." Proceedings of the Conf. on the Environmental Impact of Water Chlorination, Oak Ridge National Laboratory, Oak Ridge Tn., pp. 37-63.

Katz, B. M., (1977). "Chlorine dissipation and toxicity presence of nitrogenous compounds." J. Water Poll. Cont. Fed., Vol. 49, No. 7.

Keffer, J. F., and Baines, W. D., (1962). "The round turbulent jet in a cross-wind." J. Fluid Mech., Vol. 15, Part 4, pp. 481-497.

Lau, Y. L., and Krishnappan, B. G., (1981). "Modelling transverse mixing in natural streams." J. Hyd. Div. ASCE, Vol. 107, HY2, pp. 209-227.

Lee, J. D., (1954). "Simplified method for analysis of BOD data." Sewage and Industrial Wastes, 23 .

Lee, P.C.C., and Fung, C.T.M., (1979). The effect of chlorination on the BOD simulation on streams. B.Sc. Major Paper, Univ. of Windsor, Ontario.

McCorquodale, J. A., (1977). "Hydraulic study of the circular settling tanks at the West Windsor Pollution Control Plant." Report submitted to LaFontaine, Cowie, Buratto and Associates Limited, Consulting Engineers, Windsor, Ont.

McCorquodale, J. A., and Bewtra, J. K., (1982). "Simulation of phenol concentrations in the St. Clair River." IRI -15-24 (Part A) for Water Resources Branch, Ontario Ministry of Environment, Toronto, Ont.

McCorquodale, J. A., Imam, E. H., Bewtra, J. K., Hamdy, Y.S., and Kinkead, J. K., (1983). "Transport of pollutants in natural streams." Canadian Journal of Civil Eng., Vol. 10, No. 1, pp. 9-17.

McGuirk, J. J., and Rodi, W., (1978). "A depth-averaged mathematical model for the near field of side discharges into open channel flow." J. Fluid Mech., Vol. 86, Part 4, pp. 761-781.

Mikhail, R., Chu, V. M., and Savage, S. B., (1975). The reattachment of a two-dimensional turbulent jet in a confined cross-flow." Proc. 16th International Assoc. for Hyd. Res. Congress, Sao Paulo, Brazil, Vol. 3.

Ministry of the Environment, (1978). Water Management. Toronto, Ont.

Moussa, Z. M., Trischka, J. W., and Eskinazi, S., (1977). "The near-field in the mixing of a round jet with a cross-stream." J. Fluid Mech., Vol. 80, Part 1, pp. 49-80.

Natalizo, A., and Baines, W. D., (1977). "Simplified analysis of surface buoyant jet." J. of Hydraulics Division, ASCE, Vol. 103, No. HY2, pp. 123-132.

Neville, A. M., and Kennedy, J. B., (1964). Basic Statistical Methods for Engineers and Scientists." International Textbook Company, Scranton, Pennsylvania.

Orion Research, (1979). Instruction Manual for Ammonia Electrode, Model 95-10.

Parr, A. D., Sayre, W. W., (1979). "Multiple jets in shallow flowing receiving waters." J. Hyd. Div., ASCE, 11, pp. 1357-1374.

Patrick, M. A., (1967). "Experimental investigation of the mixing and penetration of a round turbulent jet injected perpendicularly into a transverse stream." Trans. Inst. Chem. Eng., No. 45, pp. 16-31.

Pratte, B. D., and Baines, W. D., (1967). "Profiles of the round turbulent jet in a cross-flow." J. Hyd. Div., ASCE, 6, pp. 53-64.

Prych, E. A., (1972). "A warm water effluent analyzed as a buoyant surface jet." Svergis Meterologiska Och Hydrologiska Institute, Serie Hydrologi, Nr. 21, Stockholm, Sweden.

Rajaratnam, N., (1976). Turbulent Jets. Elsevier Scientific Publishing Company.

Rajaratnam, N., and Gangadhariah, T., (1980). "Circular jets in cross-flow." Tech. Report, Univ. of Alberta, Edmonton.

Rajaratnam, N., (1984). "Non-buoyant and buoyant circular surface jets in co-flowing streams." J. of Hydraulic Research, Vol. 22, No. 2, pp. 117-140.

Rodi, W., (1980). "Turbulence Models and their application in hydraulics - A state of the art review." IAHR, June.

Rodi, W., Pavlocic, R. N., and Srivatsa, S. K., (1981). "Prediction of flow and pollutant spreading in rivers." Transport Models for Inland and Coastal Waters, Academic Press, Inc.

Rouse, H., Yih, C. S., and Humphreys, H. W., (1952). "Gravitational convection from a boundary source." Tellus, 4, pp. 201-210.

Sawyer, C. N., and Bradney, L., (1946). "Modernization of the BOD Test for determining the efficacy of sewage treatment processes." Sewage Works Journal, Vol. 18, No. 6, pp. 1113-1120.

Schlichting, H., (1968). Boundary-Layer Theory. Sixth Edition. McGraw-Hill Book Company.

Scorer, R. S., (1959). "The behaviour of chimney plumes." Int. J. Air Pollution, Vol. 1, pp. 198 -220.

Shirazi, M. A., and Davis, L. R., (1974). "Workbook of thermal plume prediction, Vol. 2: surface discharge." U.S. Environmental Protection Agency, Report EPA-R2-72-0056.

Smith, G. D., (1965). Numerical Solution of Partial Differential Equations. Oxford Univ. Press, London, England.

Snodgrass, W. J., (1980). Removal Rates of Four Chemicals from Aqueous Systems. McMaster University, Hamilton, Ont.

Snoeyink, V. L., and Markus, F. I., (1974). "Chlorine residuals in treated effluents." Water Sew. Works, No. 121, pp. 35-38.

Standard Methods for the Examination of Water and Wastewater, (1980). 15th Edition. American Public Health Association.

Steffler, P. M., (1980). Deflection of Jets by Weak Crossflows. M.Sc. Thesis, University of Alberta, Edmonton, Alberta.

Stolzenbach, K. D., and Harleman, D.R.F., (1971). "An analytical and experimental investigation of surface discharges of heated water." MIT, R. M. Parsons Lab, Report No. 135.

Stolzenbach, K. D., and Harleman, D.R.F., (1973). "Three-dimensional heated surface jets." Water Resources Research, Vol. 9, No. 1, pp. 129-132.

Strazisar, A., and Prahl, J., (1973). "The effects of bottom friction on river entrance flow with cross-flow." Proc. 16th Conf. Great Lakes Res., pp. 615-625.

Townsend, A. A. (1976). The Structure of Turbulent Shear Flow. Cambridge University Press, London.

Turner, J. S., (1960). "A comparison between buoyant vortex rings and vortex pairs." J. Fluid Mech., Vol. 7, pp. 419-432.

Turner, Filter Fluorometer Model III, (1974). Operating Instructions and Service Manual. Turner Associates Division of the American Sterilizier Company.

U.S. Army Corps of Engineers, Detroit District, (1974). "Detroit River current studies - aerial Drogue survey and mean velocity distribution study." Int. Report, Great Lakes Hydraulics and Hydrology Branch.

U.S. Department of Commerce, (1979). "St. Clair River." Chart No. 46-49/14853, 8th Ed. (Nautical Chart Catalogue No. 4, Panel C), National Oceanic and Atmospheric Administration, Washington, D. C.

U.S. Environmental Protection Agency, (1974). "Water Pollution Investigation: Detroit and St. Clair Rivers." EPA-905/9-74-013.

Varma, M. M., Horn, J. A., and Reid, G. W., (1963). "Effect of algae in BOD samples." Water and Sewage Works, pp. 191-194.

Wachs, A. M., Folkman, Y., and Shemesh, D., (1972). "Use of surface stirrers for ammonia desorption from ponds." Applications of New Concepts of Physical-Chemical Wastewater Treatment, Progress in Water Technology, Vol. 1, pp. 263-271.

Wallace, R. B., and Wright, S. J., (1984). "Spreading layer of two-dimensional buoyant jet." J. Hyd. Eng., ASCE, Vol. 110, No. 6, pp. 813-828.

Weil, J., (1972). "Mixing of a heated surface jet in turbulent channel flow." Report WHM-1, Hyd. Eng. Lab., Univ. of California, Berkeley.

Weiler, R. R., (1979). "Rate of loss of ammonia from water to the atmosphere." J. Fish. Research Board Canada, Vol. 36, No. 6, pp. 685-689.

White, G. C., (1972). Handbook of Chlorination. Van Nostrand Reinhold, New York.

Wright, S. J., (1977). "Mean behavior of buoyant jets in a cross-flow." J. Hyd. Div., ASCE, Vol. 103, HY5, pp. 499-513.

Yotsukura, N., and Sayre, W. W., (1976). "Transverse mixing in natural channels." Water Resour. Res., Vol. 12, pp. 695-704.

APPENDIX A

TABLES CONTAINING VELOCITY RESULTS

Table A.1

Velocity Results for Exp. 5

$\frac{x}{D} = 0.0$

$\frac{y}{D}$	6	9	12	15	18	21	24	27	33	39	45
Velocity at 0.2H				16.6	17.3	19.0	19.2	17.3	17.3	17.6	17.6
Velocity at 0.5H		14.4	17.6	18.4	18.7	20.9	21.2	19.0	19.1	23.5	20.0
Velocity at 0.8H	12.3	15.6	18.4	19.8	20.4	21.4	21.7	19.5	19.8	24.9	20.6
Depth-averaged velocity $\bar{U}$	12.3	15.0	18.0	18.3	18.8	20.4	20.7	18.6	18.8	22.0	19.4
Dimensionless velocity $U/\bar{U}$	.65	.80	0.96	0.97	1.0	1.09	1.1	0.99	1.0	1.17	1.03

$\frac{x}{D} = 6.0$

Velocity at 0.2H				16.6	18.4	21.7	19.5	18.2	17.4	18.4	19.3
Velocity at 0.5H		13.6	16.6	19.0	20.5	21.4	21.7	19.2	18.7	23.3	21.2
Velocity at 0.8H	11.2	17.4	17.6	20.0	20.5	21.2	22.2	19.8	19.0	24.6	20.6
Depth-averaged velocity $\bar{U}$	11.2	15.5	17.1	18.5	19.8	21.4	21.1	19.1	18.4	22.1	20.4
Dimensionless velocity $U/\bar{U}$	.61	.84	0.92	1.0	1.07	1.16	1.14	1.03	1.00	1.19	1.10

Table A.1 (continued)

$\frac{x}{D} = 12.0$

$\frac{y}{D}$	6	9	12	15	18	21	24	27	33	39	45
Velocity at 0.2H			10.9	17.1	18.2	20.0	17.6	19.5	17.1	18.4	19.4
Velocity at 0.5H		10.4	16.0	19.8	18.6	23.5	20.3	18.4	18.4	20.9	18.5
Velocity at 0.8H	8.5	16.0	16.8	19.2	19.2	23.0	20.6	19.0	19.0	21.4	19.0
Depth-averaged velocity U	8.5	13.2	14.6	18.7	18.7	22.2	19.5	19.0	18.2	20.2	19.0
Dimensionless velocity $U/\overline{U}$	0.46	0.72	0.80	1.02	1.02	1.21	1.06	1.04	.99	1.1	1.04

$\frac{x}{D} = 24.0$

Velocity at 0.2H				15.8	19.2	19.2	20.0	18.4	18.0	17.1	18.3
Velocity at 0.5H			17.6	19.8	19.0	19.2	22.4	20.6	18.4	21.2	20.7
Velocity at 0.8H	10.7	15.5	17.41	18.7	17.9	17.7	21.4	20.9	19.7	20.9	20.9
Depth-averaged velocity U	10.7	15.5	17.5	18.1	18.7	18.7	21.3	20.0	18.7	19.7	20.0
Dimensionless velocity $U/\overline{U}$	.57	.82	0.93	0.96	0.99	.99	1.13	1.06	0.99	1.05	1.06

Table A.2

Velocity Results for Exp. 8

$\frac{x}{D}$ = 0.0

$\frac{y}{D}$	6	9	12	15	18	21	24	27	33	39	45
Velocity at 0.2H				20.8	20.8	29.5	29.5	30.5	29.5	29.5	26.5
Velocity at 0.5H			26.4	26.9	26.8	32.0	34.5	34.5	32.0	33.5	29.5
Velocity at 0.8H	17.1	22.7	27.2	28.5	28.0	29.5	33.5	33.5	32.0	32.0	32.0
Depth-averaged velocity U	17.1	22.7	26.8	25.4	25.2	36.3	32.5	32.8	31.2	31.7	29.3
Dimensionless velocity U/$\overline{U}$	.60	0.80	0.95	0.9	0.90	1.07	1.15	1.16	1.1	1.12	1.04

$\frac{x}{D}$ = 6.0

Velocity at 0.2H			20.8	19.2	[illegible]0.5	28.9	26.7	29.5	29.5	28.0	26.2
Velocity at 0.5H		19.5	26.8	27.3	33.5	33.0	33.0	32.0	33.5	33.5	33.5
Velocity at 0.8H	16.0	22.4	28.0	27.0	34.5	31.4	32.0	34.5	33.5	33.5	32.0
Depth-averaged velocity U	16.0	21.0	25.2	24.5	32.8	31.1	30.6	32.0	32.2	31.7	30.6
Dimensionless velocity U/$\overline{U}$	.57	.74	0.89	0.87	1.16	1.10	1.08	1.13	1.14	1.12	1.08

Table A.2 (continued)

$\frac{x}{D}$ = 12.0

$\frac{y}{D}$	6	9	12	15	18	21	24	27	33	39	45
Velocity at 0.2H			18.2	25.4	26.6	32.0	29.5	32.0	30.5	29.5	26.2
Velocity at 0.5H		18.4	24.4	26.8	28.4	34.5	30.5	33.5	33.5	32.0	32.7
Velocity at 0.8H	16.0	24.0	26.0	29.5	30.5	36.0	33.5	34.5	33.5	33.5	32.8
Depth-averaged velocity U	16.0	21.2	22.9	27.2	28.5	34.2	31.2	33.3	32.5	31.7	30.6
Dimensionless velocity $U/\overline{U}$	.57	.75	.81	.96	1.00	1.2′	1.1	1.18	1.15	1.12	1.08

$\frac{x}{D}$ = 24.0

Velocity at 0.2H			20.8	27.0	27.0	24.6	30.5	34.5	31.0	29.5	26.5
Velocity at 0.5H		18.4	26.0	28.0	27.8	30.5	36.0	34.5	33.5	32.0	29.8
Velocity at 0.8H	16.0	24.0	29.5	29.5	29.7	30.5	37.5	33.5	33.5	33.5	32.3
Depth-averaged velocity U	16.0	21.2	25.4	28.2	28.2	28.5	34.7	39.2	32.7	31.7	29.5
Dimensionless velocity $U/\overline{U}$	.56	.75	.89	.99	0.99	1.00	1.21	1.20	1.14	1.10	1.04

Table A.3

Velocity Results for Exp. 9

	$\frac{y}{D}$	6	9	12	15	18	21	24	27	33	39	45
$\frac{x}{D} = 0$	Velocity at 0.2H			17.9	12.3	10.6	16.6	16.3	12.6	13.3	19.0	20.1
	Velocity at 0.5H		12.3	18.4	18.7	17.1	18.4	19.0	14.7	15.0	23.5	24.6
	Velocity at 0.8H	19.2	17.6	16.6	17.4	17.6	19.8	20.6	16.0	15.3	23.8	26.2
	Depth-averaged velocity U	19.2	14.9	17.6	16.1	15.1	18.3	18.6	14.4	14.5	22.1	23.6
	Dimensionless velocity	1.1	0.89	1.04	0.95	0.90	1.08	1.1	0.85	0.86	1.31	1.4
$\frac{x}{D} = 6$	Velocity at 0.2H			12.3	15.8	11.7	18.7	18.2	13.3	13.3	19.0	23.3
	Velocity at 0.5H		12.5	18.2	18.7	18.4	22.0	21.4	18.4	15.0	20.1	26.8
	Velocity at 0.8H	19.5	17.8	16.6	17.6	17.6	21.7	18.44	16.3	15.3	21.4	27.0
	Depth-averaged velocity U	19.5	15.2	15.7	17.4	15.9	20.8	19.3	16.0	14.5	20.2	25.2
	Dimensionless velocity	1.1	0.88	0.91	1.00	0.92	1.2	1.12	0.93	0.84	1.12	1.50

Table A.3 (continued)

	$\frac{y}{D}$	6	9	12	15	18	21	24	27	33	39	45
$\frac{x}{D} = 12$	Velocity at 0.2H			12.0	16.0	15.3	13.1	18.2	14.4	13.3	18.4	24.4
	Velocity at 0.5H		11.8	17.4	18.4	16.8	16.6	20.1	16.0	15.0	22.0	26.8
	Velocity at 0.8H	19.0	18.1	17.9	17.6	16.6	18.7	17.9	16.6	14.7	20.9	27.0
	Depth-averaged velocity U	19.0	15.0	15.8	17.3	16.1	16.1	18.7	15.7	14.3	20.4	26.1
	Dimensionless velocity $U/\overline{U}$	1.13	0.89	0.94	1.03	0.96	0.96	1.1	0.93	0.85	1.21	1.55
$\frac{x}{D} = 24$	Velocity at 0.2H			12.0	15.5	16.8	14.7	17.1	17.9	13.1	19.0	23.3
	Velocity at 0.5H		12.5	17.9	18.7	16.3	13.3	17.6	18.7	16.3	20.0	26.6
	Velocity at 0.8H	19.3	17.9	19.0	19.0	15.8	17.1	18.4	17.1	15.3	21.5	27.2
	Depth-averaged velocity U	19.3	15.2	16.2	17.7	16.3	15.0	17.7	17.9	14.9	20.2	25.7
	Dimensionless velocity $U/\overline{U}$	1.14	0.90	0.97	1.05	0.97	0.90	1.05	1.06	0.88	1.21	1.50

Table A.4

Velocity Results for Exp. 12

$\frac{x}{D} = 0$

$\frac{y}{D}$	6	9	12	15	18	21	24	27	33	39	45
Velocity at 0.2H				12.3	15.5	16.8	17.1	16.3	16.3	16.3	16.3
Velocity at 0.5H		6.4	10.9	16.3	21.1	21.1	20.3	20.0	20.0	20.0	22.7
Velocity at 0.8H	15.5	21.4	15.5	16.6	20.3	20.6	22.0	20.3	20.3	20.3	22.7
Depth-averaged velocity U	15.5	13.9	13.2	15.1	18.9	19.8	19.8	18.9	18.9	18.9	20.4
Dimensionless velocity $U/\overline{U}$	0.85	0.76	0.73	0.83	1.04	1.07	1.09	1.04	1.04	1.04	1.3

$\frac{x}{D} = 6$

Velocity at 0.2H				18.7	17.9	18.7	16.6	17.3	17.9	17.6	17.9
Velocity at 0.5H		9.3	20.0	20.0	20.3	21.4	20.3	20.6	20.6	20.6	20.7
Velocity at 0.8H	15.5	19.8	16.0	20.9	22.0	22.0	22.4	20.6	20.9	20.9	23.8
Depth-averaged velocity U	15.5	18.7	12.6	20.0	20.0	20.3	20.1	19.4	19.8	19.7	20.8
Dimensionless velocity $U/\overline{U}$	0.82	0.99	0.67	1.06	1.06	1.08	1.07	1.03	1.05	1.04	1.1

Table A.4 (continued)

	$\frac{y}{D}$	6	9	12	15	18	21	24	27	33	39	45
$\frac{x}{D} = 12$	Velocity at 0.2H				11.7	19.5	19.8	18.7	17.9	17.4	18.7	19.2
	Velocity at 0.5H		14.4	10.7	16.0	21.4	22.7	21.4	21.2	20.6	21.7	23.8
	Velocity at 0.8H	13.6	18.2	14.3	18.4	22.2	22.0	23.6	21.4	21.2	21.7	24.4
	Depth-averaged velocity U	13.6	16.3	12.5	15.4	21.0	21.5	21.2	20.2	19.7	20.7	22.5
	Dimensionless velocity $U/\overline{U}$	0.72	0.87	0.67	0.82	1.14	1.14	1.13	1.07	1.05	1.10	1.20
$\frac{x}{D} = 24$	Velocity at 0.2H				13.1	19.8	19.8	20.0	17.9	17.4	18.4	19.2
	Velocity at 0.5H			15.8	16.0	21.4	21.2	21.4	21.4	20.6	20.9	21.8
	Velocity at 0.8H	13.0	15.4	15.0	17.6	22.2	21.7	23.0	20.9	20.9	21.7	22.9
	Depth-averaged velocity U	13.0	15.4	15.4	15.6	21.1	20.9	21.5	20.1	19.6	20.3	21.3
	Dimensionless velocity $U/\overline{U}$	0.69	0.82	0.82	0.83	1.12	1.11	1.14	1.07	1.04	1.08	1.13

Table A.5

Velocity Results for Exp. 13

x = 0

$\frac{y}{D}$	6	9	12	15	18	21	24	27	33	39	45
Velocity at 0.2H			3.9	11.7	12.8	13.3	12.8	10.4	11.4	12.3	15.8
Velocity at 0.5H	5.2	7.7	9.0	13.6	15.0	16.0	14.4	12.3	11.5	14.4	17.6
Velocity at 0.8H	9.0	9.6	11.2	13.6	15.8	17.1	15.0	12.6	11.5	14.4	16.2
Depth-averaged velocity U	7.1	8.65	8.0	13.0	14.5	15.5	14.1	11.8	11.9	13.7	17.2
Dimensionless velocity $U/\overline{U}$	0.57	0.70	0.65	1.05	1.17	1.25	1.14	0.95	0.93	1.11	1.39

x = 6

Velocity at 0.2H			4.2	12.0	14.4	13.4	13.0	12.0	11.2	13.0	15.0
Velocity at 0.5H	5.2	8.7	8.5	12.8	15.8	17.4	15.2	13.3	12.0	15.5	17.4
Velocity at 0.8H	9.0	9.9	12.8	14.4	17.9	17.4	15.8	12.8	11.4	13.9	17.6
Depth-averaged velocity U	7.1	9.3	12.75	13.1	16.0	16.1	14.7	12.7	11.5	14.1	16.7
Dimensionless velocity $U/\overline{U}$	0.55	0.73	0.99	1.02	1.25	1.25	1.15	0.99	0.90	1.10	1.34

Table A.5 (continued)

x = 12

$\frac{y}{D}$	6	9	12	15	18	21	24	28	33	39	45
Velocity at 0.2H			6.0	12.6	14.4	13.9	13.4	12.0	10.9	13.3	16.0
Velocity at 0.5H	5.2	8.5	9.3	13.1	16.0	17.1	15.3	12.8	11.2	14.2	18.2
Velocity at 0.8H	9.9	10.9	12.8	14.7	17.9	18.2	15.0	12.8	12.6	14.4	17.6
Depth-averaged velocity $\overline{U}$	7.55	9.7	9.4	13.5	16.1	16.4	14.6	12.5	11.6	14.0	17.3
Dimensionless velocity $U/\overline{U}$	0.59	0.76	0.73	1.05	1.25	1.28	1.14	0.97	0.92	1.11	1.37

x = 24

Velocity at 0.2H				13.3	15.5	14.7	13.3	12.6	12.0	13.4	15.0
Velocity at 0.5H	5.2	10.1	10.9	12.5	16.6	16.3	15.0	13.3	13.3	14.1	17.4
Velocity at 0.8H	9.6	11.2	11.2	14.1	17.6	17.4	15.0	13.3	12.8	14.4	17.6
Depth-averaged velocity $\overline{U}$	7.4	10.65	11.05	13.3	16.6	16.1	14.4	13.1	12.7	14.0	16.7
Dimensionless velocity $U/\overline{U}$	0.58	0.83	0.86	1.04	1.29	1.25	1.12	1.02	0.99	1.11	1.34

Table A.6

Velocity Results for Exp. 20

	$\frac{y}{D}$	6	9	12	15	18	21	24	27	33	39
x = 0	Velocity at 0.2H			12.0	13.6	16.0	16.0	16.0	13.6	9.6	11.7
	Velocity at 0.5H			15.3	13.4	18.4	19.5	16.3	14.2	10.3	13.3
	Velocity at 0.8H	12.0	12.8	15.5	16.8	19.0	21.2	18.2	13.6	11.2	13.9
	Depth-averaged velocity U	12.0	12.8	14.3	14.6	17.8	18.9	16.8	13.8	10.4	13.0
	Dimensionless velocity $U/\overline{U}$	0.86	0.92	1.03	1.05	1.28	1.36	1.21	0.99	0.75	0.94
x = 6	Velocity at 0.2H			7.4	14.7	16.6	17.1	16.0	13.4	10.1	13.0
	Velocity at 0.5H		6.3	9.0	9.8	19.0	20.6	17.1	13.6	10.6	12.8
	Velocity at 0.8H	9.6	9.6	12.8	14.7	19.5	20.6	19.2	14.2	11.2	13.9
	Depth-averaged velocity U	9.6	8.0	9.7	13.1	18.4	19.4	17.4	13.7	10.6	13.2
	Dimensionless velocity $U/\overline{U}$	0.73	0.61	0.74	1.00	1.40	1.47	1.32	1.04	0.83	1.00

Table A.6 (continued)

	$\frac{y}{D}$	6	9	12	15	18	21	24	27	33	39
x = 12	Velocity at 0.2H			7.1	14.4	16.6	16.0	16.0	13.4	10.6	13.2
	Velocity at 0.5H		8.0	9.6	12.3	18.7	19.8	18.4	13.6	10.6	13.0
	Velocity at 0.8H	10.1	10.9	11.7	12.3	19.5	20.6	19.2	14.2	11.2	13.5
	Depth-averaged velocity U	10.1	9.45	9.5	13.0	18.3	18.6	17.9	13.7	10.8	13.2
	Dimensionless velocity $U/\overline{U}$	0.77	0.72	0.72	0.99	1.39	1.41	1.36	1.04	0.82	1.00
x = 24	Velocity at 0.2H			8.0	14.4	16.6	16.6	16.0	12.3	10.4	12.8
	Velocity at 0.5H		10.1	10.6	12.6	18.4	19.5	18.2	15.0	10.8	13.0
	Velocity at 0.8H	11.2	10.9	11.5	14.7	19.5	20.9	19.0	16.3	11.2	13.9
	Depth-averaged velocity U	11.2	10.5	10.0	13.9	18.2	19.0	17.7	14.5	10.8	13.2
	Dimensionless velocity $U/\overline{U}$	0.85	0.80	0.76	1.06	1.38	1.44	1.35	1.10	0.82	0.99

Table A.7

Velocity Results for Exp. 21

	$\frac{y}{D}$	6	9	12	15	18	21	24	27	33	39
x = 0	Velocity at 0.2H			16.8	16.3	15.8	16.0	15.2	13.4	12.1	12.0
	Velocity at 0.5H			32.0	13.3	15.0	17.6	15.8	13.4	12.4	13.9
	Velocity at 0.8H	13.1	14.4	19.8	15.5	15.0	18.2	18.2	13.4	13.0	13.9
	Depth-averaged velocity U	13.1	14.4	22.9	15.0	15.3	17.3	16.4	13.4	12.5	13.3
	Dimensionless velocity $U/\overline{U}$	0.92	1.01	1.60	1.05	1.07	1.21	1.15	0.94	0.90	0.93
x = 6	Velocity at 0.2H			9.0	12.3	18.4	18.2	13.4	12.8	13.0	12.0
	Velocity at 0.5H		6.6	9.6	13.4	13.4	21.2	16.0	13.6	12.8	13.8
	Velocity at 0.8H	11.5	9.8	12.8	10.1	18.7	21.2	16.8	13.9	13.9	14.0
	Depth-averaged velocity U	11.5	8.2	10.5	11.9	16.8	20.2	15.4	13.4	13.2	13.3
	Dimensionless velocity $U/\overline{U}$	0.87	0.62	0.80	0.90	1.28	1.54	1.17	1.02	1.00	1.00

Table A.7 (continued)

x = 12

$\frac{y}{D}$	6	9	12	15	18	21	24	27	33	39
Velocity at 0.2H			9.3	12.3	15.3	19.2	16.3	12.8	13.2	12.0
Velocity at 0.5H		7.4	9.3	12.6	13.9	20.9	18.4	14.7	13.4	13.9
Velocity at 0.8H	11.7	9.8	12.8	12.0	14.7	20.0	19.0	15.0	13.5	13.9
Depth-averaged velocity U	11.7	8.6	10.5	12.3	14.6	20.0	17.9	14.2	13.4	13.3
Dimensionless velocity $U/\overline{U}$	0.89	0.65	0.80	0.93	1.11	1.52	1.36	1.08	1.02	1.01

x = 24

Velocity at 0.2H			8.0	12.3	15.3	17.6	17.6	13.9	12.0	12.8
Velocity at 0.5H		7.4	9.8	13.1	14.2	17.1	20.9	15.3	13.8	13.0
Velocity at 0.8H	11.5	9.8	11.7	12.3	13.9	18.7	19.0	15.8	14.0	13.9
Depth-averaged velocity U	11.5	8.6	9.8	12.6	14.5	17.8	19.2	15.0	13.3	13.2
Dimensionless velocity $U/\overline{U}$	0.87	0.65	0.75	0.96	1.10	1.35	1.46	1.14	1.00	1.00

APPENDIX B

PHOTOGRAPHS

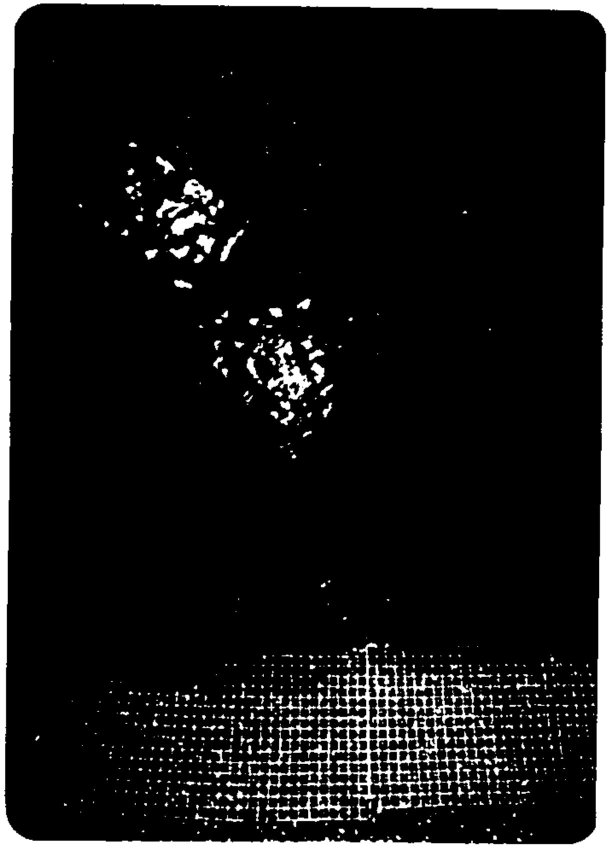

Photo B.1 Plan view of non-buoyant bottom jet - Exp. 1 (R=3.2, H/D=2.0).

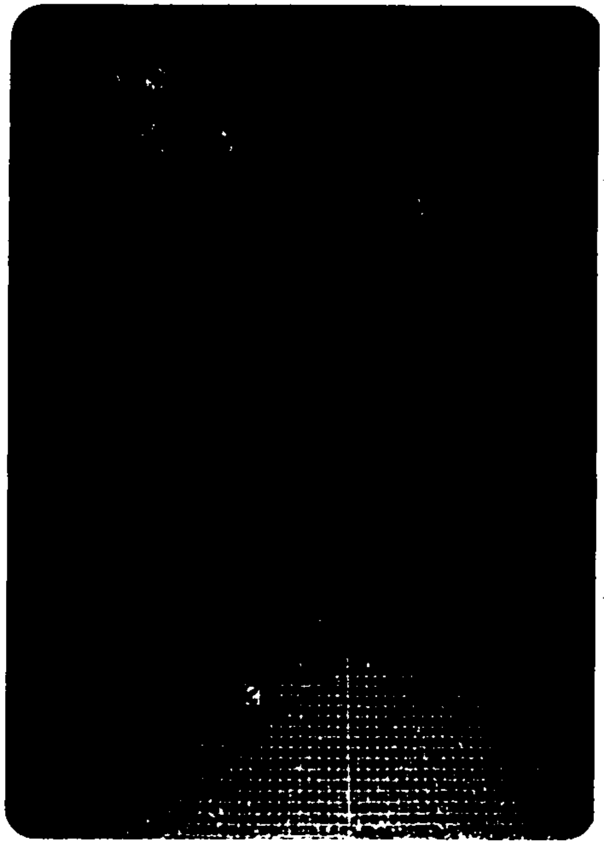

Photo B.2 Plan view of non-buoyant bottom jet - Exp. 4 (R=1.6, H/D=2.0).

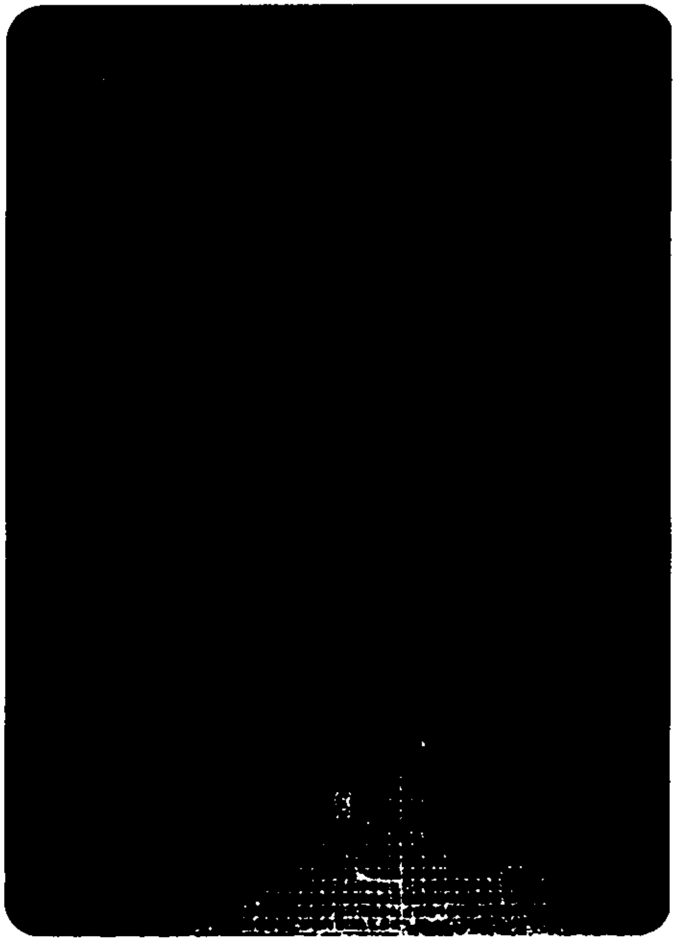

Photo B.3 Plan view of non-buoyant bottom jet - Exp. 5 (R=3.3, H/D=4.0).

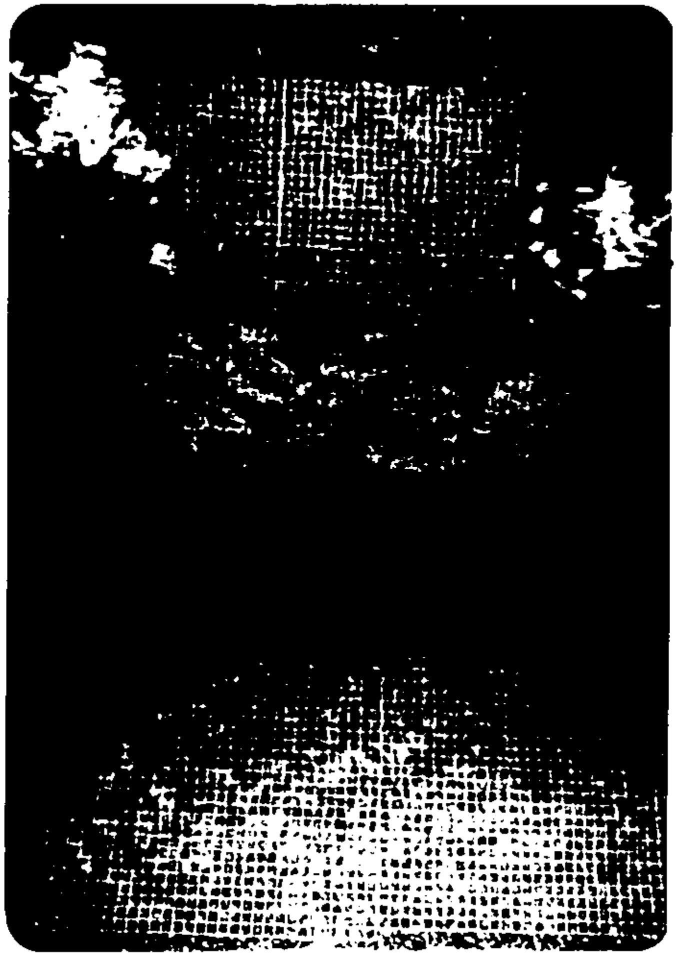

Photo B.4 Plan view of non-buoyant bottom jet - Exp. 9 (R=3.4, H/D=5.5).

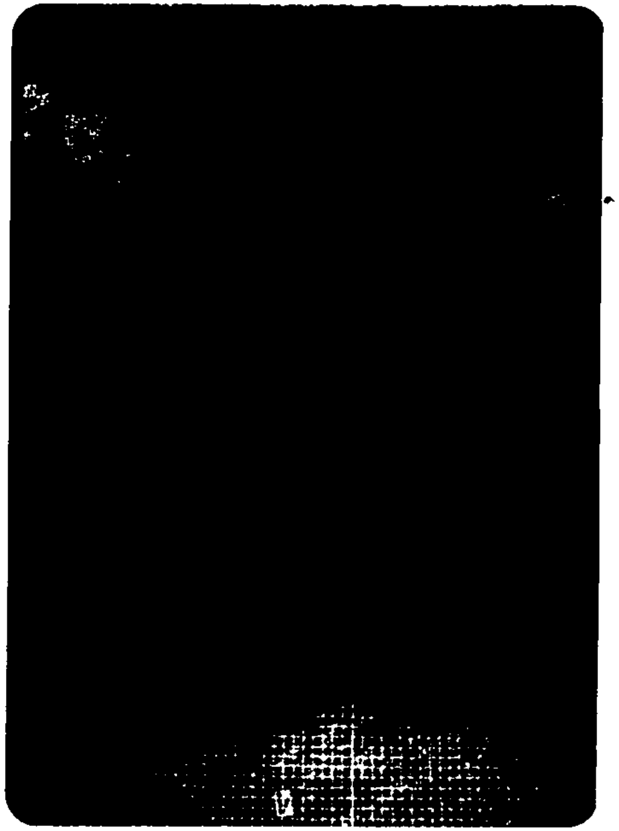

Photo B.5 Plan view of non-buoyant bottom jet - Exp. 6 (R=2.2, H/D=5.5).

Photo B.6 Plan view of non-buoyant bottom jet - Exp. 7 (R=4.9, H/D=5.5).

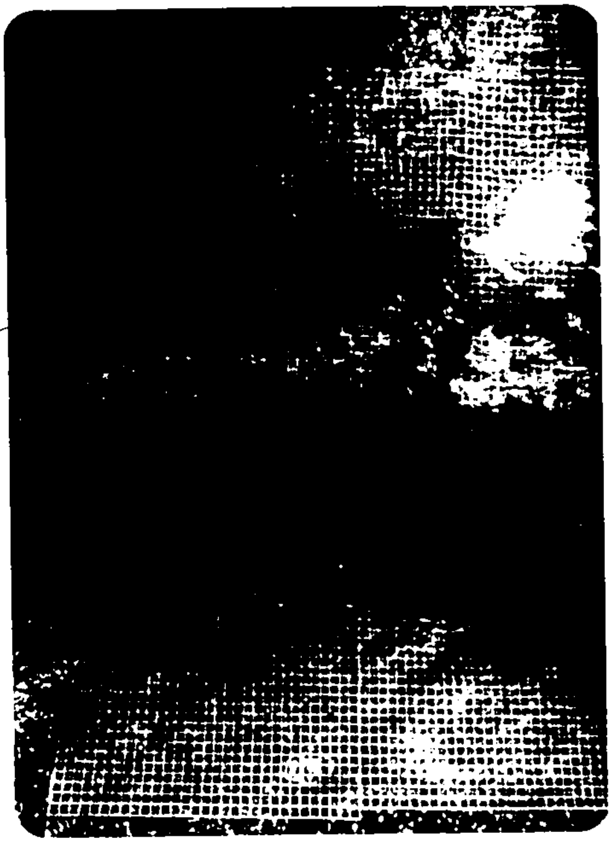

Photo B.7 Plan view of non-buoyant bottom jet - Exp. 8 (R=2.1, H/D=4.0).

COLOURED PICTURES
Images en couleur

Photo B.8 Plan view of non-buoyant submerged jet - Exp. 12 (R=4.0, H/D=4.0).

Photo B.9 Plan view of non-buoyant submerged jet - Exp. 16 (R=4.2, H/D=5.5).

Photo B.10 Plan view of non-buoyant submerged jet - Exp. 13 (R=2.2, H/D=5.5).

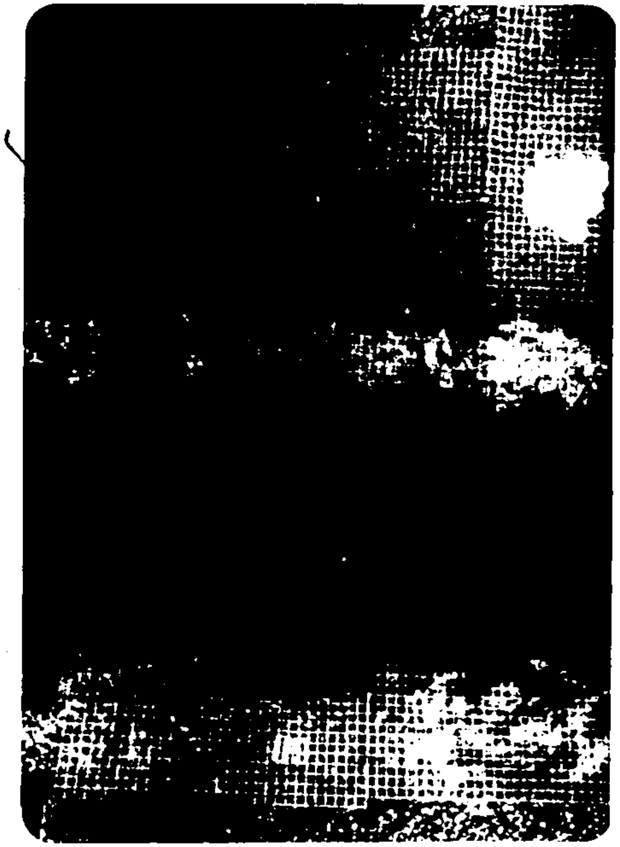

Photo B.11 Plan view of non-buoyant submerged jet - Exp. 14 (R=5.8, H/D = 5.5).

COLOURED PICTURES
Images en couleur

Photo B.12 Plan View of Non-Buoyant Submerged Jet - Exp. 15 (R=2.6, H/D=4.0).

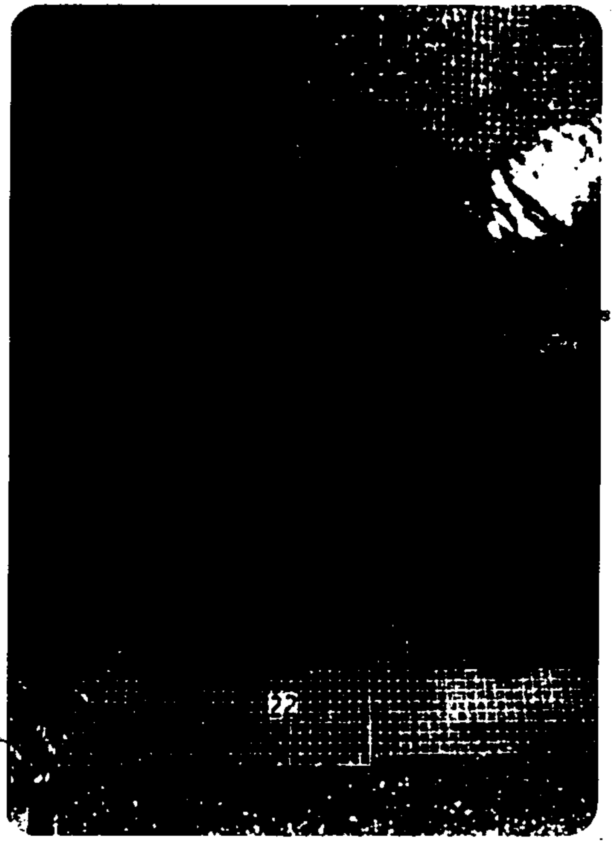

Photo B.13 Plan view of non-buoyant extended surface jet - Exp. 19 (R=4.2, H/D=4.0).

Photo B.14 Plan view of non-buoyant extended surface jet - Exp. 23 (R=4.4, H/D=5.5).

Photo B.15 Plan view of non-buoyant extended surface jet - Exp. 20 (R=2.2, H/D=5.5).

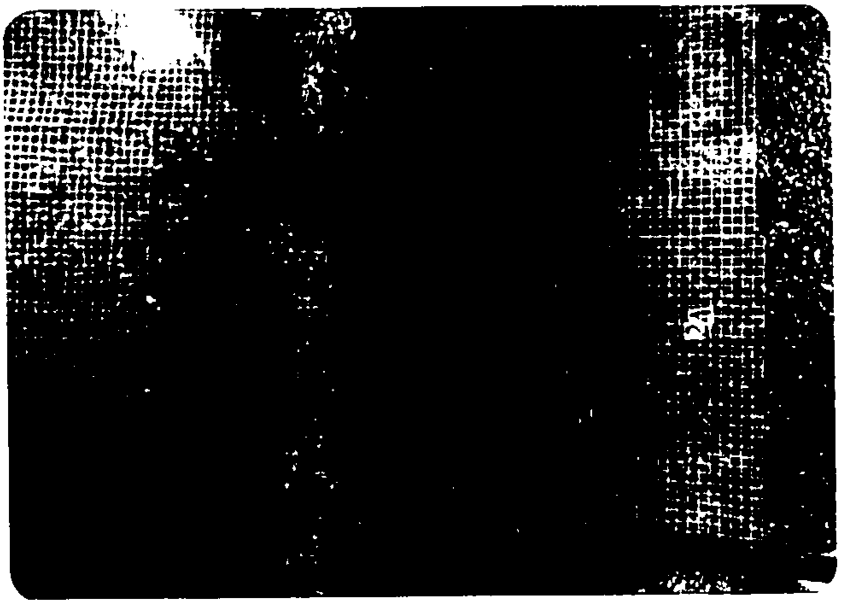

Photo B.16 Plan view of non-buoyant extended surface jet - Exp. 21 (R=5.9, H/D=5.5).

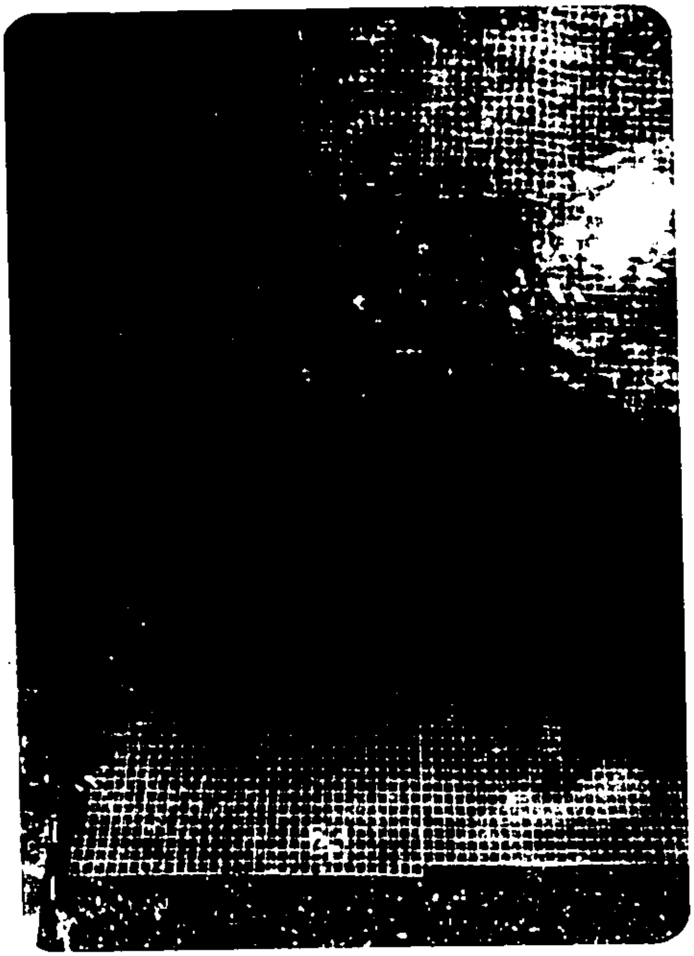

Photo B.17 Plan view of non-buoyant extended surface jet - Exp. 22 (R=2.6, H/D=4.0).

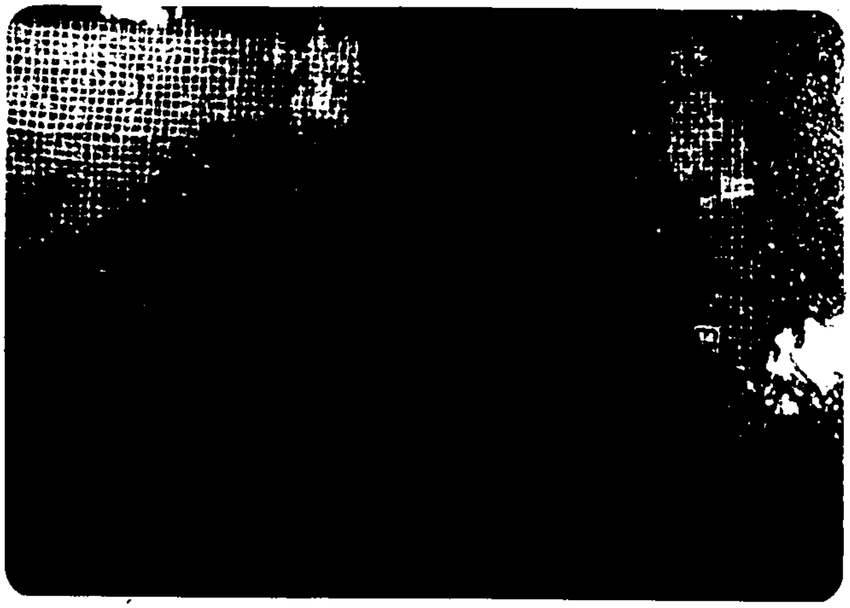

Photo B.18 Plan view of non-buoyant shore-based surface jet - Exp. 26 (R=4.9, H/D=5.5).

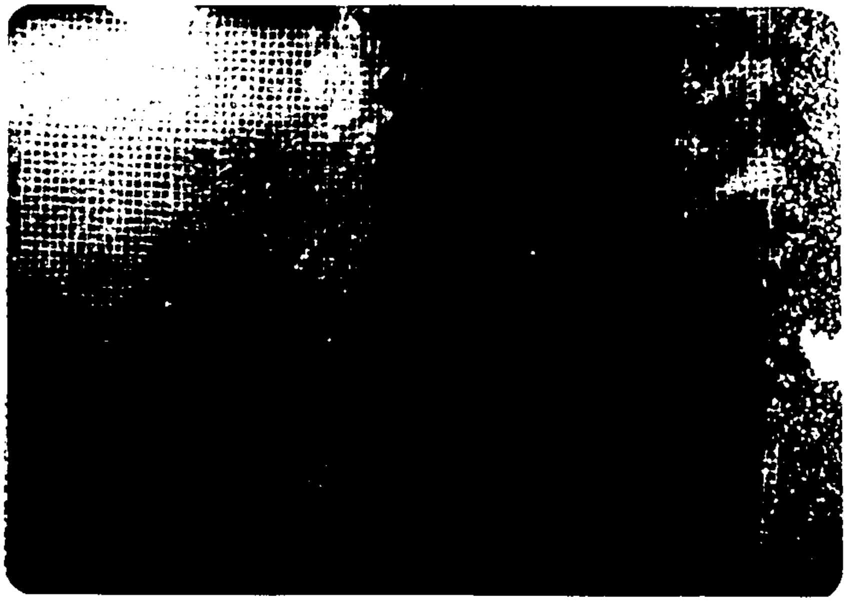

Photo B.19 Plan view of non-buoyant shore-based surface jet - Exp. 27 (R=2.0, H/D=5.5).

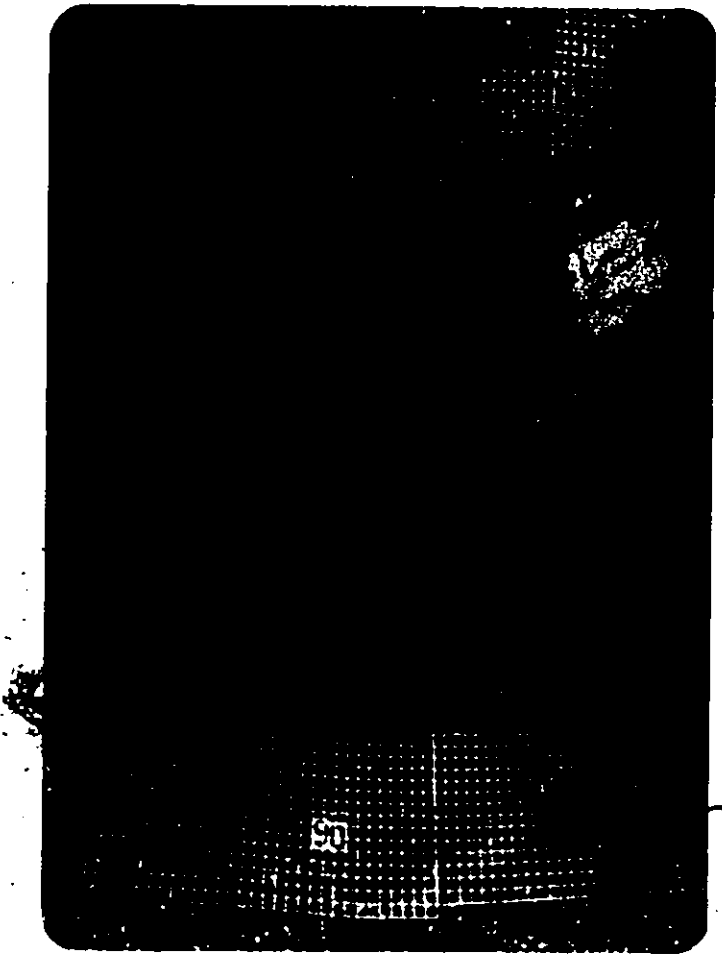

Photo B.20 Plan view of buoyant bottom jet - Exp. 1-1 (R=3.2, H/D=2.0, F_o=17.3).

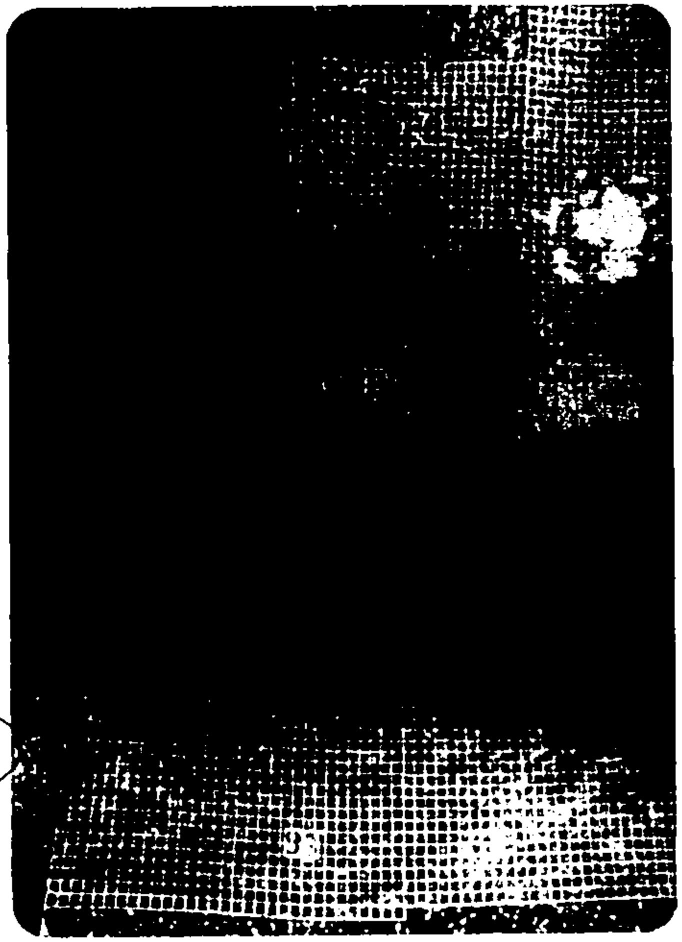

Photo B.21 Plan view of buoyant bottom jet - Exp. 5-1 (R=3.3, H/D=4.0, F_o=18.6).

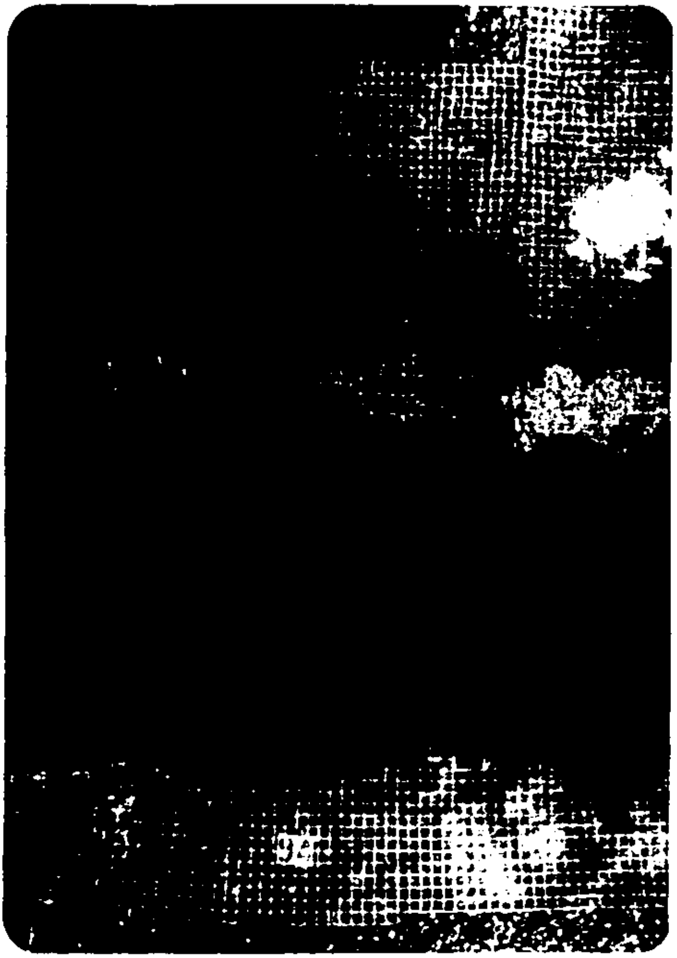

Photo B.22 Plan view of buoyant bottom jet - Exp. 6-1 (R=2.2, H/D=5.5 F_o=6.52).

Photo B.23 Plan view of buoyant bottom jet - Exp. 7-1 (R=4.9, H/D=5.5, F_o=19.30).

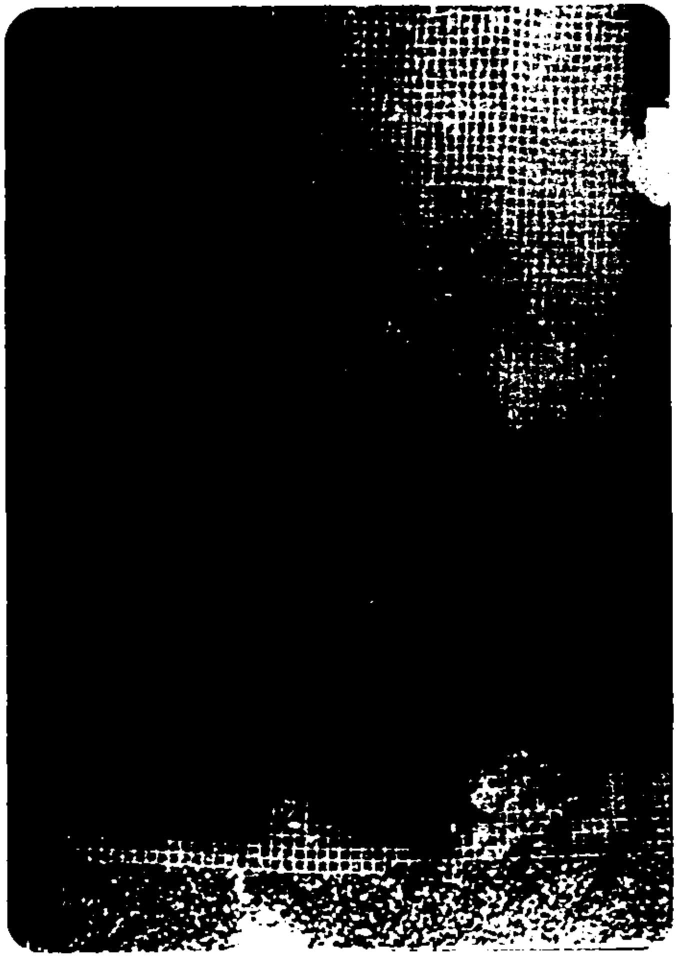

Photo B.24 Plan view of buoyant surface jet - Exp. 27-1 (R=2.0, H/D=5.5, F_o= 18.60).

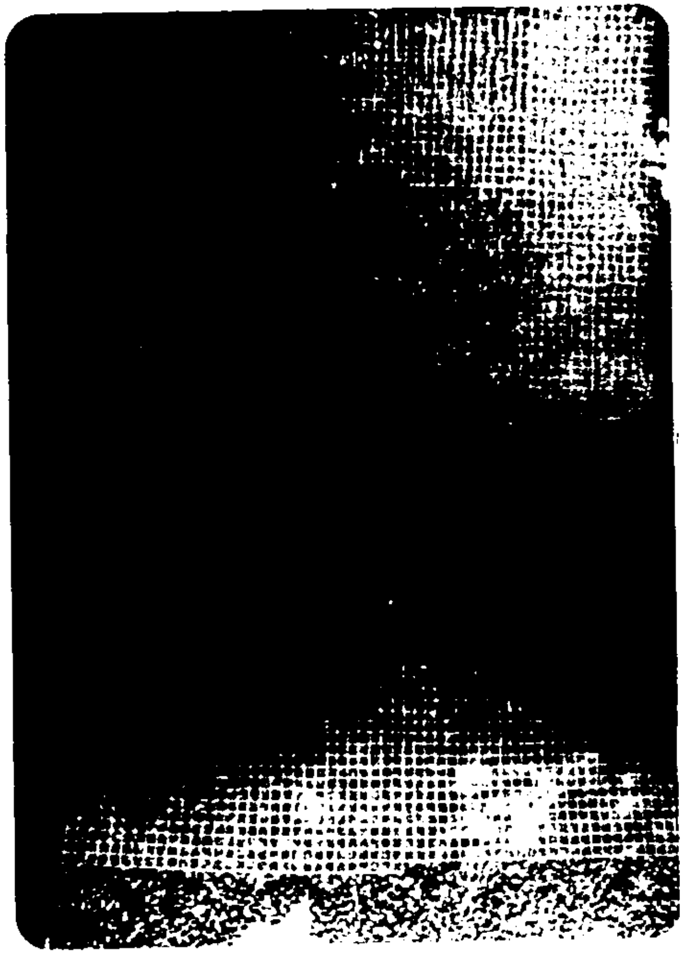

Photo B.25 Plan view of buoyant surface jet - Exp. 26-1 (R=4.9, H/D=5.5, F_o= 19.14).

APPENDIX C

THEORETICAL ANALYSIS OF NEAR-FIELD MODELS

APPENDIX C

C.1 PDS THEORETICAL ANALYSIS (after Shirazi and Davis, 1974)

The method of solution is an integral approach which assumes similarity of temperature and velocity profiles and the principle of entrainment. With the assumed temperature and velocity profiles, Eqs. 2.24 and 2.25, the volume, energy and momentum fluxes are integrated across the jet at any cross-section expressing them in terms of centreline values and plume characteristics width, B, and depth, h.

(i) Volume Flux, Q:

$$Q = \pi Bh\left(\frac{U_m}{2} + U_a \cos\theta\right) \qquad (C.1)$$

The change of volume flux, Q, with distance, $\partial Q/\partial\xi$, is presented in Chapter II, Eqs. 2.26 to 2.35.

(ii) Heat Flux, J:

$$J = \frac{Q(\Delta T_m)}{2} \qquad (C.2)$$

The change in heat flux along the plume due to exchange with the atmosphere is expressed as,

$$\frac{dJ}{d\xi} = -\sqrt{\pi}\, K_1 B \cdot \Delta T_m \qquad (C.3)$$

This yields to,

$$\frac{dT}{d\xi} = -\frac{\Delta T_m}{Q}\left(2\sqrt{\pi}\, KB + \frac{dQ}{d\xi}\right) \qquad (C.4)$$

(iii) Momentum Flux, M:

$$M = \frac{Q^2}{\pi Bh} \qquad (C.5)$$

The conservation of momentum is applied in the ξ-direction and then divided into x and y components. The forces acting on the plume which balanced by the change of momentum flux are: (a) internal pressure forces due to buoyancy, P, (b) from drag due to ambient current, F_D, and (c) interfacial shear forces in the x and y directions, SF_x and SF_y.

These forces are given by:

$$P = \sqrt{\pi}\ \Delta T_m h^2 B/2F_o^2 \tag{C.6}$$

$$F_D = \frac{1}{\sqrt{2}}\, C_D h\ U_a|U_a|\sin^2\theta \tag{C.7}$$

$$SF_x = C_F\left(\frac{1}{R_N h}\right)^{\frac{1}{4}} \int_0^{\sqrt{2}B} \Delta U_v^{3/4}\left[U_a\sin^2\theta - U\cos\theta\,\exp(-\eta^2/B^2)\right]d\eta \tag{C.8}$$

$$SF_y = -C_F\left(\frac{1}{R_N h}\right)^{\frac{1}{4}} \int_0^{\sqrt{2}B} \Delta U_v^{3/4}\left[U_a\cos\theta + U\exp(-\eta^2/B^2)\right]d\eta \tag{C.9}$$

Equating the forces to the change in momentum flux in the x and y directions and rearranging the equations yield to:

$$\frac{d\theta}{d\xi} = \frac{SF_y\cos\theta - SF_x\sin\theta - F_D - U_a\sin\theta(dQ/d\xi)}{\dfrac{Q^2}{\pi Bh} + \dfrac{\sqrt{\pi}}{2F_o^2}\,\Delta T\cdot h^2 B} \tag{C.10}$$

$$\begin{aligned}\frac{dH}{d\xi} = {} & [SF_y\sin\theta + SF_x\cos\theta + (U_a\cos\theta - 2Q/\pi Bh)\left(\frac{dQ}{d\xi}\right) \\ & - (\sqrt{\pi}Bh^2/2F_o^2)\left(\frac{dT}{d\xi}\right) + Q^2/\pi B^2h - \sqrt{\pi}h^2\Delta T/2F_o^2)\left(\frac{dB}{d\xi}\right)] \\ & [\sqrt{\pi}\Delta T\cdot hB/2F_o^2 - Q^2/\pi Bh^2]^{-1}\end{aligned} \tag{C.11}$$

Momentum in the lateral direction is included through lateral spreading. In the model, it is assumed that the contributions to spreading by non-buoyant horizontal jet and mixing and buoyancy are independent of one another such that,

$$\frac{dB}{d\xi} = \left(\frac{dB}{d\xi}\right)_{nb} + \left(\frac{dB}{d\xi}\right)_{b} \tag{C.12}$$

where the subscripts b and nb denote buoyant and nonbuoyant terms.

$$\left(\frac{dB}{d\xi}\right)_{nb} = \frac{SF_y\sin\theta + SF_x\cos\theta + \left(U_a\cos\theta - \frac{2Q}{\pi Bh}\right)\frac{dQ}{d\xi}}{-(Q^2/\pi Bh)\left[\left(\frac{dQ}{d\xi}\right)_v / \left(\frac{dQ}{d\xi}\right)_h + 1\right]} \tag{C.13}$$

$$\left(\frac{dB}{d\xi}\right)_{b} = \frac{xk_1}{\left(\frac{B}{h}F^2 - 1\right)^{½}} \tag{C.14}$$

The preceeding derivatives are integrated step-wise along the plume trajectory to give local values of x, y, ΔT, h, B, θ and Q.

C.2 MIT THEORETICAL ANALYSIS (after Stolzenbach and Harleman, 1971)

Similar to the PDS model, integral equations expressing conservation of mass, ξ-momentum and heat were found by integrating Eqs. 2.45, 2.46 and 2.48 over the domain $0<\xi<\infty$ using appropriate boundary conditions. The integral equations for detached jets with no re-entrainment is presented herein as follows:

Continuity,

$$\frac{d}{d\xi}(\bar{u}\bar{b}\bar{h}) = \bar{u}(\alpha_{y3}\bar{h} + \alpha_{z3}\bar{b}) + (\alpha_{yc}\bar{h} + \alpha_{zc}\bar{b})U_a\sin\theta\,\frac{2\bar{h}}{(\bar{h}+\bar{b})} \tag{C.15}$$

ξ-momentum,

$$\frac{d}{d\xi}\left[\bar{u}^2\bar{b}\bar{h} + ½ w_p\frac{\Delta\rho g\bar{h}^2\bar{b}}{\rho_a}\right] = q_e U_a\cos\theta \tag{C.16}$$

Heat,

$$\frac{d}{d\xi}(\bar{u}\bar{b}\bar{h}\Delta\bar{T}) = 0 \qquad (C.17)$$

Jet Spreading ,

$$\frac{d}{d\xi}\left[\bar{u}^2\bar{b}\bar{h}\left(\frac{d\bar{b}}{d\xi} - \frac{d\bar{b}}{d\xi}\bigg|_{nb}\right)\right] = \frac{1}{2}\,\frac{\Delta\rho}{\rho_a}\,g\bar{h}^2 - \frac{w_e^2\bar{b}^2\bar{h}}{2(H-\bar{h})^2} \qquad (C.18)$$

Jet Deflection,

$$\bar{u}^2\bar{b}\bar{h}\,\frac{d\theta}{d\xi} = q_e U_a \sin\theta - \frac{1}{4}c_{D_o}U_a^2 - \frac{1}{4}c_{D_2}U_a^2\sin^2\theta \qquad (C.19)$$

Geometry,

$$\frac{dx}{d\xi} = \sin\theta, \qquad (C.20)$$

$$\frac{dy}{d\eta} = \cos\theta \qquad (C.21)$$

where, α_{y3}, α_{z3} = lateral and vertical jet entrainment coefficients;

α_{yc}, α_{zc} = cross-flow entrainment coefficients;

w_p = hydrostatic pressure factor;

q_e = entrainment flow per unit length;

w_e = entrainment velocity.

The definition sketch of the MIT model is given in Fig. 2.2.

VITA AUCTORIS

1952	Born on the 9th of July in Cairo, Egypt.
1974	Graduated with a B.Sc. in Civil Engineering from Cairo University, Egypt.
1974	Appointed as a Civil Engineer at the Ministry of Housing, Cairo, Egypt.
1980	Graduated with a M.A.Sc. in Civil Engineering, Memorial University of Newfoundland, St. John's, Newfoundland.
1981	Enrolled in Faculty of Graduate Studies, University of Windsor, in a programme leading to the Degree of Doctor of Philosophy in Civil Engineering.